

R-07-48

Hydrogeological characterisation and modelling of deformation zones and fracture domains, Forsmark modelling stage 2.2

Sven Follin, SF GeoLogic AB

Jakob Levén, Svensk Kärnbränslehantering AB

Lee Hartley, Peter Jackson, Steve Joyce,
David Roberts, Ben Swift
Serco Assurance

September 2007

Svensk Kärnbränslehantering AB

Swedish Nuclear Fuel
and Waste Management Co
Box 5864
SE-102 40 Stockholm Sweden
Tel 08-459 84 00
+46 8 459 84 00
Fax 08-661 57 19
+46 8 661 57 19



ISSN 1402-3091

SKB Rapport R-07-48

ID 1203434

Updated 2013-12

Hydrogeological characterisation and modelling of deformation zones and fracture domains, Forsmark modelling stage 2.2

Sven Follin, SF GeoLogic AB

Jakob Levén, Svensk Kärnbränslehantering AB

Lee Hartley, Peter Jackson, Steve Joyce,

David Roberts, Ben Swift

Serco Assurance

September 2007

Keywords: Hydrogeology, Deformation zone, Fracture domain, Hydraulic properties.

A pdf version of this document can be downloaded from www.skb.se.

Update notice

The original report, dated September 2007, was found to contain both factual and editorial errors which have been corrected in this updated version. The corrected factual errors are presented below.

Updated 2013-08

Location	Original text	Corrected text
Page 172, Table 11-9, column 4	(0.04,)	(0.038,)
Page 174, Table 11-11, column 4	(0.04,)	(0.038,)
Page 176, Table 11-13, column 4	(0.04,)	(0.038,)
Page 181, Table 11-18, column 4	(0.04,)	(0.038,)
Page 182, Table 11-20, column 4	(0.04,)	(0.038,)
Page 182, Table 11-20, column 6, row 6	(-7.0, 1.2)	(-6.7, 1.2)
Page 186, Table 11-22, column 4	(0.04,)	(0.038,)
Page 189, Table 11-25, column 4	(0.04,)	(0.038,)
Page 192, Table 11-26		Table updated with additional data

The updated tables show what was actually used in the groundwater flow modelling for SDM-Site Forsmark.

Abstract

The work reported here collates the structural-hydraulic information gathered in 21 cored boreholes and 32 percussion-drilled boreholes belonging to Forsmark site description, modelling stage 2.2. The analyses carried out provide the hydrogeological input descriptions of the bedrock in Forsmark needed by the end users Repository Engineering, Safety Assessment and Environmental Impact Assessment; that is, hydraulic properties of deformation zones and fracture domains. The same information is also needed for constructing 3D groundwater flow models of the Forsmark site and surrounding area.

The analyses carried out render the following conceptual model regarding the observed heterogeneity in deformation zone transmissivity:

- We find the geological division of the deterministically modelled deformation zones into eight categories (sets) useful from a hydrogeological point of view. Seven of the eight categories are steeply dipping, WNW, NW, NNW, NNE, NE, ENE and EW, and on is gently dipping, G.
- All deformation zones, regardless of orientation (strike and dip), are subjected to a substantial decrease in transmissivity with depth. The data gathered suggest a contrast of c. 20,000 times for the uppermost one kilometre of bedrock, i.e. more than four orders of magnitude. The hydraulic properties below this depth are not investigated.
- The lateral heterogeneity is also substantial but more irregular in its appearance. For instance, for a given elevation and deformation zone category (orientation), the spatial variability in transmissivity within a particular deformation zone appears to be as large as the variability between all deformation zones. This suggests that the lateral correlation length is shorter than the shortest distance between two adjacent observation points and shorter than the category spacing.
- The observation that the mean transmissivity of the gently-dipping deformation zones is c. one to two orders of magnitude greater than the mean transmissivities of all categories of steeply-dipping deformation zones may be due to the anisotropy in the stress field, where the maximum stress is horizontal and has an azimuth of c. 140°. The hypothesis is supported by the deformation zones that strike WNW and NW. These two categories of steeply-dipping deformation zones have, relatively speaking, higher mean transmissivities than steeply-dipping deformation zones in other directions.

Key hydrogeological aspects of the fracture domains modelled are:

- We find the geological division of the bedrock in between the deterministically deformation zones to fall into six fracture domains useful from a hydrogeological point of view. In fact, the suggested division is consistent with the hydrogeological modelling approach reported for modelling stage 1.2.
- Three fracture domains together cover the potential repository area below the gently dipping deformation zone ZFMA2; these are FFM01, FFM02 and FFM06. One fracture domain covers the bedrock above this zone, FFM03. The remaining fracture domains, FFM04 and FFM05, border the candidate area. For modelling stage 2.2, hydrogeological data are available from hydraulic tests carried out in FFM01–FFM03 mainly. However, the work reported here suggests hydrogeological DFN (Hydro-DFN) properties for all fracture domains, FFM01–06.

- The key aspect for Forsmark is that the corrected conductive fracture frequency for the potential fracture domain FFM01 shows very strong variations with depth, and so it is suggested that the Hydro-DFN be split into three layers: above the elevation –200, between the elevations –200 and –400, and below the elevation –400. FFM01 is also very anisotropic, being dominated by the HZ set, and only with a small contribution from the NE and NS sets. The top layer of fracture domain FFM01 is similar to the Hydro-DFN parameters for fracture domain FFM02. FFM03 has less variation with depth and is comparable to the middle section of FFM01, but is more isotropic. Data for fracture domain FFM06, which is also a part of the potential target bedrock, will be treated in modelling stage 2.3. Pending this information, it is envisaged that fracture domain FFM06 can be modelled in the same fashion as fracture domain FFM01. Fracture domains FFM04 and FFM05 lie in the periphery of the candidate area. Based on the statistical analysis, FFM05 seems to be similar to FFM03, while FFM04 is of slightly higher hydraulic conductivity, but the statistical significance of the data for these fracture domains is very limited, being based on about 120–150 m of borehole data. It is proposed that fracture domains FFM04 and FFM05 are assumed to have the same properties as FFM03.

Finally, comments and recommendations are made in the report as a guidance for several aspects in forthcoming hydrogeological discrete fracture network and groundwater flow models. The comments and recommendations address the following matters:

- fracture set definitions reflecting observations made for all boreholes in modelling stage 2.2, i.e. the geological DFN results reported for modelling stage 2.2,
- semi-deterministic DFN modelling of so called possible deformation zones below the elevation –400 m RHB 70 in the potential target volume, and
- fracture domains outside the candidate area where there are no cored boreholes.

For the conclusions drawn in the work reported here these three matters are of minor importance.

Sammanfattning

Denna rapport redovisar strukturgeologisk-hydraulisk information från 21 kärnbrorhål och 32 hammarborhål tillhörande Forsmark platsbeskrivning, modelleringskede 2.2. De hydrogeologiska förhållandena i berggrundens deformationszoner och sprickdomäner är viktiga för olika användare inom förvarsdesign, säkerhetsanalys och miljökonsekvensbeskrivning. De beskrivningar som redovisas i rapporten behövs även för att bygga tredimensionella flödesmodeller över berggrunden i Forsmark med omnejd.

Den observerade rumsliga variationen i deformationszonernas transmissivitet har getts följande beskrivning:

- Vi finner den geologiska indelningen av de deterministiskt modellerade deformationszonerna i åtta kategorier (set) användbar ur hydrogeologisk synvinkel. Sju av de åtta kategorierna är brantstående, WNW, NW, NNW, NNE, NE, ENE och EW, och en är flackt lutande, G.
- Alla deformationszoner, oavsett orientering (strykning och stupning), uppvisar ett betydande djupavtagande i uppmätt transmissivitet. Uppmätta data indikerar en kontrast på ca 20 000 inom den översta kilometern under markytan, dvs mer än fyra storleksordningar. De hydrauliska egenskaperna under detta djup har inte undersökts.
- Heterogeniteten i transmissivitet är betydande också i sidled, men mer oregelbunden i sitt uttryck. För en given nivå och deformationszonskategori (orientering) är den laterala heterogeniteten inom en och samma deformationszon lika stor som variabiliteten i transmissivitet mellan olika zonerna inom aktuell kategori. Detta indikerar att den laterala korrelationslängden är kortare än det kortaste avståndet mellan två näraliggande observationspunkter och kortare än medelavståndet mellan näraliggande deformationszoner.
- Iakttagelsen att medeltransmissiviteten för flacka deformationszoner är en till två storleksordningar större än medeltransmissiviteterna för de olika kategorierna av brantstående zoner kan bero på bergspänningarnas anisotropi, där den största huvudspänningen är horisontell och har bäringen 140° (högerhandsregeln). Hypotesen stöds av observerade transmissiviteter hos de brantstående zoner som stryker WNW och NW. Medeltransmissiviteten för dessa kategorier, som är subparallella med den största huvudspänningen, är högre än för övriga kategorier av brantstående deformationzoner.

Viktiga hydrogeologiska egenskaper för sprickdomänerna i Forsmark är:

- Vi finner den geologiska indelningen av berggrunden mellan deformationszonerna i sex sprickdomäner användbar ur hydrogeologisk synvinkel. Faktum är att indelningen är påtagligt lik den domänindelning som föreslogs och tillämpades i modelleringskede 1.2 inom hydrogeologi.
- Det potentiella förvarsområdet under den flacka deformationszonen ZFMA2 utgörs av tre sprickdomäner – FFM01, FFM02 och FFM06. Berggrunden över denna zon innehåller en sprickdomän – FFM03. Resterande sprickdomäner, dvs FFM04 och FFM05, sammanfaller med berggrunden nära kandidatsområdet gränser. För modelleringskede 2.2 finns hydrogeologiska data att tillgå för FFM01–FFM03 huvudsakligen. Rapporten redovisar dock ett förslag på hydrogeologiska egenskaper för samtliga sprickdomäner.

- Den viktigaste hydrogeologiska egenskapen i Forsmark är den konduktiva sprickfrekvensens starka djupavtagande i sprickdomän FFM01. Rapporten förslår att den hydrogeologiska DFN-modelleringen i FFM01 görs med tre lager: från nivån 0 till –200, från nivån –200 till –400, och från nivån –400 och nedåt. FFM01 är också påtagligt anisotrop, där det horisontella spricksetet dominerar stort, följt av små intensiteter i NE och NS. Det översta lagret i FFM01 har samma hydrogeologiska egenskaper som sprickdomän FFM02. FFM03 uppvisar ett mindre djupavtagande än FFM01 och liknar det mellersta lagret i FFM01, men är mer isotropt. Data som beskriver förhållandena i FFM06 redovisas i modelleringsskede 2.3. I väntan på denna information förutspås att sprickdomänerna kan modelleras på samma sätt som FFM01. Sprickdomänerna FFM04 och FFM05 omgärdar kandidatområdet. FFM05 förefaller likna FFM03, medan FFM04 har en något högre hydraulisk konduktivitet. Tillgången på data är dock mycket begränsad för dessa sprickdomäner. Vi föreslår att FFM04 och FFM05 modelleras på samma sätt som FFM03.

Slutligen, rapporten kommenterar och ger rekommendationer till vägledning för kommande hydrogeologiska spricknätverks- och grundvattenflödesmodelleringar i följande frågeställning:

- spricksetsindelning baserat på alla borrhålsdata från modelleringsskede 2.2, dvs resultatet från den geologiska spricknätverksmodellen för modelleringsskede 2.2,
- semi-deterministisk modellering av s k möjliga deformationszoner i sprickdomän FFM01 under nivån –400 m RHB 70, och
- sprickdomäner utanför kandidatområdet där det inte finns några kärnborrhål.

För de slutsatser som dras i denna rapport har frågeställningarna endast en mindre betydelse.

Contents

1	Introduction	9
1.1	Background	9
1.2	Scope and objectives	11
1.2.1	Disposition	12
2	SKB's systems approach to hydrogeological modelling in the SDM	13
2.1	General	13
2.2	Bedrock hydrogeology	14
2.3	The ECPM approach	16
3	Geological setting	19
3.1	The Forsmark site	19
3.2	Overview of the deformation zone model	21
3.3	Overview of the fracture domain model	24
4	Hydraulic single-hole investigations	31
4.1	Available primary data	31
4.2	Hydraulic tests conducted on intact rock cores	35
4.3	Hydraulic tests conducted in cored boreholes	37
4.4	Hydraulic tests in percussion-drilled boreholes	48
4.5	Overview of the hydraulic characterisation of the bedrock at repository depth	48
4.6	Hydraulic characterisation of the near-surface bedrock	52
5	Structural-hydraulic data in cored boreholes	55
5.1	Deformation zones and possible deformation zones	55
5.1.1	Drill site 1	55
5.1.2	Drill site 2	56
5.1.3	Drill site 3	57
5.1.4	Drill site 4	57
5.1.5	Drill site 5	58
5.1.6	Drill site 6	58
5.1.7	Drill site 7	59
5.1.8	Drill site 8	60
5.1.9	Drill site 9	61
5.1.10	Drill site 10	62
5.1.11	Summary	62
5.2	Hydro-structural cross-correlation	63
5.2.1	Drill site 1	65
5.2.2	Drill site 2	67
5.2.3	Drill site 3	68
5.2.4	Drill site 4	69
5.2.5	Drill site 5	70
5.2.6	Drill site 6	71
5.2.7	Drill site 7	72
5.2.8	Drill site 8	74
5.2.9	Drill site 10	76
5.2.10	Data in KFM02A, KFM07C and KFM10A	77
5.2.11	Crushed rock	77
5.2.12	Errors and uncertainty in feature orientation	77
5.3	Orientation and occurrence of PFL-anomalies	78

6	Structural-hydraulic data in percussion-drilled boreholes	81
6.1	Overview	81
6.2	Plots showing HTHB transmissivity data	83
7	Hydrogeological data synthesis for possible deformation zones	101
8	Hydrogeological data synthesis for near-surface bedrock	107
8.1	Foot wall and hanging wall bedrock	107
8.2	Near-surface bedrock in the hanging wall of ZFMA2	107
8.3	Near-surface bedrock in the foot wall of ZFMA2	110
9	Hydrogeological modelling of deformation zones	113
9.1	Summary of data	113
9.2	Deformation zone thickness versus trace length	117
9.3	Heterogeneity and anisotropy	119
9.4	A preliminary model for representing observed heterogeneity in deformation zone transmissivity	122
	9.4.1 Conceptual model	122
	9.4.2 Numerical representation	122
10	Fracture data analysis	125
10.1	Methodology	125
10.2	Assumptions	126
10.3	Analysis of geological data	126
	10.3.1 Fracture orientation	126
	10.3.2 Fracture intensity	131
10.4	Analysis of hydrogeological data	143
	10.4.1 Correlation of geological and hydrogeological fracturing	143
	10.4.2 Orientation and statistics of flowing features	146
10.5	Summary	150
11	Hydrogeological DFN modelling	155
11.1	Background and overview of work performed	155
11.2	Conceptual model development	157
	11.2.1 Relation to model stage 1.2	157
	11.2.2 Definitions	157
11.3	Fracture set definitions	163
11.4	Simulations of fracture geometry	164
	11.4.1 Modelling approach	164
	11.4.2 Fracture size cases	167
	11.4.3 Calibration of fracture intensity and connectivity	167
	11.4.4 Summary of findings	178
11.5	Simulation of Posiva Flow Log (PFL-f) tests	178
	11.5.1 Modelling approach	178
	11.5.2 Fracture size to transmissivity relationships	180
11.6	Suggested update on sets for open fractures based on stage 2.2 data	192
11.7	Recommendations for implementation of DFN in groundwater flow models	193
	11.7.1 Stochastic and semi-deterministic DFN models	194
11.8	Summary	195
12	Summary and conclusions	197
13	References	201
Appendix A	Additional information on data collation	205
Appendix B	Additional results for the flow modelling in FFM01–FFM03	219

1 Introduction

1.1 Background

As part of the preliminary Site Descriptive Modelling (SDM) for the Initial Site Investigation (ISI) phase at Forsmark, Simpevarp and Laxemar, a methodology was developed for constructing hydrogeological models of the crystalline bedrock. The methodology combined a deterministic representation of the major deformation zones (DZ) with a stochastic representation of the less fractured bedrock outside these zones using a Discrete Fracture Network (DFN) concept.

The geological DZ and DFN models were parameterised hydraulically with data from single-hole Posiva Flow Log (PFL) pumping tests and single-hole Pipe String System (PSS) injection tests, see /Follin et al. 2005ab, 2006b, Hartley et al. 2005ab, 2006/. The hydrogeological descriptions of the major deformation zones and the less fractured bedrock outside these zones were referred to as Hydraulic Conductor Domains (HCD) and Hydraulic Rock Domains (HRD), respectively, according to SKB's systems approach to bedrock hydrogeology /Rhén et al. 2003/.

The hydraulic properties of the DZ and DFN models formed the basis for constructing regional-scale Equivalent Continuum Porous Medium (ECPM) flow models, which were used to simulate the palaeohydrogeological evolution over the last 10,000 years (Holocene), as a coupled process between groundwater flow and the hydrodynamic transport of several reference waters including the process of rock-matrix diffusion. Results obtained from these simulations included a prediction of hydrochemical constituents (e.g. major ions and environmental isotopes) for the present-day situation along boreholes which could be compared with corresponding groundwater samples acquired from the sites. By comparing the model predictions with measurements the models developed could be partially calibrated to improve model parameterisation, improve our understanding of the hydrogeological system, and help build confidence in the conceptual models developed for the sites.

The methodology achieved reasonable success given the restricted amounts and types of data available at the time. Notwithstanding, several issues of concern have surfaced following the reviews of the preliminary site descriptions of the three sites conducted internally by SKB's modelling teams /SKB 2005a/, by SKB's external review group (SIERG) and by the SKI's international review group (INSITE) /SKI 2005/. Moreover, the safety implications of the preliminary site descriptions have been assessed in the Preliminary Safety Evaluations (PSE) /SKB 2005b/ and in SR-Can /SKB 2006b/.

A brief summary of the issues raised is found in /Follin et al. 2007b/. Of particular importance for the work reported here are the concerns raised regarding the uncertainties in the derivation of hydraulic properties of the deterministically modelled deformation zones and the less fractured bedrock outside (in between) the deterministically modelled deformation zones. These uncertainties involve, among other things:

- the understanding of deformation zone genetics and its implication for hydrogeology,
- the spatial variation of hydraulic properties over the plane of a deformation zone,
- the evidence for dividing the less fractured bedrock between the deterministically modelled deformation zones into sub volumes of different hydrogeological DFN (Hydro-DFN) properties, e.g. with regard to depth dependence and anisotropy,
- the upscaling approach used for constructing regional scale ECPM flow models of discrete features, and
- the intrinsic complexity of the DFN concept, the properties of which are described in terms of probability distributions for the orientation, size, intensity, spatial distribution and transmissivity of discrete fracture networks.

It is recognised that a main reason for these uncertainties in the preliminary SDM model for Forsmark are few hydraulic observations in representative sub volumes and the high variability found in the existing data, as well as the significant uncertainty demonstrated by the geological (geometrical) DFN modelling derived.

For the complete site investigation (CSI) phase new types of hydrogeological data will be available and in greater amounts, and hence the issues of concern require satisfactory resolution as the site investigation work moves towards completion. In particular, the use of the integrated geological, hydrogeological, hydrogeochemical and transport models has identified the need for more robust discipline consistent and ‘partially validated’ models to be produced by the final stage of the site descriptive modelling.

Possible solutions to parts of the problems have been discussed and an integrated view and strategy forward has been formulated, see Figure 1-1. The “updated strategy” is not an entire shift in methodology, however, but a refocusing on and clarification of the key aspects of the hydrogeological SDM, i.e.:

- assessing the current understanding of the hydrogeology at the analysed site, and
- providing the hydrogeological input descriptions needed for the end users, Design, Safety Assessment and Environmental Impact Assessment. The input descriptions should especially focus on properties in the potential repository volumes of the explored sites and assess the distribution of flow paths at potential repository depth.

/Follin et al. 2007a/ suggested a procedure for integrating four kinds of data in the groundwater flow (GWF) modelling of the final SDM, see Figure 1-2, as a means of approaching the issue of confirmatory testing (Step 4 in Figure 1-1). For its demonstration /Follin et al. 2007a/ used the hydrogeological DZ and DFN models derived during modelling stage 1.2 and the hydrogeological and hydrochemical information from data freeze 2.1. Hence, the modelling study by /Follin et al. 2007a/ was not aimed at a model update, but a preparatory modelling study intended to provide some insight into new aspects of suggested procedure and the use of field data (e.g. interference tests), and therefore provide background support for the work reported here.

It is noted that a primary idea behind Figure 1-2 is that the same GWF model is used for each type of simulation to make it transparent that a single implementation of the conceptual model could be calibrated against all three types of field observation, although it may have been possible to improve the modelling of a particular data type by refining the model around a relevant observation borehole, for example.

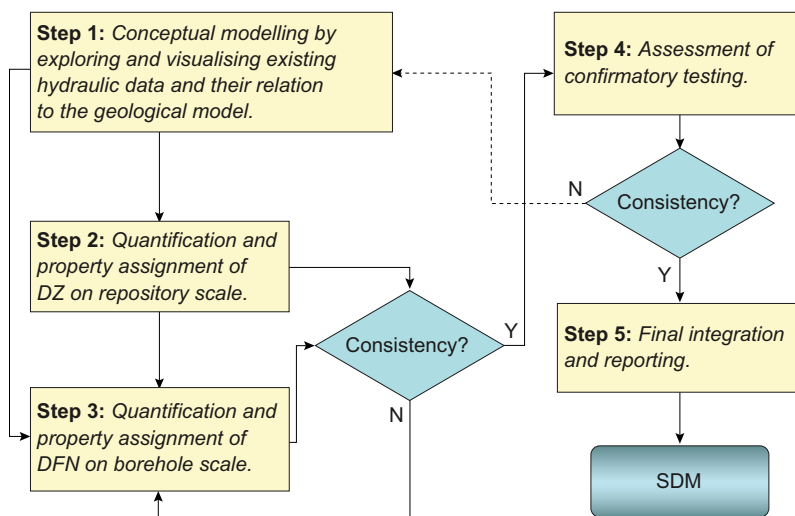


Figure 1-1. Flow chart of the five steps suggested for the hydrogeological modelling of the complete site investigation (CSI) phase.

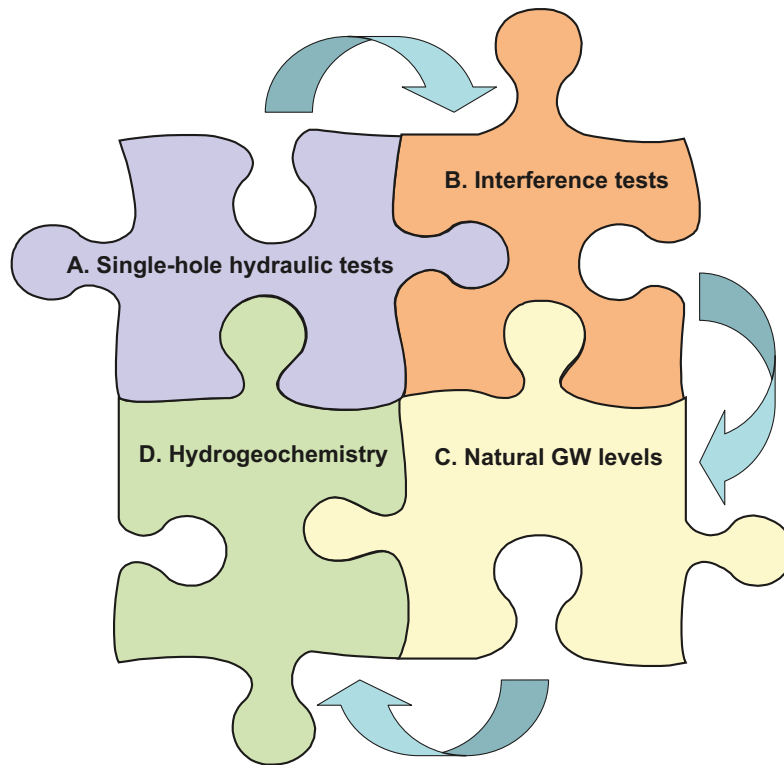


Figure 1-2. Four kinds of data are used in the numerical groundwater flow modelling of the final SDM as a means of approaching the issue of confirmatory testing, cf. Step 4 in Figure 1-1: A) Hydraulic properties of deformation zones and discrete fracture networks as deduced from single-hole hydraulic tests (this report); B) Interference tests; C) Natural groundwater levels; D) Hydrogeochemistry (see /Follin et al. 2007b/).

1.2 Scope and objectives

The primary objectives of the work reported here are:

- provide the hydrogeological input descriptions needed for the end users Repository Engineering, Safety Assessment and Environmental Impact Assessment, and
- provide a basis for constructing a 3D groundwater flow model of the site and surrounding area to assess and illustrate the conceptual understanding of the site and to build confidence in the model by testing it against a variety of field data, such as interference tests, palaeo-hydrogeology and near-surface hydrogeology.

The input descriptions should especially focus on the hydraulic properties of deformation zones and fracture domains in the potential repository volume. This requires consideration of how to parameterise the geological DZ and DFN models based on hydraulic measurements along boreholes to the entire 3D groundwater flow domain, a volume of perhaps 100 km³. Part of this is achieved by deriving specific:

- hydrogeological DZ models for the set of representative deformation zone categories which cover the regional model domain /Stephens et al. 2007/,
- hydrogeological DFN models for the set of representative fracture domains which cover the candidate area /Olofsson et al. 2007/.

There is still the issue though of where it is appropriate to use a deterministic model when particular structures have been observed in the boreholes or geophysical data, and where a stochastic model should be used as a supplement in areas less well mapped, or below the limit for resolution of deterministic structures. Another issue is how to model the hydrogeology of the top 100 m, or so, of bedrock which is generally not mapped by the core-drilled boreholes, but is known to contain sub-horizontal sheet joints of very high transmissivity forming a so called “hydraulic cage phenomenon” cf. /Follin et al. 2007b/. Recommendations on how to address these three issues in the upcoming groundwater flow modelling for stage 2.2 are made in the work reported here.

1.2.1 Disposition

This report is organised as follows:

- Section 2 presents SKB’s systems approach to groundwater flow and solute transport in fractured crystalline rocks as attempted in the SDM. This Section is important for Sections 4, 10 and 11.
- Section 3 presents an overview of the deformation zone model and the fracture domain model derived for Forsmark modelling stage 2.2 by the geological modelling group. This section is important for Sections 9, 10 and 11.
- Section 4 presents an overview of the hydraulic testing carried out up to data freeze 2.2, and the data selected for hydrogeological analysis and modelling in the work reported here. This section, in particular Section 4.2, is fundamental for the entire report.
- Section 5 presents the structural-hydraulic data gathered in core-drilled boreholes.
- Section 6 presents the structural-hydraulic data gathered in percussion-drilled boreholes.
- Section 7 deals with the concept of possible deformation zones at repository depth and presents a working hypothesis for numerical modelling.
- Section 8 deals with the concept of a ‘hydraulic cage phenomenon’ in the near-surface bedrock and presents a working hypothesis for numerical modelling.
- Section 9 deals with the concept of ‘deterministically modelled deformation zones’ and presents a working hypothesis for numerical flow modelling.
- Section 10 presents the statistical analyses of fracture domain data.
- Section 11 presents the assumptions and conceptual model development for hydrogeological DFN modelling as well as the model set-up and the results from the hydrogeological DFN modelling undertaken for Forsmark modelling stage 2.2.
- Section 12 contains a short summary of the observations made and the conclusions drawn.

2 SKB's systems approach to hydrogeological modelling in the SDM

2.1 General

The SDM is conducted on a regional scale. In modelling stage 2.2, particular attention is paid to the so called target volume, see Section 3. As a means to meet the two objectives the description of the real groundwater system is divided into different hydraulic domains. Figure 2-1 illustrates schematically SKB's systems approach as used in the hydrogeological SDM for Forsmark. The groundwater system consists of three hydraulic domains HSD, HCD and HRD, where:

- HSD represents the Quaternary deposits (or "soil"),
- HCD represents deformation zones (or "conductors"), and
- HRD represents the fractured bedrock outside (in between) the deformations zones.

The characterisation of the hydraulic domains is the main objective of the hydrogeological site investigations and constitutes the basis for the conceptual modelling and the numerical simulations carried out in support of the SDM.

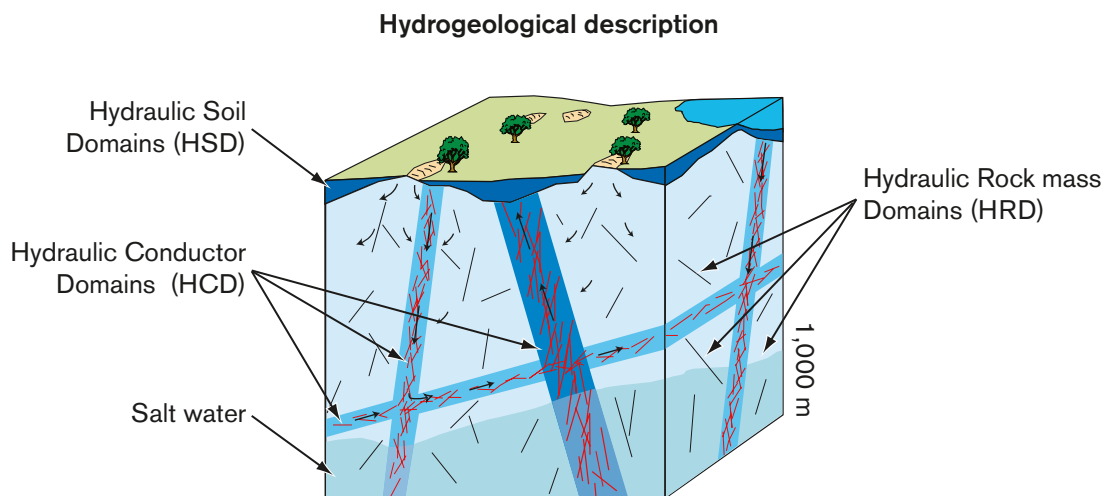


Figure 2-1. Cartoon showing the division of the crystalline bedrock and the overburden (Quaternary deposits) into hydraulic domains. Within each domain, the hydraulic properties are represented by equivalent values, or by spatially distributed statistical distributions /Rhen et al. 2003/.

The investigations and modelling of the groundwater system are split between the surface system and hydrogeological modelling groups, where the former treat the near-surface system (surface hydrology and the hydraulic properties of the HSD), and the latter the deeper (bedrock hydrology and hydraulic properties of the HCD and HRD). This division is purely pragmatic and the interface between the different descriptions is seamless from a conceptual modelling point of view. For instance, the hydraulic properties of the bedrock and the head distribution on the bottom boundary of the near-surface hydrogeological system are provided by the numerical flow modelling undertaken for the entire system /Follin et al. 2007b/. A description of the approach taken by SKB for Forsmark in stage 1.2 is found in /Bosson and Berglund 2006/.

2.2 Bedrock hydrogeology

A cornerstone of the bedrock hydrogeological description concerns the hydraulic characterisation of the more intensely fractured deformation zones and the less fractured bedrock outside (in between) these zones. The approach taken by SKB combines a deterministic representation of the major deformation zones (DZ) with a stochastic representation of the less fractured bedrock outside these zones using a Discrete Fracture Network (DFN) concept. The geological DZ and DFN models are parameterised hydraulically with data from single-hole Posiva Flow Log (PFL) pumping tests and single-hole Pipe String System (PSS) injection tests. The hydraulic description of the deformation zones is particularly important for Repository engineering and the hydraulic description of the less fractured bedrock outside (in between) the deformation is especially important for Safety Assessment.

The hydraulic characterisation of the less fractured bedrock outside the deformation zones at repository depth is a vital task, yet complex. The hydrogeological SDM is based on data from investigations in cored boreholes drilled from the surface, and the current understanding of the groundwater system at depth is bounded to be constrained by this fact. With regard to the different pros and cons of the two methods used for hydraulic borehole investigations in Forsmark, PFL and PSS, the hydraulic characterisation of less fractured bedrock outside the deformation zones may be envisaged as illustrated in Figure 2-2. The constituent parameters measured where the fractures intersect the borehole are the flow rate Q and the pressure p . Since they are coupled the parameter really studied is the specific discharge $Q/\Delta p$. The specific discharge is dependent on several important aspects, among which we particularly note:

- Q_{limi} ; the lower measurement limit of the test method.
- T_{bh} ; the transmissivities of the fractures intersecting the borehole. These can be disturbed (positive skin) or stimulated (negative skin) during the drilling.
- C ; the connectivity of the fractures intersecting the borehole to other fractures away from the borehole. Some fracture are isolated, or a part of an isolated cluster of fractures. Others, in turn, are part of the overall hydrologic system.
- T/S ; the hydraulic diffusivity of the fracture system.
- t ; the duration of the hydraulic testing, i.e. the test time.
- ΔL ; the length of the test interval (test section).

The pros and cons of the two test methods used in Forsmark, PFL and PSS, are described in detail in Section 4.2. From a site descriptive modelling point of view it is noted that the modelling approach taken by SKB focuses on the conductive fracture frequency (CFF) gathered by the so called PFL-f method. This decision means, among other things, that fracture network situations such as A and B are not honoured in modelling stage 2.2, neither in the hydrogeological DFN modelling nor in the subsequent ECPM groundwater flow modelling¹.

¹ The reason why the PFL method cannot address situations like A and B, in contrast to the PSS method, is explained in Section 4.2. It is also explained in Section 4.2 why the PSS method has problems in distinguishing situations A and B from situations C–E.

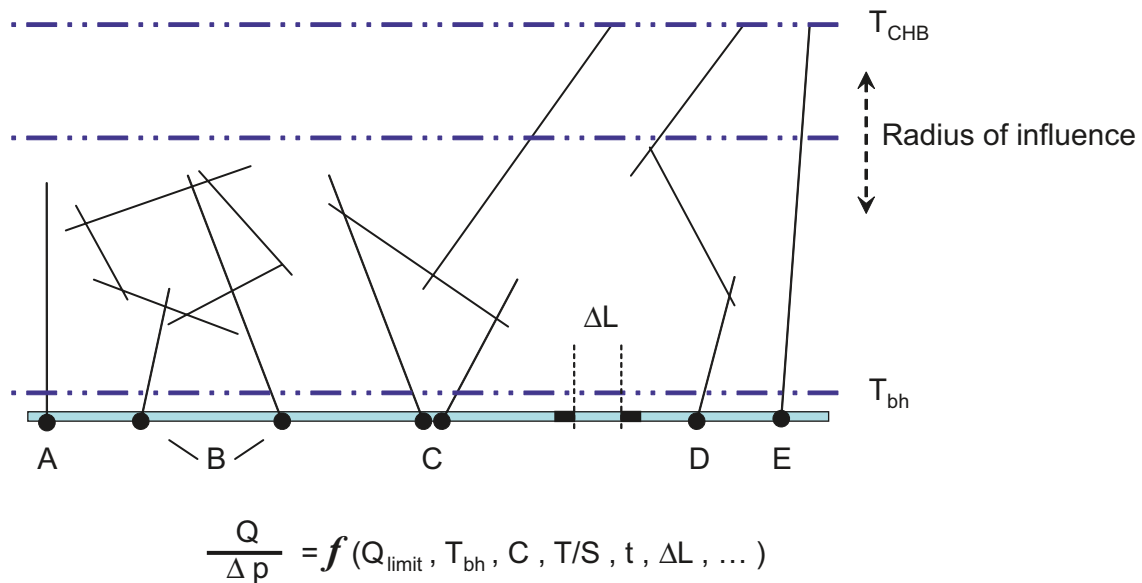


Figure 2-2. Cartoon showing different symbolic situations A–E where fractures in the less fractured bedrock connect to a borehole (bottom). The specific discharge $Q/\Delta p$ measured at the boreholes is dependent on several factors, e.g. the measurement limit Q_{limit} , the borehole transmissivity T_{bh} , the fracture connectivity C , the hydraulic diffusivity T/S , the test time t , the length of the test section ΔL , etc. As a consequence the hydraulic characterisation of the fracture system varies depending on the method used, PFL and PSS, as well as on the in situ conditions. Situations A and B represent isolated fractures and situations C–E fractures connected to the overall hydrogeological system. The latter is here indicated by a “constant head boundary” (CHB) suggesting steady-state flow once sensed at the borehole. (Note: The borehole Cartoon is rotated 90° to improve the readability.)

Ignoring situations like A and B does not mean that they are unimportant. On the contrary, the role of compartmentalised fracture systems is well recognised by the hydrogeological modelling group and a procedure for its handling in the repository modelling carried out in the forthcoming safety assessment project SR-Site has been suggested. However, situations such as C–E are regarded as more important for the groundwater flow modelling addressed in the hydrogeological SDM, see /Follin et al. 2007b/.

A pertinent question to be answered in due time though, is the role of the presumably connected fractures of less transmissivity than the practical lower measurement limit of the PFL-f method, which is c. 30 mL/h. This matter is discussed further in Section 4.2. Another circumstance to consider is that not all boreholes in the target volume of the rock will be hydraulically tested with both test methods, cf. Section 4.

The hydraulic characterisation of the deformation zones is fairly straightforward. All hydraulic data between the upper and lower bounds of a deformation zone interval, as described in the single-hole geological interpretation are considered, regardless of the test method used. The hydraulic data gathered are pooled, i.e. lumped together, to form a single transmissivity value for that interval.

Figure 2-3 illustrates the structural-hydraulic approach taken by SKB in the hydrogeological SDM for Forsmark modelling stage 2.2

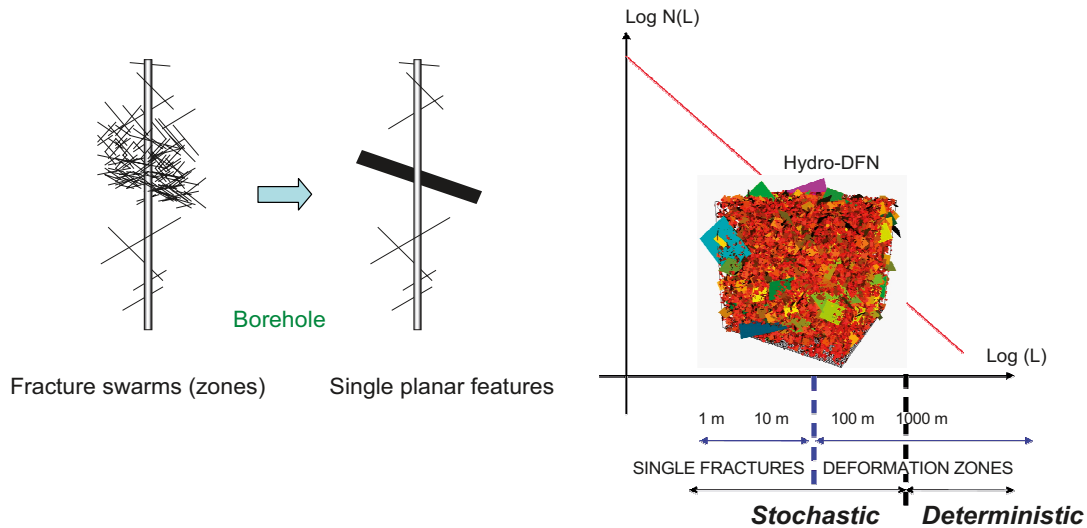


Figure 2-3. Cartoons showing the structural-hydraulic approach used for the treatment of the deformation zones, deterministically as well as possible, in the hydrogeological SDM. Left: The hydraulic data gathered between the upper and lower bounds of a deformation zone interval are lumped together to form a single transmissivity value for that interval. In the same fashion all fractures in the interval are also lumped together, to form a single planar feature. Right: A tectonic continuum is envisaged where the number of features of different sizes follows a power law relationship. Features up to $L = 1,000$ m ($r = 564$ m) are regarded as uncertain and treated stochastically using the Hydro-DFN concept.

2.3 The ECPM approach

Any groundwater model is a simplified parameterisation of a physical groundwater system. The equivalent continuous porous medium (ECPM) approach is used in the hydrogeological SDM for the transformation of geometrical and hydraulic properties of a modelled system consisting of 2D discrete features (DZ and DFN) into a 3D continuous porous medium, see Figure 2-4. Since each ECPM model studied is based on a particular underlying stochastic DFN realisation, the ECPM models are also stochastic. This circumstance is valid also for the ‘deterministically modelled’ DZ model. That is, although geometrically more certain than the DFN model, they are found to have a considerable hydraulic heterogeneity.

The hydrogeological SDM considers single realisations in modelling stage 2.2. Sensitivities to model uncertainties caused by spatial variability in the geometrical and/or hydraulic properties, i.e. multiple realisations, will be quantified in modelling stage 2.3, see Figure 2-5.

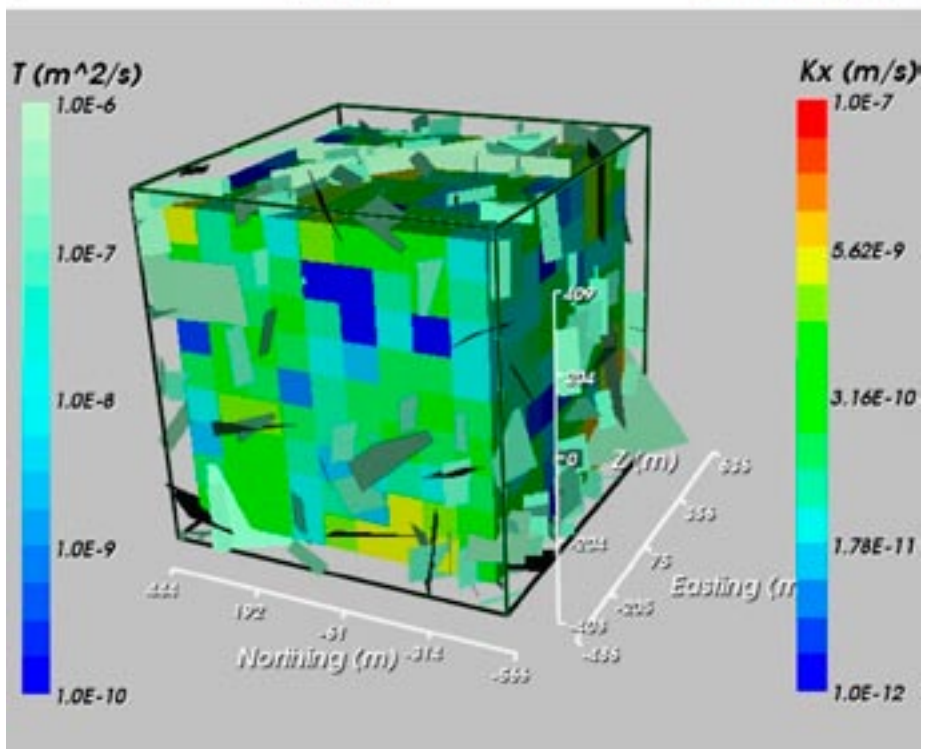
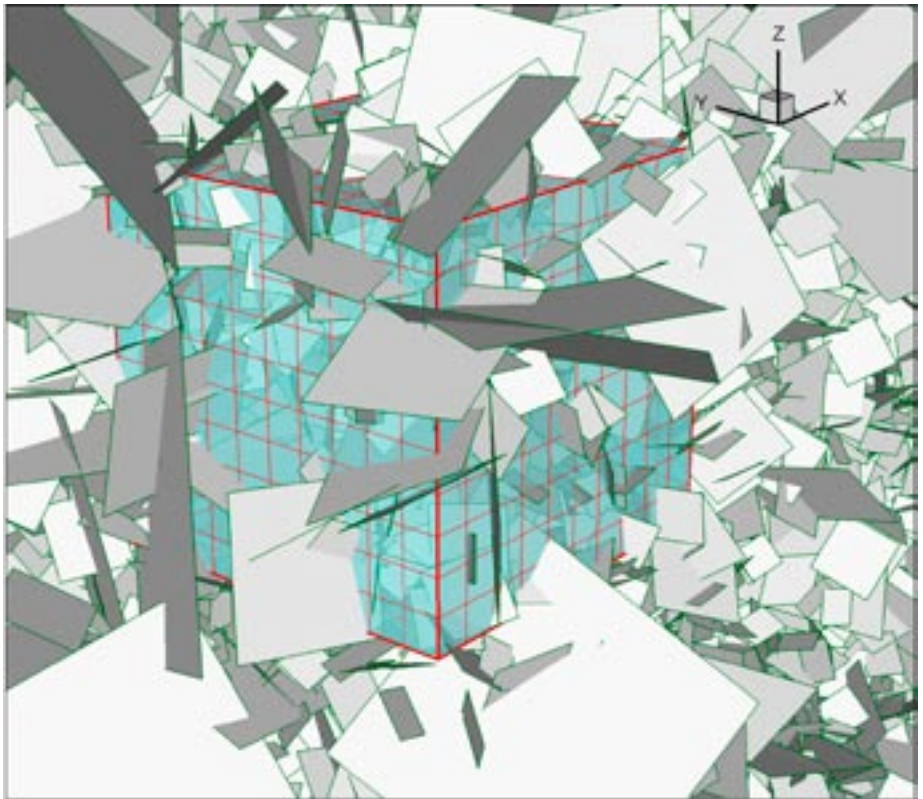


Figure 2-4. Illustrations showing of the ECPM concept. Geometrical and hydraulic properties of modelled 2D discrete features (DZ and DFN) are transformed into a 3D equivalent continuous porous medium.

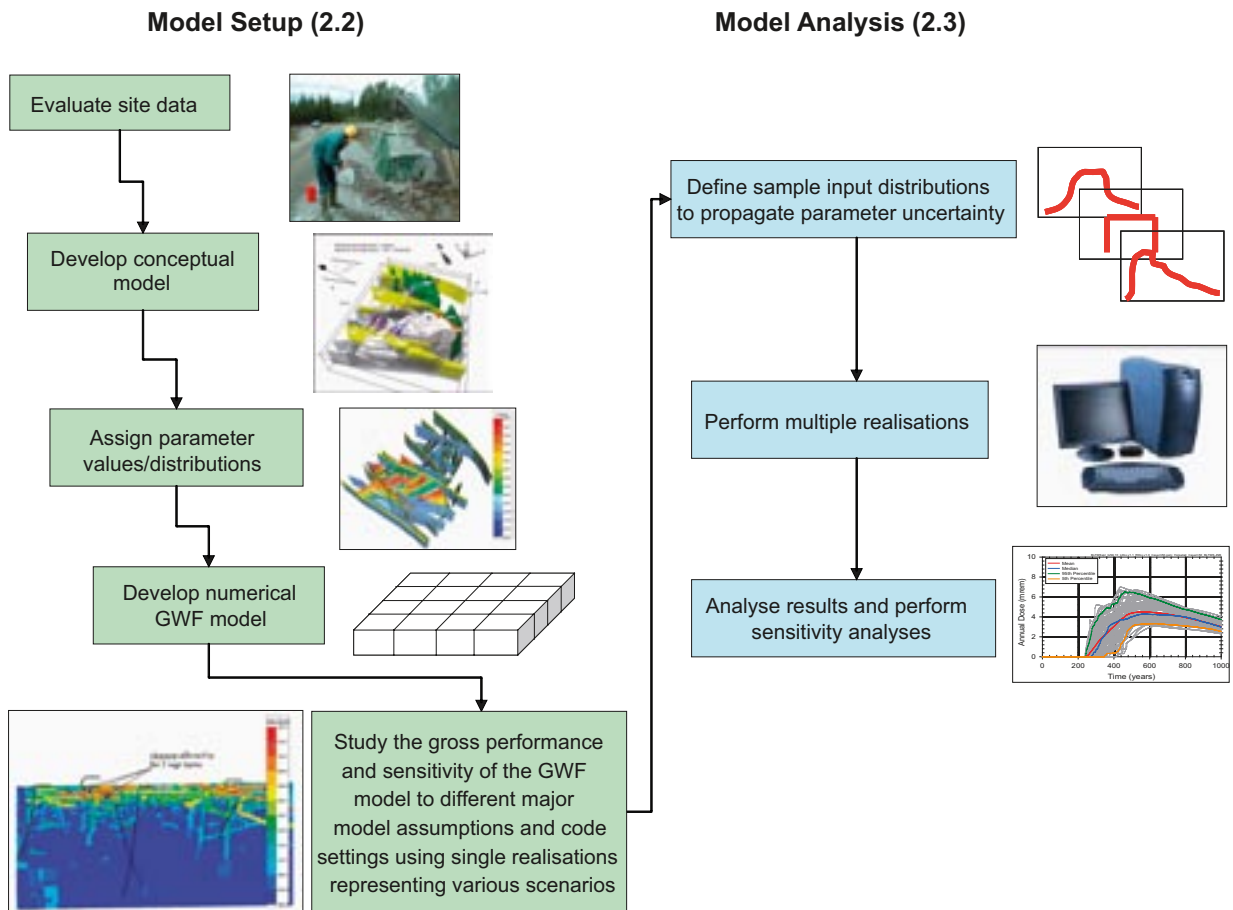


Figure 2-5. The numerical modelling in modelling stage 2.2 is focused on studying the gross performance and sensitivity of the groundwater flow model constructed to different major model assumptions and code settings using single realisations representing different scenarios. Sensitivities to model uncertainties caused by spatial variability in the geometrical and/or hydraulic properties will be quantified in modelling stage 2.3.

3 Geological setting

3.1 The Forsmark site

The Forsmark site is situated in northern Uppland within the municipality of Östhammar about 170 km north of Stockholm. Figure 3-1 illustrates the candidate area with its twelve drill sites (DS). Figure 3-2 presents detailed maps of the actual drill sites for the report. Boreholes KFM11A and -12A at drill sites 11 and 12, respectively, are not included in data freeze 2.2. This constraint applies also to data from boreholes KFM02B and KFM08D at drill sites 2 and 8, respectively. The information from these four boreholes will be treated in modelling stage 2.3.

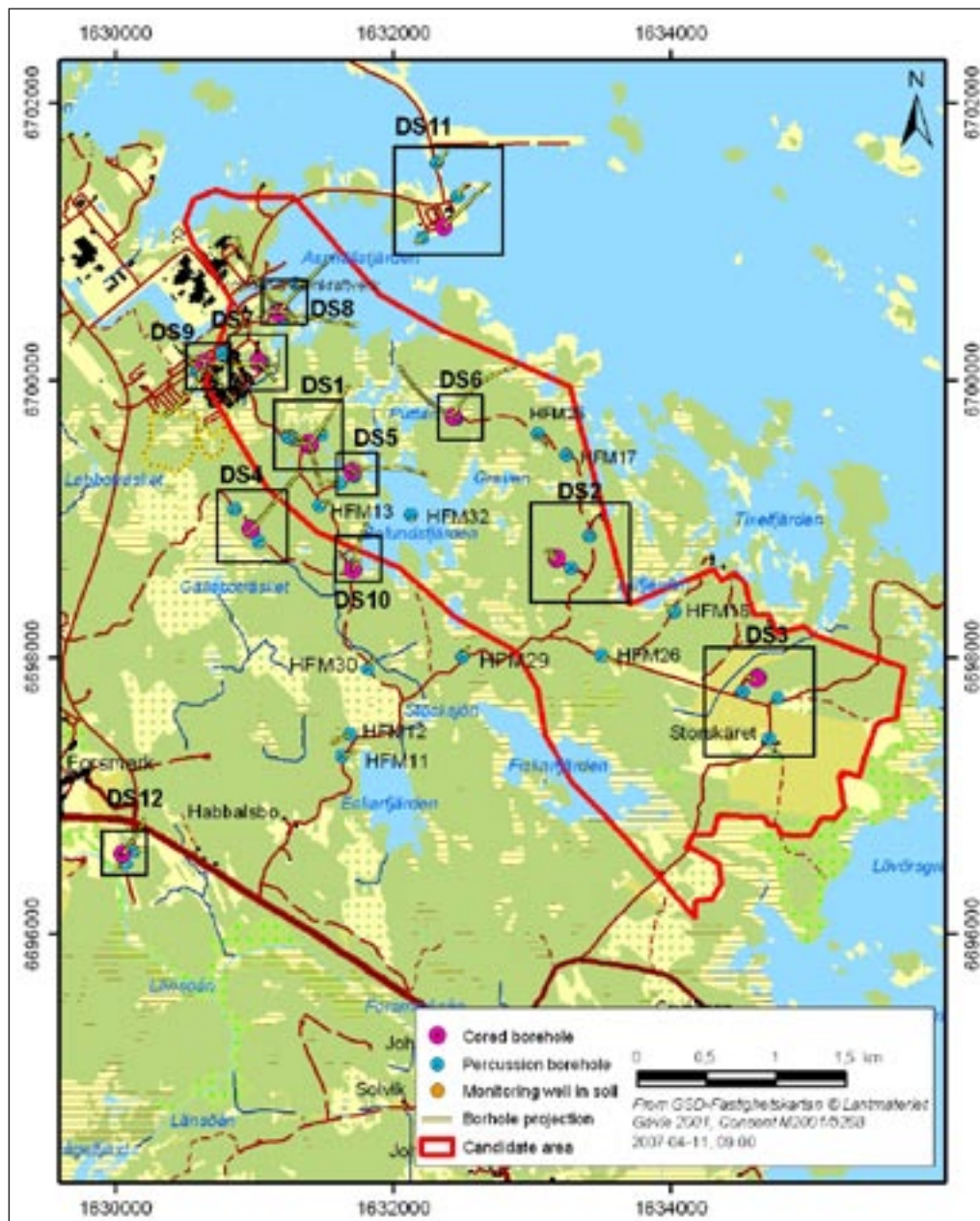


Figure 3-1. Drill sites within and close to the candidate area in Forsmark. Boreholes KFM11A and KFM12A at drill sites 11 and 12, respectively, are not included in data freeze 2.2. This constraint applies also to boreholes KFM02B and KFM08D at drill sites 2 and 8, respectively. The information from these four boreholes will be treated in modelling stage 2.3.

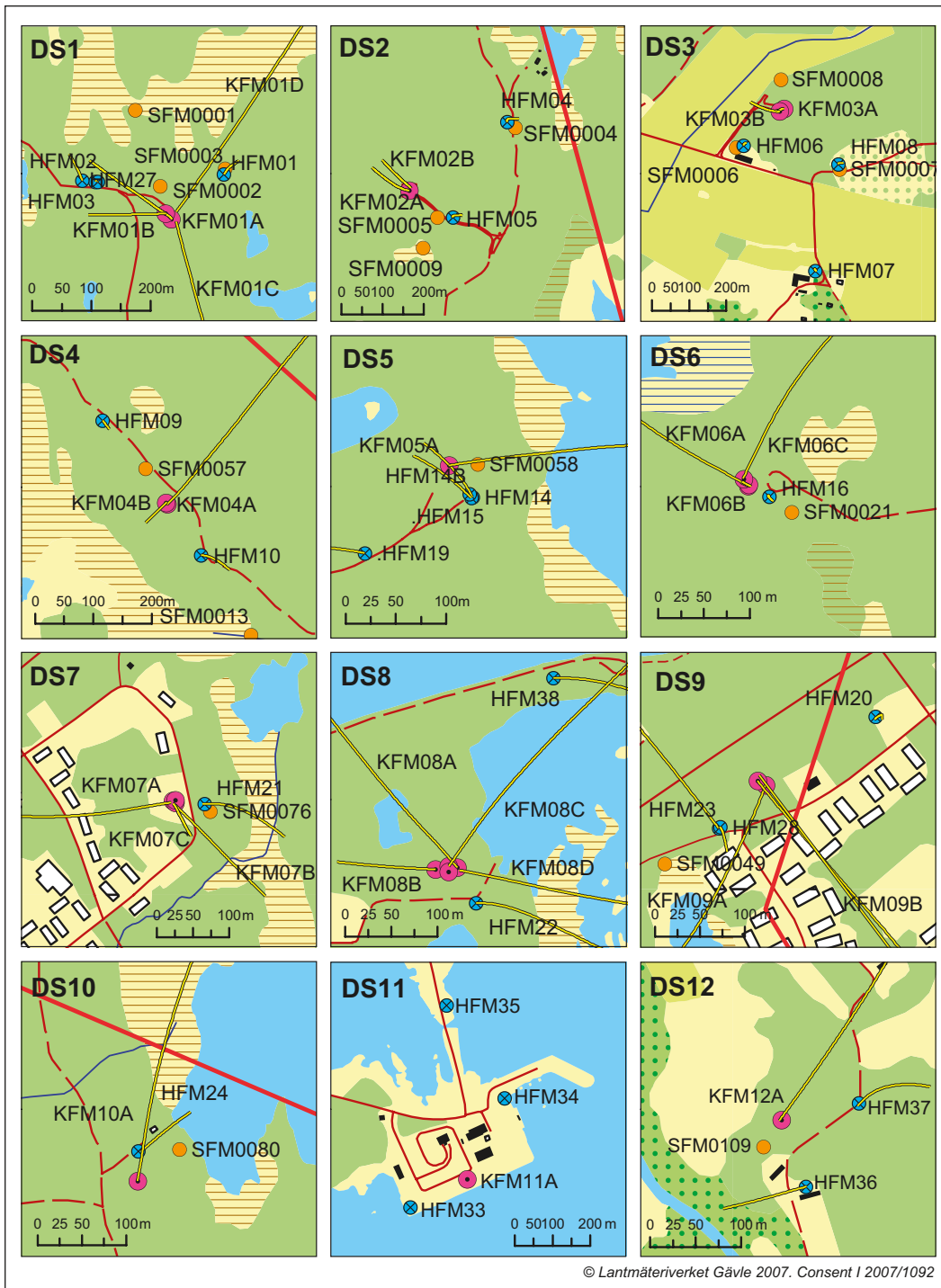


Figure 3-2. Detailed map of the drill sites in Forsmark. The legend is shown in Figure 3-1. Boreholes KFM11A and KFM12A at drill sites 11 and 12, respectively, are not included in data freeze 2.2. This constraint applies also to boreholes KFM02B and KFM08D at drill site 2 and 8, respectively. The information from these four boreholes will be treated in modelling stage 2.3.

3.2 Overview of the deformation zone model

The term deformation zone is used at all stages in the geological work, bedrock surface mapping, single-hole interpretation and 3D modelling. Hence, a deformation zone is a general term referring to an essentially 2D structure along which there is a concentration of brittle, ductile or combined brittle and ductile deformation. The term fracture zone is used to denote a brittle deformation zone without any specification whether there has or has not been a shear sense of movement along the zone. A fracture zone that shows a shear sense of movement is referred to as a fault zone. Table 3-1 presents the terminology for brittle structures based on trace length and thickness as presented in /Andersson et al. 2000/.

The borderlines between the different structures are approximate. The so called 3D DZ block model for Forsmark modelling stage 2.2 described in /Stephens et al. 2007/ contains 103 deterministically modelled deformation zones. These are referred to as ZFMxxx. All of the 103 deformation zones but eleven have trace lengths longer than one kilometre, which implies that the 3D DZ block model, in principle, consists of regional or local major deformation zones, cf. Table 3-1. The eleven deformation zones with trace lengths shorter than one kilometre are either a part (splay) of a nearby deformation zone longer than one kilometre, or gently dipping.

In addition to the 103 deterministically modelled deformation zones, /Stephens et al. 2007/ describe 28 minor deformation zones deterministically, i.e. deformation zones with trace lengths shorter than one kilometre. These are also referred to as ZFMxxx, but *not* part of the 3D DZ block model. Finally, /Stephens et al. 2007/ discuss 43 so called possible deformation zones. These are probably shorter than one kilometre, hence judged to be minor deformation zones, and not modelled deterministically.

Conceptually, the 28 minor deformation zones are no different than the possible deformation zones not modelled deterministically. Despite the conceptual inconsistency created, it was decided by the hydrogeological modelling group to incorporate the 28 deterministically modelled minor deformation zones in the deformation zone model used in the hydrogeological SDM. The motive for this decision is purely pragmatic; that is, it is better to use the geometrical data available than having them modelled as stochastic features. In effect, the deformation zone model for the hydrogeological SDM contains 131 deterministically modeled deformation zones.

Table 3-1. Terminology and general description (length and width are approximate) of brittle structures /Andersson et al. 2000/.

Terminology	Length	Width	Geometrical description
Regional deformation zone	> 10 km	> 100 m	Deterministic
Local major deformation zone	1–10 km	5–100 m	Deterministic (with scale-dependent description of uncertainty)
Local minor deformation zone	10 m–1 km	0.1–5 m	Statistical (if possible, deterministic)
Fracture	< 10 m	< 0.1 m	Statistical

Figure 3-3 shows a 3D visualisation of the 131 deformation zones modelled deterministically in the hydrogeological SDM for Forsmark stage 2.2. The steeply-dipping deformation zones (107) are shaded in different colours and labeled with regard to their principle direction of strike. The gently-dipping zones (24) are shaded in pale grey and denoted by a G. The inset shows the direction of the main principal stress, cf. /SKB 2006a/. All of the 28 minor deformation zones modelled deterministically by /Stephens et al. 2007/, but not included in the 3D DZ block model, occur inside the local model domain, see Figure 3-4. The local model domain encompasses the target volume defined in modelling stage 2.1 /SKB 2006a/, hence investigated to a greater extent than the regional model domain. The bottom of the local model ends at elevation $-1,100$ m, which means that it matches fairly well the maximum penetration depths of the deepest cored boreholes.

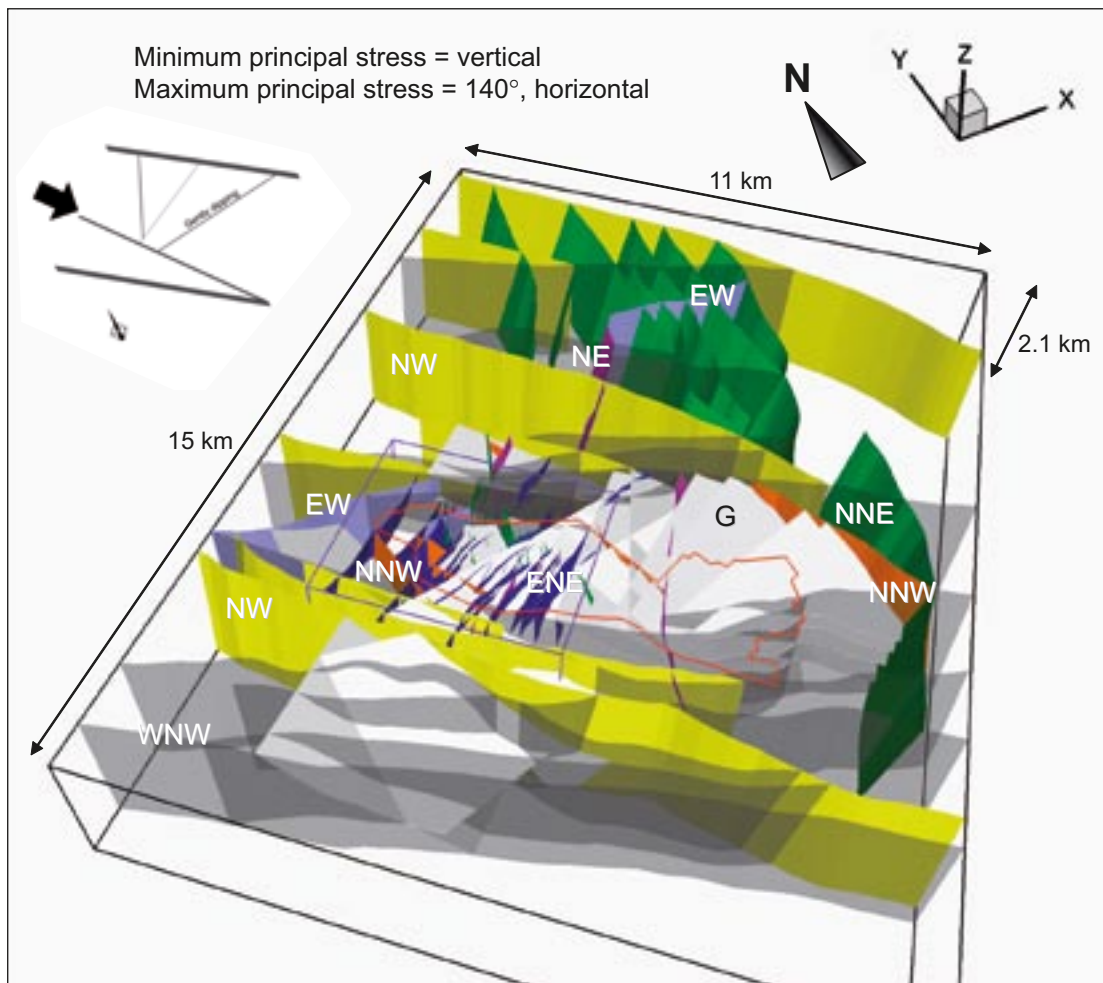


Figure 3-3. 3D visualisation of the 131 deformation zones modelled deterministically in the hydrogeological SDM for Forsmark modelling stage 2.2. The steeply-dipping deformation zones (107) are shaded in different colours and labeled with regard to their principle direction of strike. The gently-dipping zones (24) are shaded in pale grey and denoted by a G. The border of the candidate is shown in red and regional and local model domains in black and purple, respectively. The inset shows the direction of the main principal stress /SKB 2006a/.

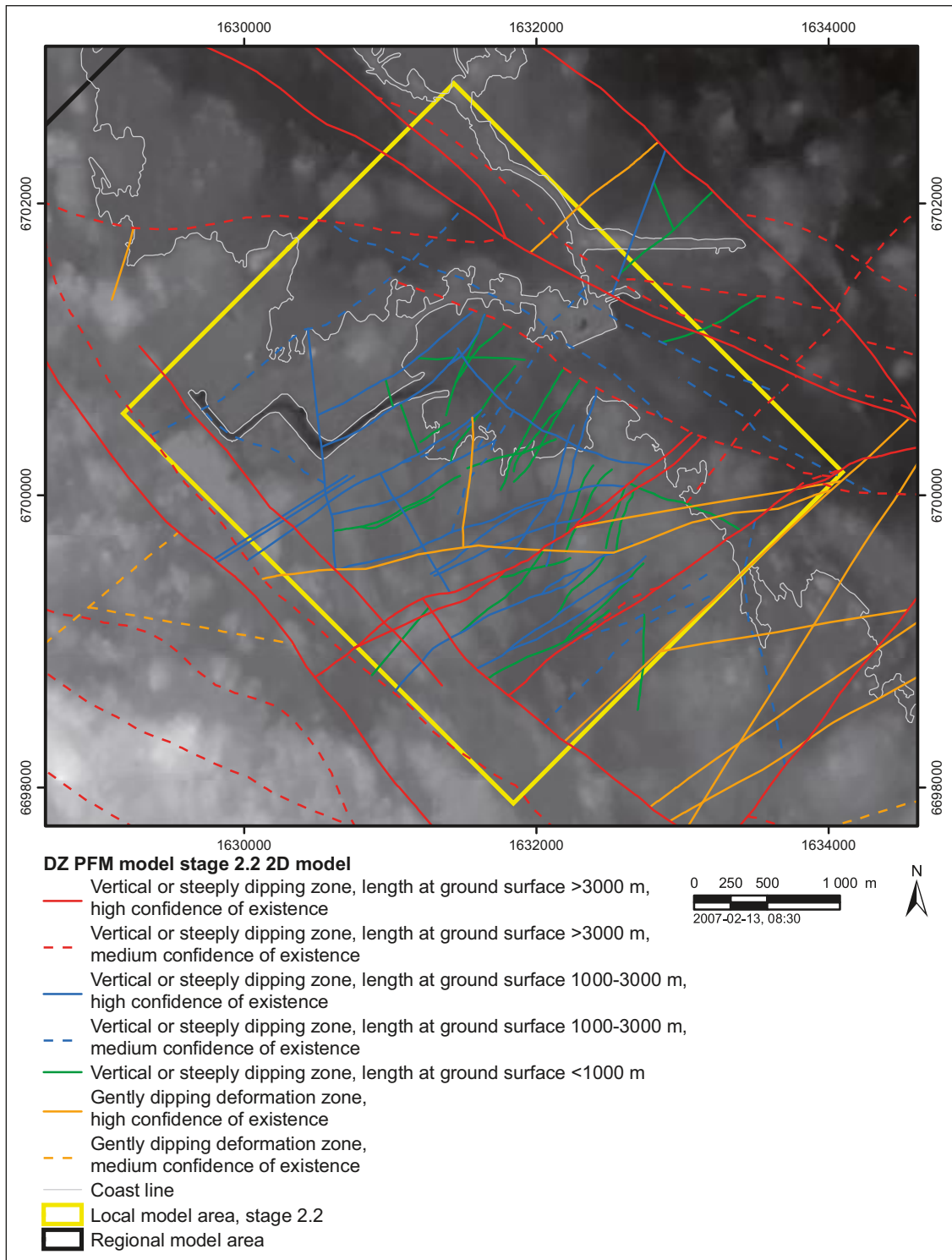


Figure 3-4. Surface intersection of deterministically modelled deformation zones in the local model area, modelling stage 2.2. The background corresponds to the digital elevation model for the site. Coordinates are provide using the RT90 (RAK) system. The 28 minor deformation zones modelled deterministically and included in the hydrogeological SDM have a green colour. Reproduced from /Olofsson et al. 2007/.

Table 3-2 shows a summary of the information presented above. We note in particular:

- 39 (28+11) deformation zones have trace lengths shorter than one kilometre and 45 deformation zones have trace lengths longer than three kilometres.
- 31 of the 103 deformation zones contained by the 3D DZ block model occur inside the local model domain solely, 43 major deformation zones occur outside the local model domain solely and 29 major deformation zones occur both inside and outside. All of the 28 minor deformation zones modelled deterministically in the hydrogeological SDM are steeply dipping and occur inside the local model domain.
- There are 43 possible deformation zones identified in the geological single-hole interpretation but not modelled deterministically for Forsmark in stage 2.2; 34 of these intersect cored boreholes and nine the percussion-drilled holes.

The colours shown in Table 3-2 correspond to the colours used in Figure 3-3 (where they are made transparent). The same colours are used in Section 5 where the hydraulic measurements associated with deformation zones are presented.

The 43 possible deformation zones not modelled deterministically were reported as borehole intervals with “deformation zone type properties”. Their orientations may be tentatively estimated from the fracture poles. However, there are no other strands of evidence to support a more deterministic interpretation, such as, e.g., magnetic lineaments or seismic reflectors. The lack of constraining deterministic information implies that they should be treated stochastically, i.e. as discrete fracture network (DFN) features, cf. Figure 2-3. Section 7 presents an approach to constrain the stochastic modelling.

3.3 Overview of the fracture domain model

A rock domain refers to a rock volume in which rock units that show similar composition, grain size, degree of bedrock homogeneity, and degree and style of ductile deformation have been combined and distinguished from each other. Rock volumes that show early-stage alteration (albitisation) are also distinguished as separate rock domains. The term rock domain is used in the 3D geometric modelling work and different rock domains at Forsmark are referred to as RFMxxx.

Table 3-2. Summary of trace length data (L) for the deterministically modelled deformation zones treated in the hydrogeological SDM. The data are tabulated with regard to orientation. Note that ten of the 24 gently-dipping deformation zones do not outcrop.

Orientation category	No. of DZ major/minor	No. of DZ L ≥ 3 km	No. of DZ 3 km > L ≥ 1 km	No. of DZ L < 1 km	No. of DZ Possible
G	24 / –	6	6	2	17
WNW	23 / 1	15	7	2	3
NW	9 / –	9	0	0	0
NNW	4 / 3	1	2	4	7
NNE	13 / 10	8	4	11	6
NE	4 / 6	2	1	7	0
ENE	24 / 7	2	17	12	9
EW	2 / 1	2	0	1	0
Total	103 / 28	45	37	39	42¹

¹ One of the 43 possible deformation zones interpreted has no orientation data.

A fracture domain refers to a rock volume outside deformation zones in which rock units show similar fracture frequency characteristics. Fracture domains are defined on the basis of the single-hole interpretation work and the results of the initial statistical treatment of fractures. The minor modifications of the single-hole interpretation performed during the stage and the higher-resolution, extended single-hole interpretation work are also accounted for in the recognition of fracture domains. The different fracture domains at Forsmark are referred to as FFMxxx.

An embryo to the fracture domain concept was suggested from a hydrogeological point of view for Forsmark already in modelling stage 1.2 by /Follin et al. 2005b/. The fracture domain definition presented above was first introduced in /SKB 2006a/ and elaborated for Forsmark stage 2.2 in /Olofsson et al. 2007/. The fracture domain concept constitutes a basis for both geological and hydrogeological DFN models.

The dominant rock domains within the north-western part of Forsmark candidate area are RFM029 and RFM045, see Figure 3-5. These two rock domains form the target volume for Forsmark stage 2.2. The target volume is located in the *foot wall* bedrock of the gently dipping deformation zone ZFMA2 (previously called ZFMNE00A2 in stages 1.2 and 2.1). Rock domain RFM029 occurs also in the *hanging wall* bedrock of ZFMA2. Figure 3-6 shows two simplified profiles of the target volume in a NW-SE direction. The profiles pass through drill sites 2 and 8 and drill site 6, respectively. The fractured bedrock outside the deterministically modelled deformation zones intersecting the rock domains RFM012, RFM018, RFM029, RFM032, RFM044 and RFM045 is divided into six fracture domains, FFM01–06:

Fracture domain FFM01: This domain is situated within rock domain RFM029 inside the target volume. It lies beneath the gently dipping or sub-horizontal zones ZFMA2, ZFMA3 and ZFMF1, and north-west of the steeply dipping zone ZFMNE0065, at a depth that varies from greater than c. –40 m elevation (large distance from ZFMA2) to greater than c. –300 m elevation (close to ZFMA2). Relative to the overlying fracture domain FFM02, the bedrock in this domain shows a lower frequency of especially open and partly open fractures. Gently dipping or sub-horizontal deformation zones are not common inside this domain. In particular, they have not been recognised in the critical depth interval 400–500 m in the north-western part of this domain. It has been suggested that high in situ rock stresses have been able to accumulate inside this volume at one or more times during geological history, in connection with, for example, sedimentary loading processes /SKB 2006a, Section 3.2.2, p. 121–126/. It should be noted that some fracture assigned to FFM01 lie between zones ZFMA2 and ZFMF1 which in fact are considered to be possible deformation zones. In consequence, the model may over predict the amount of the stochastic fractures within FFM01.

Fracture domain FFM02: This domain is situated close to the surface inside the target volume, directly above fracture domain FFM01 (Figure 3-6). The domain is characterised by a complex network of gently dipping and sub-horizontal, open and partly open fractures, which, beneath drill site 7, are known to merge into minor zones. The gently dipping and sub-horizontal fractures are oriented at a high angle to the present day minimum principal stress in the bedrock. This relationship favours their reactivation as extensional joints in the present stress regime, the development of conspicuous apertures along several fractures, and the release of high stress. The occurrence of this domain at greater depths close to ZFMA2 at drill site 1, and even above this zone at drill sites 5 and 6, is related to an inferred higher frequency of such older fractures in the vicinity of this zone, to higher rock stresses around zone ZFMA2 or to a combination of these two possibilities.

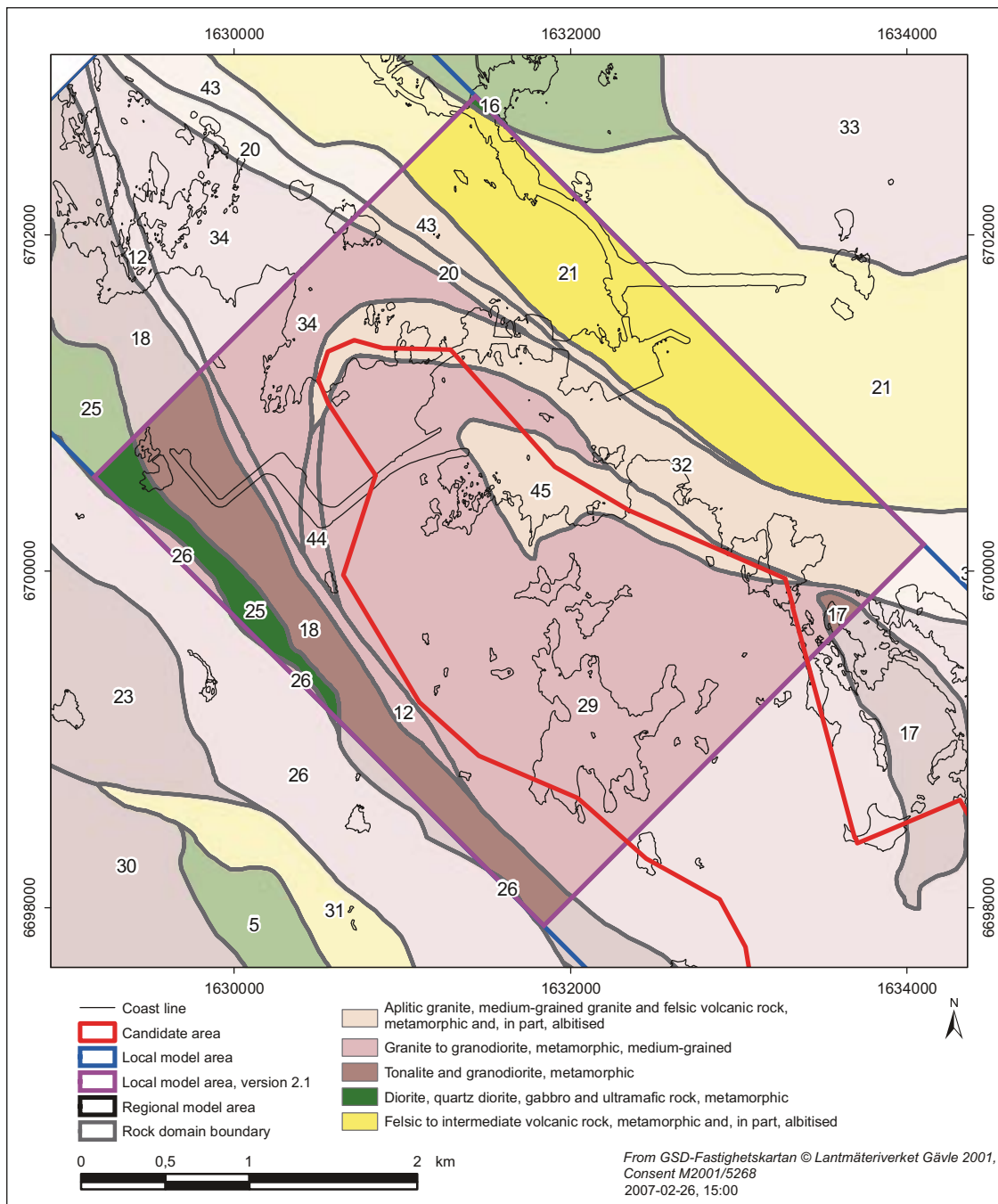


Figure 3-5. Horizontal slice at the surface for rock domains inside and immediately around the local model area in Forsmark. Modified after /Olofsson et al. 2007/.

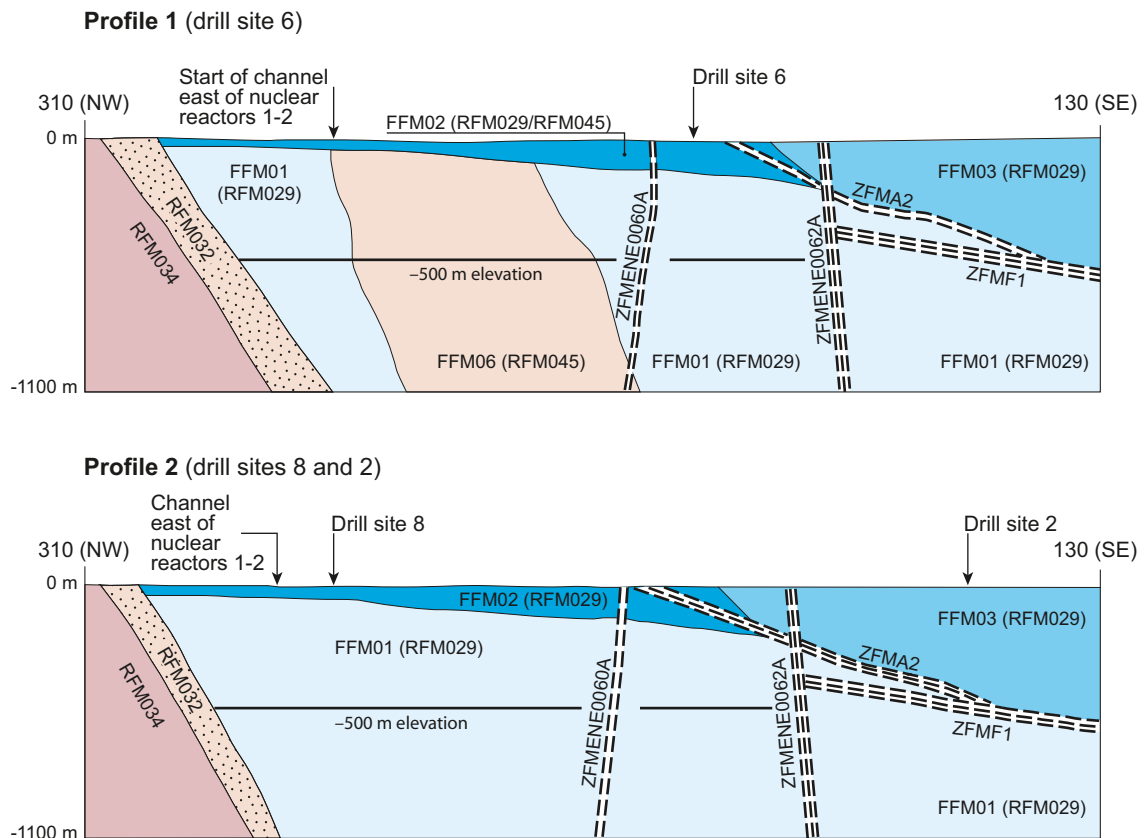


Figure 3-6. Simplified profiles in a NW-SE direction (310–130°) that pass through drill sites 2 and 8 (lower profile) and drill site 6 (upper profile). The labeled fracture domains (FFM01, FFM02, FFM03 and FFM06) occur inside rock domains RFM029 and RFM045. Only the high confidence deformation zones ZFMA2 (gently dipping), ZFMF1 (sub-horizontal), ZFMENE0060A (steeply dipping, longer than 3,000 m) and ZFMENE0062A (steeply dipping, longer than 3,000 m) are included in the profiles. Note the increased depth of fracture domain FFM02 as zone ZFMA2 is approached in the footwall to the zone, and the occurrence of this domain close to the surface directly above ZFMA2. Reproduced from /Olofsson et al. 2007/. The vertical scale shows elevation in metres RHB 70.

Fracture domain FFM03: This domain is situated within rock domains RFM017 and RFM029, outside the target volume. It lies structurally above zones ZFMA2, ZFMA3 and ZFMF1, north-west of the steeply dipping zone ZFMNE0065, and south-east of zone ZFMNE0065 (Figure 3-6). The domain is characterised by a high frequency of gently dipping deformation zones, which contain both open and sealed fractures. It is suggested that this structural feature inhibited the build-up of rock stresses in connection with, for example, sedimentary loading processes /SKB 2006a, Section 3.2.2, p. 121–126/. The development of a significant stress-release fracture domain, close to the surface, with the characteristics of domain FFM02 is also not favoured.

Fracture domain FFM04: This domain is situated within rock domains RFM012 and RFM018 along the south-western margin of and outside the target volume. Strong bedrock anisotropy with high ductile strain and ductile structures that dip steeply to the south-west are prominent in this domain.

Fracture domain FFM05: This domain is situated within rock domains RFM044 and RFM032 along the north-western and north-eastern margins of and outside the target volume. Strong bedrock anisotropy with high ductile strain and folded ductile structures, as well as the occurrence of fine-grained, felsic meta-igneous rocks characterise this domain.









Fracture domain FFM06: This domain is situated within rock domain RFM045, inside the target volume. It resembles fracture domain FFM01 in the sense that it lies beneath both zone ZFMA2 and fracture domain FFM02. It is distinguished from domain FFM01 on the basis of the common occurrence of fine-grained, altered (albitised) granitic rock, with slightly higher contents of quartz compared to unaltered granitic rock.

In summary, fracture domains FFM01–03 occur in rock domain RFM029, with FFM01–02 in the foot wall bedrock and FFM03 in the hanging wall bedrock. Fracture domains FFM04 and FFM05 coincide with rock domains RFM012+RFM018 and RFM032+RFM044, respectively, see Figure 3-3. Fracture domain FFM06 coincides with rock domain RFM045. In conclusion, the target volume consists of three fracture domains, FFM01, FFM02 and FFM06. Since the target volume lies within rock domains RFM029 and RFM045, north-west of the steeply dipping zone ZFMNE0065 and structurally beneath the gently dipping and sub-horizontal zones ZFMA2, ZFMA3 and ZFMF1, it is apparent that statistical modelling of fractures and possible minor deformation zones needs to be implemented in fracture domains FFM01, FFM02 and FFM06.

Figure 3-7 and Figure 3-8 show two 3D visualisations of the fracture domain model. The two views show the geometrical relationships between domains FFM01, FFM02, FFM03 and FFM06. Fracture domain FFM01 dominates in the lowermost part of the view. The volume coloured dark grey shows the position of FFM06. The uppermost part of the bedrock, in the north-western part of the model, is fracture domain FFM02. This domain dips gently towards the south. Fracture domain FFM03 is situated directly above the gently dipping and sub-horizontal zones ZFMA2 and ZFMF1 at depth, and above domain FFM02 close to the surface.

Table 3-3 presents a colour legend, which is used in Section 5 when the geological interpretations of the hydraulic measurements in the tested boreholes are presented with regard to fracture domains.

Table 3-3. Legend showing the geological interpretation of the hydraulic measurements in the tested boreholes with regard fracture domains.

Symbol	Meaning
	Fracture domain FFM01
	Fracture domain FFM02
	Fracture domain FFM03
	Fracture domain FFM04
	Fracture domain FFM05
	Fracture domain FFM06
	Deformation zone
	Possible deformation zone

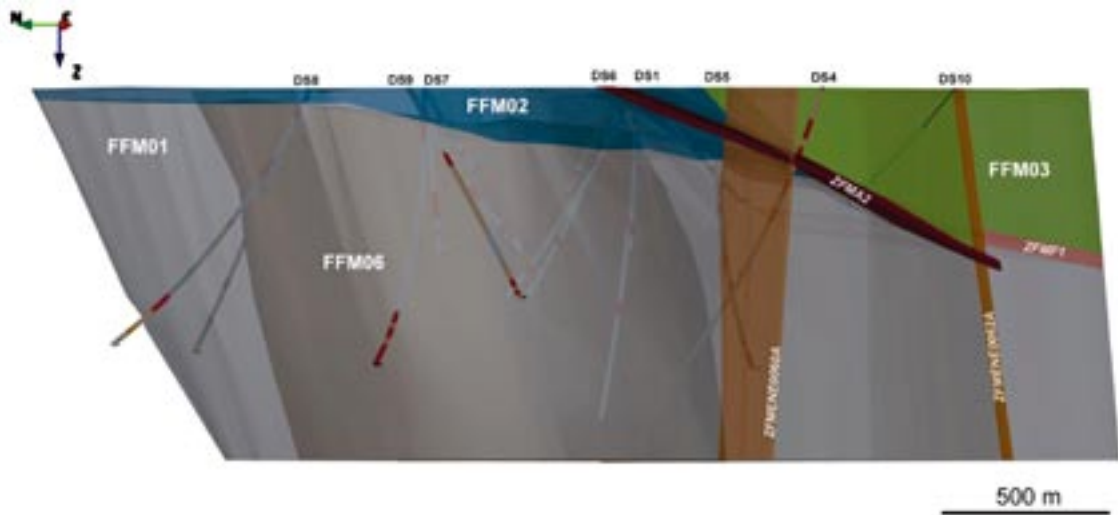


Figure 3-7. Three-dimensional view of the fracture domain model, viewed towards the east-north-east. Fracture domains FFM01, FFM02, FFM03 and FFM06 are coloured grey, dark grey, blue and green, respectively. The gently dipping and sub-horizontal zones ZFMA2 and ZFMF1 as well as the steeply dipping deformation zones ZFMENE0060A and ZFMENE0062A are also shown. Reproduced from /Olofsson et al. 2007/.

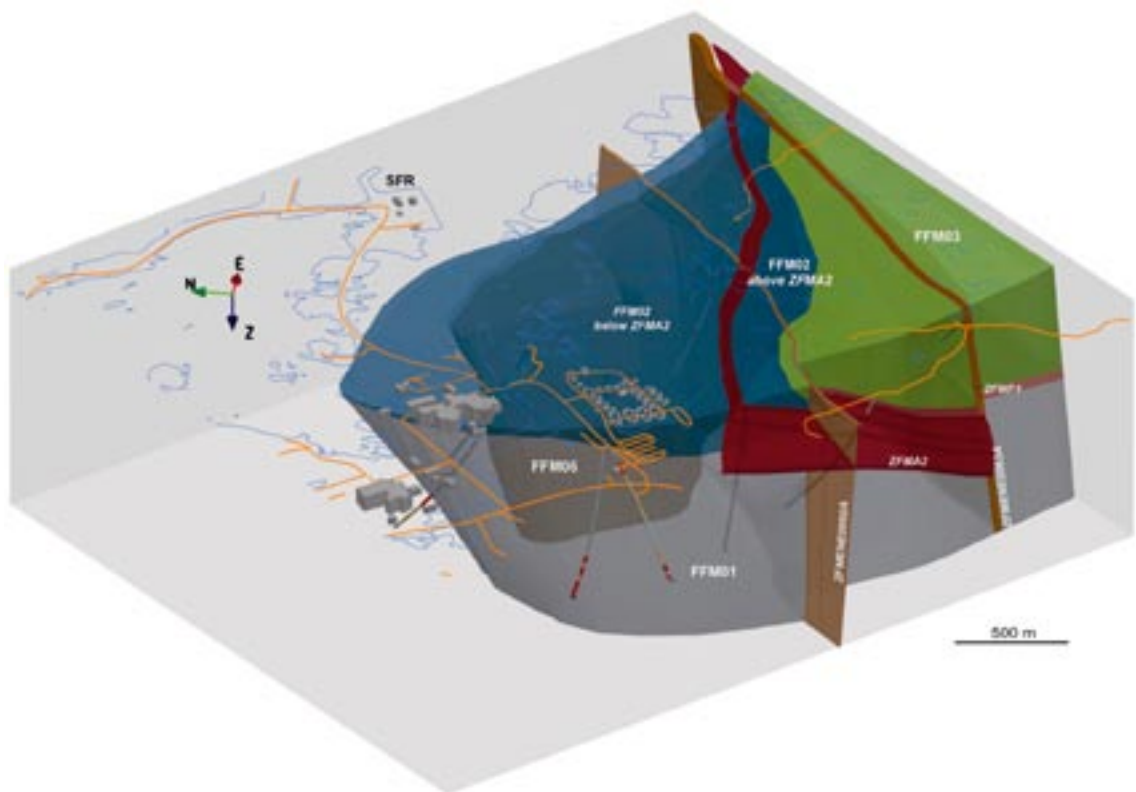


Figure 3-8. Three-dimensional view to the east-north-east showing the relationship between deformation zone ZFMA2 (red) and fracture domain FFM02 (blue). Reproduced from /Olofsson et al. 2007/.

4 Hydraulic single-hole investigations

4.1 Available primary data

Table 4-1 lists the boreholes with regard to the geological information acquired at the time of the different data freezes (modelling stages). Currently, there are 25 cored and 38 percussion-drilled boreholes planned for the site investigations in Forsmark. Figure 4-1 shows a map of completed, ongoing and upcoming cored boreholes (KFMxxx) as of 2006-05-31. The map in Figure 4-2 shows the corresponding information for the percussion-drilled boreholes (HFMxx).

Table 4-2 lists the cored boreholes investigated with the Posiva Flow Log (PLF) method and the Pipe String System (PSS) method, respectively. All percussion-drilled boreholes are investigated with the HTHB method (combined pumping and impeller flow logging) except those with a very poor yield.

The hydraulic characterisation of the bedrock differs depending on the drilling technique used. Cored boreholes are slim, c. 76 mm in diameter, and are drilled to great depths. The borehole length and inclination vary; the most important ones drilled for hydrogeological reasons mainly are c. one kilometre long and inclined c. 60° from the horizontal. In contrast, percussion-drilled boreholes have a larger diameter, c. 140 mm, and are generally not deeper than 200 m, see Figure 4-3. It is noted that the geological information provided by core drilling is superior in comparison with percussion drilling, which crushes the rock, i.e. no cores are collected.

Table 4-1. List of cored and percussion-drilled boreholes with regard to the different data freezes in Forsmark.

Data freeze	No. of core drilled boreholes	KFMxxx	No. of percussion drilled boreholes	HFMxx
1.1 2003-04-30	1	KFM01A	8	HFM01–08
1.2 2004-07-31	5	KFM02A–05A KFM01B	11	HFM09–19
2.1 2005-07-29	4	KFM06A–07A KFM03B, -06B	3	HFM020–22
2.2 2006-09-30	11	KFM08A–10A KFM06B–09B KFM01C, KFM07C–08C KFM01D	10	HFM23–32
2.3 2007-03-31	4	KFM11A–12A KFM02B KFM08D	6	HFM33–38
All	25	KFM01A–12A KFM01B–03B KFM06B–09B KFM01C, KFM07C–08C KFM01D, -08D	38	HFM01–38

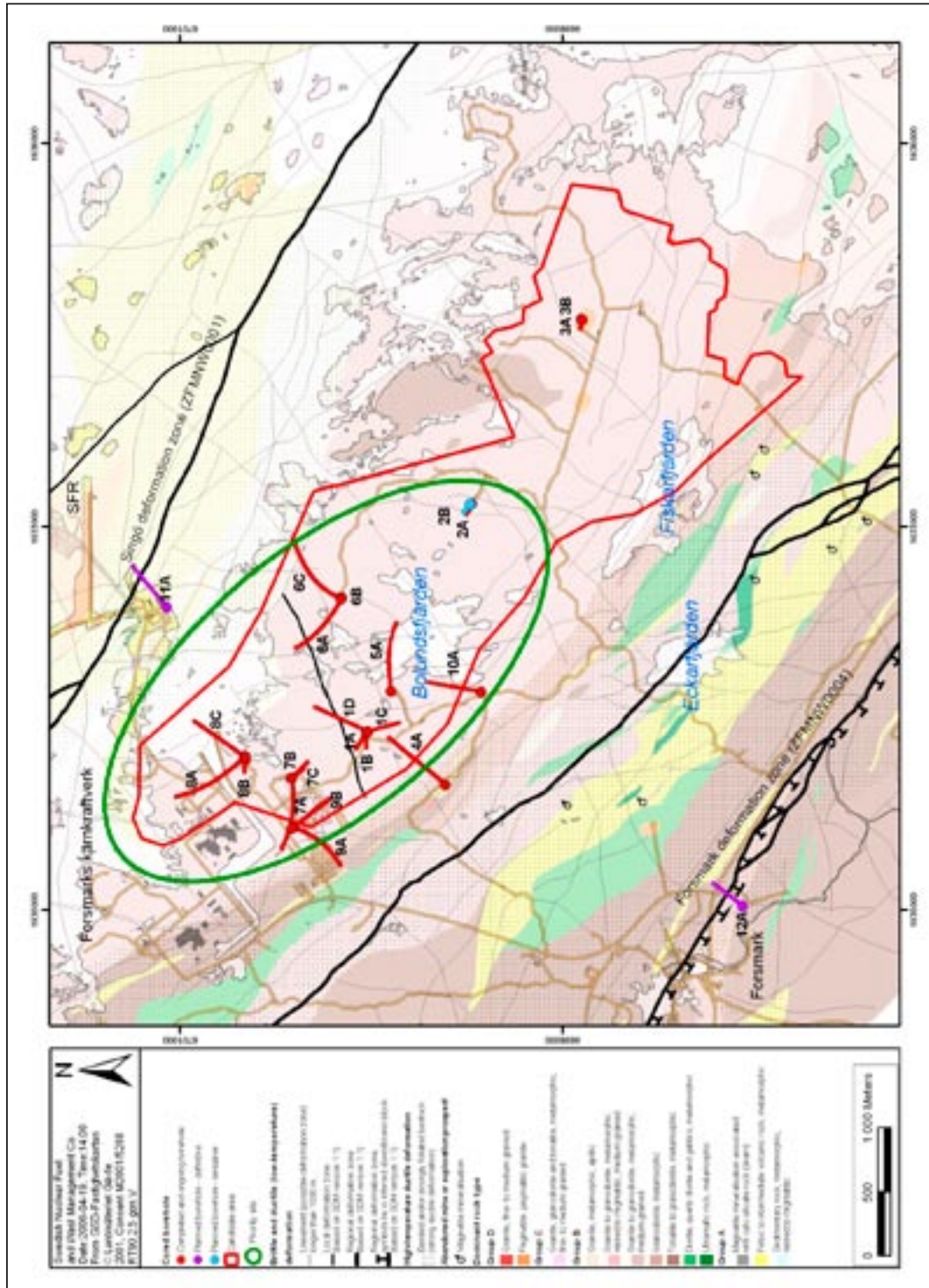


Figure 4-1. Completed and planned core-drilled boreholes in Forsmark (2006-05-31). The underlying geological map is from stage 1.2 /SKB 2005a/. The green ellipse shows the location of the target area (priority site).

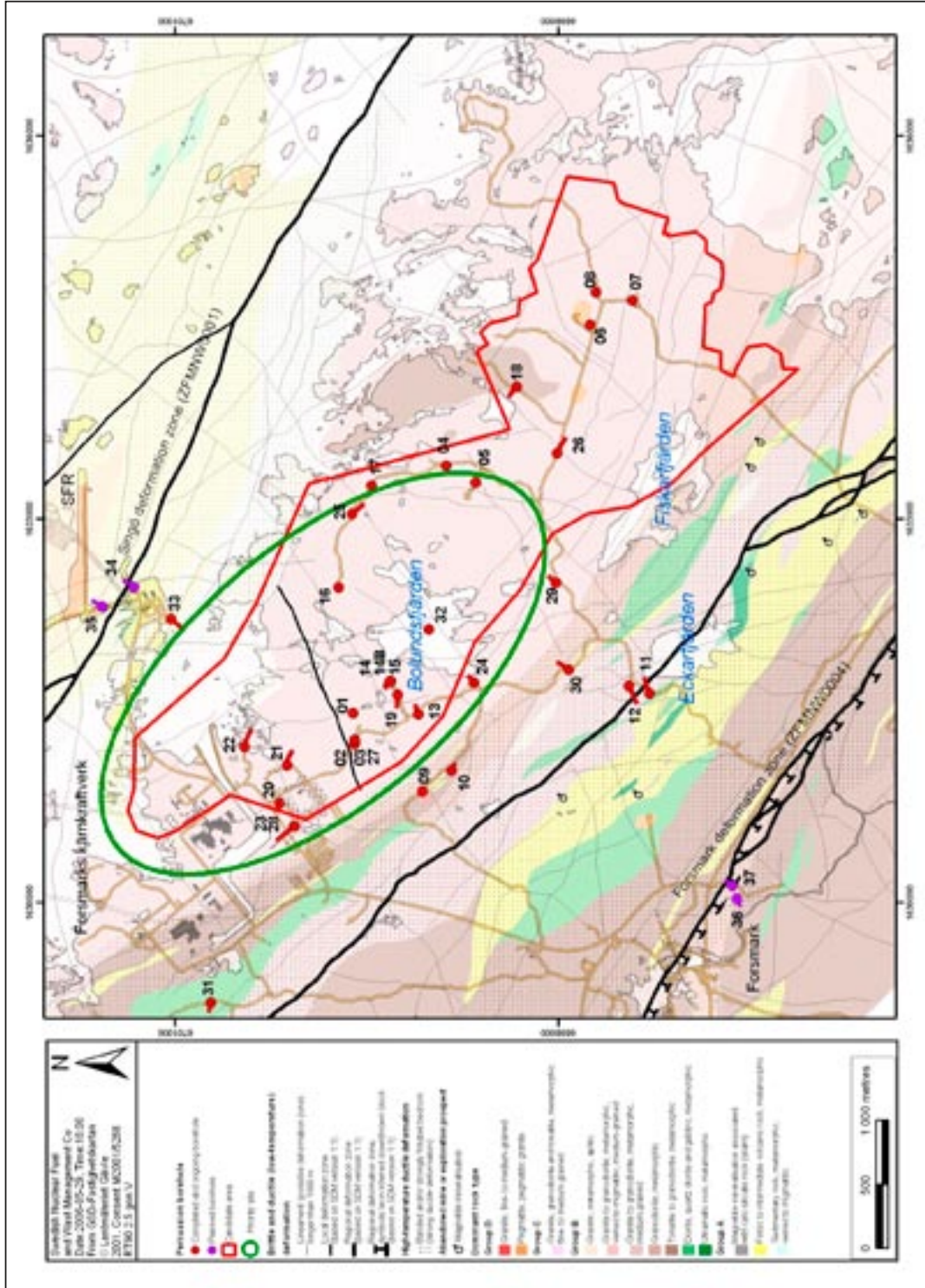


Figure 4-2. Completed and planned percussion-drilled boreholes in Forsmark (2006-05-31). The underlying geological map is from stage 1.2 /SKB 2005a/. The green ellipse shows the location of the target area (priority site).

Table 4-2. List of PFL and PSS tests in Forsmark.

Data freeze	No. of PFL tested boreholes	Tested boreholes KFMxxx	No. of PSS tested boreholes	Tested boreholes KFMxxx
1.1 2003-04-30	1	KFM01A	0	–
1.2 2004-07-31	4	KFM02A–05A	3	KFM01A–03A
2.1 2005-07-29	2	KFM06A–07A	6	KFM04A–07A KFM03B, -06B
2.2 2006-09-30	5	KFM08A, -10A KFM07C–08C KFM01D	8	KFM08A–09A KFM07B–09B KFM01C, -06C KFM01D
2.3 2007-03-31	3	KFM11A KFM02B KFM08D	5	KFM10A–12A KFM07C–08C
All	15	KFM01–08A KFM10A–11A KFM08C KFM01D, -08D	22	KFM01A–12A KFM03B, KFM06B–09B KFM01C, KFM06C–08C KFM01D

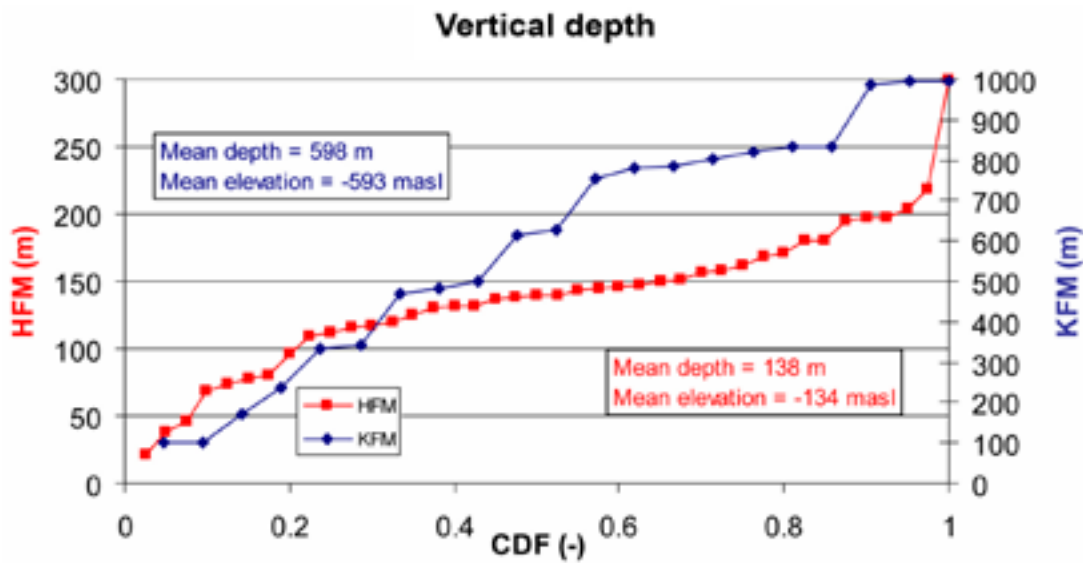


Figure 4-3. CDFs for the cored (KFM) and percussion-drilled (HFM) boreholes.

4.2 Hydraulic tests conducted on intact rock cores

Matrix permeabilities of intact rock core samples have been estimated at various confining pressures using the HPRM apparatus, described by /Drew and Vandergraaf 1989/. The HPRM consists of a core holder assembly, which is placed in a pressure vessel that can be operated with a maximum pressure of about 17 MPa. The core samples, with lengths of 0.5 to 2.0 cm, were placed between two stainless steel cylinders, see Figure 4-4.

Five successful core samples were taken from borehole KFM01D at drill site 1 at borehole lengths ranging from about 250 m to 790 m. The matrix permeability measurements were made at AECL's Whiteshell Laboratories Canada, using a range of confining pressures to simulate in situ burial conditions. Measured permeability values ranged from $6 \cdot 10^{-22}$ to $6 \cdot 10^{-19}$ m², corresponding to hydraulic conductivity values of $4 \cdot 10^{-14}$ to $5 \cdot 10^{-12}$ m/s. Table 4-3 shows average permeability and conductivity values for confining pressures greater than 14 MPa. Permeability measured normal to the core axis was a factor 3 to 5 lower than measured parallel to the core axis.

Table 4-3. Average permeability and hydraulic conductivity values for confining pressures greater than 14 MPa. A = parallel to core axis, B = normal to core axis. Sample positions along the borehole are shown between parentheses /Wilks 2007/.

Sample	Permeability (m ²)	Hydraulic conductivity (m/s)
KFM01D-3A (254.93-255.03)	$(6.8 \pm 1.6) \cdot 10^{-20}$	$(5.9 \pm 1.4) \cdot 10^{-13}$
KFM01D-3B (254.93-255.03)	$(1.3 \pm 0.9) \cdot 10^{-20}$	$(1.1 \pm 0.8) \cdot 10^{-13}$
KFM01D-8A (499.90-500.00)	$7.4 \cdot 10^{-22}$	$6.4 \cdot 10^{-15}$
KFM01D-12A (700.07-700.17)	$(2.5 \pm 0.7) \cdot 10^{-19}$	$(2.2 \pm 0.6) \cdot 10^{-12}$
KFM01D-13A (747.09-747.19)	$(9.2 \pm 1.5) \cdot 10^{-21}$	$(8.0 \pm 1.3) \cdot 10^{-14}$
KFM01D-13B (747.09-747.19)	$(2.9 \pm 1.8) \cdot 10^{-21}$	$(2.5 \pm 1.3) \cdot 10^{-14}$
KFM01D-14A* (790.38-790.48s)	$(4 \pm 5) \cdot 10^{-21}$	$(4 \pm 4) \cdot 10^{-14}$

*Average for confining pressures from 2.2 to 2.7 MPa.



Figure 4-4. Rock core sample enclosed by end pieces to be used in a permeability measurement. Reproduced from /Wilks 2007/.

Increasing the confining pressure from 2 MPa to 15 MPa resulted in a reduction of measured permeability that ranged from a factor 2 to 130, see Figure 4-5.

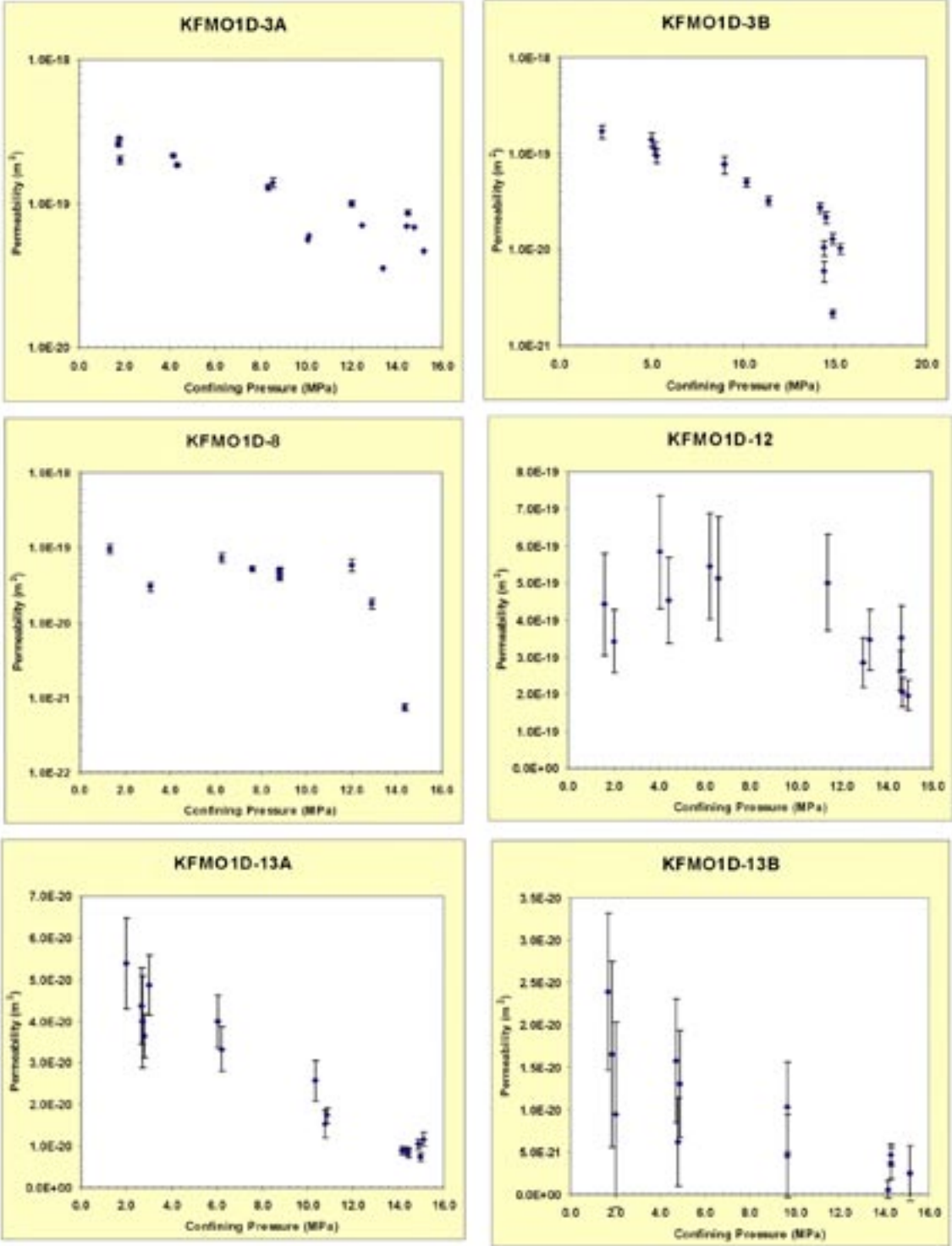


Figure 4-5. Effect of confining pressure on permeability values. Reproduced from /Vilks 2007/.

4.3 Hydraulic tests conducted in cored boreholes

Most of the cored boreholes have been characterised hydraulically with both the PFL method and the PSS method in order to allow for consistency checks of the hydraulic data acquired from repository depth. Percussion-drilled boreholes have been characterised with the HTHB method predominantly. The three test methods have different pros and cons. In particular, it is important to recognise the significant differences between the PFL and PSS methods in terms of field operation, spatial resolution and lower measurement threshold (detection limit). It is also important to recognise the fairly intricate evaluation procedure used for the interpretation and reporting of transmissivity data for the PSS method. In summary, all these differences combined have a profound impact on the use of the transmissivity values in hydrogeological modelling.

The PFL method is a geophysical logging device developed to detect *continuously flowing fractures* in sparsely fractured crystalline bedrock by means of difference flow logging, see Figure 4-6. The physical limitations of the measurement device and the principles for operation are explained in detail in SKB P-report series, see e.g. /Rouhiainen and Sokolnicki 2005/.

The flowing fractures detected with the so called PFL-f method (f stands for fracture) are traditionally called flow anomalies, or just PFL-anomalies. The PFL-f measurements are based on c. one week of pumping (~10,000 minutes) where the entire borehole acts as a line sink. The test configuration means that a radial, steady-state flow regime is prevailing. The PFL-f method is designed to detect individual fracture flows along the borehole with a high spatial resolution. A resolution of 0.1 m is used in Forsmark. The detection limit varies depending on the in situ conditions. As a rule of thumb, the lower detection limit of the flow meter device used is c. 30 mL/h.

The PFL-f method has the following characteristics:

- A radial, steady-state flow regime prevails around each test interval. The interval is probably small enough to characterise the flow from individual fractures. By combining the PFL-f method with a borehole viewer (BIPS) the orientation of the flowing fracture can be assessed. The maximum uncertainty in position along the borehole of the PFL-f method is c. ± 0.2 m /Forsman et al. 2004/.

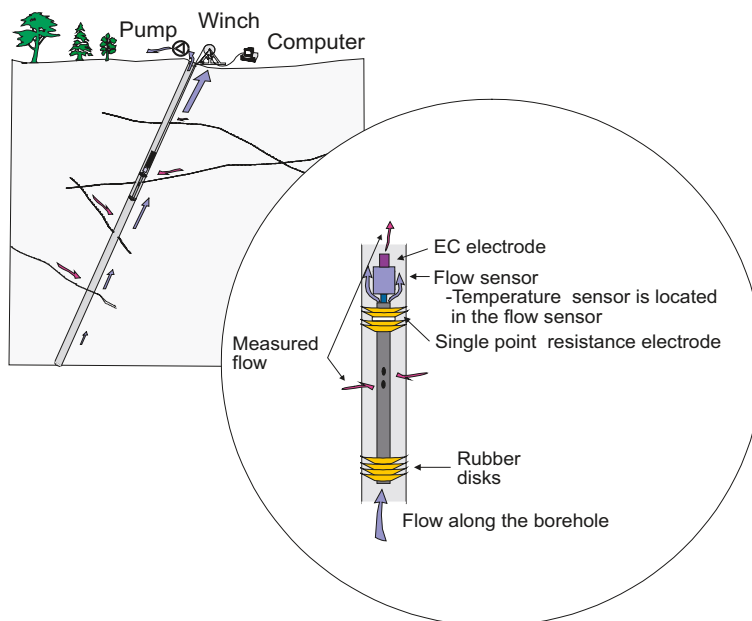


Figure 4-6. Schematic drawing of the down-hole equipment used for difference flow logging in Forsmark. Reproduced from /Rouhiainen and Sokolnicki 2005/.

- There are no problems with flowing fractures short circuiting with the borehole above and below the rubber discs since the borehole is a line sink. Problems with the rubber discs may arise however, e.g. when there are great cavities in borehole diameter or large axial flows in the borehole below test interval.
- The flow rate of isolated fractures or isolated clusters of fractures connected to the pumped borehole are not investigated; that is, only connected open fractures with a sufficient flow rate are detected and analysed.
- Fracture transmissivity values are only defined and reported to the Sicada data base for those 0.1 m long test intervals where measurable flow rates were observed. Non-flowing test intervals are not assigned a threshold value.

The PFL-f transmissivity T_{PFL-f} is calculated from Thiem's equation /Thiem 1906/, which assumes a radial, steady-state flow regime of known radius of influence. Since the actual flow geometry, skin effects, and radii of influence are unknown, transmissivity values should be taken as indicating orders of magnitude. The practical transmissivity threshold varies depending on the actual field conditions, but typical for the conditions in Forsmark is c. $1 \cdot 10^{-9} \text{ m}^2/\text{s}$.

/Rouhiainen and Sokolnicki 2005/ note that the calculated hydraulic heads do not depend on geometrical properties but only on the ratio of the flow rates measured at different heads in the borehole. Hence, they should be less sensitive to unknown fracture geometry. A discussion of potential uncertainties in the calculation of transmissivity and hydraulic head is provided in /Ludvigson et al. 2002/.

The PSS measurements apply the classic test approach known as constant-head, double-packer injection. A schematic drawing of the test equipment used in Forsmark is shown in Figure 4-7. The PSS measurements are run with different test section lengths. The shortest test section length used in Forsmark is five metres. The evaluation of the flow-time envelop is made after 20 minutes of injection, which means that the duration of the PSS measurements is much shorter than for the PFL-f measurements. As a rule of thumb, the lower detection limit of the flow meter device used is c. 60 mL/h.

The PSS method has the following characteristics:

- The test section is generally so long that several fractures are investigated at the same time. Their individual contribution or geometry cannot be inferred without an additional set of assumptions of statistical nature.
- The flow regime (linear, radial, spherical) and the state of flow (steady-state or transient) cannot be assumed with confidence, because the tested section acts like a temporary point source. Hence, the flow regime and the state of flow must be analysed and evaluated using the entire flow-time envelop.
- There may be problems with locally connected fractures short circuiting with the borehole above and below the inflatable packers (cf. Figure 4-7), in particular at locations where the fracture intensity is high close to the borehole.
- The transmissivity of some isolated fractures or isolated clusters of fractures connected to the test section may also be measured; that is, it is not only the interconnected open fractures that are detected and analysed. The hydraulic diffusivity of the more compartmentalised parts of the fracture network is also investigated. In order to resolve the connectivity issue the boundary effects must be evaluated and/or another methodology must be used.
- A test section transmissivity value is always defined and reported to the Sicada data base regardless if a measurable flow rate or not was detected during the injection period. The lower detection limit of the flow meter device used is c. 60 mL/h, which corresponds to a transmissivity of $6.7 \cdot 10^{-10} \text{ m}^2/\text{s}$ using Moye's formula for steady-state flow /Moye 1969/.

Two transmissivity values should be reported to Sicada for each PSS test conducted according to the methodology instructions for single-hole hydraulic testing; a steady-state transmissivity

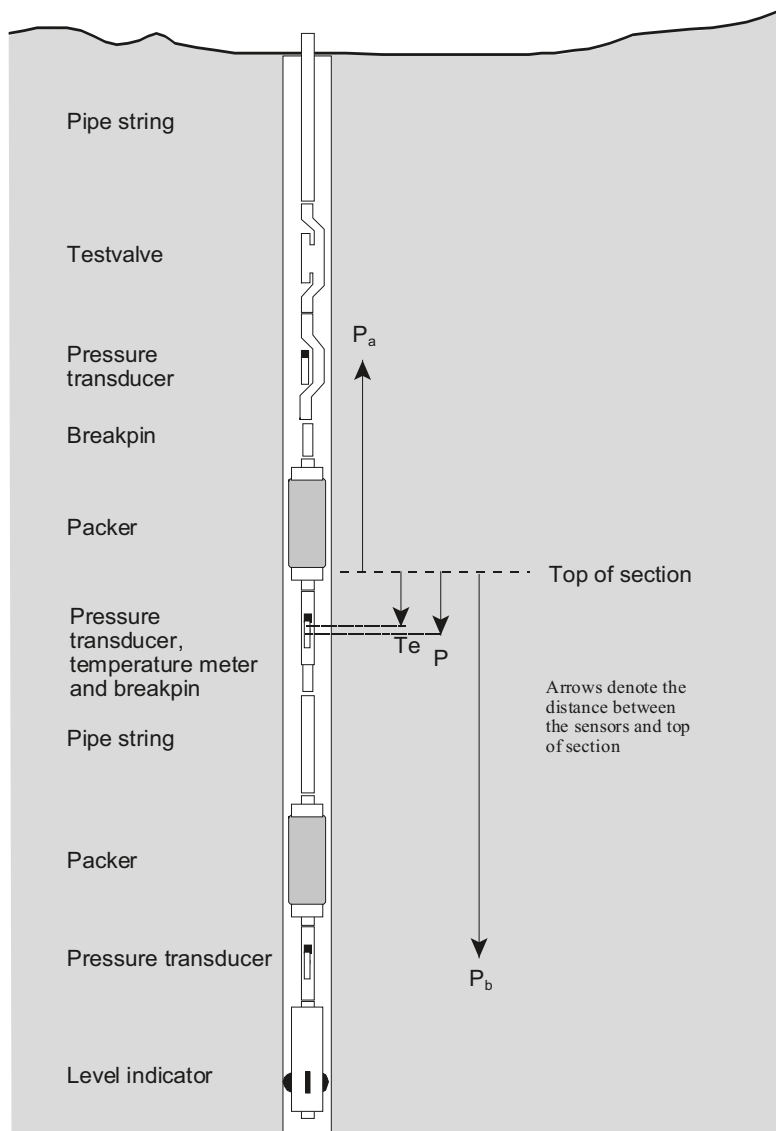


Figure 4-7. Schematic drawing of the down-hole equipment in the PSS system. Reproduced from /Walger et al. 2006/.

value T_{s-s} and a transient value T_{tr} , regardless of the in situ borehole flow conditions. The steady-state transmissivity evaluation is based on the flow rate at shut-in time (c. 20 min) using Moye's formula /Moye 1969/. The transient transmissivity evaluations have several options. Ideally, the evaluation is made for the first radial acting part of the flow-time envelope using type curve interpretation methods derived for the petroleum industry and transferred to hydrogeology, e.g. AQTESOLVE /HydroSOLVE Inc. 2007/. If there is no radial acting part the test section transmissivity value is calculated using classic linear or spherical flow models. If apparent boundary effects can be observed at shut-in time this is also reported to Sicada. The information stored in Sicada is accompanied by a recommendation regarding the best transmissivity value to be used for each test section, i.e. the steady-state transmissivity value or the transient transmissivity value. The recommended transmissivity values are denoted by T_{BC} (BC for "Best Choice").

Wellbore skin is a concept developed by the petroleum industry to describe the hydraulic contact between a production well and the geological formation surrounding it /Earlougher 1977/. A positive skin means, conceptually, that there is a resistance to flow (head loss) close to the well. Thus, a positive skin reduces the well's specific capacity. A negative skin means the opposite; that the hydraulic contact with the geological formation is enhanced and that

specific capacity has been improved. The concept of skin is not readily transferred to fractured crystalline rock, in particular not a positive skin. However, the majority of the skin factors inferred from transient analyses of 550 PSS measurements in Forsmark have a negative skin, see Figure 4-8. This suggests that the cored boreholes in Forsmark in general improve the connectivity of the near-field fracture system.

From a site characterisation point of view, a negative skin factor is preferable since the radius of influence is enhanced; that is, the testing sensors the hydraulic properties of the bedrock away from the borehole. In contrast, a positive skin factor can be detrimental for the testing since it not only restricts the radius of influence, but also endangers the transmissivity interpretation resulting in lower values than otherwise. The steady-state interpretations are particularly sensitive to positive skin. Figure 4-8 does not suggest that there is huge problem with positive skin factors in Forsmark though.

An indirect way to check for skin effects is to cross plot steady state transmissivity data and transient transmissivity data. Figure 4-9 shows a summary cross-plot of PSS 5 m steady-state transmissivity data T_{s-s} versus PSS 5 m transient transmissivity data T_{tr} gathered in cored boreholes at drill sites 1–8. The scattering around the unit slope is fairly random, thus no systematic difference between the two test interpretation methods of any major importance can be deduced. However, the tendency for positive differences of $(T_{s-s} - T_{tr})$ in the lower transmissivity range and negative differences in the upper suggests that other kinds of disturbing test conditions may be present, e.g. non-Euclidian (fractional) flow regimes, compartmentalisation and boundary effects.

/Follin et al. 2006a/ noted that the flow-time envelopes for the first seven cored boreholes in Forsmark KFM01A–KFM07A varied from one borehole to the next in a fashion that could not be explained by skin effects alone. As an example Figure 4-10 shows a cross-plot of steady-state transmissivity data with PSS T_{s-s} versus $\sum T_{PFL-f}$ data for KFM06A. The scattering around the unit slope is fairly large, with large positive differences of $(T_{s-s} - \sum T_{PFL-f})$ in the lower transmissivity range. Transmissivity data from PSS test sections without any PFL-f anomalies are plotted to the left at an arbitrary low value. Figure 4-11 shows specific capacity data for the two test methods and a test section length of 5 m. Figure 4-11 is close to identical to Figure 4-10, which implies that the major reason for the transmissivity differences seen in Figure 4-10 is the difference in specific capacity at shut-in time. In other words, the flow regime after 20 min of constant-head injection with the PSS method is generally not at steady-state, which is more likely the case after c. one week of pumping with the PFL-f method.

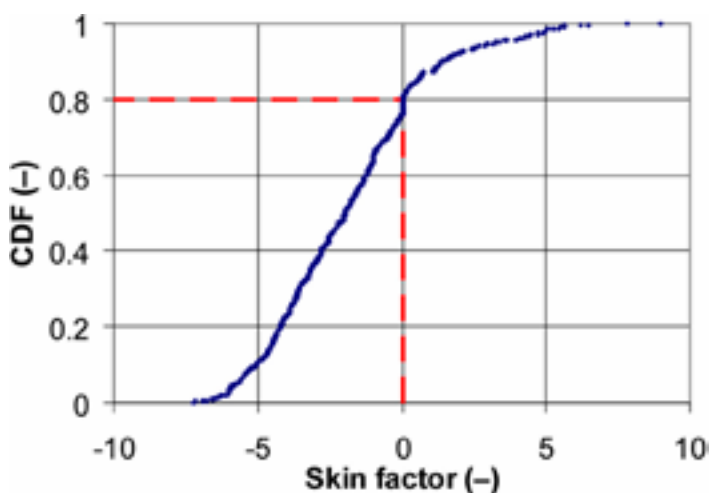


Figure 4-8. Cumulative distribution plot for the skin factors inferred from transient analyses of 550 PSS measurements (5 m test section length) in Forsmark.

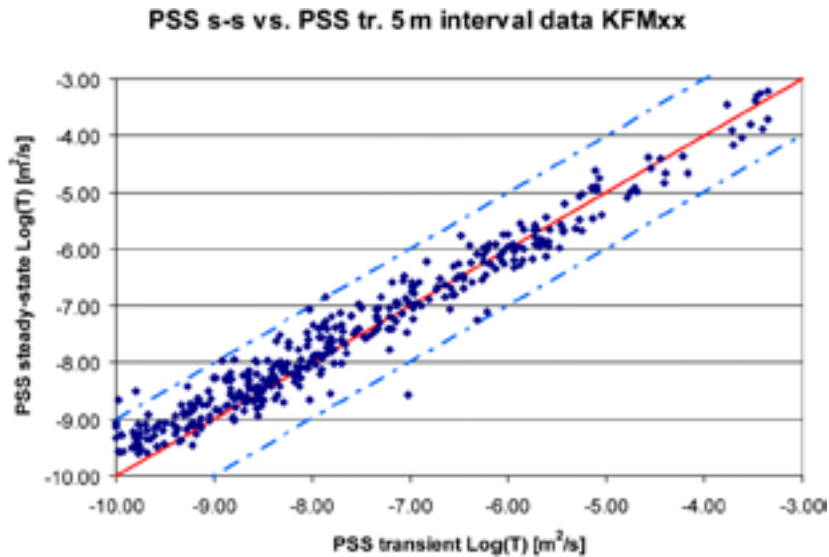


Figure 4-9. Summary cross-plot of PSS 5 m steady-state transmissivity data vs. PSS 5 m transient transmissivity data gathered in cored boreholes at drill sites 1–8. The red line indicates a 1:1 slope and the blue lines a spread of ± 1 order of magnitude.

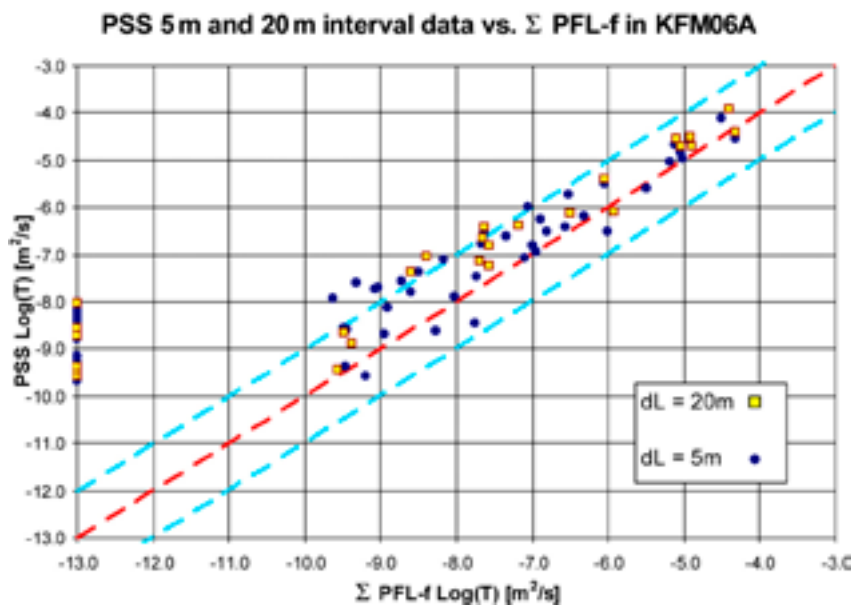


Figure 4-10. Cross-plot of PSS steady-state transmissivity data vs. Σ PFL-f transmissivity data in KFM06A. The red line indicates a unit slope and the blue lines a spread of ± 1 order of magnitude. Data are shown for two test section lengths dL between the PSS packers, i.e. 5 m and 20 m. Transmissivity data from PSS test sections without PFL-f anomalies are plotted to the left at an arbitrary low value on the abscissa.

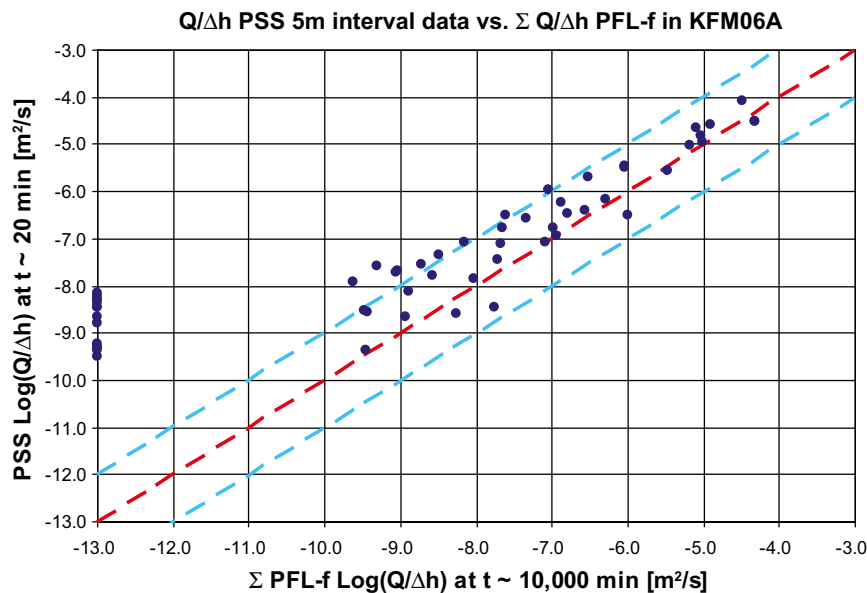


Figure 4-11. Supplementary cross-plot to Figure 4-10 showing PSS specific capacity at c. 20 min of injection vs. Σ PFL-f specific capacity at c. one week of pumping.

/Follin et al. 2006a/ applied a variant of the generalised radial flow (GRF) approach suggested by /Barker 1988/ in an attempt to assess the role of fractional flow regimes and boundary effects for a selected number of boreholes, among them borehole KFM06A. The cross-plot in Figure 4-12 indicates a fairly good agreement between the GRF transmissivity value T_{GRF} and the aforementioned “Best Choice” transmissivity value T_{BC} , except in a few cases where the T_{GRF} values are much greater. The particular cases are denoted by filled squares. The two numbers close to each case represent the associated packer position and the interpreted fractional flow dimension, n , respectively, using the GRF approach. The fractional flow dimensions are in general quite low for these cases, which may indicate either localised flow, channeling or boundary effects. A radial flow regime has a fractional flow dimension of two in theory, which happens to also be the median value of the 58 tests analysed in KFM06A, see Figure 4-13.

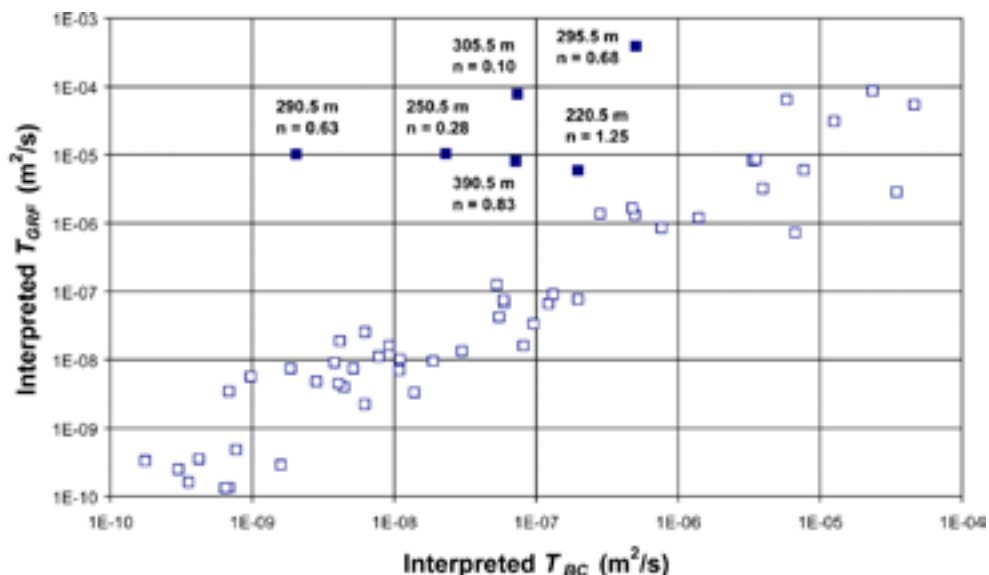


Figure 4-12. Cross-plot of transmissivities derived with the GRF approach T_{GRF} vs. the transmissivities “Best Choice” transmissivities T_{BC} reported to Sicada for KFM06A. The cross-plot indicates a fairly good agreement between the T_{GRF} and the T_{BC} values except in a few cases, where the T_{GRF} values are much greater. The cases are denoted by filled squares. The figures adjacent to the filled squares represent the associated packer positions and the interpreted fractional flow dimensions, n , using the GRF approach, respectively. Reproduced from /Follin et al. 2006a/.

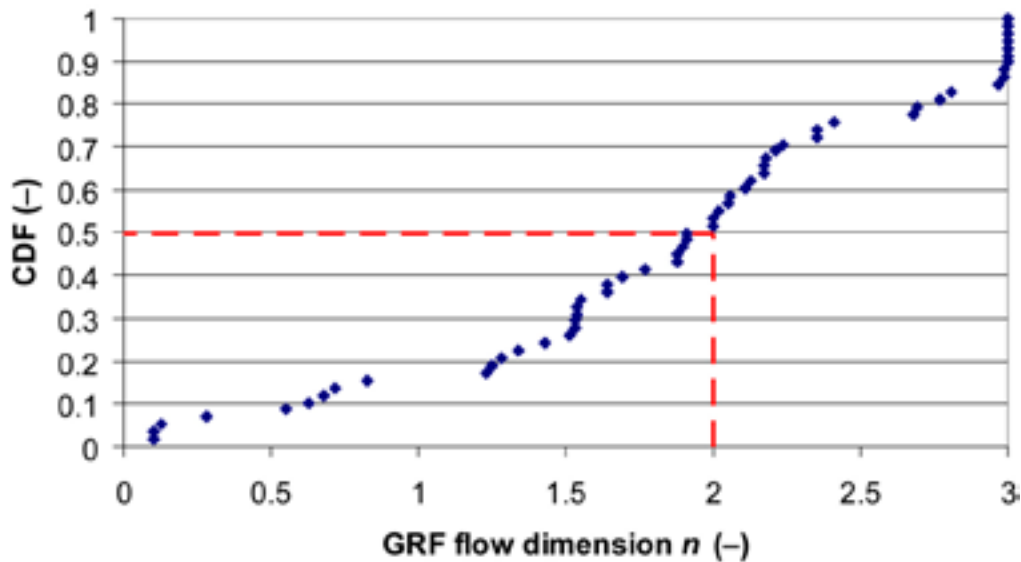


Figure 4-13. Cumulative distribution plot for the fractional flow dimensions inferred from GRF analyses of 58 PSS 5 m tests in KFM06A. Reproduced from /Follin et al. 2006a/.

Figure 4-14 shows a cross-plot of the fractional flow dimensions interpreted from the injection period versus the observed pressure recovery at the end of the recovery period for borehole KFM06A. The pressure recoveries for the sections shown by filled squares are not very good, which suggest poorly connected fracture network geometries for the associated test sections, i.e. compartmentalised fracture networks. /Follin et al. 2006a/ noted that poorly connected networks often render low values of the flow dimension, which in turn render high T_{GRF} values. More details about the analyses behind Figure 4-12 and Figure 4-14 and premises for the comparison are found in /Follin et al. 2006a/.

Figure 4-15 and Figure 4-16 show two other examples of cross-plots of steady-state transmissivity data, i.e. PSS T_{s-s} versus $\sum T_{PFL-f}$. The plot showing KFM04A data are fairly well concentrated on the unit slope throughout, whereas most of the KFM08A data are significantly off with large positive differences of $(PSS T_{s-s} - \sum T_{PFL-f})$.

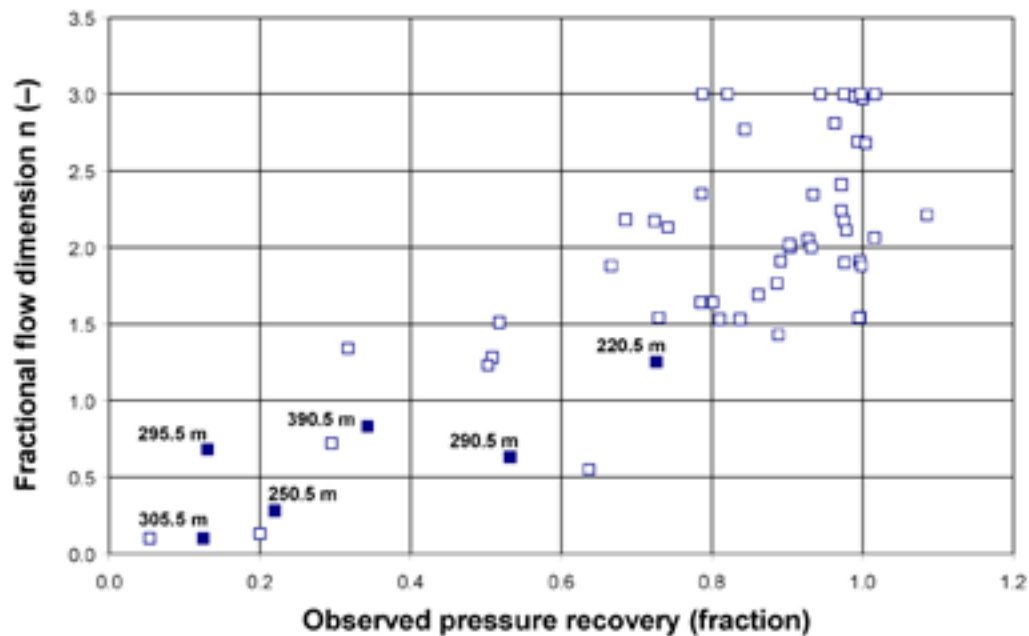


Figure 4-14. Cross-plot of computed fractional flow dimension vs. measured pressure recovery. Reproduced from /Follin et al. 2006a/.

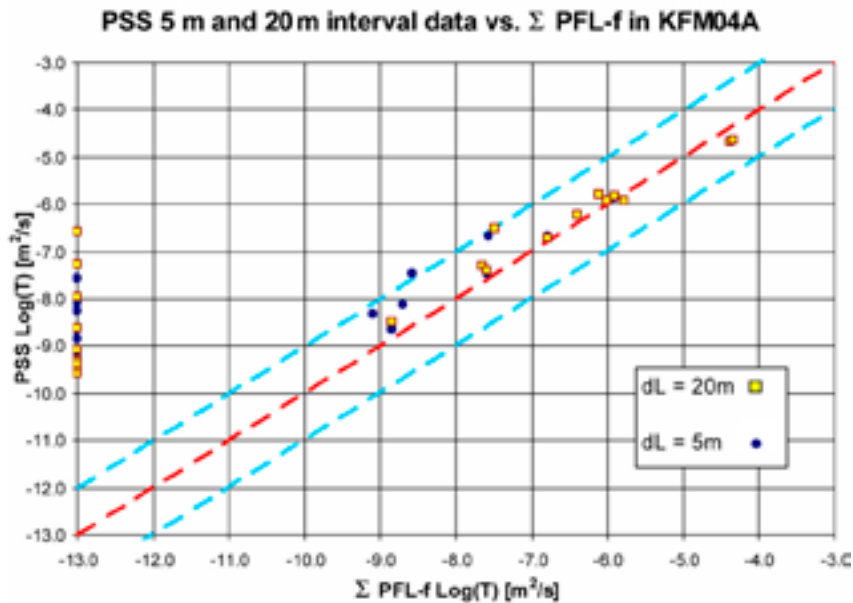


Figure 4-15. Cross-plot of PSS steady-state transmissivity data vs. Σ PFL-f transmissivity data in KFM04A. The red line indicates a unit slope and the blue lines a spread of ± 1 order of magnitude. Data are shown for two test section lengths dL between the PSS packers, i.e. 5 m and 20 m. Transmissivity data from PSS test sections without PFL-f anomalies are plotted to the left at an arbitrary low value on the abscissa.

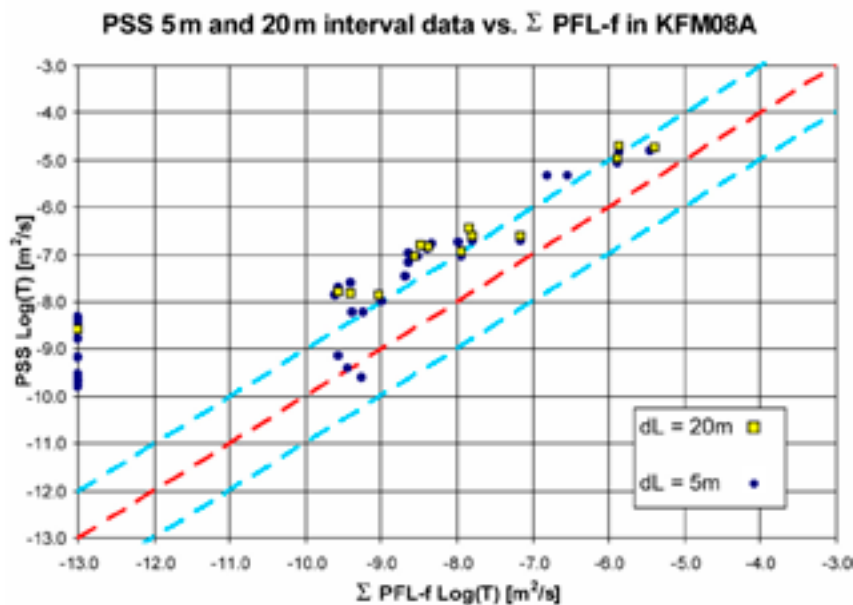


Figure 4-16. Cross-plot of PSS steady-state transmissivity data vs. Σ PFL-f transmissivity data in KFM08A. The red line indicates a unit slope and the blue lines a spread of ± 1 order of magnitude. Data are shown for two test section lengths dL between the PSS packers, i.e. 5 m and 20 m. Transmissivity data from PSS test sections without PFL-f anomalies are plotted to the left at an arbitrary low value on the abscissa.

It was previously mentioned that the flow condition at the shut-in time of the injection period is reported to Sicada. An index of three possible values ($-1, 0, +1$) is used to indicate whether positive effects, infinite acting or negative effects, respectively, could be observed. Figure 4-17 shows a histogram of reported “apparent boundary effects” as envisaged by the operators of the 5 m PSS tests conducted in KFM04A, KFM06A and KFM08A. Evidently, the shut-in conditions in KFM06A and KFM08A are more often judged to be affected by flow constraints than are the conditions in KFM04A.

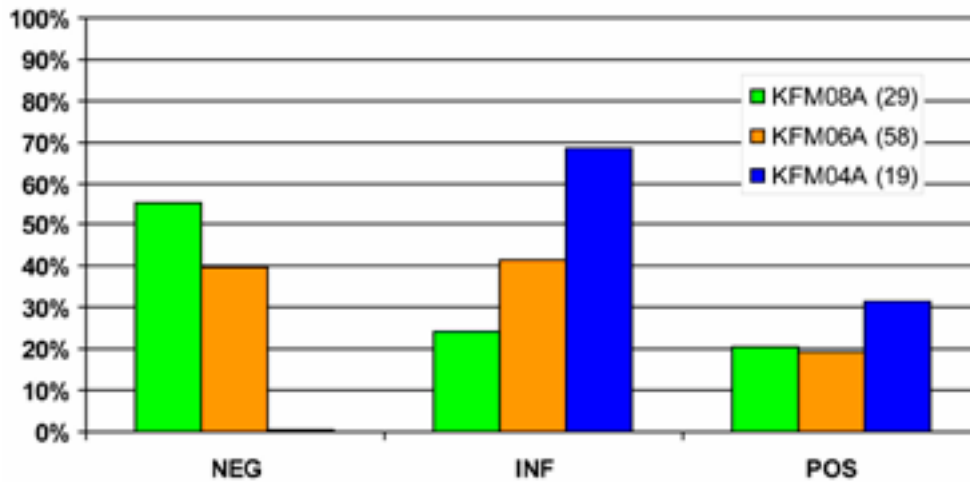


Figure 4-17. Histogram of the “boundary effects” sensed at the shut-in time for the 5 m PSS tests conducted in KFM04A, KFM06A and KFM08, respectively. (Note: There are no “negative boundary effects” reported for KFM04A.)

In summary, some of the differences seen between the cross-plots shown in Figure 4-10, Figure 4-15 and Figure 4-16 may be explained by heterogeneities in the geological conditions, e.g. compartmentalised fracture networks, whereas others may be due to differences in the test procedures including technical differences (equipment performance) rather. In particular, PSS and PFL-f tests are run on quite different temporal and spatial scales. As a consequence, the PSS measurements, as applied in the site investigation programme, focus on the hydraulic conditions close to the borehole, whereas the PFL-f measurements focus on the conditions far away from the borehole. In compartmentalised fracture network systems, this unlikeness is to be expected to make a difference in the type of cross-plots presented above. That is, the PFL-f method cannot address the presence of compartmentalised fracture networks, but is excellent for delineating interconnected flowing fractures. Another vital difference between the two test methods lays in the integration with structural data; that is, fracture orientations and frequencies. The PSS method cannot address such information to the same level of detail nearly as well as the PFL-f method.

On the transmissivity threshold of the PFL-f method

Due to the circumstance discussed above one has to be careful in assuming that the PSS packer test data can necessarily resolve the fracture transmissivity distribution to a lower measurement threshold than the PFL-f method. Notwithstanding, results are given below to quantify the consequences for groundwater flow modelling using one technique over the other.

We consider the cross-plot of PSS 5 m interval steady-state values and the sum of PFL-f fracture transmissivities for the corresponding intervals for all borehole intervals measured by both types of test, as shown in Figure 4-18.

For the PSS method, values for intervals that are indicated as being outside the detection limits for the particular measurement were assigned an arbitrary low transmissivity of $1 \cdot 10^{-13} \text{ m}^2/\text{s}$. For the PFL-f measurements, if no flow-anomalies were identified in the 5 m PSS interval, then the cumulative transmissivity was also assigned as $1 \cdot 10^{-13} \text{ m}^2/\text{s}$. Hence, the points on the ordinate axis correspond to intervals where a transmissivity has been measured by the PSS method, but is below the detection limit of the PFL-f method. Of this group of points, the ones with a larger transmissivity are likely to be associated with either localised networks or with recirculation around the borehole, whilst the lower ones may genuinely correspond to values measured below the PFL-f detection limit, but above the PSS detection limit. Two values occur on the abscissa axis where favourable conditions in the borehole give a lower detection limit for PFL-f below that of PSS.

PSS 5 m interval data vs. Σ PFL-f 5 m interval data all KFMxx

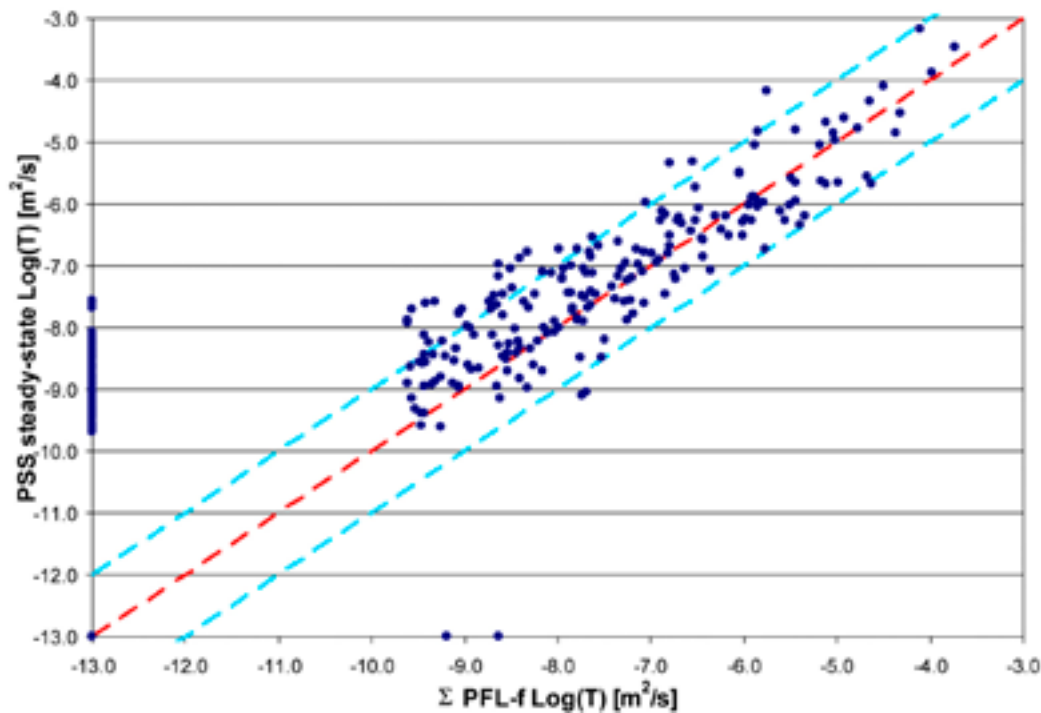


Figure 4-18. Cross-plot of PSS 5 m steady-state transmissivity data vs. Σ PFL-f transmissivity data for all borehole sections with both PSS and PFL-f data. The red line indicates a unit slope and the blue lines a spread of ± 1 order of magnitude. Transmissivity data from PSS test sections without PFL-f anomalies are plotted to the left at an arbitrary low value on the abscissa.

The overall counts of intervals with measured flow in different ranges of transmissivity are tabulated for both methods in Table 4-4. The effective total number of 5 m intervals covered by the PSS method is about 1,540 (Note: This number includes those 100-m or 20-m long packer intervals with no quantifiable flow above the lower detection limit, hence all non-flowing 5-m intervals envisaged were not measured directly²). The cumulative counts of number of intervals with transmissivities greater than the lower detection limit, $1 \cdot 10^{-9}$, $1 \cdot 10^{-8}$, $1 \cdot 10^{-7}$, $1 \cdot 10^{-6}$, $1 \cdot 10^{-5}$ and $1 \cdot 10^{-4}$ m²/s are given, and compared as a cumulative frequency with respect to the total number of measurement intervals in Figure 4-19. These show that the two methods give a very similar distribution down to about $1 \cdot 10^{-8}$ m²/s. This quantifies that the PFL-f method predicts that only 14% of the 5 m packer intervals studied contain continuously flowing fractures after several days of pumping; that is, naturally water bearing fractures connected to the hydro-geological system. The PSS method, on the other hand, predicts that 20% of the 5 m packer intervals have flowing conditions close to the borehole at test shut-in (20 minutes of injection.)

Although it is difficult to characterise the transmissivity distribution below $1 \cdot 10^{-9}$ m²/s, as will be shown in the bedrock transport properties background report, we expect such low transmissive features to have effective solute transport times many times greater than fractures featuring transmissivities greater than $1 \cdot 10^{-9}$ m²/s (allowing for matrix diffusion and possibly sorption in the case of sorbing solutes). The effective transport time for a $1 \cdot 10^{-10}$ m²/s fracture, for example,

² A telescopic approach is used for the PSS testing conducted in Forsmark. Each borehole is measured with consecutive 100-m long, 20-m long and 5-m long packer intervals beginning with the longest packer interval. However, non-flowing 100-m long packer intervals are not studied with 20-m long packer intervals, etc. The telescopic measurement approach saves time but it assumes that low transmissive sections are correctly characterised.

Table 4-4. Summary of cumulative counts of 5m intervals with different ranges of transmissivity based on data from core drilled boreholes that have both PSS and PFL measurements.

Classification	Number of 5 m packer intervals
Effective total PSS measurement coverage	1,540
PSS above detection limit*	304
PSS $T > 1 \cdot 10^{-9} \text{ m}^2/\text{s}$	254
PSS $T > 1 \cdot 10^{-8} \text{ m}^2/\text{s}$	148
PSS $T > 1 \cdot 10^{-7} \text{ m}^2/\text{s}$	84
PSS $T > 1 \cdot 10^{-6} \text{ m}^2/\text{s}$	36
Σ PFL-f T above detection limit*	208
Σ PFL-f $T > 1 \cdot 10^{-9} \text{ m}^2/\text{s}$	173
Σ PFL-f $T > 1 \cdot 10^{-8} \text{ m}^2/\text{s}$	124
Σ PFL-f $T > 1 \cdot 10^{-7} \text{ m}^2/\text{s}$	74
Σ PFL-f $T > 1 \cdot 10^{-6} \text{ m}^2/\text{s}$	40

* The measurement limits of the PSS and the PFL method are slightly different, but they both vary. The lowest real value measured for both methods, in this comparison, was c. $2.5 \cdot 10^{-10} \text{ m}^2/\text{s}$ ($\log T = -9.6$).

should be about 100 times longer than that for a $1 \cdot 10^{-9} \text{ m}^2/\text{s}$ fracture even for very weakly sorbing solutes. The main motivation for disregarding such low transmissive features is that even if they are connected to more transmissive features at a short distance from a canister deposition hole, they can only have a very weak impact on the overall rate of radionuclide release from the repository.

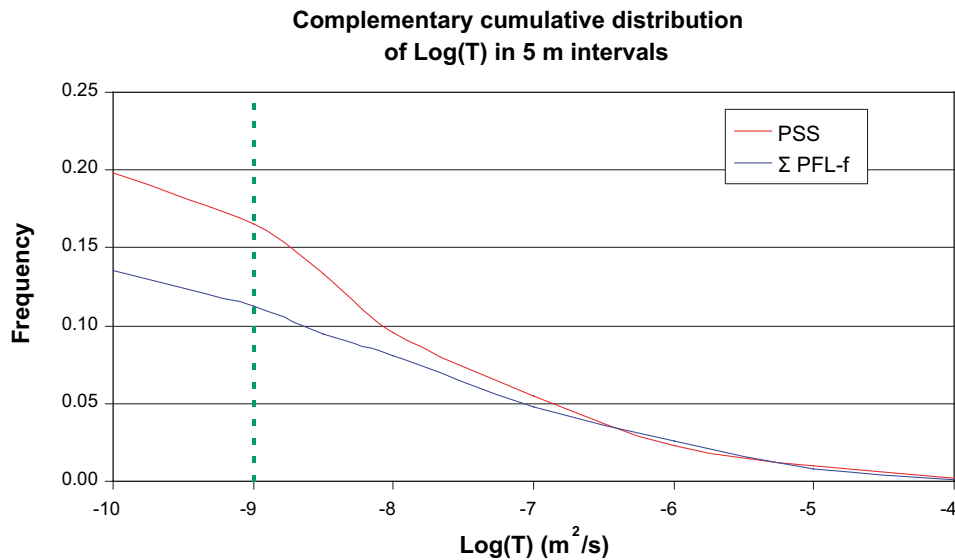


Figure 4-19. Complementary cumulative distribution plot for the frequency of Log(T) in 5 m intervals for the PSS measurements and the PFL-f measurements grouped according to the same 5 m intervals. The frequency is normalised according to the total number of 5 m intervals measured by the PSS technique (i.e. total borehole length of PSS measurements / 5 m). The typical detection limit of the PFL-f technique is shown by the green dotted line.

4.4 Hydraulic tests in percussion-drilled boreholes

The HTHB method is based on pumping and flow logging in an open borehole. The *borehole* transmissivity is determined after a few hours of pumping only and the individual flow contributions along the borehole are determined by means of a cumulative impeller flow log. The practical detection limit varies. In Forsmark a common value observed is about $1 \cdot 10^{-6} \text{ m}^2/\text{s}$.

4.5 Overview of the hydraulic characterisation of the bedrock at repository depth

For the reasons stated in Section 2.2 and in Section 4.3, fracture transmissivity data acquired by the PFL-f method using a measurement interval of 0.1 m is the primary source of data treated in the work presented here. Among the cored borehole data available at the time of data freeze 2.2, KFM01A–08A, -10A, KFM07C–08C and KFM01D were all measured with the PFL-f method using a measurement interval of 0.1 m. KFM09A, KFM03B, KFM06B–09B, KFM01C and KFM06C, were all measured with the PSS method only. Figure 4-20 through Figure 4-24 show cross-plots of PSS 5 m transmissivity data vs. Σ PFL-f (5 m) transmissivity data from the cored boreholes at drill sites 1, 2, 3, 5 and 7. (Data from drill sites 4, 6 and 8 are shown in Section 4.3.)

Figure 4-25 shows that the overall agreement between PSS 5 m test section transmissivity data and Σ PFL-f (5 m) fracture transmissivity data is fairly good for both deformation zones and fracture domains, which suggests that in general both sources of data may be used with a reasonable confidence. Figure 4-25 also suggests that the practical detection limit of c. $1 \cdot 10^{-9} \text{ m}^2/\text{s}$ of the PFL-f method is not an ultimate limit but that reliable data of less magnitudes are observed, at least occasionally. It is noted that the scattering in the data shown in Figure 4-25 is not all due to the physical differences between the PFL-f and PSS methods. The PSS 5 m data shown in Figure 4-20 through Figure 4-25 are derived by means of Moye's formula /Moye 1967/, which assumes a steady-state flow condition. For a 20-minute long testing period this assumption it is doubtful, however.

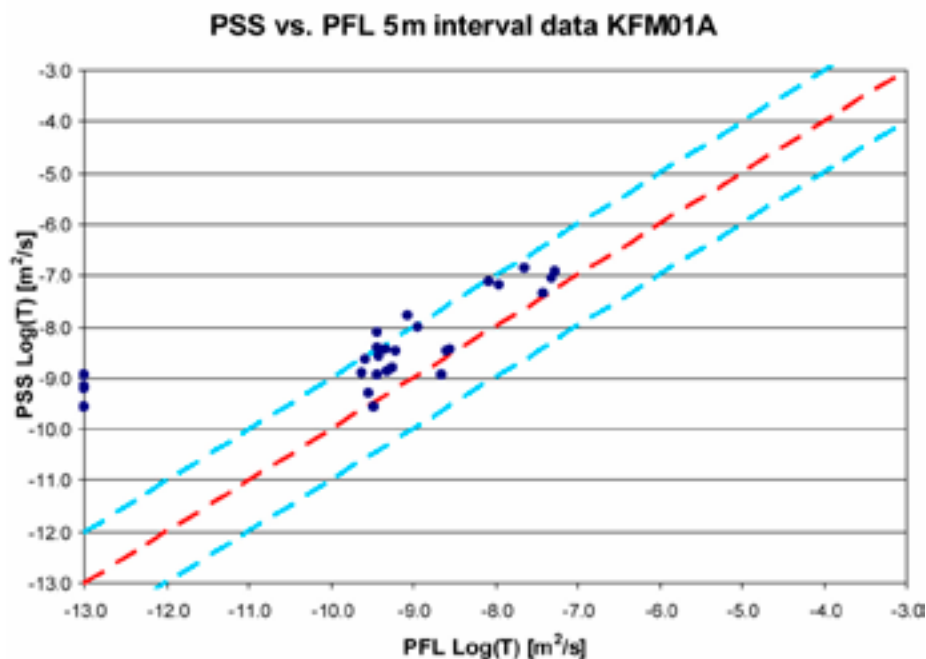


Figure 4-20. Cross-plot of PSS 5 m steady-state transmissivity data vs. Σ PFL-f (5 m) transmissivity data in KFM01A. The coloured lines are inserted to facilitate the reading; the red line indicates a 1.1 slope and the blue lines ± 1 order of magnitude. Transmissivity data from PSS test sections without PFL-f anomalies are plotted to the left at an arbitrary low value on the abscissa.

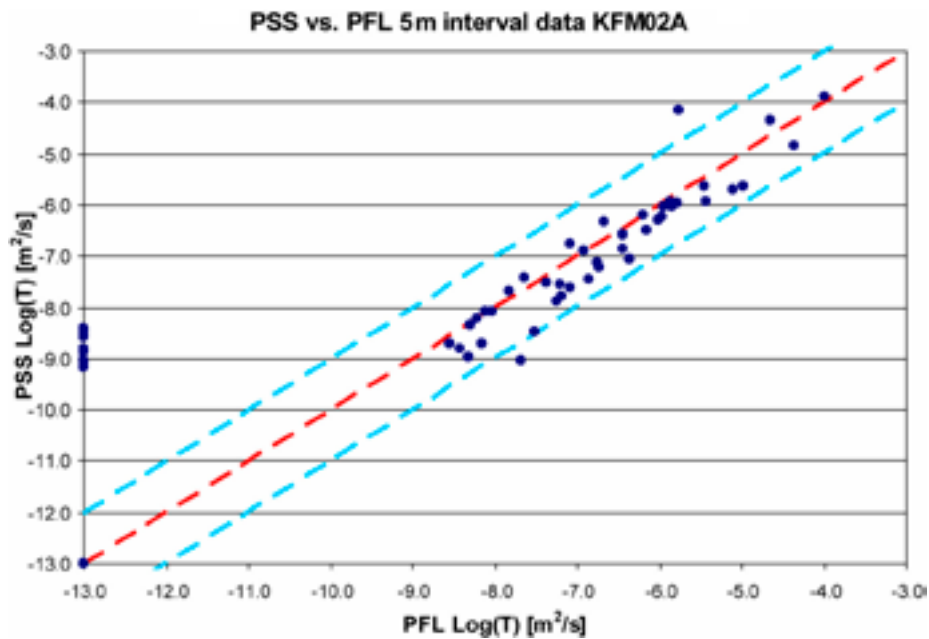


Figure 4-21. Cross-plot of PSS 5 m steady-state transmissivity data vs. Σ PFL-f (5 m) transmissivity data in KFM02A. The coloured lines are inserted to facilitate the reading; the red line indicates a 1:1 slope and the blue lines ± 1 order of magnitude. Transmissivity data from PSS test sections without PFL-f anomalies are plotted to the left at an arbitrary low value on the abscissa.

From Figure 4-20 through Figure 4-24 we conclude that the fracture network conditions close to the boreholes vary in space within the candidate area. In some boreholes several 5-m long test sections identified by the PSS method have higher transmissivities than corresponding Σ PFL-f (5 m) data. This occurs predominantly in the lower end of the cross plots, which suggests that 20-minute long injection tests in ‘low permeable rock’ occasionally emphasise the transmissivity of dead end single fractures or dead end clusters of fractures connected to the pumped borehole depending on the in situ conditions, cf. Section 4.3.

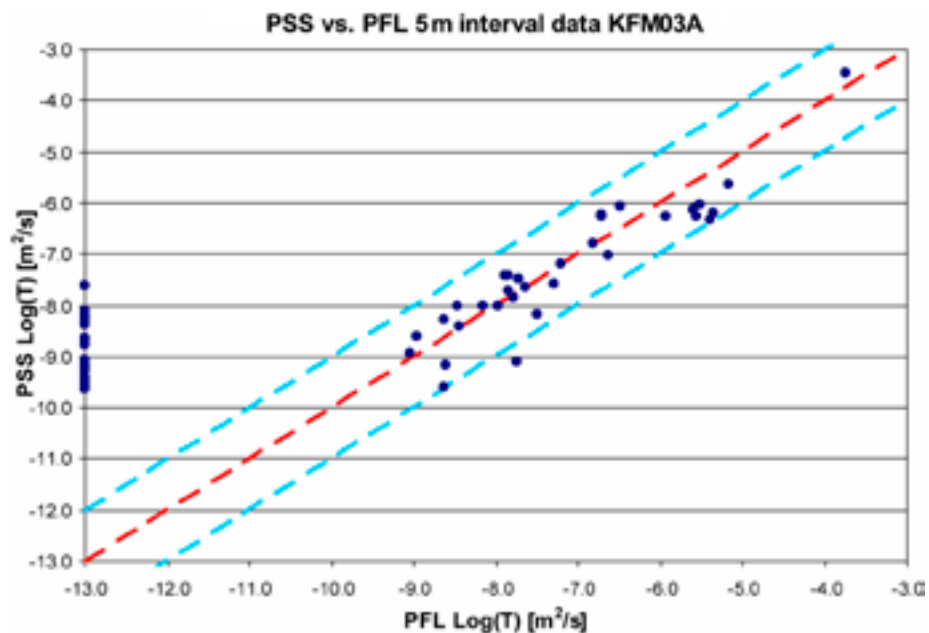


Figure 4-22. Cross-plot of PSS 5 m steady-state transmissivity data vs. Σ PFL-f (5 m) transmissivity data in KFM03A. The coloured lines are inserted to facilitate the reading; the red line indicates a 1:1 slope and the blue lines ± 1 order of magnitude. Transmissivity data from PSS test sections without PFL-f anomalies are plotted to the left at an arbitrary low value on the abscissa.

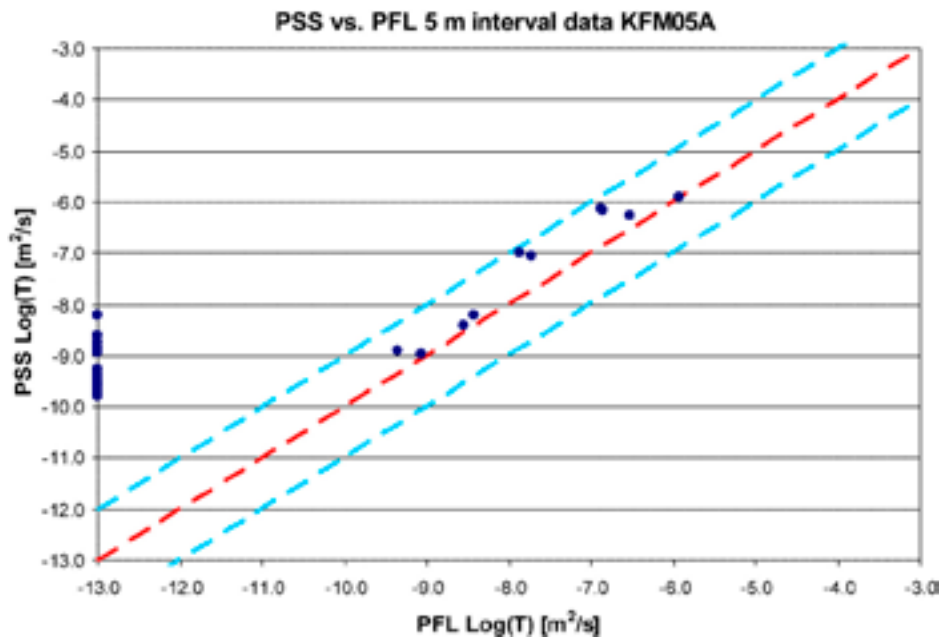


Figure 4-23. Cross-plot of PSS 5 m steady-state transmissivity data vs. Σ PFL-f (5m) transmissivity data in KFM05A. The coloured lines are inserted to facilitate the reading; the red line indicates a 1.1 slope and the blue lines ± 1 order of magnitude. Transmissivity data from PSS test sections without PFL-f anomalies are plotted to the left at an arbitrary low value on the abscissa.

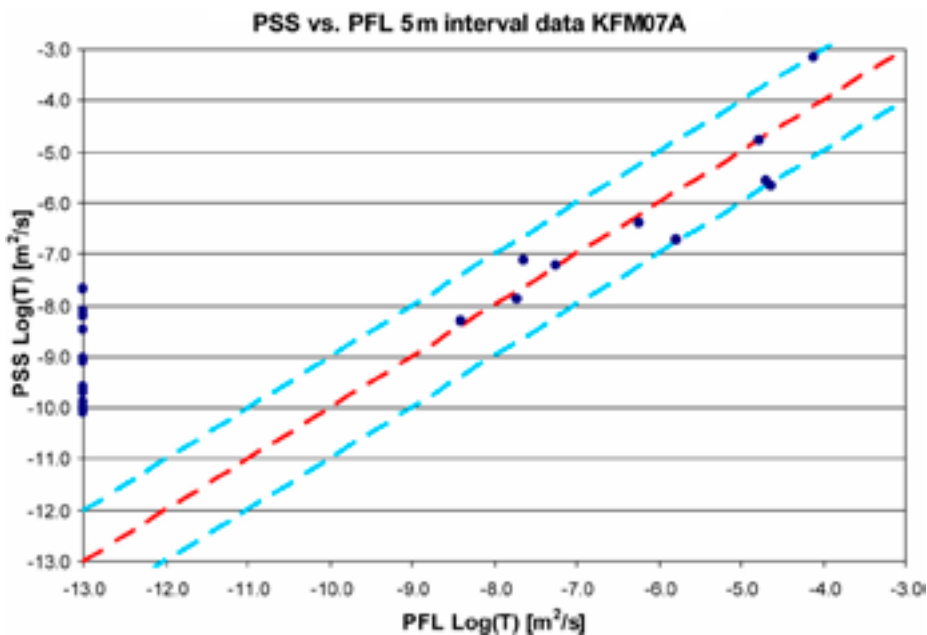


Figure 4-24. Cross-plot of PSS 5 m transmissivity data vs. Σ PFL-f (5m) transmissivity data in KFM07A. The coloured lines are inserted to facilitate the reading; the red line indicates a 1.1 slope and the blue lines ± 1 order of magnitude. Transmissivity data from PSS test sections without PFL-f anomalies are plotted to the left at an arbitrary low value on the abscissa.

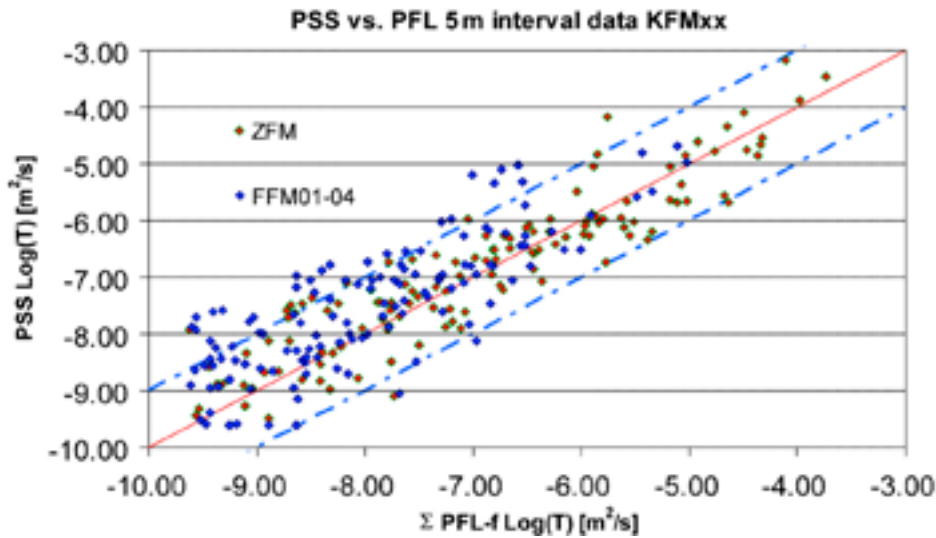


Figure 4-25. Summary cross-plot of PSS 5 m steady-state transmissivity data vs. Σ PFL-f (5m) transmissivity data gathered in cored boreholes at drill site 1–8. The coloured lines are inserted to facilitate the reading; the red line indicates a 1:1 slope and the blue lines ± 1 order of magnitude.

Figure 4-26 shows an example of the in situ condition at repository depth in the north-western part of the tectonic lens. Here the bedrock is sparsely fractured by open (naturally broken and potentially flowing) fractures. About 200 unbroken 3-m-long rock cores have been recorded during the coring drillings (total length c. 15 km). There are very few transmissive fractures above the detection limit of the Posiva Flow Log below 400 m depth.

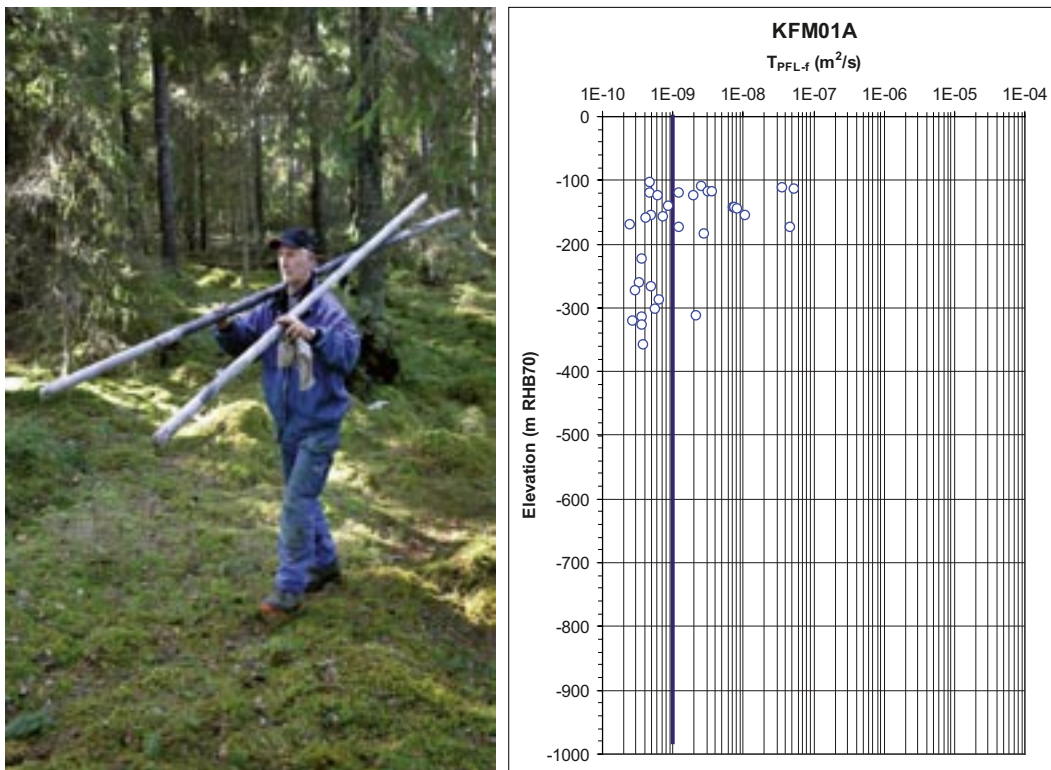


Figure 4-26. About 200 unbroken 3-m-long rock cores have been recorded during the coring drillings (total length c. 15 km). This observation suggests that the bedrock at repository depth in the north-western part of the tectonic lens is sparsely fractured by open (naturally broken) fractures. The mechanical observation is supported by thy hydraulic testing. There are few transmissive fractures above the detection limit of the Posiva Flow Log below 400 m depth. The blue line indicates the investigated depth and the typical practical detection limit of the PFL-f method ($\sim 1 \cdot 10^{-9} \text{ m}^2/\text{s}$).

4.6 Hydraulic characterisation of the near-surface bedrock

A particular problem in Forsmark concerns the geological-hydraulic characterisation of the near-surface bedrock in the north-western part of the tectonic lens. In this area the uppermost c. 100–150 m of the bedrock is heterogeneously intersected by horizontal sheet joints besides the ‘ordinary’ occurrence of fractures and fracture zones. For example, Figure 4-27 shows a picture from the construction of the cooling water canal which runs between the Baltic Sea and the nuclear power reactors parallel to HFM20 and HFM22, see Figure 4-2. The sheet joints observed range across hundreds of metres.

The frequency of sheet joints probably decreases with depth; a tentative estimation for the maximum depth of occurrence is 100–150 m. The combination of extensive near-surface sheet joints and outcropping deformation zones, both gently-dipping and steeply-dipping, is believed to form a well-connected lattice of potential flow paths, which short-circuits the groundwater flow field from above as well as from below, depending on the transmissivities of the discrete features involved. Figure 4-28 shows an illustration of the concept suggested by /Follin et al. 2007b/. The notion that the flow field is short-circuited in the near-surface bedrock is based on several strands of hydrogeological and hydrogeochemical evidence, see /Follin et al. 2007b/. In summary, the situation within the target area in Forsmark may be described as a “hydraulic cage phenomenon”, a concept first presented in /SKB 2006a/.

The cored boreholes in Forsmark generally start at –100 m elevation. The uppermost 100 m are percussion-drilled and cased with a steel casing in order to allow for a hydraulic testing with the PFL-f method, which requires a large-diameter borehole in order to host the submersible pump used for the testing. This means that there are not many cores collected nor fractures tested in detail with the PFL-f method in the uppermost part of the bedrock.



Figure 4-27. Picture from the construction of the 13 m deep and more than one kilometre long canal between the Baltic Sea and the nuclear power reactors. The horizontal fractures/ sheet joints are encountered along the entire excavation. There are several “beds” of extensive sheet joints on top of each other. The picture is taken from the southern side of the canal where the bridge crosses the canal between HFM20 and HFM22, see Figure 4-2. Reproduced from /Carlsson and Christiansson 2007/.

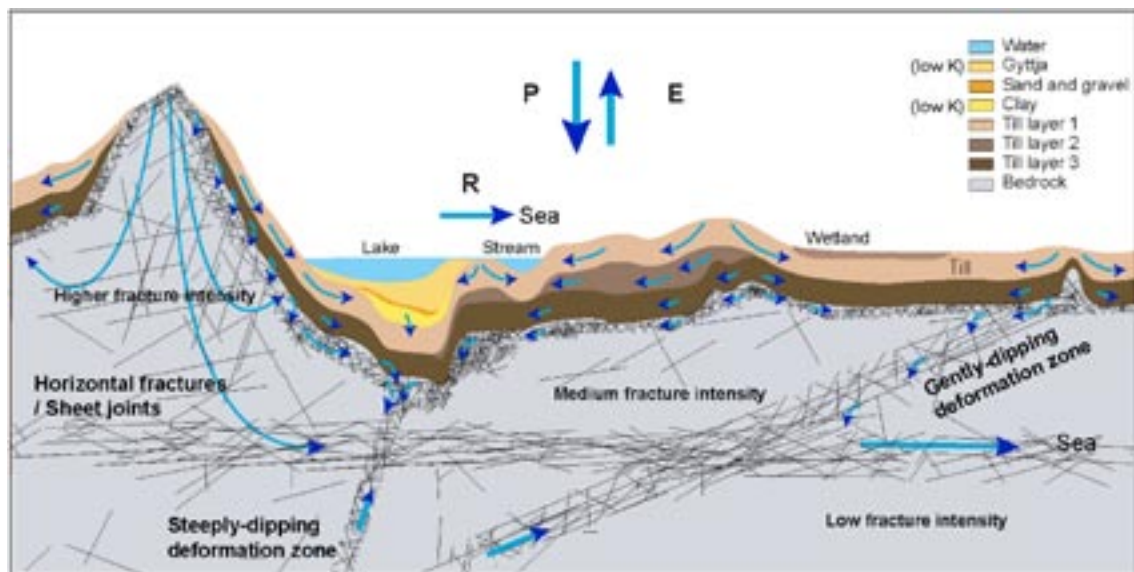


Figure 4-28. Two-dimensional cartoon of the near-surface bedrock in Forsmark. The connectivity caused by horizontal sheet joints and outcropping deformation zones is envisaged to create a hydraulic cage in the north-western part of the tectonic lens. Strands of evidence that support the envisaged hydraulic interplay between the groundwater in the superficial bedrock and in the Quaternary deposits and between surface water and the groundwater in the Quaternary deposits are presented in /Follin et al. 2007b/.

Six boreholes have been cored from the surface and tested with the PSS method in 5 m intervals (KFM01B, KFM03B, and KFM06B–9B). Some of these boreholes were drilled from a rock mechanical purpose, however, which means that they were subjected to a mechanical testing, e.g. hydraulic fracturing, before they were characterised hydraulically with the PSS method. Moreover, in order to prevent fall out in the most intensely fractured parts near the surface, it was necessary to stabilize some of the boreholes with concrete.

In conclusion, the premises for a detailed structural-hydraulic characterisation of flowing fractures in the uppermost c. 100 m of bedrock in Forsmark by means of hydraulic investigations in cored boreholes are constrained for both geological and technical reasons. Here, the many percussion-drilled boreholes shown in Figure 4-2 provide important information regarding the transmissivities of the structures intersected. However, the geological interpretations of the structures intersected by the percussion-drilled boreholes are much less certain due to lack of geological control. Hence, it is unclear if the hydrogeological data (heads) and the hydraulic test responses (transmissivities) observed represent sheet joints, outcropping deformation zones or both. Most likely the situation varies in space from one borehole to the next for one or several reasons. For instance, both the sheet joints and the outcropping deformation zones are known to be hydraulically heterogeneous depending on if they are filled with glaciofluvial sediments or not, see Figure 4-29.

Figure 4-30 shows a compilation of the inferred HTHB impeller flow logging transmissivities divided into intervals of 50 m for the uppermost 200 m of bedrock. The pattern of high and low transmissivities in the uppermost parts of the bedrock is complex and confirms the notion of a lattice of discrete features, some of which may be very transmissive. As indicated in Figure 4-28, the lattice is interpreted to be a combination of several kinds of features, where the most prominent are outcropping deformation zones (both gently and steeply dipping) and horizontal fractures/sheet joints. Further, the large number of gently dipping fractures associated with fracture domain FFM02 probably also contributes to the characteristic hydrogeology. This notion is revisited later on in this work reported here.



Figure 4-29. Two pictures of the near-surface bedrock in the north-western part of the tectonic lens (target area). The leftmost picture shows structurally dominant, but highly heterogeneous, horizontal sheet joints where the apertures are clogged by glaciofluvial sediments. This phenomenon is known to occur down to at least c. 50 m depth (KFM03A and HFM07) rightmost picture shows the flushing of a high yielding gently dipping deformation zone or sheet joint encountered at c. 40 m depth in HFM02.

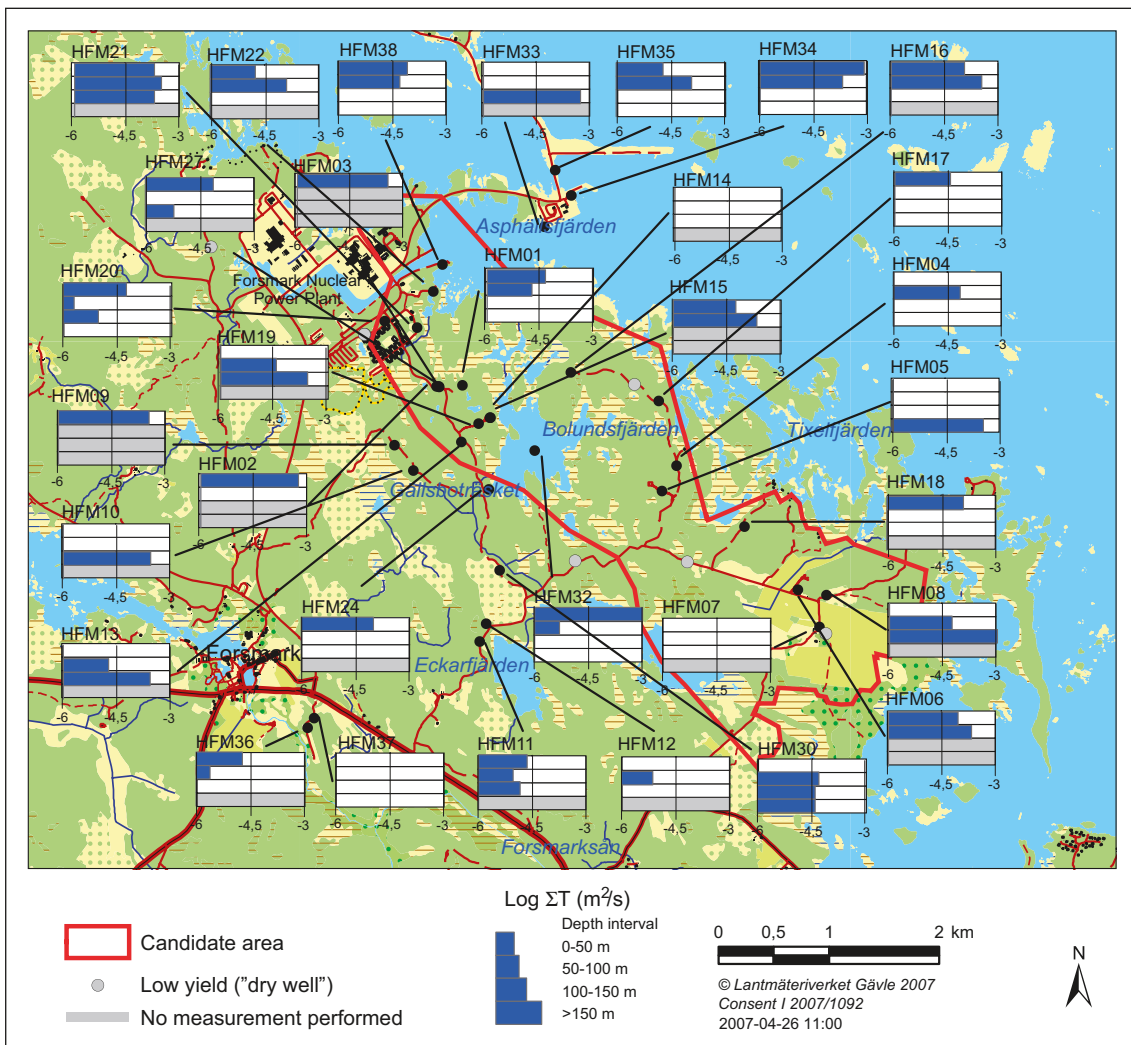


Figure 4-30. HTHB transmissivities lumped into intervals of 50 m for the uppermost 200 m of bedrock. The logarithmic transmissivity scale ranges from 10^{-6} to 10^{-3} m^2/s .

5 Structural-hydraulic data in cored boreholes

5.1 Deformation zones and possible deformation zones

Table 5-1 through Table 5-20 display PFL-f fracture transmissivity and/or PSS 5m test section transmissivity data observed in the 20 boreholes treated here; that is, KFM01A–10A, KFM03B, -06B–09B, KFM01C, -06C, -08C and KFM01D.

The columns show rock domain (RFM), deformation zone (ZFM), fracture domain (FFM), borehole length (Sec-up/-low) and elevation (Elev-up/-low) [metres RHB 70]. For those boreholes where transmissivity measurements were made with both the PFL-method and the PSS method, data from the latter method were omitted in favour of the former. All transmissivities are given in [m²/s]. The interpreted main direction of orientation of the possible deformation zones is provided between parentheses, where G = gently dipping and S = steeply dipping and xxx = bearing.

The structural interpretation in the second column uses the colour legend shown in Table 3-2. The structural interpretation in the third column uses the colour legend shown in Table 3-3.

5.1.1 Drill site 1

Table 5-1. Compilation of PFL-f transmissivity data gathered in KFM01A.

RFMxxx	ZFMxxxx	FFMxx	Sec-up	Sec-low	Elev-up	Elev-low	No. PFL-f	Σ T PFL-F
RFM029		FFM02	102	203	-98	-199	23	1.92·10 ⁻⁷
RFM029		FFM01	203	216	-199	-212	0	0
RFM029	Possible (G)		216	224	-212	-220	0	0
RFM029		FFM01	224	267	-220	-262	2	7.09·10 ⁻¹⁰
RFM029	ZFMENE1192		267	285	-262	-280	2	7.79·10 ⁻¹⁰
RFM029		FFM01	285	386	-280	-380	7	4.76·10 ⁻⁹
RFM029	ZFMENE1192		386	412	-380	-406	0	0
RFM029		FFM01	412	639	-406	-630	0	0
RFM029	ZFMENE2254		639	684	-630	-674	0	0
RFM029		FFM01	684	1,001	-674	-982	0	0

Table 5-2. Compilation of PSS transmissivity data gathered in KFM01C.

RFMxxx	ZFMxxxx	FFMxx	Sec-up	Sec-low	Elev-up	Elev-low	No. PSS 5 m	Σ T PSS 5m
RFM029		FFM02	12	23	-6	-15	23	4.19·10 ⁻⁵
RFM029	ZFMA2, ZFMENE1192		23	48	-15	-34	5	4.82·10 ⁻⁴
RFM029		FFM02	48	62	-34	-44	3	4.02·10 ⁻⁷
RFM029	ZFMA2		62	99	-44	-72	8	1.13·10 ⁻³
RFM029		FFM02	99	121	-72	-89	4	4.70·10 ⁻⁷
RFM029	Possible DZ (G)		121	124	-89	-91	2	9.03·10 ⁻⁸
RFM029		FFM02	124	235	-91	-175	23	1.96·10 ⁻⁷
RFM029	ZFMENE0060A		235	252	-175	-187	5	3.48·10 ⁻⁹
RFM029		FFM01	252	305	-187	-227	10	4.23·10 ⁻⁹
RFM029	ZFMENE0060C		305	330	-227	-245	6	3.37·10 ⁻⁹
RFM029		FFM01	330	450	-245	-332	22	3.36·10 ⁻⁸

Table 5-3. Compilation of PFL-f transmissivity data gathered in KFM01D.

RFMxxx	ZFMxxxx	FFMxx	Sec-up	Sec-low	Elev-up	Elev-low	No. PFL-f	ΣT PFL-F
RFM029		FFM02	92	176	-72	-141	23	$5.33 \cdot 10^{-6}$
RFM029	Possible DZ (S-NNW)		176	184	-141	-147	0	0.00
RFM029		FFM02	184	191	-147	-153	0	0.00
RFM029		FFM01	191	411	-153	-325	9	$4.22 \cdot 10^{-7}$
RFM029	Possible DZ (S-NNW)		411	421	-325	-332	0	0.00
RFM029		FFM01	421	488	-332	-383	1	$6.23 \cdot 10^{-8}$
RFM029	Possible DZ (S-NNW)		488	496	-383	-389	0	0.00
RFM029		FFM01	496	670	-389	-517	1	$1.59 \cdot 10^{-8}$
RFM029	ZFMENE0061		670	700	-517	-538	0	0.00
RFM029		FFM01	700	771	-538	-589	0	0.00
RFM029	Possible DZ (S-ENE)		771	774	-589	-591	0	0.00
RFM029		FFM01	774	800	-591	-609	0	0.00

5.1.2 Drill site 2

Table 5-4. Compilation of PFL-f transmissivity data gathered in KFM02A.

RFMxxx	ZFMxxxx	FFMxx	Sec-up	Sec-low	Elev-up	Elev-low	No. PFL-f	ΣT PFL-F
RFM029		FFM03	100	110	-92	-102	1	$3.28 \cdot 10^{-8}$
RFM029	ZFM866		110	122	-102	-114	14	$1.07 \cdot 10^{-4}$
RFM029		FFM03	122	160	-114	-152	5	$1.66 \cdot 10^{-7}$
RFM029	ZFMA3		160	184	-152	-176	21	$3.46 \cdot 10^{-6}$
RFM029		FFM03	184	240	-176	-232	3	$7.78 \cdot 10^{-7}$
RFM029	ZFM1189		240	310	-232	-302	10	$1.03 \cdot 10^{-6}$
RFM029		FFM03	310	417	-302	-408	3	$7.62 \cdot 10^{-8}$
RFM029	ZFMA2		417	442	-408	-433	14	$2.85 \cdot 10^{-6}$
RFM029		FFM01	442	476	-433	-467	10	$1.90 \cdot 10^{-7}$
RFM029	ZFMF1		476	520	-467	-511	22	$4.66 \cdot 10^{-6}$
RFM029	Possible DZ (G)		520	600	-511	-590	0	0.00
RFM029		FFM01	600	893	-590	-881	0	0.00
RFM029	ZFMB4		893	905	-881	-892	1	$2.62 \cdot 10^{-9}$
RFM029		FFM01	905	922	-892	-909	0	0.00
RFM029	Possible DZ (G)		922	925	-909	-912	0	0.00
RFM029		FFM01	925	976	-912	-963	0	0.00
RFM029	Possible DZ (G)		976	982	-963	-969	0	0.00
RFM029		FFM01	982	1,001	-969	-987	0	0.00

5.1.3 Drill site 3

Table 5-5. Compilation of PFL-f transmissivity data gathered in KFM03A.

RFMxxx	ZFMxxxx	FFMxx	Sec-up	Sec-low	Elev-up	Elev-low	No. PFL-f	ΣT PFL-F
RFM029		FFM03	102	220	-93	-211	9	$2.10 \cdot 10^{-7}$
RFM017		FFM03	220	293	-211	-284	0	0.00
RFM017		FFM03	293	356	-284	-347	2	$4.60 \cdot 10^{-9}$
RFM029	ZFMA4		356	399	-347	-390	20	$1.01 \cdot 10^{-4}$
RFM029		FFM03	399	448	-390	-438	2	$2.01 \cdot 10^{-8}$
RFM029	ZFMA7		448	455	-438	-445	3	$6.72 \cdot 10^{-6}$
RFM029		FFM03	455	638	-445	-627	5	$6.06 \cdot 10^{-8}$
RFM029	ZFMB1		638	646	-627	-635	2	$2.50 \cdot 10^{-6}$
RFM029		FFM03	646	803	-635	-791	0	0.00
RFM029	ZFMA3		803	816	-791	-804	2	$2.86 \cdot 10^{-8}$
RFM029		FFM03	816	942	-804	-929	0	0.00
RFM029	Possible DZ (G)		942	949	-929	-936	2	$3.46 \cdot 10^{-7}$
RFM029		FFM03	949	1,000	-936	-987	5	$3.06 \cdot 10^{-7}$

Table 5-6. Compilation of PSS transmissivity data gathered in KFM03B.

RFMxxx	ZFMxxxx	FFMxx	Sec-up	Sec-low	Elev-up	Elev-low	No. PSS 5 m	ΣT PSS 5m
RFM029		FFM03	6	24	+2	-15	3	$1.06 \cdot 10^{-6}$
RFM029	ZFMA5		24	42	-15	-33	4	$2.32 \cdot 10^{-5}$
RFM029		FFM03	42	62	-33	-53	4	$3.06 \cdot 10^{-6}$
RFM029	Possible DZ (G)		62	67	-53	-58	1	$1.01 \cdot 10^{-5}$
RFM029		FFM03	67	97	-58	-88	5	$1.55 \cdot 10^{-7}$

5.1.4 Drill site 4

Table 5-7. Compilation of PFL-f transmissivity data gathered in KFM04A.

RFMxxx	ZFMxxxx	FFMxx	Sec-up	Sec-low	Elev-up	Elev-low	No. PSS 5 m	ΣT PSS 5m
RFM018		FFM04	109	110	-87	-88	1	$1.39 \cdot 10^{-7}$
RFM018	ZFMNW1200		110	176	-88	-146	35	$6.48 \cdot 10^{-5}$
RFM018		FFM04	176	177	-146	-147	0	0.00
RFM012		FFM04	177	202	-147	-169	12	$9.88 \cdot 10^{-7}$
RFM012	ZFMA2		202	242	-169	-204	7	$8.79 \cdot 10^{-5}$
RFM012		FFM04	242	290	-204	-245	2	$2.19 \cdot 10^{-8}$
RFM012	ZFMNE1188		290	370	-245	-313	10	$1.46 \cdot 10^{-6}$
RFM012		FFM04	370	412	-313	-348	0	0.00
RFM012	ZFMNE1188		412	462	-348	-389	2	$1.38 \cdot 10^{-8}$
RFM012		FFM04	462	500	-389	-420	0	0.00
RFM029		FFM01	500	654	-420	-541	1	$1.41 \cdot 10^{-9}$
RFM029	ZFMWNW0123		654	661	-541	-546	0	0.00
RFM029		FFM01	661	953	-546	-761	0	0.00
RFM029	Possible DZ (S-NNW)		953	956	-761	-763	1	$1.29 \cdot 10^{-9}$
RFM029		FFM01	956	1,001	-763	-794	0	0.00

5.1.5 Drill site 5

Table 5-8. Compilation of PFL-f transmissivity data gathered in KFM05A.

RFMxxx	ZFMxxxx	FFMxx	Sec-up	Sec-low	Elev-up	Elev-low	No. PFL-f	Σ T PFL-F
RFM029	ZFMA2		102	114	-83	-93	6	1.25·10 ⁻³
RFM029		FFM02	114	237	-93	-199	18	1.80·10 ⁻⁶
RFM029		FFM01	237	395	-199	-333	1	1.86·10 ⁻⁸
RFM029	ZFMENE2282		395	436	-333	-366	0	0.00
RFM029		FFM01	436	590	-366	-492	0	0.00
RFM029	ZFMENE0401B		590	616	-492	-514	0	0.00
RFM029		FFM01	616	685	-514	-570	0	0.00
RFM029	ZFMENE0401A		685	720	-570	-598	2	1.20·10 ⁻⁸
RFM029		FFM01	720	892	-598	-738	0	0.00
RFM029	ZFMENE0103		892	916	-738	-757	0	0.00
RFM029		FFM01	916	936	-757	-773	0	0.00
RFM029	ZFMENE2383		936	992	-773	-818	0	0.00
RFM029		FFM01	992	1,000	-818	-825	0	0.00

5.1.6 Drill site 6

Table 5-9. Compilation of PFL-f transmissivity data gathered in KFM06A.

RFMxxx	ZFMxxxx	FFMxx	Sec-up	Sec-low	Elev-up	Elev-low	No. PFL-f	Σ T PFL-F
RFM029		FFM02	102	128	-84	-107	12	8.13·10 ⁻⁶
RFM029	Possible DZ (G)		128	146	-107	-122	17	3.90·10 ⁻⁵
RFM029		FFM01	146	195	-122	-164	19	1.42·10 ⁻⁵
RFM029	ZFMENE0060B		195	278	-164	-235	26	4.54·10 ⁻⁵
RFM029		FFM01	278	318	-235	-269	4	4.28·10 ⁻⁸
RFM029	ZFMB7, ZFMENE0060A		318	358	-269	-303	13	9.79·10 ⁻⁷
RFM029		FFM01	358	518	-303	-436	3	2.67·10 ⁻⁸
RFM029	ZFMNNE2273		518	545	-436	-459	0	0.00
RFM029		FFM01	545	619	-459	-520	0	0.00
RFM029	ZFMNNE2255		619	624	-520	-524	1	4.26·10 ⁻¹⁰
RFM029		FFM01	624	652	-524	-547	0	0.00
RFM029	Possible DZ (S-NNE)		652	656	-547	-551	1	2.74·10 ⁻¹⁰
RFM029		FFM01	656	740	-551	-620	0	0.00
RFM029	ZFMNNE0725		740	775	-620	-648	1	3.40·10 ⁻⁷
RFM045		FFM06	775	788	-648	-659	0	0.00
RFM045	ZFMENE0061		788	810	-659	-677	0	0.00
RFM045		FFM06	810	882	-677	-734	0	0.00
RFM045	Possible DZ (S-NNE)		882	905	-734	-753	0	0.00
RFM045		FFM06	905	925	-753	-769	0	0.00
RFM045	Possible DZ (S-NNE)		925	933	-769	-775	0	0.00
RFM045		FFM06	933	950	-775	-789	0	0.00
RFM045	ZFMNNE2280		950	990	-789	-820	0	0.00
RFM045		FFM06	990	998	-820	-827	0	0.00

Table 5-10. Compilation of PSS transmissivity data gathered in KFM06B.

RFMxxx	ZFMxxxx	FFMxx	Sec-up	Sec-low	Elev-up	Elev-low	No. PSS 5 m	ΣT PSS 5m
029		FFM02	6	55	-2	-51	10	$3.36 \cdot 10^{-4}$
029	ZFMA8		55	93	-51	-88	0	$2.42 \cdot 10^{-4}$
029		FFM02	93	98	-88	-93	-	-

Table 5-11. Compilation of PSS transmissivity data gathered in KFM06C.

RFMxxx	ZFMxxxx	FFMxx	Sec-up	Sec-low	Elev-up	Elev-low	No. PSS 5 m	ΣT PSS 5m
RFM029	Possible DZ (G)		102	169	-83	-140	10	$8.74 \cdot 10^{-5}$
RFM029		FFM01	169	283	-140	-234	23	$2.19 \cdot 10^{-5}$
RFM029	ZFMNNE2008		283	306	-234	-253	4	$3.40 \cdot 10^{-7}$
RFM029		FFM01	306	359	-253	-296	11	$3.48 \cdot 10^{-6}$
RFM029	ZFMB7		359	400	-296	-328	5	$5.67 \cdot 10^{-6}$
RFM029		FFM01	400	411	-328	-337	2	$2.63 \cdot 10^{-9}$
RFM045		FFM06	411	415	-337	-340	1	$1.16 \cdot 10^{-9}$
RFM045	ZFMNNE2263		415	489	-340	-397	10	$1.84 \cdot 10^{-7}$
RFM045		FFM06	489	502	-397	-407	-	-
RFM045	ZFMWNW0044		502	555	-407	-448	4	$1.22 \cdot 10^{-6}$
RFM045		FFM06	555	623	-448	-500	-	-
RFM045	Possible DZ (S-NNE/WNW)		623	677	-500	-540	9	$9.33 \cdot 10^{-8}$
RFM045		FFM06	677	898	-540	-703	14	$1.03 \cdot 10^{-8}$
RFM032		FFM05	898	1,000	-703	-776	7	$1.47 \cdot 10^{-8}$

5.1.7 Drill site 7

Table 5-12. Compilation of PFL-f transmissivity data gathered in KFM07A.

RFMxxx	ZFMxxxx	FFMxx	Sec-up	Sec-low	Elev-up	Elev-low	No. PFL-f	ΣT PFL-F
RFM029		FFM02	102	108	-85	-90	0	0.00
RFM029	ZFM1203, ZFMNNW0404		108	185	-90	-156	22	$1.41 \cdot 10^{-4}$
RFM029		FFM01	185	196	-156	-165	0	0.00
RFM029	Possible DZ (G)		196	205	-165	-173	0	0.00
RFM029		FFM01	205	417	-173	-351	1	$9.27 \cdot 10^{-8}$
RFM029	ZFMENE0159A		417	422	-351	-355	0	0.00
RFM029		FFM01	422	793	-355	-657	0	0.00
RFM044		FFM05	793	803	-657	-665	0	0.00
RFM044	ZFMENE1208B		803	840	-665	-694	0	0.00
RFM044		FFM05	840	857	-694	-708	0	0.00
RFM044	ZFMENE1208A		857	897	-708	-739	0	0.00
RFM044		FFM05	897	920	-739	-756	2	$4.00 \cdot 10^{-7}$
RFM044	ZFMB8, ZFMNNW0100		920	999	-756	-815	1	$2.00 \cdot 10^{-7}$

Table 5-13. Compilation of PSS transmissivity data gathered in KFM07B.

RFMxxx	ZFMxxxx	FFMxx	Sec-up	Sec-low	Elev-up	Elev-low	No. PSS 5 m	Σ T PSS 5m
RFM029		FFM02	5	51	-1	-38	-	-
RFM029	Possible DZ (G)		51	58	-38	-43	-	-
RFM029		FFM02	58	93	-43	-71	-	-
RFM029	ZFM1203		93	102	-71	-78	-	-
RFM029		FFM02	102	119	-78	-92	-	-
RFM029	Possible DZ (G)		119	135	-92	-104	-	-
RFM029		FFM02	135	195	-104	-151	-	-
RFM029		FFM01	195	225	-151	-175	2	3.30·10 ⁻¹⁰
RFM029	ZFMENE2320		225	245	-175	-190	4	4.36·10 ⁻⁸
RFM029		FFM01	245	298	-190	-233	-	-

Table 5-14. Compilation of PFL-f transmissivity data gathered in KFM07C.

RFMxxx	ZFMxxxx	FFMxx	Sec-up	Sec-low	Elev-up	Elev-low	No. PFL-f	Σ T PFL-F
RFM029		FFM02	85	92	-82	-88	0	0.00
RFM029	ZFM1203		92	103	-88	-99	1	4.81·10 ⁻⁵
RFM029		FFM02	103	123	-99	-119	5	1.12·10 ⁻⁷
RFM029		FFM01	123	308	-119	-303	8	4.71·10 ⁻⁵
RFM029	ZFMENE2320		308	388	-303	-383	0	0.00
RFM029		FFM01	388	429	-383	-424	0	0.00
RFM029	ZFMENE2320		429	439	-424	-434	0	0.00
RFM029		FFM01	439	498	-434	-493	0	0.00

5.1.8 Drill site 8

Table 5-15. Compilation of PFL-f transmissivity data gathered in KFM08A.

RFMxxx	ZFMxxxx	FFMxx	Sec-up	Sec-low	Elev-up	Elev-low	No. PFL-f	Σ T PFL-F
RFM029		FFM01	102	172	-86	-144	9	2.20·10 ⁻⁸
RFM029		FFM01	172	244	-144	-204	15	4.06·10 ⁻⁶
RFM029	ZFMENE1061A		244	315	-204	-262	6	1.31·10 ⁻⁶
RFM029		FFM01	315	479	-262	-392	8	1.47·10 ⁻⁸
RFM029	ZFMNNW1204		479	496	-392	-405	2	6.93·10 ⁻⁸
RFM029		FFM01	496	528	-405	-430	0	0.00
RFM029	Possible DZ (S-NNE)		528	557	-430	-451	0	0.00
RFM029		FFM01	557	624	-451	-500	0	0.00
RFM029	Possible DZ (S-NNW)		624	624	-500	-501	0	0.00
RFM029		FFM01	624	672	-501	-536	0	0.00
RFM029	Possible DZ (S-WNW)		672	693	-536	-551	1	1.41·10 ⁻⁶
RFM029		FFM01	693	775	-551	-608	0	0.00
RFM029	ZFMENE2248		775	843	-608	-654	0	0.00
RFM032		FFM05	843	915	-654	-700	0	0.00
RFM032	Possible DZ (S-WNW)		915	946	-700	-719	0	0.00
RFM034		FFM01	946	967	-719	-732	0	0.00
RFM034	Possible DZ (S-WNW)		967	976	-732	-738	0	0.00
RFM034		FFM01	976	1,001	-738	-753	0	0.00

Table 5-16. Compilation of PSS transmissivity data gathered in KFM08B.

RFMxxx	ZFMxxxx	FFMxx	Sec-up	Sec-low	Elev-up	Elev-low	No. PSS 5 m	Σ T PSS 5m
RFM029		FFM02	6	46	-3	-37	8	9.94·10 ⁻⁵
RFM029		FFM01	46	133	-37	-111	10	7.91·10 ⁻⁷
RFM029	ZFMNNW1205		133	140	-111	-117	1	1.22·10 ⁻⁹
RFM029		FFM01	140	167	-117	-139	3	8.61·10 ⁻⁸
RFM029	ZFMNNW1205		167	185	-139	-154	5	5.60·10 ⁻⁸
RFM029		FFM01	185	200	-154	-167	2	1.54·10 ⁻⁶

Table 5-17. Compilation of PFL-f transmissivity data gathered in KFM08C.

RFMxxx	ZFMxxxx	FFMxx	Sec-up	Sec-low	Elev-up	Elev-low	No. PFL-f	Σ T PFL-F
RFM029		FFM01	102	161	-86	-137	2	2.95·10 ⁻⁶
RFM029	Possible DZ (S-NNE)		161	191	-137	-162	2	6.68·10 ⁻⁹
RFM029		FFM01	191	342	-162	-289	3	8.76·10 ⁻⁹
RFM045		FFM06	342	419	-289	-353	0	0.00
RFM045	ZFMNNE2312		419	542	-353	-454	13	1.76·10 ⁻⁷
RFM045		FFM06	542	546	-454	-457	0	0.00
RFM029		FFM01	546	673	-457	-561	0	0.00
RFM029	ZFMWNW2225		673	705	-561	-586	1	2.61·10 ⁻⁹
RFM029		FFM01	705	829	-586	-685	0	0.00
RFM029	ZFMENE1061A, ZFMENE1061B		829	832	-685	-687	0	0.00
RFM029		FFM01	832	946	-687	-777	0	0.00
RFM029	ZFMENE1061A		946	949	-777	-779	0	0.00

5.1.9 Drill site 9

Table 5-18. Compilation of PSS transmissivity data gathered in KFM09A.

RFMxxx	ZFMxxxx	FFMxx	Sec-up	Sec-low	Elev-up	Elev-low	No. PSS 5 m	Σ T PSS 5m
RFM029		FFM02	8	15	-2	-9	-	-
RFM029	ZFMENE1208A		15	40	-9	-30	-	-
RFM029		FFM02	40	86	-30	-69	-	-
RFM029	ZFNENE1208B		86	116	-69	-95	2	2.50·10 ⁻⁸
RFM029		FFM02	116	124	-95	-101	2	3.57·10 ⁻⁷
RFM029		FFM01	124	217	-101	-179	17	3.36·10 ⁻⁶
RFM029	ZFMENE0159A, ZFMNNW0100		217	242	-179	-200	3	1.03·10 ⁻⁷
RFM044	ZFMENE0159A, ZFMNNW0100		242	280	-200	-232	6	1.96·10 ⁻⁸
RFM044		FFM05	280	522	-232	-424	44	8.26·10 ⁻⁷
RFM034		FFM01	522	641	-424	-513	13	1.39·10 ⁻⁷
RFM012		FFM04	641	666	-513	-531	5	6.35·10 ⁻⁹
RFM012	Possible (NNW)		666	667	-531	-531	-	-
RFM012		FFM04	667	723	-531	-570	-	-
RFM012	ZFMNW1200		723	754	-570	-591	5	7.74·10 ⁻⁹
RFM012		FFM04	754	770	-591	-602	3	1.51·10 ⁻⁸
RFM018	ZFMNW1200		770	790	-602	-615	4	4.37·10 ⁻⁸
RFM018		FFM04	790	800	-615	-621	-	-

Table 5-19. Compilation of PSS transmissivity data gathered in KFM09B.

RFMxxx	ZFMxxxx	FFMxx	Sec-up	Sec-low	Elev-up	Elev-low	No. PSS 5 m	ΣT PSS 5m
RFM029	ZFMENE1208A		9	43	-3	-31	8	$2.92 \cdot 10^{-5}$
RFM029		FFM02	43	59	-31	-44	3	$6.46 \cdot 10^{-5}$
RFM029	ZFMENE1208B		59	78	-44	-59	6	$1.01 \cdot 10^{-5}$
RFM029		FFM02	78	106	-59	-82	5	$4.78 \cdot 10^{-7}$
RFM029	ZFMENE0159A		106	132	-82	-103	6	$3.57 \cdot 10^{-6}$
RFM029		FFM01	132	284	-103	-223	23	$2.50 \cdot 10^{-6}$
RFM029	Possible (S-ENE)		284	284	-223	-223	1	$3.22 \cdot 10^{-10}$
RFM029		FFM01	284	308	-223	-242	2	$3.85 \cdot 10^{-10}$
RFM029	Possible (S-ENE)		308	340	-242	-266	0	0.00
RFM029		FFM01	340	363	-266	-284	0	0.00
RFM029	ZFMENE2320		363	413	-284	-322	5	$3.76 \cdot 10^{-8}$
RFM029		FFM01	413	520	-322	-399	5	$1.85 \cdot 10^{-9}$
RFM029	ZFMENE2325A		520	550	-399	-420	3	$1.10 \cdot 10^{-9}$
RFM029		FFM01	550	561	-420	-428	0	0.00
RFM029	ZFMENE2325B		561	574	-428	-437	3	$2.86 \cdot 10^{-7}$
RFM029		FFM01	574	616	-437	-465	3	$5.53 \cdot 10^{-10}$

5.1.10 Drill site 10

Table 5-20. Compilation of PFL-f transmissivity data gathered in KFM10A.

RFMxxx	ZFMxxxx	FFMxx	Sec-up	Sec-low	Elev-up	Elev-low	No. PFL-f	ΣT PFL-F
RFM029	ZFMWNW0123		63	145	-43	-105	34	$7.47 \cdot 10^{-5}$
RFM029		FFM03	145	275	-105	-196	1	$2.61 \cdot 10^{-9}$
RFM029	ZFMENE2403		275	284	-196	-202	0	0.00
RFM029		FFM03	284	430	-202	-296	14	$4.98 \cdot 10^{-7}$
RFM029	ZFMA2		430	449	-296	-307	3	$2.92 \cdot 10^{-5}$
RFM029		FFM03	449	478	-307	-324	0	0.00
RFM029	ZFMA2		478	490	-324	-331	4	$1.15 \cdot 10^{-6}$
RFM029		FFM01	490	500	-331	-337	0	0.00

5.1.11 Summary

Table 5-21 shows summary statistics with regard to deformation zone and possible deformation zone (PDZ) intercepts for the 20 boreholes. All in all there are 75 intercepts with deformation zones and 31 intercepts with possible deformation zones. A number of deformation zones are intercepted by different boreholes.

Table 5-21. Summary statistics with regard to deformation zone (ZFM) and possible deformation zone (PDZ).

Borehole	ZFM			PDZ		
	All	Flowing	No flowing	All	Flowing	No flowing
KFM01A	3	1	2	1	0	1
KFM01C	4	4	0	1	1	0
KFM01D	1	0	1	4	0	4
KFM02A	6	6	0	3	0	3
KFM03A	4	4	0	1	1	0
KFM03B	1	1	0	1	1	0
KFM04A	5	4	1	0	1	0
KFM05A	6	2	4	4	0	0
KFM06A	7	4	3	0	2	2
KFM06B	1	1	0	2	0	0
KFM06C	4	4	0	1	2	0
KFM07A	5	2	3	2	0	1
KFM07B	2	1	1	0	0	2
KFM07C	3	1	2	1	0	0
KFM08A	3	2	1	5	1	4
KFM08B	2	2	0	0	0	0
KFM08C	4	2	2	1	1	0
KFM09A	6	5	1	1	0	1
KFM09B	6	6	0	2	1	1
KFM10A	4	3	1	0	0	0
ALL	77	57	22	30	11	19
	100%	74%	26%	100%	37%	63%

5.2 Hydro-structural cross-correlation

Table 5-22 shows an example of the hydro-structural cross-correlation for a PFL-f anomaly recorded in borehole KFM01D; the fracture transmissivity is $1.83 \cdot 10^{-7} \text{ m}^2/\text{s}$ and the inferred strike, dip and aperture of the cross-correlated open fracture are 110° , 12° and 3 mm, respectively. The orientations of the PFL-f anomalies are determined by comparing their positions in the boreholes with the positions of the open fractures identified during the core mapping (Boremap) and the viewer logging (BIPS) /Forsman et al. 2004, Forssman et al. 2006, Teurneau et al. 2007/. The assumptions behind these important works are explained in greater detail in Section 11.

Table 5-23 shows a summary of the input data available for hydrogeological DFN analysis and modelling for Forsmark stage 2.2.

Figure 5-1 through Figure 5-12 display the geological interpretation of each PFL-f anomaly gathered in KFM01A–8A, -10A, KFM07C–08C and KFM01D. The data use the colour legend shown in Table 3-3.

Table 5-22. Example of the structural interpretation of PFL-f flow anomaly no. 27 recorded in borehole KFM01D. Modified after /Teurneau et al. 2007/.

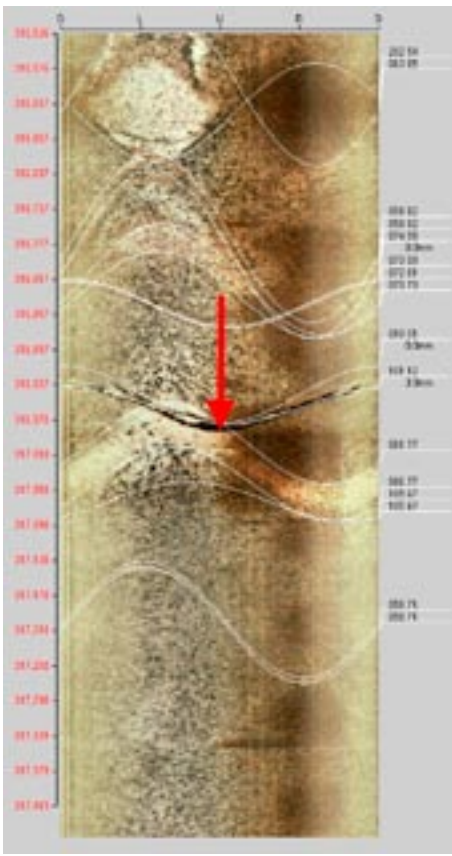
PFL-f anomaly no.	PFL-f	Boremap data	BIPS Image
27	Bh-length (m): 316.90 T (m ² /s): 1.83E-7 PFL confidence: Certain	Adjusted secup (m): 316.96 Fract_interpret: Open Frac. interp. confidence: Certain PFL-anom. confidence: 1 Strike: 110° Dip: 12° BIPS aperture: 3 mm	

Table 5-23. Summary of sample lengths and numbers of fractures according to different categories in each of the boreholes studied in F2.2. Fractures that are judged to be open are assigned a confidence: certain, probable or possible. The number of PFL flow-anomalies is also given.

Borehole	Top [m]	Bottom [m]	Length [m]	Total number	Number of open (+partly)	Open and certain	Open and prob.	Open and poss.	PFL-f anom.
KFM01A	102.67	993.49	890.82	1,517	752	174	143	435	34
KFM01D	91.67	799.62	707.95	1,636	468	99	178	191	34
KFM02A	101.54	1,000.36	898.82	2,199	443	152	267	24	104
KFM03A	102.45	999.67	897.22	1,825	375	146	137	92	52
KFM04A	109.1	985.07	875.97	4,327	1,357	257	630	470	71
KFM05A	102.27	999.62	897.35	2,838	633	91	180	362	27
KFM06A	102.21	997.37	895.16	3,680	816	172	235	409	99
KFM07A	102.04	993.77	891.73	3,183	617	103	162	352	26
KFM07C	98.62	498.67	400.05	1,765	285	78	116	91	14
KFM08A	103.36	949.67	846.31	4,268	713	149	210	354	41
KFM08C	102.29	948.99	846.70	4,198	676	56	199	421	21
KFM10A	62.86	499.98	437.12	2,755	999	264	299	436	54
All boreholes			9,485.20	34,191	8,134	1,741	2,756	3,637	577

5.2.1 Drill site 1

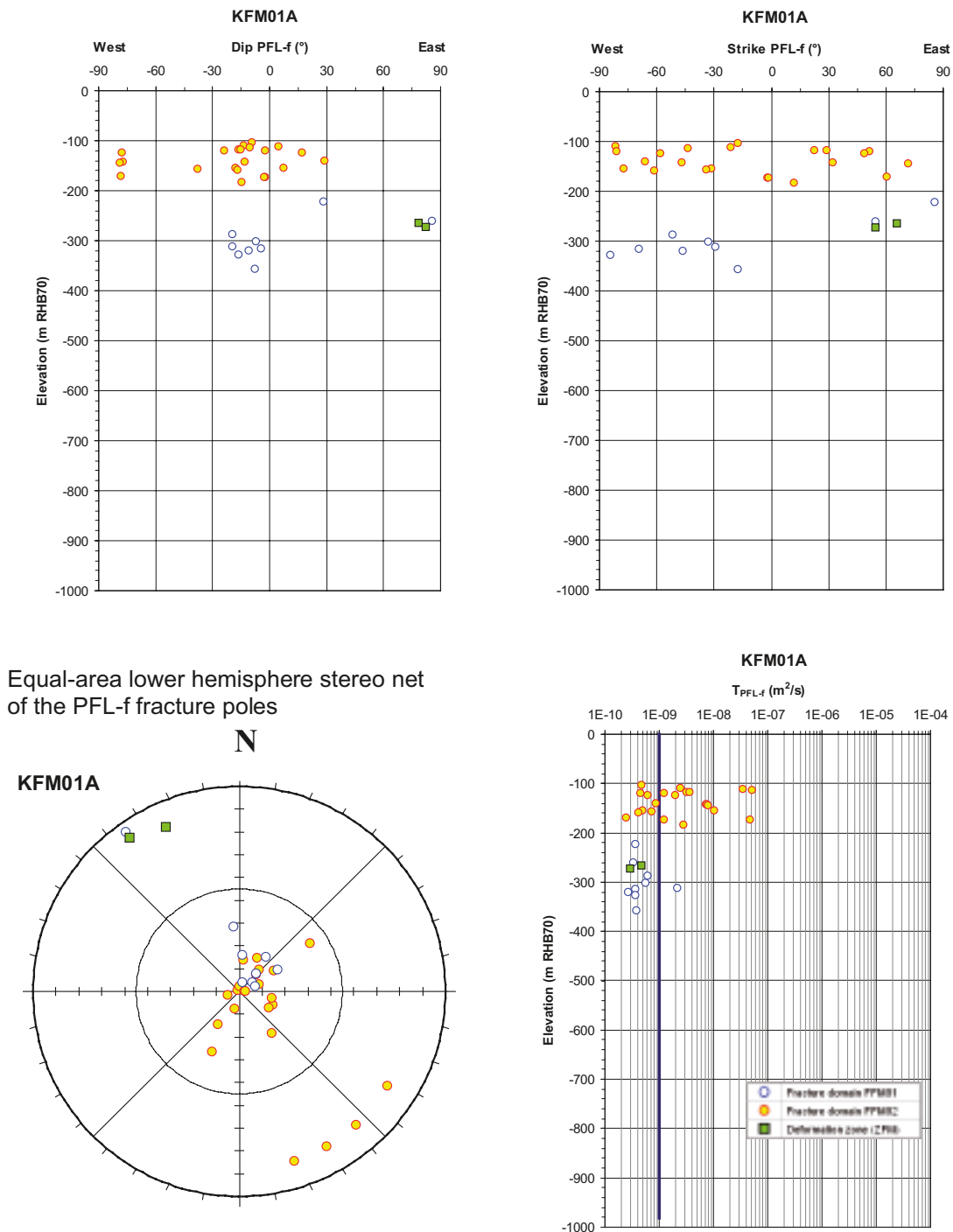
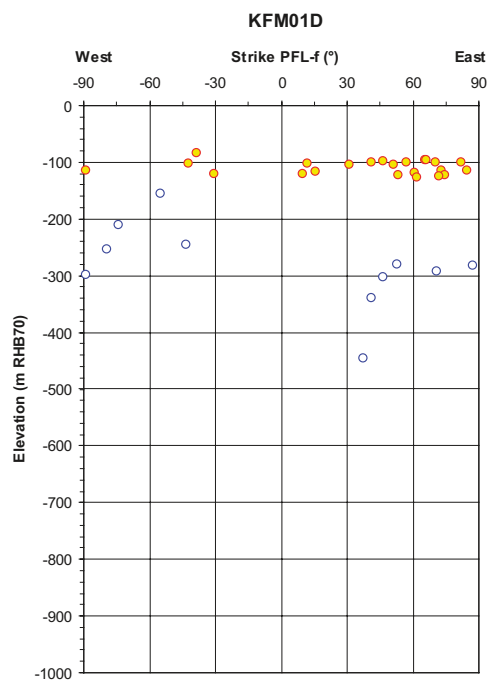
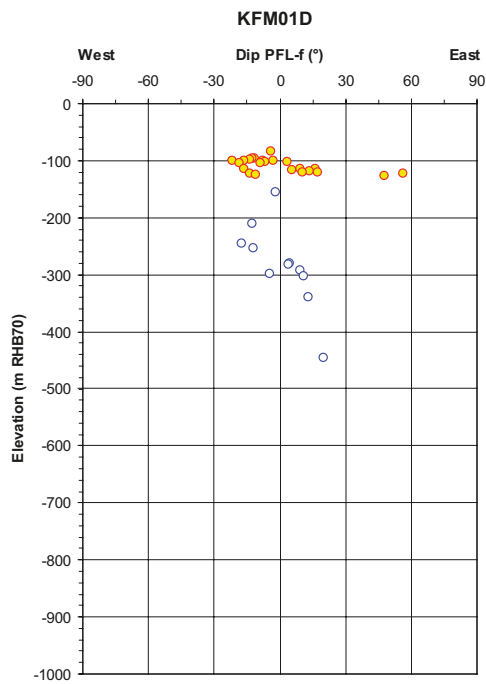


Figure 5-1. Summary plots of structural-hydraulic data gathered in the cored borehole KFM01A based on the cross-correlation analyses carried out by /Forsman et al. 2004/. KFM01A is c. 1,001 m long, has an azimuth of c. 318° and an inclination of c. 85°. There are 32 PFL-f flow anomalies associated with single fractures and 2 associated with 1 deterministically modelled deformation zone. The blue line indicates the investigated depth and the typical practical detection limit of the PFL-f method ($\sim 1 \cdot 10^{-9}$ m²/s). The legend to the colours used is explained in Table 3-3.



Equal-area lower hemisphere stereo net of the PFL-f fracture poles

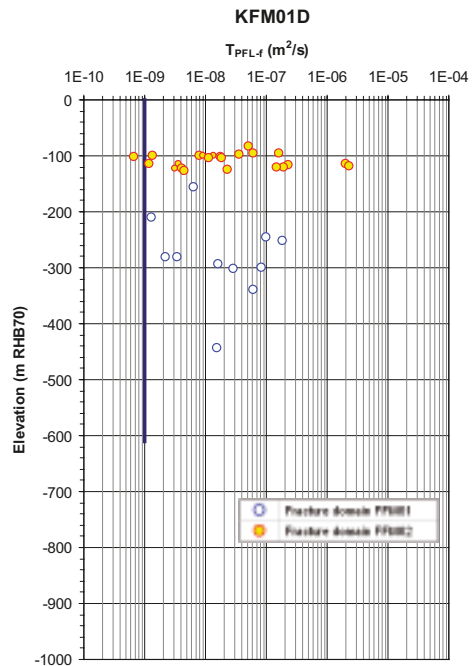
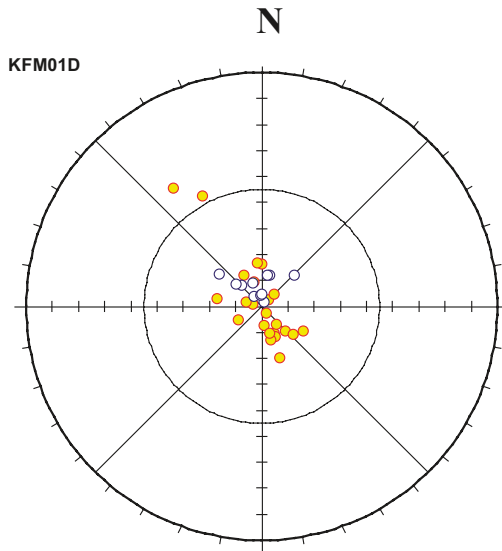
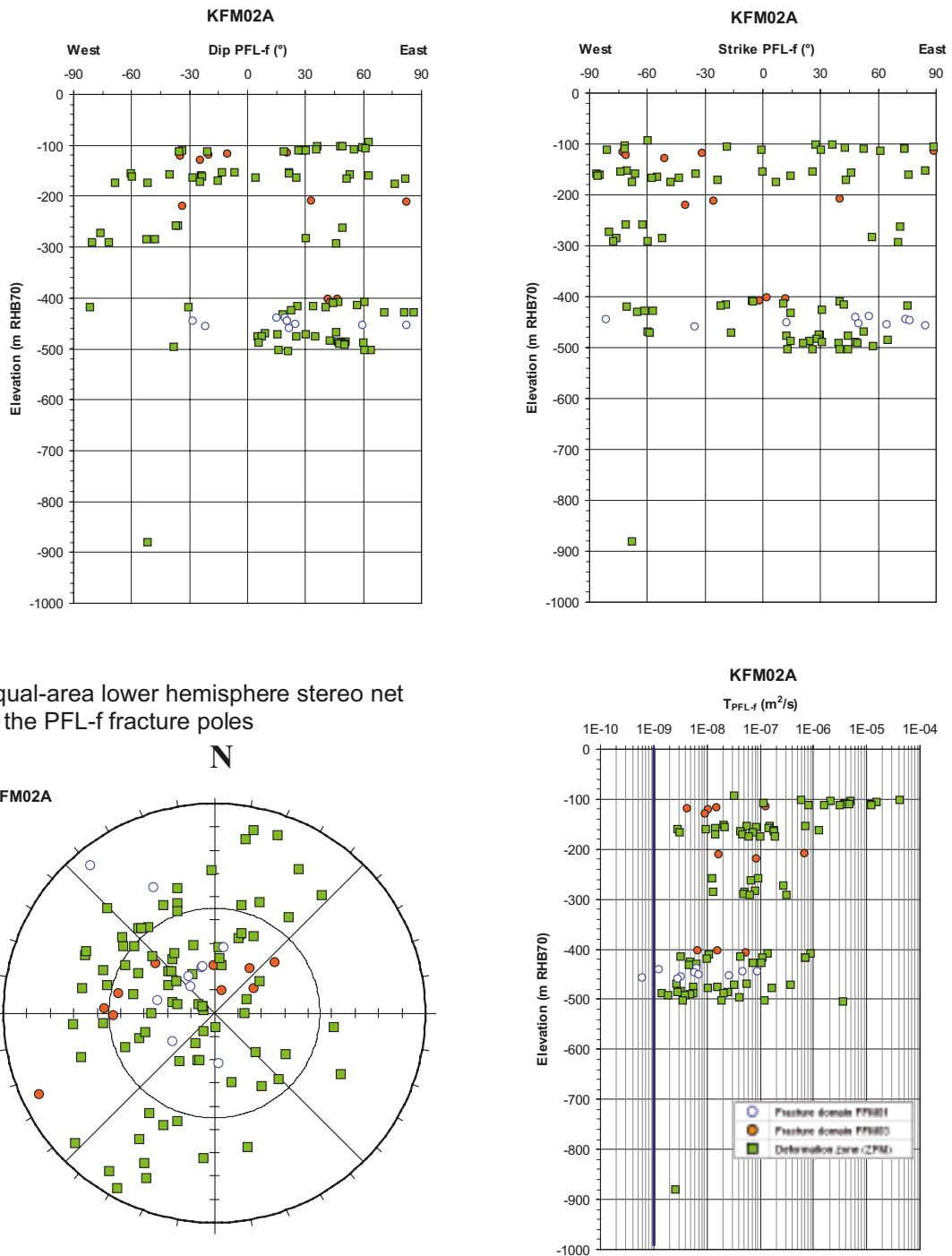


Figure 5-2. Summary plots of structural-hydraulic data gathered in the cored borehole KFM01D based on the cross-correlation analyses carried out by /Teurneau et al. 2007/. KFM01D is c. 800 m long, has an azimuth of c. 35° and an inclination of c. 55°. There are 34 PFL-f flow anomalies associated with single fractures. The blue line indicates the investigated depth and the typical practical detection limit of the PFL-f method ($\sim 1 \cdot 10^{-9} m^2/s$). The legend to the colours used is explained in Table 3-3.

5.2.2 Drill site 2



Equal-area lower hemisphere stereo net of the PFL-f fracture poles

Figure 5-3. Summary plots of structural-hydraulic data gathered in the cored borehole KFM02A based on the cross-correlation analyses carried out by Forsman et al. 2004/. KFM02A is c. 1,002 m long, has an azimuth of c. 276° and an inclination of c. 85°. There are 22 PFL-f flow anomalies associated with single fractures and 82 associated with 6 deterministically modelled deformation zones. The blue line indicates the investigated depth and the typical practical detection limit of the PFL-f method ($\sim 1 \cdot 10^{-9}$ m²/s). The legend to the colours used is explained in Table 3-3.

5.2.3 Drill site 3

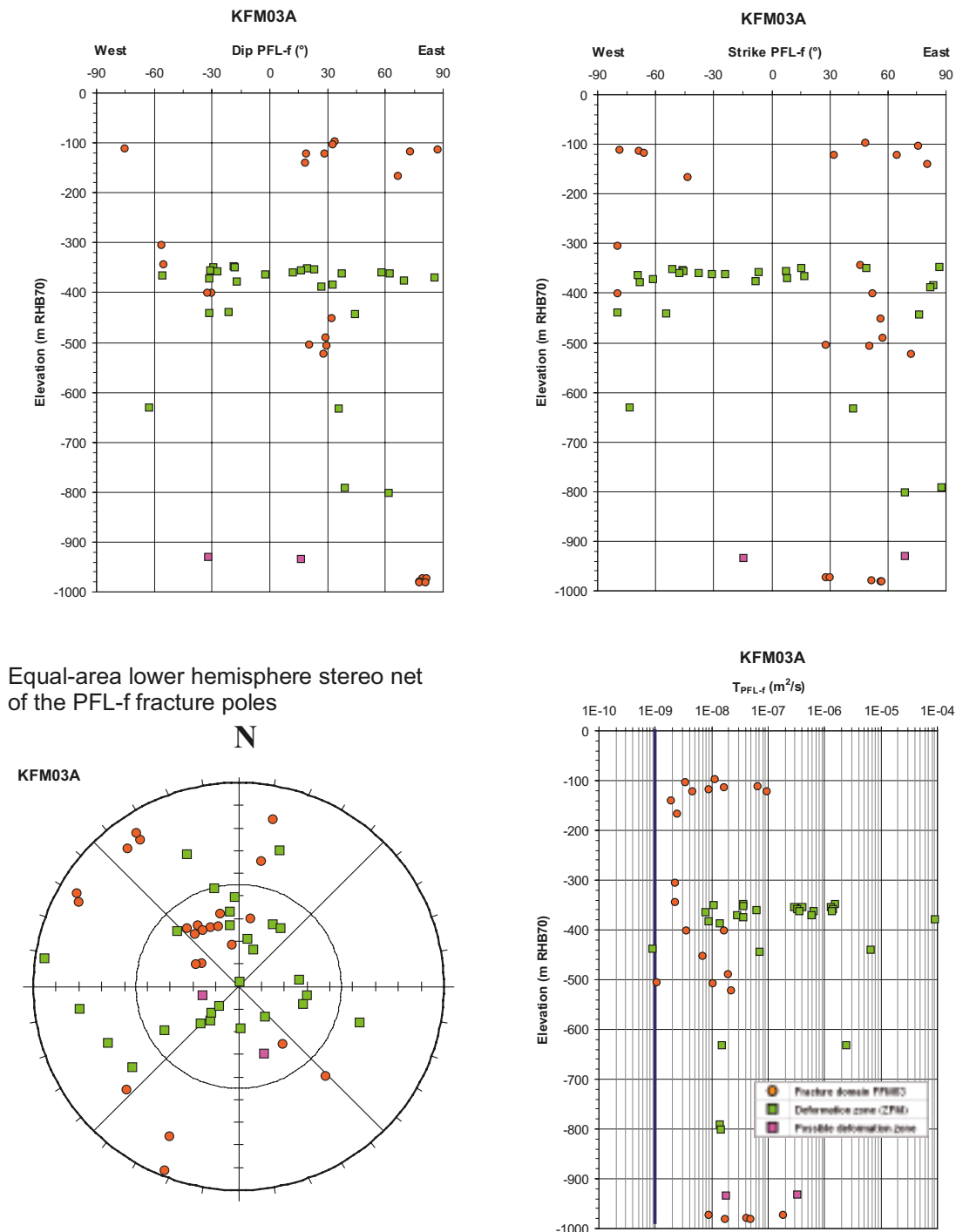


Figure 5-4. Summary plots of structural-hydraulic data gathered in the cored borehole KFM03A based on the cross-correlation analyses carried out by /Forsman et al. 2004/. KFM02A is c. 1,002 m long, has an azimuth of c. 272° and an inclination of c. 86°. There are 23 PFL-f flow anomalies associated with single fractures, 27 associated with 4 deterministically modelled deformation zones, and 2 associated with 1 possible deformation zone. The blue line indicates the investigated depth and the typical practical detection limit of the PFL-f method ($\sim 1 \cdot 10^{-9}$ m²/s). The legend to the colours used is explained in Table 3-3.

5.2.4 Drill site 4

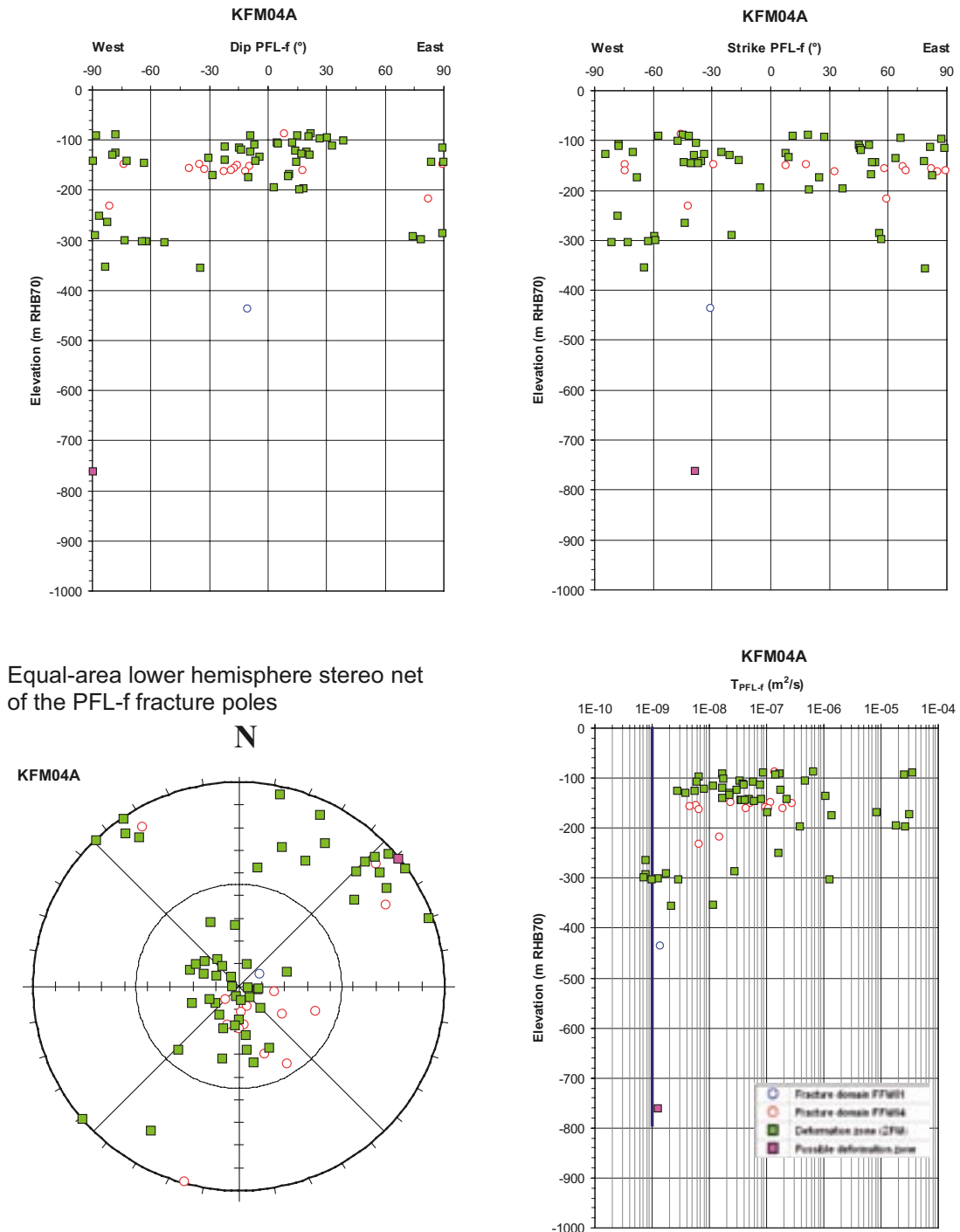


Figure 5-5. Summary plots of structural-hydraulic data gathered in the cored borehole KFM04A based on the cross-correlation analyses carried out by Forsman et al. 2004/. KFM02A is c. 1,002 m long, has an azimuth of c. 45° and an inclination of c. 60°. There are 16 PFL-f flow anomalies associated with single fractures, 54 associated with 2 deterministically modelled deformation zones, and 1 associated with 1 possible deformation zone. The blue line indicates the investigated depth and the typical practical detection limit of the PFL-f method ($\sim 1 \cdot 10^{-9}$ m²/s). The legend to the colours used is explained in Table 3-3.

5.2.5 Drill site 5

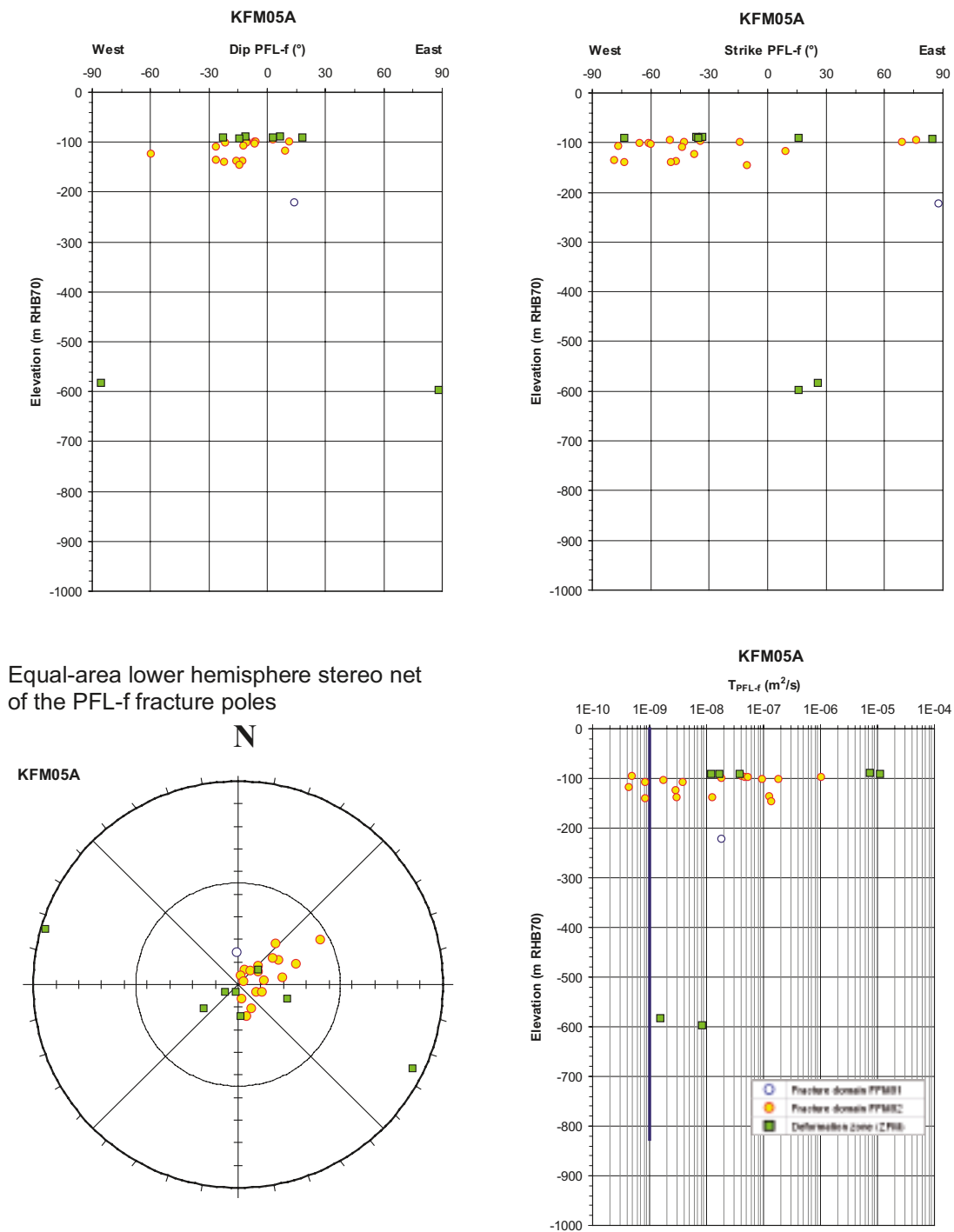
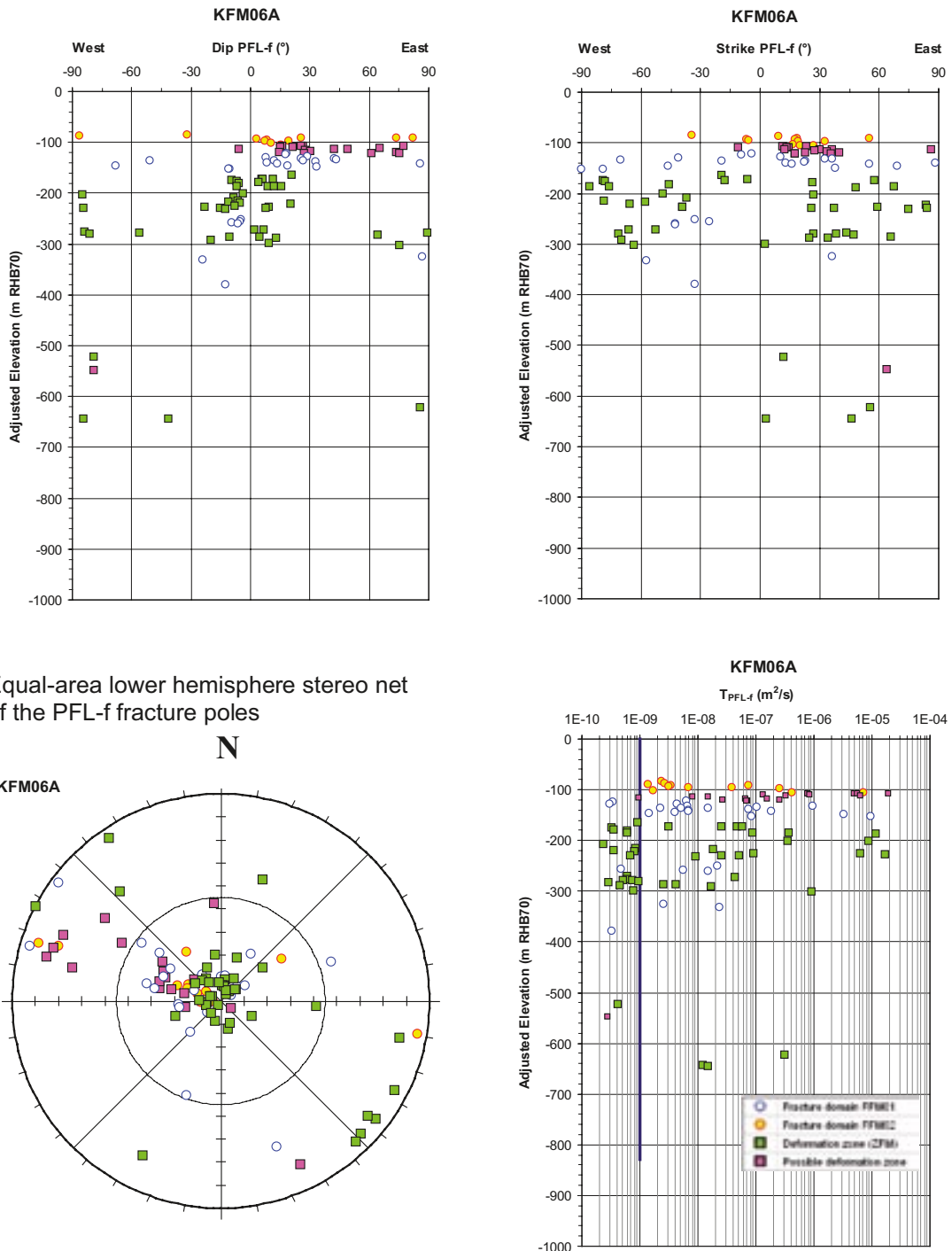


Figure 5-6. Summary plots of structural-hydraulic data gathered in the cored borehole KFM05A based on the cross-correlation analyses carried out by /Forsman et al. 2004/. KFM02A is c. 1,002 m long, has an azimuth of c. 81° and an inclination of c. 60°. There are 19 PFL-f flow anomalies associated with single fractures and 8 associated with 2 deterministically modelled deformation zones. The blue line indicates the investigated depth and the typical practical detection limit of the PFL-f method ($\sim 1 \cdot 10^{-9}$ m²/s). The legend to the colours used is explained in Table 3-3.

5.2.6 Drill site 6



Equal-area lower hemisphere stereo net of the PFL-f fracture poles

Figure 5-7. Summary plots of structural-hydraulic data gathered in the cored borehole KFM06A based on the cross-correlation analyses carried out by Forssman et al. 2006/. KFM02A is c. 1,002 m long, has an azimuth of c. 301° and an inclination of c. 60°. There are 38 PFL-f flow anomalies associated with single fractures, 43 of associated with 5 deterministically modelled deformation zones, and 18 associated with 2 possible deformation zones. The blue line indicates the investigated depth and the typical practical detection limit of the PFL-f method ($\sim 1 \cdot 10^{-9}$ m²/s). The legend to the colours used is explained in Table 3-3.

5.2.7 Drill site 7

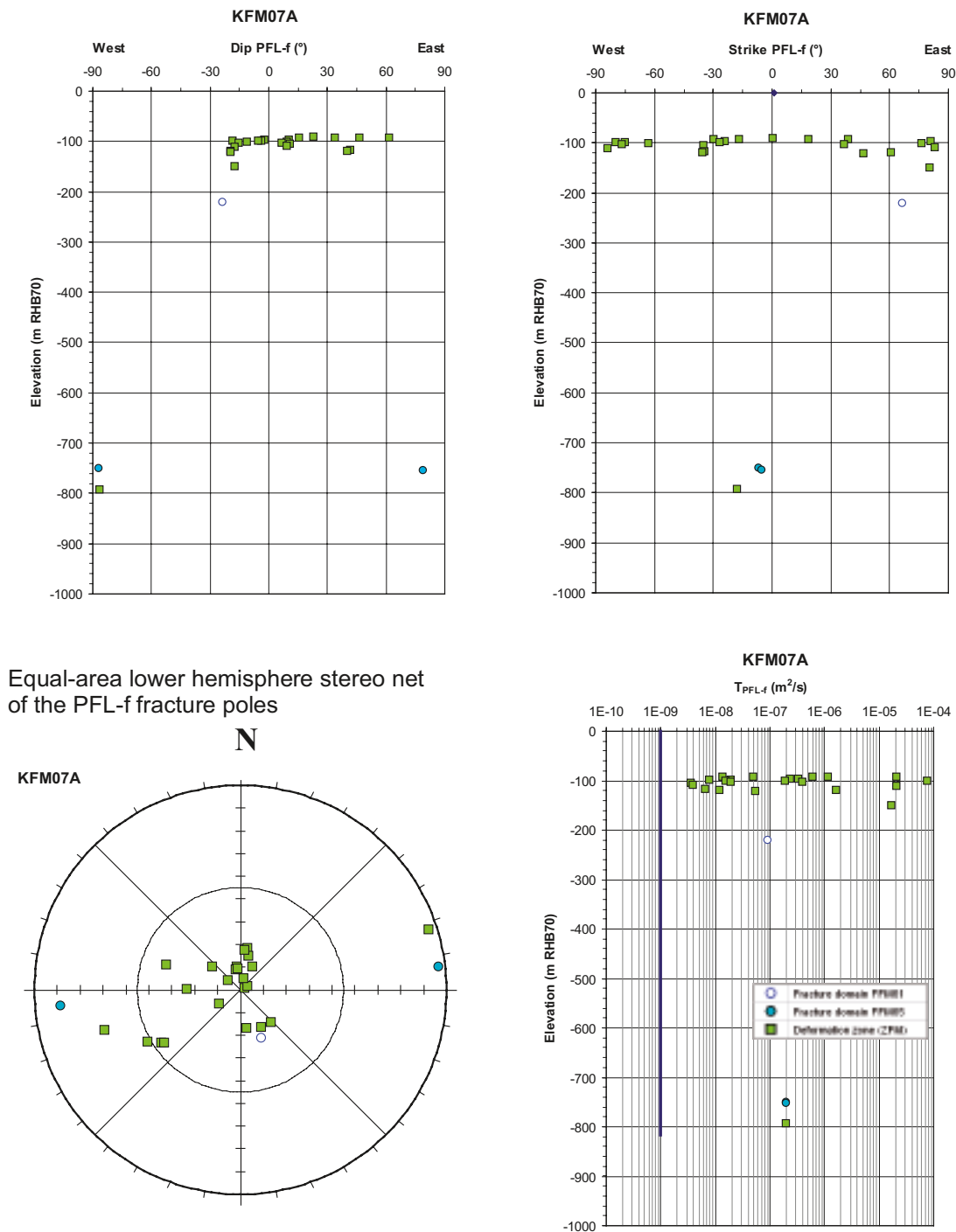
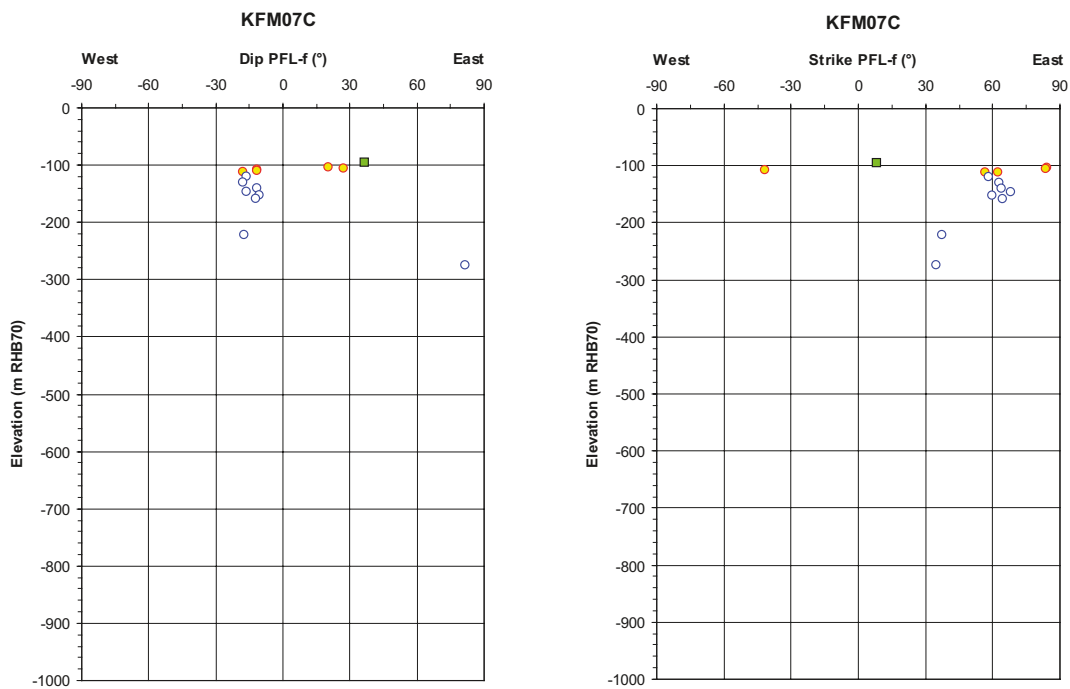


Figure 5-8. Summary plots of structural-hydraulic data gathered in the cored borehole KFM07A based on the cross-correlation analyses carried out by /Forssman et al. 2006/. KFM02A is c. 1,002 m long, has an azimuth of c. 261° and an inclination of c. 59°. There are 3 PFL-f flow anomalies associated with single fractures and 23 associated with 4 deterministically modelled deformation zones. The blue line indicates the investigated depth and the typical practical detection limit of the PFL-f method ($\sim 1 \cdot 10^{-9}$ m²/s). The legend to the colours used is explained in Table 3-3.



Equal-area lower hemisphere stereo net of the PFL-f fracture poles

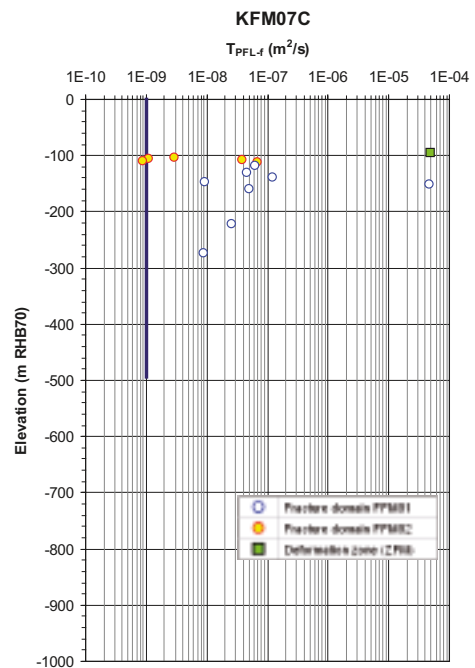
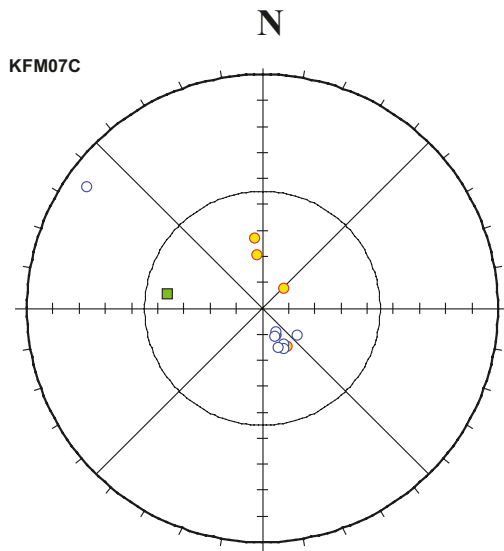


Figure 5-9. Summary plots of structural-hydraulic data gathered in the cored borehole KFM07C based on the cross-correlation analyses carried out by /Teurneau et al. 2007/. KFM02A is c. 1,002 m long, has an azimuth of c. 143° and an inclination of c. 85°. There are 13 PFL-f flow anomalies associated with single fractures and 1 associated with 1 deterministically modelled deformation zone. The blue line indicates the investigated depth and the typical practical detection limit of the PFL-f method ($\sim 1 \cdot 10^{-9} \text{ m}^2/\text{s}$). The legend to the colours used is explained in Table 3-3.

5.2.8 Drill site 8

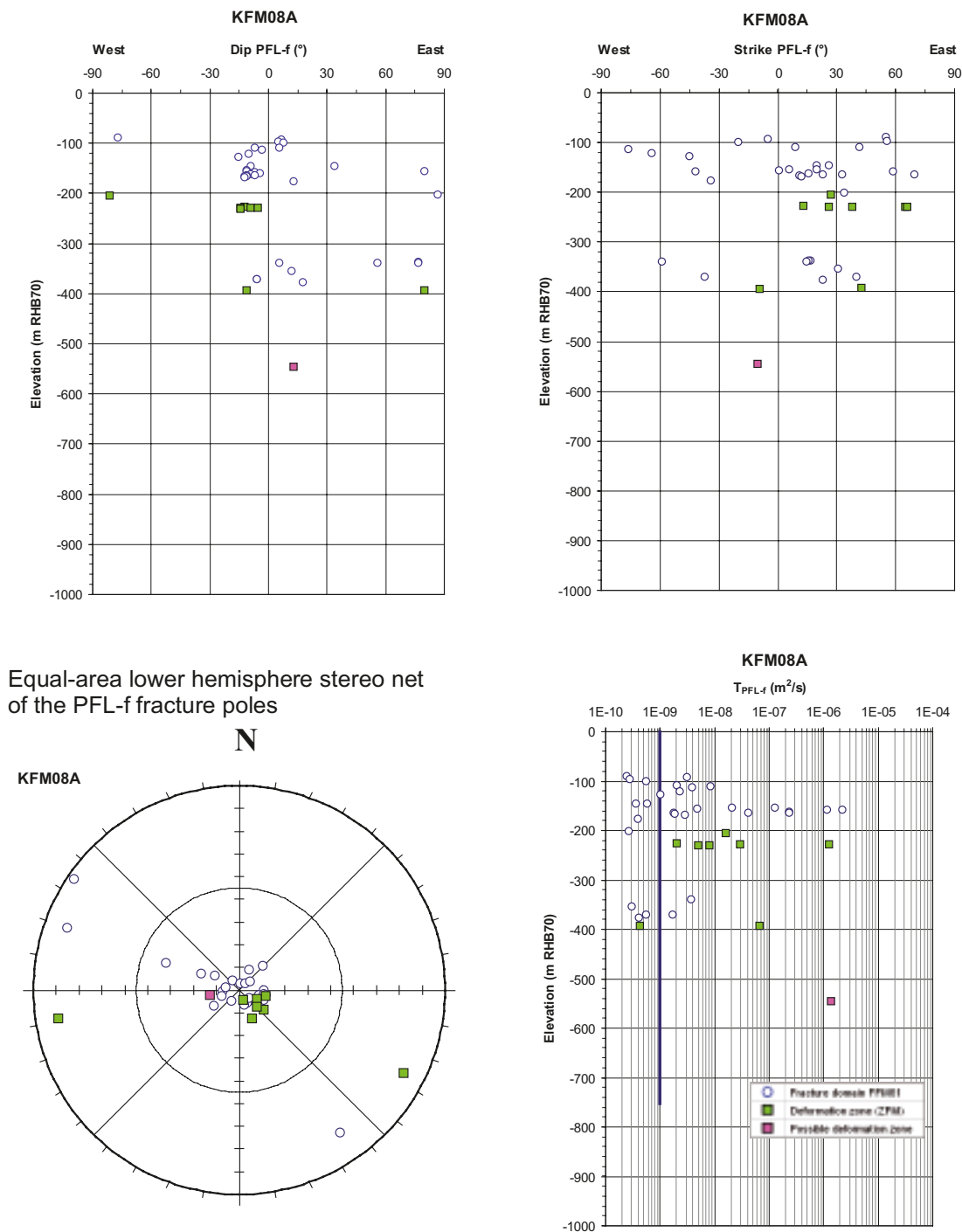
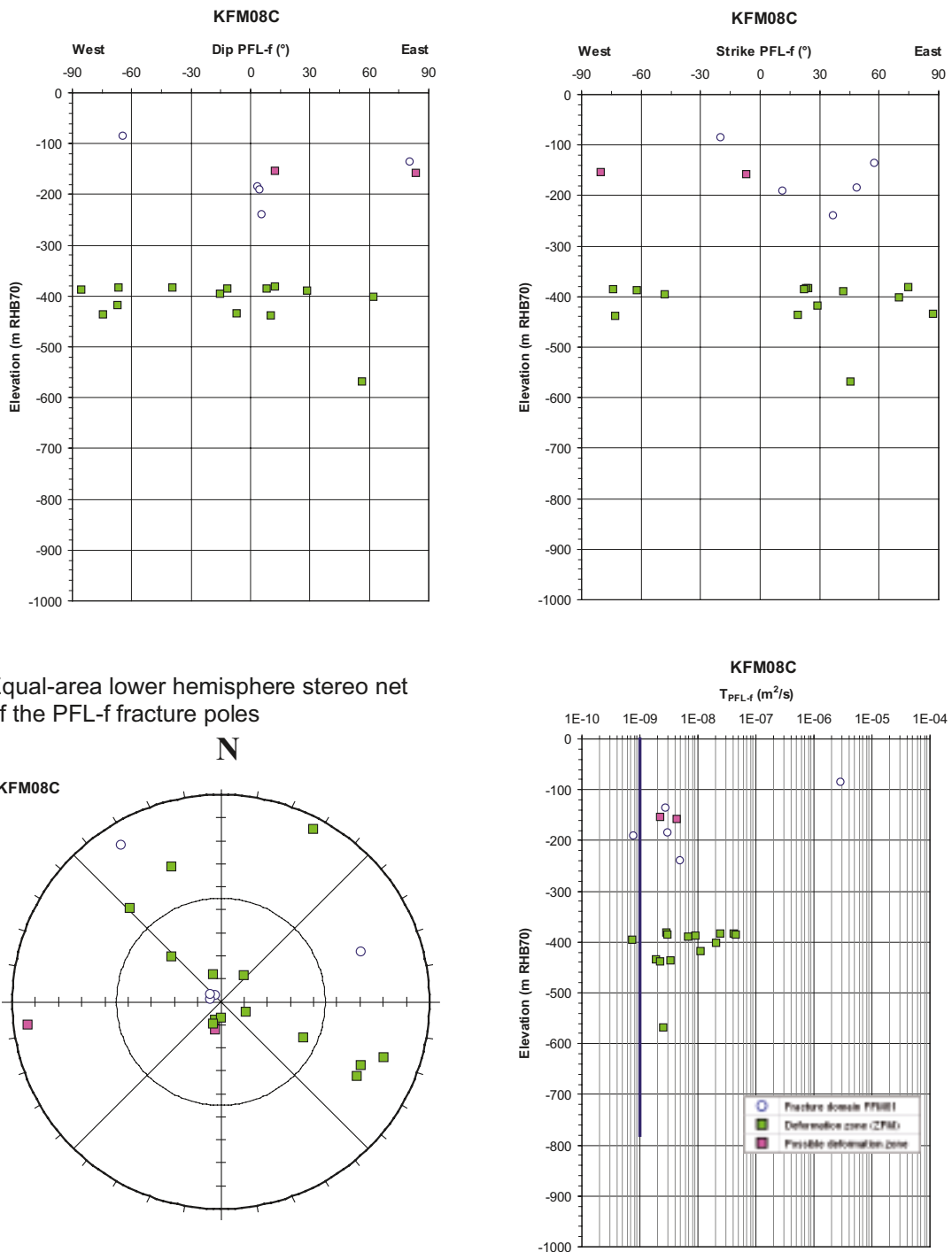


Figure 5-10. Summary plots of structural-hydraulic data gathered in the cored borehole KFM08A based on the cross-correlation analyses carried out by /Teurneau et al. 2007/. KFM02A is c. 1,002 m long, has an azimuth of c. 321° and an inclination of c. 61°. There are 32 PFL-f flow anomalies associated with single fractures, 8 associated with 2 deterministically modelled deformation zones, and 1 associated with 1 possible deformation zone. The blue line indicates the investigated depth and the typical practical detection limit of the PFL-f method ($\sim 1 \cdot 10^{-9}$ m²/s). The legend to the colours used is explained in Table 3-3.



Equal-area lower hemisphere stereo net of the PFL-f fracture poles

Figure 5-11. Summary plots of structural-hydraulic data gathered in the cored borehole KFM08C based on the cross-correlation analyses carried out by Teurneau et al. 2007/. KFM02A is c. 1,002 m long, has an azimuth of c. 36° and an inclination of c. 60°. There are 5 PFL-f flow anomalies associated with single fractures, 14 associated with 2 deterministically modelled deformation zones, and 2 associated with 1 possible deformation zone. The blue line indicates the investigated depth and the typical practical detection limit of the PFL-f method ($\sim 1 \cdot 10^{-9}$ m²/s). The legend to the colours used is explained in Table 3-3.

5.2.9 Drill site 10

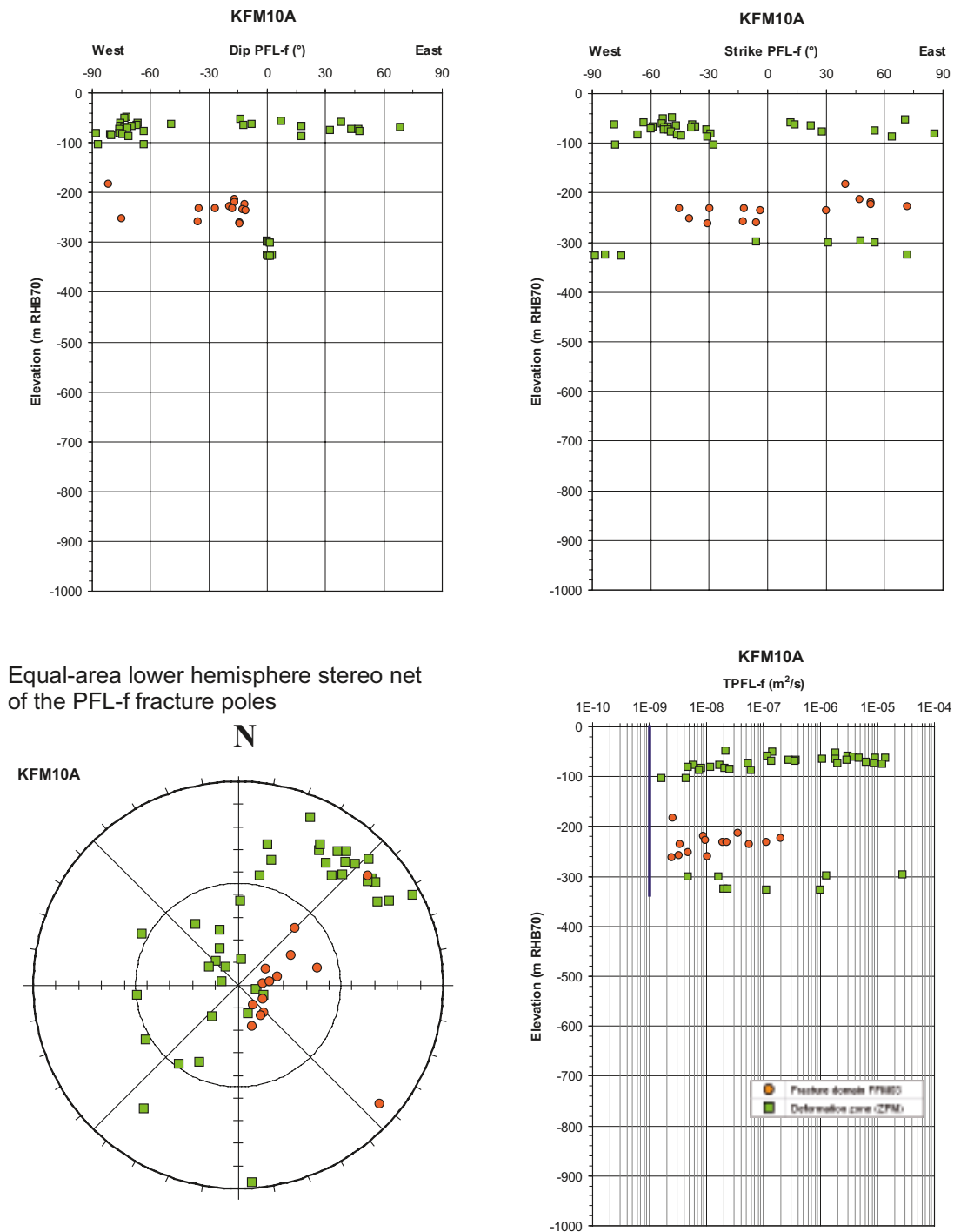


Figure 5-12. Summary plots of structural-hydraulic data gathered in the cored borehole KFM10A based on the cross-correlation analyses carried out by Teurneau et al. 2007/. KFM02A is c. 1,002 m long, has an azimuth of c. 10° and an inclination of c. 50°. There are 14 PFL-f flow anomalies associated with single fractures and 40 associated with 2 deterministically modelled deformation zones. The blue line indicates the investigated depth and the typical practical detection limit of the PFL-f method ($\sim 1 \cdot 10^{-9} \text{ m}^2/\text{s}$). The legend to the colours used is explained Table 3-3.

5.2.10 Data in KFM02A, KFM07C and KFM10A

It is noted that the reported total number of PFL-f anomalies observed in boreholes KFM02A, KFM07C and KFM10A are 125, 15 and 56, respectively, and not 104, 14 and 54, respectively, the numbers given in Table 5-23. The reasons for these discrepancies are:

- There are 28 observations of PFL-f anomalies in vuggy granite in KFM02A. 21 of these cannot be associated with discrete fractures, but suggest a porous-medium flow field rather. The remaining seven fractures show a discrete flow pattern and are therefore maintained. Hence, a balance calculation yields 104 PFL-f anomalies useful for hydrogeological DFN modelling.
- There are two PFL-f anomalies in KFM07C that are interpreted to represent the same fracture (the angle between the borehole trajectory and the dip of the flowing fracture is 3.5°). Hence, the total number of useful PFL-f transmissivity data becomes one less than the total number of PFL-f flow anomalies observed.
- The two uppermost PFL-f anomalies observed in KFM10A have no core data due to borehole fall out. Hence, the total number of useful PFL-f transmissivity data is 54.

5.2.11 Crushed rock

There are 15 PFL-f flow anomalies in data freeze 2.2 associated with intervals consisting of crushed rock; 6 in KFM02A, 1 in KFM03A, 2 in KFM04A, 2 in KFM06A, and 4 in KFM07A. All of the 15 PFL-f flow anomalies associated with crushed rock intervals coincide with deterministically modelled deformation zones implying that they do not affect the hydrogeological DFN analysis of single features.

5.2.12 Errors and uncertainty in feature orientation

After data freeze 2.2, SKB discovered two potential sources of error, which could affect the modelling work under stage 2.2 /Munier and Stigsson 2007/. The potential sources of error concerns the determination of the trajectory and position of each borehole as well as the mapping of fracture orientations. The quantification of the lumped maximum uncertainty related to these two errors was still under analysis at the time of preparation of this report including the supporting works conducted by /Forsman et al. 2004, Forssman et al. 2006, Teurneau et al. 2007/.

/Stigsson 2007/ investigated the effect of the orientation uncertainties for the flowing fractures associated with the different fracture domains in due time and concluded that the lumped maximum uncertainty in the dihedral angle (Ω) is less than 30° except for eleven fractures, see Figure 5-13. After inspection we can confirm that the eleven fractures occur outside the target fracture domain at repository depth, i.e. in the hanging wall bedrock, in the bedrock bordering the tectonic lens, or near the surface. Many of these fractures are already from the onset determined to be steeply dipping, which means that a further correction of dip is insignificant for the hydrogeological DFN model.

In conclusion, none of the two orientation errors identified has any practical implication for the analysis of PFL-f fracture transmissivity data associated with the fracture domains modelled in stage 2.2. This means that all tables and figures in this report showing PFL-f orientation data are considered to be relevant and reliable for Hydro-DFN modelling with regard to the uncertainty caused by the two orientation errors.

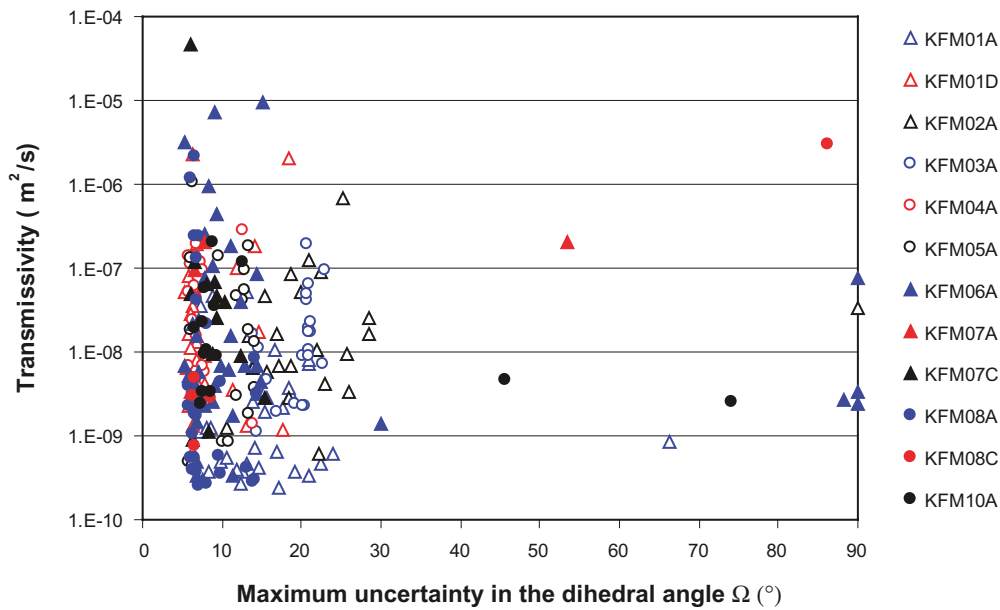


Figure 5-13. Scatter plot showing the maximum uncertainty for each PFL-f fracture transmissivity value associated with the different fracture domains. Eleven fractures have a maximum uncertainty in the dihedral (Ω) angle greater than 30° . Reproduced from /Stigsson 2007/.

5.3 Orientation and occurrence of PFL-anomalies

Figure 5-14 shows the cumulative frequency distributions for the dip of the PFL-f anomalies encountered in the foot wall and hanging wall bedrock of ZFMA2 as well as and bedrock bordering the tectonic lens, respectively. No distinction is made with regard to deformation zones, possible deformation zones and fracture domains in this plot. The foot wall bedrock contains more gently-dipping flowing fractures than encountered in the hanging wall bedrock and the bordering bedrock.

Figure 5-15 shows the cumulative frequency distributions for the dip of the PFL-f anomalies encountered in the foot wall bedrock only (data representing deformation zones and possible deformation zones are excluded.) The data in FFM01 are divided into three depth intervals, 100–200 m, 200–400 m and 400–1,000 m. The data for FFM02 represent the depth interval 100–200 m.

Figure 5-15 reveals that c. 80% of the observations have a dip angle of 30° or less. The foot wall bedrock below elevation -400 contains 12 PFL-f anomalies, 10 of which are squeezed between ZFMA2 and ZFMF1 in borehole KFM02A, cf. Figure 3-6. In effect, there are only five PFL-f anomalies in the target volume below -400 m elevation; three PFL-f anomalies associated with possible deformation zones in KFM04A, KFM06A, and KFM08A, and two PLF-f anomalies associated with FFM01 in KFM01D and KFM04A. A fourth possible deformation zone in the target volume below -400 m elevation occurs in KFM06C, which is investigated with the PSS method only.

It should be noted that Figure 5-14 and Figure 5-15 show measured data and that due to the steep inclination of the boreholes there is a bias to favour observations of gently-dipping fractures. In the fracture data analyses presented in Section 10 we account for this bias by means of a Terzaghi correction.

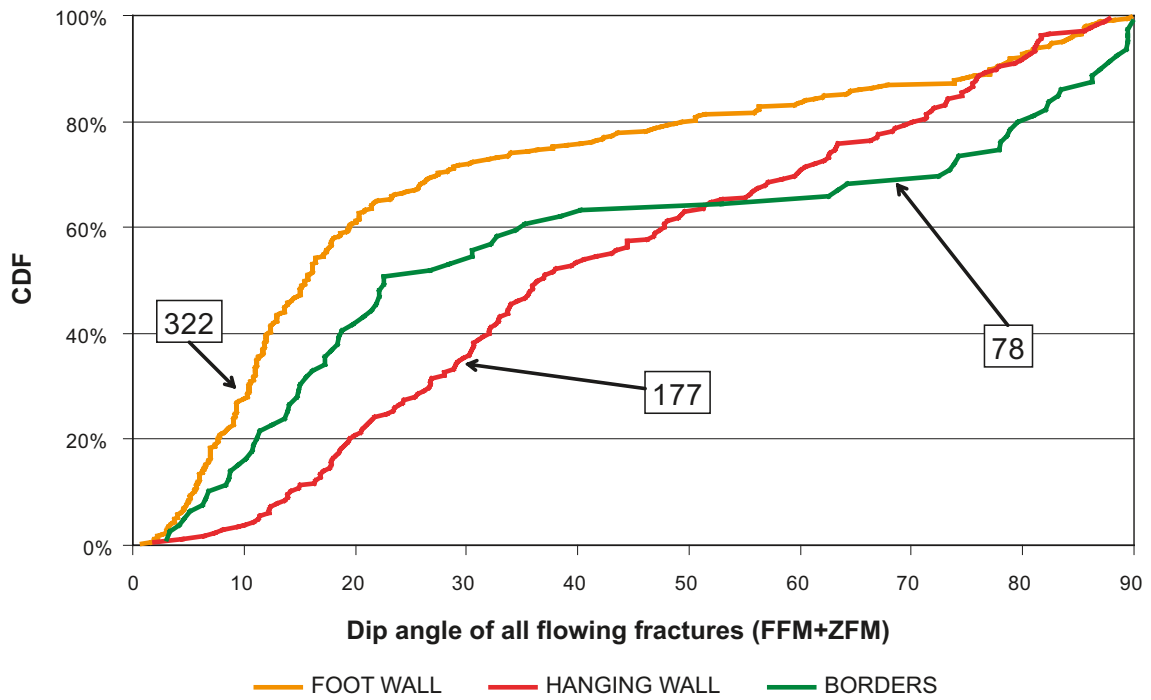


Figure 5-14. Dip distributions for the 577 PFL-f anomalies encountered in KFM01A–8A, -10A, -08C and -01D. The data are split between the foot wall bedrock, the hanging wall bedrock and the bedrock bordering the tectonic lens. The graphs are not corrected for borehole orientation bias (cf. Section 10).

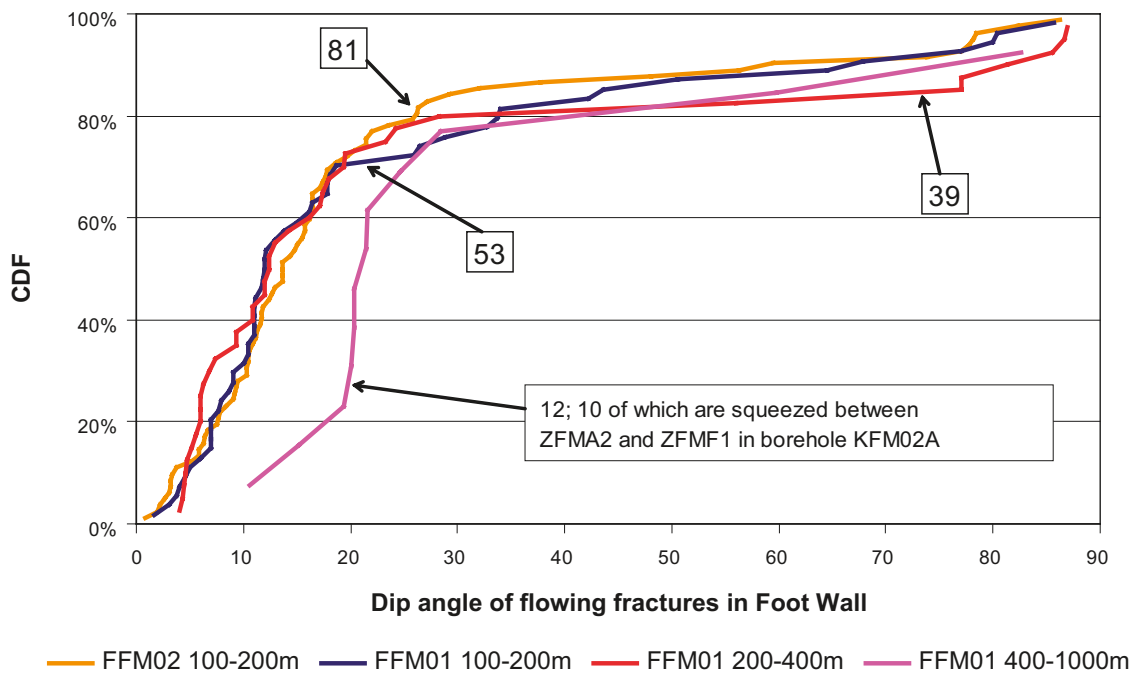


Figure 5-15. There are 185 PFL-f anomalies encountered in the cored boreholes drilled in the foot wall outside the deterministically modelled deformation zones; 81 in FFM02 and 104 in FFM01. The graphs are not corrected for borehole orientation bias (cf. Section 10).

6 Structural-hydraulic data in percussion-drilled boreholes

6.1 Overview

Table 6-1 presents the structural-hydraulic data gathered in the 32 percussion-drilled boreholes. The columns show rock domain (RFM), deformation zone (ZFM), fracture domain (FFM), borehole length (Sec-up/-low) and elevation (Elev-up/-low) [metres RHB 70]. All HTHB transmissivities are given in [m²/s]. The interpreted main direction of orientation of the possible deformation zones is provided between parentheses, where G = gently dipping and S-xxx = steeply dipping and xxx = bearing. The structural interpretation in the third column uses the colour legend shown in Table 3-2. The structural interpretation in the fourth column uses the colour legend shown in Table 3-3.

Table 6-1. Compilation of HTHB transmissivity data* gathered in HFM01–32.

HFMxx	RFMxxx	ZFMxxxx	FFMxx	Sec-up	Sec-low	Elev-up	Elev-low	Σ T HTHB
HFM01	RFM029		FFM02	31	35	29	33	0.00
HFM01	RFM029	ZFMA2		35	44	33	41	4.50·10 ⁻⁵
HFM01	RFM029		FFM02	44	197	41	192	2.05·10 ⁻⁵
HFM02	RFM029		FFM02	25	42	22	39	0.00
HFM02	RFM029	ZFM1203		42	47	39	44	5.90·10 ⁻⁴
HFM02	RFM029		FFM02	47	99	44	96	0.00
HFM03	RFM029		FFM02	13	26	10	23	4.20·10 ⁻⁴
HFM04	RFM029		FFM03	12	61	8	57	0.00
HFM04	RFM029	ZFM866		61	64	57	60	7.87·10 ⁻⁵
HFM04	RFM029		FFM03	64	183	60	177	0.00
HFM04	RFM029	ZFMA3		183	187	177	181	0.00
HFM04	RFM029		FFM03	187	222	181	214	0.00
HFM05	RFM029		FFM03	12	153	4	144	0.00
HFM05	RFM029	ZFM866		153	154	144	145	3.96·10 ⁻⁴
HFM05	RFM029		FFM03	154	199	145	189	0.00
HFM06	RFM029		FFM03	11	61	4	54	1.03·10 ⁻⁴
HFM06	RFM029	ZFMA5		61	71	54	64	2.29·10 ⁻⁴
HFM06	RFM029		FFM03	71	108	64	101	0.00
HFM07	RFM029		FFM03	11	54	5	48	Low yield
HFM07	RFM029	ZFMA6		54	66	48	60	Low yield
HFM07	RFM029		FFM03	66	109	60	103	Low yield
HFM08	RFM029		FFM03	17	136	10	128	5.70·10 ⁻⁵
HFM08	RFM029	ZFMA5		136	141	128	133	1.20·10 ⁻³
HFM08	RFM029		FFM03	141	142	133	134	0.00
HFM09	RFM018		FFM04	17	18	11	12	0.00
HFM09	RFM018	ZFMENE0060A		18	28	12	21	3.26·10 ⁻⁴
HFM09	RFM018		FFM04	28	50	21	41	4.67·10 ⁻⁵
HFM10	RFM018		FFM04	12	65	6	56	0.00
HFM10	RFM018	Possible DZ (S-ENE)		65	69	56	60	0.00
HFM10	RFM018		FFM04	69	108	60	96	0.00
HFM10	RFM018	Possible DZ (S-ENE)		108	117	96	104	3.11·10 ⁻⁴
HFM10	RFM018		FFM04	117	149	104	133	0.00
HFM11	RFM026		FFM04	12	83	1	53	2.25·10 ⁻⁵
HFM11	RFM026	ZFMNW0003		83	160	53	105	2.80·10 ⁻⁵
HFM11	RFM026		FFM04	160	182	105	118	0.00

HFMxx	RFMxxx	ZFMxxxx	FFMxx	Sec-up	Sec-low	Elev-up	Elev-low	Σ T HTHB
HFM12	RFM026		FFM04	15	91	4	60	9.00·10 ⁻⁶
HFM12	RFM026	ZFMNW0003		91	179	60	118	7.87·10 ⁻⁶
HFM12	RFM026		FFM04	179	209	118	136	0.00
HFM13	RFM029		FFM03	15	162	7	135	2.11·10 ⁻⁵
HFM13	RFM029	ZFMENE0401A		162	176	135	147	2.91·10 ⁻⁴
HFM14	RFM029		FFM02	3	68	1	56	7.01·10 ⁻⁴
HFM14	RFM029	ZFMA2		68	76	56	63	1.64·10 ⁻⁴
HFM14	RFM029		FFM02	76	92	63	77	0.00
HFM14	RFM029	ZFMA2		92	104	77	87	2.49·10 ⁻⁴
HFM14	RFM029		FFM02	104	149	87	126	0.00
HFM15	RFM029		FFM02	4	86	1	56	2.17·10 ⁻⁴
HFM15	RFM029	ZFMA2		86	96	56	63	1.02·10 ⁻⁴
HFM15	RFM029		FFM02	96	99	63	65	0.00
HFM16	RFM029	ZFMA8		12	71	9	68	5.26·10 ⁻⁴
HFM16	RFM029		FFM02	71	130	68	126	0.00
HFM17	RFM029		FFM03	8	209	4	202	3.93·10 ⁻⁵
HFM18	RFM017	Possible DZ (G)		9	11	3	4	2.73·10 ⁻⁵
HFM18	RFM017		FFM03	11	30	4	20	0.00
HFM18	RFM029		FFM03	30	36	20	25	0.00
HFM18	RFM029	ZFMA4		36	49	25	36	1.62·10 ⁻⁴
HFM18	RFM029		FFM03	49	119	36	94	0.00
HFM18	RFM029	ZFMA7, ZFMNE0065		119	148	94	117	0.00
HFM18	RFM029		FFM03	148	180	117	142	0.00
HFM19	RFM029		FFM03	11	121	6	94	4.24·10 ⁻⁵
HFM19	RFM029	ZFMA2		121	148	94	115	1.55·10 ⁻⁵
HFM19	RFM029		FFM02	148	168	115	131	6.18·10 ⁻⁶
HFM19	RFM029	ZFMA2		168	185	131	144	2.75·10 ⁻⁴
HFM20	RFM029		FFM02/FFM01	12	301	9	298	7.00·10 ⁻⁵
HFM21	RFM029		FFM02	12	94	6	74	1.71·10 ⁻⁴
HFM21	RFM029	ZFM1203		94	102	74	80	3.01·10 ⁻⁴
HFM21	RFM029		FFM02	102	160	80	124	0.00
HFM21	RFM029	Possible DZ (G)		160	177	124	136	2.08·10 ⁻⁴
HFM21	RFM029		FFM02	177	202	136	153	0.00
HFM22	RFM029		FFM02/FFM01	12	110	9	86	1.65·10 ⁻⁴
HFM22	RFM029	ZFMENE2120		110	129	86	99	0.00
HFM22	RFM029		FFM01	129	216	99	152	0.00
HFM23	RFM029		FFM02/FFM01	21	26	13	18	Low yield
HFM23	RFM029	ZFMENE1208A		26	42	18	30	Low yield
HFM23	RFM029		FFM02/FFM01	42	82	30	56	Low yield
HFM23	RFM029	ZFMNNW0100		82	95	56	62	Low yield
HFM23	RFM029		FFM02/FFM01	95	146	62	76	Low yield
HFM23	RFM044		FFM05	146	166	76	77	Low yield
HFM23	RFM044	Possible DZ (S-ENE)		166	169	77	77	Low yield
HFM23	RFM044		FFM05	169	181	77	77	Low yield
HFM24	RFM029	ZFMWNNW0123		18	32	12	24	3.01·10 ⁻⁵
HFM24	RFM029		FFM04	32	42	24	32	0.00
HFM24	RFM029	ZFMWNNW0123		42	63	32	50	7.99·10 ⁻⁵
HFM24	RFM029		FFM04	63	67	50	54	0.00
HFM24	RFM029	ZFMWNNW0123		67	103	54	86	0.00
HFM24	RFM029		FFM03	103	151	86	129	0.00
HFM25	RFM029	Possible DZ (S-ENE)		9	36	4	26	Low yield
HFM25	RFM029		FFM03	36	42	26	31	Low yield

HFMxx	RFMxxx	ZFMxxxx	FFMxx	Sec-up	Sec-low	Elev-up	Elev-low	Σ T HTHB
HFM25	RFM029	Possible DZ (S-ENE)		42	54	31	41	Low yield
HFM25	RFM029		FFM03	54	80	41	61	Low yield
HFM25	RFM029	Possible DZ (S-ENE)		80	92	61	70	Low yield
HFM25	RFM029		FFM03	92	143	70	105	Low yield
HFM25	RFM029	ZFMENE0062A		143	155	105	113	Low yield
HFM25	RFM029		FFM03	155	169	113	122	Low yield
HFM25	RFM029	ZFMENE0062A		169	187	122	134	Low yield
HFM26	RFM029	ZFMA4		12	46	7	33	Low yield
HFM26	RFM029		FFM03	46	60	33	44	Low yield
HFM26	RFM029	ZFMA4		60	95	44	70	Low yield
HFM26	RFM029		FFM03	95	161	70	116	Low yield
HFM26	RFM029	ZFMNE0065		161	203	116	144	Low yield
HFM27	RFM029		FFM02	12	26	9	22	1.30·10 ⁻⁵
HFM27	RFM029	ZFMA2		26	30	22	25	2.30·10 ⁻⁵
HFM27	RFM029		FFM02	30	45	25	39	0.00
HFM27	RFM029	ZFM1203		45	63	39	56	4.00·10 ⁻⁵
HFM27	RFM029		FFM02	63	117	56	105	0.00
HFM27	RFM029	Possible DZ (G)		117	123	105	111	6.70·10 ⁻⁶
HFM27	RFM029		FFM02	123	127	111	115	0.00
HFM28	RFM029	ZFMENE1208A		12	65	8	60	Low yield
HFM28	RFM029		FFM02/FFM01	65	148	60	141	Low yield
HFM29	RFM029		FFM03	9	19	3	12	Low yield
HFM29	RFM029	ZFMWNNW0123		19	25	12	17	Low yield
HFM29	RFM029		FFM03	25	62	17	50	Low yield
HFM29	RFM029	ZFMWNNW0123		62	81	50	67	Low yield
HFM29	RFM029		FFM03	81	146	67	127	Low yield
HFM29	RFM029	ZFMWNNW0123		146	150	127	131	Low yield
HFM29	RFM029		FFM03	150	200	131	178	Low yield
HFM30	RFM026		FFM04	19	57	12	45	0.00
HFM30	RFM018		FFM04	57	79	45	63	6.90·10 ⁻⁶
HFM30	RFM018	ZFMNW0017		79	201	63	170	1.28·10 ⁻⁴
HFM30	RFM018			0	0	0	0	0.00
HFM31	RFM025		FFM04	9	200	2	177	Low yield
HFM32	RFM029		FFM03	6	29	5	28	8.17·10 ⁻⁴
HFM32	RFM029		FFM03	29	122	28	120	1.30·10 ⁻⁴
HFM32	RFM029		FFM03	122	203	120	198	0.00

* Low yield means that the borehole was too dry to be tested. A zero transmissivity means that the impeller logging could detect any flow.

6.2 Plots showing HTHB transmissivity data

Figure 6-1 through Figure 6-16 display the HTHB transmissivity values gathered in the percussion-drilled boreholes HFM01–32. The left hand plot shows all transmissivity data gathered and the right hand plot shows the transmissivity data associated with deformation zones. The legend to the colours used in the right hand plot is shown in Table 3-2. Possible deformation zones are coloured grey. It is noted that the structural interpretation of the HTHB transmissivities identified in HFM01, -02, -04, -05, -06, -08, -14, -15, -16, -18, and -19 are predominantly associated with gently-dipping features.

In a few of the percussion-drilled boreholes, the PSS method has been used as a means to enhance the data acquisition, e.g. when the drawdown of the HTHB pumping test drops far below the elevation of the casing shoe.

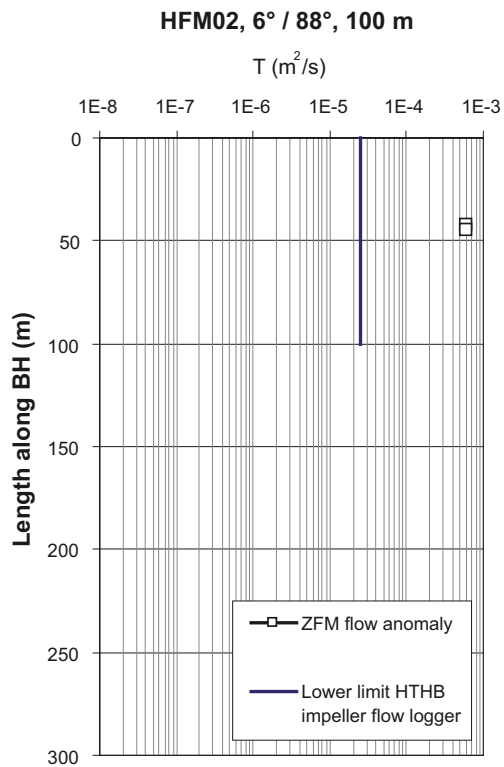
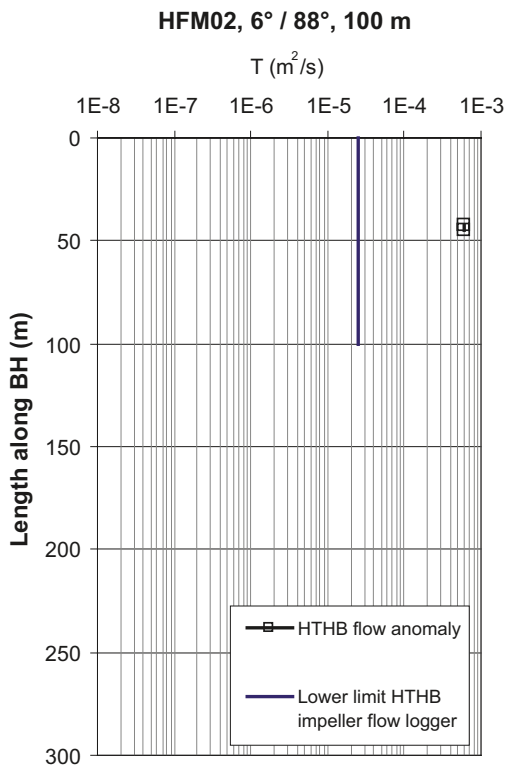
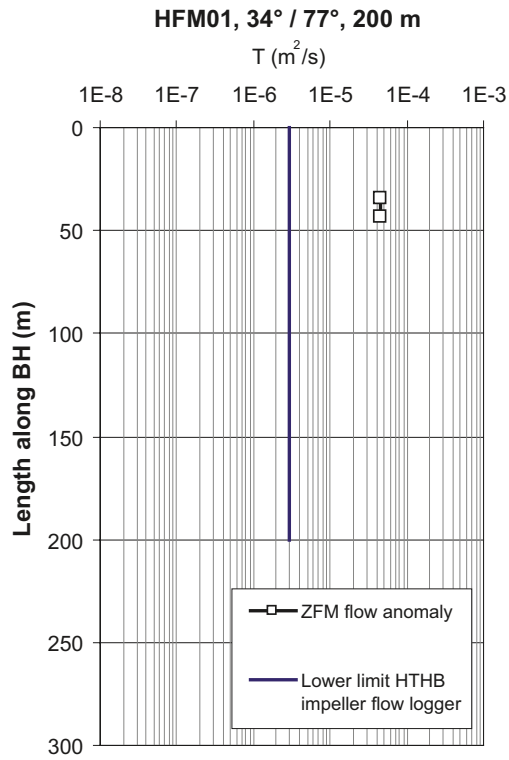
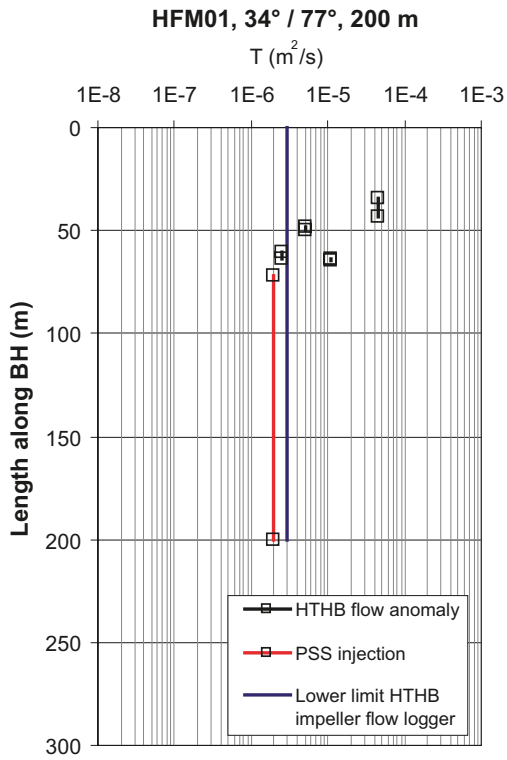


Figure 6-1. HTHB transmissivities acquired in HFM01 and HFM02. The plots to the left shows all transmissivity data and the plots to the right shows the transmissivity data associated with deformation zones. Colours according to Table 3-2.

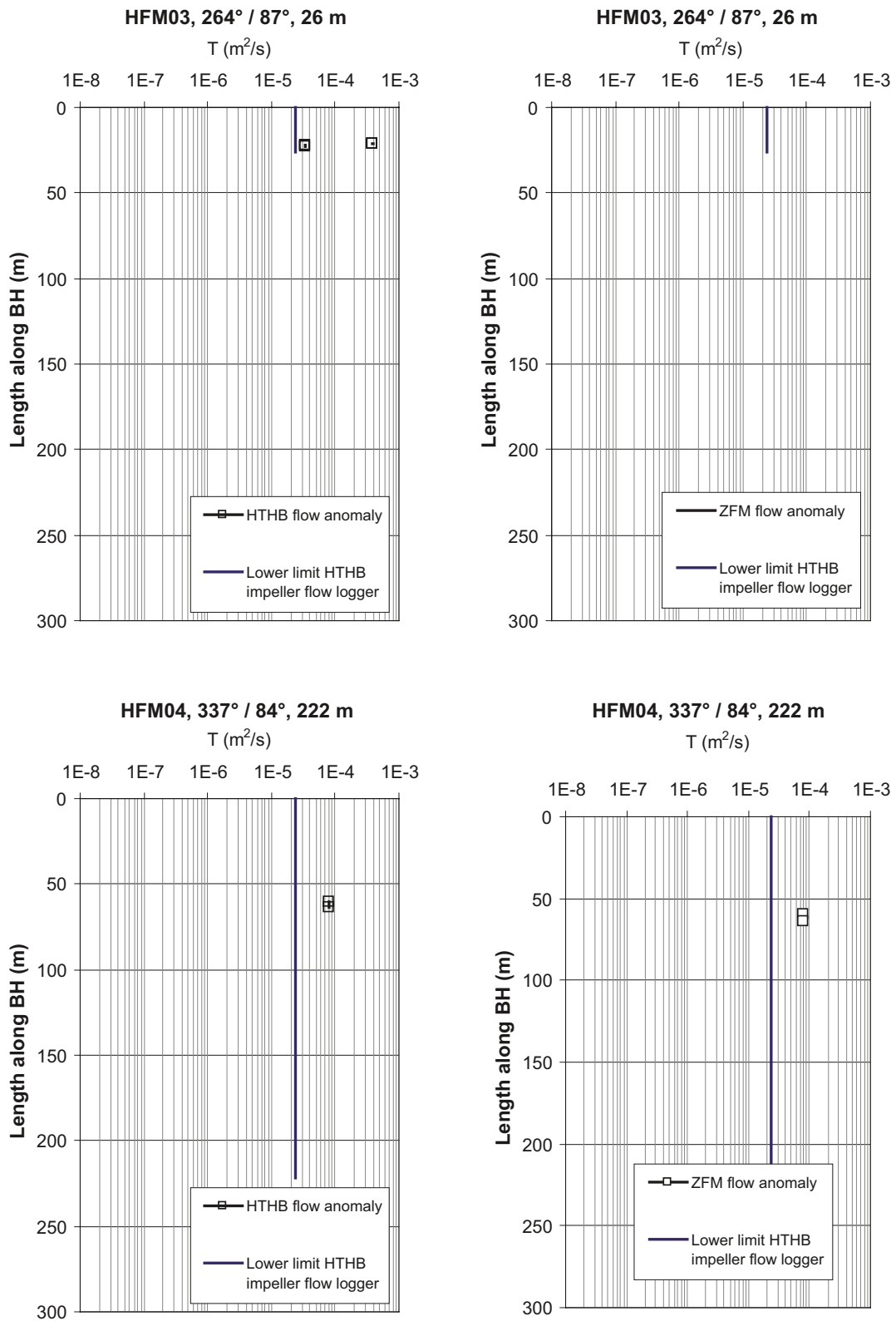


Figure 6-2. HTHB transmissivities acquired in HFM03 and HFM04. The plots to the left shows all transmissivity data and the plots to the right shows the transmissivity data associated with deformation zones. Colours according to Table 3-2.

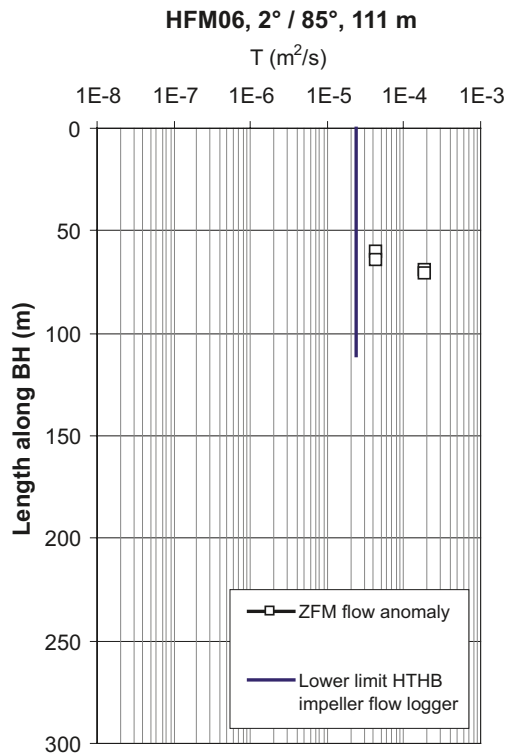
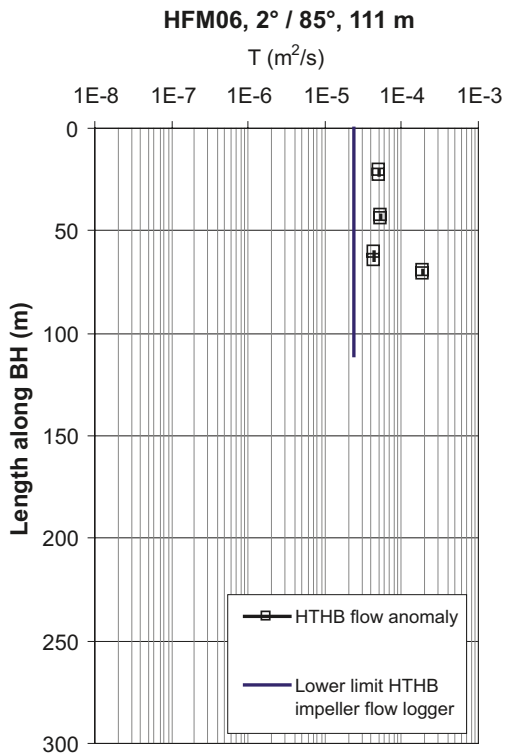
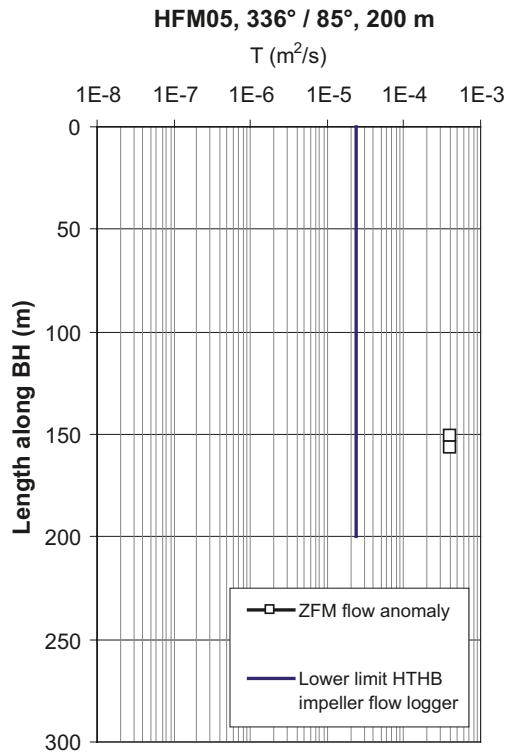
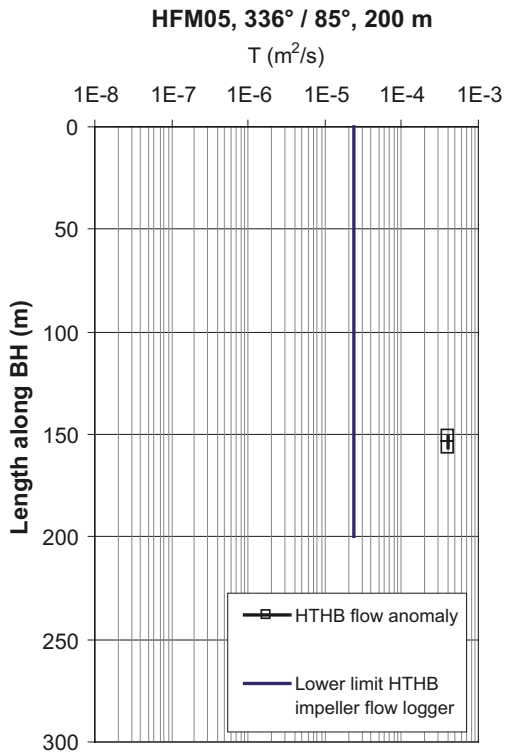


Figure 6-3. HTHB transmissivities acquired in HFM05 and HFM06. The plots to the left shows all transmissivity data and the plots to the right shows the transmissivity data associated with deformation zones. Colours according to Table 3-2.

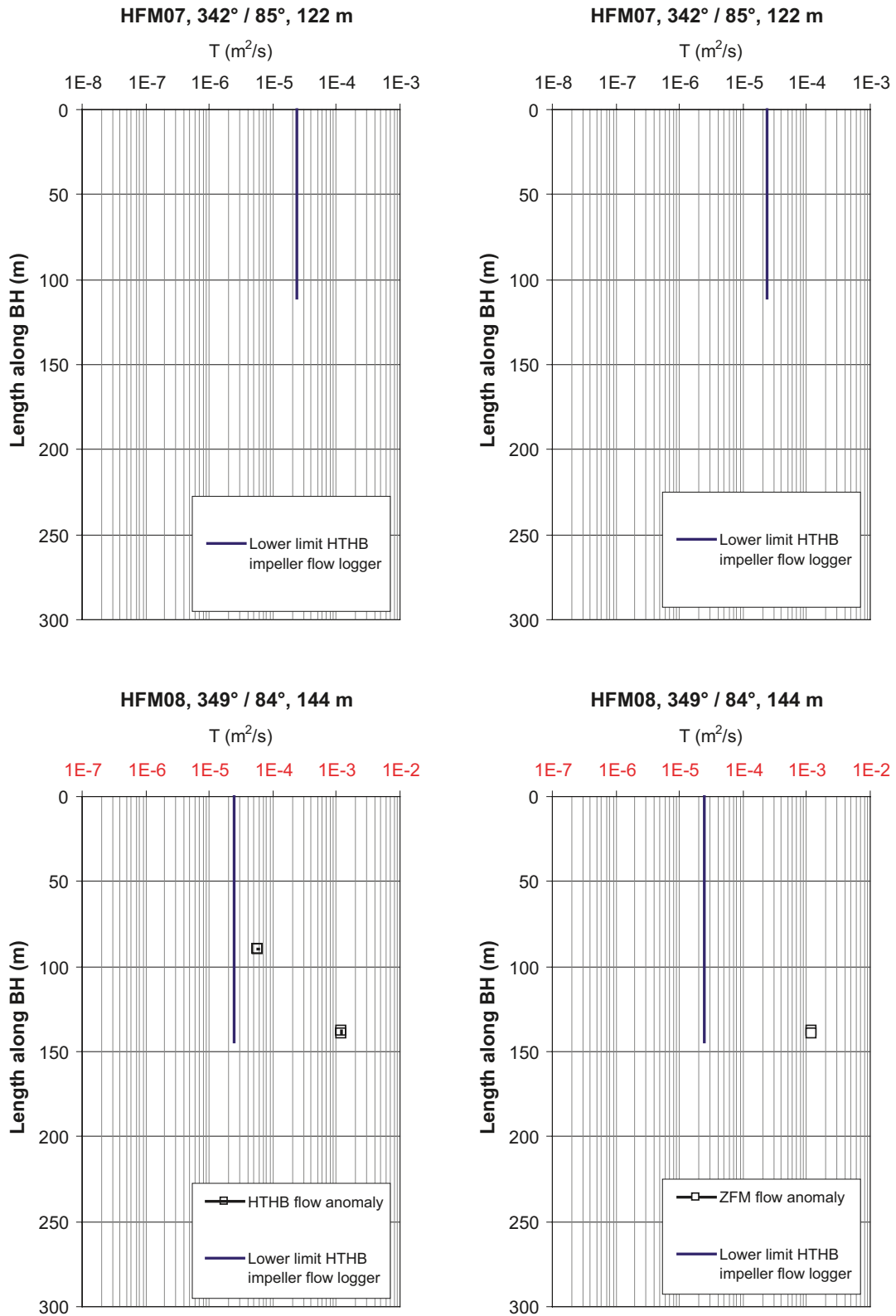


Figure 6-4. HTHB transmissivities acquired in HFM07 and HFM08. The plots to the left show all transmissivity data and the plots to the right show the transmissivity data associated with deformation zones. Colours according to Table 3-2. Note the difference in the transmissivity range in this plot.

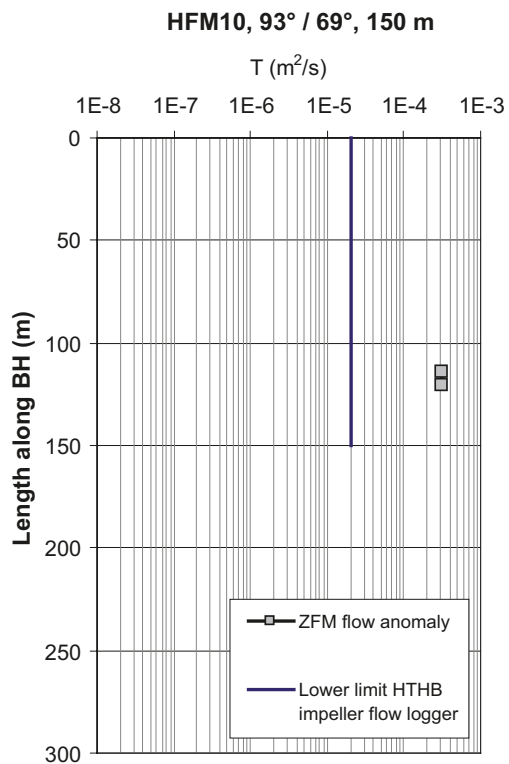
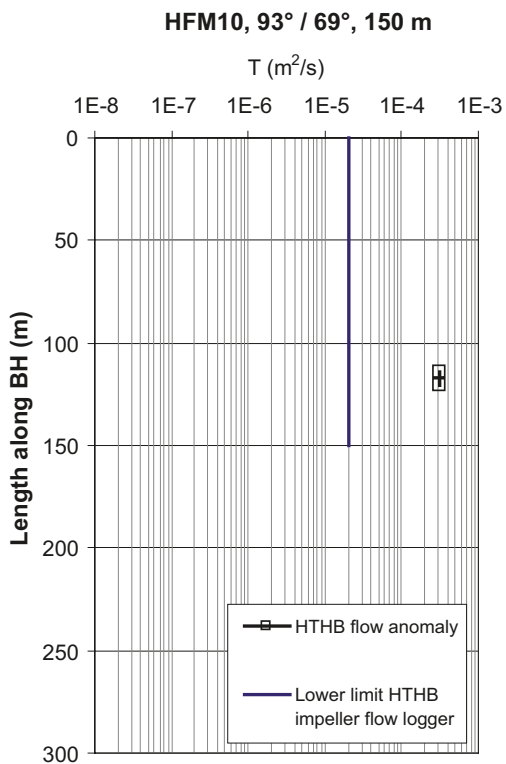
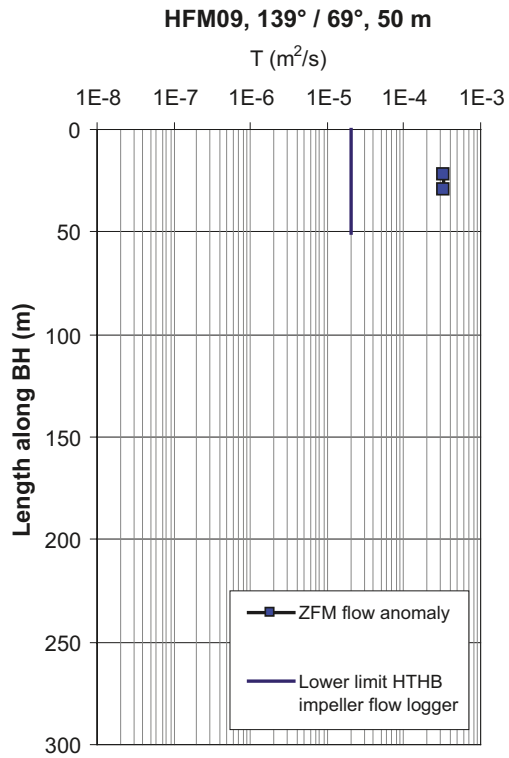
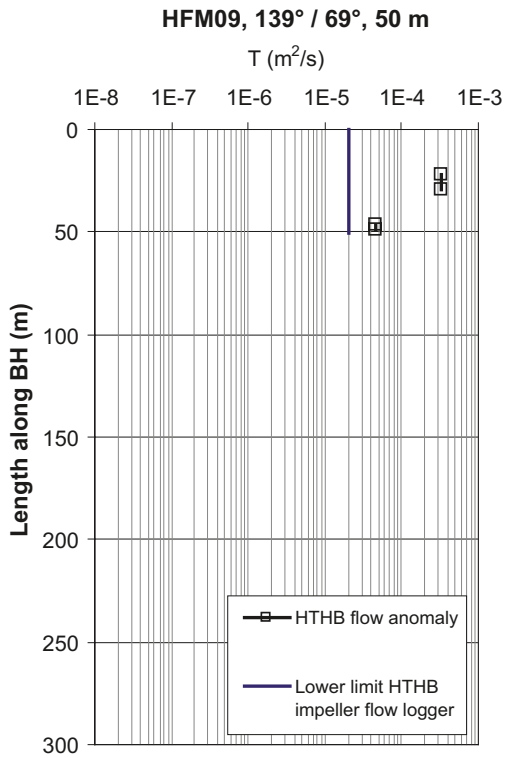


Figure 6-5. HTHB transmissivities acquired in HFM09 and HFM10. The plots to the left shows all transmissivity data and the plots to the right shows the transmissivity data associated with deformation zones. Colours according to Table 3-2.

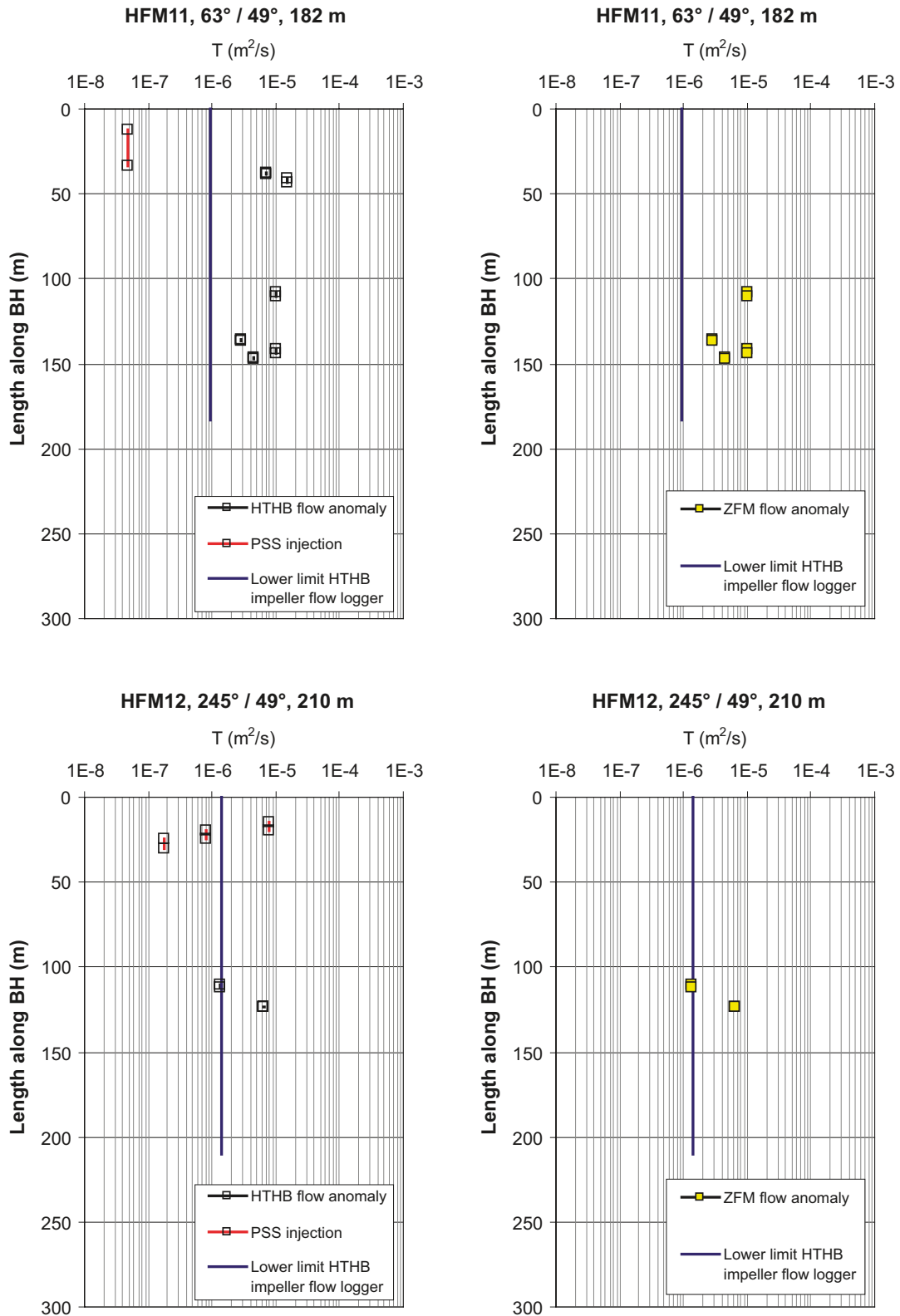


Figure 6-6. HTHB transmissivities acquired in HFM11 and HFM12. The plots to the left shows all transmissivity data and the plots to the right shows the transmissivity data associated with deformation zones. Colours according to Table 3-2.

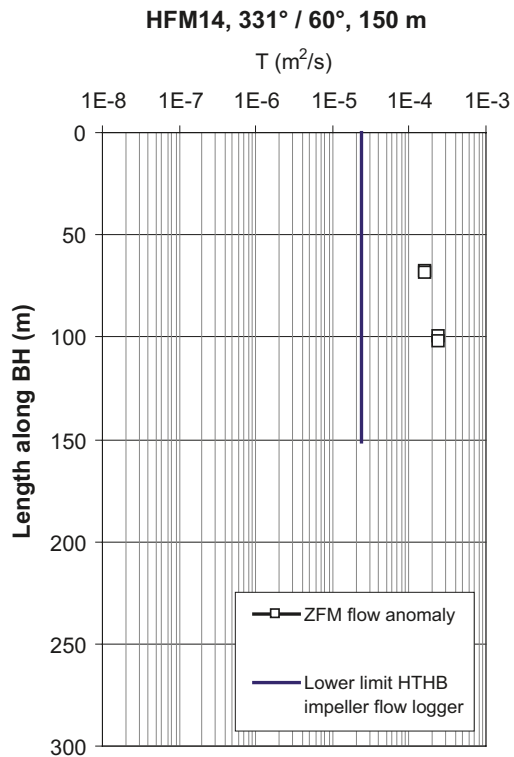
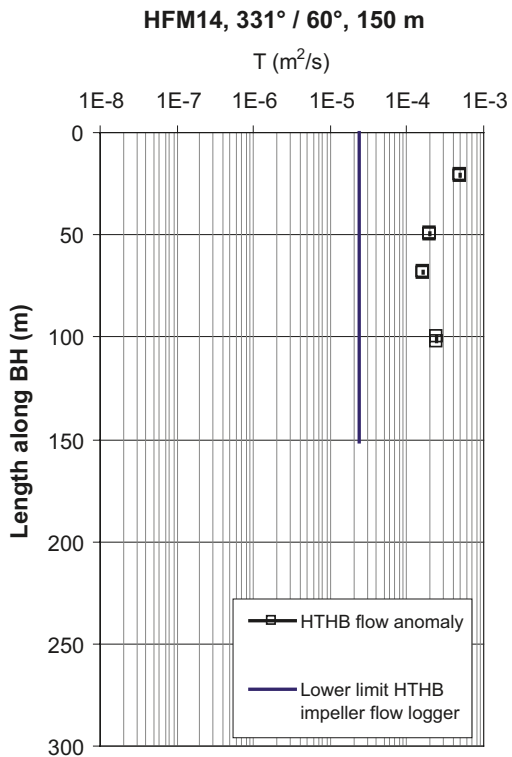
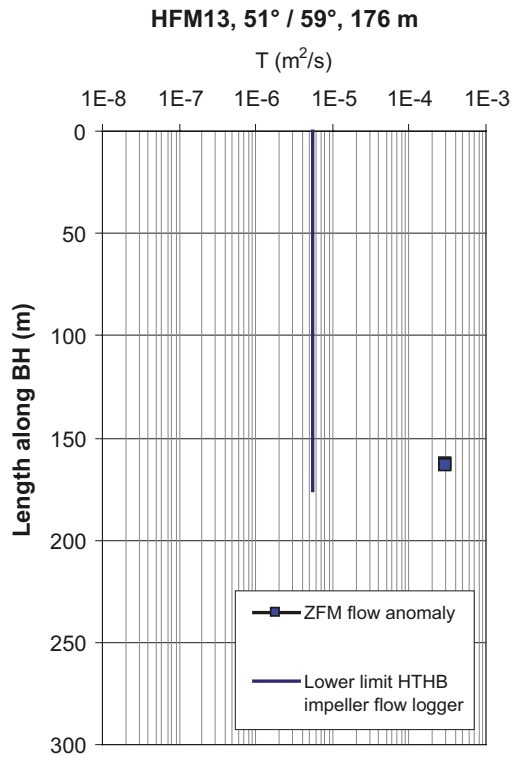
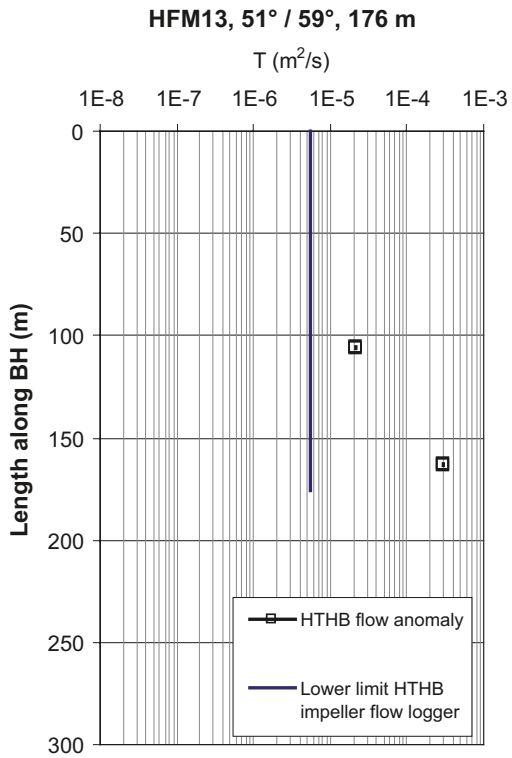


Figure 6-7. HTHB transmissivities acquired in HFM13 and HFM14. The plots to the left shows all transmissivity data and the plots to the right shows the transmissivity data associated with deformation zones. Colours according to Table 3-2.

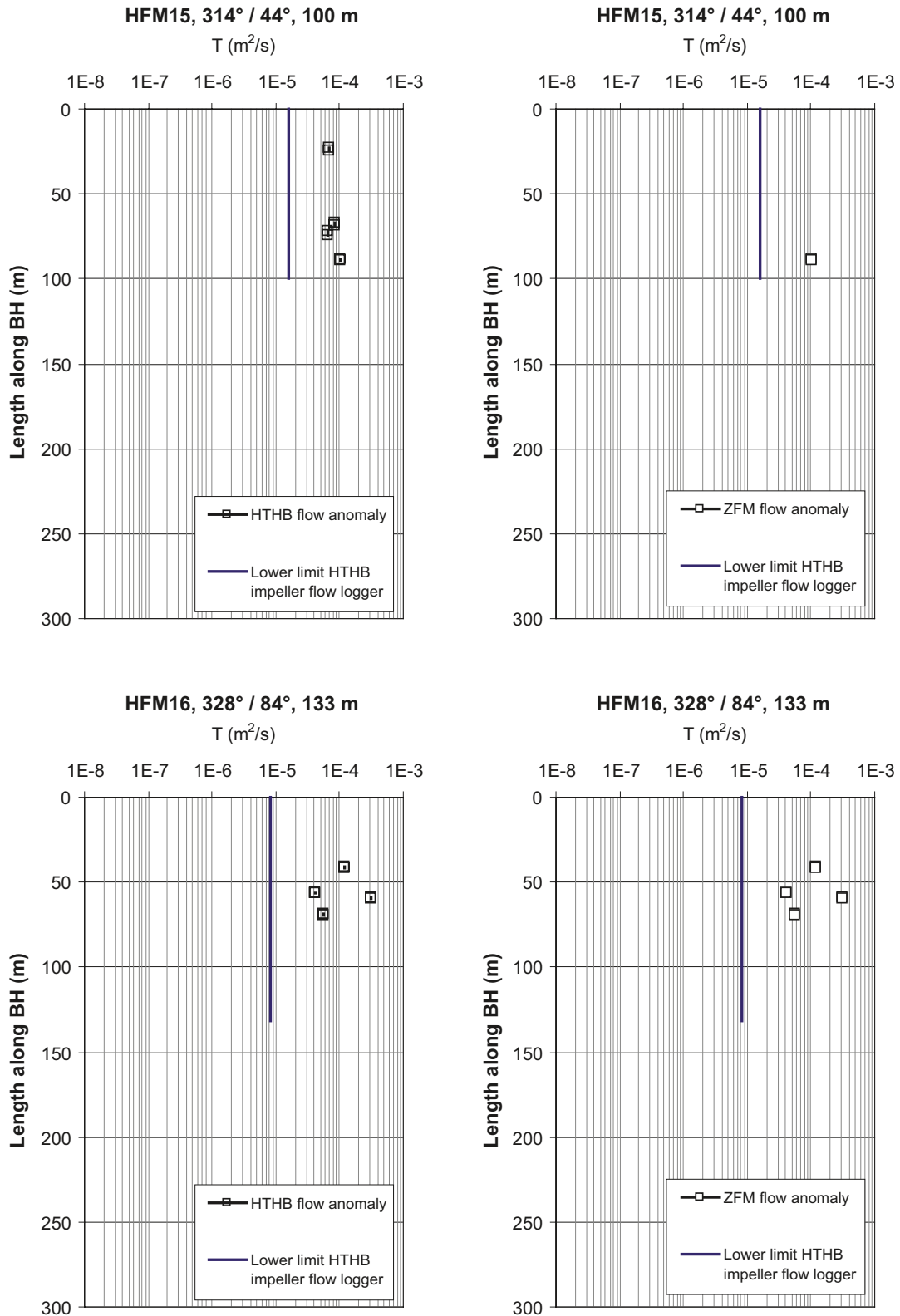


Figure 6-8. HTHB transmissivities acquired in HFM15 and HFM16. The plots to the left shows all transmissivity data and the plots to the right shows the transmissivity data associated with deformation zones. Colours according to Table 3-2.

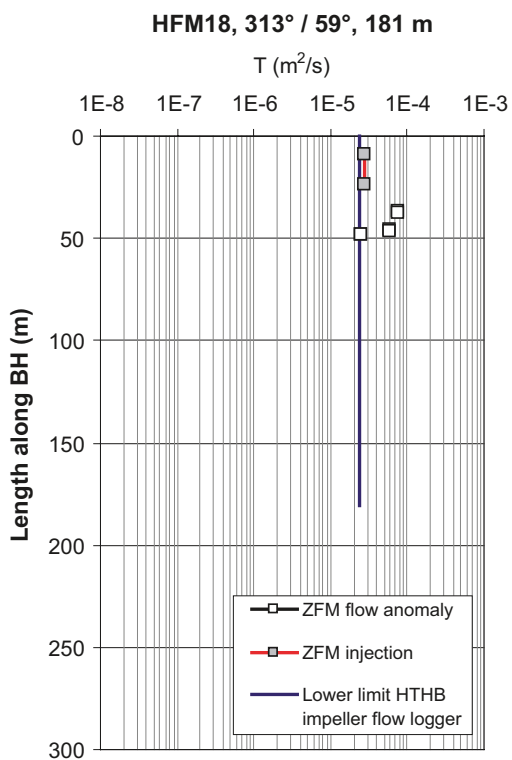
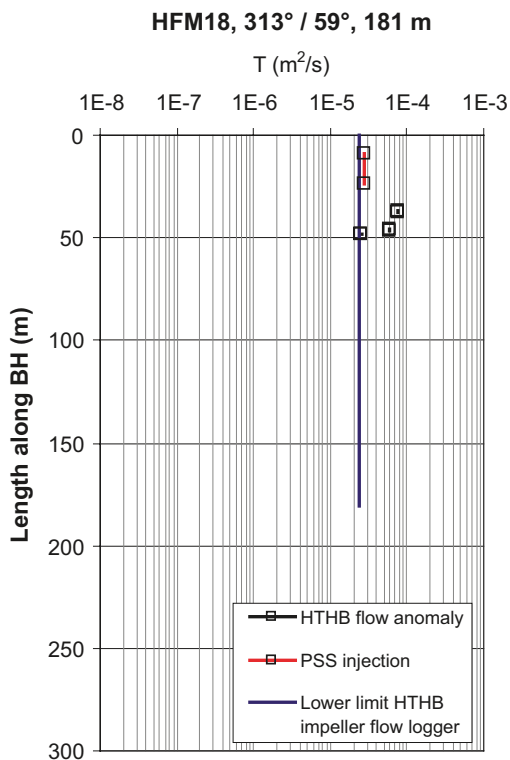
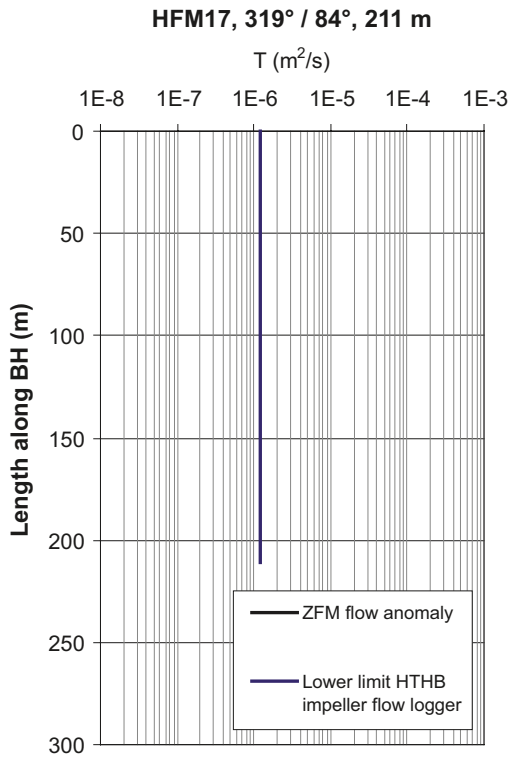
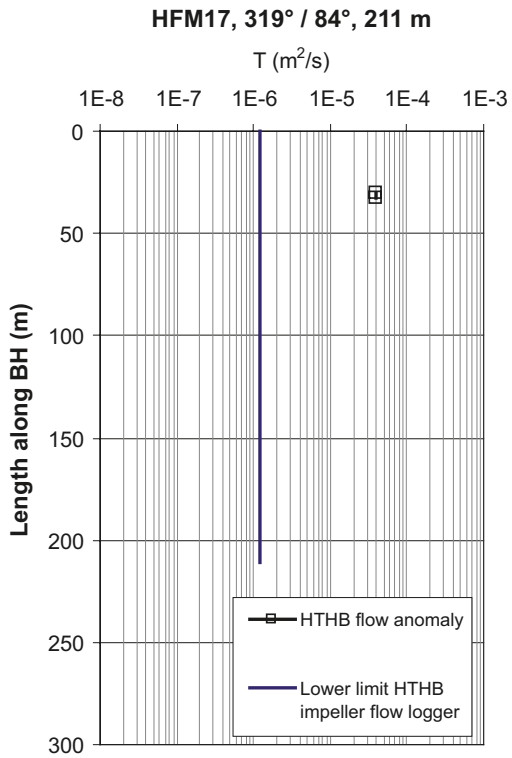


Figure 6-9. HTHB transmissivities acquired in HFM17 and HFM18. The plots to the left shows all transmissivity data and the plots to the right shows the transmissivity data associated with deformation zones. Colours according to Table 3-2.

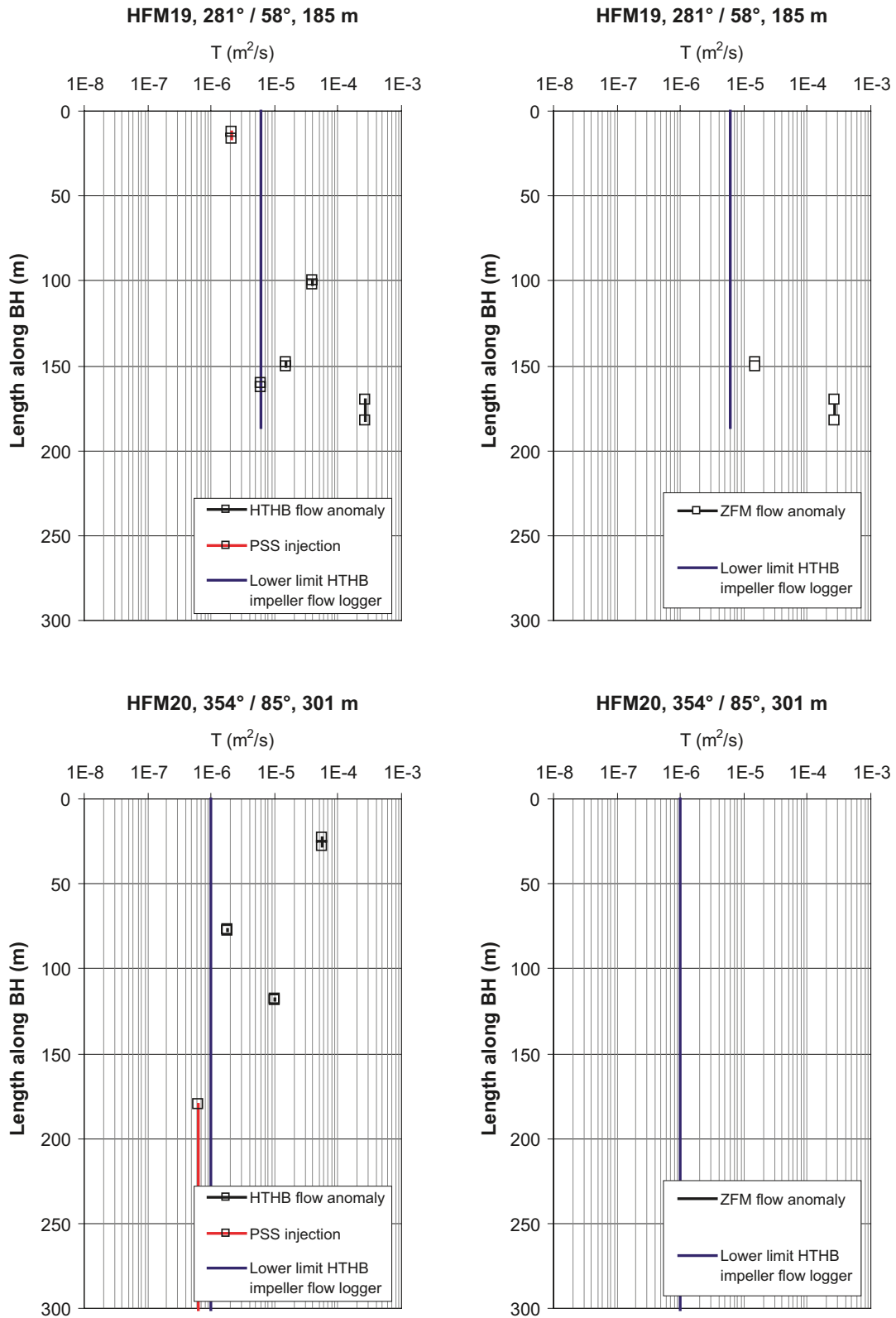


Figure 6-10. HTHB transmissivities acquired in HFM19 and HFM20. The plots to the left shows all transmissivity data and the plots to the right shows the transmissivity data associated with deformation zones. Colours according to Table 3-2.

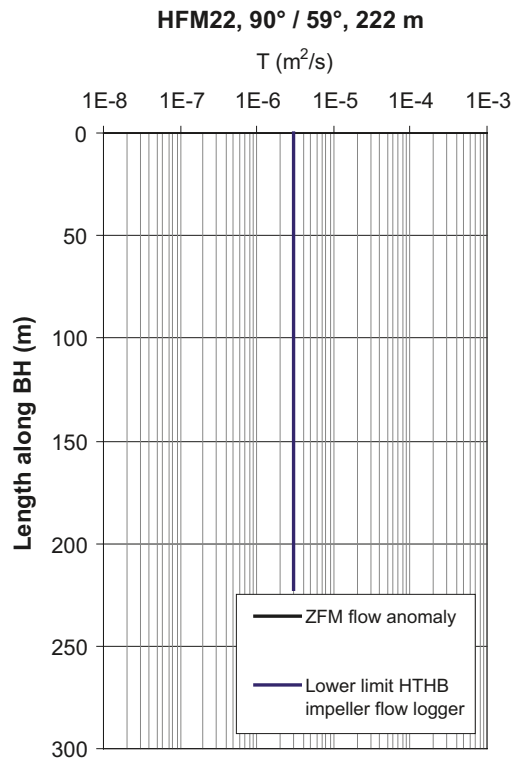
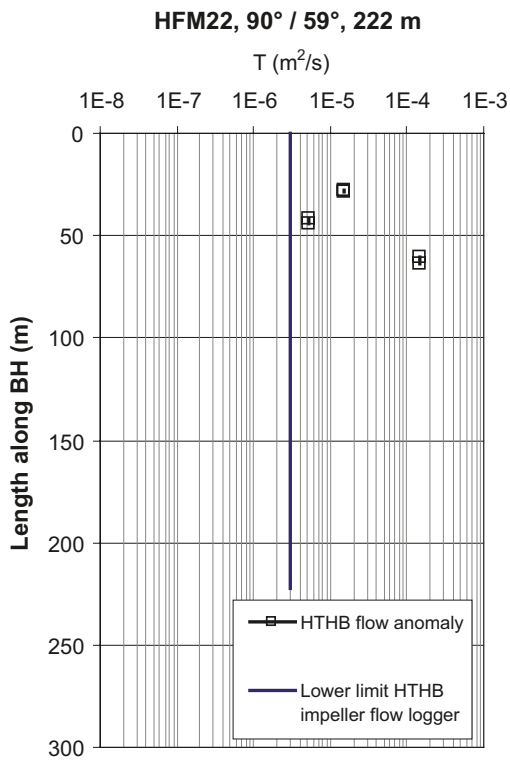
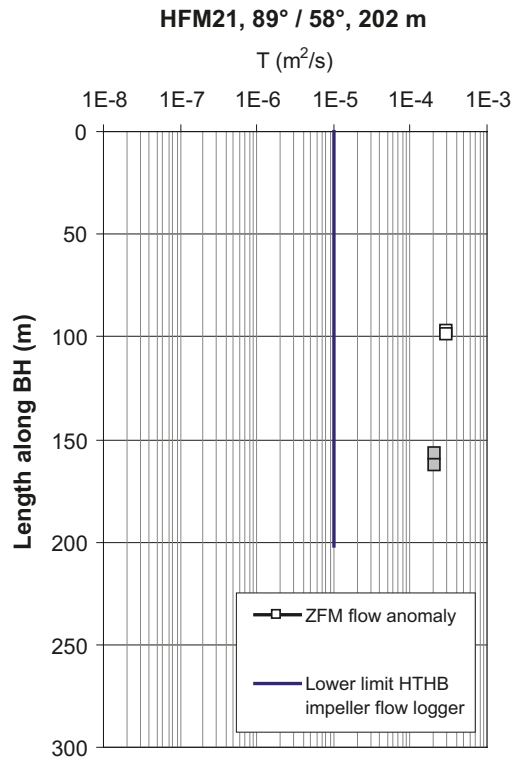
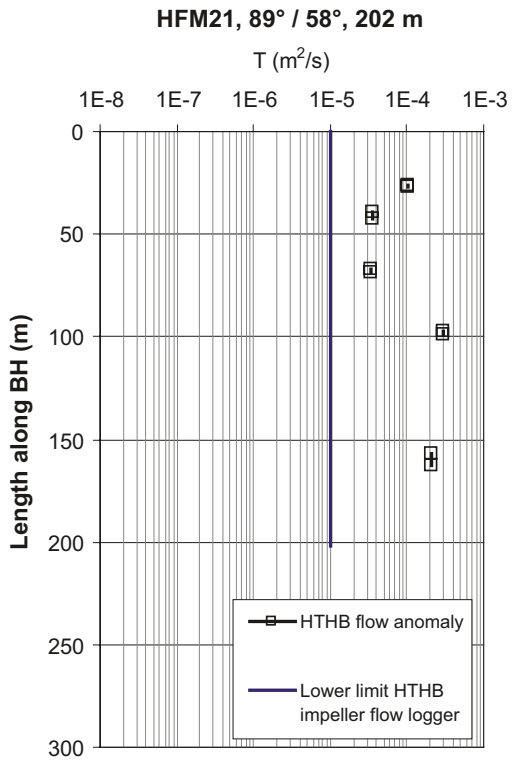


Figure 6-11. HTHB transmissivities acquired in HFM21 and HFM22. The plots to the left shows all transmissivity data and the plots to the right shows the transmissivity data associated with deformation zones. Colours according to Table 3-2.

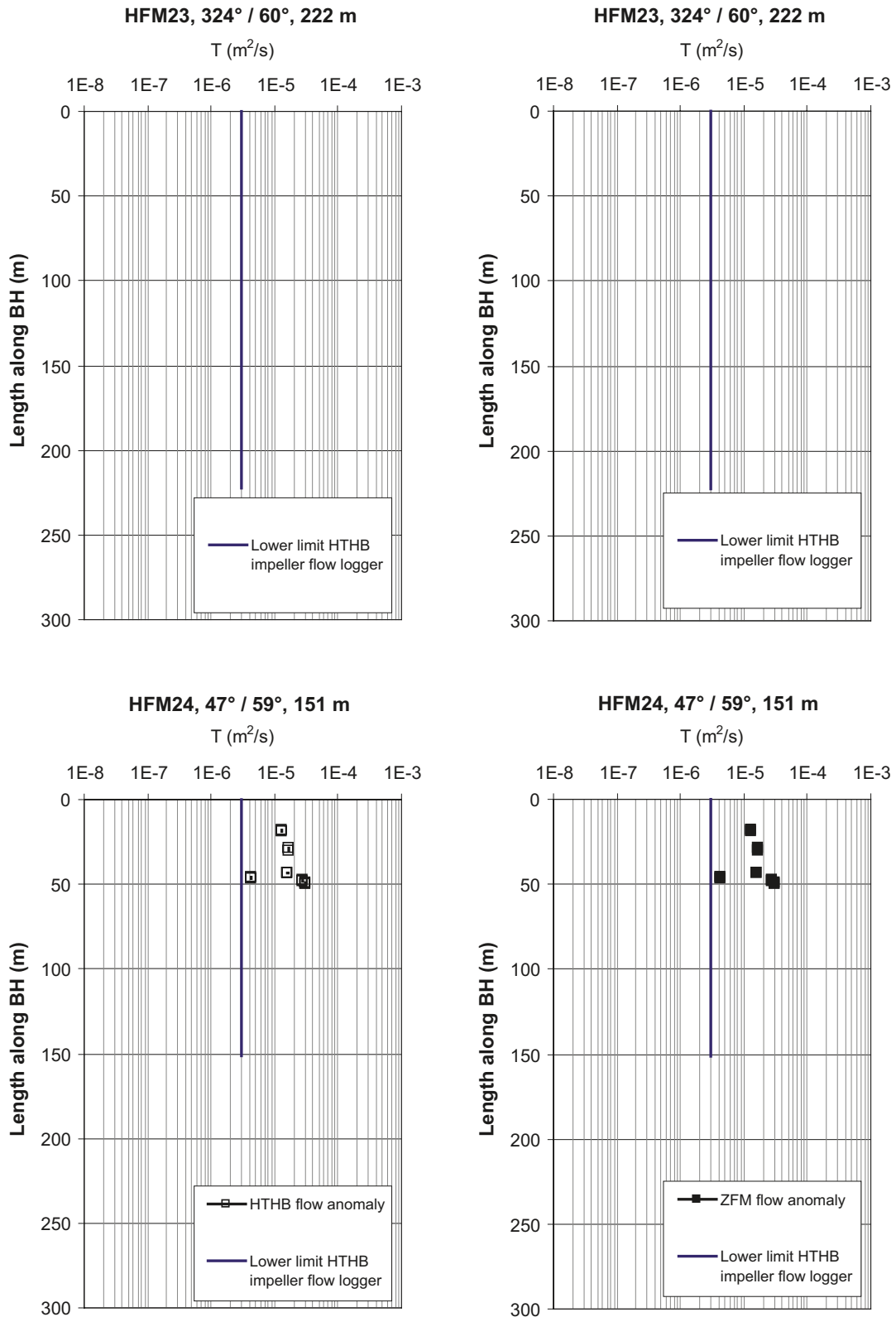


Figure 6-12. HTHB transmissivities acquired in HFM23 and HFM24. The plots to the left shows all transmissivity data and the plots to the right shows the transmissivity data associated with deformation zones. Colours according to Table 3-2.

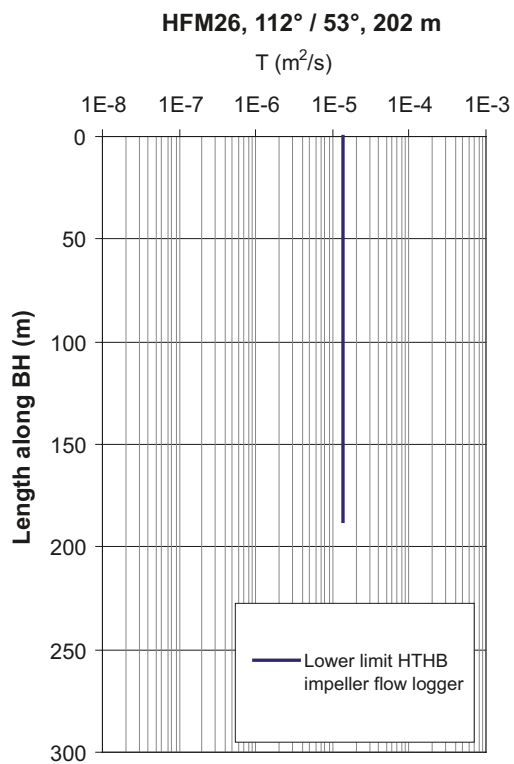
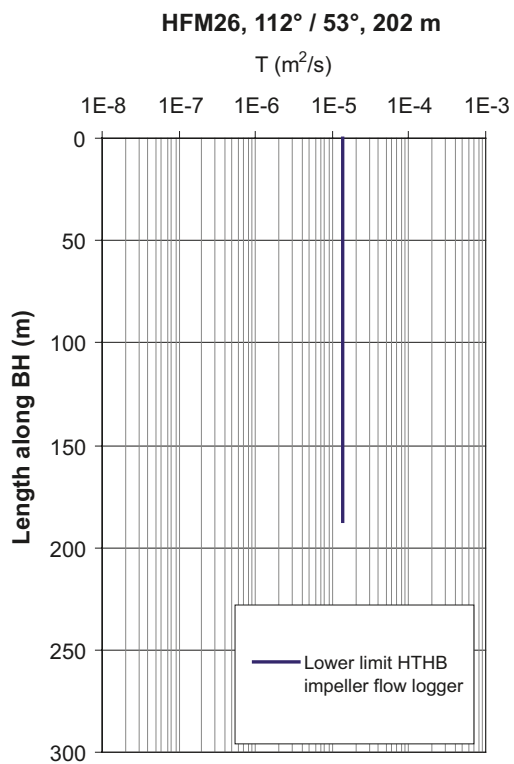
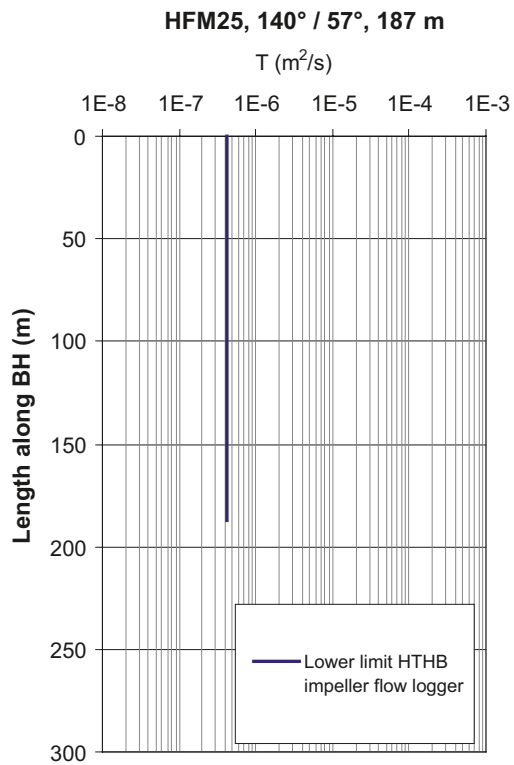
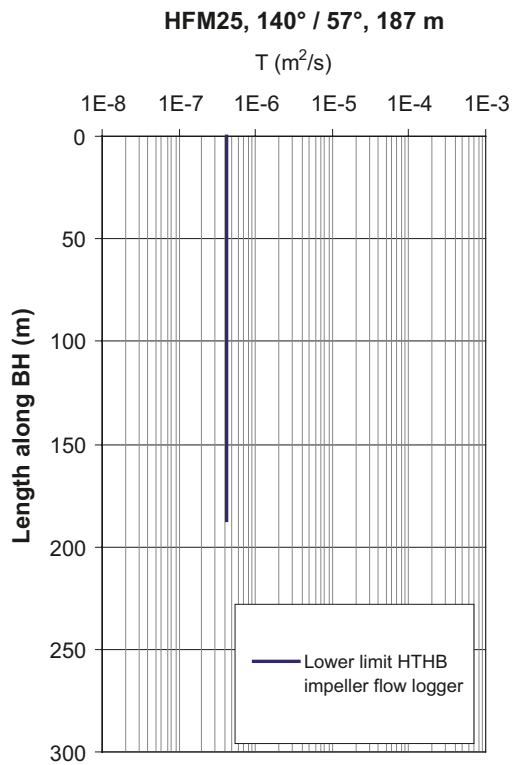


Figure 6-13. HTHB transmissivities acquired in HFM25 and HFM26. The plots to the left shows all transmissivity data and the plots to the right shows the transmissivity data associated with deformation zones. Colours according to Table 3-2.

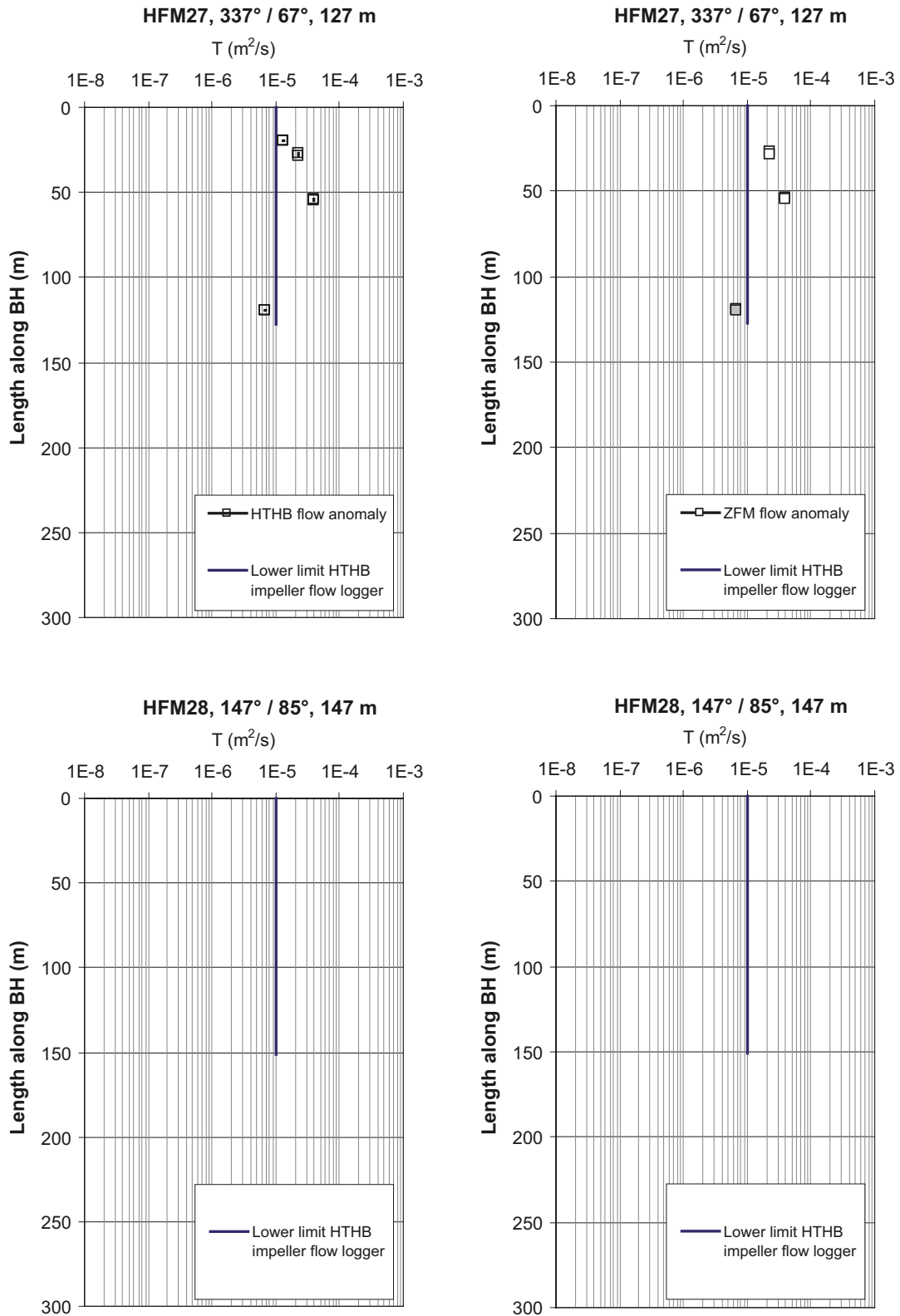


Figure 6-14. HTHB transmissivities acquired in HFM27 and HFM28. The plots to the left shows all transmissivity data and the plots to the right shows the transmissivity data associated with deformation zones. Colours according to Table 3-2.

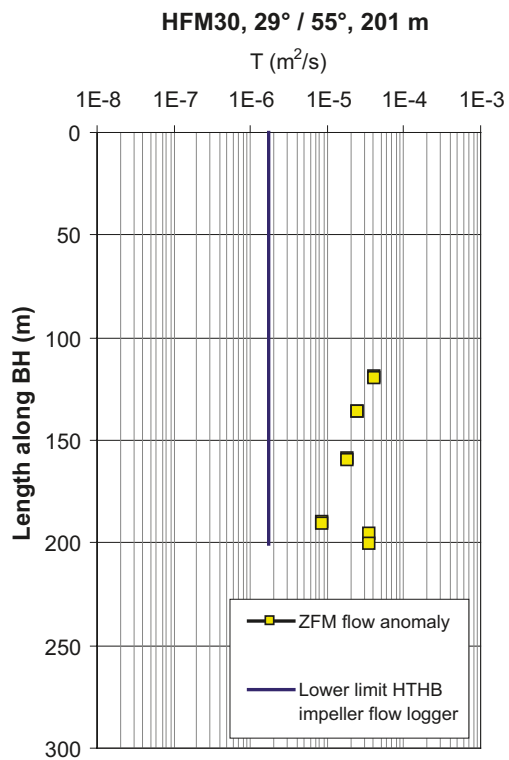
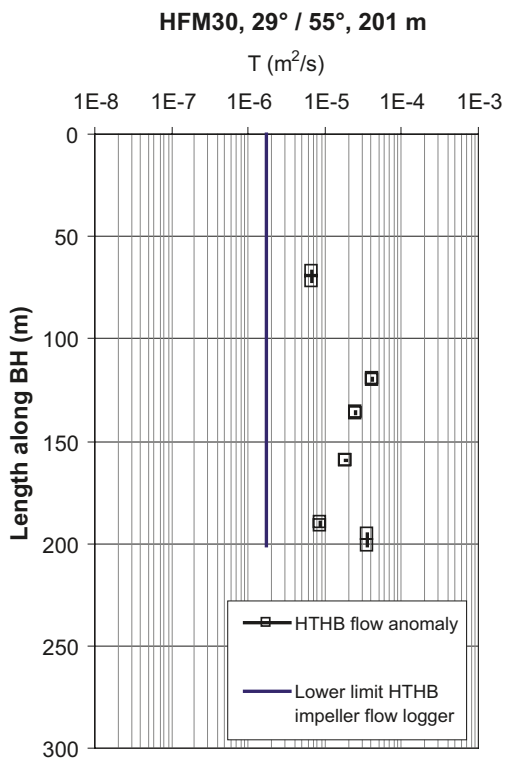
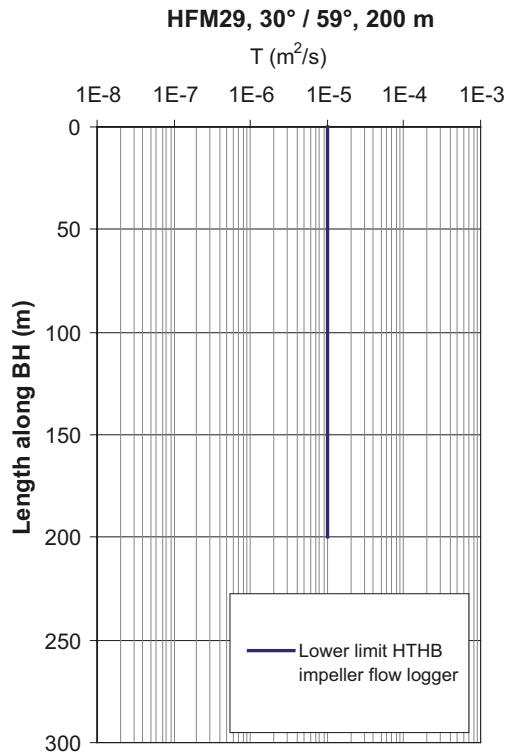
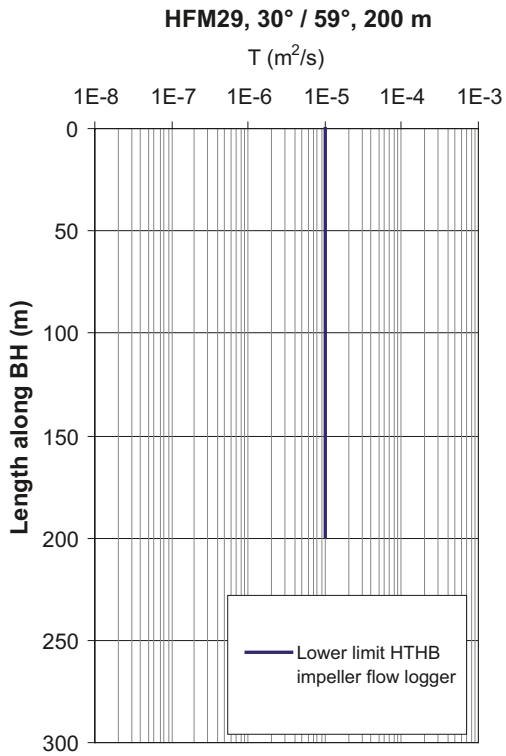


Figure 6-15. HTHB transmissivities acquired in HFM29 and HFM30. The plots to the left shows all transmissivity data and the plots to the right shows the transmissivity data associated with deformation zones. Colours according to Table 3-2.

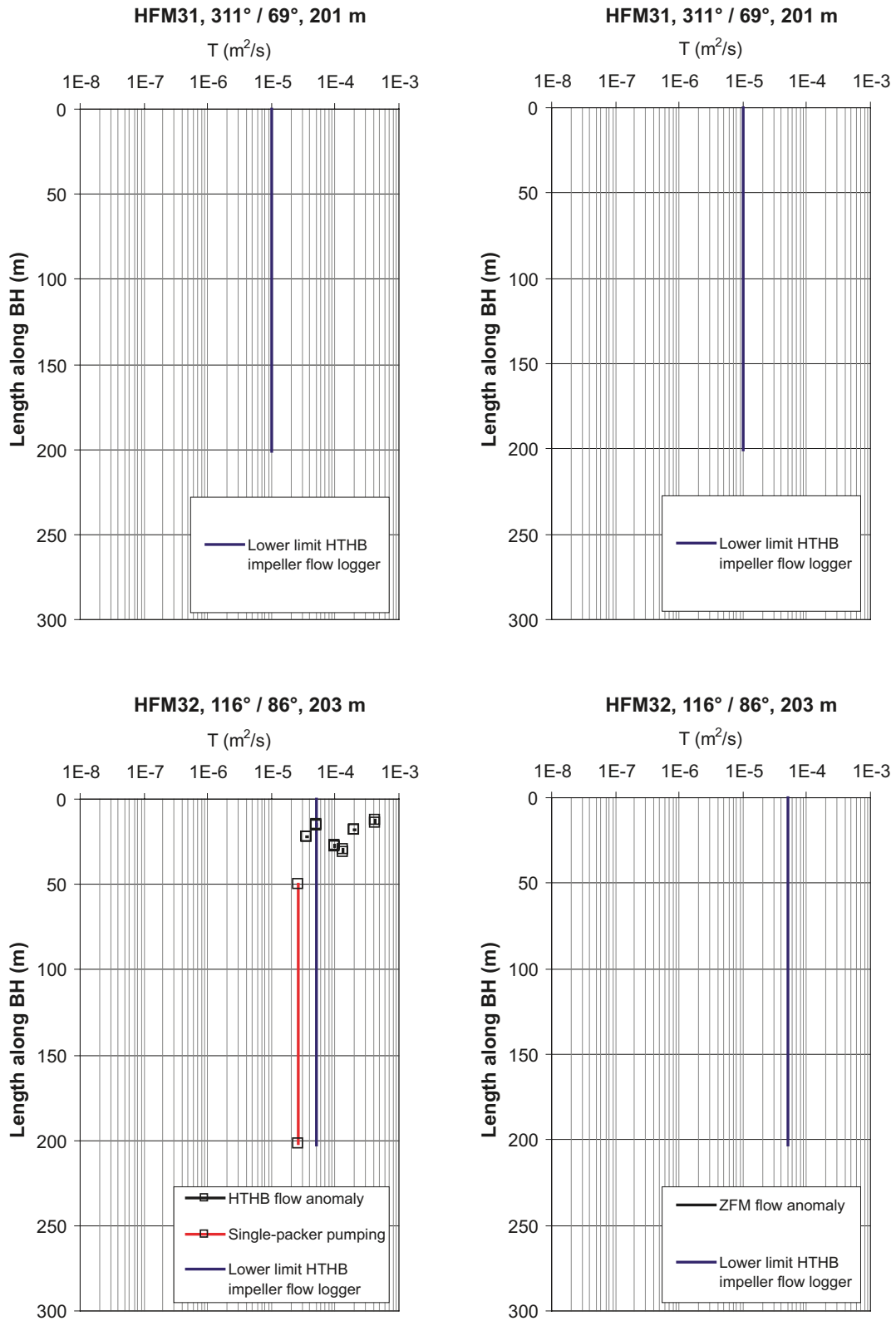


Figure 6-16. HTHB transmissivities acquired in HFM31 and HFM32. The plots to the left shows all transmissivity data and the plots to the right shows the transmissivity data associated with deformation zones. Colours according to Table 3-2.

7 Hydrogeological data synthesis for possible deformation zones

Table 5-23 reveals that c. 24% (8,191) of the 34,191 fractures identified in KFM01A–8A, -10A, -08C and -01D, are determined to be open at the point of observation. 577 of the open fractures are identified as interconnected and flowing fractures with the PFL-f method, which corresponds to 1.7% of all fractures and to 7.0% of the open fractures. About 44% (251) of the PFL-f anomalies are associated with single fractures, c. 52% (302) are associated with 30 deterministically modelled deformation zones and c. 4% (24) are associated with 6 “possible deformation zones”.

The boreholes studied with the PFL-f method KFM01A–8A, -10A, -08C and -01D contain all together 21 borehole intervals interpreted as deformation zone intercepts but not modelled deterministically; that is, possible deformation zones. Table 7-1 summarises the structural-hydraulic data for the 21 borehole intervals. Possible deformation zones with little or no flow are marked up as “ $< T_{limit}$ ”.

Table 7-1. Summary of structural-hydraulic data interpreted for the 21 borehole intervals in KFM01A–8A, -10A, -08C and -01D investigated with the PFL-f method and demarked as “possible deformation zones”. The first column shows the structural interpretation as suggested by the geological single-hole interpretation. The third column shows the elevation of the centre of each intercept. ‘b’ denotes is the estimated geological thickness. Note that the possible deformation zones associated with little or no flow are marked up as “ $< T_{limit}$ ”. Flowing “possible deformation zones” encountered below –400 m RHB 70 within the target volume are highlighted with red letters.

Category	Borehole	Elevation (m RHB 70)	b (m)	No. of PFL-f (–)	ΣT PFL-f (m ² /s)	T_{limit}
G	KFM01A	–216.0	8	0	$< T_{limit}$	$1 \cdot 10^{-9}$
NNW	KFM01D	–144.0	6	0	$< T_{limit}$	$1 \cdot 10^{-9}$
NNW	KFM01D	–328.5	7	0	$< T_{limit}$	$1 \cdot 10^{-9}$
NNW	KFM01D	–386.0	6	0	$< T_{limit}$	$1 \cdot 10^{-9}$
ENE	KFM01D	–590.0	2	0	$< T_{limit}$	$1 \cdot 10^{-9}$
G	KFM02A	–550.5	79	0	$< T_{limit}$	$1 \cdot 10^{-9}$
G	KFM02A	–910.5	3	0	$< T_{limit}$	$1 \cdot 10^{-9}$
G	KFM02A	–966.0	6	0	$< T_{limit}$	$1 \cdot 10^{-9}$
G	KFM03A	–932.5	7	2	$3.46 \cdot 10^{-7}$	$1 \cdot 10^{-9}$
NNW	KFM04A	–762.0	2	1	$1.29 \cdot 10^{-9}$	$1 \cdot 10^{-9}$
G	KFM06A	–114.5	15	17	$3.90 \cdot 10^{-5}$	$1 \cdot 10^{-9}$
NNE	KFM06A	–549.0	4	1	$2.74 \cdot 10^{-10}$	$1 \cdot 10^{-9}$
NNE	KFM06A	–743.5	19	0	$< T_{limit}$	$1 \cdot 10^{-9}$
NNE	KFM06A	–772.0	6	0	$< T_{limit}$	$1 \cdot 10^{-9}$
G	KFM07A	–169.0	8	0	$< T_{limit}$	$1 \cdot 10^{-9}$
NNE	KFM08A	–440.5	21	0	$< T_{limit}$	$1 \cdot 10^{-9}$
NNW	KFM08A	–500.5	1	0	$< T_{limit}$	$1 \cdot 10^{-9}$
WNW	KFM08A	–543.5	15	1	$1.41 \cdot 10^{-6}$	$1 \cdot 10^{-9}$
WNW	KFM08A	–712.5	19	0	$< T_{limit}$	$1 \cdot 10^{-9}$
WNW	KFM08A	–735.0	6	0	$< T_{limit}$	$1 \cdot 10^{-9}$
NNE	KFM08C	–149.5	25	2	$6.68 \cdot 10^{-9}$	$1 \cdot 10^{-9}$

Table 7-1 suggests that the geological thickness of the possible deformation zones varies widely (1–80 m) and that about 2/3 of them are either no flowing or have a transmissivity value lower than the detection limit of the test method used. Moreover, possible deformation zones with little or no flow can occur at any depth. With one exception the flowing possible deformation zones tend to be very discrete; 1 or 2 flowing fractures despite their geological thickness. The exception is found in KFM06A where a c. 15 m thick possible deformation zone occurs close to surface. This zone has 17 flow anomalies.

The evident interpretation from these observations is that “possible deformation zones” is not a well defined class of objects, at least not from a hydrogeological point of view. If the deeper zones conform to the same tectonic evolution as envisaged for single fractures, see Figure 2-3, their size can be modelled stochastically. However, the possible deformation zones that occur in the uppermost part of the bedrock may be stress induced sheet joints rather, the sizes of which may be arbitrary.

The classic Monte Carlo approach to hydrogeological DFN analysis and modelling entails multiple realisations. The approach invokes a statistical homogeneous medium. However, Figure 5-1 through Figure 5-12 suggest quite extraordinary hydrogeological conditions, where large volumes of rock may be below the percolation threshold, in particular below –400 m elevation. The overall impression of the data displayed suggests a significant depth dependence, lateral heterogeneity and anisotropy, properties which make it difficult to invoke statistical homogeneity.

An excellent example, which demonstrates some of the conceptual complexities involved, is the possible deformation zone, DZ4, between 672–693 m borehole length (–536 to –551 m RHB 70) in borehole KFM08A. This interval contains one (1) PLF-f flow anomaly with a transmissivity of $1.41 \cdot 10^{-6} \text{ m}^2/\text{s}$ /Teurneau et al. 2007/. The possible deformation zone interval has a geological thickness of c. 15 m. The stereo nets of the sealed and open fractures associated with the zone are shown in Figure 7-1 together with a BIPS image of the flowing fracture correlated to the anomaly. The geological motivation for the interpretation of the interval as a possible deformation zone is /Carlsten et al. 2005/:

Increased frequency of sealed fractures, sealed fracture networks and open fractures. Sealed fractures dominate. Steeply dipping fractures that strike WNW and ENE as well as some gently dipping fractures are present. Open and partly open fractures are mostly gently dipping. Distinct low resistivity and low P-wave velocity anomalies at 686–689 m. Six radar reflectors identified, two of them are oriented, 20/072 (675.4 m) and 30/001 (686.1 m). One very clear reflector, identified in all three dipole antenna frequencies at a depth of 687 m. Fracture apertures are typically less than 1 mm, with one that is 7 mm. The most frequent fracture filling minerals in the order of decreasing abundance include chlorite, calcite, adularia and laumontite.

A pertinent question for the hydrogeological DFN modelling of DZ4 in KFM08A is if this “zone” should be modelled as a 15 m thick feature with a steep dip following the majority of the fractures, which are sealed according to Figure 7-1, or as a single open feature with a very gentle dip as suggested by the dip of the open fracture correlated to the PFL-f anomaly?

The uncertainty in the dip of DZ4 in KFM08A is decisive for the modelling considering the fact that there are no other open, interconnected and flowing fractures in KFM08A close to DZ4. This leads to a question about size; that is, how large must the fracture in Figure 7-1 be in order to form a flow path if it is gently dipping and there are no other flowing fractures nearby? The modelling of DZ4 in KFM08A at repository depth has a quite different impact on the site description compared to the aforementioned 15 m thick DZ1 in KFM06A, which has 17 flow anomalies (cf. Table 7-1) and occurs in the heavily fractured uppermost part of the bedrock, see Figure 5-7.

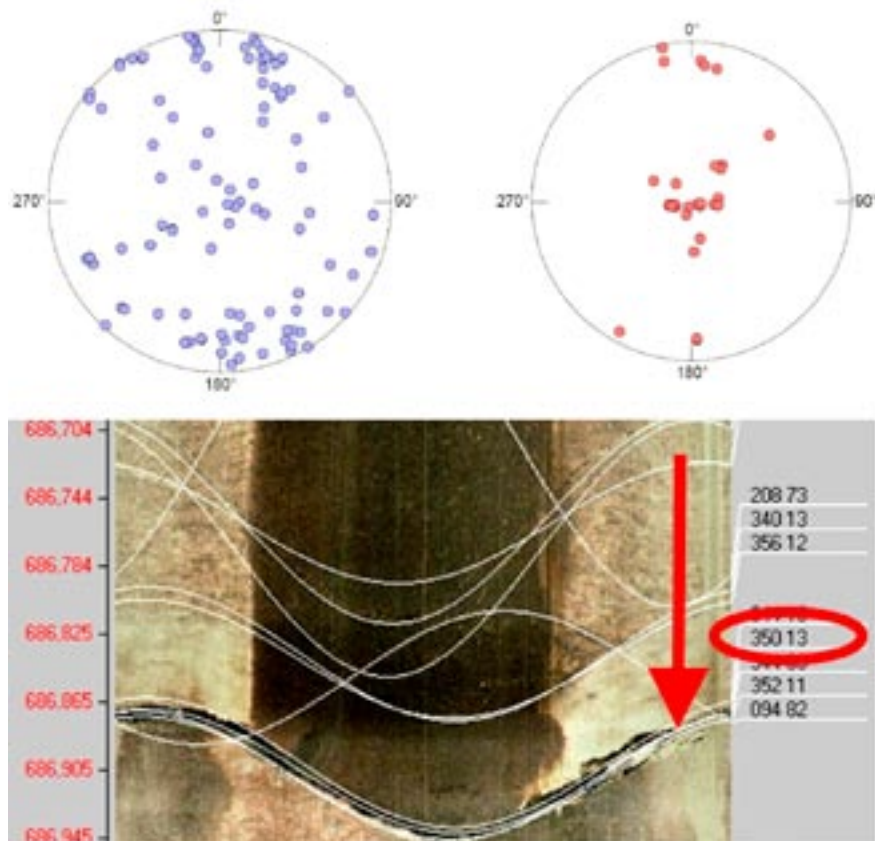


Figure 7-1. Structural data for the possible deformation zone DZ4 in KFM08A. Top: Stereo nets for 91 sealed (left) and 25 open (right) fractures. Reproduced from /Carlsten et al. 2005/. Bottom: Structural interpretation of the flow anomaly correlated with DZ4. Reproduced from /Teurneau et al. 2007/.

It is of great interest to also look at data from the cored boreholes investigated with the PSS method only, i.e. KFM09A, KFM03B, -06B–09B and KFM06C as well as the boreholes investigated with the HTHB method only, i.e. HFM01–HFM32. A compilation of all information available information is provided in Table 7-2. All together there are 40 possible deformation zones identified in the boreholes available for modelling in stage 2.2. Only 14 of the 40 possible deformation zones are found to be transmissive, however, four of which are encountered below –400 m elevation in the target volume. The four zones show up as single fractures and not as fracture networks in contrast to most of the possible deformation zones encountered in the uppermost part of the bedrock close to surface. Moreover, half of the possible deformation zones tested hydraulically are either no flowing or have a transmissivity value lower than the detection limit of the test methods used.

Table 7-2. Summary of structural-hydraulic data interpreted for the 40 borehole intervals demarked as “possible deformation zones” in stage 2.2. The first column shows the structural interpretation as suggested by the geological single-hole interpretation. The third column shows the elevation of the centre of each intercept. The column named LOC shows in what part of the tectonic lens the transmissivity value of the deformation zone is measured; where F = foot wall of ZFMA2, H = hanging wall of ZFMA2 and B = border. NF means “no flow” and NT means “not tested”. Note that the possible deformation zones associated with little or no flow are marked up as “< T_{limit} ”. Flowing “possible deformation zones” encountered close to repository depth in the target volume are highlighted with red letters. Possible deformation zones in the uppermost c. 150 m of bedrock of the target volume interpreted as stress induced sheet joints are highlighted with bold black letters.

Category	Borehole	Elevation [m RHB 70]	T [m ² /s]	LOC	Method	T_{limit}
ENE	HFM10	-57.9	< T_{limit}	B, NF	HTHB	c. $1 \cdot 10^{-6}$
ENE	HFM10	-100.0	$3.11 \cdot 10^{-4}$	B, NF	HTHB	c. $1 \cdot 10^{-6}$
G	HFM18	-3.5	$2.73 \cdot 10^{-5}$	H	HTHB	c. $1 \cdot 10^{-6}$
G	HFM21	-130.3	$2.08 \cdot 10^{-4}$	F	HTHB	c. $1 \cdot 10^{-6}$
ENE	HFM23	-76.9	< T_{limit}	B, NF	HTHB	c. $1 \cdot 10^{-6}$
ENE	HFM25	-15.0	< T_{limit}	H, NF	HTHB	c. $1 \cdot 10^{-6}$
ENE	HFM25	-35.9	< T_{limit}	H, NF	HTHB	c. $1 \cdot 10^{-6}$
ENE	HFM25	-65.2	< T_{limit}	H, NF	HTHB	c. $1 \cdot 10^{-6}$
G	HFM27	-108.1	$6.70 \cdot 10^{-6}$	F	HTHB	c. $1 \cdot 10^{-6}$
G	KFM01A	-216.0	< T_{limit}	F, NF	Σ PFL-f	c. $1 \cdot 10^{-9}$
G	KFM01B	-115.5	–	F, NT	–	
G	KFM01B	-215.5	–	F, NT	–	
G	KFM01C	-90.0	$9.03 \cdot 10^{-8}$	F	Σ PSS 5m	c. $7 \cdot 10^{-10}$
NNW	KFM01D	-144.0	< T_{limit}	F, NF	Σ PFL-f	c. $1 \cdot 10^{-9}$
NNW	KFM01D	-328.5	< T_{limit}	F, NF	Σ PFL-f	c. $1 \cdot 10^{-9}$
NNW	KFM01D	-386.0	< T_{limit}	F, NF	Σ PFL-f	c. $1 \cdot 10^{-9}$
ENE	KFM01D	-590.0	< T_{limit}	F, NF	Σ PFL-f	c. $1 \cdot 10^{-9}$
G	KFM02A (percussion)	-77.0	–	H, NT	–	
G	KFM02A	-550.5	< T_{limit}	F, NF	Σ PFL-f	c. $1 \cdot 10^{-9}$
G	KFM02A	-910.5	< T_{limit}	F, NF	Σ PFL-f	c. $1 \cdot 10^{-9}$
G	KFM02A	-966.0	< T_{limit}	F, NF	Σ PFL-f	c. $1 \cdot 10^{-9}$
G	KFM03A	-932.5	$3.46 \cdot 10^{-7}$	H	Σ PFL-f	c. $1 \cdot 10^{-9}$
G	KFM03B	-55.5	< T_{limit}	H	Σ PSS 5m	c. $7 \cdot 10^{-10}$
NNW	KFM04A	-762.0	$1.29 \cdot 10^{-9}$	F / B	Σ PFL-f	c. $1 \cdot 10^{-9}$
G	KFM06A	-114.5	$3.90 \cdot 10^{-5}$	F	Σ PFL-f	c. $1 \cdot 10^{-9}$
NNE	KFM06A	-549.0	$2.74 \cdot 10^{-10}$	F	Σ PFL-f	c. $1 \cdot 10^{-9}$
NNE	KFM06A	-743.5	< T_{limit}	F, NF	Σ PFL-f	c. $1 \cdot 10^{-9}$
NNE	KFM06A	-772.0	< T_{limit}	F, NF	Σ PFL-f	c. $1 \cdot 10^{-9}$
G	KFM06C	-111.5	$8.74 \cdot 10^{-5}$	F	Σ PSS 5m	c. $7 \cdot 10^{-10}$
WNW	KFM06C	-520.0	$9.33 \cdot 10^{-8}$	F	Σ PSS 5m	c. $7 \cdot 10^{-10}$
G	KFM07A	-169.0	< T_{limit}	F, NF	Σ PFL-f	c. $1 \cdot 10^{-9}$
G	KFM07B	-40.5	–	F	–	
G	KFM07B	-98.0	–	F	–	
NNE	KFM08A	-440.5	< T_{limit}	F, NF	Σ PFL-f	c. $1 \cdot 10^{-9}$
NNW	KFM08A	-500.5	< T_{limit}	F, NF	Σ PFL-f	c. $1 \cdot 10^{-9}$
WNW	KFM08A	-543.5	$1.41 \cdot 10^{-6}$	F	Σ PFL-f	c. $1 \cdot 10^{-9}$
WNW	KFM08A	-712.5	< T_{limit}	F, NF	Σ PFL-f	c. $1 \cdot 10^{-9}$
WNW	KFM08A	-735.0	< T_{limit}	F, NF	Σ PFL-f	c. $1 \cdot 10^{-9}$
NNE	KFM08C	-149.5	$6.68 \cdot 10^{-9}$	F	Σ PFL-f	c. $1 \cdot 10^{-9}$
NNW	KFM09A	-531.0	< T_{limit}	B, NF	Σ PSS 5m	c. $7 \cdot 10^{-10}$

Figure 7-2 shows a plot of the transmissivities of the possible deformation zones observed in the cored boreholes versus depth. The data from the percussion-drilled boreholes are excluded due to the significantly more uncertain determination of both orientation and transmissivity. The transmissivities are coloured with regard to the orientation of the possible deformation zones. Possible deformation zones with little or no flow are marked up as “ $<T_{limit}$ ”, but shown as $1 \cdot 10^{-10} \text{ m}^2/\text{s}$ in Figure 7-2.

Figure 7-2 suggests a substantial depth trend, a considerable heterogeneity in the lateral direction, and an indication of a difference in transmissivity with regard to orientation, i.e. anisotropy. The depth trend observed can be thought of as vertical heterogeneity in the plane of the deformation zones. It is noteworthy that the most transmissive possible deformation zones in Figure 7-2 are more or less parallel with the direction of to the current principal stress (WNW and G), cf. Figure 3-3. It is also noteworthy that the transmissivity value representing KFM08A coincides with a gently-dipping fracture.

In conclusion, it is important to take the four possible deformation zones encountered at repository depth in the target volume into account since there are practically no other flowing fractures nearby. A conditioned stochastic, or semi-deterministic, modelling approach is suggested in Section 11, which honours the position, orientation and transmissivity of each of the four possible deformation zones.

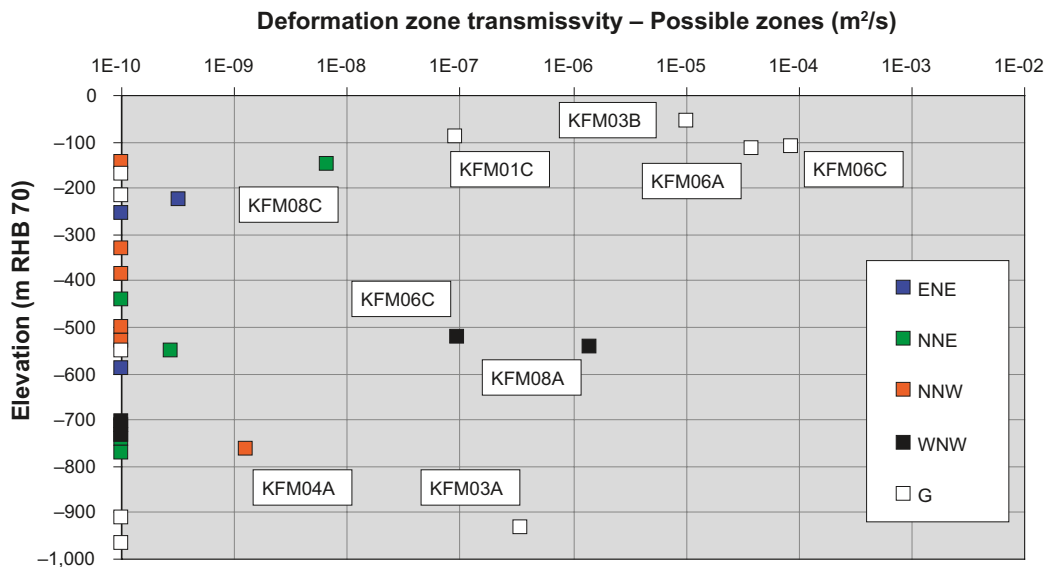


Figure 7-2. Transmissivity versus depth for the possible deformation zones observed in cored boreholes. The transmissivities are coloured with regard to the estimated orientations of the possible deformation zones, cf. Table 3-2. Possible deformation zones with little or no flow are assigned a low transmissivity value of $1 \cdot 10^{-10} \text{ m}^2/\text{s}$.

8 Hydrogeological data synthesis for near-surface bedrock

8.1 Foot wall and hanging wall bedrock

Figure 8-1 shows a NW-SE cross section across the candidate area. There is a significant structural difference with regard to the occurrence of gently-dipping deformation zones. In the bedrock below the vital deformation zone ZFMA2, i.e. the foot wall bedrock, the number of extensive gently-dipping deformation zones is considerably less than in the bedrock above, i.e. the hanging wall bedrock.

Figure 4-28 shows a cartoon of the conceptual model of the near-surface bedrock in the foot wall of ZFMA2. The combination of near-surface sheet joints and outcropping deformation zones, both gently-dipping and steeply-dipping, is envisaged to form a well-connected lattice of flow paths, which short-circuits the groundwater recharge from above as well as a potential discharge from below /Follin et al. 2007b/. The frequency of the horizontal fractures/sheet joints is uncertain but forecasted to decrease significantly with depth; the maximum depth of occurrence is estimated to c. 100–150 m /Stephens et al. 2007/. The description of their lateral extent is also somewhat faint, but presumable horizontal fractures/sheet-joints are more extensive in the foot wall bedrock than in the hanging wall bedrock /Stephens et al. 2007/.

In what follows we analyse the hydraulic differences between the foot wall bedrock and the hanging wall bedrock as perceived from the hydraulic tests conducted in cored and percussion drilled boreholes.

8.2 Near-surface bedrock in the hanging wall of ZFMA2

Table 8-1 shows transmissivity data from 35 deformation zones (7 possible and 28 deterministic) associated with the hanging wall bedrock. Twelve deformation zones (4 possible and 8 deterministic) with little or no flow are marked up as “ $< T_{limit}$ ”. Three deformation zones (1 possible and 2 deterministic) have not been tested hydraulically.



Figure 8-1. Cross section of the deformation model. The profile is circa six kilometres long and two kilometres deep. Modified after /Stephens et al. 2007/.

Table 8-1. Summary of structural-hydraulic data of the deformation zone intercepts encountered in the uppermost 200 m of the hanging wall bedrock above ZFMA2. The second column shows the structural interpretation as suggested by the geological single-hole interpretation, cf. Table 3-2. The fourth column shows the elevation of the centre of each intercept. Deformation zones associated with little or no flow are marked up as “< T_{limit}”. Deformation zones not tested hydraulically have no values.

DZ	Category	Borehole	Elevation [m RHB 70]	T [m ² /s]	Method	T _{limit}
POSS	ENE	HFM25	-15	< T _{limit}	HTHB	c. 1·10 ⁻⁶
ZFMENE0060A	ENE	HFM09	-16	3.26·10 ⁻⁴	HTHB	c. 1·10 ⁻⁶
POSS	ENE	HFM25	-36	< T _{limit}	HTHB	c. 1·10 ⁻⁶
POSS	ENE	HFM10	-58	< T _{limit}	HTHB	c. 1·10 ⁻⁶
POSS	ENE	HFM25	-65	< T _{limit}	HTHB	c. 1·10 ⁻⁶
POSS	ENE	HFM10	-100	3.11·10 ⁻⁴	HTHB	c. 1·10 ⁻⁶
ZFMENE0062A	ENE	HFM25	-109	< T _{limit}	HTHB	c. 1·10 ⁻⁶
ZFMENE0062A	ENE	HFM25	-128	< T _{limit}	HTHB	c. 1·10 ⁻⁶
ZFMENE0401A	ENE	HFM13	-141	2.91·10 ⁻⁴	HTHB	c. 1·10 ⁻⁶
POSS	G	HFM18	-4	2.73·10 ⁻⁵	HTHB	c. 1·10 ⁻⁶
ZFMA4	G	HFM26	-20	< T _{limit}	HTHB	c. 1·10 ⁻⁶
ZFMA2	G	HFM27	-23	2.30·10 ⁻⁵	HTHB	c. 1·10 ⁻⁶
ZFMA5	G	KFM03B	-24	2.32·10 ⁻⁵	Σ PSS 5m	c. 7·10 ⁻¹⁰
ZFMA2, ZFMENE1192	G	KFM01C	-25	4.83·10 ⁻⁴	Σ PSS 5m	c. 7·10 ⁻¹⁰
ZFMA4	G	HFM18	-31	1.62·10 ⁻⁴	HTHB	c. 1·10 ⁻⁶
ZFMA2	G	KFM01B	-37	–	–	
ZFMA2	G	KFM01A (percussion)	-37	–	–	
ZFMA2	G	HFM01	-37	4.50·10 ⁻⁵	HTHB	c. 1·10 ⁻⁶
ZFMA6	G	HFM07	-54	< T _{limit}	HTHB	c. 1·10 ⁻⁶
POSS	G	KFM03B	-56	1.01·10 ⁻⁵	Σ PSS 5m	c. 7·10 ⁻¹⁰
ZFMA4	G	HFM26	-57	< T _{limit}	HTHB	c. 1·10 ⁻⁶
ZFMA2	G	KFM01C	-58	1.13·10 ⁻³	Σ PSS 5m	c. 7·10 ⁻¹⁰
ZFM866	G	HFM04	-58	7.87·10 ⁻⁵	HTHB	c. 1·10 ⁻⁶
ZFMA5	G	HFM06	-59	2.29·10 ⁻⁴	HTHB	c. 1·10 ⁻⁶
ZFMA2	G	HFM14	-59	1.64·10 ⁻⁴	HTHB	c. 1·10 ⁻⁶
ZFMA2	G	HFM15	-60	1.02·10 ⁻⁴	HTHB	c. 1·10 ⁻⁶
POSS	G	KFM02A (percussion)	-77	–	–	
ZFMA2	G	HFM14	-82	2.49·10 ⁻⁴	HTHB	c. 1·10 ⁻⁶
ZFMA2	G	KFM05A	-88	1.25·10 ⁻³	Σ PFL-f	
ZFMA2	G	HFM19	-105	1.55·10 ⁻⁵	HTHB	c. 1·10 ⁻⁶
ZFMA7, ZFMNE0065	G	HFM18	-106	< T _{limit}	HTHB	c. 1·10 ⁻⁶
ZFM866	G	KFM02A	-108	1.07·10 ⁻⁴	Σ PFL-f	c. 1·10 ⁻⁹
ZFMA5	G	HFM08	-130	1.20·10 ⁻³	HTHB	c. 1·10 ⁻⁶
ZFMA2	G	HFM19	-137	2.75·10 ⁻⁴	HTHB	c. 1·10 ⁻⁶
ZFM866	G	HFM05	-145	3.96·10 ⁻⁴	HTHB	c. 1·10 ⁻⁶
ZFMA3	G	KFM02A	-164	3.46·10 ⁻⁶	Σ PFL-f	c. 1·10 ⁻⁹
ZFMA3	G	HFM04	-179	< T _{limit}	HTHB	c. 1·10 ⁻⁶
ZFMNE0065	NE	HFM26	-130	< T _{limit}	HTHB	c. 1·10 ⁻⁶

Figure 8-2 shows a plot of the deformation zone transmissivity data for the near-surface bedrock in the hanging wall bedrock.

There are no PFL-f data gathered in the uppermost c. 100 m of bedrock because of the drilling technique used. Figure 8-3 shows the dips of 16 PFL-f anomalies observed in FFM03, which is the fracture domain associated with the hanging wall bedrock of ZFMA2. The data come from two boreholes, KFM02A and KFM03A, which are both sub vertical. The data shown in Figure 8-3 are not Terzaghi corrected (cf. Section 10).

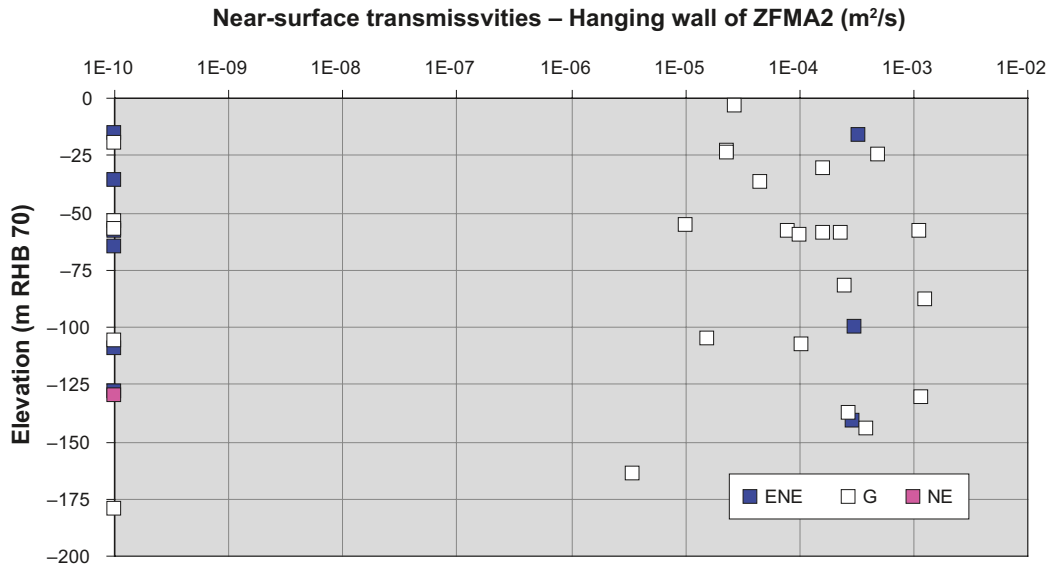


Figure 8-2. Transmissivity data for the near-surface bedrock in the hanging wall of deformation zone ZFMA2, cf. Table 8-1. The twelve deformation zones (4 possible and 8 deterministic) zones with little or no flow are here assigned a low transmissivity value of $1 \cdot 10^{-10} \text{ m}^2/\text{s}$. The specific measurement limits for these zones are provided in Table 8-1.

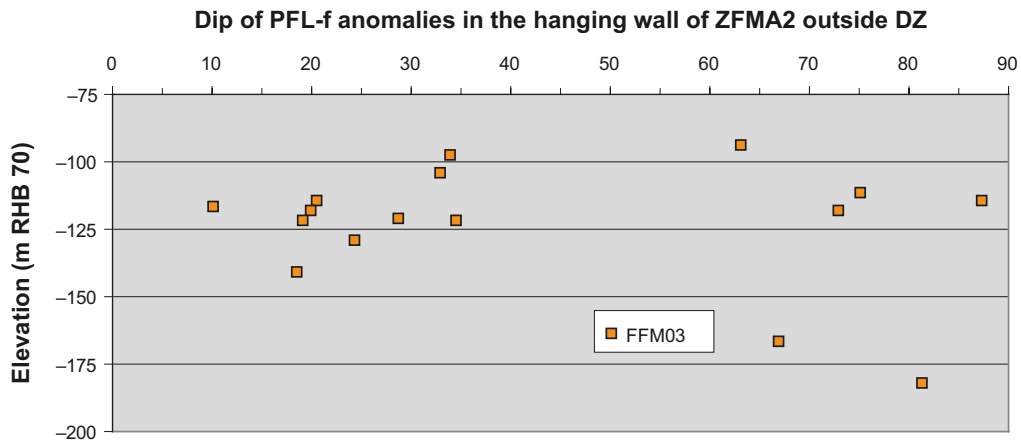


Figure 8-3. Dip data for 16 PFL-f anomalies in the interval -100 to -200 m RHB 70 (roughly) gathered in FFM03. 7 of the PFL-f anomalies have a dip of 30° or less. The data shown are not Terzaghi corrected.

8.3 Near-surface bedrock in the foot wall of ZFMA2

Table 8-2 shows transmissivity data from 27 deformation zones (8 possible and 19 deterministic) associated with the foot wall bedrock. Five deformation zones (2 possible and 3 deterministic) with little or no flow are marked up as “ $< T_{limit}$ ”. Five deformation zones (3 possible and 2 deterministic) have not been tested hydraulically.

Table 8-2. Summary of structural-hydraulic data of the deformation zone intercepts encountered in the uppermost 200 m of the foot wall bedrock below ZFMA2. The second column shows the structural interpretation as suggested by the geological single-hole interpretation, cf. Table 3-2. The fourth column shows the elevation of the centre of each intercept. Deformation zones associated with little or no flow are marked up as “ $< T_{limit}$ ”. Deformation zones not tested hydraulically have no values.

DZ	Category	Borehole	Elevation [m RHB 70]	T [m ² /s]	Method	T _{limit}
ZFMENE1208A	ENE	KFM09B	-17	2.92·10 ⁻⁵	Σ PSS 5m	c. 7·10 ⁻¹⁰
ZFMENE1208A	ENE	KFM09A	-20	–	–	
ZFMENE1208A	ENE	HFM23	-24	< T _{limit}	HTHB	c. 1·10 ⁻⁶
ZFMENE1208A	ENE	HFM28	-34	< T _{limit}	HTHB	c. 1·10 ⁻⁶
ZFNENE1208B	ENE	KFM09B	-52	1.01·10 ⁻⁵	Σ PSS 5m	c. 7·10 ⁻¹⁰
ZFMENE1208B	ENE	KFM09A	-82	2.50·10 ⁻⁸	Σ PSS 5m	c. 7·10 ⁻¹⁰
ZFMENE2120	ENE	HFM22	-92	< T _{limit}	HTHB	c. 1·10 ⁻⁶
ZFNENE0159A	ENE	KFM09B	-93	3.57·10 ⁻⁶	Σ PSS 5m	c. 7·10 ⁻¹⁰
ZFMENE0060A	ENE	KFM01C	-181	3.48·10 ⁻⁹	Σ PSS 5m	c. 7·10 ⁻¹⁰
ZFMENE2320	ENE	KFM07B	-183	4.36·10 ⁻⁸	Σ PSS 5m	c. 7·10 ⁻¹⁰
ZFMENE0159A, ZFMNNW0100	ENE	KFM09A	-190	1.03·10 ⁻⁷	Σ PSS 5m	c. 7·10 ⁻¹⁰
ZFMA8	G	HFM16	-38	5.26·10 ⁻⁴	HTHB	c. 1·10 ⁻⁶
POSS	G	KFM07B	-41	–	–	
ZFM1203	G	HFM02	-41	5.90·10 ⁻⁴	HTHB	c. 1·10 ⁻⁶
ZFM1203	G	HFM27	-47	4.00·10 ⁻⁵	HTHB	c. 1·10 ⁻⁶
ZFMA8	G	KFM06B	-70	2.42·10 ⁻⁴	Σ PSS 5m	c. 7·10 ⁻¹⁰
ZFM1203	G	KFM07B	-75	–	–	
ZFM1203	G	HFM21	-77	3.01·10 ⁻⁴	HTHB	c. 1·10 ⁻⁶
POSS	G	KFM01C	-90	9.03·10 ⁻⁸	Σ PSS 5m	c. 7·10 ⁻¹⁰
ZFM1203	G	KFM07C	-94	4.81·10 ⁻⁵	Σ PFL-f	c. 1·10 ⁻⁹
POSS	G	KFM07B	-98	–	–	
POSS	G	HFM27	-108	6.70·10 ⁻⁶	HTHB	c. 1·10 ⁻⁶
POSS	G	KFM06C	-112	8.74·10 ⁻⁵	Σ PSS 5m	c. 7·10 ⁻¹⁰
POSS	G	KFM06A	-115	3.90·10 ⁻⁵	Σ PFL-f	c. 1·10 ⁻⁹
POSS	G	KFM01B	-116	–	–	
ZFM1203, ZFMNNW0404	G	KFM07A	-123	1.41·10 ⁻⁴	Σ PFL-f	c. 1·10 ⁻⁹
POSS	G	HFM21	-130	2.08·10 ⁻⁴	HTHB	c. 1·10 ⁻⁶
POSS	G	KFM07A	-169	< T _{limit}	Σ PFL-f	c. 1·10 ⁻⁹
POSS	NNE	KFM08C	-150	6.68·10 ⁻⁹	Σ PFL-f	c. 1·10 ⁻⁹
ZFMNNW1205	NNW	KFM08B	-114	1.22·10 ⁻⁹	Σ PSS 5m	c. 7·10 ⁻¹⁰
POSS	NNW	KFM01D	-144	< T _{limit}	Σ PFL-f	c. 1·10 ⁻⁹
ZFMNNW1205	NNW	KFM08B	-147	5.60·10 ⁻⁸	Σ PSS 5m	c. 7·10 ⁻¹⁰

Figure 8-4 shows a plot of the transmissivity data for the near-surface bedrock in the foot wall bedrock.

Figure 8-5 shows the dips of 134 PFL-f anomalies observed in FFM01 (53) and FFM02 (81) in the foot wall bedrock. The data come from six boreholes, KFM01A, -01D, -05A, and -06A, -08A and -08C. Fracture domain FFM02 is not observed at drill site 8.

Figure 8-3 and Figure 8-5 suggest that the frequency of water conducting gently dipping fractures $P_{10,PFL}$ in the uppermost part of the bedrock is between 2–3 times greater in FFM02 than in FFM01 or FFM03; that is $81/(4 \cdot 100 \text{ m}) = 0.20 \text{ m}^{-1}$ in FFM02, $53/(6 \cdot 100 \text{ m}) = 0.088 \text{ m}^{-1}$ in FFM01 and $16/(2 \cdot 100 \text{ m}) = 0.080 \text{ m}^{-1}$ in FFM03.

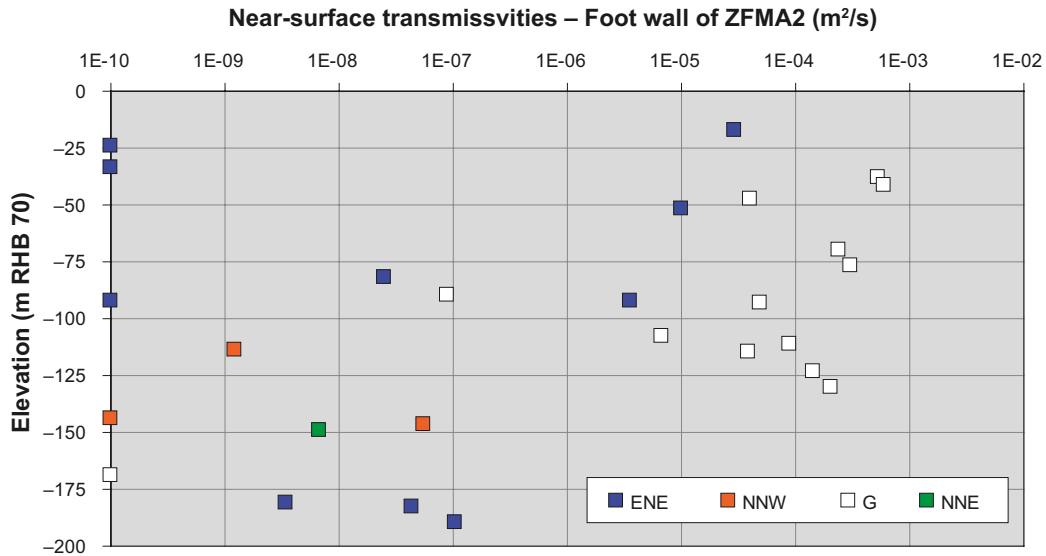


Figure 8-4. Transmissivity data for the near-surface bedrock in the foot wall of deformation zone ZFMA2, cf. Table 8-2. The five deformation zones (2 possible and 3 deterministic) with little or no flow are assigned a low transmissivity value of $1 \cdot 10^{-10} \text{ m}^2/\text{s}$. The specific measurement limits for these zones are provided in Table 8-2.

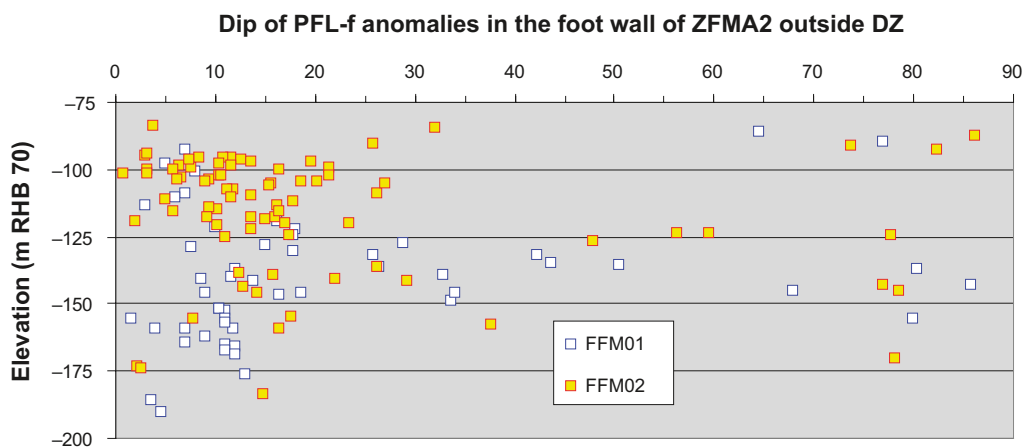


Figure 8-5. Dip data for 134 PFL-f anomalies in the interval -100 to -200 m RHB 70 (roughly) gathered in FFM01 and FFM02. About 82% (110) of the data have a dip of 30° or less. The data shown are not Terzaghi corrected.

The relationship between the fractures associated with FFM01 or FFM02 shown in Figure 8-3 and Figure 8-5 and horizontal sheet joints is not addressed in the geological modelling provided by /Stephens et al. 2007, Olofsson et al. 2007/. A reasonable notion is that the envisaged lattice of near-surface sheet joints and outcropping deformation zones, both gently-dipping and steeply-dipping, is also intersected by the large number of gently-dipping single fractures belonging to FFM01 and FFM02, thus reinforcing the hydraulic anisotropy of the near-surface bedrock in the foot wall.

From a hydrogeological point of view it is considered more important to mimic the spatially varying and quite anisotropic hydraulic behaviour of this near-surface lattice of features instead of modelling the structural-hydraulic properties of the individual discrete features involved. It is recalled that the aforementioned notion that the groundwater flow field in the near-surface bedrock is horizontally anisotropic is based on several strands of hydrogeological and hydro-geochemical evidence:

- abnormally high flow rates in many shallow percussion boreholes,
- a smooth distribution of head independent of topography,
- limited penetration of freshwater below about 100 m, and
- rapid responses to large scale interference tests in the near-surface.

A very simple representation of the ‘hydraulic cage phenomenon’ was implemented in /Follin et al. 2007b/ using a single 100 m thick feature extending throughout the candidate area and having a homogeneous transmissivity of about 10^{-3} m²/s.

For the groundwater flow modelling in stage 2.2 it is proposed that a more sophisticated representation be used. It is recommended that the finite-element grid resolution used be refined in both horizontal and vertical directions within the candidate area in order to better honour the spatial variability and anisotropy observed.

9 Hydrogeological modelling of deformation zones

9.1 Summary of data

Table 5-1 through Table 5-20 and Table 6-1 contain 116 borehole intervals which are interpreted as deformation zone intercepts and modelled deterministically for Forsmark in modelling stage 2.2. 77 of the intervals occur in cored boreholes and 39 occur in percussion-drilled boreholes. In addition to the 116 intervals there are additional 3 intercepts with deterministically modelled deformation zones in KFM01B (2) and in KFM01A (1) not tested hydraulically; that is, all in all there are 119 borehole intervals interpreted as deformation zone intercepts and modelled deterministically for Forsmark in stage 2.2.

Table 9-1 summarises the structural-hydraulic data of the 119 borehole intervals. The column named **LOC** shows in what part of the tectonic lens the transmissivity value of the deformation zone is acquired; where **F** = foot wall, **H** = hanging wall and **B** = border. **NF** means “no flow” and **NT** means “not tested”. The deformation zones associated with little or no flow are marked up as “ $< T_{limit}$ ”. Table 9-1 suggests that:

- about one third of the deformation zones tested hydraulically has a transmissivity value lower than the detection limit of the test methods used, and
- deformation zones with little or no flow can occur at any depth.

Figure 9-1 shows a plot of the transmissivities of the deterministically modelled deformations zones observed in the cored boreholes versus depth. Data from the percussion-drilled boreholes are excluded in the analyses presented here due to the significantly more uncertain determination of both orientation and transmissivity. The transmissivities are coloured with regard to the orientation of the deformation zones, cf. Table 3-2. Deformation zones with little or no flow are in this plot assigned a low transmissivity value of $1 \cdot 10^{-10}$ m²/s.

Figure 9-1 suggests a substantial depth trend and a significant difference in transmissivity with regard to the orientation, i.e. anisotropy. The reasons for the anisotropy observed are not fully understood, but it is noteworthy that the deformation zone denoted by WNW and G are more or less parallel with the direction of to the current main principal stress, whereas the ENE type of deformation zones are essentially perpendicular to the current main principal stress, cf. Figure 3-3.

All but five of the 23 gently-dipping deformation zones shown in Figure 9-1 are located in the hanging wall, and all of the 45 steeply-dipping deformation zones are located in the foot wall, i.e. none in the hanging wall. Twelve deformation zones are drilled through the bedrock bordering the tectonic lens.

Table 9-1. Summary of structural-hydraulic data of the 119 deterministically modelled deformation zones in stage 2.2. The second column shows the structural interpretation as suggested by the geological single-hole interpretation, cf. Table 3-2. The fourth column shows the elevation of the centre of each intercept and the maximum geological thickness. The column named LOC shows in what part of the tectonic lens the transmissivity value of the deformation zone is measured; where F = foot wall of ZFMA2, H = hanging wall of ZFMA2 and B = border. NF means “no flow” and NT means “not tested”. The deformation zones associated with little or no flow are marked up as “ $< T_{limit}$ ”.

ZFM	Category	Borehole	Elevation / b [m RHB 70] / [m]	T [m ² /s]	LOC	Method	T _{limit}
ZFMA2	G	HFM01	-37 / 8	4.50·10 ⁻⁵	H	HTHB	c. 1·10 ⁻⁶
ZFM1203	G	HFM02	-41 / 5	5.90·10 ⁻⁴	F	HTHB	c. 1·10 ⁻⁶
ZFM866	G	HFM04	-58 / 3	7.87·10 ⁻⁵	H	HTHB	c. 1·10 ⁻⁶
ZFMA3	G	HFM04	-179 / 4	< T _{limit}	H, NF	HTHB	c. 1·10 ⁻⁶
ZFM866	G	HFM05	-145 / 1	3.96·10 ⁻⁴	H	HTHB	c. 1·10 ⁻⁶
ZFMA5	G	HFM06	-59 / 10	2.29·10 ⁻⁴	H	HTHB	c. 1·10 ⁻⁶
ZFMA6	G	HFM07	-54 / 12	< T _{limit}	H, NF	HTHB	c. 1·10 ⁻⁶
ZFMA5	G	HFM08	-130 / 5	1.20·10 ⁻³	H	HTHB	c. 1·10 ⁻⁶
ZFMENE0060A	ENE	HFM09	-16 / 9	3.26·10 ⁻⁴	B	HTHB	c. 1·10 ⁻⁶
ZFMNW0003	NW	HFM11	-79 / 52	2.80·10 ⁻⁵	B	HTHB	c. 1·10 ⁻⁶
ZFMNW0003	NW	HFM12	-89 / 58	7.87·10 ⁻⁶	B	HTHB	c. 1·10 ⁻⁶
ZFMENE0401A	ENE	HFM13	-141 / 12	2.91·10 ⁻⁴	H	HTHB	c. 1·10 ⁻⁶
ZFMA2	G	HFM14	-59 / 7	< T _{limit}	H, NF	HTHB	c. 1·10 ⁻⁶
ZFMA2	G	HFM14	-82 / 10	< T _{limit}	H, NF	HTHB	c. 1·10 ⁻⁶
ZFMA2	G	HFM15	-60 / 7	1.02·10 ⁻⁴	H	HTHB	c. 1·10 ⁻⁶
ZFMA8	G	HFM16	-38 / 59	5.26·10 ⁻⁴	H	HTHB	c. 1·10 ⁻⁶
ZFMA4	G	HFM18	-31 / 11	1.62·10 ⁻⁴	H	HTHB	c. 1·10 ⁻⁶
ZFMA7, ZFMNE0065	G	HFM18	-106 / 23	< T _{limit}	H, NF	HTHB	c. 1·10 ⁻⁶
ZFMA2	G	HFM19	-105 / 21	1.55·10 ⁻⁵	H	HTHB	c. 1·10 ⁻⁶
ZFMA2	G	HFM19	-137 / 13	2.75·10 ⁻⁴	H	HTHB	c. 1·10 ⁻⁶
ZFM1203	G	HFM21	-77 / 6	3.01·10 ⁻⁴	F	HTHB	c. 1·10 ⁻⁶
ZFMENE2120	ENE	HFM22	-92 / 13	< T _{limit}	F, NF	HTHB	c. 1·10 ⁻⁶
ZFMENE1208A	ENE	HFM23	-24 / 12	< T _{limit}	B, NF	HTHB	c. 1·10 ⁻⁶
ZFMNNW0100	NNW	HFM23	-59 / 6	< T _{limit}	B, NF	HTHB	c. 1·10 ⁻⁶
ZFMWNW0123	WNW	HFM24	-18 / 8	3.01·10 ⁻⁵	B	HTHB	c. 1·10 ⁻⁶
ZFMWNW0123	WNW	HFM24	-41 / 18	7.99·10 ⁻⁵	B	HTHB	c. 1·10 ⁻⁶
ZFMWNW0123	WNW	HFM24	-70 / 32	< T _{limit}	B, NF	HTHB	c. 1·10 ⁻⁶
ZFMENE0062A	ENE	HFM25	-109 / 8	< T _{limit}	H, NF	HTHB	c. 1·10 ⁻⁶
ZFMENE0062A	ENE	HFM25	-128 / 12	< T _{limit}	H, NF	HTHB	c. 1·10 ⁻⁶
ZFMA4	G	HFM26	-20 / 26	< T _{limit}	H, NF	HTHB	c. 1·10 ⁻⁶
ZFMA4	G	HFM26	-57 / 26	< T _{limit}	H, NF	HTHB	c. 1·10 ⁻⁶
ZFMNE0065	NE	HFM26	130 / 28	< T _{limit}	H, NF	HTHB	c. 1·10 ⁻⁶
ZFMA2	G	HFM27	-23 / 3	2.30·10 ⁻⁵	H	HTHB	c. 1·10 ⁻⁶
ZFM1203	G	HFM27	-47 / 17	4.00·10 ⁻⁵	F	HTHB	c. 1·10 ⁻⁶
ZFMENE1208A	ENE	HFM28	-34 / 52	< T _{limit}	B, NF	HTHB	c. 1·10 ⁻⁶
ZFMWNW0123	WNW	HFM29	-14 / 5	< T _{limit}	B, NF	HTHB	c. 1·10 ⁻⁶
ZFMWNW0123	WNW	HFM29	-58 / 17	< T _{limit}	B, NF	HTHB	c. 1·10 ⁻⁶
ZFMWNW0123	WNW	HFM29	-129 / 4	< T _{limit}	B, NF	HTHB	c. 1·10 ⁻⁶
ZFMNW0017	NW	HFM30	-117 / 107	1.28·10 ⁻⁴	B	HTHB	c. 1·10 ⁻⁶
ZFMA2	G	KFM01A (percussion)	-37 / 22	–	H, NT	–	
ZFMENE1192	ENE	KFM01A	-271 / 18	7.79·10 ⁻¹⁰	F, NF	Σ PFL-f	c. 1·10 ⁻⁹
ZFMENE1192	ENE	KFM01A	-393 / 26	< T _{limit}	F, NF	Σ PFL-f	c. 1·10 ⁻⁹
ZFMENE2254	ENE	KFM01A	-652 / 44	< T _{limit}	F, NF	Σ PFL-f	c. 1·10 ⁻⁹

ZFM	Category	Borehole	Elevation / b [m RHB 70] / [m]	T [m ² /s]	LOC	Method	T _{limit}
ZFMA2	G	KFM01B	-37 / 47	–	H, NT	–	
ZFMNNW0404	NNW	KFM01B	-417 / 37	–	F, NT	–	
ZFMA2, ZFMENE1192	G	KFM01C	-25 / 19	4.83·10 ⁻⁴	H	Σ PSS 5m	c. 7·10 ⁻¹⁰
ZFMA2	G	KFM01C	-58 / 28	1.13·10 ⁻³	H	Σ PSS 5m	c. 7·10 ⁻¹⁰
ZFMENE0060A	ENE	KFM01C	-181 / 12	3.48·10 ⁻⁹	F	Σ PSS 5m	c. 7·10 ⁻¹⁰
ZFMENE0060C	ENE	KFM01C	-236 / 18	3.37·10 ⁻⁹	F	Σ PSS 5m	c. 7·10 ⁻¹⁰
ZFMENE0061	ENE	KFM01D	-528 / 21	< T _{limit}	F, NF	Σ PFL-f	c. 1·10 ⁻⁹
ZFM866	G	KFM02A	-108 / 12	1.07·10 ⁻⁴	H	Σ PFL-f	c. 1·10 ⁻⁹
ZFMA3	G	KFM02A	-164 / 24	3.46·10 ⁻⁶	H	Σ PFL-f	c. 1·10 ⁻⁹
ZFM1189	G	KFM02A	-267 / 70	1.03·10 ⁻⁶	H	Σ PFL-f	c. 1·10 ⁻⁹
ZFMA2	G	KFM02A	-421 / 25	2.85·10 ⁻⁶	H	Σ PFL-f	c. 1·10 ⁻⁹
ZFMF1	G	KFM02A	-489 / 44	4.66·10 ⁻⁶	H	Σ PFL-f	c. 1·10 ⁻⁹
ZFMB4	G	KFM02A	-887 / 11	2.62·10 ⁻⁶	H	Σ PFL-f	c. 1·10 ⁻⁹
ZFMA4	G	KFM03A	-369 / 43	1.01·10 ⁻⁶	H	Σ PFL-f	c. 1·10 ⁻⁹
ZFMA7	G	KFM03A	-442 / 7	6.72·10 ⁻⁶	H	Σ PFL-f	c. 1·10 ⁻⁹
ZFMB1	G	KFM03A	-631 / 8	2.50·10 ⁻⁶	H	Σ PFL-f	c. 1·10 ⁻⁹
ZFMA3	G	KFM03A	-798 / 13	2.86·10 ⁻⁸	H	Σ PFL-f	c. 1·10 ⁻⁹
ZFMA5	G	KFM03B	-24 / 18	2.32·10 ⁻⁵	H	Σ PSS 5m	c. 7·10 ⁻¹⁰
ZFMNW1200	NW	KFM04A	-117 / 58	6.48·10 ⁻⁵	B	Σ PFL-f	c. 1·10 ⁻⁹
ZFMA2	G	KFM04A	-187 / 35	8.79·10 ⁻⁵	B	Σ PFL-f	c. 1·10 ⁻⁹
ZFMNE1188	NE	KFM04A	-279 / 68	1.46·10 ⁻⁶	B	Σ PFL-f	c. 1·10 ⁻⁹
ZFMNE1188	NE	KFM04A	-369 / 41	1.38·10 ⁻⁸	B	Σ PFL-f	c. 1·10 ⁻⁹
ZFMWNW0123	WNW	KFM04A	-544 / 5	< T _{limit}	F B, NF	Σ PFL-f	c. 1·10 ⁻⁹
ZFMA2	G	KFM05A	-88 / 10	1.25·10 ⁻³	H	Σ PFL-f	c. 1·10 ⁻⁹
ZFMENE2282	ENE	KFM05A	-350 / 33	< T _{limit}	F, NF	Σ PFL-f	c. 1·10 ⁻⁹
ZFMENE0401B	ENE	KFM05A	-503 / 22	< T _{limit}	F, NF	Σ PFL-f	c. 1·10 ⁻⁹
ZFMENE0401A	ENE	KFM05A	-584 / 28	1.20·10 ⁻⁸	F	Σ PFL-f	c. 1·10 ⁻⁹
ZFMENE0103	ENE	KFM05A	-748 / 19	< T _{limit}	F, NF	Σ PFL-f	c. 1·10 ⁻⁹
ZFMENE2383	ENE	KFM05A	-796 / 45	< T _{limit}	F, NF	Σ PFL-f	c. 1·10 ⁻⁹
ZFMENE0060B	ENE	KFM06A	-200 / 71	4.54·10 ⁻⁵	F	Σ PFL-f	c. 1·10 ⁻⁹
ZFMB7, ZFMENE0060A	G	KFM06A	-286 / 34	9.79·10 ⁻⁷	F	Σ PFL-f	c. 1·10 ⁻⁹
ZFMNNE2273	NNE	KFM06A	-448 / 23	< T _{limit}	F, NF	Σ PFL-f	c. 1·10 ⁻⁹
ZFMNNE2255	NNE	KFM06A	-522 / 4	< T _{limit}	F, NF	Σ PFL-f	c. 1·10 ⁻⁹
ZFMNNE0725	NNE	KFM06A	-634 / 28	3.40·10 ⁻⁷	F	Σ PFL-f	c. 1·10 ⁻⁹
ZFMENE0061	ENE	KFM06A	-668 / 18	< T _{limit}	F, NF	Σ PFL-f	c. 1·10 ⁻⁹
ZFMNNE2280	NNE	KFM06A	-805 / 31	< T _{limit}	F, NF	Σ PFL-f	c. 1·10 ⁻⁹
ZFMA8	G	KFM06B	-70 / 37	2.42·10 ⁻⁴	F	Σ PSS 5m	c. 7·10 ⁻¹⁰
ZFMNNE2008	NNE	KFM06C	-244 / 19	3.40·10 ⁻⁷	F	Σ PSS 5m	c. 7·10 ⁻¹⁰
ZFMB7	G	KFM06C	-312 / 32	5.67·10 ⁻⁶	F	Σ PSS 5m	c. 7·10 ⁻¹⁰
ZFMNNE2263	NNE	KFM06C	-369 / 57	1.84·10 ⁻⁷	F	Σ PSS 5m	c. 7·10 ⁻¹⁰
ZFMWNW0044	WNW	KFM06C	-428 / 41	1.22·10 ⁻⁶	F	Σ PSS 5m	c. 7·10 ⁻¹⁰
ZFM1203, ZFMNNW0404	G	KFM07A	-123 / 66	1.41·10 ⁻⁴	F	Σ PFL-f	c. 1·10 ⁻⁹
ZFMENE0159A	ENE	KFM07A	-353 / 4	< T _{limit}	F, NF	Σ PFL-f	c. 1·10 ⁻⁹
ZFMENE1208B	ENE	KFM07A	-680 / 29	< T _{limit}	F, NF	Σ PFL-f	c. 1·10 ⁻⁹
ZFMENE1208A	ENE	KFM07A	-724 / 31	< T _{limit}	F, NF	Σ PFL-f	c. 1·10 ⁻⁹
ZFMB8, ZFMNNW0100	G	KFM07A	-786 / 59	2.00·10 ⁻⁷	F	Σ PFL-f	c. 1·10 ⁻⁹
ZFM1203	G	KFM07B	-75 / 7	–	F, NT	–	
ZFMENE2320	ENE	KFM07B	-183 / 15	4.36·10 ⁻⁸	F	Σ PSS 5m	c. 7·10 ⁻¹⁰
ZFM1203	G	KFM07C	-94 / 11	4.81·10 ⁻⁵	F	Σ PFL-f	c. 1·10 ⁻⁹
ZFMENE2320	ENE	KFM07C	-343 / 80	< T _{limit}	F, NF	Σ PFL-f	c. 1·10 ⁻⁹
ZFMENE2320	ENE	KFM07C	-429 / 10	< T _{limit}	F, NF	Σ PFL-f	c. 1·10 ⁻⁹

ZFM	Category	Borehole	Elevation / b [m RHB 70] / [m]	T [m ² /s]	LOC	Method	T _{limit}
ZFMENE1061A	ENE	KFM08A	-233 / 58	1.31·10 ⁻⁶	F	Σ PFL-f	c. 1·10 ⁻⁹
ZFMNNW1204	NNW	KFM08A	-399 / 13	6.93·10 ⁻⁸	F	Σ PFL-f	c. 1·10 ⁻⁹
ZFMENE2248	ENE	KFM08A	-631 / 46	< T _{limit}	F, NF	Σ PFL-f	c. 1·10 ⁻⁹
ZFMNNW1205	NNW	KFM08B	-114 / 6	1.22·10 ⁻⁹	F	Σ PSS 5m	c. 7·10 ⁻¹⁰
ZFMNNW1205	NNW	KFM08B	-147 / 15	5.60·10 ⁻⁸	F	Σ PSS 5m	c. 7·10 ⁻¹⁰
ZFMNNE2312	NNE	KFM08C	-404 / 101	1.76·10 ⁻⁷	F	Σ PFL-f	c. 1·10 ⁻⁹
ZFMWNW2225	WNW	KFM08C	-574 / 27	2.61·10 ⁻⁹	F	Σ PFL-f	c. 1·10 ⁻⁹
ZFMENE1061A, ZFMENE1061B	ENE	KFM08C	-686 / 2	< T _{limit}	F, NF	Σ PFL-f	c. 1·10 ⁻⁹
ZFMENE1061A	ENE	KFM08C	-778 / 2	< T _{limit}	F, NF	Σ PFL-f	c. 1·10 ⁻⁹
ZFMENE1208A	ENE	KFM09A	-20 / 23	–	B, NT	–	
ZFMENE1208B	ENE	KFM09A	-82 / 26	2.50·10 ⁻⁸	B	Σ PSS 5m	c. 7·10 ⁻¹⁰
ZFMENE0159A, ZFMNNW0100	ENE	KFM09A	-190 / 21	1.03·10 ⁻⁷	B	Σ PSS 5m	c. 7·10 ⁻¹⁰
ZFMENE0159A, ZFMNNW0100	ENE	KFM09A	-216 / 32	1.96·10 ⁻⁸	B	Σ PSS 5m	c. 7·10 ⁻¹⁰
ZFMNW1200	NW	KFM09A	-581 / 21	7.74·10 ⁻⁹	B	Σ PSS 5m	c. 7·10 ⁻¹⁰
ZFMNW1200	NW	KFM09A	-609 / 13	4.37·10 ⁻⁸	B	Σ PSS 5m	c. 7·10 ⁻¹⁰
ZFMENE1208A	ENE	KFM09B	-17 / 28	2.92·10 ⁻⁵	F	Σ PSS 5m	c. 7·10 ⁻¹⁰
ZFNENE1208B	ENE	KFM09B	-52 / 25	1.01·10 ⁻⁵	F	Σ PSS 5m	c. 7·10 ⁻¹⁰
ZFNENE0159A	ENE	KFM09B	-93 / 21	3.57·10 ⁻⁶	F	Σ PSS 5m	c. 7·10 ⁻¹⁰
ZFMENE2320	ENE	KFM09B	-303 / 38	3.76·10 ⁻⁸	F	Σ PSS 5m	c. 7·10 ⁻¹⁰
ZFMENE2325A	ENE	KFM09B	-410 / 21	1.10·10 ⁻⁹	F	Σ PSS 5m	c. 7·10 ⁻¹⁰
ZFMENE2325B	ENE	KFM09B	-433 / 9	2.86·10 ⁻⁷	F	Σ PSS 5m	c. 7·10 ⁻¹⁰
ZFMWNW0123	WNW	KFM10A	-74 / 62	7.47·10 ⁻⁵	H	Σ PFL-f	c. 1·10 ⁻⁹
ZFMENE2403	ENE	KFM10A	-199 / 6	< T _{limit}	H, NF	Σ PFL-f	c. 1·10 ⁻⁹
ZFMA2	G	KFM10A	-302 / 7	2.92·10 ⁻⁵	H	Σ PFL-f	c. 1·10 ⁻⁹
ZFMA2	G	KFM10A	-327 / 7	1.15·10 ⁻⁶	H	Σ PFL-f	c. 1·10 ⁻⁹

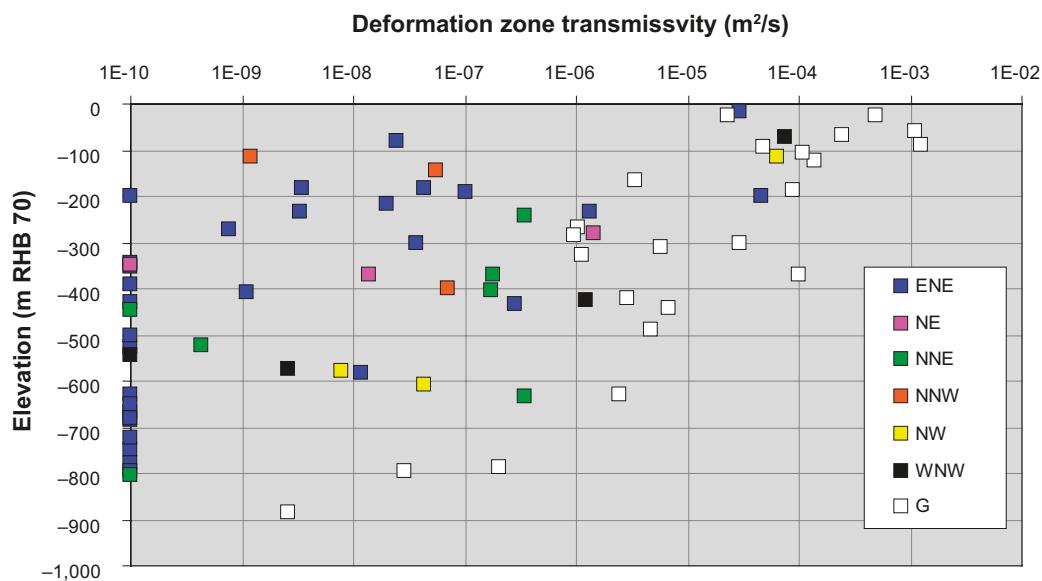


Figure 9-1. Transmissivity versus depth for the deterministically modelled deformations zones observed in cored boreholes. The transmissivities are coloured with regard to the orientations of the deformation zones. The colour legend is explained in Table 3-2. Deformation zones with little or no flow are assigned a low transmissivity value of 1·10⁻¹⁰ m²/s. The specific measurement limits for these zones are provided in Table 9-1.

9.2 Deformation zone thickness versus trace length

Table 9-2 shows estimated trace lengths and mean geological thicknesses of outcropping steeply-dipping deformation zones modelled by /Stephens et al. 2007/. The deformation zones taper and widen due to intersection with other structures, which means that the uncertainty in the mean value is large.

Figure 9-2 shows a plot of the same data. The correlation between geological thickness and length is weak. Apparently, the geological thickness of a steeply-dipping deformation zone with $L = 400\text{--}1,000$ m can be any value between 2–50 m. Furthermore, it is important to note that Table 5-1 through Table 5-20 suggest that groundwater flow in fairly thick deformation zones, i.e. thick from a geological point of view, is often constrained to one or a few flowing fractures only.

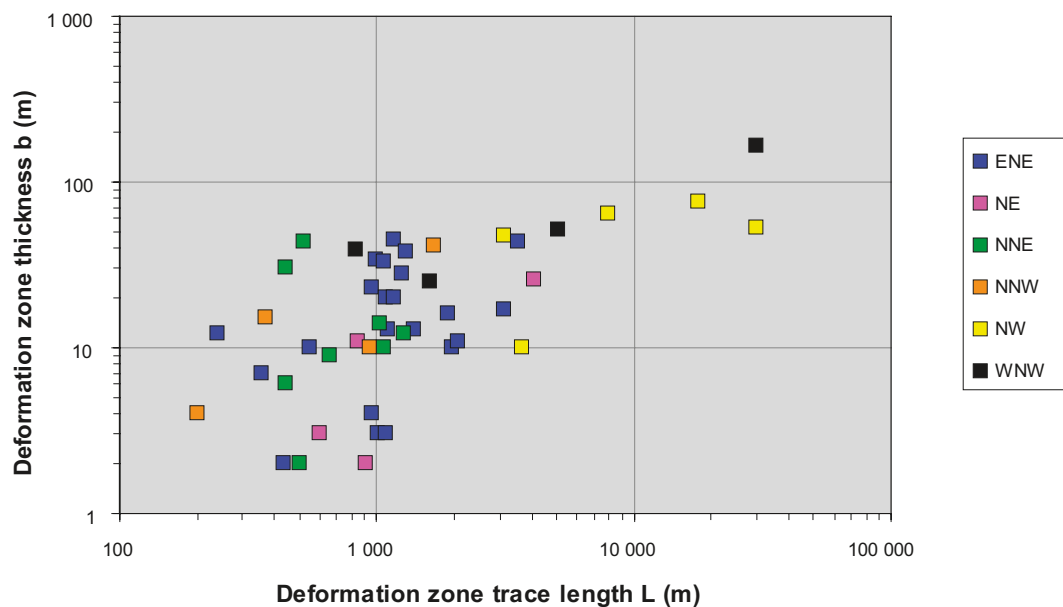


Figure 9-2. Deformation zone mean thickness versus trace length for outcropping steeply-dipping deformation zones.

Table 9-2. Summary of 2D data of outcropping steeply-dipping deformation zones in stage 2.2. The second column shows the structural interpretation as suggested by the geological single-hole interpretation. b denotes the geological thickness [m]. The table is based on data reported by /Stephens et al. 2007/.

ZFM	Category	Trace length	b
ZFMENE2120	ENE	239	12
ZFMENE0401B	ENE	358	7
ZFMENE1061B	ENE	436	2
ZFMENE2325B	ENE	553	10
ZFMENE2403	ENE	954	4
ZFMENE2325A	ENE	963	23
ZFMENE2383	ENE	1,000	34
ZFMENE2254	ENE	1,021	3
ZFMENE0060B	ENE	1,070	33
ZFMENE1208A	ENE	1,081	20
ZFMENE1192	ENE	1,090	3
ZFMENE1208B	ENE	1,112	13
ZFMENE1061A	ENE	1,158	45
ZFMENE0060C	ENE	1,161	20
ZFMENE2320	ENE	1,251	28
ZFMENE2248	ENE	1,298	38
ZFMENE0103	ENE	1,399	13
ZFMENE0159A	ENE	1,909	16
ZFMENE0401A	ENE	1,961	10
ZFMENE0061	ENE	2,081	11
ZFMENE0060A	ENE	3,120	17
ZFMENE0062A	ENE	3,543	44
ZFMNE1188	NE	606	3
ZFMNE2282	NE	842	11
ZFMNE0870	NE	903	2
ZFMNE0065	NE	4,068	26
ZFMNNE2008	NNE	441	6
ZFMNNE2263	NNE	446	30
ZFMNNE2255	NNE	507	2
ZFMNNE2312	NNE	519	43
ZFMNNE2273	NNE	657	9
ZFMNNE2280	NNE	1,035	14
ZFMNNE0869	NNE	1,072	10
ZFMNNE0725	NNE	1,274	12
ZFMNNW1204	NNW	201	4
ZFMNNW1205	NNW	368	15
ZFMNNW0404	NNW	947	10
ZFMNNW0100	NNW	1,673	41
ZFMNW1200	NW	3,121	47
ZFMNW0805	NW	3,694	10
ZFMNW0017	NW	7,923	64
ZFMNW0002	NW	18,000	75
ZFMNW0003	NW	30,000	53
ZFMWNW0044	WNW	834	39
ZFMWNW2225	WNW	1,613	25
ZFMWNW0123	WNW	5,086	52
ZFMWNW0001	WNW	30,000	165

9.3 Heterogeneity and anisotropy

Among the 131 deformation zones modelled deterministically within the regional model domain (cf. Figure 3-3), 57 deformation zones have been investigated hydraulically. Twenty-six of the 57 deformation zones are assessed by two or more hydraulic tests, see Figure 9-3. Multiple observations in individual zones imply that deformation zone heterogeneity and anisotropy can be addressed more thoroughly, which is a vital improvement of the site descriptive hydrogeological modelling compared to stage 1.2.

From Figure 9-1 we note the following hydraulic features for the deformation zones modelled deterministically in stage 2.2:

- *Vertical heterogeneity (depth trend)*: The transmissivity observations for the gently-dipping deformation zones vary from c. 10^{-3} m²s close to the bedrock surface to 10^{-9} m²s at an elevation of c. -900 m, which suggests a transmissivity contrast of several orders of magnitude.
- *Anisotropy*: On all elevations the mean transmissivity of the gently-dipping deformations zones is always more transmissive than any of the mean transmissivities of the seven steeply-dipping categories of deformation zones regardless of elevation.
- *Anisotropy*: On all elevations the mean transmissivities associated with the WNW and NW categories of the steeply-dipping deformation zones appear to greater than the mean transmissivities of the NNW and NNE categories, which in turn are greater than the mean transmissivities of the NE and ENE categories.
- *Lateral heterogeneity*: On all elevations each deformation zone category, cf. Table 3-2, display a substantial spatial variability in transmissivity.

From these four observations we conclude that hydraulic anisotropy and heterogeneity are vital characteristics of the deformation zones modelled deterministically.

The vertical heterogeneity (depth trend) displayed in Figure 9-1 is striking. However, a closer look at the data reveals that lateral heterogeneity is also a considerable feature (aspect) and must be taken into account. Conceptually, one could perhaps think of two kinds of lateral heterogeneity:

- *Intra-category lateral heterogeneity*, which concerns the differences in transmissivity observed between all deformation zones belonging to a particular category of deformation zones, e.g. all deformation zones striking ENE.
- *Intrinsic lateral heterogeneity*, which concerns the spatial variability in transmissivity observed within a single (specific) deformation zone.

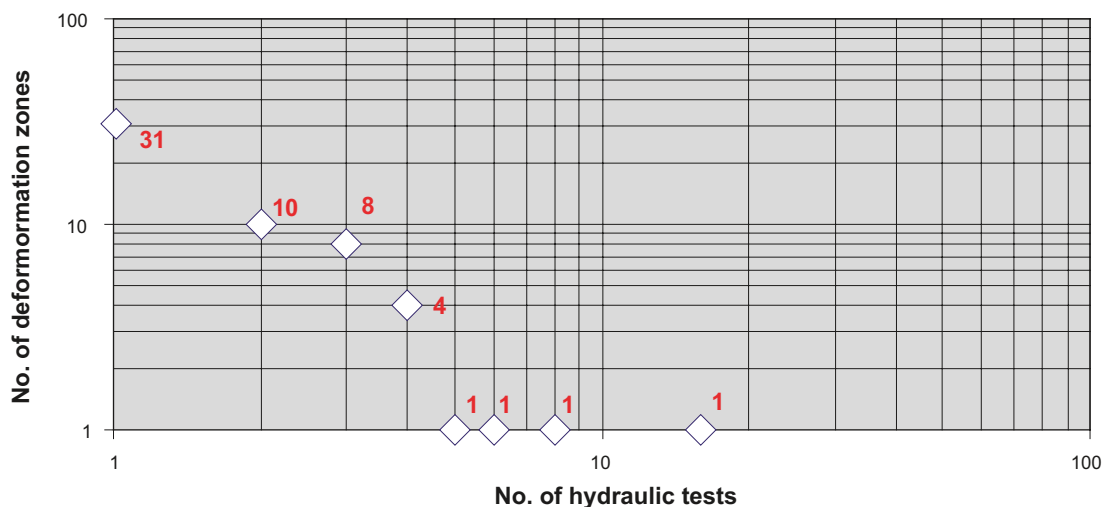


Figure 9-3. Plot of the number of deformation zones versus the number of hydraulic tests.

The two types of lateral heterogeneity addresses different scales of observation and one would expect the intrinsic lateral heterogeneity to be greater than the intra-category lateral heterogeneity. Unfortunately, some of the 26 zones with multiple transmissivity recordings intersect other zones as well, which means that there are 17 deformation zones only, which can be used to visualise and evaluate the differences between the two kinds of lateral heterogeneity. Figure 9-4 shows available transmissivity data for the ENE deformation zone category, which is the most abundant category among the steeply-dipping deformation zones. This plot can be used to address both types of lateral heterogeneity. Figure 9-5 shows available transmissivity data for the NE, NNW, NW, and WNW categories of the steeply-dipping deformation zones. Figure 9-6 shows available transmissivity data for the gently-dipping deformation zones. Figure 9-5 and Figure 9-6 can be used to address the magnitude of the intrinsic lateral heterogeneity.

From Figure 9-4 we make the following hypotheses regarding the lateral heterogeneity of the ENE steeply-dipping deformation zones:

- The magnitudes of the intra-category lateral heterogeneity as well as the intrinsic lateral heterogeneity depend on the elevation.
- The ranges of the intra-category and intrinsic lateral heterogeneities are both substantial but in principal very similar. The heterogeneities observed are c. four orders of magnitude at elevation c. -200 m and two to three orders of magnitude at elevation c. -500 m.

From Figure 9-5 we make the following hypothesis regarding the lateral heterogeneity of the NE, NNW, NW, and WNW steeply-dipping deformation zones:

- The range of the intrinsic lateral heterogeneity is difficult to generalise due to the scarce amount of data, but the data available suggest between one to two orders of magnitude at the elevations -150 (NNW), -300 (NE) and -600 (NW).

From Figure 9-6, finally, we make the following observations regarding the lateral heterogeneity of the gently-dipping deformation zones:

- The intra-category lateral heterogeneity is c. 300 times at all elevations.
- The intrinsic lateral heterogeneity is presumably smaller; the range appears to be between one to two orders of magnitude.

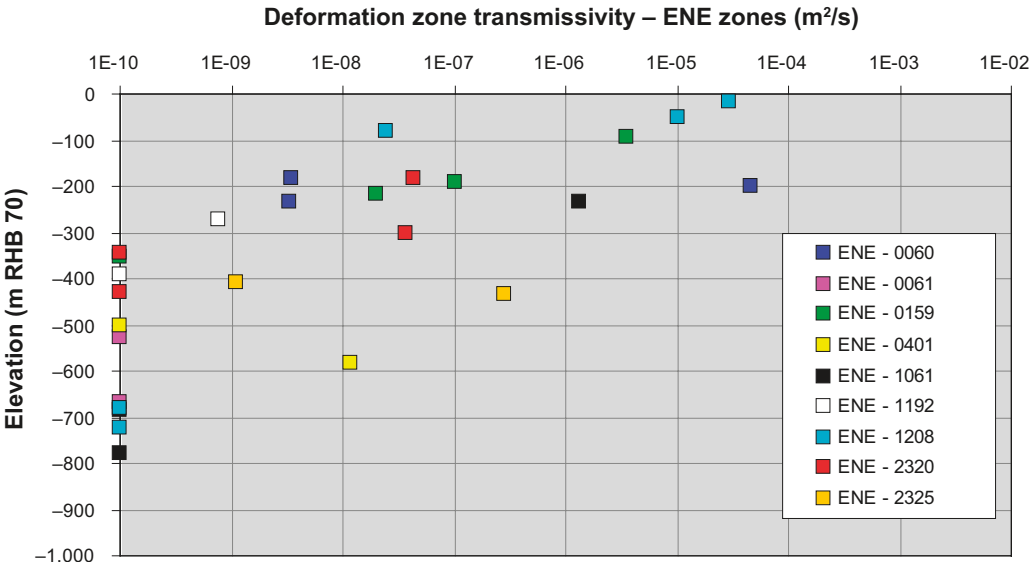


Figure 9-4. Plot of transmissivity data for the ENE category of the steeply-dipping deformation zones. A reasonable estimation of the intra-category lateral heterogeneity is c. four orders of magnitude at the elevation c. -200 and c. three orders of magnitude at elevation c. -500. Concerning intrinsic lateral heterogeneity, data from ZFMENE0060 suggest c. four orders of magnitude at the elevation c. -200 and data from ZFMENE2325 suggest c. two orders of magnitude at the elevation c. -400.

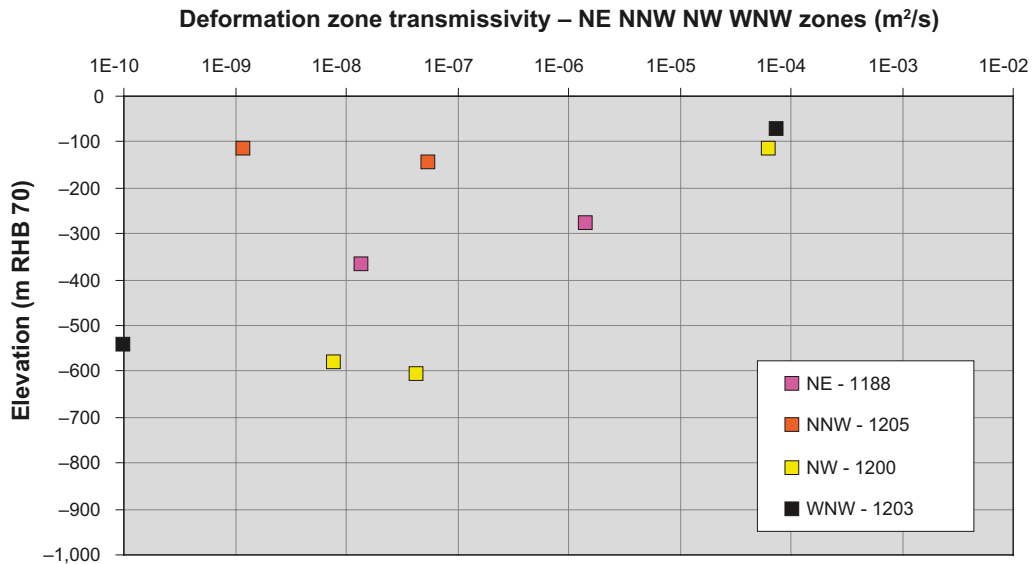


Figure 9-5. Plot of transmissivity data for the NE, NNW, NW, and WNW categories of the steeply-dipping deformation zones. The magnitude of the intrinsic lateral heterogeneity is difficult to generalise due to the scarce amount of data, but the data available suggest between one to two orders of magnitude at the elevations -150 (NNW), -300 (NE) and -600 (NW).

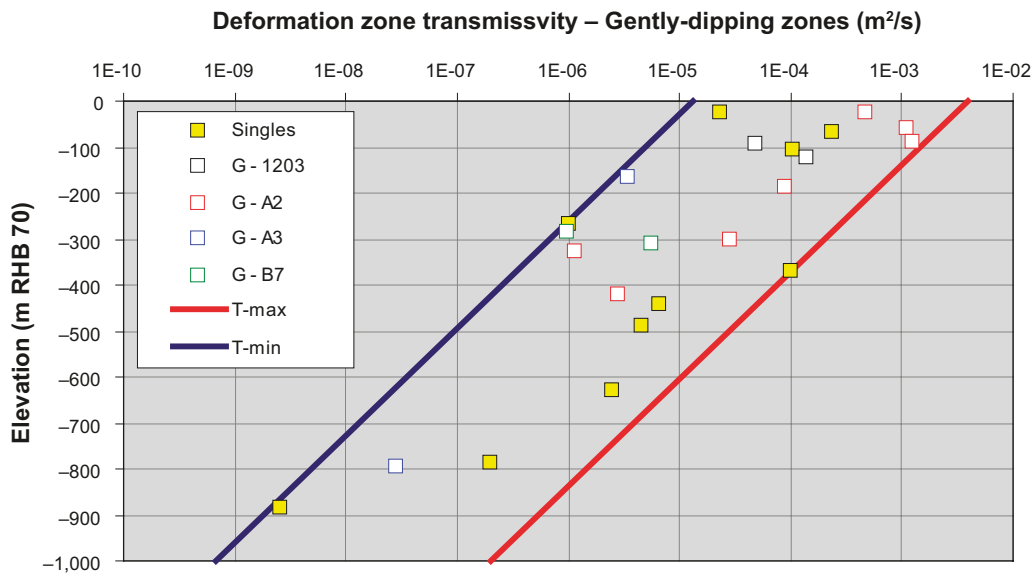


Figure 9-6. Plot of single-transmissivity zones as well as multiple-transmissivity zones for the gently-dipping deformation zones. The envisaged magnitude of the intra-category lateral heterogeneity is *c.* 300 times at all elevations. The range of the intrinsic lateral heterogeneity is presumably less; the range appears to be between one to two orders of magnitude.

The reason for incorporating single-zone transmissivity data in Figure 9-6 is the substantial conceptual contribution provided by these measurements, which should be recognised while addressing the intra-category lateral heterogeneity. Figure 9-6 does not indicate that the range of the intra-category lateral heterogeneity decreases with depth for the gently-dipping zones. On the contrary, the range of this kind of lateral heterogeneity appears to be more or less constant with a suggested value of *c.* 300 times, i.e. 2.5 orders of magnitude on all elevations.

9.4 A preliminary model for representing observed heterogeneity in deformation zone transmissivity

9.4.1 Conceptual model

The observations listed above render the following preliminary conceptual model of the observed heterogeneity in deformation zone transmissivity:

- All deformation zones, regardless of orientation, are subjected to a substantial transmissivity decrease with depth. The upper and lower bounds shown in Figure 9-6 suggest a contrast of c. 20,000 times for the uppermost one kilometre of bedrock, which corresponds to a contrast of c. 4.3 orders of magnitude.
- The lateral heterogeneity is also substantial but more irregular in its appearance. The difference between the two kinds of lateral heterogeneity discussed, intra-category vs. intrinsic, is arbitrary though.
- If there is any particular directional difference between the different sets of deformation zones, the ENE set appears to have the largest range and the gently dipping set the smallest. The ENE set can easily vary four orders of magnitude in transmissivity on any elevation, whereas the gently-dipping set appears to vary c. two and half orders of magnitude rather.
- The observation that the mean transmissivity of the gently-dipping deformation zones is c. one to two orders of magnitude greater than the mean transmissivities of all categories of steeply-dipping deformation zones may be due to the anisotropy in the stress field. There is an indication that large values in the data representing the steeply-dipping deformation zones are often associated with the WNW and NW sets. These two sets and the gently-dipping set are all parallel with the main horizontal stress.

9.4.2 Numerical representation

Figure 9-7 shows a combination of the cross-plots shown in Figure 9-1 and Figure 9-6, respectively. Based on the information shown in Figure 9-7 the following scheme for numerical modelling of deformation zone heterogeneity is proposed for modelling stage 2.2:

1. The discretisation of the computational grid should not exceed 20 m in any direction above the elevation -1,100.
2. A linear model for the common logarithm of the vertical heterogeneity in transmissivity is suggested for all deformation zones regardless of category:

$$\log(T(z)) = (z - m) / k \quad (9-1)$$

where k is determined from the slope of the red line denoted by “T-max”) in Figure 9-7:

$$T_{max}(0) = 4 \cdot 10^{-3} \text{ m}^2\text{s}; T_{max}(-1,000) = 2 \cdot 10^{-7} \text{ m}^2\text{s} \rightarrow k = 232.50.$$

The value of m for the red line is computed from $T_{max}(0) = 4 \cdot 10^{-3} \text{ m}^2\text{s}$:

$$m_{max} = -232.50 \log(4 \cdot 10^{-3}) = 557.53.$$

3. Local conditioning is suggested for the computation of m for the hydraulically tested deformation zones. The values of z and T to be used for the computations of the local m values are shown in Table 9-1.

$$m(\text{ZFM}_{xxx}) = z(\text{ZFM}_{xxx}) - k \log(T(\text{ZFM}_{xxx})) \quad (9-2)$$

If local conditioning is too complex to accomplish for the few cases where there are several observations of transmissivity in the same deformation zone, it is suggested that the arithmetic mean for the zone’s category is used as a start value.

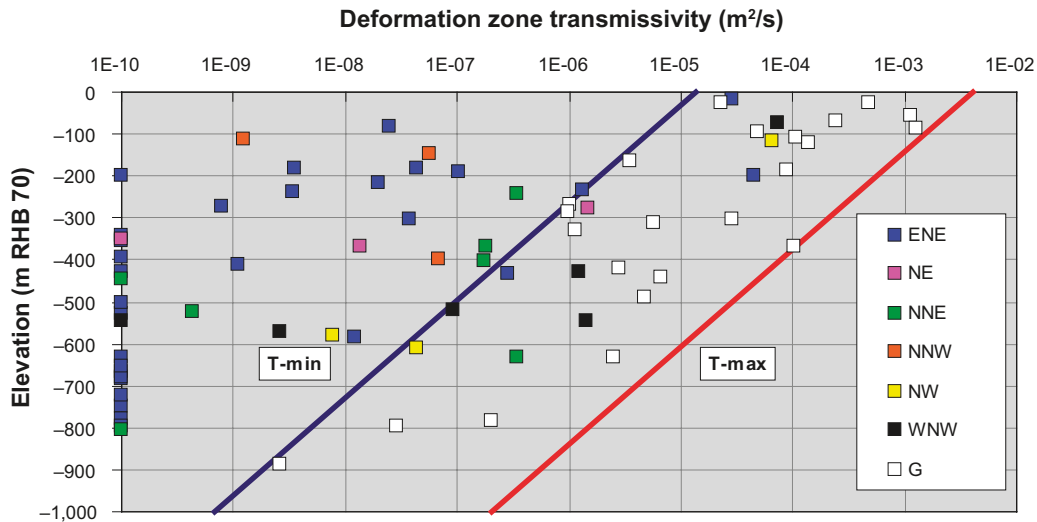


Figure 9-7. Combination of the cross-plots shown in Figure 9-1 and Figure 9-6, respectively.

4. For the deformation zones not tested hydraulically, it is also suggested that the arithmetic mean for the zone's category is used as a start value. For instance, for all NNE deformation zones not tested hydraulically, the arithmetic mean of m of the tested NNE deformation zones on that elevation is used as a start value.
5. Lateral heterogeneity away from the borehole intercepts is suggested to be modelled without a trend or a correlation as a start value. Here, two approaches are envisaged:

Approach 1: Uniformly distributed lateral $\log(T(z))$ variability

$$T(x,y|z) = \min(T_{max}(z); \{ 10^{\text{U}[\{\log(T(z) / \sqrt{D}\}); \{\log(T(z) \sqrt{D}\})\}]} \}) \quad (9-3)$$

where $D = 300$.

D is determined from the ratio between the blue and red lines in Figure 9-6, which define T_{min} and T_{max} , respectively, of the gently-dipping zones. $T_{max} / T_{min} = 300$ implies a lateral heterogeneity of c. two and half orders of magnitude.

Approach 2: Normally distributed lateral $\log(T(z))$ variability

$$T(x,y|z) = \min(T_{max}(z); 10^{(\log(T(z)) + \sigma_{\log(T)} \text{N}[0, 1]))} \quad (9-4)$$

If one assumes that $\log(D)$ is fair approximation of the 95% confidence interval of $\log(T)$, the standard deviation for the generation of lateral values of $\log(T)$ can be estimated as:

$$\sigma_{\log(T)} = \log(D) / (2 \cdot 1.96) = 0.632.$$

10 Fracture data analysis

10.1 Methodology

A methodology for analysis and collation of fracture geological and hydrogeological information has been previously applied to the Forsmark modelling stage 1.2 data /Follin et al. 2005b, Hartley et al. 2005b/. For modelling stage 2.2, a much greater quantity of data is available, and in particular data is available for core drilled boreholes in a variety of orientations. Hence the workflow has been enhanced and follows the steps:

1. Group fractures from the borehole core-logs according to whether they are inside a deformation zone identified in the geological single-hole interpretations, or in one of the Forsmark fracture domains.
2. Calculate linear fracture intensities, P_{10} , in each borehole according to various sub-sets of types of fracture.
3. Calculate Terzaghi corrected linear fracture intensities, $P_{10,corr}$, in each borehole according to various sub-sets of types of fracture.
4. The sub-sets of fractures to be quantified include all fractures, open or partly open fractures, and fractures associated with PFL flow-anomalies based on the PFL-f hydraulic tests. In this analysis, no distinction is made between open and partly open fractures.
5. Investigate possible correlations between fracture intensity and fracture domain, inside or outside a deformation zone, and by depth.
6. Calculate average fracture intensities across boreholes by using borehole length weighted averages, and use Terzaghi corrected fracture intensities to limit the bias due to borehole orientations.
7. Generate equal area lower hemisphere stereonet for each borehole to investigate variations in fracture orientations between boreholes, and consider variations in fracture orientation by depth.
8. Use Terzaghi corrected stereographic density plots for each borehole to identify major sets and compare these with the hard sector definitions of sets defined in geological DFN model for Forsmark modelling stage 1.2 /La Pointe et al. 2005/.
9. Generate stereographic pole plots for the fractures associated with PFL flow-anomalies colouring the poles according to the interpreted transmissivity to identify the orientation of fractures with the greatest hydrogeological significance.
10. Collate fracture intensities for various fracture sub-sets with each of the fracture sets identified in modelling stage 1.2.
11. Calculate fracture intensities within each deformation zone.

The objectives of this analysis are to collate basic statistics of the fractures in a variety of ways to guide and support the development of a conceptual model for fracture characteristics including fracture hydrogeology. This requires the exploration of any correlations in fracture occurrence with depth, rock domain, or geological structures for different categories of fractures including all fractures, those judged as open which might potentially contributed to flow and aqueous diffusion, and those where a flow has been measured in hydraulic tests.

In the following we use the notation F 1.2 and F 2.2 as acronyms for Forsmark modelling stage 1.2 and 2.2, respectively. DZ and ZFM are used as synonyms and denote a deformation zone in Forsmark. Likewise, FFM denote a fracture domain. The geological DFN model for Forsmark modelling stage 1.2 is denoted by Geo-DFN F 1.2.

10.2 Assumptions

The following assumptions have been made in the data compilation:

- The locations of the first and last fracture mapped in the borehole core logs approximates well the total length of borehole mapped.
- Fracture sets can be categorised based on orientation only and using the definitions defined in the Geo-DFN for F 1.2 with predefined hard sectors.
- Fracture with dips $\geq 50^\circ$ belong to sub-vertical sets. Fractures with dips $< 50^\circ$ are assigned to the sub-horizontal set.
- The Terzaghi correction can be used to estimate fracture intensities unbiased by the direction of a sample borehole. Having calculated unbiased or corrected linear fracture intensities, $P_{10,corr}$, for individual boreholes, these can be combined over boreholes of varying trajectories to estimate average areal fracture intensities, P_{32} .
- The maximum correction factor used in the Terzaghi correction process is 7, equivalent to an angle of 8.2° between the borehole and the fracture plane.
- Stereonets are plotted as equal area lower hemisphere plots with Terzaghi correction.
- The PFL-anomalies identified in each borehole are comparable, i.e. have similar practicable detection limits.
- The BIPS errors in the F 2.2 orientation data are small.
- The measurement process for recording length down the borehole for the occurrence of PFL flow-anomalies are sufficiently consistent with the measurement process for the BIPS logs that the correlations of flows and individual fractures made by Sweco Viak are valid.
- Open fractures are a subset of all fractures, and the PFL-anomalies are a subset of the open fractures.

10.3 Analysis of geological data

This section considers the basic geometrical attributes of the fractures mapped in the deep cored drilled boreholes. The main attributes of the borehole fractures are their orientation, classification into sets, spatial distribution, and intensity. The fracture statistics are collated in a variety of ways to try to discover any patterns in the occurrence and nature of open, interconnected, flowing fractures.

10.3.1 Fracture orientation

The global Geo-DFN model derived for Forsmark modelling stage 1.2 was used as a starting point. However, it is noted that the only significant result of that work used here is the hard sector classification of the fracture sets based on orientation as detailed in Table 10-1.

Table 10-1. Hard sector definitions. Modified after the global Geo-DFN model for Forsmark stage 1.2 /La Pointe et al. 2005/.

Set	Trend	Plunge	Dip	Strike
1 NS	65–110, 245–290	0–40	50–90	335–20, 155–200
2 NE	110–170, 290–350	0–40	50–90	20–80, 200–260
3 NW	25–65, 205–245	0–40	50–90	115–155, 295–335
4 EW	350–25, 170–205	0–40	50–90	80–115, 260–295
5 HZ	0–360	40–90	0–50	0–360

Terzaghi correction

Measurements along a scanline or borehole preferentially detect fractures orthogonal to the scanline than at an oblique angle, which will bias measures of fracture intensity such as frequency or stereographic concentration contour plots heavily in favour of fracture sets orthogonal to the borehole. To compensate for this bias, calculations of fracture intensity are accumulated in terms of a weighted sum rather than a simple count with a geometrical weighting factor calculated and applied to each fracture measured. This weighting, W , is used in calculating statistics such as the corrected linear fracture intensity, $P_{10,corr}$, when comparing between different borehole orientations, or can be applied to concentration plots for identifying sets. The process is called Terzaghi correction /Terzaghi 1965/ and is illustrated in Figure 10-1.

Fracture sets in boreholes

In order to evaluate the validity of the fracture sets used in F 1.2 for the new boreholes, stereographic concentration plots were created for all boreholes in the F 2.2 data freeze and compared with the F 1.2 hard sector definitions given in Table 10-1. Stereonets are plotted as Terzaghi corrected Fisher concentration plots using equal area lower hemisphere projection. Concentration plots are used since they indicate which sets have the highest density of fractures, and Terzaghi correction is used to reduce the bias due to the orientation of the borehole to make comparisons between boreholes of different orientation more meaningful than simple pole plots. Figure 10-2 shows an example of a plot for the F 1.2 borehole, KFM01A. Here, all fractures (open and sealed) are included that occur within one of the fracture domains (FFMs), but not part of a deformation zone (ZFM). The measure of concentration is a relative one defined in terms of % of total per 1.0% area, meaning the percentage of the total number of poles in each 1% area of the hemisphere. That is, for each 1% area on the hemisphere, the number of poles are counted and divided by the total number of poles to give the percentage. For KFM01A the most concentrated sets are the HZ, NS and NE sets. KFM02A shows similar patterns, while KFM04A and KFM05A have higher concentrations in the sub-vertical sets NE, NS and NW (see Figure 10-3).

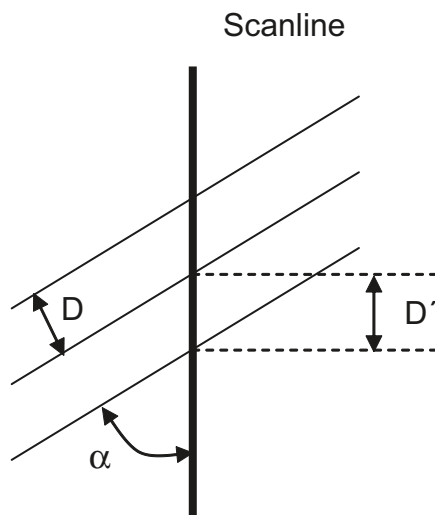


Figure 10-1. α = minimum angle between plane and the borehole scanline, D' = apparent spacing along traverse, $D = D' \sin(\alpha) = D' (1/W) =$ true spacing of discontinuity set, $W = \text{cosec}(\alpha) =$ weighting applied to individual pole before density calculation.

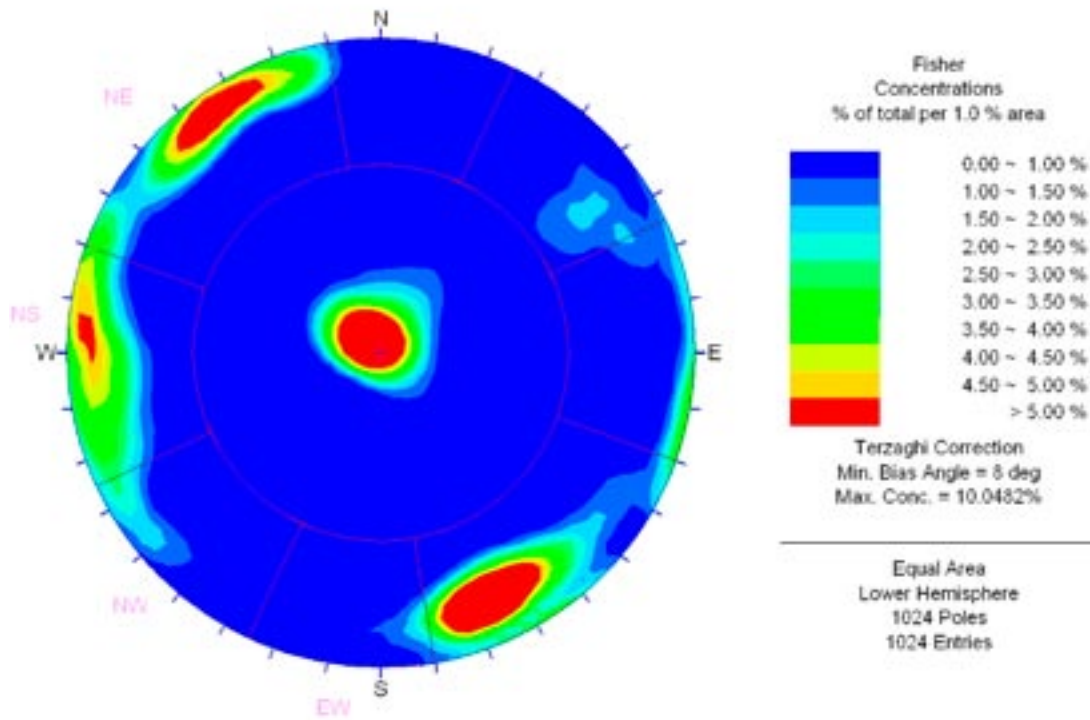


Figure 10-2. Fisher concentration plot for all fractures in KFM01A for all FFM fracture domains (i.e. excluding deformation zones). The concentrations are Terzaghi corrected and use an equal area lower hemisphere projection.

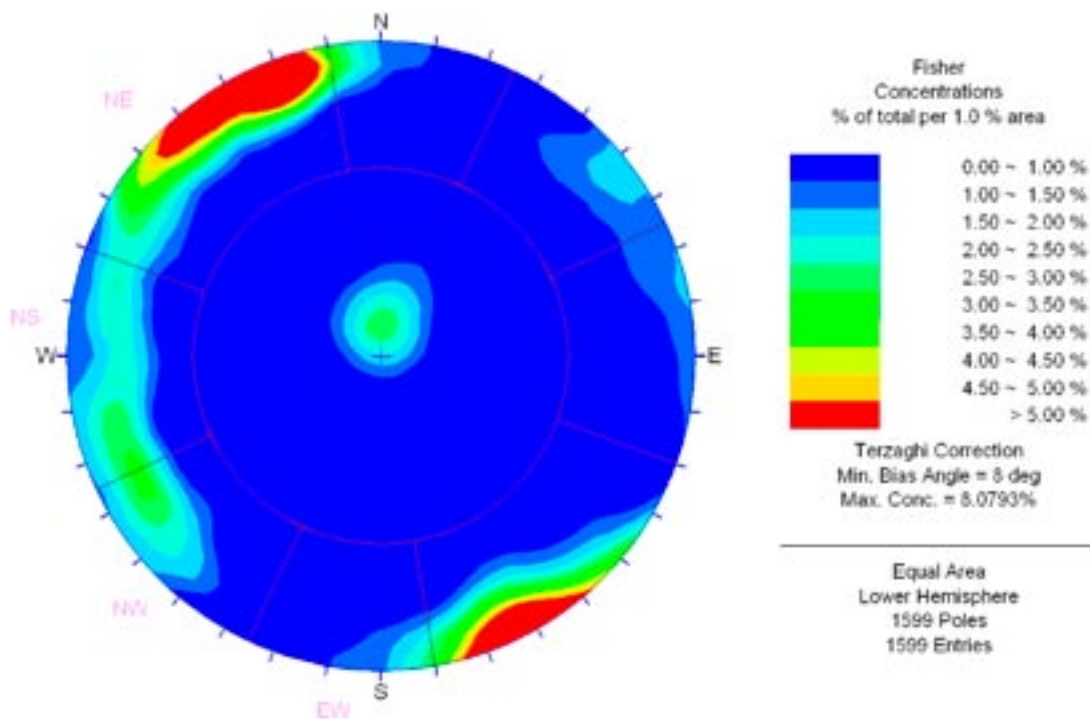


Figure 10-3. Fisher concentration plot for all fractures in KFM05A for all FFM fracture domains (i.e. excluding deformation zones). The concentrations are Terzaghi corrected and use an equal area lower hemisphere projection.

The new F 2.2 borehole KFM01D also confirms the geological importance of these 3 sub-vertical sets, as seen in Figure 10-4. KFM06A in Figure 10-5 reveals the presence of a NNE set that overlaps the 2 sectors defined for F 1.2, NS and NE. This borehole is oriented NW, which is a direction not previously sampled. KFM08A is also in this direction and confirms the presence of a NNE set, as well as suggesting a small EW set rarely seen in the other boreholes (see Figure 10-6). A complete set of stereonets for all boreholes is given in Appendix A. The EW oriented KFM07A is dominated by the NE, NS and HZ sets; and near vertical KFM07C largely encounters the HZ and NE sets. The NE oriented KFM08C confirms the NNE set, together with observing the HZ, NS and NE sets. KFM10A is oriented NNE, and encounters the NE, NS, NW and HZ sets.

In summary, the sets identified in the F 1.2 Geo-DFN still seem to give a valid way of grouping the fractures by orientation, although some of the new boreholes suggest a NNE set that smears between the F 1.2 NE and NS sets. In terms of updating the hard sector definitions for F 2.2, it could be speculated that there are two possible choices: either to introduce a new NNE sector, or to simplify the definition of the sub-vertical sets by merging the NE-NS sets and the NW-EW sets. The second of these two options would probably require a more diffuse distribution of strike for modelling the data, and this might lead to the necessity for using Bivariate Fisher distributions.

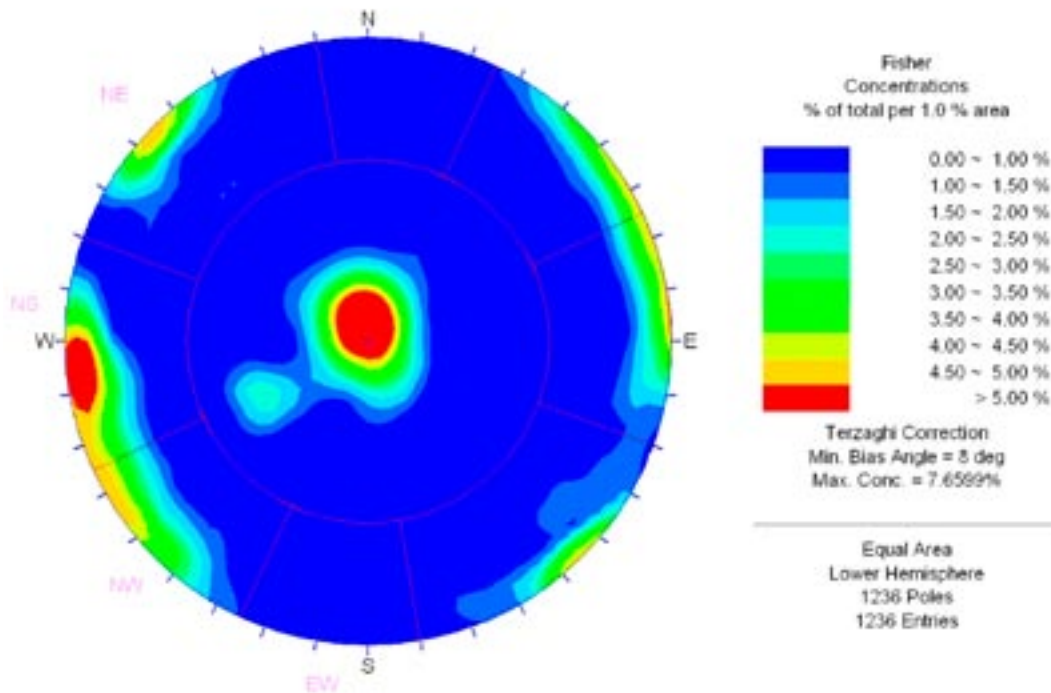


Figure 10-4. Fisher concentration plot for all fractures in KFM01D for all FFM fracture domains (i.e. excluding deformation zones). The concentrations are Terzaghi corrected and use an equal area lower hemisphere projection.

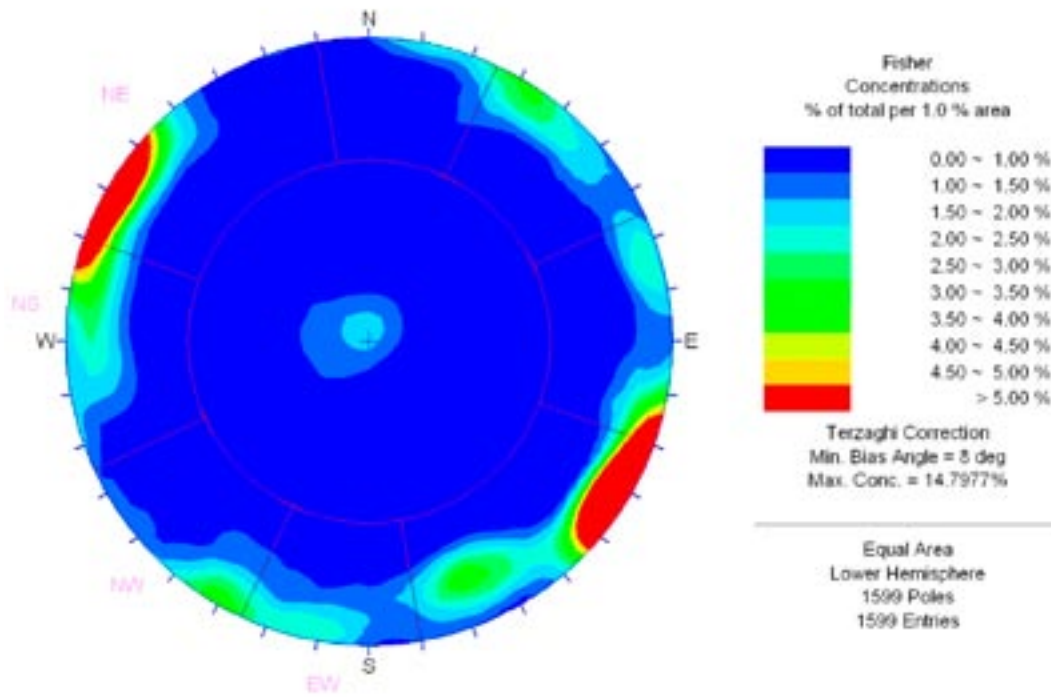


Figure 10-5. Fisher concentration plot for all fractures in KFM06A for all FFM fracture domains (i.e. excluding deformation zones). The concentrations are Terzaghi corrected and use an equal area lower hemisphere projection.

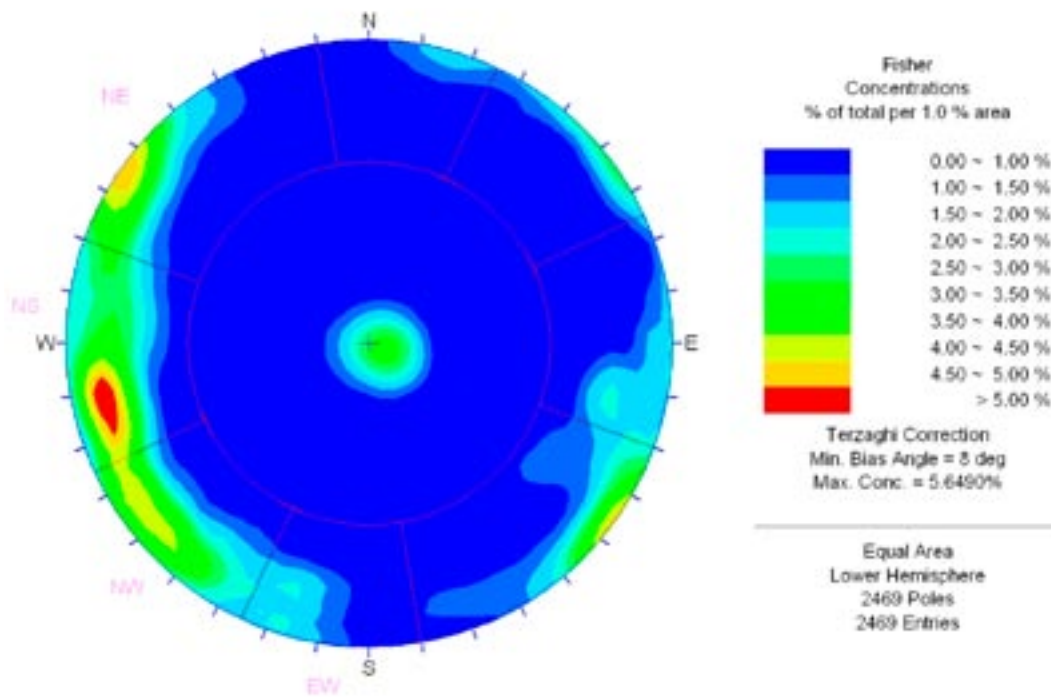


Figure 10-6. Fisher concentration plot for all fractures in KFM08A for all FFM fracture domains (i.e. excluding deformation zones). The concentrations are Terzaghi corrected and use an equal area lower hemisphere projection.

10.3.2 Fracture intensity

In this section a variety of ways of collating the observed fracture intensities in the F 2.2 core-drilled borehole are presented to identify possible correlations between fracture occurrence and controlling factors such as position, depth, rock domain, and geological structures.

Statistics are collected for different classification of fractures. One key fracture attribute used is whether the fracture is open or sealed in the core since this is considered useful in indicating whether the fracture forms a possible flow conduit for the movement of water primarily by advection through connected channels, but also possibly by diffusion in stagnant flow volumes. A small number of fractures are recorded as partly-open where there is an opening in the core, but it is not a complete break. Since these features may also potentially conduct flow, they are grouped with the open fractures. Fractures judged to be open are classified as such with a degree of confidence described as certain, probable or possible. This could be considered as an indication of the uncertainty in a fractures potential to form part of a connected network. However, even if a fracture is open and certain it does not necessarily mean it carries flow, as this will depend on the fractures connectivity to a water bearing network. To quantify statistics for water bearing fractures, a classification of fractures associated with observed PFL flow-anomalies is used. Flow-anomalies are identified in intervals about 10 cm in length where flows corresponding to a feature transmissivity of about 10^{-9} m²/s or more have been measured using the PFL-f tests. Sweco Viak have associated each of these flow-anomalies to individual fractures observed in the core and BIPS logs according to rules based on position in the borehole and the classification of the fractures as potential flowing features in the core logs /Forsman et al. 2004; Forsman et al. 2006; Teurneau et al. 2007/.

The numbers of fractures recorded in each borehole according to the different classifications is given in Table 10-2 along with the length of borehole mapped. As can be seen, only about 24% of fractures are judged to be open, and of these only about 1.7% are associated with flowing features. Hence, open fractures represent a small sub-set of the total number of fractures, and only a tiny proportion contributes to flow in the bedrock. An important consideration is whether these sub-sets important to flow are uniform percentage of fractures or belong to particular fracture sets in spatial positions. This issue will be considered in tabulations of the data in this section and using stereonet in Section 10.4. Of the fractures considered to be open, about half of these are only possibly open.

Table 10-2. Summary of sample lengths and numbers of fractures according to different categories in each of the boreholes studied in F2.2. Fractures that judged to be open are assigned a confidence: certain, probable or possible. The number of PFL flow-anomalies is also given.

Borehole	Top [m]	Bottom [m]	Length [m]	Total number	Number of open (+partly)	Open and certain	Open and prob.	Open and poss.	PFL-anom.
KFM01A	102.67	993.49	890.82	1,517	752	174	143	435	34
KFM01D	91.67	799.62	707.95	1,636	468	99	178	191	34
KFM02A	101.54	1,000.36	898.82	2,199	443	152	267	24	104
KFM03A	102.45	999.67	897.22	1,825	375	146	137	92	52
KFM04A	109.1	985.07	875.97	4,327	1,357	257	630	470	71
KFM05A	102.27	999.62	897.35	2,838	633	91	180	362	27
KFM06A	102.21	997.37	895.16	3,680	816	172	235	409	99
KFM07A	102.04	993.77	891.73	3,183	617	103	162	352	26
KFM07C	98.62	498.67	400.05	1,765	285	78	116	91	14
KFM08A	103.36	949.67	846.31	4,268	713	149	210	354	41
KFM08C	102.29	948.99	846.70	4,198	676	56	199	421	21
KFM10A	62.86	499.98	437.12	2,755	999	264	299	436	54
All bh			9,485.20	34,191	8,134	1,741	2,756	3,637	577

Fracture intensity in a borehole is simply the number of fractures divided by length. This is called the linear intensity or P_{10} . To mitigate for orientation bias the fracture intensity can be corrected by calculating the sum of Terzaghi weights divided by length, $P_{10,corr}$. Fracture intensities for the various categories of fractures: all, open, open and certain, open and probable, and PFL flow-anomalies are given in Table 10-3. This table averages over all fracture domain and deformation zone volumes within the boreholes. Note: the explanation of the shorthand notation given for each of the P_{10} statistics is given in the caption. Fracture intensities are given for all the boreholes as well as a borehole length weighted average in the row denoted “All bh”. The fracture intensity for all fractures is notably lower for KFM01A than all other boreholes. Using the estimate of “true” intensity $P_{10,a,corr}$, suggests an overall average intensity of just over 8 m^{-1} and varying between about 4.5 to 14.5 m^{-1} with the lowest intensity at KFM01A, KFM01D and KFM02A. Considering open fractures, the “true” intensity $P_{10,o,corr}$ reduces to an average of 1.8 m^{-1} with the highest values above 2.5 m^{-1} occurring in KFM04A and KFM10A, which lie around the periphery of the tectonic lens. For PFL flow-anomalies, the “true” intensity $P_{10,PFL,corr}$ averages to about 0.09 m^{-1} , but this statistic is very heterogeneous. The boreholes with a relatively high intensity of PFL flow-anomalies are KFM02A which intersects the major deformation zone ZFMA2, KFM04A which is inclined to penetrate the candidate area from outside the tectonic lens, KFM06A which intersects an abnormally high number of deformation zones, and KFM10A which is on the periphery of the candidate area.

Fracture intensity for sets

Together with the stereonet given in Section 10.3.1, the Terzaghi corrected intensities of fractures associated with each of the fracture sets defined in the F 1.2 Geo-DFN interpretation are tabulated in Table 10-4. The HZ and NE sets are the primary orientations in terms of both all and open fractures, followed by NW and NS as secondary sets, and EW as a minor set. However, there are considerable variations between individual boreholes as to the order of importance. The NW set is only a relatively major set in KFM04A and KFM10A, which both cross the NW oriented southern edge of the tectonic lens. Likewise, the NS is only a relatively major set on the NS oriented western edge of the tectonic lens. Thus, there is some evidence for enhanced tangential sub-vertical fracturing around the edges of the tectonic lens that are sub-parallel to the boundary of the lens. The HZ and NE are consistently important in all boreholes. Stereographic concentration plots are presented in Figure 10-7 and Figure 10-8 based

Table 10-3. Summary of various linear fracture intensities, P_{10} , in each of the boreholes studied in F2.2. The subscripts relate to: a = all, corr = Terzaghi corrected, o = open, c = certain, cpr = certain or probable, PFL = PFL-f anomalies, a comma signifies a logical AND function.

Borehole	Fracture linear intensity, P_{10} [1/m]							
	$P_{10,a}$	$P_{10,a,corr}$	$P_{10,o}$	$P_{10,o,c}$	$P_{10,o,cpr}$	$P_{10,o,corr}$	$P_{10,PFL}$	$P_{10,PFL,corr}$
KFM01A	1.70	4.17	0.84	0.20	0.36	1.64	0.038	0.078
KFM01D	2.31	4.86	0.66	0.14	0.39	1.09	0.048	0.062
KFM02A	2.45	4.76	0.49	0.17	0.47	0.93	0.116	0.199
KFM03A	2.03	5.33	0.42	0.16	0.32	0.84	0.058	0.105
KFM04A	4.94	11.87	1.55	0.29	1.01	2.80	0.081	0.137
KFM05A	3.16	7.25	0.71	0.10	0.30	1.24	0.030	0.036
KFM06A	4.11	8.37	0.91	0.19	0.45	1.49	0.111	0.161
KFM07A	3.57	7.52	0.69	0.12	0.30	1.28	0.029	0.037
KFM07C	4.41	11.45	0.71	0.19	0.48	1.75	0.035	0.052
KFM08A	5.04	10.76	0.84	0.18	0.42	1.43	0.048	0.069
KFM08C	4.96	10.81	0.80	0.07	0.30	1.54	0.025	0.041
KFM10A	6.30	13.52	2.29	0.60	1.29	3.68	0.124	0.232
All bh	3.60	8.02	0.86	0.18	0.47	1.55	0.061	0.098

Table 10-4. Summary of Terzaghi corrected linear fracture intensities by set for all fractures and open fractures.

Borehole	$P_{10,a,corr}$ [1/m]					$P_{10,o,corr}$ [1/m]				
	Fracture set					Fracture set				
	NS	NE	NW	EW	HZ	NS	NE	NW	EW	HZ
KFM01A	0.69	2.30	0.29	0.13	0.76	0.17	0.69	0.12	0.08	0.58
KFM01D	1.26	1.27	0.85	0.18	1.29	0.13	0.20	0.23	0.04	0.49
KFM02A	0.69	1.13	0.86	0.36	1.72	0.12	0.17	0.23	0.05	0.37
KFM03A	1.41	1.63	0.74	0.39	1.16	0.14	0.18	0.13	0.08	0.32
KFM04A	1.66	4.65	2.68	0.78	2.11	0.17	0.68	0.85	0.19	0.91
KFM05A	1.12	3.71	0.90	0.47	1.06	0.16	0.46	0.18	0.04	0.40
KFM06A	1.48	3.87	0.87	0.81	1.34	0.16	0.59	0.12	0.12	0.50
KFM07A	1.71	2.89	0.77	0.74	1.41	0.35	0.37	0.13	0.08	0.35
KFM07C	1.15	6.53	1.04	0.44	2.30	0.18	0.91	0.15	0.07	0.44
KFM08A	2.97	3.00	1.99	1.21	1.59	0.22	0.43	0.16	0.19	0.43
KFM08C	3.07	3.29	1.67	1.13	1.65	0.22	0.46	0.21	0.26	0.39
KFM10A	2.03	4.69	2.39	0.91	3.49	0.15	0.70	0.95	0.31	1.57
All bh	1.60	3.04	1.21	0.63	1.54	0.18	0.46	0.27	0.12	0.52

on the combined data for all fractures in the background rock between the deformation zones (FFMs) for all fractures and just open fractures, respectively. These show: that the HZ set has a relatively high proportion of open fractures compared to the sub-vertical sets, and the NS set has the least proportion of open sets; gently dipping open fractures have no preferred strike; the HZ and NE sets have high Fisher concentrations; NW set as a secondary effect. In terms of hydraulic importance, the HZ set clearly stands out in the statistics presented for PFL flow-anomalies given in Table 10-5. About 56% of the PFL flow-anomaly intensity belongs to set HZ. NE is the secondary hydraulic set, with NS, NW and EW as tertiary sets. For 5 of the 12 boreholes, PFL flow-anomalies cluster in only 2–3 sets. KFM06A is the only borehole entirely within the candidate area that contains PFL flow-anomalies in all 5 sets. Figure 10-9 shows a stereographic concentration plot for only PFL flow-anomalies in FFMs. This plot confirms the dominance of the HZ set with only very weak hydraulic signatures for sub-vertical fractures with either NNE or NE strike.

Table 10-5. Summary of linear fracture intensities with and without Terzaghi correction Terzaghi corrected by fracture set for PFL fractures.

Borehole	$P_{10,PFL}$ [1/m]					$P_{10,PFL,corr}$ [1/m]				
	Fracture set					Fracture set				
	NS	NE	NW	EW	HZ	NS	NE	NW	EW	HZ
KFM01A	0.000	0.008	0.000	0.000	0.030	0.000	0.045	0.000	0.000	0.032
KFM01D	0.000	0.001	0.000	0.000	0.047	0.000	0.002	0.000	0.000	0.059
KFM02A	0.004	0.012	0.010	0.010	0.079	0.008	0.025	0.039	0.034	0.093
KFM03A	0.004	0.008	0.002	0.006	0.038	0.014	0.023	0.004	0.021	0.043
KFM04A	0.001	0.006	0.018	0.005	0.051	0.002	0.028	0.031	0.008	0.068
KFM05A	0.001	0.001	0.001	0.000	0.027	0.002	0.002	0.001	0.000	0.031
KFM06A	0.010	0.015	0.001	0.001	0.084	0.020	0.034	0.008	0.002	0.097
KFM07A	0.004	0.000	0.000	0.000	0.025	0.008	0.000	0.000	0.000	0.029
KFM07C	0.000	0.002	0.000	0.000	0.032	0.000	0.017	0.000	0.000	0.034
KFM08A	0.005	0.005	0.000	0.000	0.039	0.008	0.011	0.000	0.000	0.050
KFM08C	0.004	0.006	0.001	0.000	0.014	0.008	0.013	0.002	0.000	0.018
KFM10A	0.000	0.002	0.041	0.009	0.071	0.000	0.012	0.062	0.011	0.146
All bh	0.003	0.006	0.005	0.002	0.044	0.007	0.018	0.011	0.007	0.056

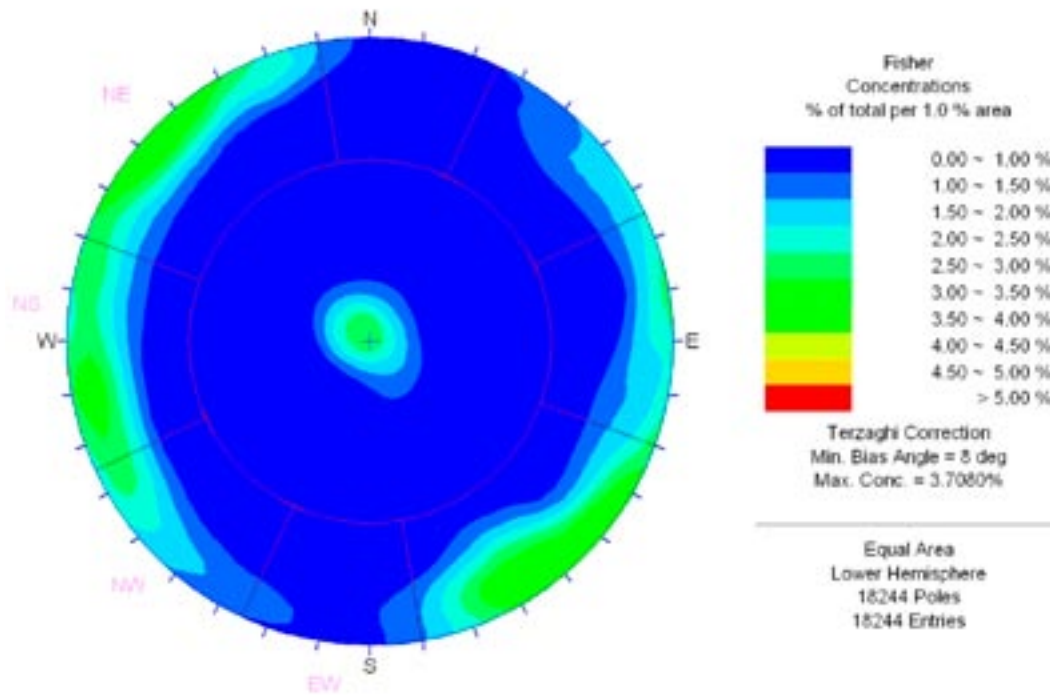


Figure 10-7. Fisher concentration plot for all (open and sealed) fractures in all boreholes and for all FFM fracture domains (i.e. excluding deformation zones). The concentrations are Terzaghi corrected and use an equal area lower hemisphere projection.

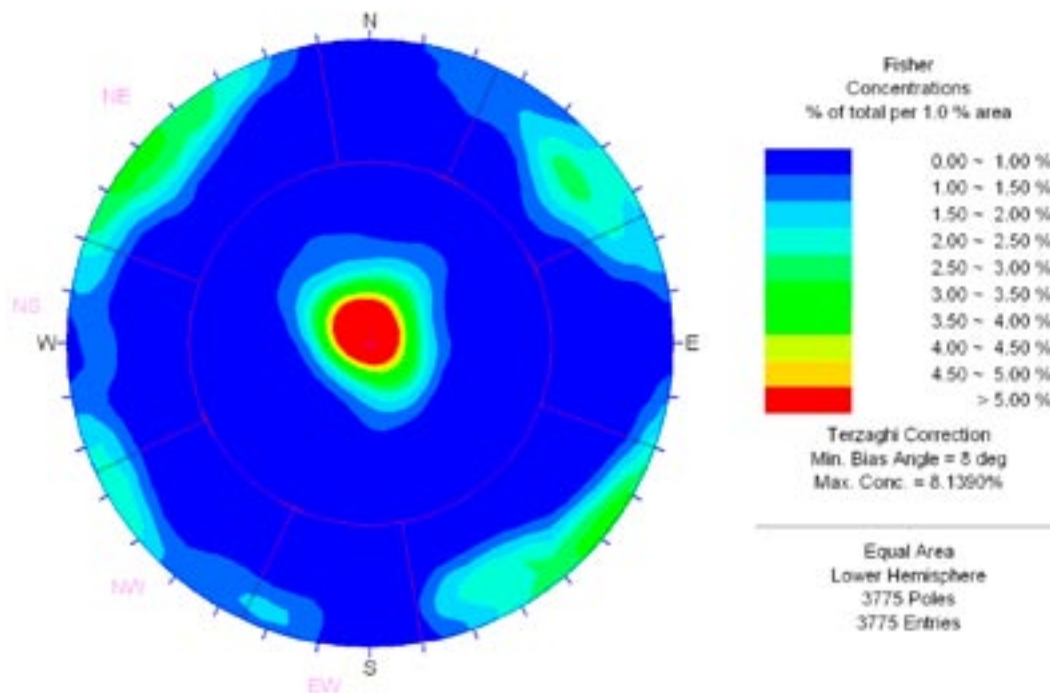


Figure 10-8. Fisher concentration plot for open fractures in all boreholes and for all FFM fracture domains (i.e. excluding deformation zones). The concentrations are Terzaghi corrected and use an equal area lower hemisphere projection.

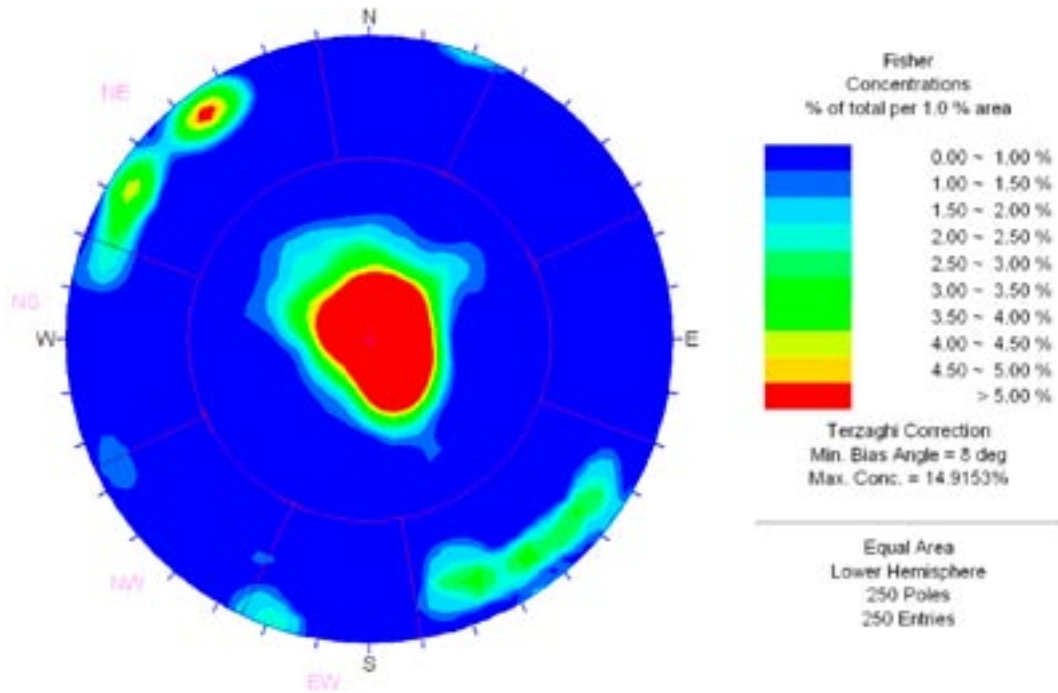


Figure 10-9. Fisher concentration plot for fractures associated with PFL flow-anomalies in all bore-holes and for all FFM fracture domains (i.e. excluding deformation zones). The concentrations are Terzaghi corrected and use an equal area lower hemisphere projection.

Fracture intensity for deformation zones and fracture domains

As part of the geological interpretation every interval of core has been uniquely assigned to either a deformation zone (ZFM) or to one of six fracture domains (FFMs). Using this information it is possible to compute statistics for the fracture intensity for individual FFMs and ZFMs as well as take an ensemble over all ZFM and FFM to contrast the fracturing and associated flow between the deformation zones and background rock (fracture domains). Table 10-6 compares such statistics between the ZFMs taken as a whole and the FFMs. Based on all fractures, the intensity in the FFMs is about one third of that in the ZFMs. For open fractures this reduces to less than one quarter, suggesting that fractures have a higher probability of being active in the vicinity of a deformation zone. Further, considering the PFL flow-anomalies, the intensity of these fractures in the background rock is less than 20% of the intensity in the deformation zones. Still, even for ZFM the proportion of mapped fractures that can be associated with a flowing feature is only about 1.5%.

Table 10-7 gives fracture intensities for all, open and PFL-anomaly fractures for each deformation zone individually. For sub-vertical deformation zones, their names reflect their strike, but the strike is not appended to the names of the sub-horizontal ZFM. The fracture intensities vary considerably between zones, but one obvious feature is the higher values of $P_{10,PFL,corr}$ that tend to correspond to gently dipping ZFM.

Table 10-8 and Table 10-9 compare statistics between the six fracture domains (FFMs). The vast majority of the data, over 5 km of core, is from the candidate domain FFM01 together with several hundred metres from FFM03 and FFM02, while there is only 100–200 m of core for each of FFM04–FFM06. The lowest fracture intensity of both all and open fractures occur in FFM01 and FFM03, with average values of about 0.8 and 1.0 m^{-1} for $P_{10,o,corr}$, respectively.

The fracture intensities in the other fracture domains, including FFM02, are more than 3 times higher. The average intensity of PFL flow-anomalies is 0.0256 m^{-1} for FFM01, or an average true spacing of about 40 m. The equivalent numbers are 0.0774 m^{-1} or 13 m for FFM03, and 0.2772 m^{-1} or 4 m for FFM02. FFM04, FFM04 and FFM06 also have an average flow-anomaly true spacing about 10 m. Hence, from a hydrogeological perspective, FFM01 is the best rock in the area for a repository.

The distribution of fracture intensity for open and PFL flow-anomaly fractures between the sets for FFM01 is studied in Table 10-10. For open fractures, the primary sets are HZ and NE, the secondary sets are NS and NW, and the minor set is EW. However, according to the PFL flow-anomalies, there are only 3 hydraulically active sets in FFM01: HZ, NS and NE. The fracture intensities given confirm the stereonet shown in Figure 10-9 with a dominant HZ and minor NE and NNE sets (showing up as NS for the F 1.2 Geo-DFN). The true spacing for flowing features in these two sub-vertical sets is about 300 m though.

Figure 10-10 to Figure 10-12 explore the sets associated with open fractures for each of the fracture domains in the candidate area: FFM01 to FFM03, respectively. FFM01 is dominated by the HZ set, but the NE, a NNE, and the NW set also present. FFM02 is even more dominated by the HZ set as conceptualised in Section 7, but also has some NE set fractures. FFM03 has more diffuse HZ set with some tendency towards fracture that dip gently to the SE, and has sub-vertical fractures in the NE and NW sets.

Table 10-6. Summary of Terzaghi corrected linear fracture intensities of all, open and PFL-anomalies within deformations zones (ZFM = regional deformation zones, DZ = single-hole interpreted deformations zones) and the background fractured rock (FFM).

Borehole	$P_{10,a,corr}$ [1/m]		$P_{10,o,corr}$ [1/m]		$P_{10,PFL,corr}$ [1/m]	
	ZFM/DZ	FFM	ZFM/DZ	FFM	ZFM/DZ	FFM
KFM01A	12.82	3.12	4.25	1.32	0.076	0.078
KFM01D	17.11	3.74	4.10	0.81	0.000	0.067
KFM02A	8.58	3.07	2.29	0.33	0.524	0.055
KFM03A	8.60	5.02	2.30	0.71	0.552	0.062
KFM04A	20.02	8.69	6.47	1.37	0.389	0.039
KFM05A	13.09	5.64	2.28	0.95	0.055	0.031
KFM06A	13.43	5.75	2.43	1.00	0.293	0.093
KFM07A	14.86	4.79	3.18	0.58	0.117	0.007
KFM07C	22.09	8.17	4.00	1.05	0.014	0.064
KFM08A	16.41	8.55	2.63	0.96	0.064	0.071
KFM08C	21.49	7.70	4.30	0.73	0.156	0.008
KFM10A	21.62	10.39	7.62	2.16	0.624	0.081
All bh	15.49	5.84	3.62	0.94	0.253	0.053

Table 10-7. Summary of various linear fracture intensities of all, open and PFL-anomalies within each deformation zone.

Name	Length [m]	P _{10,a} [1/m]	P _{10,a,corr} [1/m]	P _{10,o} [1/m]	P _{10,o,corr} [1/m]	P _{10,PFL} [1/m]	P _{10,PFL,corr} [1/m]
ZFMA2	107.73	10.52	20.07	5.24	7.70	0.32	0.62
ZFMA3	37.00	6.08	10.54	1.95	3.16	0.62	1.10
ZFMA4	43.00	4.21	6.73	1.88	2.78	0.47	0.71
ZFMA7	7.00	6.86	17.63	0.43	0.53	0.43	0.52
ZFMB1	8.00	5.75	10.64	1.13	1.36	0.25	0.41
ZFMB4	12.00	4.75	10.85	1.08	1.78	0.08	0.13
ZFMB7	20.00	11.20	19.92	1.70	2.78	0.30	0.64
ZFMB8	34.27	6.92	13.49	1.87	3.24	0.03	0.07
ZFMF1	44.00	7.16	11.35	2.02	2.94	0.50	0.64
ZFMENE0060A	20.00	8.35	16.94	1.50	2.31	0.35	0.60
ZFMENE0060B	83.00	5.94	10.84	1.12	1.64	0.31	0.39
ZFMENE0061	52.00	6.00	17.33	1.52	4.46	0.00	0.00
ZFMNNW0100	39.50	10.23	17.01	1.49	2.83	0.00	0.00
ZFMENE0103	24.00	6.58	14.52	0.42	0.99	0.00	0.00
ZFMWNNW0123	89.14	11.91	21.65	4.81	7.66	0.36	0.68
ZFMENE0159A	5.00	11.80	22.97	3.00	5.05	0.00	0.00
ZFMENE0401A	35.50	6.82	15.24	0.76	1.46	0.06	0.10
ZFMENE0401B	26.00	8.54	16.61	1.73	2.99	0.00	0.00
ZFMNNW0404	38.50	6.65	13.82	1.48	2.27	0.03	0.03
ZFMNNE0725	35.00	9.20	18.72	2.37	4.09	0.09	0.18
ZFM866	12.00	7.42	10.62	5.58	7.83	1.17	1.68
ZFMENE1061A	75.49	9.34	19.78	2.42	4.52	0.08	0.13
ZFMENE1061B	1.50	14.00	26.00	2.67	5.53	0.00	0.00
ZFMNE1188	130.00	8.52	19.21	3.06	5.92	0.09	0.21
ZFM1189	70.00	2.84	5.68	0.37	0.90	0.14	0.32
ZFMENE1192	44.00	4.80	13.92	2.41	5.94	0.05	0.17
ZFMNW1200	66.00	8.18	18.03	3.56	6.91	0.53	0.89
ZFM1203	42.88	8.61	14.84	3.50	4.83	0.51	0.61
ZFMNNW1204	17.00	7.06	15.37	1.41	2.24	0.12	0.24
ZFMENE1208A	40.00	6.70	14.94	1.18	2.36	0.00	0.00
ZFMENE1208B	37.00	6.11	14.41	0.95	2.08	0.00	0.00
ZFMWNNW2225	32.00	11.31	22.83	2.06	4.18	0.03	0.07
ZFMENE2248	68.00	7.38	17.42	0.87	1.56	0.00	0.00
ZFMENE2254	45.00	5.49	12.14	1.20	2.26	0.00	0.00
ZFMNNE2255	5.00	10.60	21.18	3.20	6.01	0.20	0.66
ZFMNNE2273	27.00	4.19	6.87	1.15	1.60	0.00	0.00
ZFMNNE2280	40.00	5.45	11.32	0.45	0.81	0.00	0.00
ZFMENE2282	41.00	4.68	10.50	1.20	2.41	0.00	0.00
ZFMNNE2312	123.00	10.64	21.72	2.21	4.12	0.11	0.16
ZFMENE2320	90.00	7.70	21.64	1.49	3.82	0.00	0.00
ZFMENE2383	56.00	5.73	11.58	0.71	1.32	0.00	0.00
ZFMENE2403	8.70	9.77	26.15	1.72	2.70	0.00	0.00
Possible DZ	309.50	5.91	12.10	1.52	2.72	0.08	0.11

Table 10-8. Summary of borehole lengths and corrected linear fracture intensities of all fractures within each fracture domain excluding deformation zones.

Borehole	Length [m]						P _{10,a,corr} [1/m]					
	FFM01	FFM02	FFM03	FFM04	FFM05	FFM06	FFM01	FFM02	FFM03	FFM04	FFM05	FFM06
KFM01A	693	100	0	0	0	0	2.14	9.84	–	–	–	–
KFM01D	558	91	0	0	0	0	3.23	6.86	–	–	–	–
KFM02A	413	0	209	0	0	0	2.80	–	3.62	–	–	–
KFM03A	0	0	819	0	0	0	–	–	5.02	–	–	–
KFM04A	475	0	0	155	0	0	6.56	–	–	15.21	–	–
KFM05A	580	123	0	0	0	0	4.88	9.22	–	–	–	–
KFM06A	435	26	0	0	0	129	5.18	6.70	–	–	–	7.50
KFM07A	594	6	0	0	50	0	4.20	13.84	–	–	10.74	–
KFM07C	286	20	0	0	0	0	8.12	8.85	–	–	–	–
KFM08A	537	0	0	0	72	0	8.36	–	–	–	9.98	–
KFM08C	575	0	0	0	0	81	7.51	–	–	–	–	9.06
KFM10A	10	0	305	0	0	0	15.12	–	10.24	–	–	–
All bh	5,156	366	1,334	155	122	210	5.12	8.68	5.99	15.21	10.29	8.10

Table 10-9. Summary of Terzaghi corrected linear fracture intensities of open fractures and PFL-anomalies within each fracture domain excluding deformation zones.

Borehole	P _{10,o,corr} [1/m]						P _{10,PFL,corr} [1/m]					
	FFM01	FFM02	FFM03	FFM04	FFM05	FFM06	FFM01	FFM02	FFM03	FFM04	FFM05	FFM06
KFM01A	0.71	5.50	–	–	–	–	0.019	0.481	–	–	–	–
KFM01D	0.57	2.28	–	–	–	–	0.024	0.329	–	–	–	–
KFM02A	0.34	–	0.31	–	–	–	0.036	–	0.091	–	–	–
KFM03A	–	–	0.71	–	–	–	–	–	0.062	–	–	–
KFM04A	0.70	–	–	3.43	–	–	0.002	–	–	0.152	–	–
KFM05A	0.67	2.24	–	–	–	–	0.002	0.165	–	–	–	–
KFM06A	0.91	2.87	–	–	–	0.91	0.090	0.604	–	–	–	0.000
KFM07A	0.51	2.71	–	–	1.15	–	0.002	0.000	–	–	0.067	–
KFM07C	1.00	1.79	–	–	–	–	0.049	0.268	–	–	–	–
KFM08A	1.05	–	–	–	0.30	–	0.081	–	–	–	0.000	–
KFM08C	0.74	–	–	–	–	0.67	0.009	–	–	–	–	0.000
KFM10A	5.21	–	2.06	–	–	–	0.000	–	0.083	–	–	–
All bh	0.72	3.17	0.95	3.43	0.65	0.82	0.029	0.326	0.072	0.152	0.027	0.000

Table 10-10. Summary of Terzaghi corrected linear fracture intensities of open fractures and PFL-anomalies within fracture domain FFM01 excluding deformation zones and divided into fracture sets.

Borehole	$P_{10,o,corr}$ [1/m]					$P_{10,PFL,corr}$ [1/m]				
	Set					Set				
	NS	NE	NW	EW	HZ	NS	NE	NW	EW	HZ
KFM01A	0.113	0.234	0.047	0.015	0.302	0.000	0.007	0.000	0.000	0.012
KFM01D	0.103	0.018	0.181	0.017	0.255	0.000	0.000	0.000	0.000	0.024
KFM02A	0.099	0.093	0.104	0.005	0.040	0.000	0.016	0.000	0.000	0.021
KFM03A	–	–	–	–	–	–	–	–	–	–
KFM04A	0.109	0.094	0.197	0.022	0.273	0.000	0.000	0.000	0.000	0.002
KFM05A	0.117	0.237	0.135	0.027	0.155	0.000	0.000	0.000	0.000	0.002
KFM06A	0.091	0.358	0.073	0.083	0.309	0.012	0.020	0.000	0.000	0.058
KFM07A	0.065	0.260	0.054	0.048	0.081	0.000	0.000	0.000	0.000	0.002
KFM07C	0.063	0.591	0.047	0.063	0.233	0.000	0.025	0.000	0.000	0.025
KFM08A	0.151	0.302	0.154	0.118	0.325	0.008	0.012	0.000	0.000	0.061
KFM08C	0.105	0.217	0.074	0.143	0.205	0.002	0.000	0.000	0.000	0.006
KFM10A	0.701	0.575	0.522	0.595	2.818	0.000	0.000	0.000	0.000	0.000
All bh	0.105	0.226	0.108	0.055	0.224	0.002	0.007	0.000	0.000	0.020

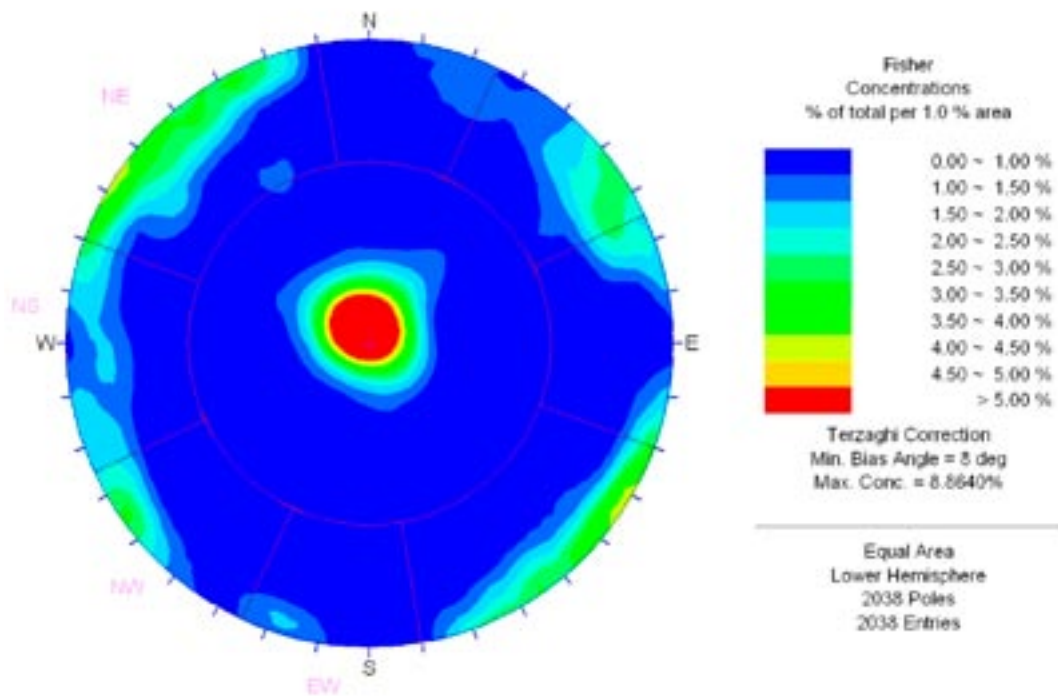


Figure 10-10. Fisher concentration plot for open fractures within FFM01 and any borehole. The concentrations are Terzaghi corrected and use an equal area lower hemisphere projection.

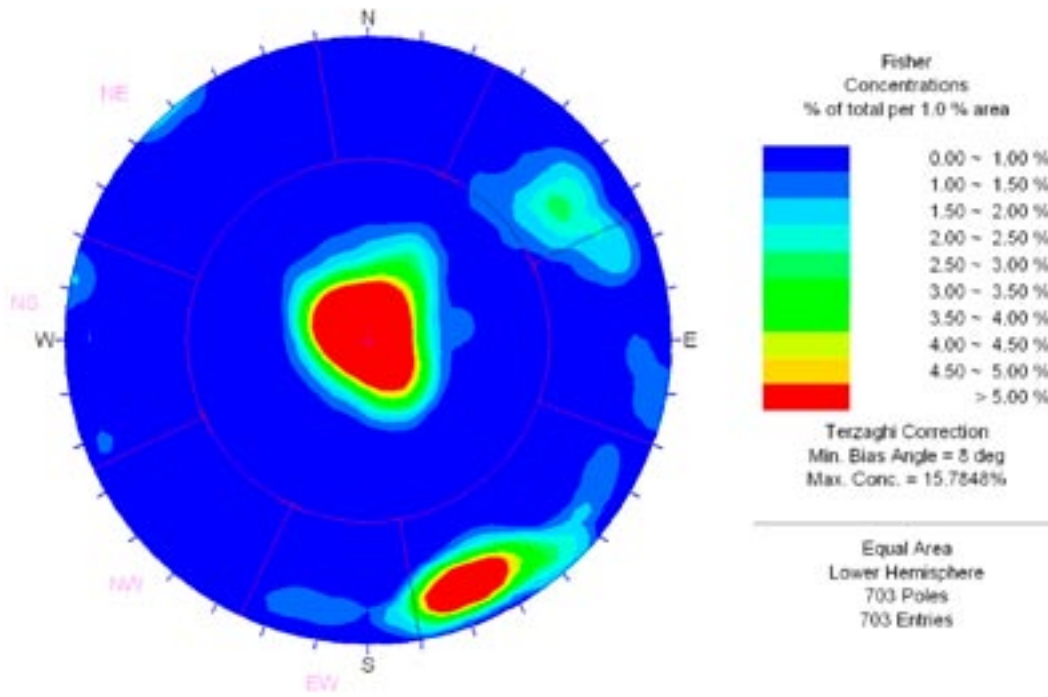


Figure 10-11. Fisher concentration plot for open fractures within FFM02 and any borehole. The concentrations are Terzaghi corrected and use an equal area lower hemisphere projection.

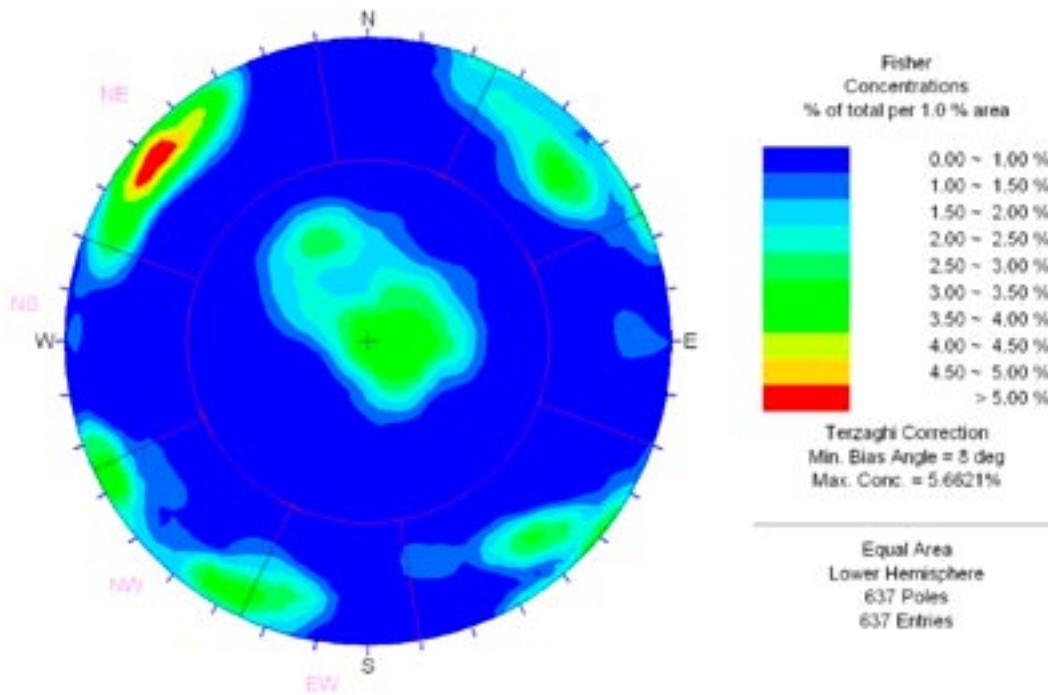


Figure 10-12. Fisher concentration plot for open fractures within FFM03 and any borehole. The concentrations are Terzaghi corrected and use an equal area lower hemisphere projection.

Fracture intensity by depth

One key hypothesis made in the F 1.2 Hydro-DFN was a strong depth dependency. With the more abundant data available for F 2.2 it is interesting to examine the support for such an assumption in more detail. Table 10-11 and Table 10-12 present the variation with depth of the Terzaghi corrected fracture intensities for open and PFL flow-anomaly related fractures in all FFM, respectively. Values are given for each 100 m of depth from near surface to 1 km down. Broadly, the open fracture intensity is about 2 m⁻¹ in the top 200 m, then drops to about 1.2 m⁻¹ down to 400 m, and falls again to about 0.6 m⁻¹ below that. The effect on the frequency of flowing features is far more marked with very sharp fall off in the top 400–500 m. The corrected intensity of flowing features at the surface is high at about 0.4 m⁻¹ in the top 100 m, and then proceeds to fall by about a half in each 100 m interval until 500 m depth, below which it averages about 0.02 m⁻¹. Hence, the F 2.2 fracture and PFL hydraulic data also indicates a strong depth variation. It is suggested that it would be appropriate to develop the conceptual model for fracturing in flow in terms of the three depth zones: the top 200 m, 200–400 m, and below 400 m depth, recognising there is probably an uncertainty in the position of these zonations of about 50 m. This uncertainty reflects the natural variations in the depths at which the fracture intensity distribution changes from borehole to borehole.

Considering the transition at an elevation of –400 m, Table 10-13 and Table 10-14 summarise the change in fracture intensity for open and PFL flow-anomaly fractures in FFM01 for above and below –400 m, respectively. For the top 400 m of FFM01, the HZ and NE sets dominate the open fractures, followed by the NS set and then the NW and EW sets. However, for the flow-anomalies, only there are 3 sets: HZ, NS and NE with HZ very dominant. Below –400 m in FFM01, the only PFL flow-anomaly fractures occur in the HZ and NE sets with an average true spacing of about 200 m. Hence, below –400 m the flowing fractures in FFM01 are almost exclusively restricted to deformation zones, symptomatic of a very sparse and poorly connected network of fracture that does not reach a threshold for percolation of water into the deep rock.

Table 10-11. Summary of Terzaghi corrected linear fracture intensities of open fractures within the fracture domains (FFMs) excluding deformation zones and divided into depth below sea level in 100 m intervals.

Borehole	P _{10,0,corr} [1/m]									
	0	100	200	300	400	500	600	700	800	900
	100	200	300	400	500	600	700	800	900	1,000
KFM01A	2.47	5.46	3.16	0.96	0.75	0.25	0.55	0.09	0.41	0.02
KFM01D	1.84	1.73	0.68	0.67	0.44	0.36	0.41	–	–	–
KFM02A	1.49	0.37	0.22	0.20	0.94	0.47	0.66	0.22	0.00	0.16
KFM03A	1.88	0.79	0.26	0.62	0.34	1.26	0.80	0.49	0.46	1.29
KFM04A	2.78	6.60	3.57	2.83	0.57	0.84	0.60	0.89	–	–
KFM05A	3.10	2.16	0.56	0.68	0.37	1.84	0.65	0.17	0.94	–
KFM06A	3.63	1.56	0.51	0.91	0.67	0.76	1.36	0.80	1.51	–
KFM07A	2.76	0.99	0.97	0.55	0.43	0.05	0.46	1.17	–	–
KFM07C	0.00	0.75	0.94	1.41	1.47	–	–	–	–	–
KFM08A	1.12	1.64	2.00	1.19	0.46	0.38	0.38	1.95	–	–
KFM08C	0.82	1.06	0.79	0.79	0.37	0.60	0.55	0.89	–	–
KFM10A	–	2.04	2.00	3.29	–	–	–	–	–	–
All bh	2.00	1.92	1.22	0.98	0.59	0.65	0.64	0.56	0.35	0.50

Table 10-12. Summary of Terzaghi corrected linear fracture intensities of PFL-anomalies within the fracture domains (FFMs) excluding deformation zones and divided into to depth below sea level in 100 m intervals.

Borehole	P _{10,PFL,corr} [1/m]									
	0	100	200	300	400	500	600	700	800	900
	100	200	300	400	500	600	700	800	900	1,000
KFM01A	0.000	0.479	0.098	0.077	0.000	0.000	0.000	0.000	0.000	0.000
KFM01D	0.275	0.189	0.065	0.023	0.010	0.000	0.000	–	–	–
KFM02A	0.343	0.088	0.238	0.000	0.447	0.000	0.000	0.000	0.000	0.000
KFM03A	0.195	0.211	0.000	0.067	0.050	0.032	0.000	0.000	0.000	0.211
KFM04A	1.388	0.671	0.104	0.000	0.009	0.000	0.000	0.000	–	–
KFM05A	0.732	0.126	0.010	0.000	0.000	0.000	0.000	0.000	0.000	–
KFM06A	0.691	0.580	0.121	0.037	0.000	0.000	0.000	0.000	0.000	–
KFM07A	0.000	0.000	0.012	0.000	0.000	0.000	0.000	0.101	–	–
KFM07C	0.000	0.114	0.080	0.000	0.000	–	–	–	–	–
KFM08A	0.335	0.215	0.033	0.090	0.000	0.000	0.000	0.000	–	–
KFM08C	0.083	0.027	0.010	0.000	0.000	0.000	0.000	0.000	–	–
KFM10A	–	0.042	0.137	0.000	–	–	–	–	–	–
All bh	0.343	0.195	0.062	0.029	0.025	0.003	0.000	0.005	0.000	0.072

Table 10-13. Summary of Terzaghi corrected linear fracture intensities by set of open fractures and PFL-anomalies within fracture domain FFM01 above an elevation of –400 m and excluding deformation zones.

Borehole	P _{10,o,corr} [1/m]					P _{10,PFL,corr} [1/m]				
	NS	NE	NW	EW	HZ	NS	NE	NW	EW	HZ
KFM01A	0.195	0.790	0.119	0.066	0.824	0.000	0.033	0.000	0.000	0.053
KFM01D	0.116	0.004	0.185	0.010	0.404	0.000	0.000	0.000	0.000	0.040
KFM02A	–	–	–	–	–	–	–	–	–	–
KFM03A	–	–	–	–	–	–	–	–	–	–
KFM04A	–	–	–	–	–	–	–	–	–	–
KFM05A	0.097	0.177	0.154	0.055	0.120	0.000	0.000	0.000	0.000	0.006
KFM06A	0.071	0.291	0.085	0.053	0.508	0.025	0.042	0.000	0.000	0.123
KFM07A	0.107	0.409	0.051	0.086	0.148	0.000	0.000	0.000	0.000	0.005
KFM07C	0.020	0.443	0.067	0.037	0.238	0.000	0.035	0.000	0.000	0.035
KFM08A	0.208	0.473	0.188	0.166	0.466	0.014	0.021	0.000	0.000	0.107
KFM08C	0.135	0.281	0.106	0.151	0.277	0.006	0.000	0.000	0.000	0.017
KFM10A	0.707	0.580	0.526	0.600	2.841	0.000	0.000	0.000	0.000	0.000
All bh	0.125	0.339	0.126	0.083	0.374	0.006	0.015	0.000	0.000	0.049

Table 10-14. Summary of Terzaghi corrected linear fracture intensities by set of open fractures and PFL-anomalies within fracture domain FFM01 below an elevation of –400 m and excluding deformation zones.

Borehole	P _{10,o,corr} [1/m]					P _{10,PFL,corr} [1/m]				
	NS	NE	NW	EW	HZ	NS	NE	NW	EW	HZ
KFM01A	0.089	0.072	0.026	0.000	0.150	0.000	0.000	0.000	0.000	0.000
KFM01D	0.087	0.034	0.178	0.026	0.080	0.000	0.000	0.000	0.000	0.006
KFM02A	0.099	0.094	0.104	0.005	0.040	0.000	0.016	0.000	0.000	0.021
KFM03A	–	–	–	–	–	–	–	–	–	–
KFM04A	0.109	0.094	0.198	0.022	0.273	0.000	0.000	0.000	0.000	0.002
KFM05A	0.127	0.270	0.127	0.013	0.174	0.000	0.000	0.000	0.000	0.000
KFM06A	0.110	0.426	0.062	0.112	0.134	0.000	0.000	0.000	0.000	0.000
KFM07A	0.030	0.133	0.057	0.016	0.024	0.000	0.000	0.000	0.000	0.000
KFM07C	0.168	0.953	0.000	0.128	0.222	0.000	0.000	0.000	0.000	0.000
KFM08A	0.077	0.078	0.108	0.055	0.142	0.000	0.000	0.000	0.000	0.000
KFM08C	0.088	0.180	0.056	0.138	0.163	0.000	0.000	0.000	0.000	0.000
KFM10A	–	–	–	–	–	–	–	–	–	–
All bh	0.094	0.163	0.098	0.039	0.141	0.000	0.002	0.000	0.000	0.003

10.4 Analysis of hydrogeological data

Extra analysis is performed in this section to help guide the development of the hydrogeological fracture model. Aspects considered are the correlation between the intensities of flowing features and the intensity of open and all fractures; the consistency in fracture transmissivity measured using the Posiva flow log (PFL-f) and the Pipe-string system double packer tests; preferences in the orientation of flowing features and resulting flow anisotropy; and overall summary of the fracture transmissivity statistic for each fracture domain, FFM.

10.4.1 Correlation of geological and hydrogeological fracturing

One question of interest is whether the fractures considered to be open or associated with flow are a sub-set of all fractures that have been mapped, or distributed in quite a different way. This is difficult to answer, but one simple guide is check whether there is a correlation in the intensity of the various categories for fractures; all, open, PFL flow-anomaly. Figure 10-13 and Figure 10-14 present plots of the Terzaghi corrected fracture intensities for P_{10,a,corr} against P_{10,o,corr} and P_{10,o,corr} against P_{10,PFL,corr}. The points shown represent the overall intensities in each cored drilled borehole; one point per borehole. The intensities are only calculated in the fracture domains, (i.e. excluding deformation zones) FFM01–03, which are the ones associated with the candidate area. Broadly, these plots suggest a correlation between the intensity of the different categories of fractures, though there is considerable variation. Therefore, where high fracture intensities occur, there is likely to be an increased frequency of flow. It may be inferred that fracture connectivity is a large factor in determining where flow occurs, which tends to be higher where fracture intensity is greatest. Since FFM01 is the primary fracture domain of interest, similar plots are plotted for the rock above and below an elevation of –400 m in Figure 10-15 and Figure 10-16. Again, there is reasonable correlation between all and open fracture at both depths. Above –400 m there is evidence of a correlation between open and PFL flow-anomaly intensity. Below –400 m the PFL flow-anomaly intensity is zero. These observations are consistent with a concept that flow and connectivity are controlled by fracture intensity above a percolation threshold, but there is a sharp drop off in flow at fracture intensities below the percolation threshold. The percolation threshold will be governed by a number of geometrical characteristics of the fracturing, mainly size distribution, and orientation to a lesser extent.

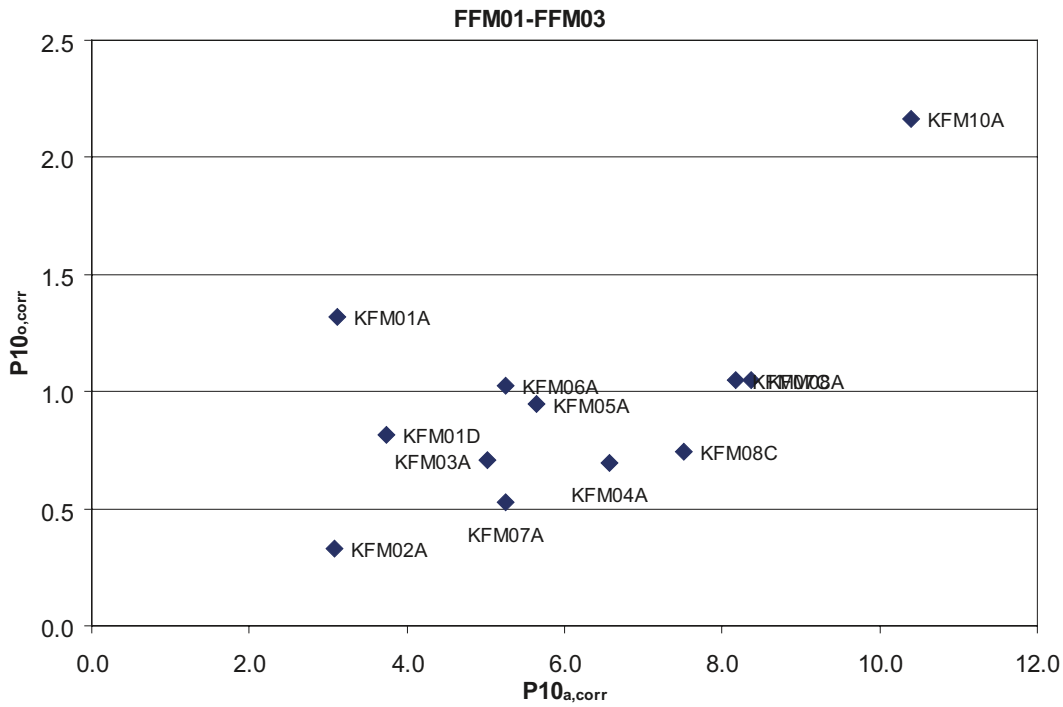


Figure 10-13. Plot comparing Terzaghi corrected fracture intensity for all (sealed and open) fractures against corrected fracture intensity for only open fractures for fracture domains FFM01–FFM03 in each of the F 2.2 core-drilled boreholes.

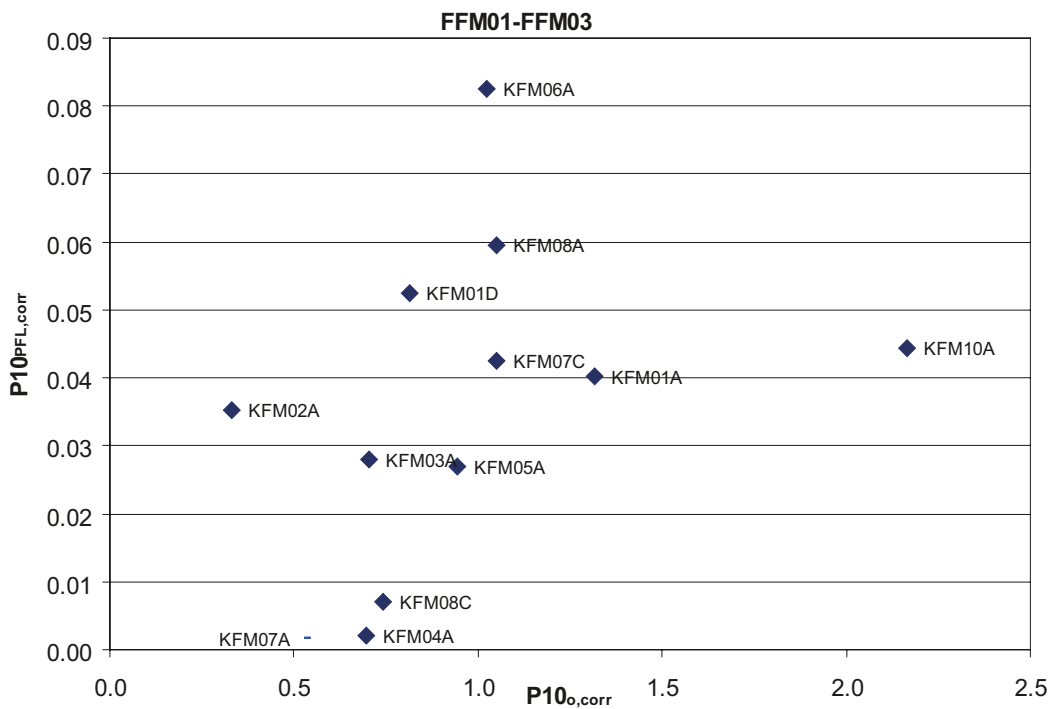


Figure 10-14. Plot comparing Terzaghi corrected fracture intensity for open fractures against corrected fracture intensity for only fractures associated with PFL flow-anomalies for fracture domains FFM01–FFM03 in each of the F 2.2 core-drilled boreholes.

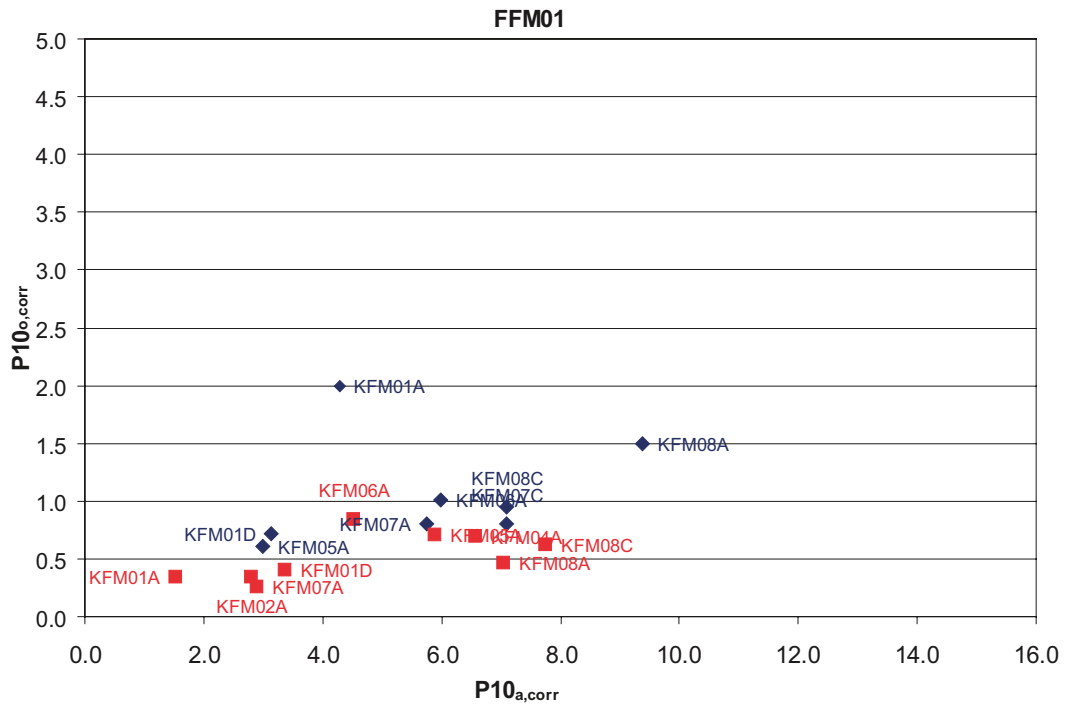


Figure 10-15. Plot comparing Terzaghi corrected fracture intensity for all (sealed and open) fractures against corrected fracture intensity for only open fractures above -400 m (blue diamonds) and below -400 m (red squares) in fracture domain FFM01 and each of the F 2.2 core-drilled borehole.

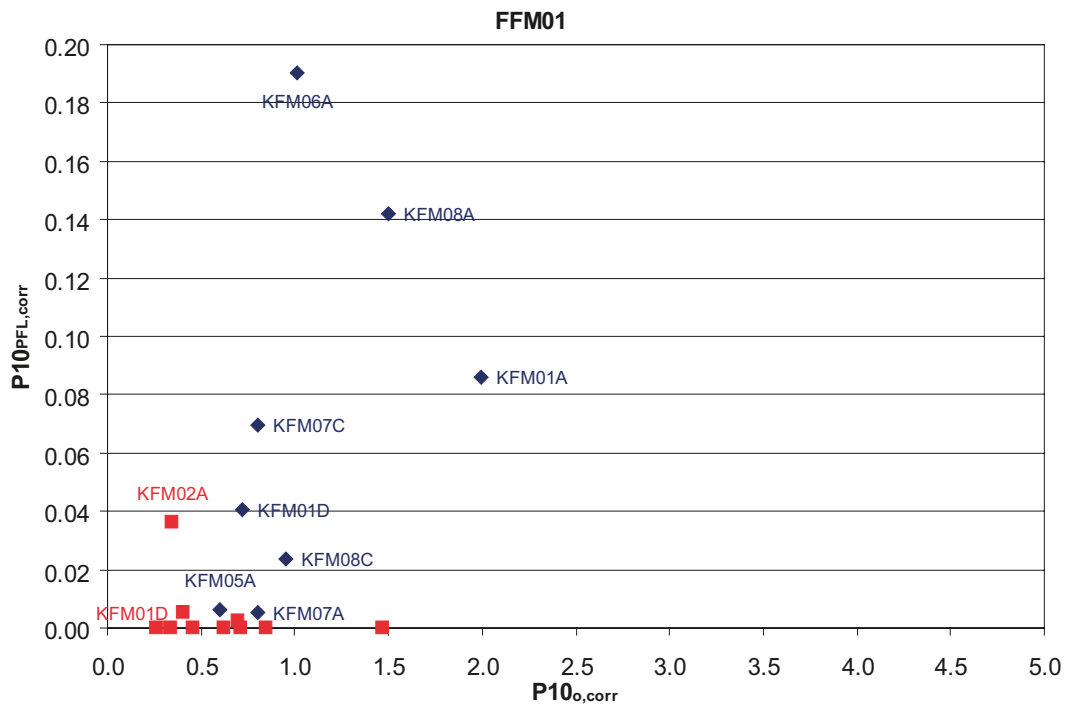


Figure 10-16. Plot comparing Terzaghi corrected fracture intensity for open fractures against corrected fracture intensity for fractures associated with PFL flow-anomalies above -400 m (blue diamonds) and below -400 m (red squares) in fracture domain FFM01 and each of the F 2.2 core-drilled borehole.

10.4.2 Orientation and statistics of flowing features

Section 11.3 considered the validity of the F 1.2 fracture sets for the updated geological fracture data. Here, we considered if these sets also useful in interpreting the orientations of flowing features and any anisotropy in flow. Figure 10-17, Figure 10-18 and Figure 10-19 show stereographic pole plots of the orientations of each of the fractures associated with PFL flow-anomalies in fracture domains FFM01, FFM02, and FFM03, respectively. For FFM01, the flow is strongly dominated by the HZ set, with a small handful of features with strike NE or NNE. This is also true of FFM02. In both cases, the highest transmissivities are all in the HZ set. The orientation of the gently dipping fractures has a NNE component within the HZ set. Hence, flow is strongly anisotropic in FFM01 and FFM02. For FFM03, flow is more dispersed in terms of orientation, or more isotropic. Although the HZ set still dominates, it is less concentrated at the centre of the stereonet, and the NW, NE and even EW sets appear.

In order to identify any depth dependence, Figure 10-20 and Figure 10-21 show stereonet for FFM01–FFM03 for above and below -400 m elevation. The interesting thing here is that even with FFM03 included, flowing features are restricted to the HZ and NE sets below -400 m. Therefore, flow is strongly anisotropic for much of the rock influencing the hydrogeology of the site even many kilometres away within the tectonic lens.

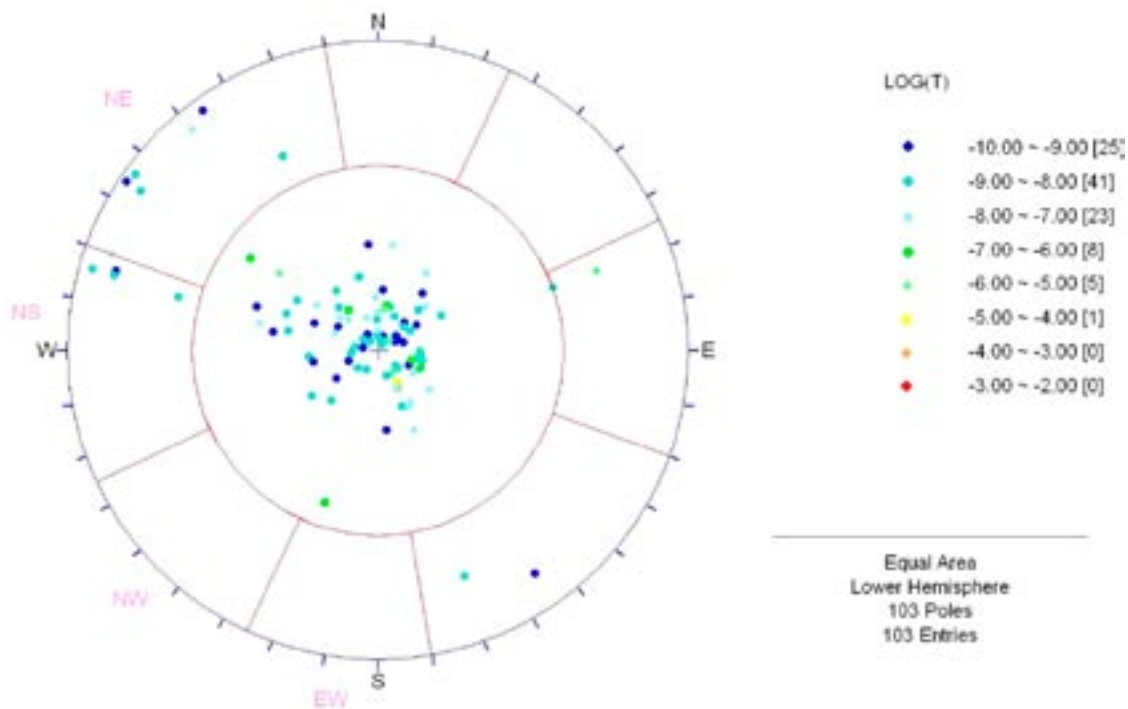


Figure 10-17. Pole plot for PFL flow-anomaly fractures within fracture domain FFM01 and any borehole. The poles are coloured by $\text{Log}_{10}(\text{transmissivity})$ and use an equal area lower hemisphere projection.

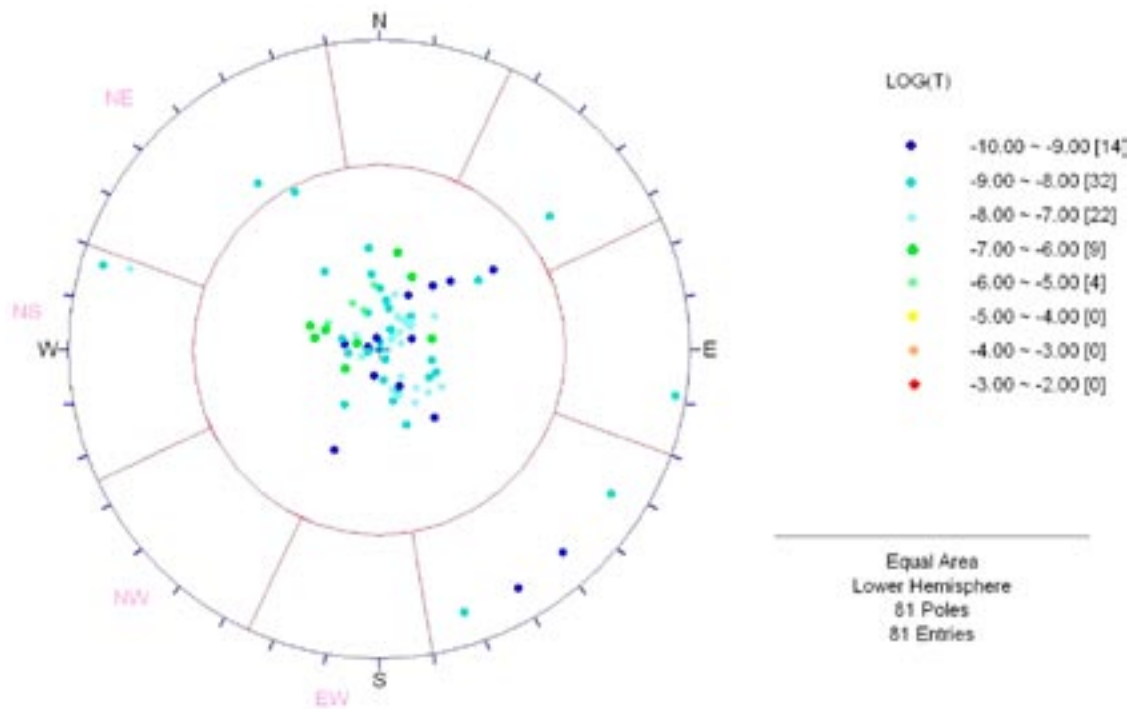


Figure 10-18. Pole plot for PFL flow-anomaly fractures within fracture domain FFM02 and any borehole. The poles are coloured by $\text{Log}_{10}(\text{transmissivity})$ and use an equal area lower hemisphere projection.

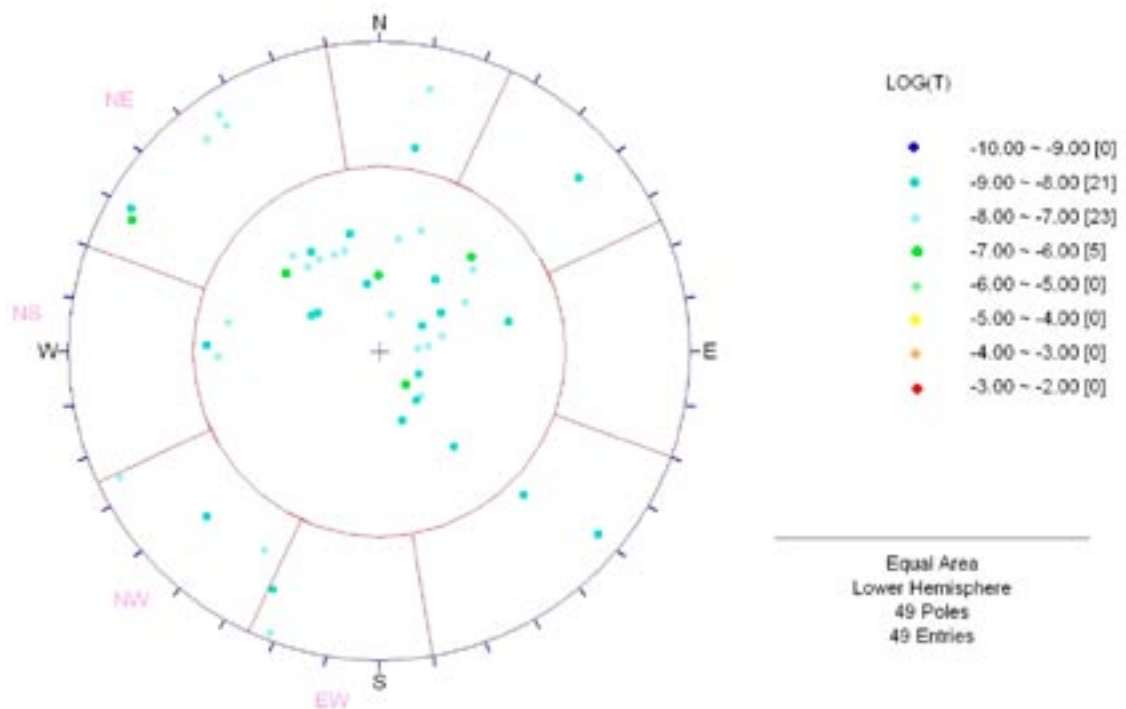


Figure 10-19. Pole plot for PFL flow-anomaly fractures within fracture domain FFM03 and any borehole. The poles are coloured by $\text{Log}_{10}(\text{transmissivity})$ and use an equal area lower hemisphere projection.

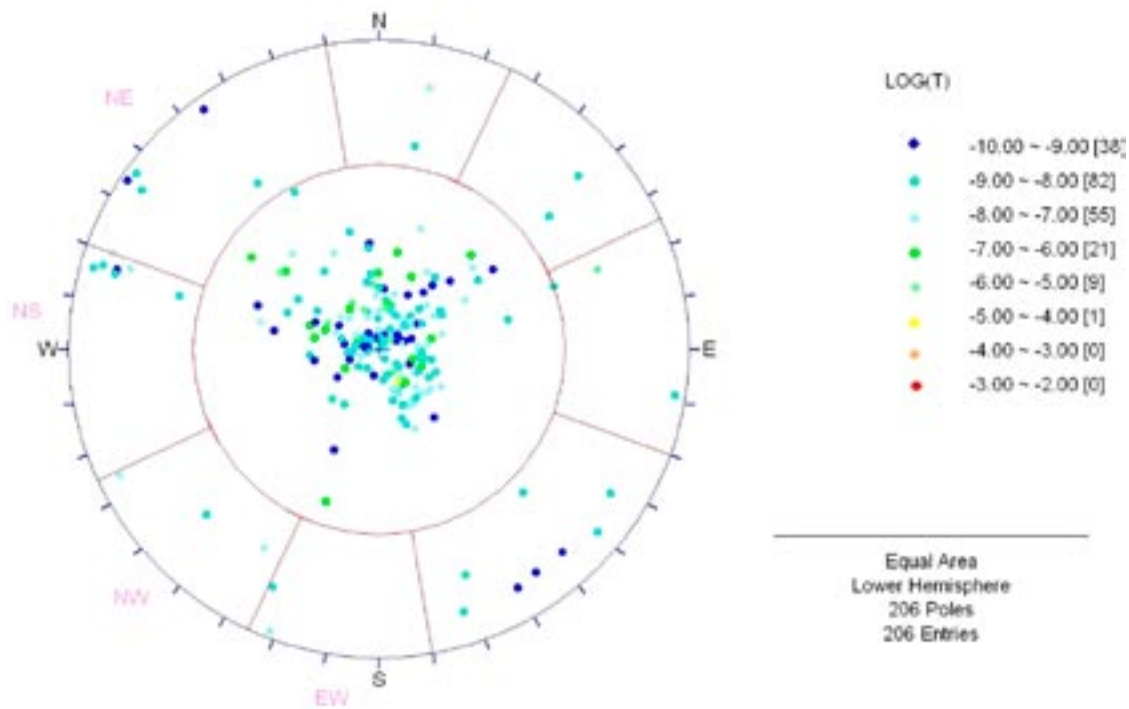


Figure 10-20. Pole plot for PFL flow-anomaly fractures within fracture domains FFM01–FFM03 above an elevation of -400 m and any borehole. The poles are coloured by $\text{Log}_{10}(\text{transmissivity})$ and use an equal area lower hemisphere projection.

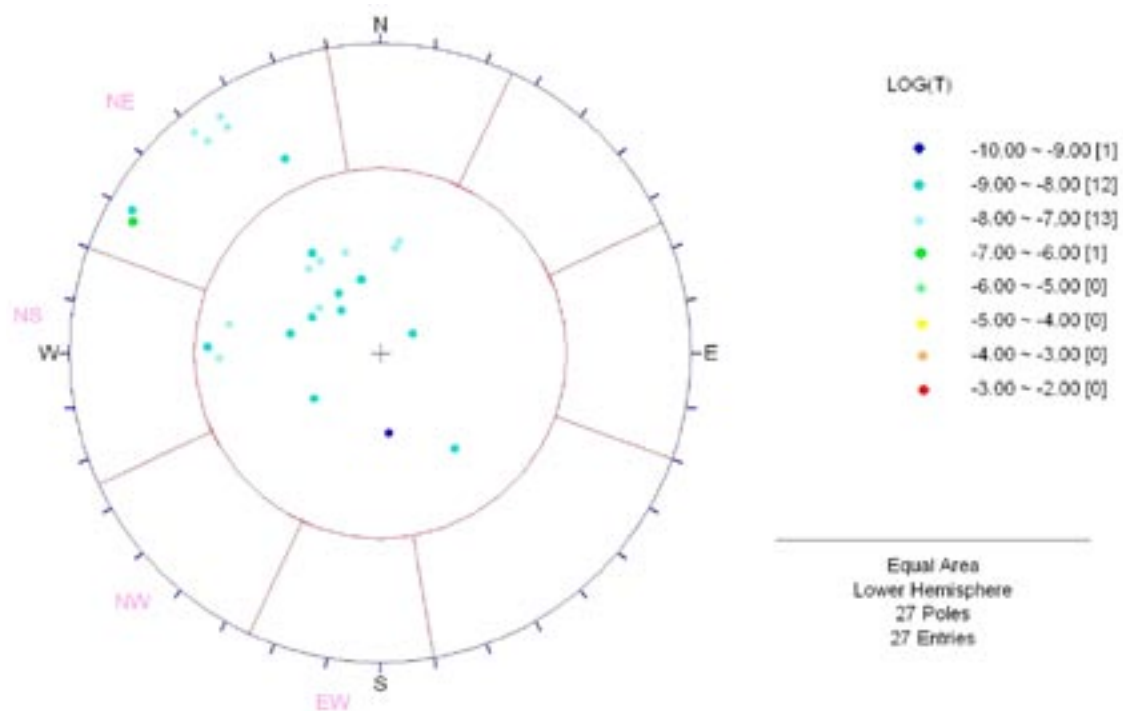


Figure 10-21. Pole plot for PFL flow-anomaly fractures within fracture domains FFM01–FFM03 below an elevation of -400 m and any borehole. The poles are coloured by $\text{Log}_{10}(\text{transmissivity})$ and use an equal area lower hemisphere projection.

A summary of statistics for PFL flow-anomalies for each fracture domain FFM01–06 is given in Table 10-15 to Table 10-20. Rough estimates of the bulk hydraulic conductivity taken over the whole volume of rock for each FFM gives values of around 10^{-9} to 10^{-8} m/s, but of course this is not evenly distributed, being much higher in the upper rock.

Table 10-15. Summary of PFL flow-anomaly statistics for fracture domain FFM01. T denotes transmissivity, and ξ is a sum over all flow-anomalies. The P_{10} values are length weighted mean values.

Borehole	Σ Length	No. PFL	$P_{10,PFL}$	$P_{10,PFL,corr}$	Σ T-PFL	Max T	Min T
KFM01A	693.49	9	0.013	0.019	$5.47 \cdot 10^{-9}$	$2.19 \cdot 10^{-9}$	$2.67 \cdot 10^{-10}$
KFM01D	557.62	11	0.020	0.024	$5.01 \cdot 10^{-7}$	$1.83 \cdot 10^{-7}$	$1.30 \cdot 10^{-9}$
KFM02A	413.36	10	0.024	0.036	$1.90 \cdot 10^{-7}$	$8.89 \cdot 10^{-8}$	$6.16 \cdot 10^{-10}$
KFM03A	0.00	0	0.000	0.000	0.00	0.00	0.00
KFM04A	475.07	1	0.002	0.002	$1.41 \cdot 10^{-9}$	$1.41 \cdot 10^{-9}$	$1.41 \cdot 10^{-9}$
KFM05A	580.12	1	0.002	0.002	$1.86 \cdot 10^{-8}$	$1.86 \cdot 10^{-8}$	$1.86 \cdot 10^{-8}$
KFM06A	435.00	26	0.060	0.090	$1.42 \cdot 10^{-5}$	$9.43 \cdot 10^{-6}$	$3.02 \cdot 10^{-10}$
KFM07A	594.00	1	0.002	0.002	$9.27 \cdot 10^{-8}$	$9.27 \cdot 10^{-8}$	$9.27 \cdot 10^{-8}$
KFM07C	285.67	8	0.028	0.049	$4.71 \cdot 10^{-5}$	$4.68 \cdot 10^{-5}$	$8.78 \cdot 10^{-9}$
KFM08A	536.81	32	0.060	0.081	$4.10 \cdot 10^{-6}$	$2.20 \cdot 10^{-6}$	$2.48 \cdot 10^{-10}$
KFM08C	574.71	4	0.007	0.009	$2.96 \cdot 10^{-6}$	$2.95 \cdot 10^{-6}$	$7.72 \cdot 10^{-10}$
KFM10A	9.98	0	0.000	0.000	0.00	0.00	0.00
All bh	5,155.83	103	0.020	0.029	$6.92 \cdot 10^{-5}$	$4.68 \cdot 10^{-5}$	$2.48 \cdot 10^{-10}$

Table 10-16. Summary of PFL flow-anomaly statistics for fracture domain FFM02. T denotes transmissivity, and ξ is a sum over all flow-anomalies. The P_{10} values are length weighted mean values.

Borehole	Σ Length	No. PFL	$P_{10,PFL}$	$P_{10,PFL,corr}$	Σ T-PFL	Max T	Min T
KFM01A	100.33	23	0.229	0.481	$1.92 \cdot 10^{-7}$	$5.31 \cdot 10^{-8}$	$2.45 \cdot 10^{-10}$
KFM01D	91.33	23	0.252	0.329	$5.33 \cdot 10^{-6}$	$2.30 \cdot 10^{-6}$	$6.59 \cdot 10^{-10}$
KFM05A	123.00	18	0.146	0.165	$1.80 \cdot 10^{-6}$	$1.06 \cdot 10^{-6}$	$4.45 \cdot 10^{-10}$
KFM06A	25.79	12	0.465	0.604	$8.13 \cdot 10^{-6}$	$7.31 \cdot 10^{-6}$	$1.37 \cdot 10^{-9}$
KFM07A	5.96	0	0.000	0.000	0.00	0.00	0.00
KFM07C	20.00	5	0.250	0.268	$1.12 \cdot 10^{-7}$	$6.86 \cdot 10^{-8}$	$8.99 \cdot 10^{-10}$
All bh	366.41	81	0.221	0.326	$1.56 \cdot 10^{-5}$	$7.31 \cdot 10^{-6}$	$2.45 \cdot 10^{-10}$

Table 10-17. Summary of PFL flow-anomaly statistics for fracture domain FFM03. T denotes transmissivity, and ξ is a sum over all flow-anomalies. The P_{10} values are length weighted mean values.

Borehole	Σ Length	No. PFL	$P_{10,PFL}$	$P_{10,PFL,corr}$	Σ T-PFL	Max T	Min T
KFM02A	209.46	12	0.057	0.091	$1.05 \cdot 10^{-6}$	$6.77 \cdot 10^{-7}$	$4.26 \cdot 10^{-9}$
KFM03A	819.22	23	0.028	0.062	$6.02 \cdot 10^{-7}$	$1.89 \cdot 10^{-7}$	$1.09 \cdot 10^{-9}$
KFM10A	305.30	14	0.046	0.083	$4.98 \cdot 10^{-7}$	$2.04 \cdot 10^{-7}$	$2.46 \cdot 10^{-9}$
All bh	1,333.98	49	0.037	0.072	$2.15 \cdot 10^{-6}$	$6.77 \cdot 10^{-7}$	$1.09 \cdot 10^{-9}$

Table 10-18. Summary of PFL flow-anomaly statistics for fracture domain FFM04. T denotes transmissivity, and Σ is a sum over all flow-anomalies.

Borehole	Σ Length	No. PFL	$P_{10,PFL}$	$P_{10,PFL,corr}$	Σ T-PFL	Max T	Min T
KFM04A	154.90	15	0.097	0.152	$1.15 \cdot 10^{-6}$	$2.80 \cdot 10^{-7}$	$4.59 \cdot 10^{-9}$
All bh	154.90	15	0.097	0.152	$1.15 \cdot 10^{-6}$	$2.80 \cdot 10^{-7}$	$4.59 \cdot 10^{-9}$

Table 10-19. Summary of PFL flow-anomaly statistics for fracture domain FFM05. T denotes transmissivity, and Σ is a sum over all flow-anomalies.

Borehole	Σ Length	No. PFL	$P_{10,PFL}$	$P_{10,PFL,corr}$	Σ T-PFL	Max T	Min T
KFM07A	50.00	2	0.040	0.067	$4.00 \cdot 10^{-7}$	$2.00 \cdot 10^{-7}$	$2.00 \cdot 10^{-7}$
KFM08A	72.00	0	0.000	0.000	0.00	0.00	0.00
All bh	122.00	2	0.016	0.027	$4.00 \cdot 10^{-7}$	$2.00 \cdot 10^{-7}$	$2.00 \cdot 10^{-7}$

Table 10-20. Summary of PFL flow-anomaly statistics for fracture domain FFM06. T denotes transmissivity, and Σ is a sum over all flow-anomalies.

Borehole	Σ Length	No. PFL	$P_{10,PFL}$	$P_{10,PFL,corr}$	Σ T-PFL	Max T	Min T
KFM06A	129.37	0	0.000	0.000	0.00	0.00	0.00
KFM08C	81.00	0	0.000	0.000	0.00	0.00	0.00
All bh	210.37	0	0.000	0.000	0.00	0.00	0.00

10.5 Summary

Key findings of this study include:

- The hard sector definition of sets developed as part of the F 1.2 Geo-DFN still provide reasonable classification of fracture orientations.
- For both all fractures and open fractures, the HZ set is the most prevalent, followed by the NE set, then the NS and NW set, and the EW set has the lowest intensity.
- For PFL fractures, the HZ set is very dominant, followed by the NE. Other sets only affect flow for some fracture domains. HZ and NE (and NNE) feature for FFM01 and FFM02, NW and EW also occur for FFM03. Hence, flow is very anisotropic in FFM01, FFM02, but less so in FFM03.
- The intensity of all fractures in deformation zones is on average about 3 times that in the fracture domains, and for PFL fractures, the intensity is five times higher in the deformation zones.
- Fracture intensity varies significantly between fracture domains. For open fractures it is highest in FFM02 and FFM04, followed by FFM05, and then similar relatively low values in FFM01, FFM03 and FFM06. FFM01 has the lowest fracture intensity.
- Fracture intensity of open fractures varies strongly with depth. The Terzaghi corrected open fracture intensity averaged over all FFM is about 2 m^{-1} above -200 m , about 1.2 m^{-1} between -200 m and -400 m , and about 0.7 m^{-1} below -400 m . For PFL fractures, the equivalent numbers are about 0.29 m^{-1} , 0.05 m^{-1} and 0.01 m^{-1} , respectively.

- The intensity of open fractures correlates reasonably with that of all fractures with a ratio of about 1:6, but the relationship between PFL fracture intensity with open fracture intensity is more erratic.
- Fracture transmissivities measured by the PFL-f technique are consistent with those measured by the PSS method, apart from some discrepancies in KFM01D and KFM08A where there is a tendency for the PSS method to measured higher transmissivities. An explanation to this phenomenon is presented in Section 4.

Figure 10-22 shows a NW-SE cross section through the centre of the candidate area. The target volume is divided into depth intervals. The PFL-f statistics collated for the different intervals are shown in Table 10-21 through Table 10-25.

Table 10-21. Summary of PFL flow-anomaly statistics for fracture domain FFM02 between –100 and –200 m RHB 70. T denotes transmissivity, and ξ is a sum over all flow-anomalies. The P_{10} values are length weighted mean values.

Borehole	Σ Length	No. PFL	$P_{10,PFL}$	$P_{10,PFL,corr}$	Σ T-PFL	Max T	Min T
KFM01A	100.33	23	0.229	0.481	$1.92 \cdot 10^{-7}$	$5.31 \cdot 10^{-8}$	$2.45 \cdot 10^{-10}$
KFM01D	91.33	23	0.252	0.329	$5.33 \cdot 10^{-6}$	$2.30 \cdot 10^{-6}$	$6.59 \cdot 10^{-10}$
KFM02A	–	–	–	–	–	–	–
KFM03A	–	–	–	–	–	–	–
KFM04A	–	–	–	–	–	–	–
KFM05A	123.00	18	0.146	0.165	$1.80 \cdot 10^{-6}$	$1.06 \cdot 10^{-6}$	$4.45 \cdot 10^{-10}$
KFM06A	25.79	12	0.465	0.604	$8.13 \cdot 10^{-6}$	$7.31 \cdot 10^{-6}$	$1.37 \cdot 10^{-9}$
KFM07A	5.96	0	0.000	0.000	0.00	0.00	0.00
KFM07C	20.00	5	0.250	0.268	$1.12 \cdot 10^{-7}$	$6.86 \cdot 10^{-8}$	$8.99 \cdot 10^{-10}$
KFM08A	–	–	–	–	–	–	–
KFM08C	–	–	–	–	–	–	–
KFM10A	–	–	–	–	–	–	–
All bh	366.41	81	0.221	0.326	$1.56 \cdot 10^{-5}$	$7.31 \cdot 10^{-6}$	$2.45 \cdot 10^{-10}$

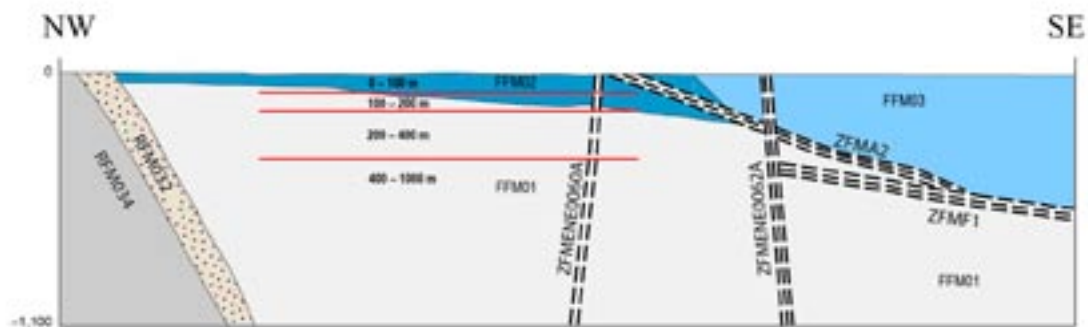


Figure 10-22. NW-SE Cross section through the centre of the candidate area showing a division of the target volume into depth intervals. The vertical scale shows elevation in metres RHB 70.

Table 10-22. Summary of PFL flow-anomaly statistics for fracture domain FFM01 between –100 and –200 m RHB 70. T denotes transmissivity, and Σ is a sum over all flow-anomalies. The P_{10} values are length weighted mean values.

Borehole	Σ Length	No. PFL	$P_{10,PFL}$	$P_{10,PFL,corr}$	Σ T-PFL	Max T	Min T
KFM01A	1.49	0	0.000	0.000	0.00	0.00	0.00
KFM01D	59.23	1	0.017	0.020	$6.53 \cdot 10^{-9}$	$6.53 \cdot 10^{-9}$	$6.53 \cdot 10^{-9}$
KFM02A	–	–	–	–	–	–	–
KFM03A	–	–	–	–	–	–	–
KFM04A	–	–	–	–	–	–	–
KFM05A	0.90	0	0.000	0.000	0.00	0.00	0.00
KFM06A	49.31	19	0.385	0.608	$1.42 \cdot 10^{-5}$	$9.43 \cdot 10^{-6}$	$3.02 \cdot 10^{-10}$
KFM07A	42.76	0	0.000	0.000	0.00	0.00	0.00
KFM07C	81.30	6	0.074	0.075	$4.71 \cdot 10^{-5}$	$4.68 \cdot 10^{-5}$	$9.26 \cdot 10^{-9}$
KFM08A	135.59	23	0.170	0.229	$4.09 \cdot 10^{-6}$	$2.20 \cdot 10^{-6}$	$2.48 \cdot 10^{-10}$
KFM08C	103.86	3	0.029	0.036	$2.95 \cdot 10^{-6}$	$2.95 \cdot 10^{-6}$	$7.72 \cdot 10^{-10}$
KFM10A	–	–	–	–	–	–	–
All bh	474.42	52	0.110	0.152	$6.83 \cdot 10^{-5}$	$4.68 \cdot 10^{-5}$	$2.48 \cdot 10^{-10}$

Table 10-23. Summary of PFL flow-anomaly statistics for fracture domain FFM01 between –200 and –400 m RHB 70. T denotes transmissivity, and Σ is a sum over all flow-anomalies. The P_{10} values are length weighted mean values.

Borehole	Σ Length	No. PFL	$P_{10,PFL}$	$P_{10,PFL,corr}$	Σ T-PFL	Max T	Min T
KFM01A	155.26	9	0.058	0.087	$5.47 \cdot 10^{-9}$	$2.19 \cdot 10^{-9}$	$2.67 \cdot 10^{-10}$
KFM01D	241.82	9	0.037	0.045	$4.78 \cdot 10^{-7}$	$1.83 \cdot 10^{-7}$	$1.30 \cdot 10^{-9}$
KFM02A	–	–	–	–	–	–	–
KFM03A	–	–	–	–	–	–	–
KFM04A	–	–	–	–	–	–	–
KFM05A	197.79	1	0.005	0.006	$1.86 \cdot 10^{-8}$	$1.86 \cdot 10^{-8}$	$1.86 \cdot 10^{-8}$
KFM06A	155.91	7	0.045	0.058	$6.95 \cdot 10^{-8}$	$2.38 \cdot 10^{-8}$	$3.31 \cdot 10^{-10}$
KFM07A	231.44	1	0.004	0.006	$9.27 \cdot 10^{-8}$	$9.27 \cdot 10^{-8}$	$9.27 \cdot 10^{-8}$
KFM07C	120.87	2	0.017	0.066	$3.44 \cdot 10^{-8}$	$2.56 \cdot 10^{-8}$	$8.78 \cdot 10^{-9}$
KFM08A	168.93	9	0.053	0.072	$1.50 \cdot 10^{-8}$	$4.46 \cdot 10^{-9}$	$2.75 \cdot 10^{-10}$
KFM08C	105.55	1	0.009	0.011	$4.97 \cdot 10^{-9}$	$4.97 \cdot 10^{-9}$	$4.97 \cdot 10^{-9}$
KFM10A	9.90	0	0.000	0.000	0.00	0.00	0.00
All bh	1,387.46	39	0.028	0.042	$7.19 \cdot 10^{-7}$	$1.83 \cdot 10^{-7}$	$2.67 \cdot 10^{-10}$

Table 10-24. Summary of PFL flow-anomaly statistics for fracture domain FFM01 below –400 m RHB 70. T denotes transmissivity and Σ is a sum over all flow-anomalies. The P_{10} values are length weighted mean values. Note that the 10 PFL-f anomalies in borehole KFM02A are squeezed between the deformation zones ZFMA2 and ZFMF1. The thickness of this interval is 34 m. The location of the interval is far from the target area close to the hanging wall bedrock, cf. Figure 3-6.

Borehole	Σ Length	No. PFL	$P_{10,PFL}$	$P_{10,PFL,corr}$	Σ T-PFL	Max T	Min T
KFM01A	535.14	0	0.000	0.000	0.00	0.00	0.00
KFM01D	254.99	1	0.004	0.006	$1.59 \cdot 10^{-8}$	$1.59 \cdot 10^{-8}$	$1.59 \cdot 10^{-8}$
KFM02A	411.80	10	0.024	0.036	$1.90 \cdot 10^{-7}$	$8.89 \cdot 10^{-8}$	$6.16 \cdot 10^{-10}$
KFM03A	–	–	–	–	–	–	–
KFM04A	474.54	1	0.002	0.002	$1.41 \cdot 10^{-9}$	$1.41 \cdot 10^{-9}$	$1.41 \cdot 10^{-9}$
KFM05A	379.72	0	0.000	0.000	0.00	0.00	0.00
KFM06A	225.95	0	0.000	0.000	0.00	0.00	0.00
KFM07A	317.02	0	0.000	0.000	0.00	0.00	0.00
KFM07C	83.29	0	0.000	0.000	0.00	0.00	0.00
KFM08A	231.98	0	0.000	0.000	0.00	0.00	0.00
KFM08C	365.26	0	0.000	0.000	0.00	0.00	0.00
KFM10A	–	–	–	–	–	–	–
All bh	3,279.66	12	0.004	0.005	$2.07 \cdot 10^{-7}$	$8.89 \cdot 10^{-8}$	$6.16 \cdot 10^{-10}$

Table 10-25. Summary of PFL flow-anomaly statistics for FFM02 and the proposed elevation intervals of FFM01.

Statistic	FFM02, –100 to –200 m RHB 70		FFM01, –100 to –200 m RHB 70		FFM01, –200 to –400 m RHB 70		FFM01, < –400 m RHB 70	
	Log(T)	$P_{10,PFL}$	Log(T)	$P_{10,PFL}$	Log(T)	$P_{10,PFL}$	Log(T)	$P_{10,PFL}$
Min	–9.61	0.146	–9.61	0.000	–9.57	0.004	–9.21	0.000
Mean	–8.02	0.221	–7.84	0.110	–8.51	0.028	–8.19	0.004
Max	–5.14	0.465	–4.33	0.385	–6.74	0.058	–7.05	0.024
StDev	1.00	–	1.28	–	0.88	–	0.66	–

11 Hydrogeological DFN modelling

11.1 Background and overview of work performed

Both geological DFN (Geo-DFN) and hydrogeological DFN (Hydro-DFN) models were developed based on the Forsmark modelling stage 1.2 (F 1.2) data freeze. The Geo-DFN provided definitions of the geometrical characteristics of the DFN such as fracture set definitions and orientation distributions, as well as some suggestions for fracture size distributions. The Hydro-DFN modelling considered aspects of the intensity of open fractures, fracture network connectivity and flow. Some quantitative calibration of fracture connectivity /Follin et al. 2005b/ and transmissivity /Hartley et al. 2005b/ was made for alternative relationships between fracture size and transmissivity, but data available was limited within the target area. This made it difficult to assess spatial controls and heterogeneity in fracture occurrence, as well as issues such as anisotropy in flow. A much greater amount of data is available in data freeze 2.2, especially in the target area, where several inclined (~ 50–60°) long boreholes, which give a better indication of sub-vertical fracturing and anisotropy, are drilled, cf. Figure 4-1.

The Geo-DFN for Forsmark modelling stage 2.2 was not available during this project. For this reason the set classifications and fracture orientation distributions determined as part of the Geo-DFN F 1.2 are also used here, although some tentative suggestions are made for an update appropriate to the F 2.2 data for open fractures. In the absence of guidance from the Geo-DFN F 2.2 on the distribution of fracture sizes, fracture size models for open fractures are derived here based on the power-law concept. The key data used to determine the size distributions are the fracture intensities of open fractures observed in the boreholes and those implied by the F 2.2 deformation zone model for large deterministic fractures. The size distributions of open fractures considered are calibrated based on simulations of fracture connectivity against the frequency of flow-anomalies observed in PFL-f hydraulic tests. The methodology used was developed and practiced during the initial site investigation stage by /Follin et al. 2005ab, 2006b/. The underlying principle is simple:

$$P_{10,all} > P_{10,open} > P_{10,cof} > P_{10,PFL} \quad (11-1)$$

where $P_{10,cof}$ denotes the frequency of “connected open fractures”, the key property of any hydrogeological DFN model. The notion is illustrated in Figure 11-1.

Further, the concept of fracture domains proposed by /Olofsson et al. 2007/ is used to define a framework for splitting the Hydro-DFN accordingly. A summary description of the fracture domain concept is given in Section 2. Additional sub-domains are defined for FFM01, the candidate volume, based on distinct changes in flow characteristics with depth observed in Section 10. A Hydro-DFN parameterisation is determined for the fracture domains FFM01, FFM02 and FFM03, which correspond to rock domain RFM029 (and a tiny piece of RFM034) the host rock domain studied at Forsmark. In each case, alternative relationships between fracture size and transmissivity including a direct correlation, a semi-correlation and uncorrelated are considered.

In summary, the methodology used here in deriving the Hydro-DFN is principally driven by the F 2.2 data for open fractures and PFL flow-anomalies, along with geological concepts of fracture domains and the structural model. These inputs to the modelling were finalised during the present study, and so the majority of input to this Hydro-DFN study will not change. Therefore, it is anticipated that the delivery of the Geo-DFN for F 2.2 will have limited bearing on the results and conclusions of the present study. It is noteworthy that the Geo-DFN model for Forsmark stage 2.2 treats all fractures, sealed as well as open, and mixes fractures gathered on outcrops with fractures gathered in boreholes. In contrast, the Hydro-DFN model focuses on open (and partly open) fractures gathered in core boreholes below 100 m depth solely. The motive for this difference is well founded for Forsmark given the PFL-f statistics provided in Section 10.5. Finally, unlike outcrop fractures borehole fractures are possible to test hydraulically and occur at repository depth, a decisive condition given the objectives of the work reported here.

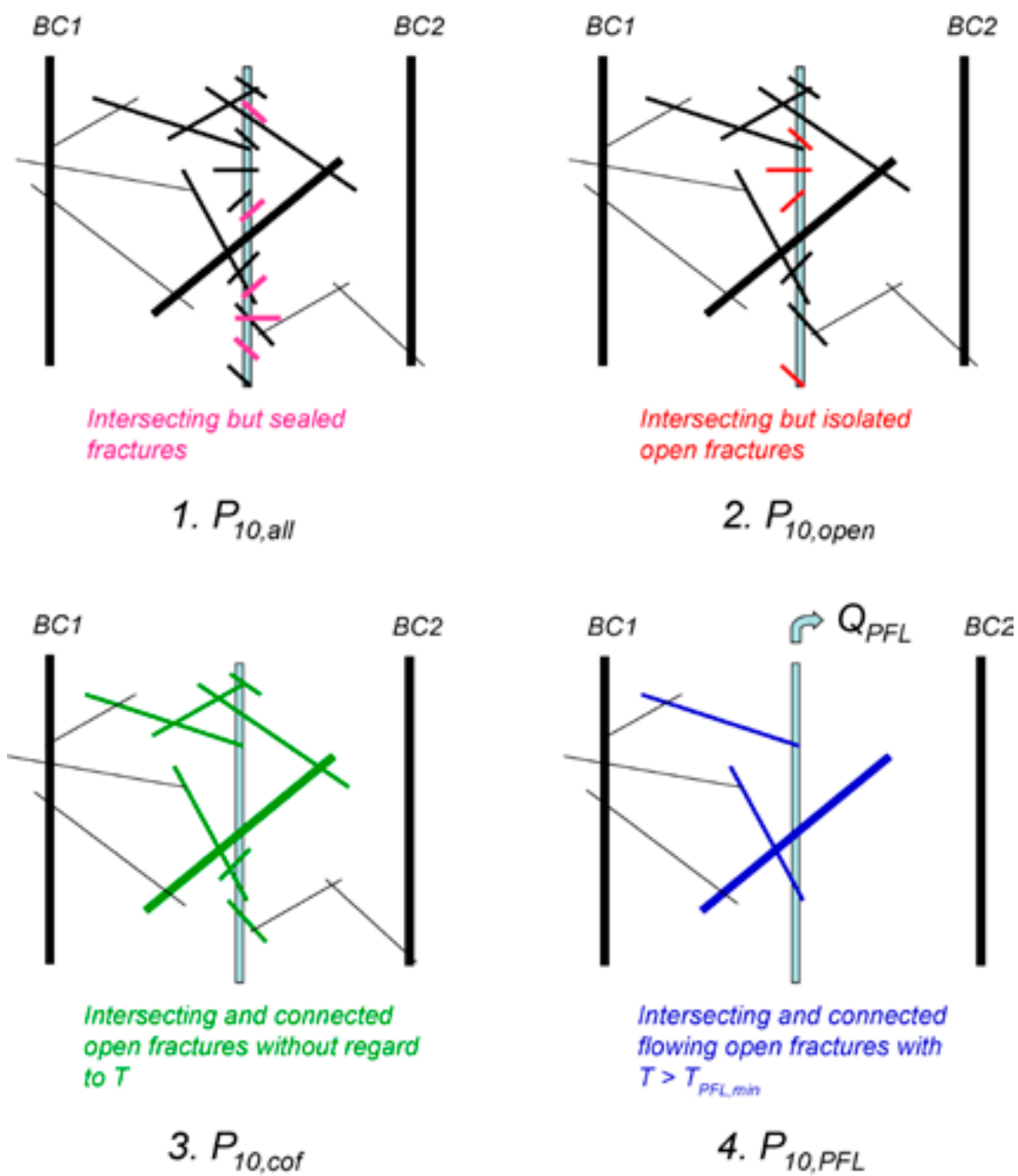


Figure 11-1. $P_{10,all}$ is the frequency of all fractures intersecting the borehole, $P_{10,open}$ the frequency of all open fractures, $P_{10,cof}$ of “all connected open fractures” and $P_{10,PFL}$ of all interconnected, open, flowing fractures that have a transmissivity greater than $c. 1 \cdot 10^{-9} \text{ m}^2/\text{s}$. BC means boundary condition. Reproduced from /Follin et al. 2007d/.

11.2 Conceptual model development

11.2.1 Relation to model stage 1.2

In the modelling stage 1.2 for Forsmark, Simpevarp and Laxemar two slightly different modelling approaches for hydrogeological DFN modelling were used in parallel. In short, the modelling approach developed by /Follin et al. 2005ab, 2006b/ stressed the importance of understanding the role of different geometrical DFN model parameters for the connectivity of open and flowing fractures. Sensitivity tests were carried out and the intensity of interconnected and flowing fractures in 3D was deduced by a calibration against the observed frequency of open fractures ($P_{10,open}$) and the frequency of flowing fractures identified with the PFL method ($P_{10,PFL}$). A graphical-statistical technique was derived for the evaluation of the parameter values of a power-law regression model $T = a r^b$. /Hartley et al. 2005ab, 2006/ started with a given set of parameter values provided by the Geo-DFN for F 1.2 and calibrated the intensity of the generated fractures for that model by means of flow simulations. The results from the flow simulations were compared with the histogram of observed specific discharges identified with the PFL-f method. Three different kinds of correlations between fracture transmissivity versus fracture size were tested; correlated, semi-correlated and uncorrelated:

$$T = a r^b \quad (11-2)$$

$$T = I0^{(\log(a r^b) + \sigma N(0,1))} \quad (11-3)$$

$$T = I0^{N(\mu, \sigma)} \quad (11-4)$$

In the work reported here, we have combined the two modelling approaches. We start with a connectivity-sensitivity analysis and end with flow simulations using the most trusted DFN model deduced in the connectivity analysis. The flow simulations are carried out using the different kinds of correlations between fracture transmissivity versus fracture size.

11.2.2 Definitions

Here, some of the concepts and terminology used in the Hydro-DFN modelling are defined (repeated).

Fracture classification

Each of the fractures mapped in the cores are classified according to a range of different properties. One main classification used in this study is an indication of whether the fracture corresponds with some void space in the borehole core indicating a potential contribution to flow:

- Sealed fractures – fractures mapped in the core that do not correspond with a visible natural break in the core.
- Open – fractures mapped in the core that correspond with a natural complete break in the core.
- Partly open – fractures mapped in the core that correspond with a partial natural break in the core.

The term “All fractures” will be used here to denote fractures which are sealed, open or partly open, whereas “Open fractures” will be used to denote only those fractures which are either open or partly open. The numbers of partly open fractures is generally very small, only 0.5–1.5% of all fractures.

Another key classification used in this study is:

- PFL-anomaly fracture – a fracture which is judged to be the most likely to be associated with an observed flow-anomaly in a PFL-f hydraulic test.

Conceptually, it is assumed that open fractures form potential conduits for groundwater flow, whether they actually provide paths for flow depending on their connectivity and transmissivity. The PFL-anomaly fractures represent a sub-set of the open fractures that are both connected to a wider network and have a transmissivity above a threshold which will give flow measurable by the PFL-f method.

Fracture size distribution

One of the most difficult characteristics of fractures to measure directly in the sub-surface rock is fracture size. Fracture trace length can be measured on outcrops for fractures on the scale of metres to tens of metres, and data is available for lineaments on the scale of 1 km to several kilometres, but this leaves a gap between the scales. (The minimum lineament length mapped at Forsmark is around 1 km). A widely used assumption is one of a continuous scale of fracturing that spans all scales in a continuous manner which can be described by a power-law relationship between fracture intensity and fracture size. The key parameters for a power-law distribution for fractures of different sizes, measured in terms of the radius of a disc, are the shape parameter (k_r) and the location parameter (r_0). The distribution, $f(r)$, is often defined only in a truncated range, between r_{min} and r_{max} .

$$f(r) = \frac{k_r r_0^{k_r}}{r^{k_r+1}} \quad (11-5)$$

where $r_{max} \geq r \geq r_{min} \geq r_0$, $r_0 > 0$, and $k_r > 0$.

The outcrop and lineament fracture size data can be used to derive measures of fracture frequency by using so called area-normalised frequency plots to combine structural data gathered on different scales of observation so as to guide the choice of fracture size parameters. Fracture frequency is also measured along core-drilled boreholes, which gives another scale of measurement resolution. Small scale fractures generally show up well on the surfaces of cored rock cylinder, so it is possible to observe fractures on the scale of the borehole diameter, 0.076 m. Figure 11-2 illustrates the fracture size windows measured by each of the fracture characterisation techniques used in SKB's site investigations.

Typically in the geological DFN modelling, the fracture size parameters are determined from combining fracture frequency data for deformation zones, outcrop maps and possibly borehole cores. Such models are developed based on all fractures mapped in the cores and outcrop without consideration for the flow characteristics of the interpreted fracture system.

In this study, we are interested in the fracture size distribution of only those fractures that contribute to the hydrogeological system, i.e. open fractures and PFL-anomaly fractures. Clearly this will be a sub-set of all fractures, but the parameter distributions of this sub-set do not necessarily bare a simple relationship to those for all fractures derived in Geo-DFN models. Since, the distribution of fracture sizes for open fractures cannot be measured directly; here we develop methods for calibrating the size distribution of open fractures based on characteristics such as the observed frequency of PFL-anomaly fractures, since this indicates the connectivity of the fracture system which is strongly dependent on the fracture size distribution given the measured frequency of open fractures.

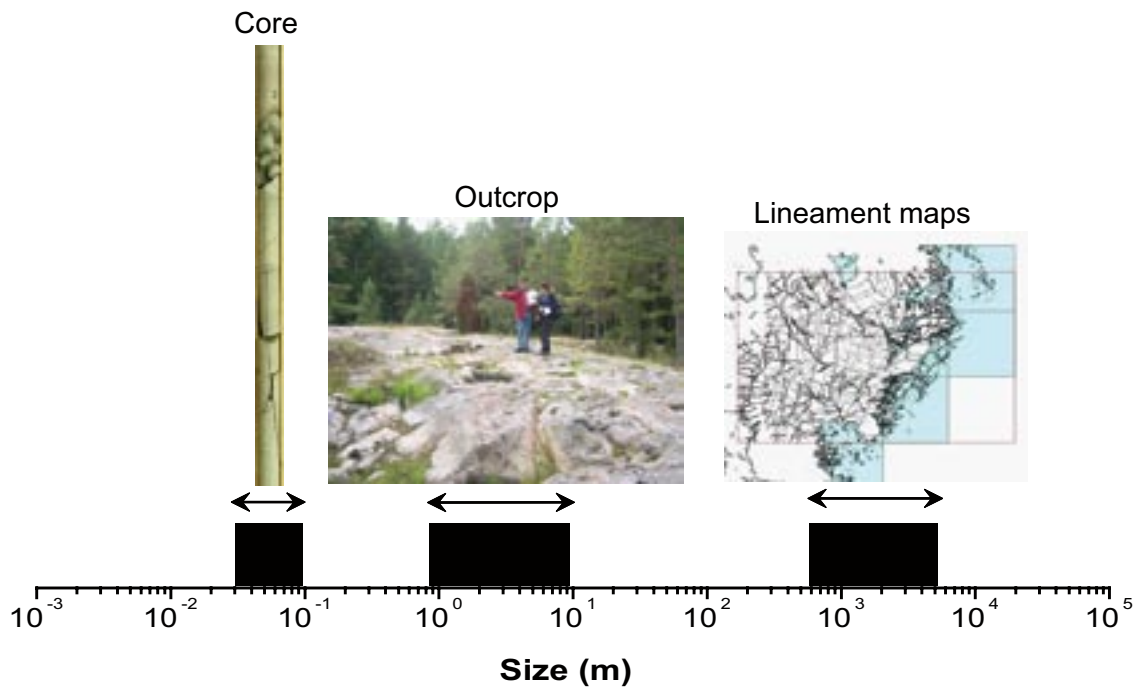


Figure 11-2. Three scales of fracture trace observations. Outcrop fracture and Lineament trace lengths are used for the construction of a fracture size model in the geological DFN. In this study, we modify the fracture size model to honour fracture frequency data from core and hydraulic tests in boreholes /Follin et al. 2006b/.

Fracture intensity

The intensity of fracturing can be measured in several ways usually depending on the method by which fracture are mapped. The main ones are defined as:

- P_{10} – average fracture frequency along a borehole or scan-line.
- P_{21} – average fracture trace length per unit area, e.g. on an outcrop or lineament map.
- P_{32} – average fracture area per unit volume of rock.

The first two of these are used commonly to collate field data since they can be computed readily. However, both are subject to bias introduced by the orientation in which a measurement is made relative to the orientation of fractures. Measurements along a scanline or borehole preferentially detect fractures orthogonal to the scanline than at an oblique angle, which will bias measures of fracture intensity such as frequency or stereographic concentration contour plots heavily in favour of fracture sets orthogonal to the borehole. To compensate for this bias, calculations of fracture intensity can be accumulated in terms of a weighted sum rather than a simple count with a geometrical weighting factor calculated and applied to each fracture measured. This weighting, W , is used in calculating statistics such as the corrected linear fracture intensity, $P_{10,corr}$, when comparing between different borehole orientations, or can be applied to concentration plots for identifying sets. The process of Terzaghi correction /Terzaghi 1965/ and is illustrated in Figure 10-1 (see Section 10.3).

The last measure, P_{32} , is an unbiased fracture intensity statistic, although it is obviously difficult to measure in the field directly. Still, it is used to parameterise fracture intensity in models because of its independence from the definition of orientations. In practice, P_{32} can be estimated from $P_{10,corr}$ and adjusted if necessary by calibration against numerical simulations.

For the power-law size distribution it is useful to be able to calculate the P_{32} fracture intensity associated with different ranges of fracture size using the following formulae. If $P_{32}[r > r_0]$ denotes the fracture surface area of all fractures greater than the location parameter, r_0 , we can write:

$$P_{32}[r > r_1] = P_{32}[r > r_0] \left(\frac{r_0}{r_1} \right)^{(k_r - 2)} \quad (11-6)$$

where $P_{32}[r > r_1]$ is the fracture surface area of all fractures r greater than the size r_1 . From a modelling point of view, it is necessary to decide the size range $[r_{\max}, r_{\min}]$ that will be used in the numerical simulations and, equally important, the intensity value $P_{32}[r > r_0]$ that corresponds to the smallest value of the underlying data set. For fractures in the size interval $[r_{\min}, r_{\max}]$, the fracture intensity of a DFN model is given by:

$$P_{32}[r_{\min}, r_{\max}] = P_{32}[r > r_0] \left[\frac{(r_{\min})^{(2-k_r)} - (r_{\max})^{(2-k_r)}}{(r_0)^{(2-k_r)}} \right] \quad (11-7)$$

In modelling a hydrogeological DFN, it is important to quantify both the geometrical connectivity of the network and the distribution of fractures that conduct flow. Figure 11-3 illustrates the concept of fracture connectivity and flow as modelled in a borehole. Here, N_{OPEN} is the number of all open fractures seen in the borehole section; N_{COF} is the number of open connected fractures; and N_{PFL} is the number of PFL-anomaly fractures observed with flow above the detection limit, typically corresponding to a transmissivity above about $10^{-9} \text{ m}^2/\text{s}$. Then the corresponding measures of fracture intensity would be:

- $P_{10} = N_{OPEN} / D$
- $P_{10,cof} = N_{COF} / D$
- $P_{10,PFL} = N_{PFL} / D$

where D is the length of borehole section mapped.

One method used for deriving a set of power-law size distribution parameters is to assume a value for r_0 and then fit values of k_r such that the distribution gives a consistent fracture intensity for all fracture lengths, based on that observed in the boreholes, and for all large deterministic fractures above the resolution for mapping local and regional scale deformation zones. That is, using Equation 10-7 it is assumed that $P_{32}(r > r_0) = P_{10,o,corr}$ based on “All bh” in Table 10-10 for FFM01, and $P_{32}[r > 560 \text{ m}] = P_{32}[\text{deformation zone model}] (r > 560 \text{ m})$ is based on an assumption of a minimum trace-length of 1 km). The deformation zone model is shown as a trace map

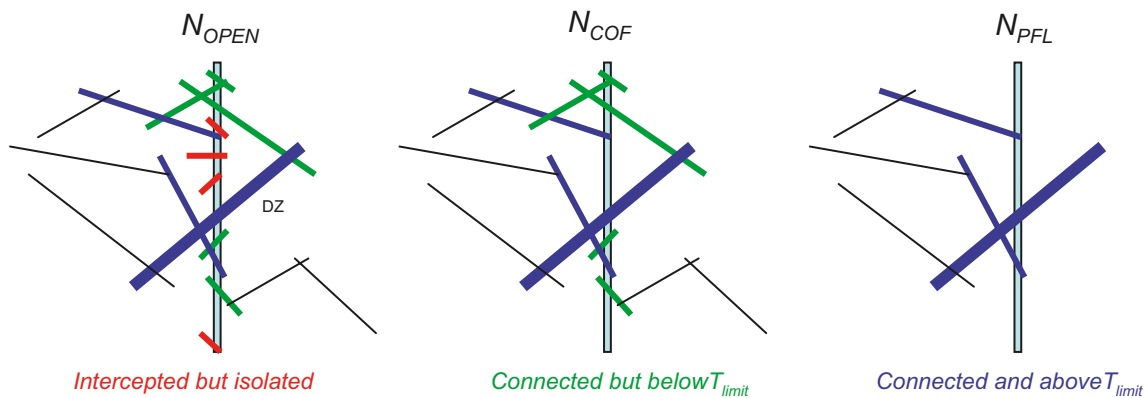


Figure 11-3. The definition of N_{OPEN} , N_{COF} and N_{PFL} for open fractures. T_{limit} denotes the lower measurement limit for transmissivity, which is typically around $10^{-9} \text{ m}^2/\text{s}$ for the Posiva Flow Log (PFL-f) /Follin et al. 2005b/.

just below the surface in Figure 3-4 and in 3D in Figure 11-4 to show the sub-horizontal zones. Because there is a different resolution scale in mapping deformation zones within the local and regional-scale areas, fracture intensity was calculated only within the local-scale area indicated in Figure 11-4 and to a depth of 1 km, and using a minimum deformation zone length of 1 km. The fracture intensity calculated as fracture area per unit volume with the local-scale area was computed for each of the fracture sets defined as hard sectors in F 1.2 (see Section 11.3). The results are given in Table 11-1.

We can also anticipate what the Geo-DFN model might give for a fracture size model if it were to just match the fracture intensity for all fractures, $P_{32}(r > r_0) = P_{10,a,corr}$, at the boreholes for FFM01 and the deformations zones. Assuming an r_0 equal to the borehole radius of 0.038 m gave the k_r values given in Table 11-2, which range from 2.6 to 2.82. As is shown in Section 11.4.2 these are higher than those used in the modelling of open fractures.

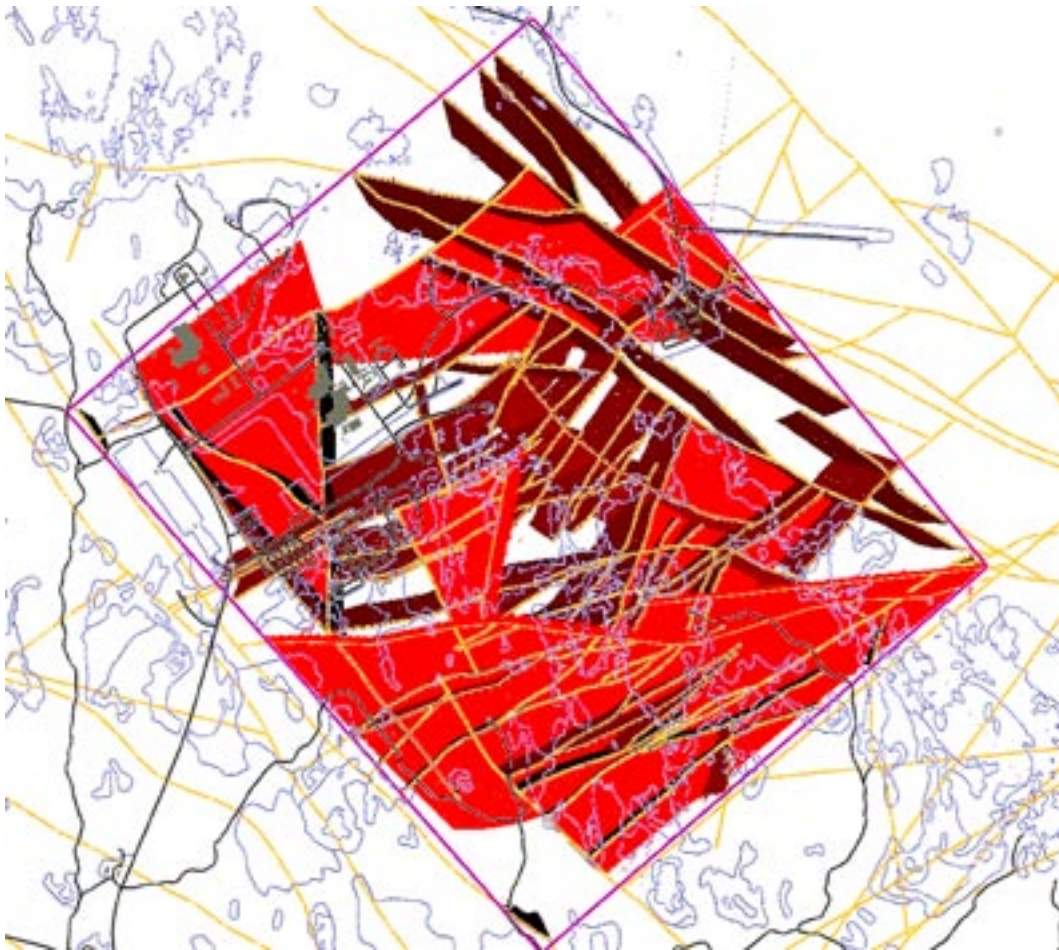


Figure 11-4. 3D view of the deformation zone model for F 2.2 as of 27/02/2007 used to derive one alternative power-law size model on matching the P_{32} for deformation zones ($r > 560$ m) to the $P_{10,o,corr}$ for boreholes ($r > r_0$). Fracture intensity for the deformation zones is calculated within the local area indicated by the purple lines (about 3.7 km by 3.1 km) and the upper 1 km. Deformation zones within the local model area are shown in 3D coloured red, outside they are just shown as traces at -10 m elevation coloured orange.

Table 11-1. Calculated fracture intensity for each of F 1.2 fracture sets for the deformation zone model within the local model volume.

Set	$P_{32}[r > 560 \text{ m}] \text{ (m}^2/\text{m}^3\text{)}$
NS	$4.87 \cdot 10^{-4}$
NE	$3.54 \cdot 10^{-3}$
NW	$1.60 \cdot 10^{-3}$
EW	$6.18 \cdot 10^{-4}$
HZ	$8.40 \cdot 10^{-4}$

Table 11-2. Power-law size models based on fitting the fracture intensity for all fractures, $P_{10,a,corr}$, in the boreholes for fracture domain FFM01 and the deformation zone model given in Table 11-1.

k_r						$r_o \text{ [m]}$
NS	NE	NW	EW	HZ		
2.82	2.64	2.60	2.66	2.70	0.038	

Identification of PFL fractures

To help interpret the flow data measured by the Posiva Flow Log (PFL), borehole fractures that correspond to the borehole lengths at which flow anomalies have been identified in the PFL-f tests have been identified by SWECO VIAK. This allows identified flows to be linked to particular fractures seen in the borehole core and image logs. The methodology followed is described in /Forsmann et al. 2005/. The methodology followed by Forsmann and co-authors when assigning a fracture orientation to each flow anomaly is described below.

For each anomaly, the fracture (or fractures) most ‘consistent’ with the anomaly is (are) selected. If there is more than one equally consistent fracture associated with an anomaly, then the orientations of each of the fractures are used. Generally, there are only one or two consistent fractures, but sometimes there are 3–5 equally consistent fractures. The assumptions made by Forsmann and co-authors when correlating the Boremap data to the PFL-anomalies were:

- As a first assumption, the open and partly-open fractures as well as crush zones are assumed to be possible flowing features. This is an important assumption on which all subsequent analysis relies. Alternative possibilities, which were not considered in this work, include the suggestion that fractures mapped as sealed could contain flow. For instance, fractures that are considered sealed when viewed from the Boremap data within the diameter of the borehole may have a conductive (flowing) section further away from the borehole.
- It is assumed that the precision of the position (L) in the borehole of the PFL-anomaly is not on the 1 dm level. If an open, partly-open fracture or crush zone is within $\pm 0.5 \text{ m}$ of a PFL-anomaly it is assumed that it could potentially correspond to the PFL-anomaly (in a few cases larger differences have been accepted). The nearest distance in dm from the fractures trace (a sinus-shape line) on the borehole wall to depth L is judged and documented in the database (PFL-anom. Confidence). This distance is estimated in dm as the deviation of each potential open, partly-open fractures or crush zones from L , defined positive if the fracture is located below L .
- A few **sealed fractures** were indicated as possible flowing features if the core has been broken AND adjusted secup (Boremap) $\approx L$ (Borehole length) for the PFL-anomaly AND that no open fracture was $< 0.6 \text{ m}$ from L OR that the nearest open fracture is positioned closer than 0.6 m but matches another anomaly very well. When interpreting these broken/ sealed fractures, only the ones located $\pm 0.1 \text{ m}$ from the anomaly have been mapped. These are fractures considered to be very uncertain and may be excluded from the analysis. “PFL-Confidence” is set to zero (0) in the database for these cases.

- Occasionally, several **open fractures** are within $\pm 0.1\text{--}0.2\text{m}$ of L for the PFL-anomaly and it is judged that one or all of them may be flowing features. If “FRACT_INTERPRET” is used in the database, the “Certain, Probable, Possible” entries can be used to decide whether one is more likely to be the flowing feature. In a few cases, the mapped open fractures are so close ($< 1\text{ cm}$) that possibly one could consider them as one fracture. In some cases where open fractures have been identified within $\pm 0.1\text{--}0.2\text{ m}$ of L , there may be more open fractures at a distance $\pm 0.2\text{--}0.5\text{ m}$ that are not included in the database as possible flowing features.
- In a few cases several PFL-anomalies may be connected to a single geological feature, generally a crush zone but sometimes also an open fracture.
- Some open, possibly flowing, fractures have very high amplitudes in the BIPS log, stretching over up to several metres of the borehole wall. These fractures can, because of their shape, have an influence on the flow conditions quite a long distance from the level indicated by the fractures “secup”-value. When evaluating the data, these fractures are given a lower “PFL-confidence” than suggested only by the distance between the fractures secup and the level of the PFL-anomaly. If the fracture cuts the level of the PFL-anomaly, the PFL-confidence is set to one (1, which is the highest confidence), independent of how long the distance between the secup value and the level of the anomaly is. In consequence, some fractures with high amplitudes that almost ($\pm 0.2\text{ m}$) cut the PFL-anomaly level are also included in the analysis. The PFL-confidence has been set to 2 in these cases.
- If several fractures are considered as possible objects for the PFL-f flow anomaly, as an option for the modeller, one fracture chosen as “Best Choice” (BC) based on mainly mapping parameters such as the confidence, if the fracture is open or not and the distance to the PFL-f anomaly, as well as the fracture appearance in the BIPS image /Forsman et al. 2004, Forsman et al. 2006, Teurneau et al. 2007/.

11.3 Fracture set definitions

All modelling performed in this study uses the hard sector definition of fracture sets defined in the F 1.2 Geo-DFN /La Pointe et al. 2005/. The sector definitions along with parameters used in the Univariate Fisher distribution for fracture orientations are given in Table 11-3.

A suggested update of the set classifications and statistical model for open fractures based on the F 2.2 data is made in Section 11.6.

Table 11-3. Hard sector definitions of fracture orientation sets from the F 1.2 Geo-DFN /La Pointe et al. 2005/ and recommended parameters for a Univariate Fisher distribution.

Set	Trend	Plunge	Dip	Strike	Orientation Fisher distribution (trend, plunge), concentration
1 NS	65–110, 245–290	0–40	50–90	335–20, 155–200	(87, 2) 21.7
2 NE	110–170, 290–350	0–40	50–90	20–80, 200–260	(135, 3) 21.5
3 NW	25–65, 205–245	0–40	50–90	115–155, 295–335	(41, 2) 23.9
4 EW	350–25, 170–205	0–40	50–90	80–115, 260–295	(190, 1) 30.6
5 HZ	0–360	40–90	0–50	0–360	(343, 80) 8.2

11.4 Simulations of fracture geometry

11.4.1 Modelling approach

In previous Hydro-DFN studies, data has only been available for a handful of boreholes, and so it was appropriate to develop Hydro-DFN models based on explicit models of each of a small number of boreholes. For F 2.2, 12 core drilled boreholes are considered, and hence it is impractical to develop an explicit DFN model for each borehole. Instead, DFN models are developed for each of the fracture domains FFM01–FFM03 within the candidate area. To characterise statistics for each fracture domain, data is pooled over several boreholes for the same fracture domain, but respecting any additional partitions of the data such as depth dependency. Therefore, in the initial modelling phase, models are developed based on statistics homogenised over the fracture domains, so as to derive models that capture the overall characteristic of each fracture domain without conditioning in the local conditions around each borehole. Hence, the DFN models developed here might be considered as spatially unconditioned stochastic models appropriate to each fracture domain. Later in this report we consider how conditioning the DFN around the boreholes might be performed.

The methodology for deriving a Hydro-DFN model for each fracture domain involves the following steps:

1. Perform DFN simulations of open fractures based on the F 1.2 set and orientation models and based on several different power-law models for fracture size to check the simulated fracture frequency in boreholes for each set.
2. Use the open fracture models to perform connectivity analyses to test the simulated frequency of potential flow channels for each of the fracture size models and assess which best reproduce the frequency of PFL flow-anomalies measured in the boreholes.
3. Based on step 2, optimise the choice of power-law size parameters for each set to give a frequency of connected fractures consistent with the frequency of PFL flow-anomalies measured in the boreholes.
4. Perform DFN flow simulations to calibrate hydraulic parameters and possible relationships between fracture size and transmissivity. The parameters are derived for each set, and potentially with a depth dependency. A direct correlation between fracture size and transmissivity is considered, as well as alternatives based on a semi-correlation and a completely uncorrelated model.

The sensitivities quantified as part of steps 1) and 2) to the magnitude of the shape parameter k_r and the location parameter r_0 are calculated based on the following five different combinations of k_r and r_0 to illustrate the importance of these parameters in determining the nature of network connectivity and flow prior to seeking optimised parameters that best match the field-data as part of step 3):

- a) Small k_r and r_0 , (2.6 and 0.038 m).
- b) Large k_r and r_0 , (2.9 and 0.282 m).
- c) Large k_r and small r_0 , (2.9 and 0.038 m).
- d) Small k_r and large r_0 , (2.6 and 0.282 m).
- e) A case based on matching the open fracture intensity in boreholes and the fracture intensity of the local-scale deformation zone model.

Of the core drilled boreholes, KFM01A, KFM02A, KFM03A and KFM07C are vertical, while the others are inclined at 60° to the horizontal, mostly dipping toward approximately NW or NE. Most boreholes are 1 km long, but are cased in the top 100 m. One of the issues dealt with in the data compilation was how to combine data from boreholes of different trajectory so as to avoid bias caused by the preferential sampling of fractures oriented orthogonal to the borehole axis. The approach used there was to collate statistics using Terzaghi weightings to correct for the bias. Similarly, in the simulations fracture frequencies are calculated according to the Terzaghi weighted values, e.g. $P_{10,corr}$, $P_{10,o,corr}$ and $P_{10,PFL,corr}$. Initially, simulations were performed only for a generic 1 km long vertical borehole within a model domain 400 m by 400 m horizontal and 1,200 m vertical. A 400 m horizontal cross-section was chosen since it is approximately the average spacing between the sub-vertical deformation zones for the local-scale model using the fracture frequencies given in Table 11-1. For each model case, 10 realisations were performed and statistics of $P_{10,corr}$ (for all, open, or connected open fractures depending on the application) were calculated along the borehole. The average $P_{10,corr}$ values calculated for the simulations were then compared with the average values measured over all boreholes. An example of a DFN model for this domain is shown in Figure 11-5. Fractures were generated of sizes varying from r_0 to 560 m according to a power-law distribution. For practical reasons, small fractures of size from r_0 to 1.1 m were only generated within a cylinder of radius 1.4 m around the borehole axis. Larger fractures, of radius greater than 1.1 m are generated within a volume 500 m larger than the model domain in each direction in order to avoid reduced fracture intensities at the model boundaries. The borehole was modelled as a straight line such that intersections with the borehole core were approximated by the intersection of a square fracture plane with a line. The software used in this study was ConnectFlow Stage 9.3 with DFN-only models.

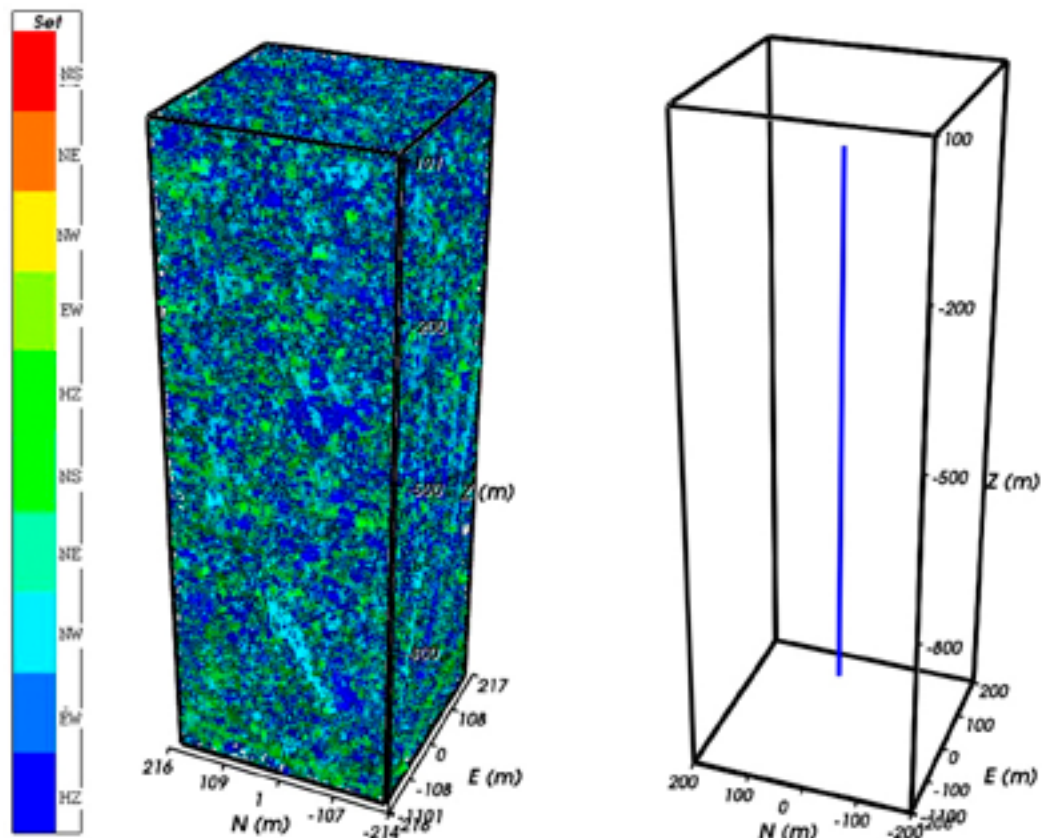


Figure 11-5. Example DFN simulation of fracturing surrounding a generic vertical borehole for a domain 400 m by 400 m by 1,200 m. Left: a simulation of open fractures coloured by fracture set (5 sets for large fractures $r > 1.1$ m, 5 sets for small fractures around the borehole $r_0 < r < 1.1$ m). Right: just the model domain and 1 km vertical borehole.

By only modelling a single vertical borehole, the results for the sub-vertical sets may be unrepresentative of a data set that includes inclined boreholes, even if Terzaghi correction is used. To quantify the sensitivity to this simplification an alternative approach was considered to generate fractures in a larger domain 1 km (E-W) by 700 m (N-S) and 1.2 km vertical and insert 3 generic boreholes: 1 vertical, 1 dipping 60° NW, and 1 dipping 60° NE. The objective being to better reflect the mix of borehole trajectories we have data for which have been grouped as approximately:

- Vertical – KFM01A, KFM02A, KFM03A and KFM07C.
- NE – KFM01D, KFM04A, KFM08C and KFM10A.
- NW – KFM05A, KFM06A, KFM07A and KFM08A.

Then, for each realisation Terzaghi corrected fracture intensities were calculated along each of the three boreholes: $P_{10,corr,Z}$, $P_{10,corr,NE}$ and $P_{10,corr,NW}$. Finally, an overall average simulated Terzaghi corrected $P_{10,corr}$ was computed as a length weighted average:

$$P_{10,corr} = (L_Z P_{10,corr,Z} + L_{NE} P_{10,corr,NE} + L_{NW} P_{10,corr,NW}) / (L_Z + L_{NE} + L_{NW}), \quad (11-8)$$

where L_Z , L_{NE} and L_{NW} are the lengths of boreholes in each of the 3 directions. For fracture domain FFM01, $L_Z = 1,393$ m, $L_{NE} = 1,617$ m, and $L_{NW} = 2,146$ m. This the same procedure used for calculating the overall borehole averaged, “All bh”, statistics given in the data compilation in Section 9. The domain and boreholes for this model is shown in Figure 11-6.

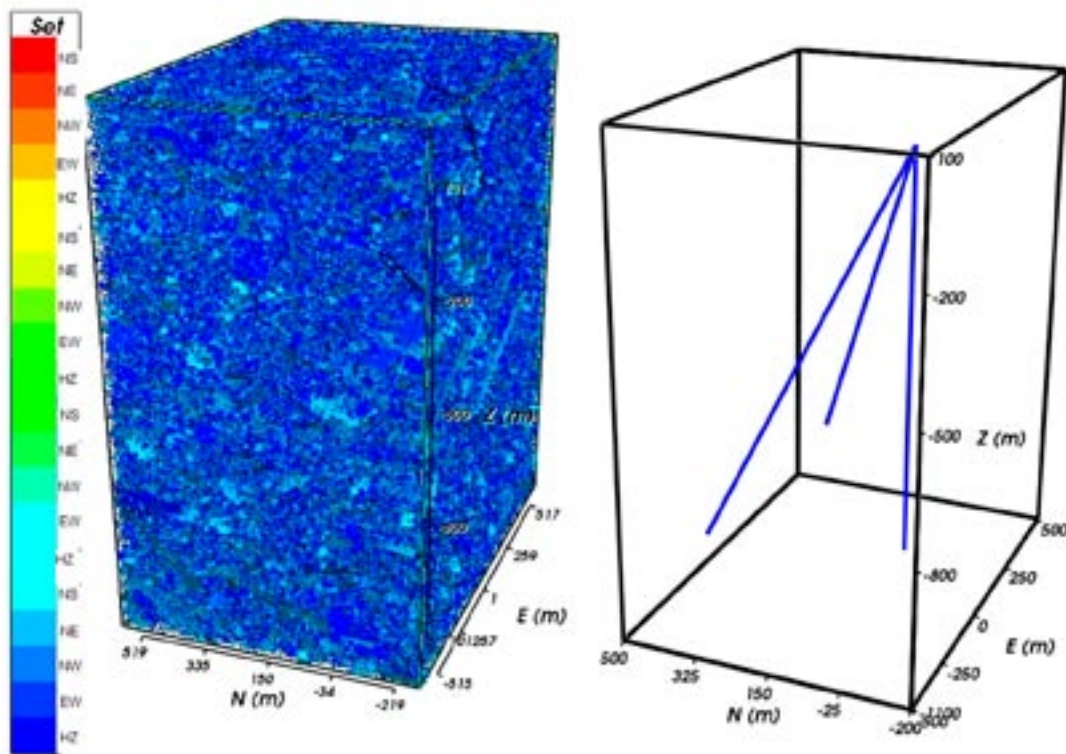


Figure 11-6. Example DFN simulation of fracturing surrounding 3 generic vertical, NE and NW boreholes for a domain 1,000 m by 700 m by 1,200 m. Left: a simulation of open fractures coloured by fracture set (5 sets for large fractures $r > 1.1$ m, 15 sets for small around the boreholes $r_0 < r < 1.1$ m, i.e. 5 sets for each borehole). Right: just the model domain and 1 km long vertical, NE and NW boreholes.

11.4.2 Fracture size cases

The connectivity of sparse fracture networks, such as encountered at Forsmark, is highly sensitive to the power-law size distribution. This has been illustrated in generic F 2.2 pre-modelling studies performed by /Follin et al. 2007a/. There, the approach was to calculate the fracture intensity of connected open fractures, $P_{10,cof}$, in a vertical borehole for different combinations of shape parameter k_r , location parameter r_0 and open fracture intensity $P_{32}[r > r_0]$. They considered approximate extreme values of the parameters: $r_0 = 0.038 - 0.282$ m; $k_r = 2.6 - 2.9$; $P_{32}[r > r_0] = 0.6 - 6.0$; and either 2 sets or completely isotropic fracture orientations. The choice of $r_0 = 0.038$ m is based on the borehole diameter, and 0.282 m is based on the approximate minimum trace length mapped on outcrops, i.e. 0.5 m. Here, we follow the same approach using the same combinations of r_0 and k_r , but taking $P_{32}[r > r_0] = P_{10,corr}$ from the borehole data for each fracture set. This was done for simulations of open fractures when considering the connectivity of potential water-bearing fractures. The names given to these cases are given in Table 11-4 for reference. An additional case, KRDZ_RMIN, was derived based on matching the borehole open fracture intensity to the deformation zone intensity and assuming $r_0 = 0.038$ m, as detailed above. It can be seen that this actually suggests k_r values less than 2.6 for all sets, down to 2.39, which will give a network more connected than the KRMIN_RMIN case.

11.4.3 Calibration of fracture intensity and connectivity

The first step in the fracture modelling was to simulate 10 realisations of open fractures using the F 1.2 sets and orientations and compare the modelled linear intensities, $P_{10,o,corr}$, for each set with those measured over all boreholes given in Table 10-10. This was done for each of the power-law size models, but it is expected that the linear intensity in a borehole will not be sensitive to the distribution of fracture sizes, since all cases have the same input areal fracture intensity P_{32} . The second step was to perform a network connectivity analysis to compare the simulated $P_{10,cof,corr}$ with the measured $P_{10,PFL,corr}$ given in Table 10-10. These results are expected to show a strong sensitivity to the choice of power-law size parameters since models with a higher proportion of long fractures tend to be more connected, at least for low fracture intensity. For simplicity, this was done for models without depth trends and for a vertical borehole to explore the basic dependence of connectivity on size distribution to identify which cases showed most consistency with data before introducing extra complexity of depth dependency and considering intersections with boreholes in three different directions.

Fracture domain FFM01

The parameter setting used for simulating open fractures in FFM01 without a depth trend are given in Table 11-5. The P_{32} input is taken from Table 10-10.

The resulting predictions of $P_{10,o,corr}$ for each set and power-law distribution model are tabulated in Table 11-6 and presented graphically in Figure 11-7.

Table 11-4. Summary of power-law size models considered and the parameters defining them. The KRDZ_RMIN is based on fitting the fracture intensity for open fractures in the boreholes and deformation zone model given in Table 11-1.

Case	k_r					r_0 [m]
	NS	NE	NW	EW	HZ	
KRMIN_RMIN	2.60	2.60	2.60	2.60	2.60	0.038
KRMAX_RMAX	2.90	2.90	2.90	2.90	2.90	0.282
KRMAX_RMIN	2.90	2.90	2.90	2.90	2.90	0.038
KRMIN_RMAX	2.60	2.60	2.60	2.60	2.60	0.282
KRDZ_RMIN	2.57	2.40	2.39	2.45	2.56	0.038

Table 11-5. Description of DFN parameters and F 1.2 fracture set orientations used for simulation of open fractures in FFM01 without depth dependency.

Fracture domain	Fracture set name	Orientation set pole: (trend, plunge), conc.	Size model, power-law (r_0, k_r) (m)	Intensity, (P_{32}), valid size interval: ($r_0, 560$ m) (m^2/m^3)	Transmissivity model Eq. no, constants T (m^2s^{-1})
FFM01	NS	(87, 2) 21.7	Cases in Table 11-4	0.105	–
	NE	(135, 3) 21.5		0.226	
	NW	(41, 2) 23.9		0.108	
	EW	(190, 1) 30.6		0.055	
	HZ	(343, 80) 8.2		0.224	

Table 11-6. Comparison of measured Terzaghi corrected linear intensities of open fractures, $P_{10,o,corr}$, in fracture domain FFM01 for each fracture set with simulation results for 10 realisations of a 1 km vertical borehole for different power-law size models (see Table 11-4).

Case	ALL	NS	NE	NW	EW	HZ
Measured FFM01 (all bh)	0.718	0.105	0.226	0.108	0.055	0.224
KRMIN_RMIN	0.572	0.079	0.147	0.083	0.039	0.224
KRMAX_RMAX	0.589	0.069	0.173	0.081	0.037	0.229
KRMAX_RMIN	0.574	0.072	0.162	0.074	0.037	0.229
KRMIN_RMAX	0.608	0.083	0.175	0.087	0.040	0.223
KRDZ_RMIN	0.608	0.086	0.170	0.088	0.037	0.227

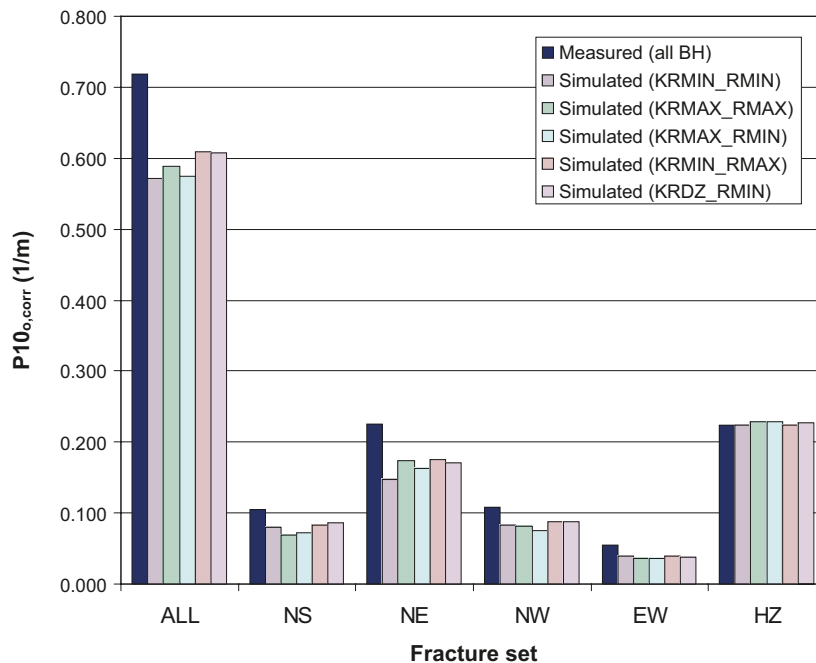


Figure 11-7. Graphical comparison of measured Terzaghi corrected linear intensities of open fractures, $P_{10,o,corr}$, for fracture domain FFM01 for each fracture set with simulation results for 10 realisations of a 1 km vertical borehole for different power-law size models.

As anticipated, the difference between the simulations for different power-law models is very small and only results from the stochastic process of generating the DFN's, and would be expected to be identical if more realisations were performed. Comparing with the measured data suggests the model is under-predicting the intensities of the sub-vertical sets slightly, particularly the NE set. This implies that the F 1.2 fracture set definitions and orientations is not giving an entirely satisfactory prediction of the distribution of fracture orientations observed in the F 2.2 data overall. It is notable that the NE set gives the poorest result, and this is where we suggest introducing a NNE set for F 2.2 data Section 11.6.

More interesting differences between the power-law models are seen when simulating fracture connectivity. This is done by generating models containing only fractures, but no boreholes. Then, a connectivity analysis is performed to identify any open fractures without a connection to one of the boundary surfaces of the model, which are then removed. The boreholes are then re-inserted in the model and the Terzaghi corrected frequency of occurrence of connected open fractures in the boreholes, $P_{10, \text{cof, corr}}$, is calculated. Results for each power-law size model are given in Table 11-7 and in Figure 11-8 which are compared with the frequency of PFL flow-anomalies taken from Table 10-10. It should be noted that a connectivity analysis is based purely on geometrical connections and does not take account of the transmissivity of fractures relative to the detection limit of the PFL-f test method. Hence, it is possible that in reality more fractures are geometrically connected, but these connections have a flow capacity below the measurement threshold. Hence, models that give connected open fracture frequencies above the measured PFL fracture frequency are plausible scenarios, provided a suitable transmissivity distribution can be found, although models far more connected than suggested by the PFL-f tests will probably require assumptions about transmissivity that are difficult to substantiate. The KRMIN_RMAX case gives a relatively connected network with about 10 times too high a connected open fracture frequency than measured by PFL-f test, while the KRMAX_RMIN case has a completely unconnected network, and so both these cases do not reflect the observed network properties. The KRMAX_RMAX case also gives 4 times too high a connected open fracture frequency than measured by PFL-f test. As a reference to the earlier F 1.2 Hydro-DFN, this used size distribution parameters close to the KRMAX_RMAX case, although with slightly higher k_r values. In conclusion, the only 2 candidates as plausible models are the KRMIN_RMIN and KRDX_MIN cases, with KRMIN_RMIN giving the best results. Visualisations to show the contrast in connectivity between the KRMIN_RMAX and KRMIN_RMIN are shown in Figure 11-9.

The next step was to quantify the variations in fracture intensity between the 3 different borehole orientations (vertical, NW 60° dip and NE 60° dip) to check whether the F 1.2 set and orientation model were giving a reasonable representation of the variation in open fracture intensity between different borehole trajectories. Simulations were only performed for the KRMIN_RMIN case using the domain shown in Figure 11-7. In Table 11-8, values for the Terzaghi corrected open fracture intensity are given for the boreholes and the mean of 10 realisations for each of the 3 orientations of borehole and for a length weighted mean based on Equation 10-8. Some aspects of the simulations show the right sort of behaviour. For example, the intensities of NS and NE fractures are highest for NW oriented boreholes, and the NW fracture intensity is highest for NE oriented boreholes. However, the data shows larger differences in fracture intensity between the boreholes than calculated in the simulations. This may suggest that there is larger anisotropy in the orientations of fractures than is produced by the F 1.2 model of fracture sets and orientations. The data seems to suggest a greater clustering of fractures around the NE direction, and hence the model with NE and NNE sets suggested in Section 11.6 may be expected to give better agreement, although simulations were not performed for this alternative model. Comparing the simulation results between Table 11-6 and Table 11-8 using the more complicated model set up with 3 boreholes did not seem to make a significant difference to results. Given this and the belief that the most significant improvement in matching variations in intensity between the different borehole orientations would only come if the set definitions were updated, it was decided to use the single vertical borehole model set up for the remaining simulations.

Table 11-7. Comparison of measured Terzaghi corrected linear intensities of PFL fractures, $P_{10,PFL,corr}$, in fracture domain FFM01 for each fracture set with simulation results of connected open fractures, $P_{10,cof,corr}$ for 10 realisations of a 1 km vertical borehole for different power-law size models (see Table 11-4).

Case	ALL	NS	NE	NW	EW	HZ
Measured FFM01 (all bh)	0.029	0.002	0.007	0.000	0.000	0.020
KRMIN_RMIN	0.023	0.005	0.007	0.002	0.001	0.008
KRMAX_RMAX	0.086	0.010	0.020	0.016	0.007	0.033
KRMAX_RMIN	0.000	0.000	0.000	0.000	0.000	0.000
KRMIN_RMAX	0.227	0.027	0.063	0.036	0.014	0.086
KRDZ_RMIN	0.064	0.004	0.023	0.015	0.004	0.018

Table 11-8. Comparison of measured Terzaghi corrected linear intensities of open fractures, $P_{10,o,corr}$, for fracture domain FFM01 for each fracture set with simulation results for 10 realisations of a 1 km vertical borehole for the KRMIN_RMIN power-law size models (see Table 11-4).

Case	ALL	NS	NE	NW	EW	HZ
Measured FFM01 (all bh)	0.718	0.105	0.226	0.108	0.055	0.224
Measured FFM01 (vert bh)	0.660	0.099	0.266	0.064	0.022	0.210
Measured FFM01 (NE bh)	0.698	0.109	0.114	0.150	0.067	0.258
Measured FFM01 (NW bh)	0.770	0.106	0.284	0.105	0.067	0.208
KRMIN_RMIN (all bh)	0.650	0.091	0.192	0.091	0.050	0.226
KRMIN_RMIN (vert bh)	0.611	0.070	0.183	0.085	0.042	0.231
KRMIN_RMIN (NE bh)	0.662	0.100	0.172	0.101	0.064	0.225
KRMIN_RMIN (NW bh)	0.677	0.105	0.221	0.085	0.044	0.222

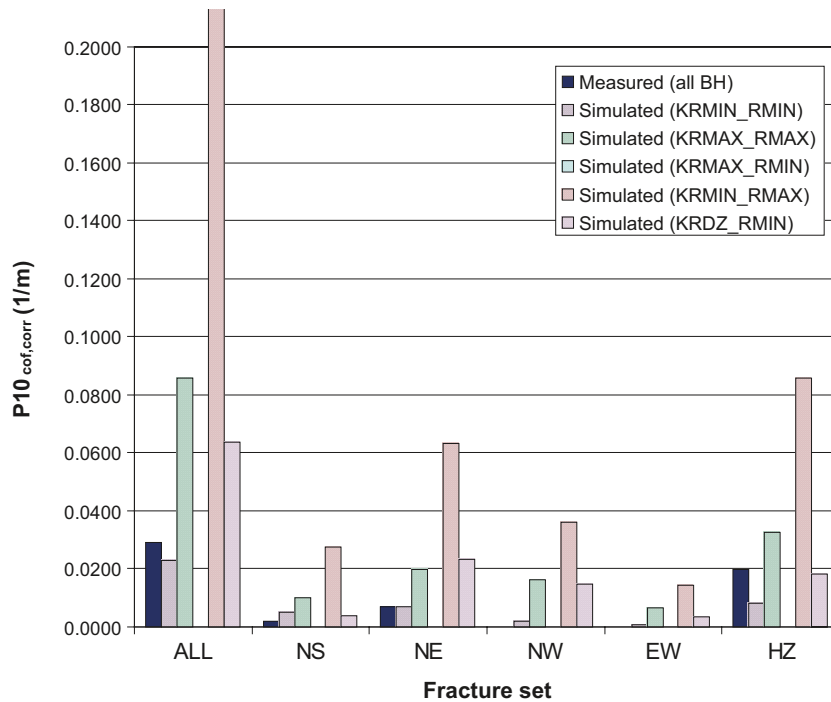


Figure 11-8. Graphical comparison of measured Terzaghi corrected linear intensities of open fractures, $P_{10,PFL,corr}$, for fracture domain FFM01 for each fracture set with simulation results of connected open fractures, $P_{10,cof,corr}$ for 10 realisation of a 1 km vertical borehole for different power-law size models.

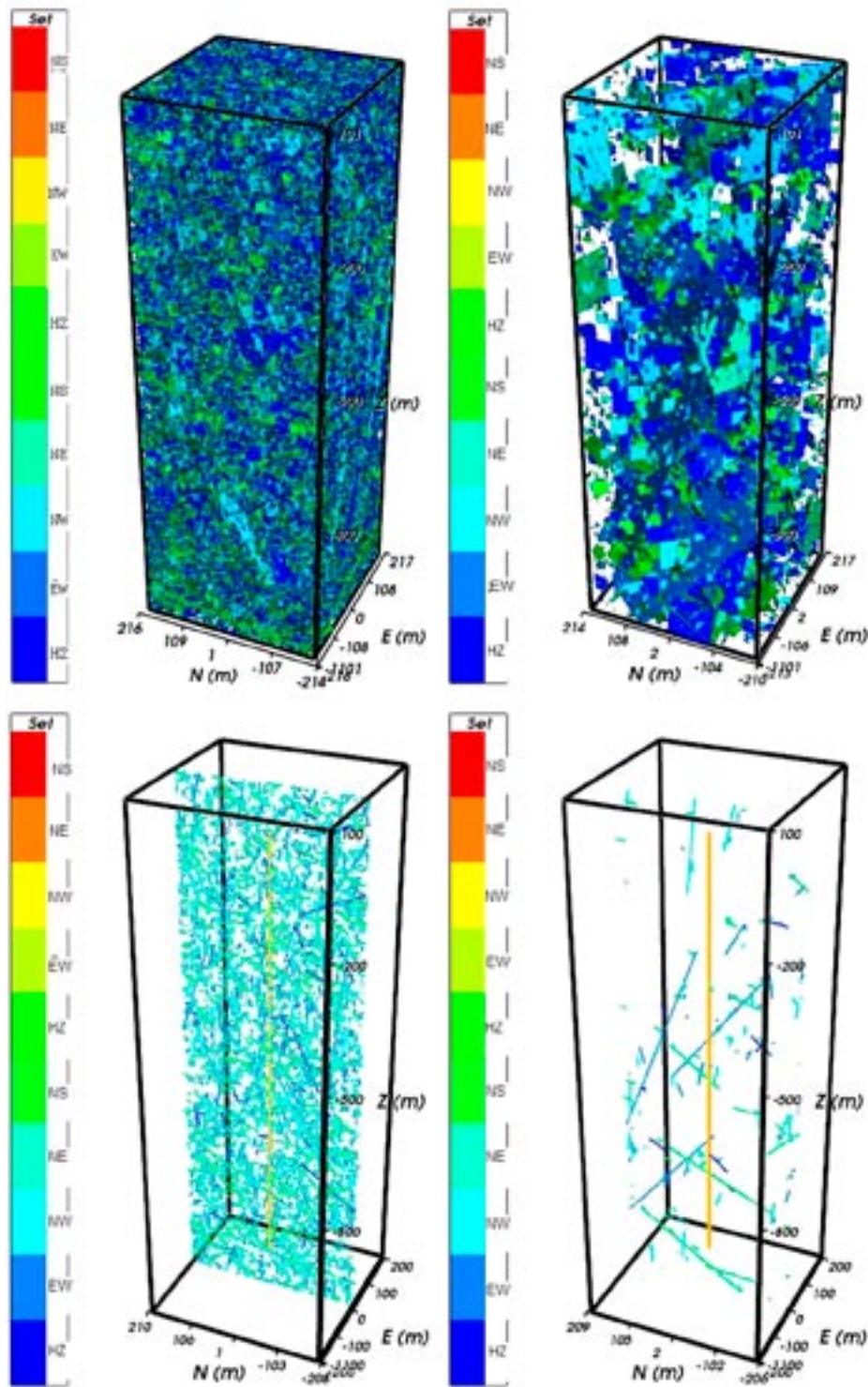


Figure 11-9. Visual comparison of connected open fractures for the very connected KRMIN_RMAX case (left) and KRMIN_RMIN case (right) for fracture domain FFM01 around a single vertical borehole. Top: 3D plots of all connected open fractures; Bottom: a vertical slice through the same networks. Fractures are coloured by fracture set (5 sets for large fractures $r > 1.1$ m, 5 for small $r_0 < r < 1.1$ m).

Finally, the sophistication of the model was increased to include the significant variations with depth above and below -400 m and check the performance of the model in reproducing the frequency of connected open fractures in these two depth zonations. In addition, a ‘fine-tuning’ of the power-law size parameters for each fracture set was carried out to produce an accurate match between $P_{10,cof,corr}$ and $P_{10,PFL,corr}$. The starting point for this was the KRMIN_RMIN case, since this gave the closest match, then the shape parameter, k_r , was modified for each set keeping the location parameter, r_0 , constant at 0.038 m. This optimised case is referred to as the KROPT_RMIN case. The complete DFN parameters for this case for the DFN above and below an elevation -400 m are given in Table 11-9. The input values for open fracture intensity are taken from Table 10-13 and Table 10-14 for above and below -400 m, respectively. The same power-law size distributions parameters are used for both elevations, but are different between sets. It is assumed that the large change in flow-anomaly frequency is due to the reduction in fracture intensity with depth. A comparison of the simulated intensity of connected open fractures, $P_{10,cof,corr}$, for the KRMIN_RMIN and KROPT_RMIN cases with the frequency of PFL flow-anomalies above and below -400 m are given in Table 11-10. The optimisation of size parameters was based on data above -400 m since the values are non-zero. Figure 11-10 illustrates graphically the match for the optimised case above and below -400 m for each set. Below -400 m, the model predicts very low mean connected open fracture intensities using the optimised model, but it does not reproduce the zeros observed in the data. Partly, this is to be expected since we are using a stochastic approach, and some realisations happen to have a small number of connected fractures intersecting the borehole. One way of reconciling the Hydro-DFN model is to also consider a depth variation in the hydraulic properties such that fractures below -400 m have a lower fracture transmissivity as well as intensity chosen so that a number of the fractures simulated below -400 m have transmissivities below the detection limit for PFL flow-anomalies. This aspect is explored in the flow simulations documented in Section 11.5.

Table 11-9. Description of DFN parameters for the KROPT_KRMIN simulations of open fractures in fracture domain FFM01 with depth dependency above and below -400 m elevation.

Fracture domain	Fracture set name	Orientation set pole: (trend, plunge), conc.	Size model, power-law (r_0 , k_r) (m, -)	Intensity ($P_{32,open}$) valid size interval: (r_0 , 560 m) (m^2/m^3)	Transmissivity model
FFM01 > -400 m	NS	(87, 2) 21.7	(0.038, 2.60)	0.125	–
	NE	(135, 3) 21.5	(0.038, 2.70)	0.339	
	NW	(41, 2) 23.9	(0.038, 3.10)	0.126	
	EW	(190, 1) 30.6	(0.038, 3.10)	0.083	
	HZ	(343, 80) 8.2	(0.038, 2.42)	0.374	
FFM01 < -400 m	NS	(87, 2) 21.7	(0.038, 2.60)	0.094	–
	NE	(135, 3) 21.5	(0.038, 2.70)	0.163	
	NW	(41, 2) 23.9	(0.038, 3.10)	0.098	
	EW	(190, 1) 30.6	(0.038, 3.10)	0.039	
	HZ	(343, 80) 8.2	(0.038, 2.42)	0.141	

Table 11-10. Comparison of measured Terzaghi corrected linear intensities of PFL fractures, $P_{10,PFL,corr}$ for fracture domain FFM01 above and below -400 m for each fracture set with simulation results of connected open fractures, $P_{10,cof,corr}$ for 10 realisations of a vertical borehole for the KRMIN_MIN and KROPT_RMIN power-law size models.

Case	ALL	NS	NE	NW	EW	HZ
Above -400 m						
Measured FFM01 (all bh)	0.070	0.006	0.015	0.000	0.000	0.049
KRMIN_RMIN	0.068	0.003	0.025	0.006	0.004	0.030
KROPT_RMIN	0.078	0.007	0.015	0.004	0.002	0.051
Below -400 m						
Measured FFM01 (all bh)	0.005	0.000	0.002	0.000	0.000	0.003
KRMIN_RMIN	0.007	0.002	0.002	0.000	0.001	0.003
KROPT_RMIN	0.006	0.001	0.001	0.000	0.000	0.004

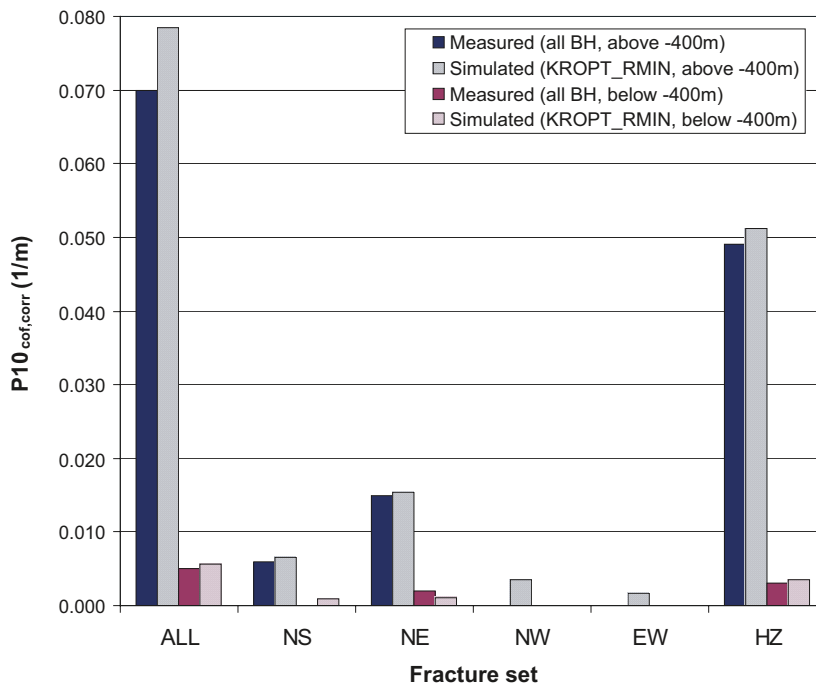


Figure 11-10. Graphical comparison of measured Terzaghi corrected linear intensities of PFL fractures, $P_{10,PFL,corr}$ for fracture domain FFM01 above and below -400 m for each fracture set with simulation results of connected open fractures, $P_{10,cof,corr}$ for 10 realisations of a vertical borehole for the KROPT_RMIN power-law size model.

Fracture domain FFM02

FFM02 is mapped primarily on the basis of approximately 100 m sections in 3 different boreholes all located above –400 m elevation, and so there is no need to consider depth dependency in this fracture domain. Again, an optimisation process was performed to derive a shape parameter, k_r , for each set assuming a location parameter, r_0 , of 0.038 m so as to reproduce a network with connected open fracture intensities consistent with the observed frequency of PFL fractures. Table 11-11 gives the full set of DFN parameters used to construct an optimised model. The resulting comparison of measured and simulated fracture frequencies for open and connected open fractures is given in Table 11-12 and illustrated in Figure 11-11. The fracture size parameters used are broadly consistent with FFM01 in that a high k_r , around 3 is used for the NW and EW sets, a value around 2.8 is used for the NE set, and a value around 2.6 or lower is used for the HZ set. The higher value of k_r , around 2.6 rather than 2.4, used in FFM02 compared to FFM01 for fracture domains located closely together in the footwall of ZFMA2 may indicate that actually 2.6 would be a good choice for the footwall of ZFMA2 overall, but the high intensities of flow-anomalies observed in FFM01 above –200 m elevation (see Table 10-12) drives the choice k_r down a bit in FFM01. From Figure 11-11 it is clear that the network of flowing fractures is anisotropic since it is dominated by the sub-horizontal set, and the NE and NS (actually NNE) sets.

Table 11-11. Description of DFN parameters for the KROPT_KRMIN simulations of open fractures in fracture domain FFM02 (which only exists above –400 m elevation).

Fracture domain	Fracture set name	Orientation set pole: (trend, plunge), conc.	Size model, power-law (r_0, k_r) (m, –)	Intensity ($P_{32,open}$) valid size interval: ($r_0, 560$ m) (m^2/m^3)	Transmissivity model
FFM02	NS	(87, 2) 21.7	(0.038, 2.86)	0.342	–
	NE	(135, 3) 21.5	(0.038, 2.68)	0.752	
	NW	(41, 2) 23.9	(0.038, 3.30)	0.335	
	EW	(190, 1) 30.6	(0.038, 3.40)	0.156	
	HZ	(343, 80) 8.2	(0.038, 2.65)	1.582	

Table 11-12. Comparison of measured Terzaghi corrected linear intensities of PFL fractures, $P_{10,PFL,corr}$, for fracture domain FFM02 for each fracture set with simulation results of connected open fractures, $P_{10,cof,corr}$, for 10 realisations of a vertical borehole for the KROPT_RMIN power-law size model.

Case	ALL	NS	NE	NW	EW	HZ
$P_{10,o,corr}$						
Measured FFM02 (all bh)	3.168	0.342	0.752	0.335	0.156	1.582
KROPT_RMIN	2.762	0.271	0.546	0.246	0.110	1.588
$P_{10,cof,corr}$						
Measured FFM02 (all bh)	0.326	0.015	0.081	0.003	0.000	0.227
KROPT_RMIN	0.364	0.025	0.074	0.015	0.004	0.246

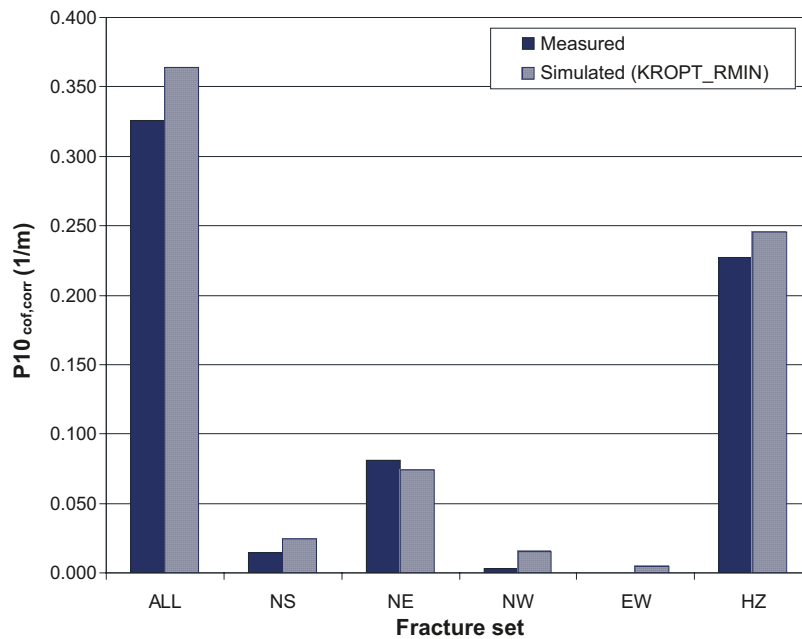


Figure 11-11. Graphical comparison of measured Terzaghi corrected linear intensities of PFL fractures, $P_{10,PFL,corr}$, for fracture domain FFM02 for each fracture set with simulation results of connected open fractures, $P_{10,cof,corr}$, for 10 realisations of a vertical borehole for the KROPT_RMIN power-law size model.

Fracture domain FFM03

FFM03 is intersected by mainly KFM02A and KFM03A and contains data from above and below -400 m elevation. As for FFM01, the data suggest a significantly higher intensity of both open and PFL fractures above -400 m, and so depth dependency is also considered in this fracture domain in a similar way to FFM01. An optimisation process was performed to derive a shape parameter, k_r , for each set assuming a location parameter, r_0 , of 0.038 m so as to reproduce a network with connected open fracture intensities consistent with the observed frequency of PFL fractures. Table 11-13 gives the full set of DFN parameters used to construct an optimised model. The resulting comparison of measured and simulated fracture frequencies for open fractures is given in Table 11-14 and Figure 11-12, and for connected open fractures in Table 11-15 and Figure 11-13. One problem for the simulations was a much higher proportion of NE oriented fractures below -400 m elevation than above, which made it hard to match both regions using the same size parameters for both depths. Hence, the choice of size parameters was a bit of a compromise with respect to the NE set. Figure 11-13 shows the choice of k_r values gives some very small numbers of flows in the NW and EW set below -400 m elevation that is not in the data, which point to the model needing low transmissivities in these sets. In simple terms, the match of the fracture size parameters for FFM03 seems to require a fairly isotropic model with k_r around 2.6 for all sets.

Table 11-13. Description of DFN parameters for the KROPT_KRMIN simulations of open fractures in fracture domain FFM03 with depth dependency above and below –400 m elevation.

Fracture domain	Fracture set name	Orientation set pole: (trend, plunge), conc.	Size model, power-law (r_0, k_r) (m, –)	Intensity ($P_{32,open}$) valid size interval: ($r_0, 560$ m) (m^2/m^3)	Transmissivity model
FFM03 > –400 m	NS	(87, 2) 21.7	(0.038, 2.60)	0.091	–
	NE	(135, 3) 21.5	(0.038, 2.50)	0.253	
	NW	(41, 2) 23.9	(0.038, 2.55)	0.258	
	EW	(190, 1) 30.6	(0.038, 2.40)	0.097	
	HZ	(343, 80) 8.2	(0.038, 2.55)	0.397	
FFM03 < –400 m	NS	(87, 2) 21.7	(0.038, 2.60)	0.102	–
	NE	(135, 3) 21.5	(0.038, 2.50)	0.243	
	NW	(41, 2) 23.9	(0.038, 2.55)	0.103	
	EW	(190, 1) 30.6	(0.038, 2.40)	0.068	
	HZ	(343, 80) 8.2	(0.038, 2.55)	0.250	

Table 11-14. Comparison of measured Terzaghi corrected linear intensities of open fractures, $P_{10,o,corr}$, for fracture domain FFM03 above and below –400 m for each fracture set with simulation results for 10 realisations of a vertical borehole for the KROPT_RMIN power-law size model.

Case	ALL	NS	NE	NW	EW	HZ
Above –400 m						
Measured FFM03 (all bh)	1.096	0.091	0.253	0.258	0.097	0.397
KROPT_RMIN	0.880	0.077	0.210	0.157	0.058	0.378
Below –400 m						
Measured FFM03 (all bh)	0.765	0.102	0.243	0.103	0.068	0.250
KROPT_RMIN	0.575	0.065	0.151	0.069	0.042	0.248

Table 11-15. Comparison of measured Terzaghi corrected linear intensities of PFL fractures, $P_{10,PFL,corr}$, for fracture domain FFM03 above and below –400 m for each fracture set with simulation results of connected open fractures, $P_{10,cof,corr}$, for 10 realisations of a vertical borehole for the KROPT_RMIN power-law size model.

Case	ALL	NS	NE	NW	EW	HZ
Above –400 m						
Measured FFM03 (all bh)	0.087	0.000	0.010	0.014	0.021	0.042
KROPT_RMIN	0.092	0.004	0.021	0.013	0.011	0.042
Below –400 m						
Measured FFM03 (all bh)	0.051	0.000	0.030	0.000	0.000	0.021
KROPT_RMIN	0.054	0.007	0.017	0.007	0.006	0.017

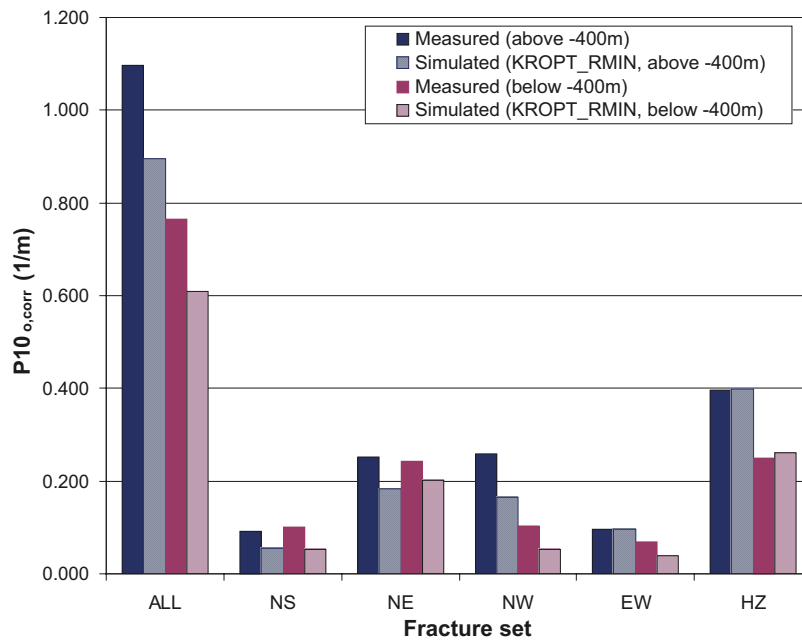


Figure 11-12. Graphical comparison of measured Terzaghi corrected linear intensities of open fractures, $P_{10,o,corr}$, for fracture domain FFM03 above and below -400 m for each fracture set with simulation results for 10 realisations of a vertical borehole for the KROPT_RMIN power-law size model.

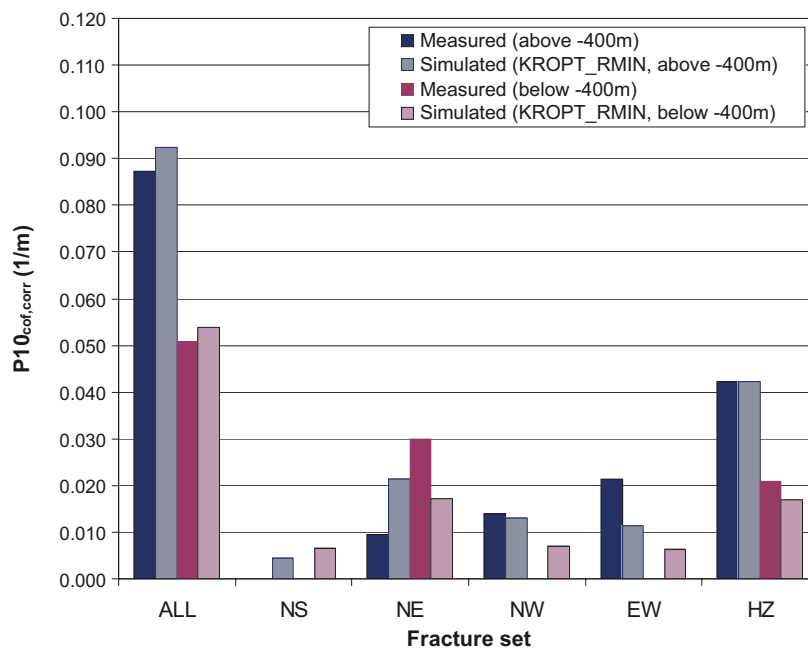


Figure 11-13. Graphical comparison of measured Terzaghi corrected linear intensities of PFL fractures, $P_{10,PFL,corr}$, for fracture domain FFM03 above and below -400 m for each fracture set with simulation results of connected open fractures, $P_{10,cof,corr}$, for 10 realisations of a vertical borehole for the KROPT_RMIN power-law size model.

11.4.4 Summary of findings

The results of the geometry and fracture network connectivity simulations can be summarised in the simplest terms that overall a power-law model with r_0 set to the borehole radius 0.04 m, and shape parameter k_r set to around 2.6 best represents the observation of open fractures mapped in cores and the flows mapped by the PFL-f technique. More specific details are that the NW and EW sets seem to be especially poorly connected, consistent with a k_r around 3.0 in fracture domains FFM01 and FFM02, and the NE also has perhaps a higher k_r of around 2.8 in the same domains. In contrast, the upper part of fracture domain FFM01 shows evidence of abnormally high connectivity requiring a lower k_r of around 2.4, at least for the sub-horizontal set.

The set definitions and orientation distributions derived for F 1.2, and maintained in the modelling here, have given an adequate framework for the preliminary modelling used here. However, the F 2.2 data suggests changing the NS set to NNE and making the sub-horizontal set significantly more concentrated in terms of a Univariate Fisher model. Given this study has shown that flow is dominated by a restricted number of sets – HZ, NE and NS – the suggested changes are only going to make the Hydro-DFN model more anisotropic.

11.5 Simulation of Posiva Flow Log (PFL-f) tests

To complete the Hydro-DFN parameterisation, flow simulations were performed to calibrate a set of alternative relationships between fracture transmissivity and size that reproduced the numbers of inflows and the distribution of their magnitude as measured in the PFL-f tests. The geometrical parameters used were taken from the optimised models developed from connectivity analysis in Section 11.3. The hydraulic calibration was performed for each of the fracture domains within the target host rock: FFM01, FFM02 and FFM03.

11.5.1 Modelling approach

A methodology to parameterise a Hydro-DFN model for PFL-f tests has been developed in previous studies /Hartley et al. 2005b/ for example. The primary calibration targets in those studies were the distribution of flow-rates per unit drawdown in the abstraction borehole, and the total flow to the borehole. The same approach is followed here using an identical model domain to that used in Section 11.3 for connectivity simulation, i.e. a 400 m horizontal cross-section and 1 km generic vertical boreholes within a 1,200 m deep domain such that there is 100 m of model above and below the borehole. To account for depth dependency in fracture intensity, the top 400 m of borehole are surrounded by a Hydro-DFN based on the parameters for rock above an elevation of –400 m, and the bottom 600 m of borehole are surrounded by rock that uses parameters for below –400 m elevation. Flow simulations are performed for 10 realisations of each fracture domain FFM01–FFM03. The boundary conditions used are zero head on the vertical sides and the top, no-flow on the bottom, and –10 m of head at the borehole to simulate the abstraction. The steady-state flow-field is then calculated using a DFN flow model to obtain the inflows to the boreholes at each fracture intersected by the borehole. The borehole is represented by a vertical line. An example of a flow simulation is shown in Figure 11-14. Here, the fractures are coloured by head, or coloured grey where they are not connected to the network. To assess the ‘goodness of fit’, the following statistics are calculated:

- Average total flow to the abstraction borehole over the 10 realisations.
- Histogram of flow rate to borehole divided by drawdown (notated Q/s) as an average over 10 realisations.
- Bar and whisker plot of minimum, mean minus standard deviation, mean, mean plus standard deviation, maximum of $\text{Log}_{10}(\text{Q/s})$ for the inflows within each fracture set taken over all realisations.
- The average numbers of fractures within each set giving inflows to the abstraction borehole above the measurement limit for the PFL-f tests.

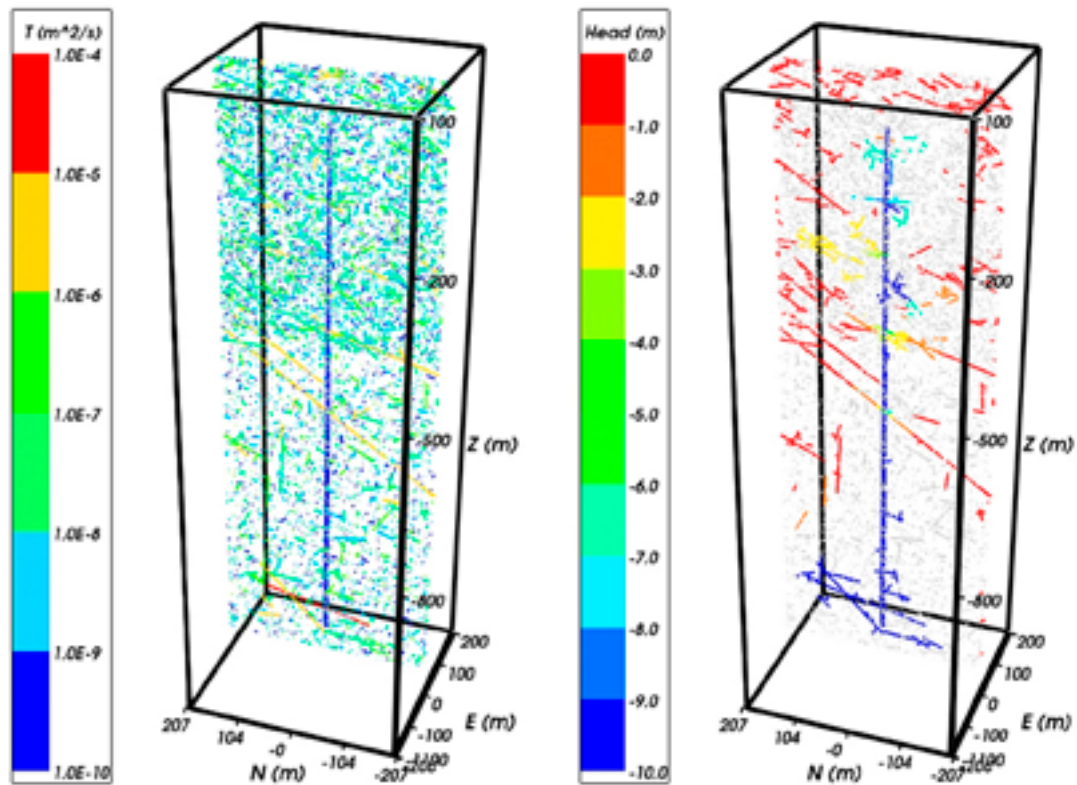


Figure 11-14. Vertical cross-section through one realisation of the Hydro-DFN model for the semi-correlated model of fracture domain FFM01 with different fracture intensity above and below -400 m elevation. Left: all open fractures coloured by transmissivity. The 1 km generic vertical borehole is coloured blue in the middle. Right: all open fractures coloured by drawdown with unconnected fractures coloured grey.

The only cases considered in the flow modelling were those based on the optimised power-law size distributions. In the initial modelling, the same transmissivity assignments were used for each fracture set and at each depth in order to quantify how well a simplistic model could reproduce the data. That is, in the first instance we try to explain variations in flow by variations in fracture intensity and the resultant network connectivity. Later, the necessity to introduce further complexity such as depth dependence in transmissivity and anisotropy between sets are discussed.

A key issue to assess in these simulations was to explore uncertainties that arise from assumptions made about the relationship between fracture transmissivity and size. Two extreme assumptions are to assume a direct correlation between transmissivity and size or to assume no correlation, or uncorrelated. Between these two extremes there is a continuous range of possibility that can be called semi-correlated, by which we imply that the mean transmissivity of a fracture increases with its size, but there is some random component or spread of values for any given fracture size. This is perhaps the most realistic situation. Hence, in the flow calibration the aim is to establish appropriate choices for the parameters for a correlated, semi-correlated and uncorrelated relationship between size and transmissivity that gives a match to the magnitude of the inflows.

11.5.2 Fracture size to transmissivity relationships

Fracture domain FFM01

The initial flow simulations of FFM01 contained a depth dependency only in terms of fracture intensity above and below -400 m elevation. One of the key objective measures of the performance of the simulations was to compare the measured total flow to boreholes within the relevant rock volume (e.g. FFM01 above -400 m) with the mean total over the realisations. The total flows were normalised to a 400 m section of borehole above -400 m, a 600 m section below above -400 m. This measure was used to adjust the overall magnitude of transmissivity, while histograms of Q/s were used to ensure fine-tuned parameters to get the right distribution of inflows to the pumped borehole. An initial guess for the parameters as specified in Table 11-16 was based on those used in the F 1.2 modelling. The transmissivity parameters were then modified to match the inflows above -400 m elevation and without any variation with depth. For each of the 3 transmissivity models, parameters were found that gave a reasonable match to the total flow above -400 m elevation as seen in Table 11-17. However, this model gave only slightly lower total flow rates, about a factor half, below -400 m whereas the PFL-f data suggested a factor $2 \cdot 10^{-4}$. Hence, it seems a necessity to introduce extra depth dependency to use a transmissivity of a factor 10^{-3} lower below -400 m in addition to the lower fracture intensity. The complete set of calibrated parameters for FFM01 is given in Table 11-18, which resulted in the total flows given in Table 11-19. A complete set of plots showing the comparison between the model simulations and the PFL-f data are given in Appendix B. The comparisons show that the semi-correlated and correlated model reproduce the numbers and shape of distribution of inflows reasonably well, giving a wedge shaped distribution characteristic of having some size-transmissivity correlation. The uncorrelated model is much flatter and less representative of the PFL-f data.

The relatively high flow rates above -400 m are actually concentrated at shallow depths, and hence the model was refined further to introduce a further depth zone in the top 200 m to give a 3 layer model: above -200 m, between -200 m and -400 m, and below -400 m. The measured open fracture intensities in each of these section was used as input data for the Hydro-DFN model and the transmissivity parameters were adjusted within each depth zone until a reasonable match to the inflow distribution and total flow was achieved. The resulting Hydro-DFN parameterisation for a 3 layer model of FFM01 is given in Table 11-20. It can be seen that the coefficients, exponents or standard deviations as appropriate to each transmissivity model are significantly lower for the band between -200 m and -400 m compared to above -400 m reflecting the rapid reduction in inflow magnitudes with depth. This trend is quantified in the comparison of measured and simulated total flow rate for each of the 3 transmissivity models tabulated in Table 11-21 measured. The flow rates decrease by about 2 orders of magnitude below -200 m, then by about another order of magnitude below -400 m.

Table 11-16. Initial transmissivity parameters used for all sets when matching PFL-f flow distribution based on F 1.2 Hydro-DFN.

Type	Description	Relationship	Parameters
Semi-correlated	Log-normal distribution about a power-law correlated mean	$\text{Log}_{10}T = \text{Log}_{10}(a r^b) + \sigma N(0.1)$	$a = 4.2 \cdot 10^{-8}$, $b = 0.6$, $\sigma = 1.0$
Correlated	Power-law relationship	$T = a r^b$	$a = 1.8 \cdot 10^{-9}$, $b = 1.0$
Uncorrelated	Log-normal distribution about a specified mean	$\text{Log}_{10}T = \mu + \sigma N(0.1)$	$\mu = -6.5$, $\sigma = 0.9$

Table 11-17. Initial comparison of total inflows to boreholes between PFL-f data and mean of 10 Hydro-DFN realisations of fracture domain FFM01 for a 2 layer without depth variations in transmissivity. The flow rates are normalised to a 400 m section above –400 m, and a 600 m section below –400 m.

Case	Total flow rate divided by drawdown Q/s [m ² /s]	
	FFM01 > –400 m per 400 m of borehole	FFM01 < –400 m per 600 m of borehole
PFL-f data	1.5·10 ⁻⁵	3.4·10 ⁻⁹
Semi-correlated	1.3·10 ⁻⁵	6.2·10 ⁻⁶
Correlated	1.7·10 ⁻⁶	8.1·10 ⁻⁶
Uncorrelated	9.1·10 ⁻⁶	4.2·10 ⁻⁵

Table 11-18. Description of Hydro-DFN parameters for the simulations of flow in open fractures in FFM01 with depth dependency above and below –400 m elevation.

Fracture domain	Fracture set name	Orientation set pole: (trend, plunge), conc.	Size model, power-law (r ₀ , k _r) (m, –)	Intensity (P _{32,open}) valid size interval: (r ₀ , 560 m) (m ² /m ³)	Transmissivity model Eq. (11-3) Eq. (11-2) Eq. (11-4)
FFM01 > –400 m	NS	(87, 2) 21.7	(0.038, 2.60)	0.125	Semi-correlated: (a,b,σ) (2.0·10 ⁻⁹ , 1.2, 1.0); Correlated: (a,b) (1.5·10 ⁻⁹ , 1.6); Uncorrelated: (μ, σ) (–7.0, 1.7)
	NE	(135, 3) 21.5	(0.038, 2.75)	0.339	
	NW	(41, 2) 23.9	(0.038, 3.10)	0.126	
	EW	(190, 1) 30.6	(0.038, 3.10)	0.083	
	HZ	(343, 80) 8.2	(0.038, 2.45)	0.374	
FFM01 < –400 m	NS	(87, 2) 21.7	(0.038, 2.60)	0.094	Semi-correlated: (a,b,σ) (2.0·10 ⁻¹² , 1.2, 1.0); Correlated: (a,b) (1.5·10 ⁻¹² , 1.6); Uncorrelated: (μ, σ) (–10.0, 1.7)
	NE	(135, 3) 21.5	(0.038, 2.75)	0.163	
	NW	(41, 2) 23.9	(0.038, 3.10)	0.098	
	EW	(190, 1) 30.6	(0.038, 3.10)	0.039	
	HZ	(343, 80) 8.2	(0.038, 2.45)	0.141	

Table 11-19. Comparison of total inflows to boreholes between PFL-f data and mean of 10 Hydro-DFN realisations of fracture domain FFM01 for a 2 layer with depth dependency in transmissivity as detailed in Table 11-18. The flow rates are normalised to a 400 m section above –400 m, and a 600 m section below –400 m.

Case	Total flow rate divided by drawdown Q/s [m ² /s]	
	FFM01 > –400 m per 400 m of borehole	FFM01 < –400 m per 600 m of borehole
PFL-f data	1.5·10 ⁻⁵	3.8·10 ⁻⁹
Semi-correlated	1.3·10 ⁻⁵	4.0·10 ⁻⁸
Correlated	1.7·10 ⁻⁶	2.6·10 ⁻⁸
Uncorrelated	9.1·10 ⁻⁶	4.3·10 ⁻⁸

Table 11-20. Description of Hydro-DFN parameters for the simulations of flow in open fractures in FFM01 with depth dependency above –200 m, –200 m to –400 m and below –400 m elevation.

Fracture domain	Fracture set name	Orientation set pole: (trend, plunge), conc.	Size model, power-law (r_0, K_r) (m, –)	Intensity ($P_{32,open}$) valid size interval: ($r_0, 560$ m) (m^2/m^3)	Transmissivity model Eq. (11-3) Eq. (11-2) Eq. (11-4)
FFM01 > –200 m	NS	(87, 2) 21.7	(0.038, 2.50)	0.073	Semi-correlated: (a, b, σ) ($6.3 \cdot 10^{-9}, 1.3, 1.0$); Correlated: (a, b) ($6.7 \cdot 10^{-9}, 1.4$); Uncorrelated: (μ, σ) (–6.7, 1.2)
	NE	(135, 3) 21.5	(0.038, 2.70)	0.319	
	NW	(41, 2) 23.9	(0.038, 3.10)	0.107	
	EW	(190, 1) 30.6	(0.038, 3.10)	0.088	
	HZ	(343, 80) 8.2	(0.038, 2.38)	0.543	
FFM01 –200 m to –400 m	NS	(87, 2) 21.7	(0.038, 2.50)	0.142	Semi-correlated: (a, b, σ) ($1.3 \cdot 10^{-9}, 0.5, 1.0$); Correlated: (a, b) ($1.6 \cdot 10^{-9}, 0.8$); Uncorrelated: (μ, σ) (–7.5, 0.8)
	NE	(135, 3) 21.5	(0.038, 2.70)	0.345	
	NW	(41, 2) 23.9	(0.038, 3.10)	0.133	
	EW	(190, 1) 30.6	(0.038, 3.10)	0.081	
	HZ	(343, 80) 8.2	(0.038, 2.38)	0.316	
FFM01 < –400 m	NS	(87, 2) 21.7	(0.038, 2.50)	0.094	Semi-correlated: (a, b, σ) ($5.3 \cdot 10^{-11}, 0.5, 1.0$); Correlated: (a, b) ($1.8 \cdot 10^{-10}, 1.0$); Uncorrelated: (μ, σ) (–8.8, 1.0)
	NE	(135, 3) 21.5	(0.038, 2.70)	0.163	
	NW	(41, 2) 23.9	(0.038, 3.10)	0.098	
	EW	(190, 1) 30.6	(0.038, 3.10)	0.039	
	HZ	(343, 80) 8.2	(0.038, 2.38)	0.141	

Table 11-21. Comparison of total inflows to boreholes between PFL-f data and mean of 10 Hydro-DFN realisations of FFM01 for a 3 layer model with depth dependency in transmissivity as detailed in Table 11-20. The flow rates are normalised to a 200 m section above –200 m and between –200 m and –400 m, and a 600 m section below –400 m.

Case	Total flow rate divided by drawdown Q/s [m^2/s]		
	FFM01 > –200 m per 200 m of borehole	–200 m < FFM01 < –400 m per 200 m of borehole	FFM01 < –400 m per 600 m of borehole
PFL-f data	$2.9 \cdot 10^{-5}$	$1.0 \cdot 10^{-7}$	$3.8 \cdot 10^{-8}$
Semi-correlated	$3.1 \cdot 10^{-5}$	$1.1 \cdot 10^{-7}$	$5.4 \cdot 10^{-8}$
Correlated	$3.0 \cdot 10^{-5}$	$2.0 \cdot 10^{-8}$	$5.4 \cdot 10^{-8}$
Uncorrelated	$1.4 \cdot 10^{-5}$	$2.1 \cdot 10^{-8}$	$8.1 \cdot 10^{-9}$

An example of the comparison of inflows between model and data is given for this 3 layer model using a semi-correlation between fracture size and transmissivity in Figure 11-15 and Figure 11-16. In Figure 11-16 a bar and whisker plot that compares the measured and simulated inflows, normalised to appropriate borehole length sections. The numbers alongside the bars represent the numbers of inflows per 200 m or 600 m sections of borehole corresponding to each set above the detection limit. The detection limit is assumed to be the minimum transmissivity measured for a flow-anomaly in the modelled volume ($2.5 \cdot 10^{-10} m^2/s$ for FFM01). This figure show the inflows are dominated by the HZ set with a small contribution from the NS and NE, and the NW and EW sets make no contribution. The frequency of inflows decreases by about a quarter below –200 m, by almost a further order of magnitude below –400 m. A complete set of comparisons for the 3 layer model is given in Appendix B. The matches for all three transmissivity models are reasonable. Given the strong variations with depth and the fact that a depth of around 400 m was considered for a repository in the SR-Can assessment, it is recommended that a 3 layer model be the basis for further hydrogeological modelling of fracture domain FFM01. It should be noted the top 200 m of FFM01 shows similar fracture hydrogeological characteristics to FFM02, as will be seen in the next section.

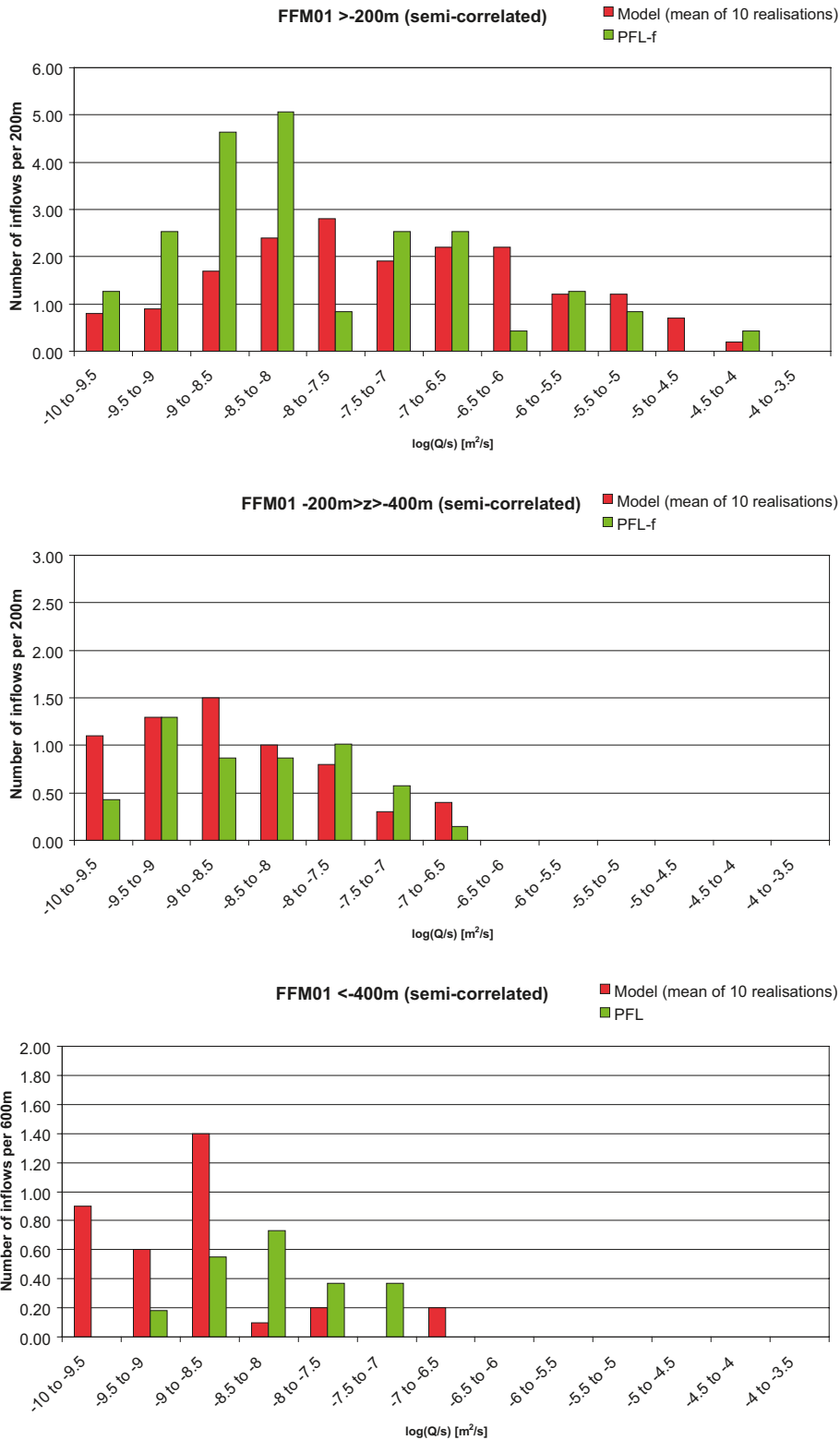


Figure 11-15. Histogram comparing the distribution of the magnitude of inflows divided by drawdown, Q/s , at abstraction boreholes in fracture domain FFM01 with a semi-correlated transmissivity (see Table 11-20 for parameter values). Top: above an elevation of -200 m; Middle: between -200 m and -400 m; Bottom: below -400 m. The PFL-f measurements are treated as ensemble over all boreholes sections within FFM01. Above -200 m and between -200 m and -400 m, the number of inflows is normalised with respect to a borehole section of 200 m length, and below -400 m relative to a 600 m section. The simulations represent statistics taken from an ensemble over 10 realisations of the HydroDFN model.

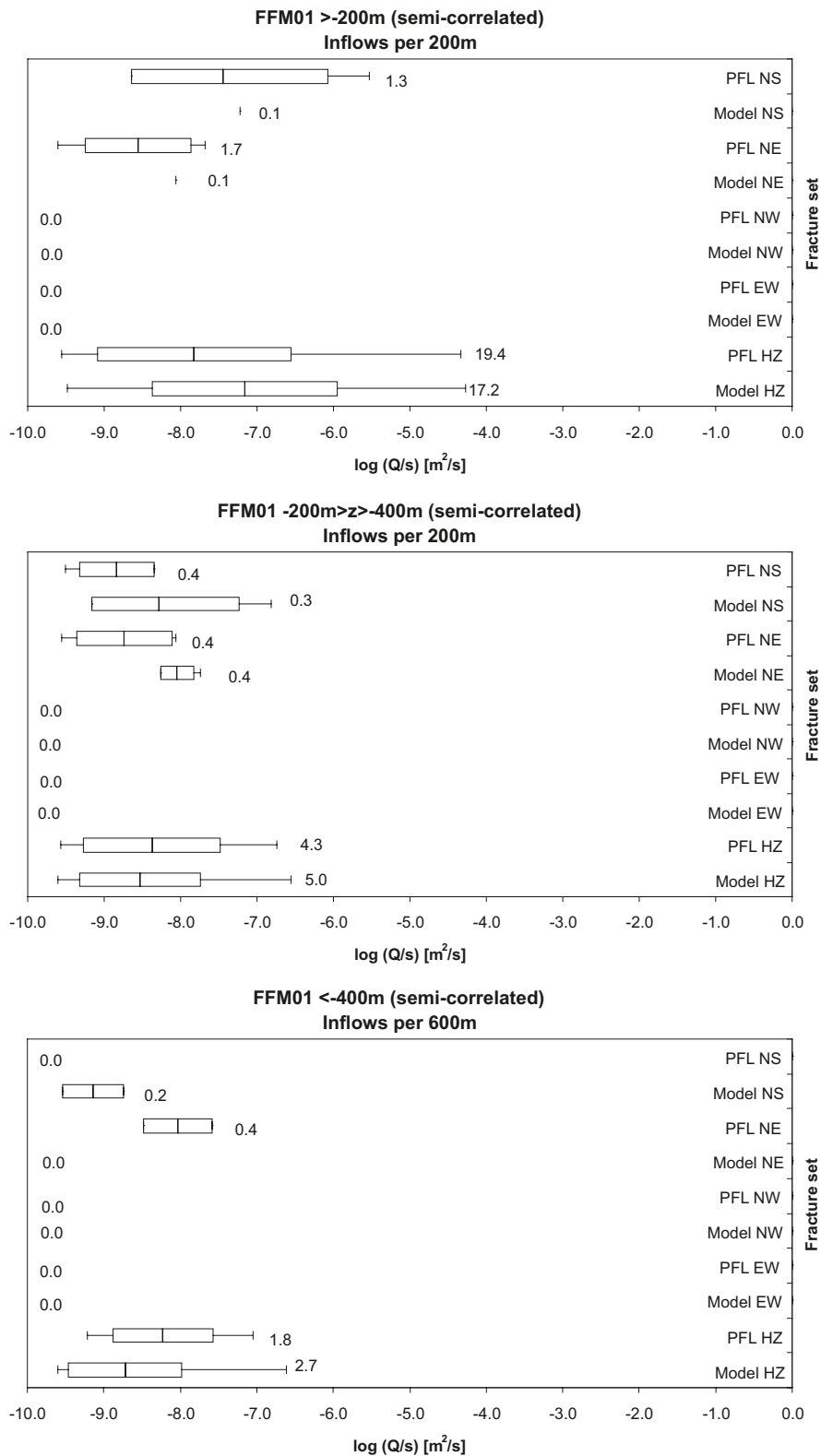


Figure 11-16. Bar and whisker plots comparing statistics taken over each fracture set for the individual inflows, Q/s , for the PFL-f data from borehole sections within FFM01 against statistics taken from an ensemble over 10 realisations of the Hydro-DFN model with a semi-correlated transmissivity. Top: above an elevation of -200 m; Middle: between -200 m and -400 m; Bottom: below -400 m. The centre of the bar indicates the mean value, the ends of the bar indicate ± 1 standard deviation, and the error bars indicate the minimum and maximum values. Above -200 m and between -200 m and -400 m, the total numbers of fractures with inflows per 200 m section of borehole above the detection limits is given; below -400 m the numbers of inflows per 600 m section of borehole is given. For the data, statistics are taken over the identified flow-anomalies within each set, and for the model are taken over the fractures generated within each set and an ensemble over 10 realisations.

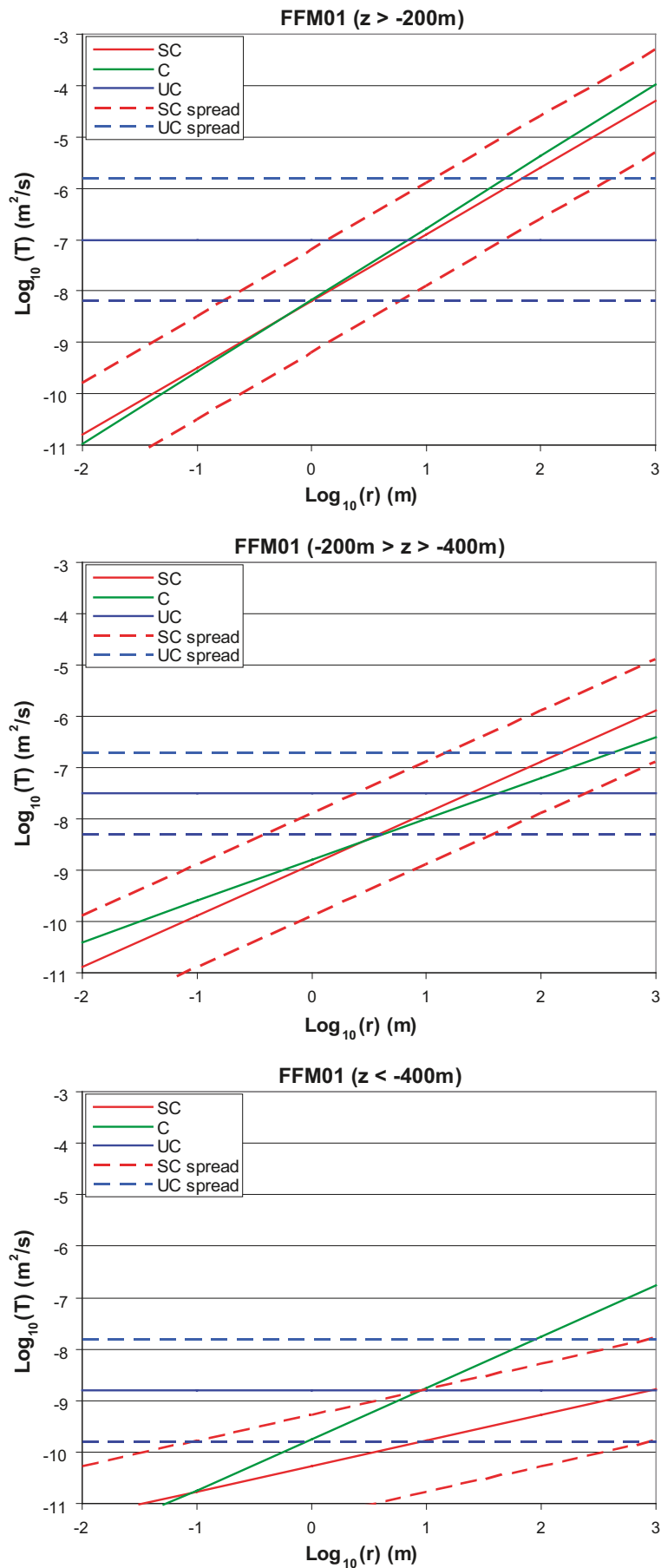


Figure 11-17. Plots of the profile of transmissivity as a function of fracture radius for the 3 layer model of fracture domain FFM01 for each of the 3 transmissivity versus size relationships (SC = semi-correlated, C = correlated, UC = uncorrelated) based on the parameterisation given in Table 11-20.

To illustrate how the different transmissivity-size relationships compare, they are plotted as log-log plots in Figure 11-17 for each of the 3 depth layers based on the parameters given in Table 11-20. The semi-correlated and correlated follow similar trends and also intercept the uncorrelated model for fractures of about 10 m radius. This to be expected since fractures around 10–100 m are the ones that form the connected network giving the inflows in the simulations. There is less consistency between the transmissivity models below –400 m as the distribution of inflows is poorly determined at these depths, there being so few data points to guide the fit.

Fracture domain FFM02

FFM02 is limited to the upper section of bedrock above about –200 m, so no depth variations are considered. The Hydro-DFN parameters derived FFM02 are given in Table 11-22. Example comparisons of the match for the semi-correlated case are given in Figure 11-18 to Figure 11-19, and the total flows are given in Table 11-23. The magnitudes of flow for this fracture domain are similar to FFM01 above –200 m, but here the frequency of inflows is about twice as high. A complete set of simulation results and their comparison to the PFL-f data is given in Appendix B. The semi-correlated and correlated models give the best match to the shape of distribution of inflows. Again, the HZ set dominates with small contributions from the NE and NS sets. An illustration of the 3 alternative modelled relationships between fracture transmissivity and size is given in Figure 11-20.

Table 11-22. Description of Hydro-DFN parameters for the simulations of flow in open fractures in FFM02 (which only exists above about –200 m elevation).

Fracture domain	Fracture set name	Orientation set pole: (trend, plunge), conc.	Size model, power-law (r_o, k_r) (m, –)	Intensity ($P_{32,open}$) valid size interval: ($r_o, 560$ m) (m^2/m^3)	Transmissivity model Eq. (11-3) Eq. (11-2) Eq. (11-4)
FFM02	NS	(87, 2) 21.7	(0.038, 2.75)	0.342	Semi-correlated: (a, b, σ); ($9.0 \cdot 10^{-9}$, 0.7, 1.0) Correlated: (a, b) ($5.0 \cdot 10^{-9}$, 1.2); Uncorrelated: (μ, σ) (–7.1, 1.1)
	NE	(135, 3) 21.5	(0.038, 2.62)	0.752	
	NW	(41, 2) 23.9	(0.038, 3.20)	0.335	
	EW	(190, 1) 30.6	(0.038, 3.40)	0.156	
	HZ	(343, 80) 8.2	(0.038, 2.58)	1.582	

Table 11-23. Comparison of total inflows to boreholes between PFL-f data and mean of 10 Hydro-DFN realisations of FFM02 with the flow rates normalised to a 200 m section.

Case	Total flow rate divided by drawdown Q/s [m^2/s] FFM02 > per 200 m of borehole
PFL-f data	$8.5 \cdot 10^{-6}$
Semi-correlated	$6.1 \cdot 10^{-6}$
Correlated	$8.1 \cdot 10^{-6}$
Uncorrelated	$5.4 \cdot 10^{-6}$

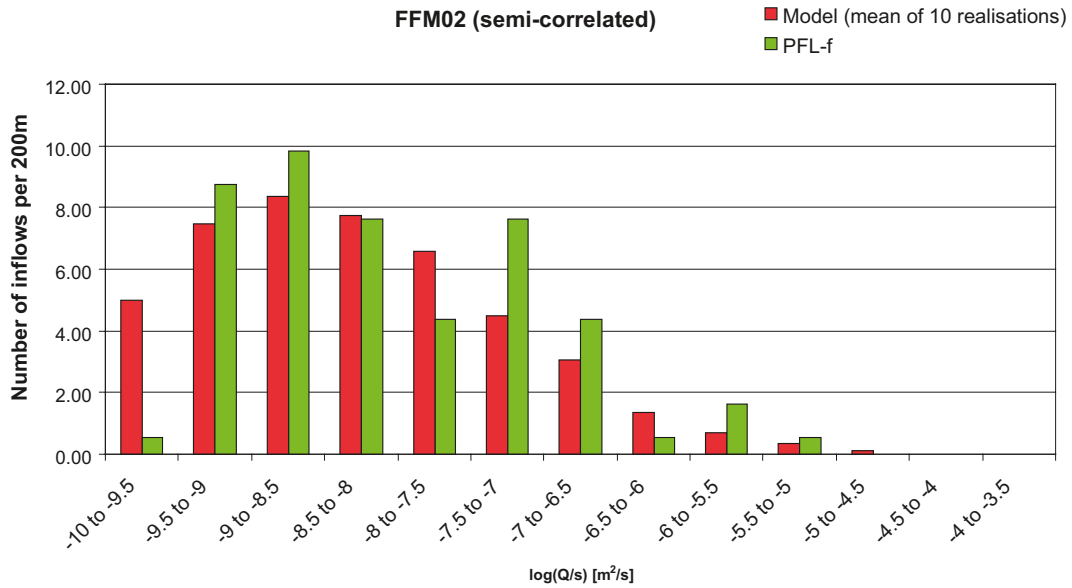


Figure 11-18. Histogram comparing the distribution of the magnitude of inflows divided by drawdown, Q/s , at abstraction boreholes in FFM02 with a semi-correlated transmissivity (see Table 11-22 for parameter values). The PFL-f measurements are treated as ensemble over all boreholes sections within FFM02. The number of inflows is normalised with respect to a borehole section of 200 m length. The simulations statistics are taken from an ensemble over 10 realisations of the Hydro-DFN model.

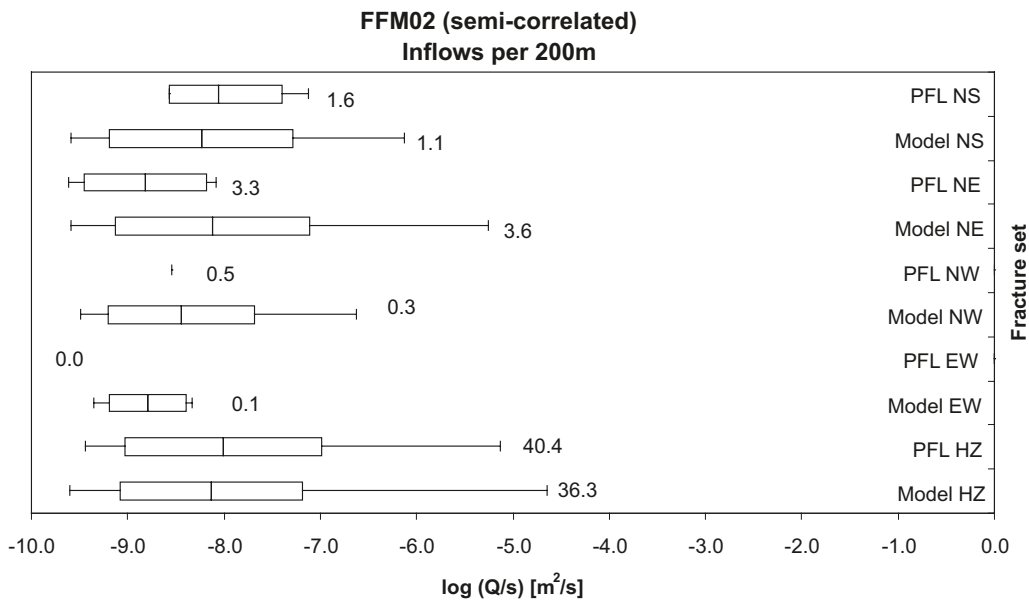


Figure 11-19. Bar and whisker plots comparing statistics taken over each fracture set for the individual inflows, Q/s , for the PFL-f data from borehole sections within FFM02 against statistics taken from an ensemble over 10 realisations of the Hydro-DFN model with a semi-correlated transmissivity. The centre of the bar indicates the mean value, the ends of the bar indicate ± 1 standard deviation, and the error bars indicate the minimum and maximum values. The total numbers of fractures with inflows per 200 m section of borehole above the detection limits is given. For the data, statistics are taken over the identified flow-anomalies within each set, and for the model are taken over the fractures generated within each set and an ensemble over 10 realisations.

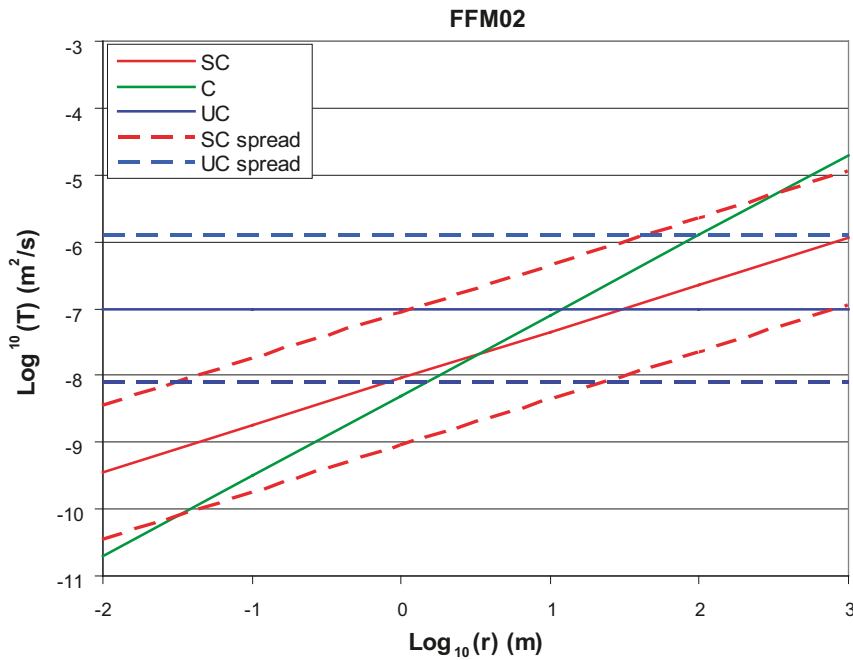


Figure 11-20. Plots of the profile of transmissivity as a function of fracture radius for FFM02 for each of the 3 transmissivity versus size relationships (SC = semi-correlated, C = correlated, UC = uncorrelated) based on the parameterisation given in Table 11-22.

Fracture domain FFM03

The variation of fracture intensity and flow in FFM03 is much less dramatic than in FFM01. Compared to FFM01, the flow rates in FFM03 are much lower than the top 200 m of FFM01, but higher than those in the middle section of FFM01 between -200 m and -400 m. The transmissivity relationships used for the upper and lower sections of FFM03 to get a match are very similar with a weak depth dependency in total flow arising from a change in the frequency of open fractures. The Hydro-DFN parameters used are given in Table 11-25, and the comparison of total inflows to the upper and lower depth zones between the model simulations and the PFL-f data are tabulated in Table 11-24. An example of the match for FFM03 is given as bar and whisker plots for each of the two depths using a semi-correlated transmissivity-size model is given in Figure 11-21. This shows that once again the HZ set dominates, but unusually each of the other 4 sub-vertical sets also contribute to flow giving a more isotropic flow hydraulic behaviour than the other fracture domains. A complete set of matching results for FFM03 is presented in Appendix B. The 3 transmissivity to size relationships derived are compared graphically for both depth zones in Figure 11-22.

Table 11-24. Comparison of total inflows to boreholes between PFL-f data and mean of 10 Hydro-DFN realisations of FFM03 for a 2 layer model with depth dependency in transmissivity as detailed in Table 11-25. The flow rates are normalised to a 400 m section above –400 m, and a 600 m section below –400 m.

Case	Total flow rate divided by drawdown Q/s [m ² /s]	
	FFM03 > –400 m per 400 m of borehole	FFM03 < –400 m per 600 m of borehole
PFL-f data	8.8·10 ⁻⁷	4.9·10 ⁻⁷
Semi-correlated	9.9·10 ⁻⁷	5.2·10 ⁻⁷
Correlated	8.7·10 ⁻⁷	3.9·10 ⁻⁷
Uncorrelated	8.2·10 ⁻⁷	2.9·10 ⁻⁷

Table 11-25. Description of DFN parameters for the simulations of flow in open fractures in FFM03 with depth dependency above and below –400 m elevation.

Fracture domain	Fracture set name	Orientation set pole: (trend, plunge), conc.	Size model, power-law (r_o, k_r) (m, –)	Intensity ($P_{32,open}$) valid size interval: ($r_o, 560$ m) (m ² /m ³)	Transmissivity model Eq. (11-3) Eq. (11-2) Eq. (11-4)
FFM03 > –400 m	NS	(87, 2) 21.7	(0.038, 2.60)	0.091	Semi-correlated: (a, b, σ); (1.3·10 ⁻⁸ , 0.4, 0.8) Correlated: (a, b) (1.4·10 ⁻⁸ , 0.6); Uncorrelated: (μ, σ) (–7.2, 0.8)
	NE	(135, 3) 21.5	(0.038, 2.50)	0.253	
	NW	(41, 2) 23.9	(0.038, 2.55)	0.258	
	EW	(190, 1) 30.6	(0.038, 2.40)	0.097	
	HZ	(343, 80) 8.2	(0.038, 2.55)	0.397	
FFM03 < –400 m	NS	(87, 2) 21.7	(0.038, 2.60)	0.102	Semi-correlated: (a, b, σ); (1.8·10 ⁻⁸ , 0.3, 0.5) Correlated: (a, b) (7.1·10 ⁻⁹ , 0.6); Uncorrelated: (μ, σ) (–7.2, 0.8)
	NE	(135, 3) 21.5	(0.038, 2.50)	0.247	
	NW	(41, 2) 23.9	(0.038, 2.55)	0.103	
	EW	(190, 1) 30.6	(0.038, 2.40)	0.068	
	HZ	(343, 80) 8.2	(0.038, 2.55)	0.250	

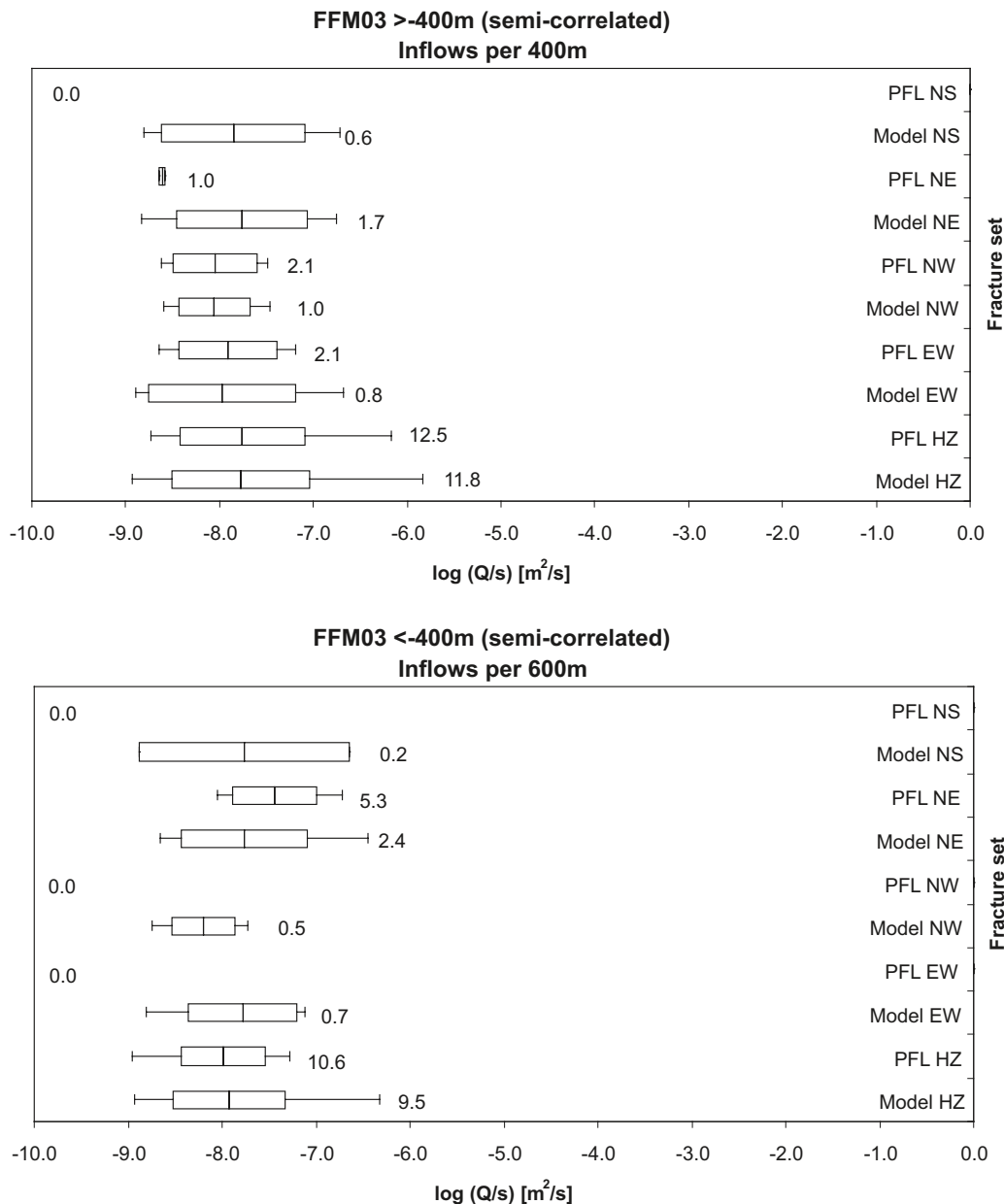


Figure 11-21. Bar and whisker plots comparing statistics taken over each fracture set for the individual inflows, Q/s , for the PFL-f data from borehole sections within FFM03 against statistics taken from an ensemble over 10 realisations of the Hydro-DFN model with a semi-correlated transmissivity. Top: above an elevation of -400 m; Bottom: below an elevation of -400 m. The centre of the bar indicates the mean value, the ends of the bar indicate ± 1 standard deviation, and the error bars indicate the minimum and maximum values. Above -400 m the total numbers of fractures with inflows per 400 m section of borehole above the detection limits is given; below -400 m the numbers of inflows per 600 m section of borehole is given. For the data, statistics are taken over the identified flow-anomalies within each set, and for the model are taken over the fractures generated within each set and an ensemble over 10 realisations.

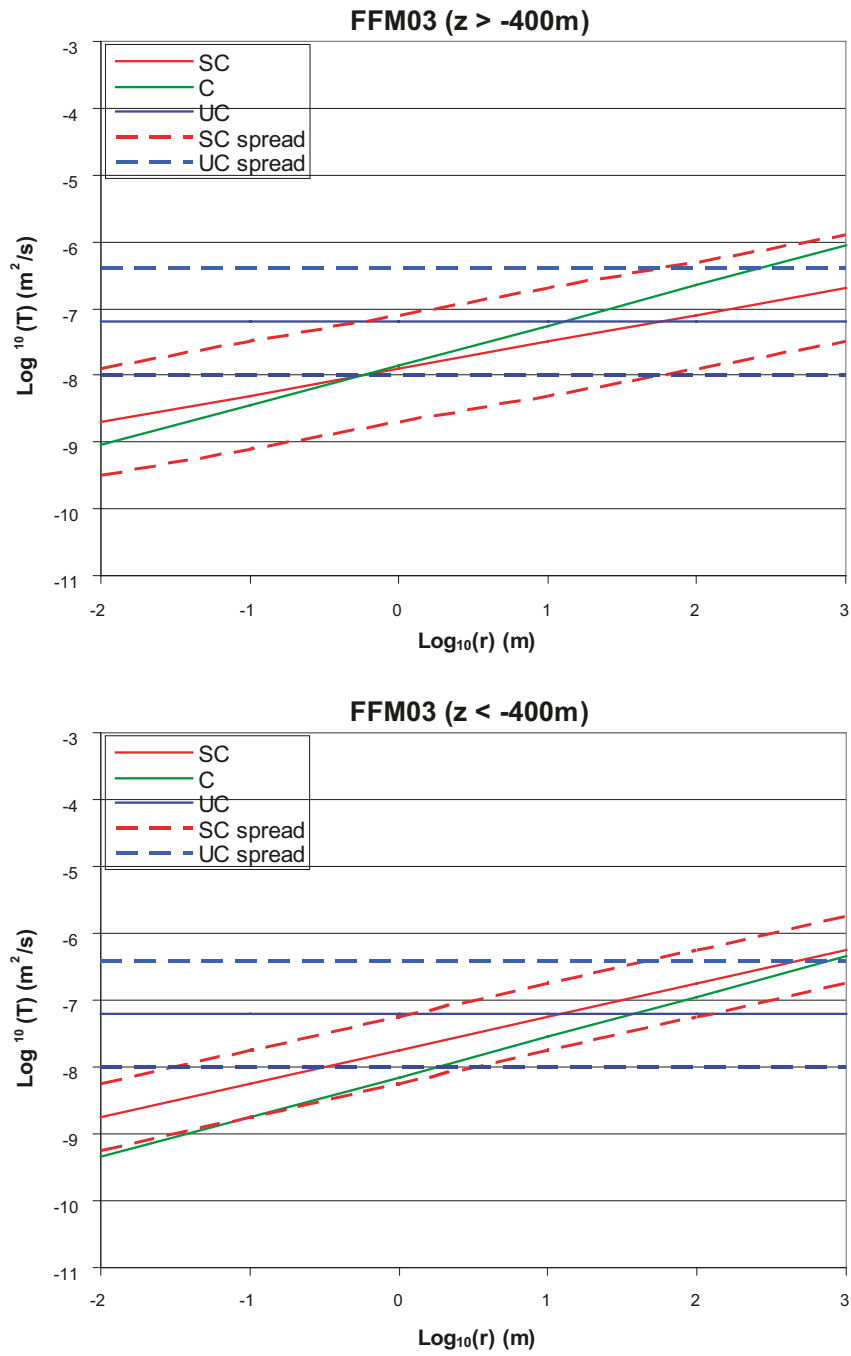


Figure 11-22. Plots of the profile of transmissivity as a function of fracture radius for a 2 layer model of FFM03 for each of the 3 transmissivity versus size relationships (SC = semi-correlated, C = correlated, UC = uncorrelated) based on the parameterisation given in Table 11-25.

11.6 Suggested update on sets for open fractures based on stage 2.2 data

Based on stereonet plots of the sub-vertical fractures corresponding to the open fracture and PFL fracture categories, updated hard sector definitions are suggested in Table 11-26 appropriate for use in a Hydro-DFN model based on all cored drilled borehole data for F 2.2. One key change is to modify the sectors to introduce a NNE set to replace the NS set. This is primarily driven by the presence of the NNE set in the key PFL fracture category that represents measured flow. It is difficult to differentiate this set clearly on the stereonet for open fractures (see Figure 11-23) from the NE set since the 2 sets overlap, although it does show up on the stereonet for PFL fractures (see Figure 11-24) and in a small number of zones in the deformation zone model. Figure 11-23 and Figure 11-24 have the alternative hard sectors superimposed on the stereonet.

Table 11-26. Suggestion for hard sector set definitions and recommended Univariate Fisher distribution parameters based on open fractures in F 2.2 borehole data. The data in the upper row are suggested for FFM01, FFM03–FFM06, whereas the data in the lower row (printed in italics) are suggested for FFM02.

Set	Orientation Fisher distribution (trend, plunge), concentration	Trend	Plunge	Dip	Strike
1 NS	(292, 1) 17.8 <i>(83, 10) 16.9</i>	90–130, 270–310 <i>240–280, 60–100</i>	0–40 <i>0–40</i>	50–90 <i>50–90</i>	0–40, 180–220 <i>330–10, 150–190</i>
2 NE	(326, 2) 14.3 <i>(143, 9) 11.7</i>	130–170, 310–350 <i>310–350, 130–170</i>	0–40 <i>0–40</i>	50–90 <i>50–90</i>	40–80, 220–260 <i>220–260, 40–80</i>
3 NW	(60, 6) 12.9 <i>(51, 15) 12.1</i>	30–90, 210–270 <i>20–80, 200–260</i>	0–40 <i>0–40</i>	50–90 <i>50–90</i>	120–180, 300–360 <i>110–190, 290–350</i>
4 EW	(15, 2) 14.0 <i>(12, 0) 13.3</i>	350–30, 170–210 <i>350–30, 170–210</i>	0–40 <i>0–40</i>	50–90 <i>50–90</i>	80–120, 260–300 <i>80–120, 260–300</i>
5 HZ	(5, 86) 15.2 <i>(71, 87) 20.4</i>	0–360 <i>0–360</i>	40–90 <i>40–90</i>	0–50 <i>0–50</i>	0–360 <i>0–360</i>

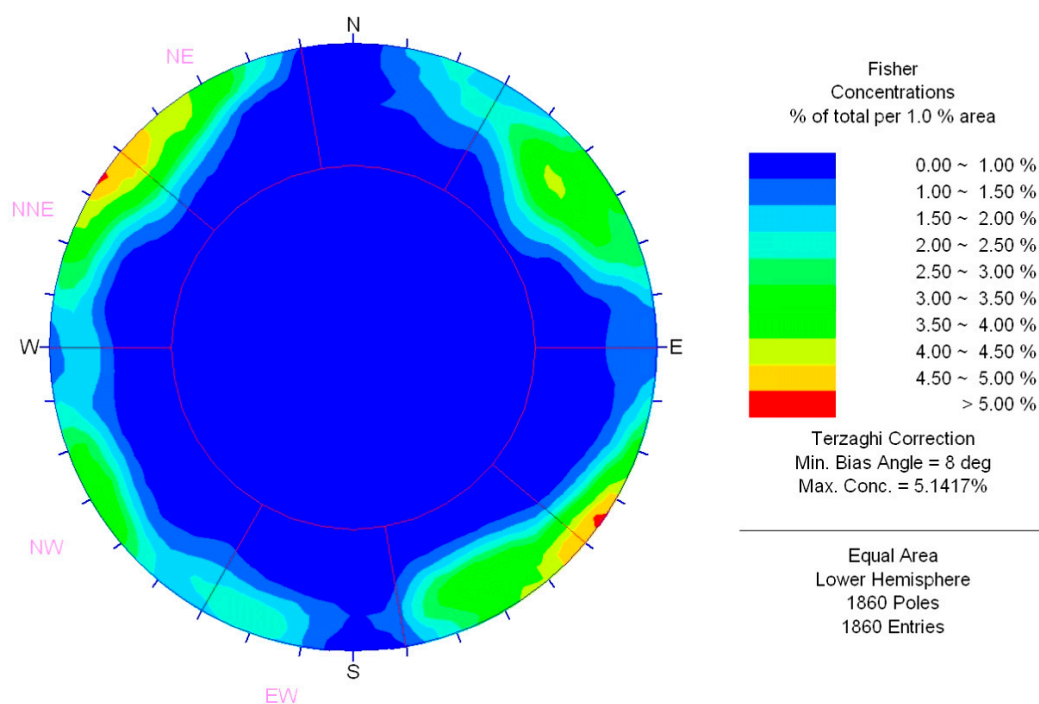


Figure 11-23. Fisher concentration plot for sub-vertical open fractures within fracture domains FFM01–06 and any borehole. The concentrations are Terzaghi corrected and use an equal area lower hemisphere projection.

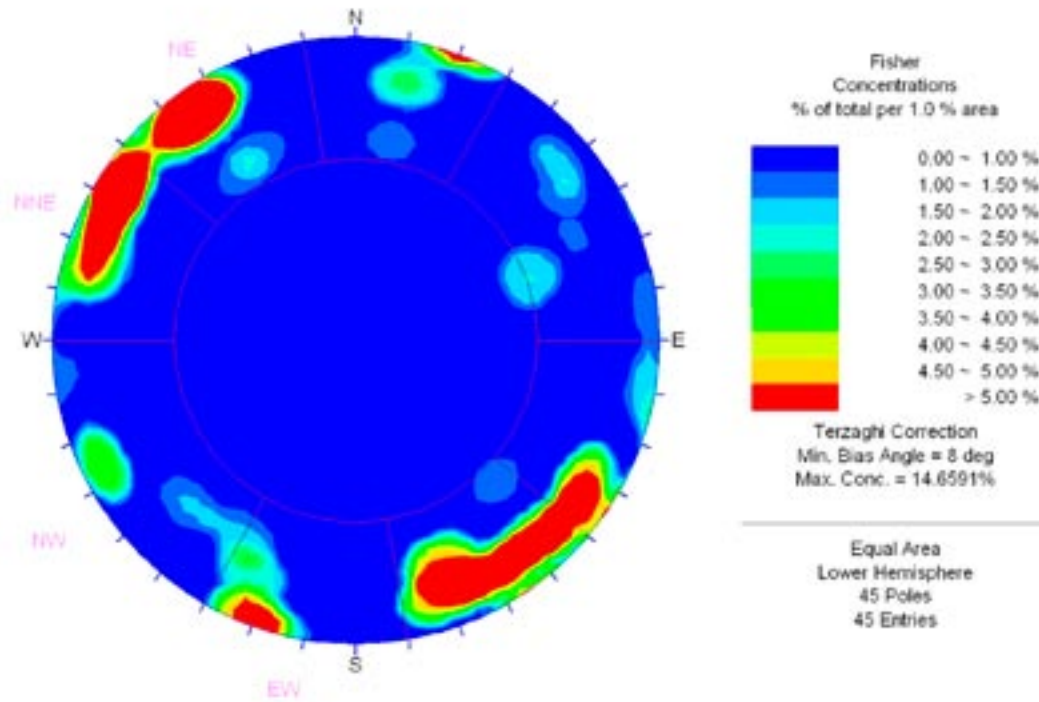


Figure 11-24. Fisher concentration plot for sub-vertical PFL fractures within fracture domains FFM01–06 and any borehole. The concentrations are Terzaghi corrected and use an equal area lower hemisphere projection.

Table 11-26 also gives revised parameters for Univariate Fisher distributions for each set. The parameters are based on fitting equal area stereonet using a Terzaghi weighting. Notably, the NW and EW sub-vertical sets become less concentrated, presumably because of the variations in fracture orientation between a larger number of boreholes, and the sub-horizontal set has become more concentrated. This alternative definition of the sets has been derived merely to indicate how much the sets might change using F 2.2 data, and to consider the restricted set of fractures appropriate to hydrogeology rather than all fractures as considered in the Geo-DFN. All subsequent modelling in study still uses the F 1.2 sets and orientation distributions.

11.7 Recommendations for implementation of DFN in groundwater flow models

The Hydro-DFN will form the basis for assigning hydraulic and transport properties in the groundwater flow calculations carried out in the upcoming F 2.2 hydrogeological site descriptive modelling. There, the approach will be to generate explicitly a DFN model and then convert this to an equivalent continuum porous medium (ECPM) model to simulate flow and solute transport on the regional scale. The transformation between explicit fractures to equivalent continuum properties is performed for each finite-element in the ECPM model using upscaling methods based on DFN flow simulations for the fracture network formed within each finite-element. The first step then is to generate a DFN model that covers the candidate area and the immediate vicinity. A natural choice for the volume in which a DFN model is generated is the rock volume covered by the six fracture domains FFM01–FFM06. However, a Hydro-DFN parameterisation has only been developed for FFM01, FFM02 and FFM03 (Section 11.5), which leaves the question of how to parameterise a Hydro-DFN for FFM04, FFM05 and

FFM06 since they have very limited data. FFM06 is within the candidate area, but as yet has very little data. Based on the description of the fracture domains in Section 3 and the fracture statistics in Table 10-9, it is proposed that FFM06 is assumed to have the same DFN properties as FFM01. FFM04 and FFM05 lie in the periphery of the candidate area. Based on the statistics in Table 10-17, Table 10-18 and Table 10-19, FFM05 seems to be similar to FFM03, while FFM04 is of slightly higher hydraulic conductivity, but the statistical significance of the data for these fracture domains is very limited being based on about 120–150 m of borehole data. It is proposed that fracture domains FFM04 and FFM05 are assumed to have the same properties as FFM03. For convenience, the 3D visualisation of the locations of the fracture domains shown in Figure 3-8 is repeated in Figure 11-25.

Outside of the fracture domains there are no core-drilled boreholes, and so a simplified approach will have to be used by defining homogeneous hydraulic properties based on well yield from water supply wells, for example.

11.7.1 Stochastic and semi-deterministic DFN models

For the fracture domains, several realisations of a stochastic DFN model will be used to parameterise a corresponding number of realisations of regional-scale ECPM groundwater flow models. Such DFN realisations can be expected to reflect the flow characteristics within each fracture domain in a statistical sense since the Hydro-DFN has been calibrated against PFL-f data, but the occurrence of particular flows and their magnitudes will not occur exactly as observed, and so the realisations can be viewed as unconditioned. In areas of relatively high intensity of flowing fractures, such as FFM02 and the upper part of FFM01, there are likely

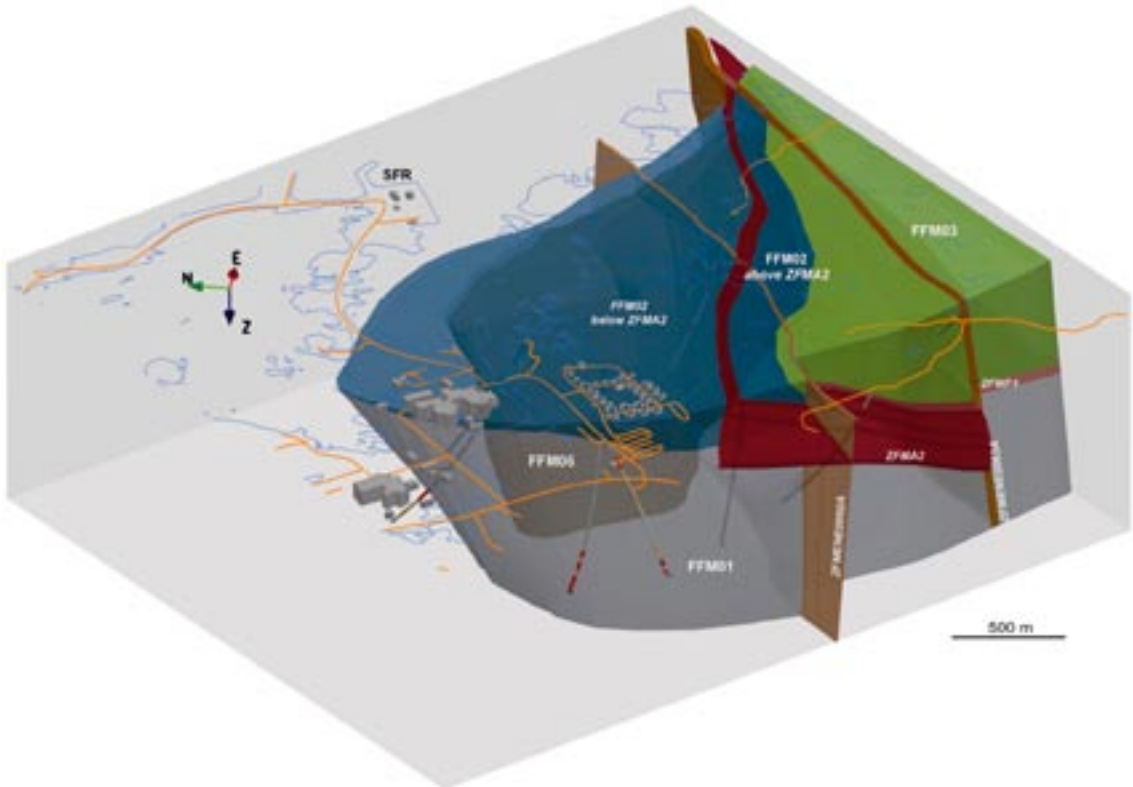


Figure 11-25. 3D visualisation of the fracture domains in and around the candidate area (FFM01, FFM02, FFM03 and FFM06). The view is from the south west.

to be several stochastic fractures with an element of the ECPM, typically 20 m contributing to the equivalent hydraulic property of the element, and so the locations and transmissivity of individual parameters is perhaps less important. However, in the base of FFM01, below –400 m, flowing fractures are much less frequent than the size of the elements in the ECPM model, and hence the locations where the limited numbers of flows occur become more important. Therefore, some method of conditioning the stochastic DFN realisations locally where flow data is available needs to be implemented to give semi-deterministic realisations that are consistent with the observations at the boreholes, but still reflect the statistics developed by the Hydro-DFN model where data is unavailable.

The positions, orientations and transmissivities of flowing features intercepting the boreholes in fracture domain FFM01 below 400 m depth are known and have been tabulated in Section 5. The size of the fractures is unknown, but they should be at least long enough to connect with more dense fracture near the surface, and so a radius of about 500 m could be an initial guess. As part of the geological characterisation some flowing features belong to the mapped deterministic deformation zone model, while others are described as possible deformation zones are as part of the background fracture domain. A methodology proposed for producing mixed stochastic and semi-deterministic models would follow the following steps:

1. Generate a stochastic DFN model based on the Hydro-DFN parameterisation for FFM01.
2. Perform a connectivity analysis and remove any fractures that are isolated or dead-ends.
3. Insert the hydraulic conditioning boreholes and remove any connected fractures with transmissivities above the PFL-f detection limit, about 10^{-9} m²/s, that intersect the boreholes in FFM01 below 400 m depth.
4. Insert the deterministic fractures with a radius chosen such that the total area of the inserted fractures is similar to that of the fractures removed in Step 3.

11.8 Summary

A set of parameterisations for a Hydro-DFN model for fracture domains FFM01, FFM02 and FFM03 necessary for the F 2.2 groundwater flow modelling has been derived here. A set of power-law size models for open fractures have been derived for each fracture domain and each fracture set based on a network connectivity analysis compared with the frequency of flowing features observed in the PFL-f hydraulic tests. DFN flow simulations based on 10 realisations have been used as a basis for deriving possible relationships between fracture transmissivity and size. A direct correlation, no correlation and a semi-correlation between fracture size and transmissivity has been considered as alternative models to quantify uncertainties. Although it is difficult to establish which of these models may best reflect reality, all three models give similar ranges of transmissivities for fractures in the size range 10–100 m, and so in fact all three models are likely to show similar flow characteristics.

The key aspect for Forsmark is that fracture domain FFM01 shows very strong variations with depth, and so it is suggested that Hydro-DFN be split into 3 layers: above –200 m, between –200 m and –400 m, and below –400 m. FFM01 is also very anisotropic, being dominated by the HZ set, and only a small contribution from the NE and possibly NS sets. The top layer of FFM01 is similar to the Hydro-DFN parameters for FFM02. FFM03 has less variation with depth and is comparable to the middle section of FFM01, but is more isotropic.

Recommendations have been made for the modelling of several aspects of the hydrogeological modelling for F 2.2 including semi-deterministic DFN models below –400 m.

12 Summary and conclusions

The work reported here collates the structural-hydraulic information gathered in 21 cored boreholes and 32 percussion-drilled boreholes belonging to Forsmark site description, modelling stage 2.2. The analyses carried out provide the hydrogeological input descriptions of the bedrock in Forsmark needed by the end users Repository Engineering, Safety Assessment and Environmental Impact Assessment; that is, hydraulic properties of deformation zones and fracture domains. The same information is also needed for constructing 3D groundwater flow models of the Forsmark site and surrounding area.

The analyses carried out render the following conceptual model regarding the observed heterogeneity in deformation zone transmissivity:

- We find the geological division of the deterministically modelled deformation zones into eight categories (sets) useful from a hydrogeological point of view. Seven of the eight categories are steeply dipping, WNW, NW, NNW, NNE, NE, ENE and EW, and one is gently dipping, G.
- All deformation zones, regardless of orientation (strike and dip), are subjected to a substantial decrease in transmissivity with depth. The data gathered suggest a contrast of c. 20,000 times for the uppermost one kilometre of bedrock, i.e. more than four orders of magnitude. The hydraulic properties below this depth are not investigated.
- The lateral heterogeneity is also substantial but more irregular in its appearance. For instance, for a given elevation and deformation zone category (orientation), the spatial variability in transmissivity within a particular deformation zone appears to be as large as the variability between all deformation zones. This suggests that the lateral correlation length is shorter than the shortest distance between two adjacent observation points and shorter than the category spacing.
- The observation that the mean transmissivity of the gently-dipping deformation zones is c. one to two orders of magnitude greater than the mean transmissivities of all categories of steeply-dipping deformation zones may be due to the anisotropy in the stress field, where the maximum stress is horizontal and has an azimuth of c. 140°. The hypothesis is supported by the deformation zones that strike WNW and NW. These two categories of steeply-dipping deformation zones have, relatively speaking, higher mean transmissivities than steeply-dipping deformation zones in other directions.

Key hydrogeological aspects of the fracture domains modelled are:

- We find the geological division of the bedrock in between the deterministically deformation zones to fall into six fracture domains useful from a hydrogeological point of view. In fact, the suggested division is consistent with the hydrogeological modelling approach reported for modelling stage 1.2.
- Three fracture domains together cover the potential repository area below the gently dipping deformation zone ZFMA2; these are FFM01, FFM02 and FFM06. One fracture domain covers the bedrock above this zone, FFM03. The remaining fracture domains, FFM04 and FFM05, border the candidate area. For modelling stage 2.2, hydrogeological data are available from hydraulic tests carried out in FFM01–FFM03 mainly. However, the work reported here suggests hydrogeological DFN (Hydro-DFN) properties for all fracture domains, FFM01–06.
- The work leading to the proposed Hydro-DFN parameters reported here is carried out in four steps:

- a) hydraulic analysis of the flow rate data measured at the borehole test sections,
- b) statistical analysis of mapped borehole fracture frequencies,
- c) 3D discrete fracture network connectivity modelling, and
- d) 3D discrete fracture network flow modelling.

The flow rate data are measured with two types of test methods, difference flow logging (notated PFL-f), and double-packer injection tests (notated PSS). The two test methods are run in parallel for a majority of the boreholes investigated. We demonstrate in the work reported here that the differences observed in terms of measured flow rates at the tested borehole intervals reflect how the two types of hydraulic testing are carried out, and that, due to the significant differences in the test configuration, the two test methods sense different properties of the fracture network system. In conclusion, we advocate that it is incorrect to assume that the PSS data necessarily can resolve the fracture transmissivity distribution to a lower measurement threshold than the PFL-f difference flow logging data, which is the impression one gets if PSS data are cross-plotted against PFL-f data without consideration of the differences in test configuration. However, the data gathered with the PSS method suggest that open fractures exist although they are poorly connected (compartmentalised) and have little or no flow. Based on the flow logging investigations made prior to pumping we conclude that the boreholes drilled in Forsmark increase the connectivity of the naturally flowing fractures.

The statistical analysis of mapped borehole fracture frequencies is straight forward in terms of data handling. The major assumptions in the work reported here are: (i) there are five fracture sets (NS, NE, NW, EW and HZ), (ii) the division of all fractures into “sealed fractures”, “open fractures” and “partly open fractures” is relevant, and (iii) the sampling bias caused by the orientation of the borehole trajectory can be compensated for using a weighting factor (called Terzaghi correction). In this work we adopted the geological DFN model reported for modelling stage 1.2 with regard to items (i) and (ii). However, we collated the open and partly open fractures into one population (called “open fractures” for simplicity reasons). Regarding item (iii), we used a Terzaghi correction factor of seven. With these assumptions the results from the statistical analysis carried out suggests:

- The corrected frequency of open fractures (notated $P_{10,o,corr}$) in the potential target fracture domain FFM01 above the elevation -400 m RHB 70 is c. 1.05 m^{-1} and c. 0.54 m^{-1} below. The corresponding figures for the corrected frequency of flowing open fractures with a flow rate greater than c. 30 mL/h (notated $P_{10,PFL,corr}$) are 0.070 m^{-1} and 0.005 m^{-1} , respectively.
- The dominating fracture sets among the open fractures above the elevation -400 in FFM01 are NE (32% of $P_{10,o,corr}$) and HZ (36%), and below this elevation NE (30%) and HZ (26%). The dominating fracture sets among the flowing open fractures above the elevation -400 in FFM01 are NE (21% of $P_{10,PFL,corr}$) and HZ (70%), and below this elevation NE (40%) and HZ (60%).

The fracture connectivity analysis undertaken is a cornerstone in SKB’s systems approach to hydrogeological modelling in the site descriptive modelling (SDM). The methodology is based on the capabilities of the PFL-f method to detect flowing open fractures and was developed during modelling stage 1.2. The methodology provides a means to calibrate the fracture size distribution, where the values of $P_{10,o,corr}$ and $P_{10,PFL,corr}$ deduced in the aforementioned statistical analysis are used as calibration targets. The DFN model used in the work reported here has the same key geometrical components as the geological DFN model reported for Forsmark in modelling stage 1.2, however, the parameter values used reflect the greater amount of data available in modelling stage 2.2. The key geometrical components are: (i) five fracture sets (NS, NE, NW, EW and HZ), which are assumed to be Fisher distributed, (ii) fracture size is power-law distributed (notated “tectonic continuum”), and (iii) the spatial distribution of the fracture centre positions in 3D are random and uncorrelated (Poisson process). With these assumptions the results from the connectivity analysis undertaken for the potential target fracture domain FFM01 suggest that the HZ fracture set has much longer fractures than the other fracture sets. The power-law shape factors (notated as k_r) are 2.38 for the HZ set, 2.50 for the NS set, 2.70 for the NE set and 3.10 for the NW and EW sets.

The flow simulations carried out apply the findings from the previous steps. A series of ten DFN realisations were generated using three different relationships between fracture transmissivity and fracture size – directly correlated, semi-correlated and completely uncorrelated – as alternative models to quantify uncertainty in fracture transmissivity. The parameters for each model were calibrated against the measured flow rates gathered from the hydraulic testing with PFL-f method. Although it is difficult to establish which of these models may best reflect reality, all three models give similar ranges of transmissivities for fractures in the size range 10-100 m, and so in fact all three models are likely to show similar flow characteristics. However, if one relationship is to be used over the others, the choice would be the semi-correlated model.

- The key aspect for Forsmark is that the corrected conductive fracture frequency for the potential fracture domain FFM01 shows very strong variations with depth, and so it is suggested that the Hydro-DFN be split into three layers: above the elevation –200, between the elevations –200 and –400, and below the elevation –400. FFM01 is also very anisotropic, being dominated by the HZ set, and only with a small contribution from the NE and possibly NS sets. The top layer of fracture domain FFM01 is similar to the Hydro-DFN parameters for fracture domain FFM02. FFM03 has less variation with depth and is comparable to the middle section of FFM01, but is more isotropic. Data for fracture domain FFM06, which is also a part of the potential target bedrock, will be treated in modelling stage 2.3. Pending this information, it is envisaged that fracture domain FFM06 can be modelled in the same fashion as fracture domain FFM01. Fracture domains FFM04 and FFM05 lie in the periphery of the candidate area. Based on the statistical analysis, FFM05 seems to be similar to FFM03, while FFM04 is of slightly higher hydraulic conductivity, but the statistical significance of the data for these fracture domains is very limited, being based on about 120-150 m of borehole data. It is proposed that fracture domains FFM04 and FFM05 are assumed to have the same properties as FFM03. For convenience, the 3D visualisation of the locations of the fracture domains shown in Figure 3-8 and Figure 11-25 is repeated in Figure 12-1.

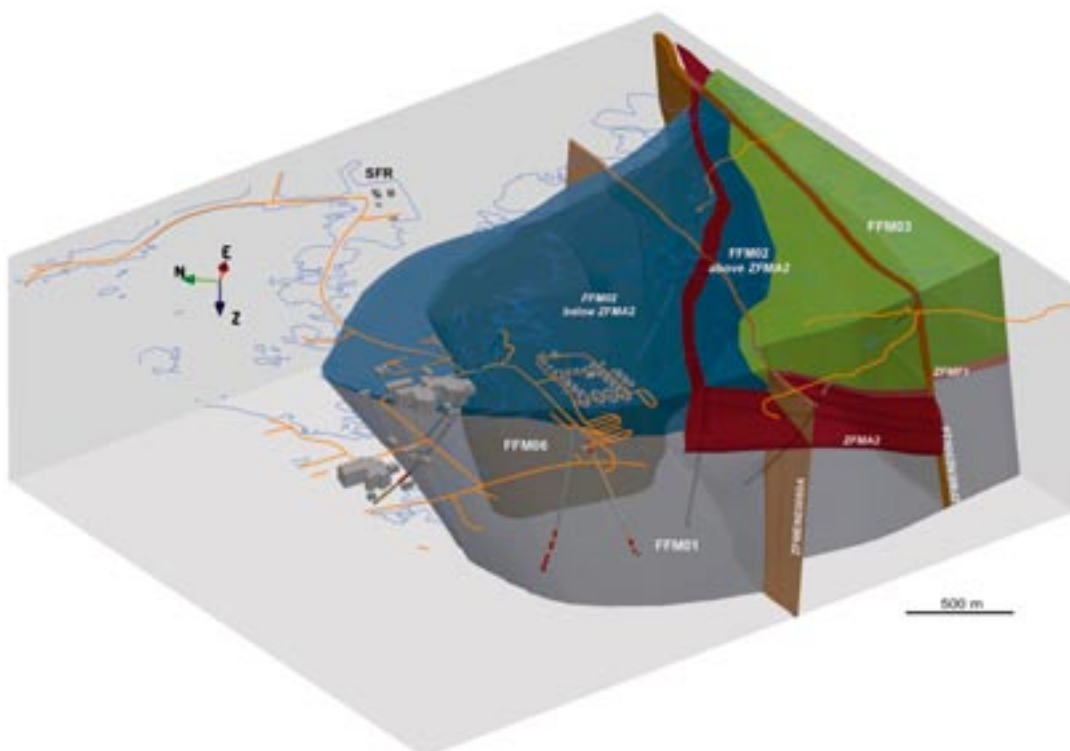


Figure 12-1. 3D visualisation of the fracture domains in and around the candidate area (FFM01, FFM02, FFM03 and FFM06). The view is from the south west.

Finally, comments and recommendations are made in the report as a guidance for several aspects in forthcoming hydrogeological discrete fracture network and groundwater flow models. The comments and recommendations address the following matters:

- fracture set definitions reflecting observations made for all boreholes in modelling stage 2.2, i.e. the geological DFN results reported for modelling stage 2.2,
- semi-deterministic DFN modelling of so called possible deformation zones below the elevation –400 m RHB 70 in the potential target fracture volume, and
- fracture domains outside the candidate area where there are no cored boreholes.

For the conclusions drawn in the work reported here these three matters are of minor importance.

13 References

- Andersson J, Ström A, Almén K-E, Ericsson LO, 2000.** Vilka krav ställer djupförvaret på berget? Geovetenskapliga lämplighetsindikationer och kriterier för lokalisering och plats-utvärdering. SKB R-00-15, Svensk Kärnbränslehantering AB.
- Bosson E, Berglund S, 2006.** Near-surface hydrogeological model of Forsmark. Open repository and solute transport applications – Forsmark 1.2. SKB R-06-52, Svensk Kärnbränslehantering AB.
- Barker J A, 1988.** A generalised radial flow model for hydraulic tests in fractured rock, *Water Resour. Res.*, v. 24, 1796-1804.
- Carlsson A, Christiansson R, 2007.** Construction experiences from underground works at Forsmark. Compilation Report. SKB R-07-10, Svensk Kärnbränslehantering AB.
- Carlsten S, Gustafsson J, Sandström R, Wallin L, Taxén C, 2005.** Forsmark site investigation, Geological single-hole interpretation of KFM08A, KFM08B and HFM22 (DS8). SKB P-05-262, Svensk Kärnbränslehantering AB.
- Drew D J, Vandergraaf T T, 1989.** Construction and operation of a high-pressure radioisotope migration apparatus. Atomic Energy of Canada Limited Technical Record, TR-476.
- Earlougher R C, 1977.** *Advances in Well Test Analysis*, Henry L. Doherty Series, 5. SPE, Dallas.
- Follin S, Stigsson M, Svensson U, 2005a.** Variable-density groundwater flow simulations and particle tracking – numerical modelling using DarcyTools. Preliminary site description Simpevarp subarea – stage 1.2. SKB R-05-11, Svensk Kärnbränslehantering AB.
- Follin S, Stigsson M, Svensson U, 2005b.** Regional hydrogeological simulations for Forsmark – numerical modelling using DarcyTools. Preliminary site description Forsmark area – stage 1.2. SKB R-05-60, Svensk Kärnbränslehantering AB.
- Follin S, Ludvigson J-E, Levén J, 2006a.** A comparison between standard well test evaluation methods used in SKB's site investigations and the Generalised Radial Flow concept. SKB P-06-54, Svensk Kärnbränslehantering AB.
- Follin S, Stigsson M, Svensson U, 2006b.** Hydrogeological DFN modelling using structural and hydraulic data from KLX04. Preliminary site description Laxemar subarea – stage 1.2. SKB R-06-24, Svensk Kärnbränslehantering AB.
- Follin S, Stigsson M, Svensson U, 2007a.** Sensitivity of the connected open fracture surface area per unit volume to the orientation, size and intensity of Poissonian discrete fracture network (DFN) models. SKB R-07-28, Svensk Kärnbränslehantering AB.
- Follin S, Johansson P-O, Levén J, Hartley L, Holton D, McCarthy R, Roberts D, 2007b.** Updated strategy and test of new concepts for groundwater flow modelling in Forsmark in preparation of site descriptive modelling stage 2.2. SKB R-07-20, Svensk Kärnbränslehantering AB.
- Forsman I, Zetterlund M, Rhén I, 2004.** Forsmark site investigation. Correlation of Posiva Flow Log anomalies to core mapped features in KFM01A to KFM05A. SKB R-04-77, Svensk Kärnbränslehantering AB.

- Forssman I, Zetterlund M, Forsmark T, Rhén I, 2006.** Forsmark site investigation, Correlation of Posiva Flow Log anomalies to core mapped features in KFM06A and KFM07A. SKB P-06-56, Svensk Kärnbränslehantering AB.
- Hartley L, Hoch A, Hunter F, Jackson P, Marsic N, 2005a.** Regional hydrogeological simulations – numerical modelling using Connectflow. Preliminary site description Simpevarp subarea – stage 1.2. SKB R-05-12, Svensk Kärnbränslehantering AB.
- Hartley L, Cox I, Hunter F, Jackson P, Joyce S, Swift B, Gylling B, Marsic N, 2005b.** Regional hydrogeological simulations for Forsmark – numerical modelling using CONNECTFLOW, Preliminary site description Forsmark area – stage 1.2. SKB R-05-32, Svensk Kärnbränslehantering AB.
- Hartley L, Hunter F, Jackson P, McCarthy R, Gylling B, Marsic N, 2006.** Regional hydrogeological simulations using CONNECTFLOW, Preliminary site description Laxemar subarea – stage 1.2. SKB R-06-23, Svensk Kärnbränslehantering AB.
- HydroSOLVE Inc., 2007.** AQTESOLV v. 4.5, Reston.
- LaPointe P, Olofsson I, Hermanson J, 2005.** Statistical model of fractures and deformation zones for Forsmark. Preliminary site description Forsmark area – stage 1.2. SKB R-05-26, Svensk Kärnbränslehantering AB.
- Ludvigson J-E, Hanson K, Rouhiainen P, 2002.** Methodology study of Posiva difference flow meter in borehole KLX02 at Laxemar. SKB R-01-52, Svensk Kärnbränslehantering AB.
- Moye D G, 1969.** Diamond drilling for foundation exploration, Civil Eng. Trans. Inst. Eng. Australia, p. 95–100.
- Munier R, Stigsson M, 2007.** Implementation of Uncertainties in borehole geometries and geological orientation data in SICADA. SKB R-07-19, Svensk Kärnbränslehantering AB.
- Olofsson I, Simeonov A, Stephens M, Follin S, Nilsson A-C, Röshoff K, Lindberg U, Lanaro F, Fredriksson A, Persson L, 2007.** Site descriptive modelling Forsmark, stage 2.2: Presentation of a fracture domain concept as a basis for the statistical modelling of fractures and minor deformation zones, and interdisciplinary coordination. SKB R-07-15, Svensk Kärnbränslehantering AB.
- Rhén I, Follin S, Hermanson J, 2003.** Hydrological Site Descriptive Model – a strategy for its development during Site Investigations. SKB R-03-08, Svensk Kärnbränslehantering AB.
- Rouhiainen P, Sokolnicki M, 2005.** Difference flow logging in borehole KFM06A. SKB P-05-15, Svensk Kärnbränslehantering AB.
- SKB, 2005a.** Preliminary site description Forsmark area-stage 1.2. SKB R-05-18, Svensk Kärnbränslehantering AB.
- SKB, 2005b.** Preliminary safety evaluation for the Forsmark area. Based on data and site descriptions after the initial site investigation stage. SKB TR-05-16, Svensk Kärnbränslehantering AB.
- SKB, 2006a.** Site descriptive modelling Forsmark stage 2.1 – Feedback for completion of the site investigation including from safety assessment and repository engineering. SKB R-06-38, Svensk Kärnbränslehantering AB.
- SKB, 2006b.** Long-term safety for KBS-3 repositories at Forsmark and Laxemar – a first evaluation. Main Report of the SR-Can project. SKB TR-06-09, Svensk Kärnbränslehantering AB.
- SKI, 2005.** Need for Confirmatory Testing of Upscaled Flow and Transport Models. INSITE Report TRD-05-08, Statens Kärnkraftsinspektion.

Stephens M B, Fox A, La Pointe P R, Isaksson H, Simeonov A, Hermanson J, Öhman J, 2007. Geology – Site descriptive modelling Forsmark stage 2.2. SKB R-07-45, Svensk Kärnbränslehantering AB.

Stigsson M, 2007. Forsmark site investigation, Analysis of uncertainty and changes in orientation of fractures coupled to PFL anomalies. SKB P-07-178, Svensk Kärnbränslehantering AB.

Terzaghi R, 1965. Sources of error in joint surveys. *Geotechnique* 15(3): 287–304.

Teurneau B, Forsmark T, Forssman I, Rhén I, Zinn E, 2007. Forsmark site investigation, Correlation of Posiva Flow Log anomalies to core mapped features in KFM01D, -07C, -08A, -08C, -08D and -10A. SKB P-07-127, Svensk Kärnbränslehantering AB.

Thiem G, 1906. *Hydrologische Methoden*, J M Gebhardt, Leipsig.

Walger E, Hjerne C, Ludvigson J-E, Harrström J, 2006. Single-hole injection tests and pressure tests in borehole KFM08A. SKB P-06-194, Svensk Kärnbränslehantering AB.

Vilks P, 2007. Rock matrix permeability measurements on core samples from borehole KFM01D. SKB P-07-162, Svensk Kärnbränslehantering AB.

Additional information on data collation

Stereonet

Stereographic concentration plots are presented for each borehole for all fractures in a fracture domain (i.e. excluding deformation zones) in Figure A-1 to Figure A-12. All use Terzaghi correction with a minimum weighting of 5, bias angle 12° , and an equal area lower hemisphere projection.

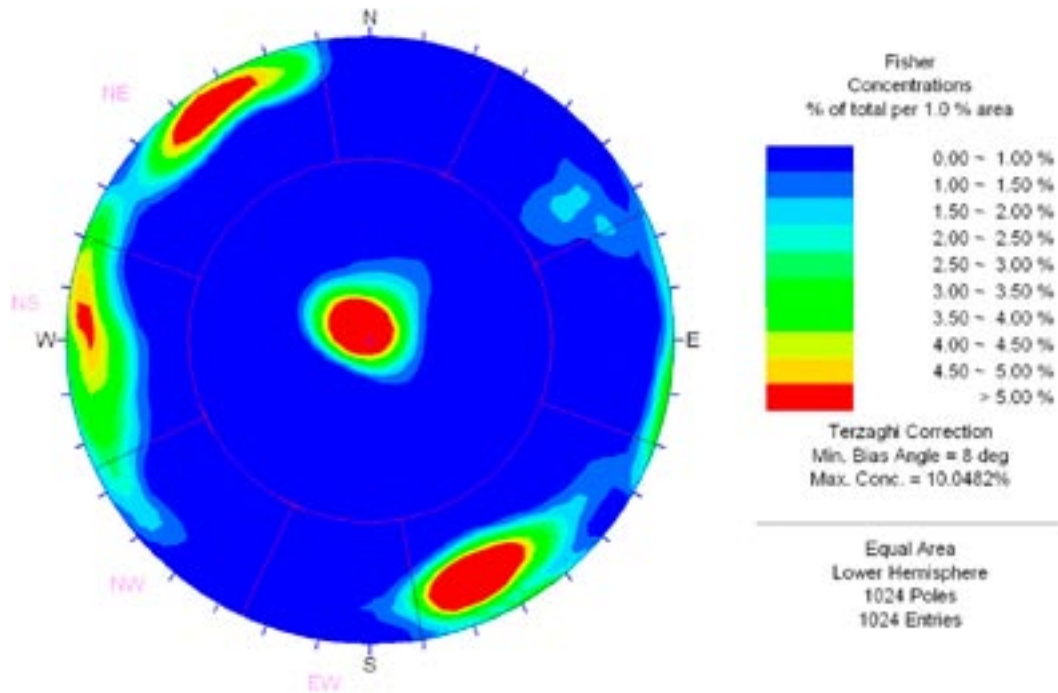


Figure A-1. Fisher concentration plot for all fractures in KFM01A for all FFM fracture domains (i.e. excluding deformation zones). The concentrations are Terzaghi corrected and use an equal area lower hemisphere projection.

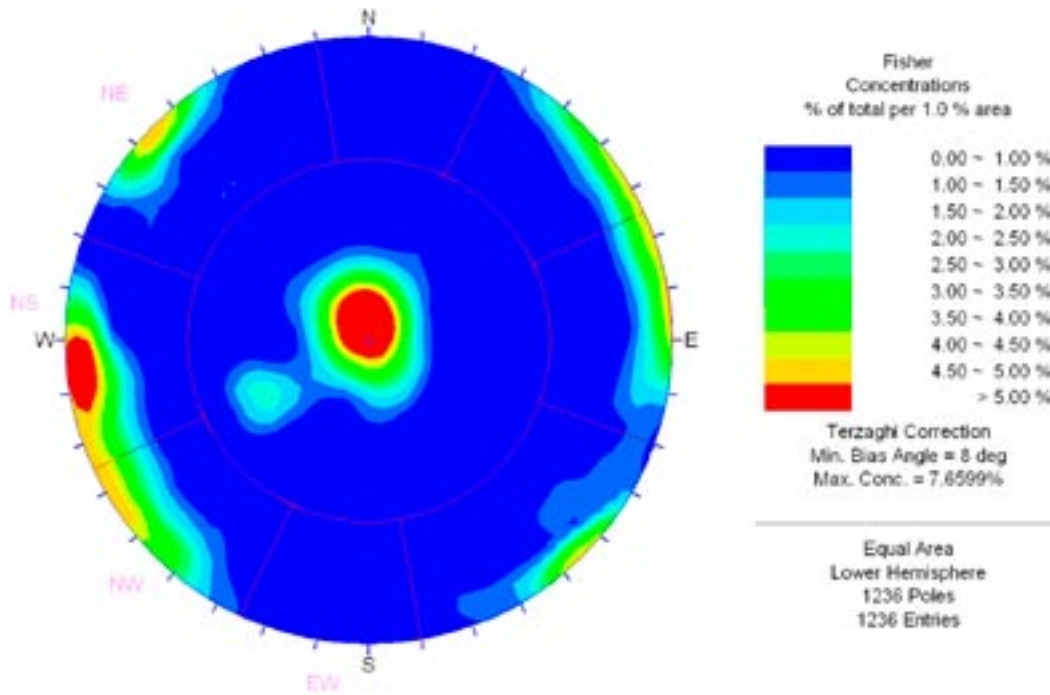


Figure A-2. Fisher concentration plot for all fractures in KFM01D for all FFM fracture domains (i.e. excluding deformation zones). The concentrations are Terzaghi corrected and use an equal area lower hemisphere projection.

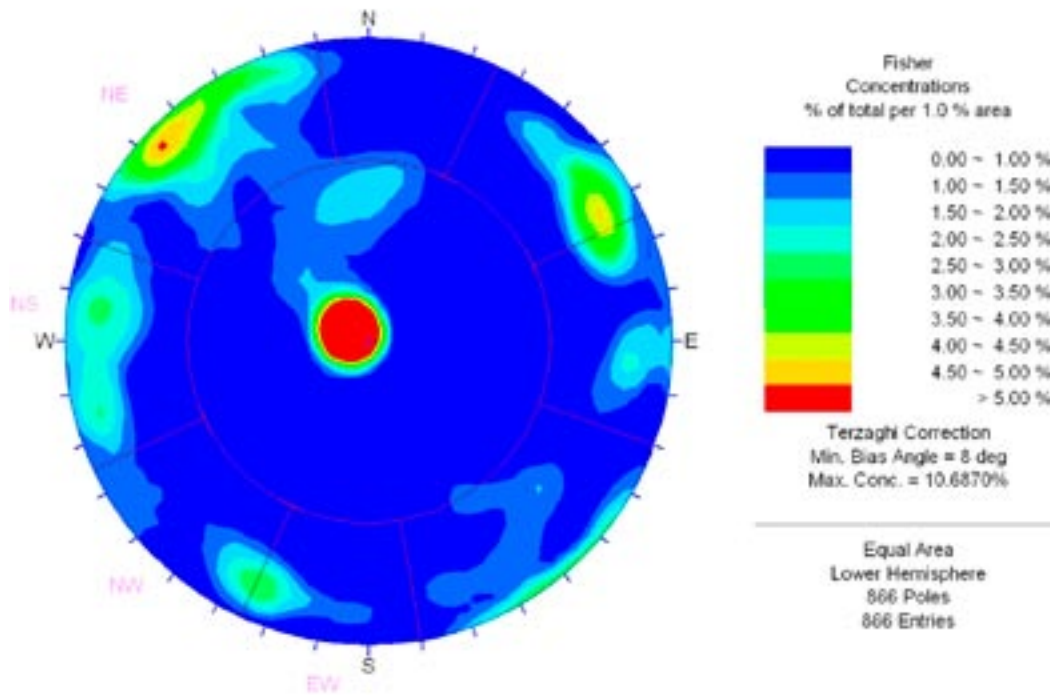


Figure A-3. Fisher concentration plot for all fractures in KFM02A for all FFM fracture domains (i.e. excluding deformation zones). The concentrations are Terzaghi corrected and use an equal area lower hemisphere projection.

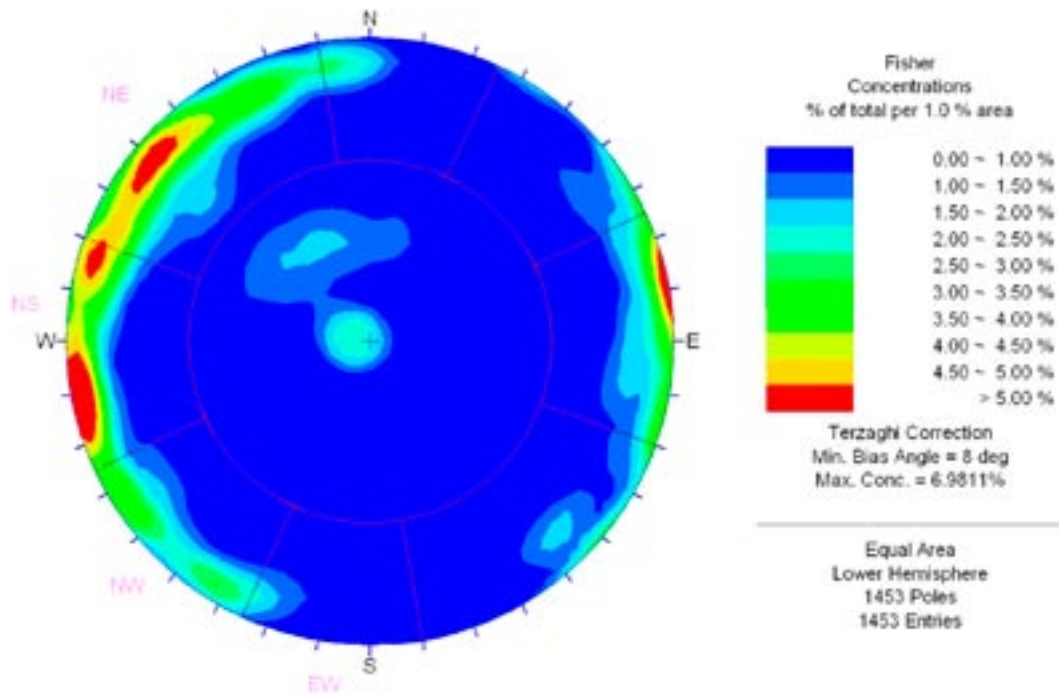


Figure A-4. Fisher concentration plot for all fractures in KFM03A for all FFM fracture domains (i.e. excluding deformation zones). The concentrations are Terzaghi corrected and use an equal area lower hemisphere projection.

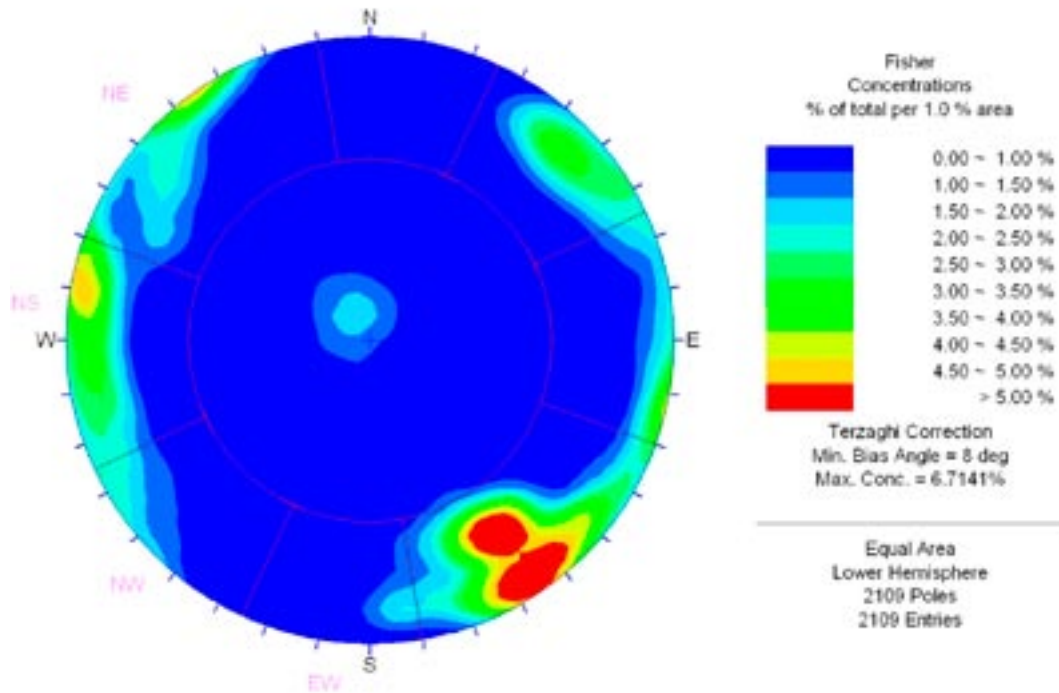


Figure A-5. Fisher concentration plot for all fractures in KFM04A for all FFM fracture domains (i.e. excluding deformation zones). The concentrations are Terzaghi corrected and use an equal area lower hemisphere projection.

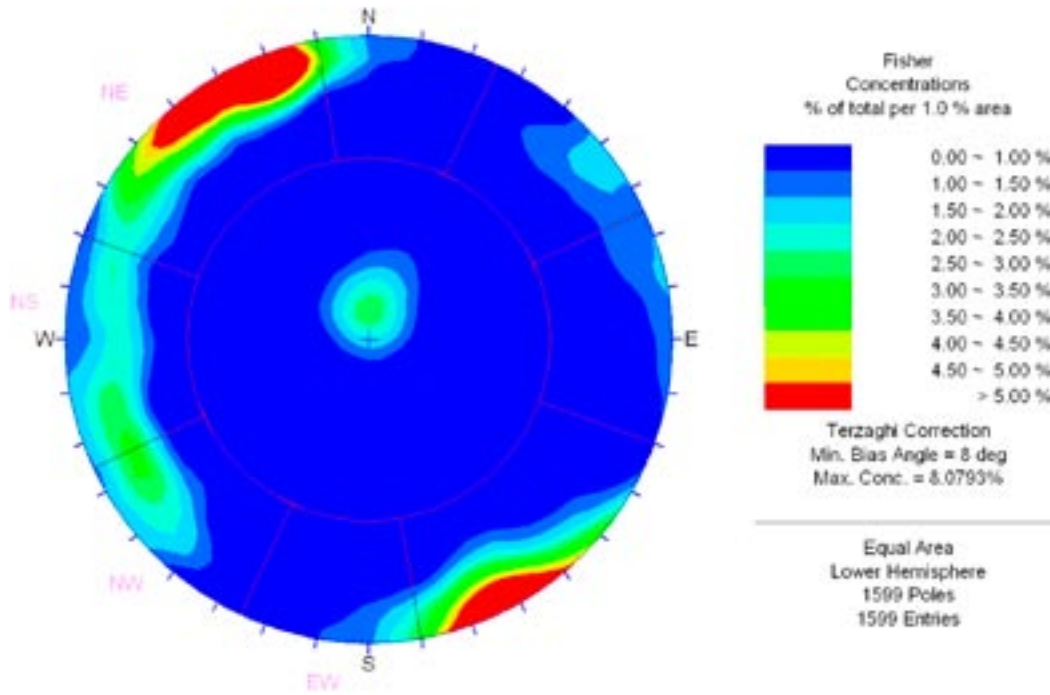


Figure A-6. Fisher concentration plot for all fractures in KFM05A for all FFM fracture domains (i.e. excluding deformation zones). The concentrations are Terzaghi corrected and use an equal area lower hemisphere projection.

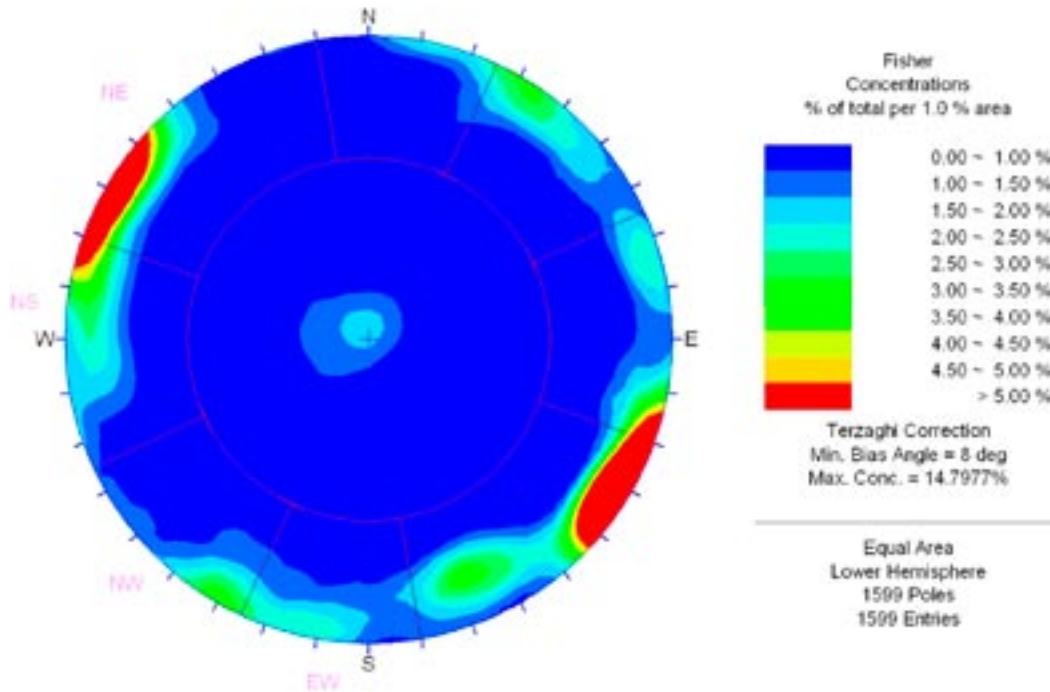


Figure A-7. Fisher concentration plot for all fractures in KFM06A for all FFM fracture domains (i.e. excluding deformation zones). The concentrations are Terzaghi corrected and use an equal area lower hemisphere projection.

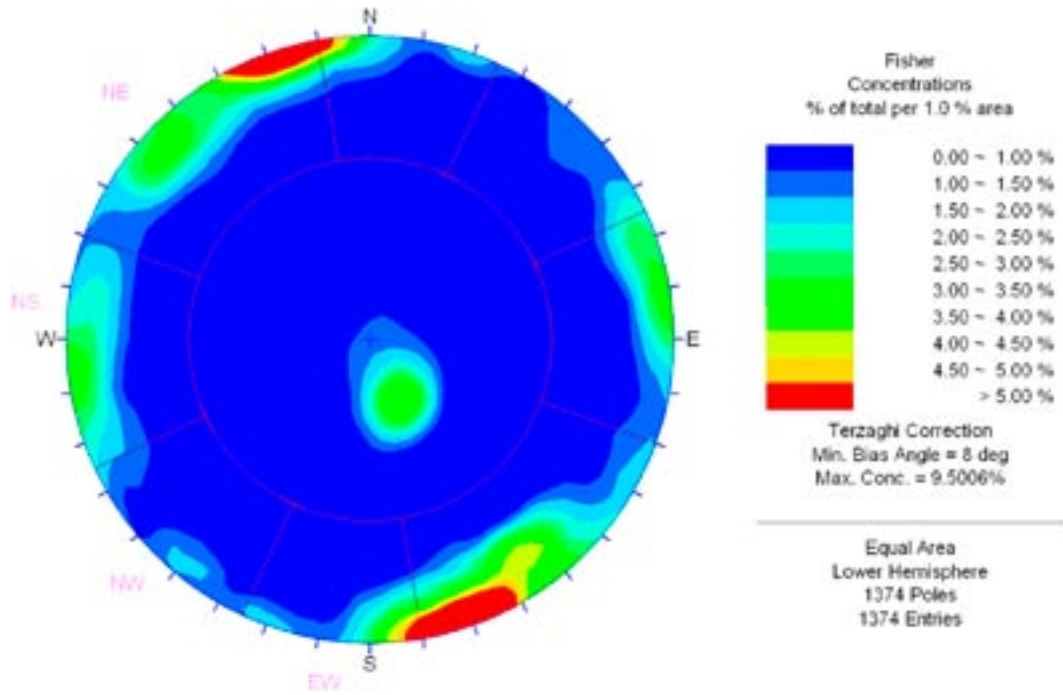


Figure A-8. Fisher concentration plot for all fractures in KFM07A for all FFM fracture domains (i.e. excluding deformation zones). The concentrations are Terzaghi corrected and use an equal area lower hemisphere projection.

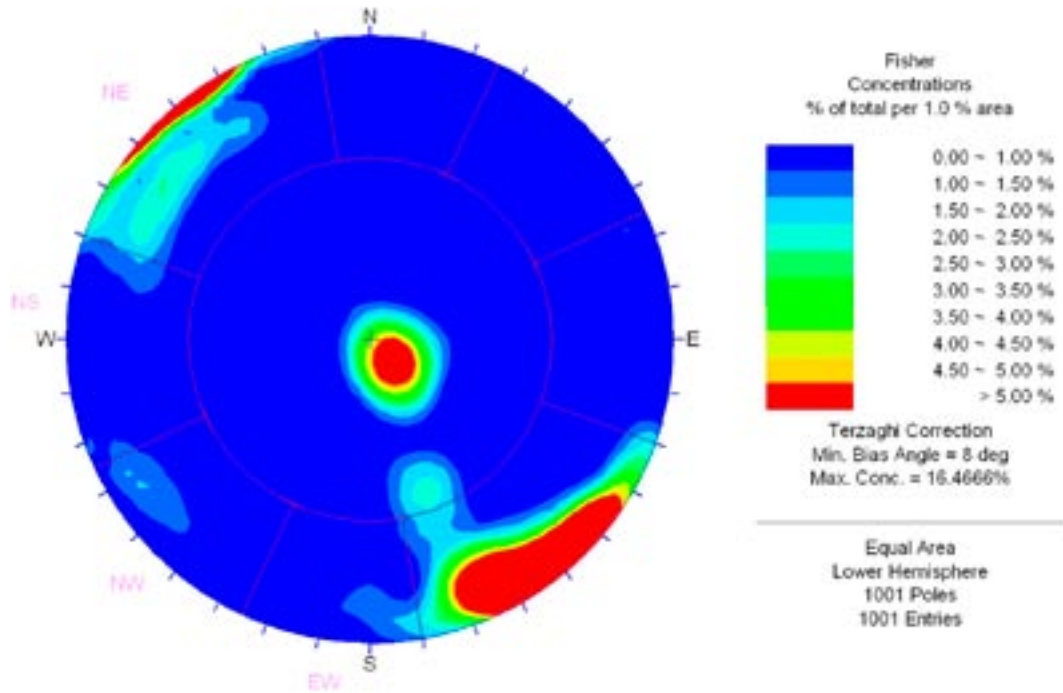


Figure A-9. Fisher concentration plot for all fractures in KFM07C for all FFM fracture domains (i.e. excluding deformation zones). The concentrations are Terzaghi corrected and use an equal area lower hemisphere projection.

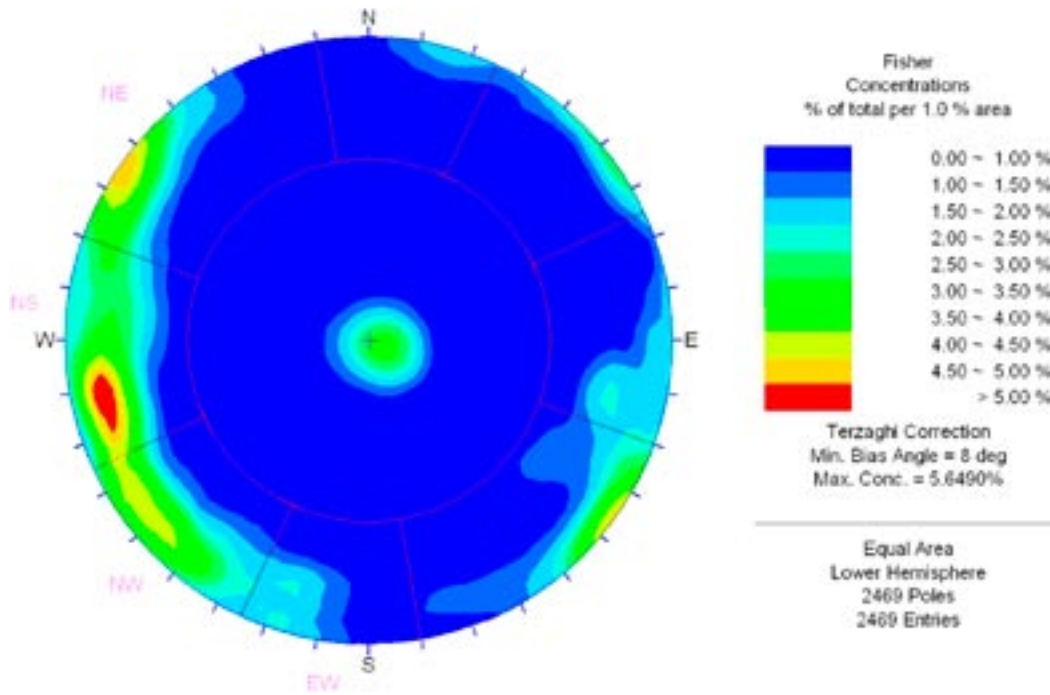


Figure A-10. Fisher concentration plot for all fractures in KFM08A for all FFM fracture domains (i.e. excluding deformation zones). The concentrations are Terzaghi corrected and use an equal area lower hemisphere projection.

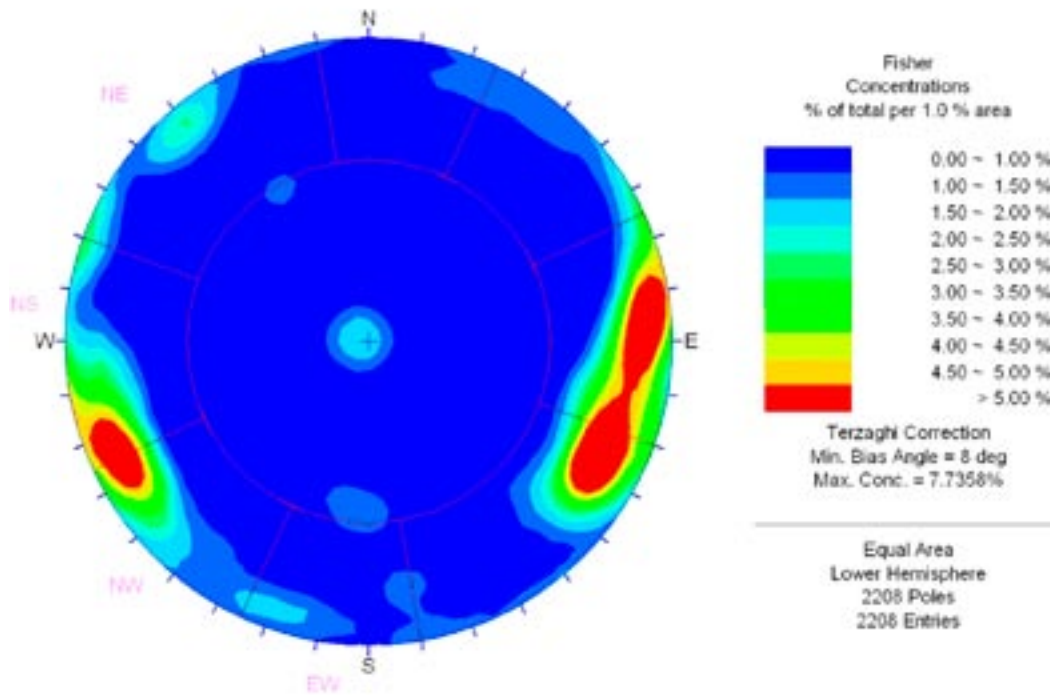


Figure A-11. Fisher concentration plot for all fractures in KFM08C for all FFM fracture domains (i.e. excluding deformation zones). The concentrations are Terzaghi corrected and use an equal area lower hemisphere projection.

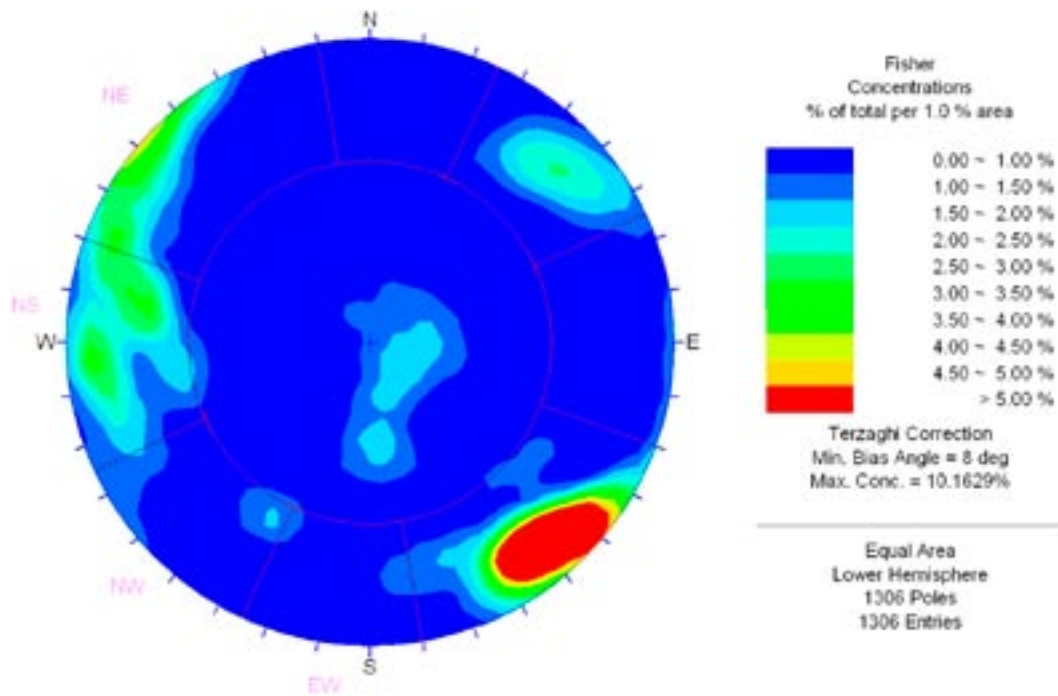


Figure A-12. Fisher concentration plot for all fractures in KFM10A for all FFM fracture domains (i.e. excluding deformation zones). The concentrations are Terzaghi corrected and use an equal area lower hemisphere projection.

Orientations of PFL flow-anomalies

Stereographic pole plots showing the orientations of all flow-anomalies for each borehole in which PFL-f tests were performed are shown in Figure A-13 to Figure A-24. The poles are coloured by the logarithm of the interpreted transmissivity and the hard sector classification of sets from F 1.2 is superimposed.

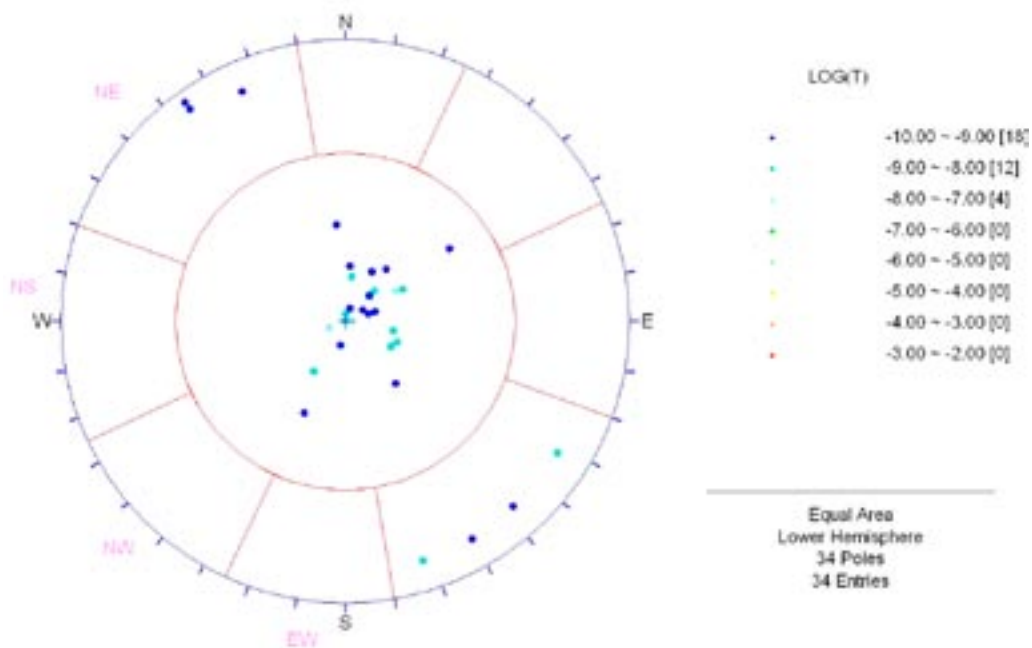


Figure A-13. Pole plot for all PFL flow-anomaly fractures in KFM01A. The poles are coloured by $\text{Log}_{10}(\text{transmissivity})$ and use an equal area lower hemisphere projection.

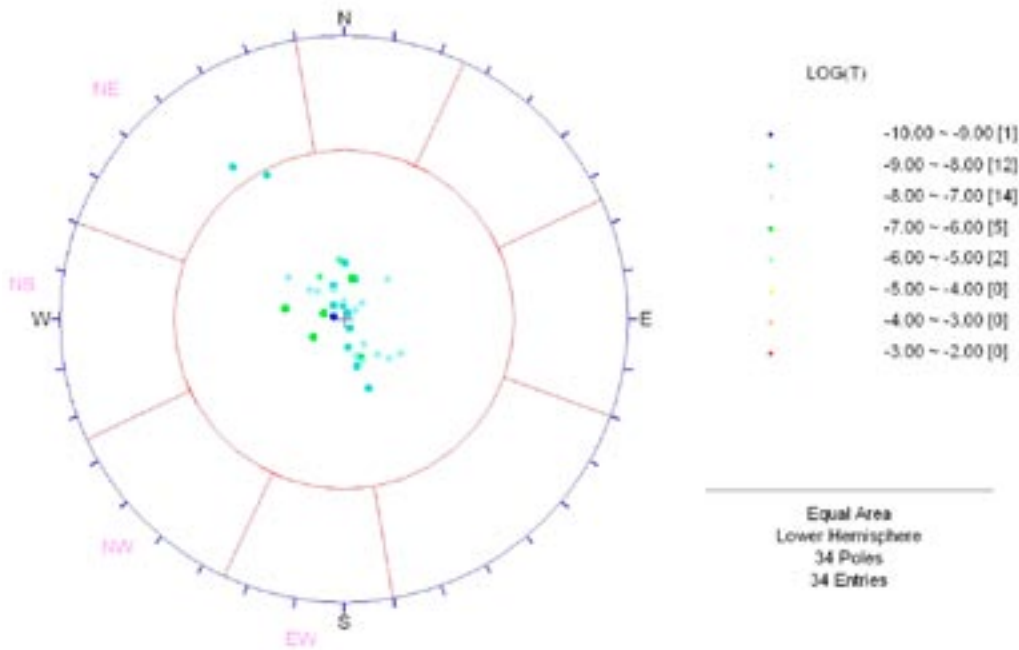


Figure A-14. Pole plot for all PFL flow-anomaly fractures in KFM01D. The poles are coloured by $\text{Log}_{10}(\text{transmissivity})$ and use an equal area lower hemisphere projection.

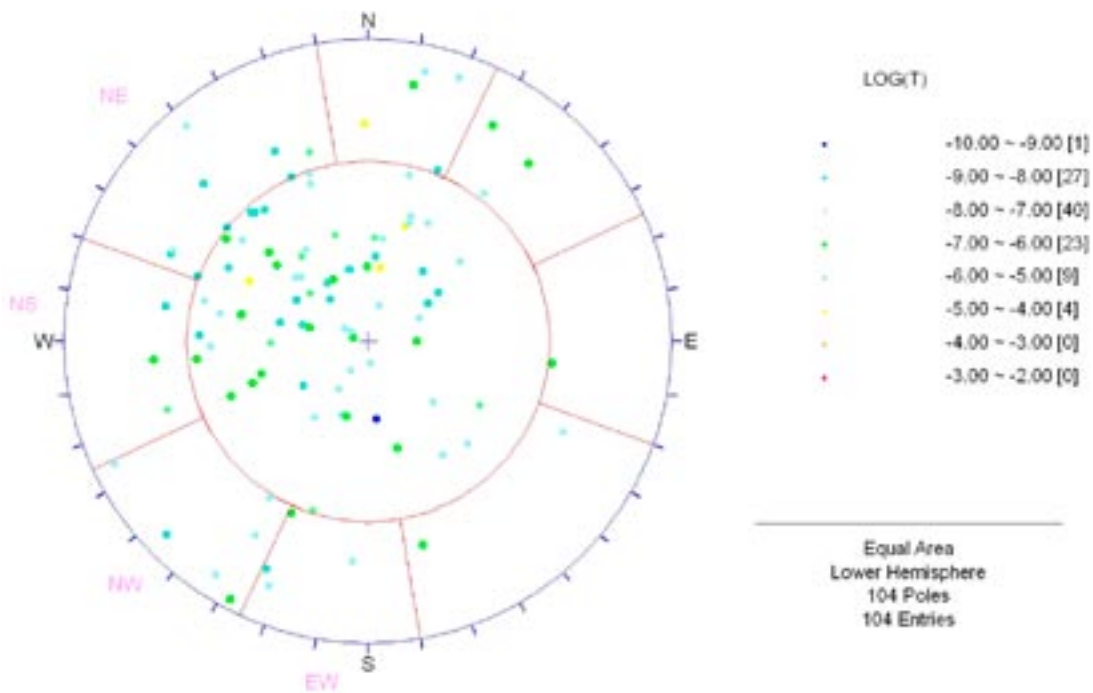


Figure A-15. Pole plot for all PFL flow-anomaly fractures in KFM02A. The poles are coloured by $\text{Log}_{10}(\text{transmissivity})$ and use an equal area lower hemisphere projection.

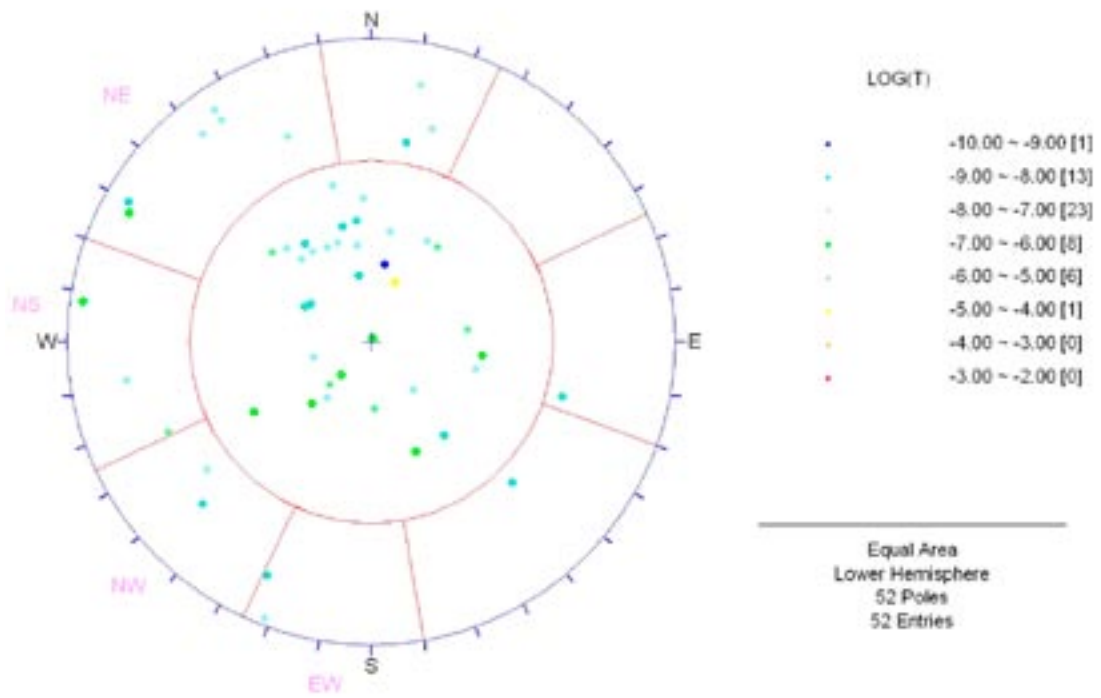


Figure A-16. Pole plot for all PFL flow-anomaly fractures in KFM03A. The poles are coloured by $\text{Log}_{10}(\text{transmissivity})$ and use an equal area lower hemisphere projection.

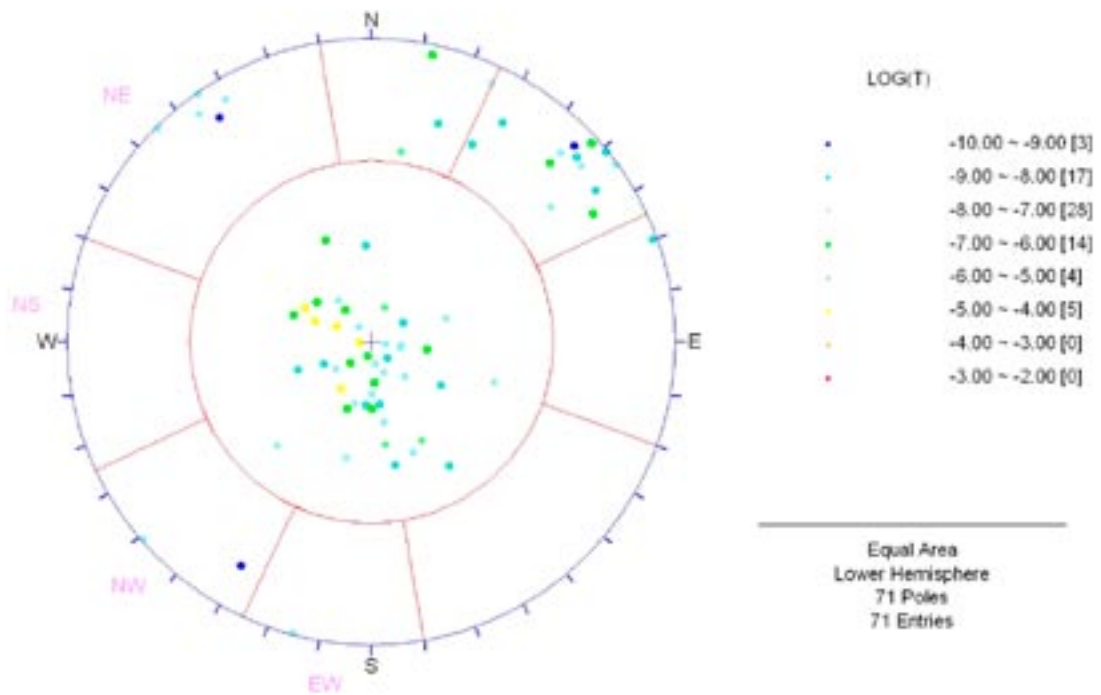


Figure A-17. Pole plot for all PFL flow-anomaly fractures in KFM04A. The poles are coloured by $\text{Log}_{10}(\text{transmissivity})$ and use an equal area lower hemisphere projection.

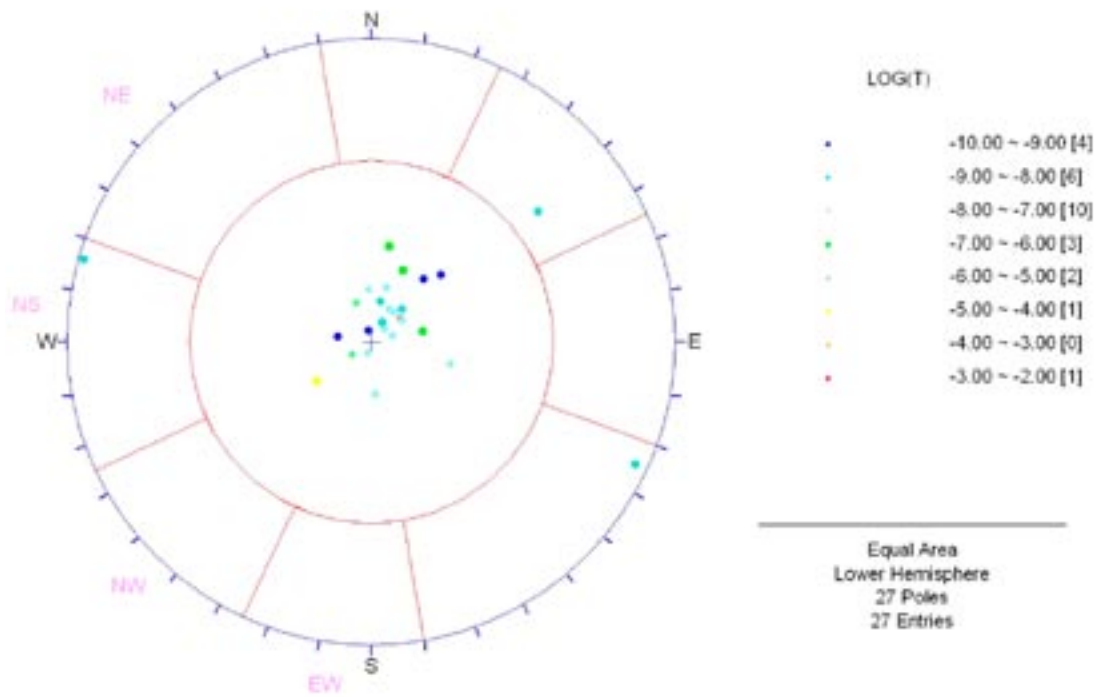


Figure A-18. Pole plot for all PFL flow-anomaly fractures in KFM05A. The poles are coloured by $\text{Log}_{10}(\text{transmissivity})$ and use an equal area lower hemisphere projection.

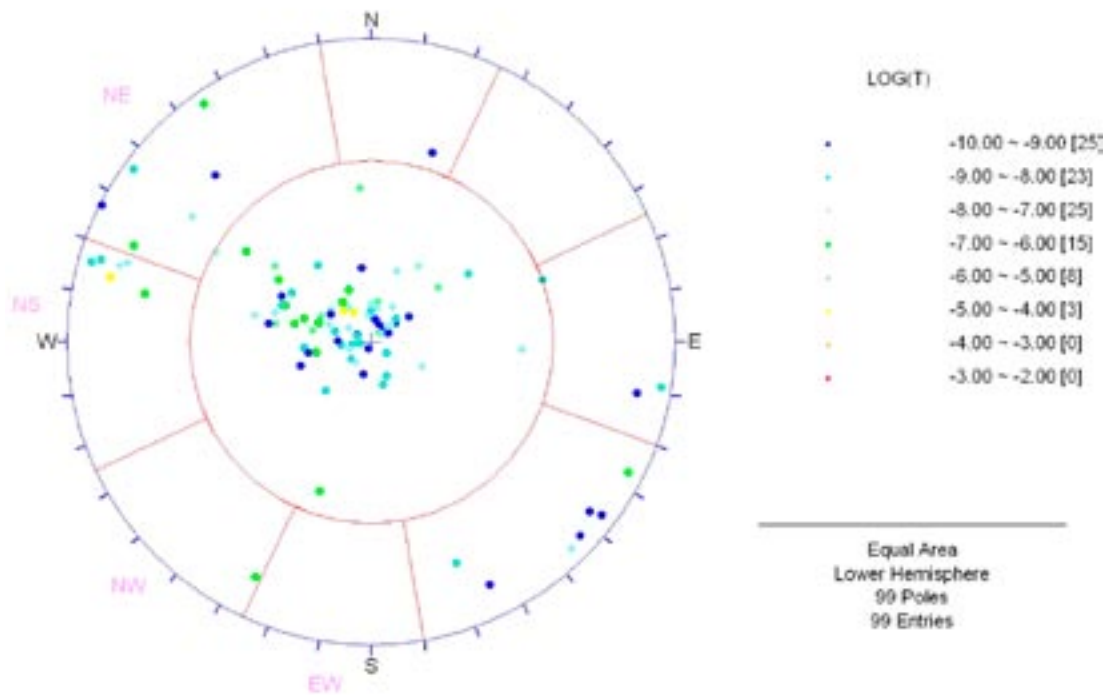


Figure A-19. Pole plot for all PFL flow-anomaly fractures in KFM06A. The poles are coloured by $\text{Log}_{10}(\text{transmissivity})$ and use an equal area lower hemisphere projection.

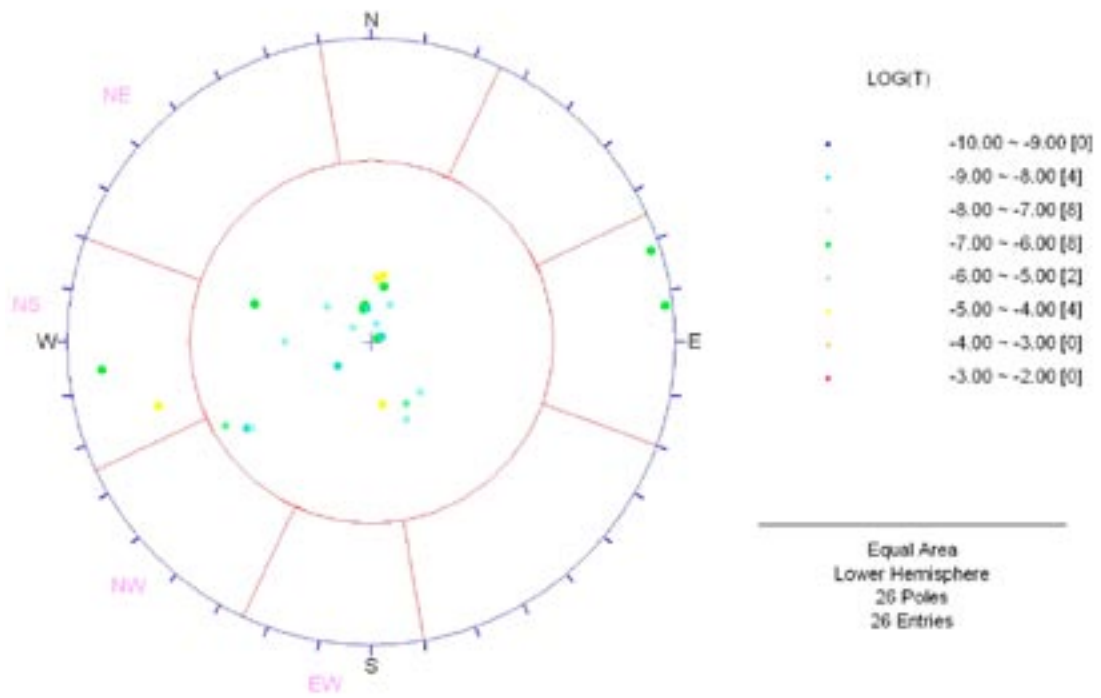


Figure A-20. Pole plot for all PFL flow-anomaly fractures in KFM07A. The poles are coloured by $\text{Log}_{10}(\text{transmissivity})$ and use an equal area lower hemisphere projection.

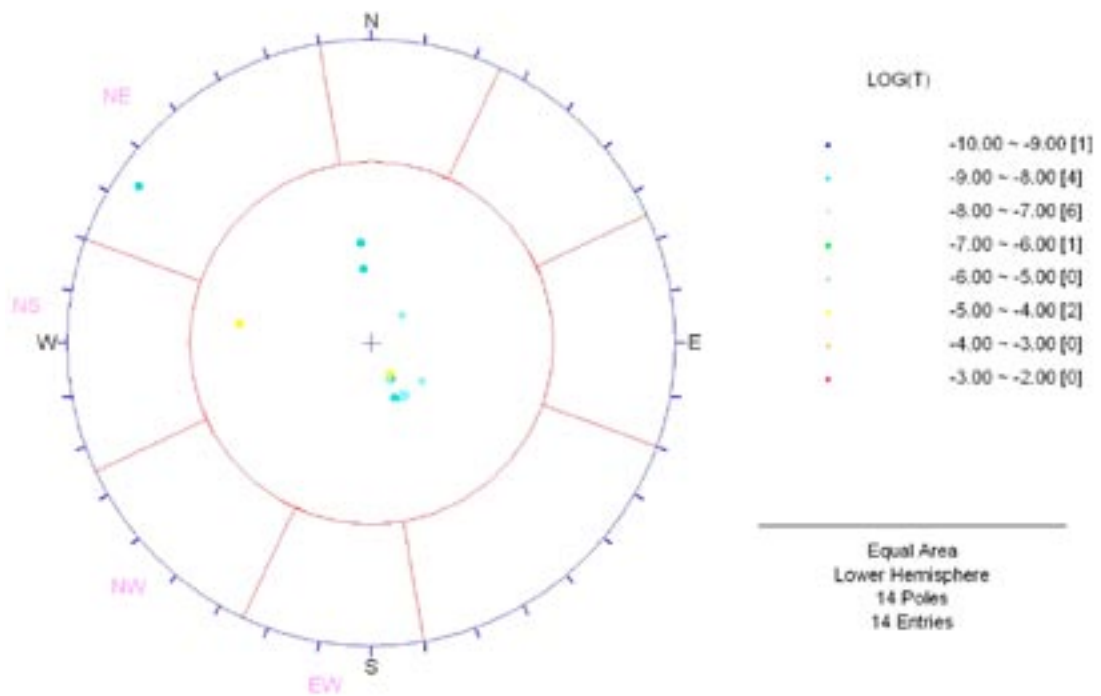


Figure A-21. Pole plot for all PFL flow-anomaly fractures in KFM07C. The poles are coloured by $\text{Log}_{10}(\text{transmissivity})$ and use an equal area lower hemisphere projection.

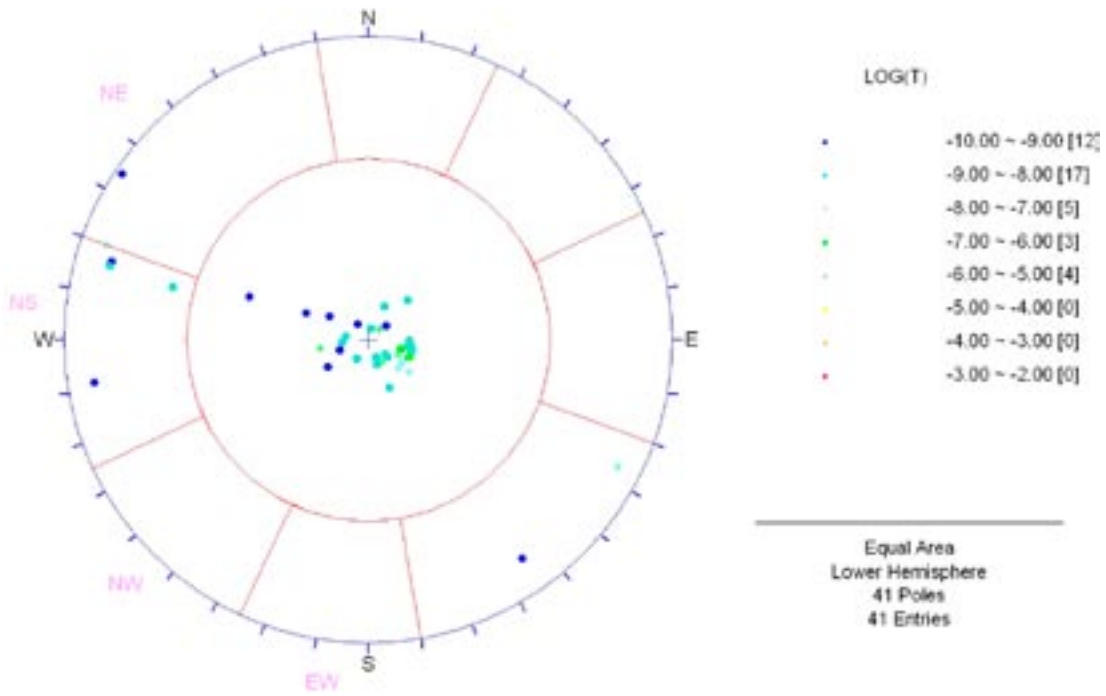


Figure A-22. Pole plot for all PFL flow-anomaly fractures in KFM08A. The poles are coloured by $\text{Log}_{10}(\text{transmissivity})$ and use an equal area lower hemisphere projection.

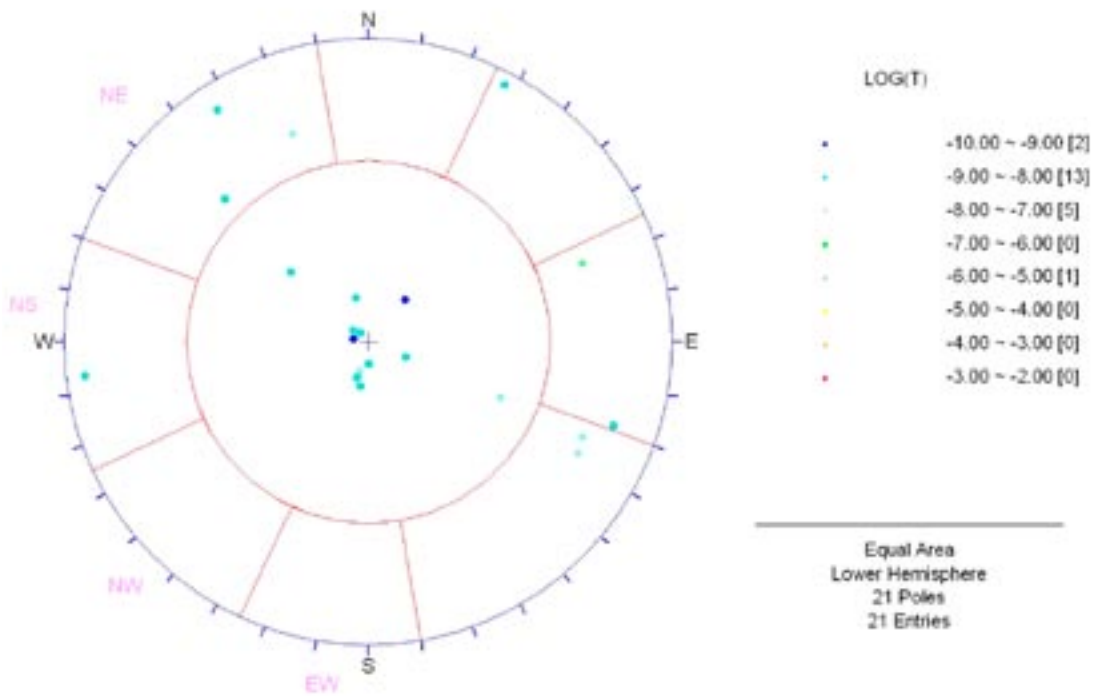


Figure A-23. Pole plot for all PFL flow-anomaly fractures in KFM08C. The poles are coloured by $\text{Log}_{10}(\text{transmissivity})$ and use an equal area lower hemisphere projection.

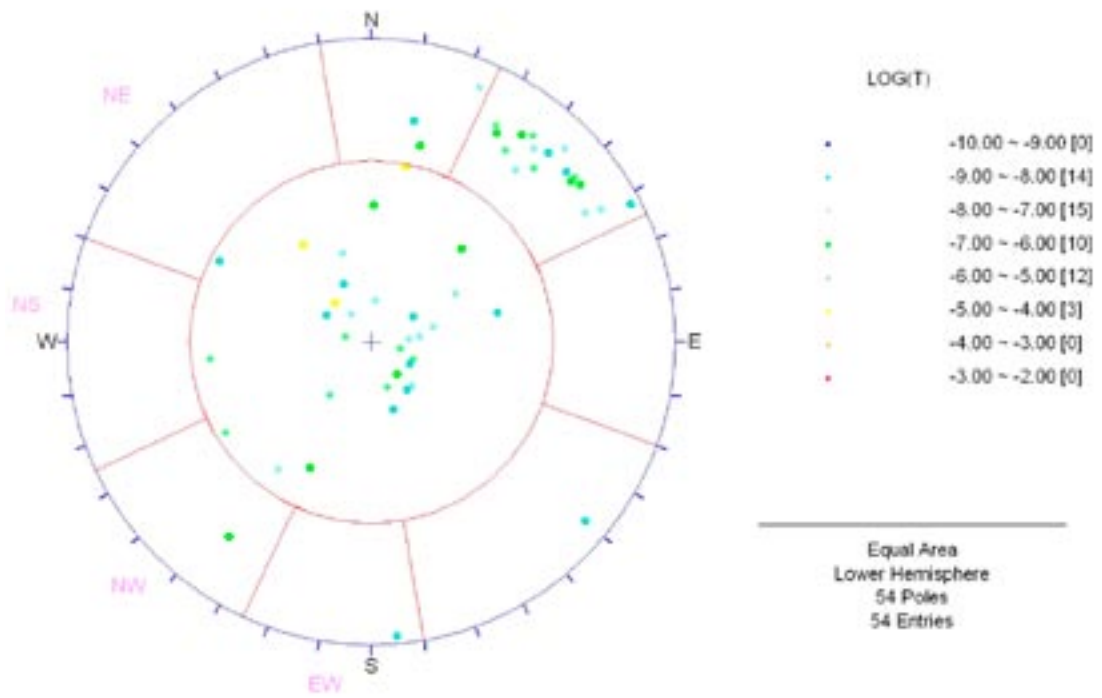


Figure A-24. Pole plot for all PFL flow-anomaly fractures in KFM10A. The poles are coloured by $\text{Log}_{10}(\text{transmissivity})$ and use an equal area lower hemisphere projection.

Additional results for the flow modelling in FFM01–FFM03

Here, all final results for matching Hydro-DFN models to the PFL-f data are presented to illustrate the quality of the match. For each fracture domain FFM01–03, the comparison of flow distribution within specified borehole intervals between model simulations and the PFL-f measurements is made. The comparisons are made both as histograms and as bar and whisker plots for each of the F 1.2 sets with annotation of the numbers of inflows per borehole section length. These matches were used in guiding the selection of parameters recommended in Table 11-18, Table 11-20, Table 11-22, and Table 11-25.

For a 2 layer model of FFM01, above and below an elevation of –400 m, Figure B-1 to Figure B-6 show the comparisons of inflow distributions for the semi-correlated, correlated and uncorrelated transmissivity relationships. The semi-correlated and correlated model reproduce the numbers and shape of distribution of inflows reasonably well, giving a wedge shaped distribution characteristic of having some size-transmissivity correlation. The uncorrelated model is much flatter and less representative of the PFL-f data.

The 3 layer model of FFM01 which divides depth dependence into above –200 m, between –200 m and –400 m, and below –400 m is presented in Figure B-7 to Figure B-12 for the semi-correlated, correlated and uncorrelated transmissivity relationships. This case demonstrates the strong variations with depth in terms of numbers and magnitudes of inflows. The matches for all three transmissivity models are reasonable.

FFM02 is limited to the upper section of bedrock above about –200 m, so no depth variations are considered. The results for FFM02 are shown in Figure B-13 to Figure B-18 for the semi-correlated, correlated and uncorrelated transmissivity relationships. The magnitudes of flow for this section are similar to FFM01 above –200 m, but here in FFM02 the frequency of inflows is about twice as high. Again, the semi-correlated and correlated models give the best match to the shape of distribution of inflows.

A 2 layer is used for FFM03 in the hanging wall of ZFM0A2, above and below an elevation of –400 m, as shown in Figure B-19 to Figure B-24. The frequency of inflows is only about 65% higher above –400 m compared to below, which is less of a marked depth variation compared to FFM01 and FFM02 in the footwall of ZFM0A2. The magnitudes are also similar between the two depths. The results for numbers and magnitudes of flow for each set and for each of the size-transmissivity relationships are good.

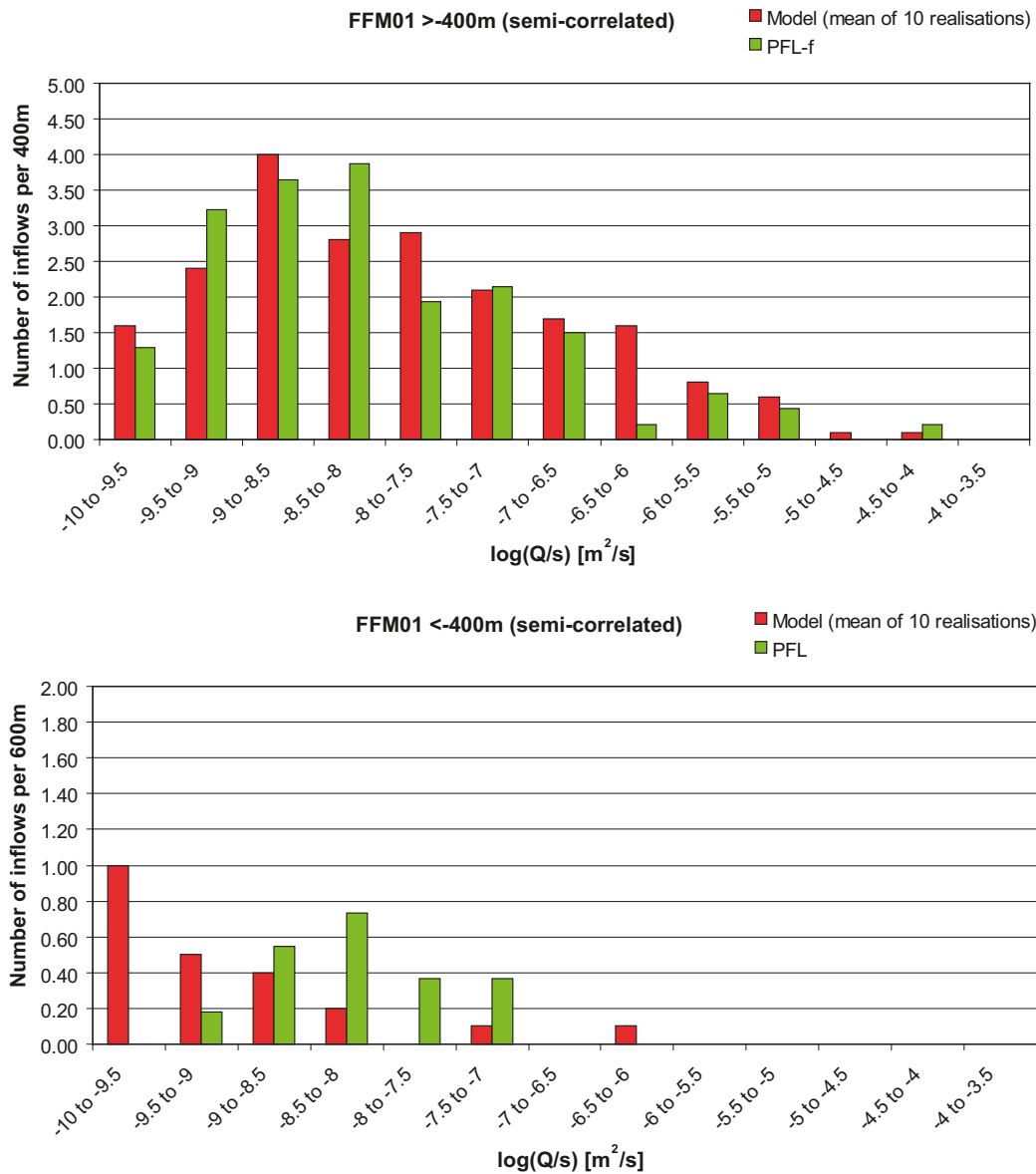


Figure B-1. Histogram comparing the distribution of the magnitude of inflows divided by drawdown, Q/s , at abstraction boreholes in FFM01 with a semi-correlated transmissivity (see Table 11-18 for parameter values). Top: above an elevation of -400 m; Bottom: below -400 m. The PFL-f measurements are treated as ensemble over all boreholes sections within FFM01. Above -400 m the number of inflows is normalised with respect to a borehole section of 400 m length, and below relative to a 600 m section. The simulations are represented by statistics taken from an ensemble over 10 realisations of the Hydro-DFN model.

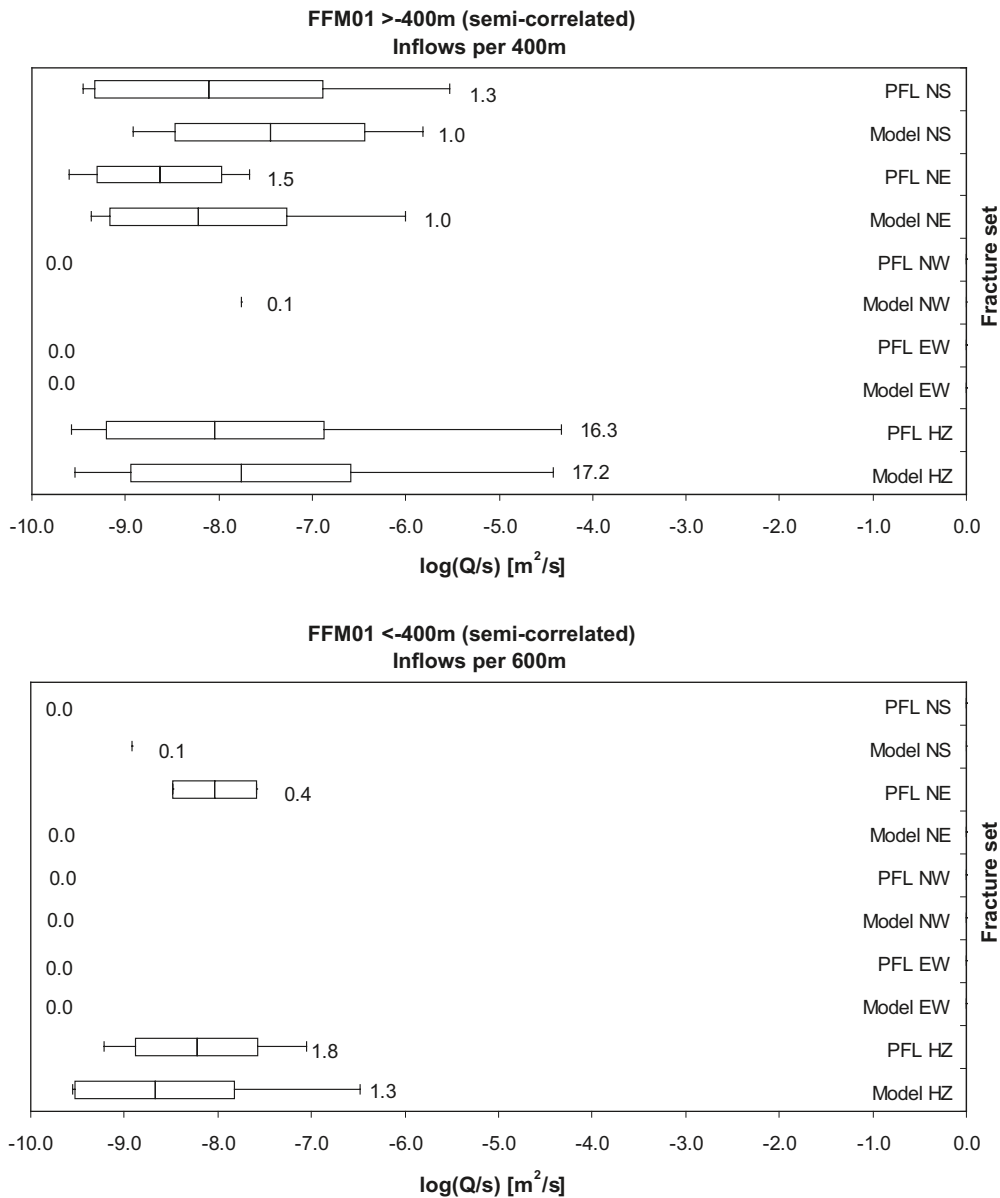


Figure B-2. Bar and whisker plots comparing statistics taken over each fracture set for the individual inflows, Q/s , for the PFL-f data from borehole sections within FFM01 against statistics taken from an ensemble over 10 realisations of the Hydro-DFN model with a semi-correlated transmissivity. Top: above an elevation of -400 m; Bottom: below -400 m. The centre of the bar indicates the mean value, the ends of the bar indicate ± 1 standard deviation, and the error bars indicate the minimum and maximum values. Above -400 m the total numbers of fractures with inflows per 400 m section of borehole above the detection limits is given; below -400 m the numbers of inflows per 600 m section of borehole is given. For the data, statistics are taken over the identified flow-anomalies within each set, and for the model are taken over the fractures generated within each set and an ensemble over 10 realisations.

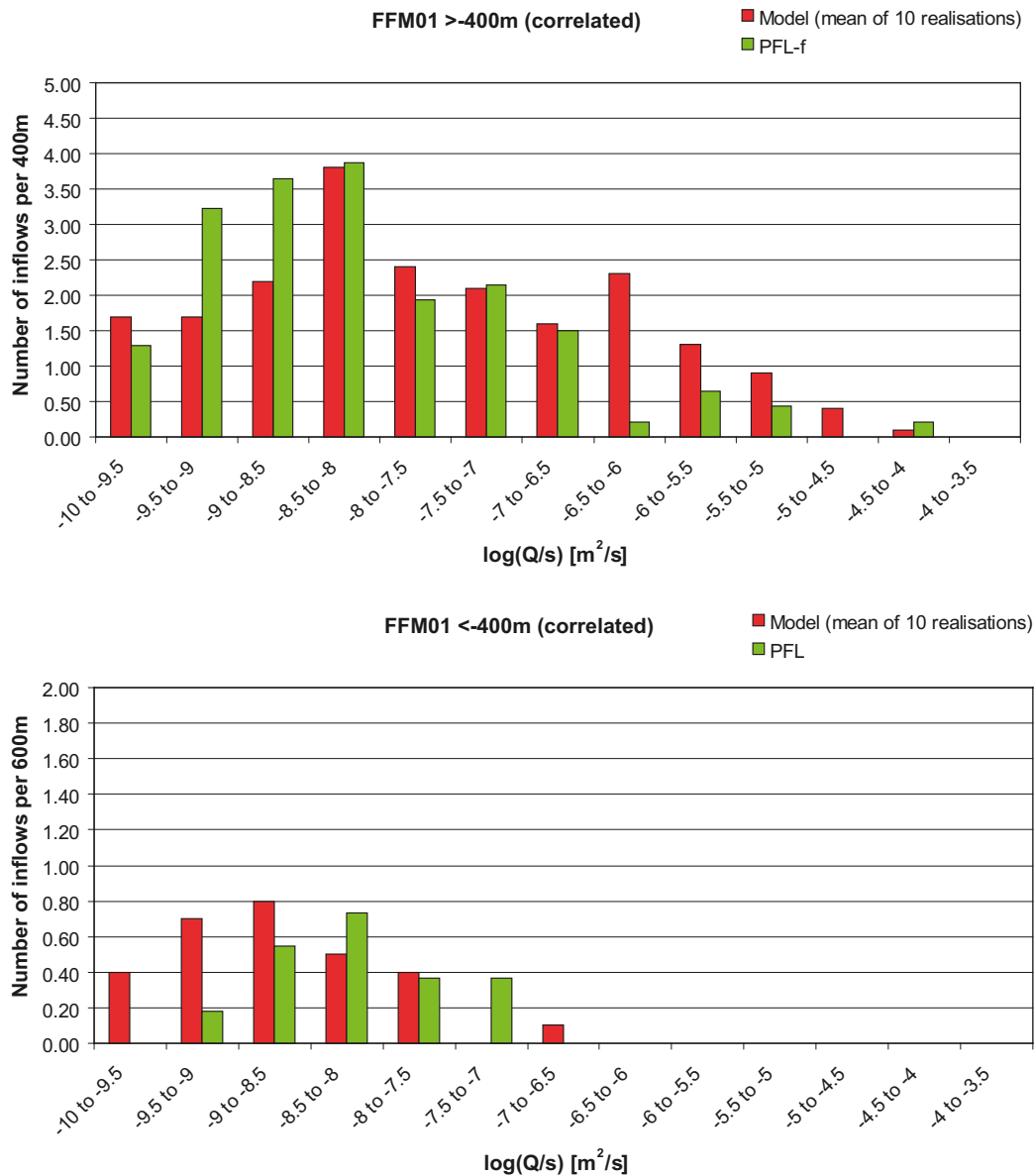


Figure B-3. Histogram comparing the distribution of the magnitude of inflows divided by drawdown, Q/s , at abstraction boreholes in FFM01 with a correlated transmissivity (see Table 11-18 for parameter values). Top: above an elevation of -400 m; Bottom: below -400 m. The PFL-f measurements are treated as ensemble over all boreholes sections within FFM01. Above -400 m the number of inflows is normalised with respect to a borehole section of 400 m length, and below relative to a 600 m section. The simulations are represented by statistics taken from an ensemble over 10 realisations of the Hydro-DFN model.

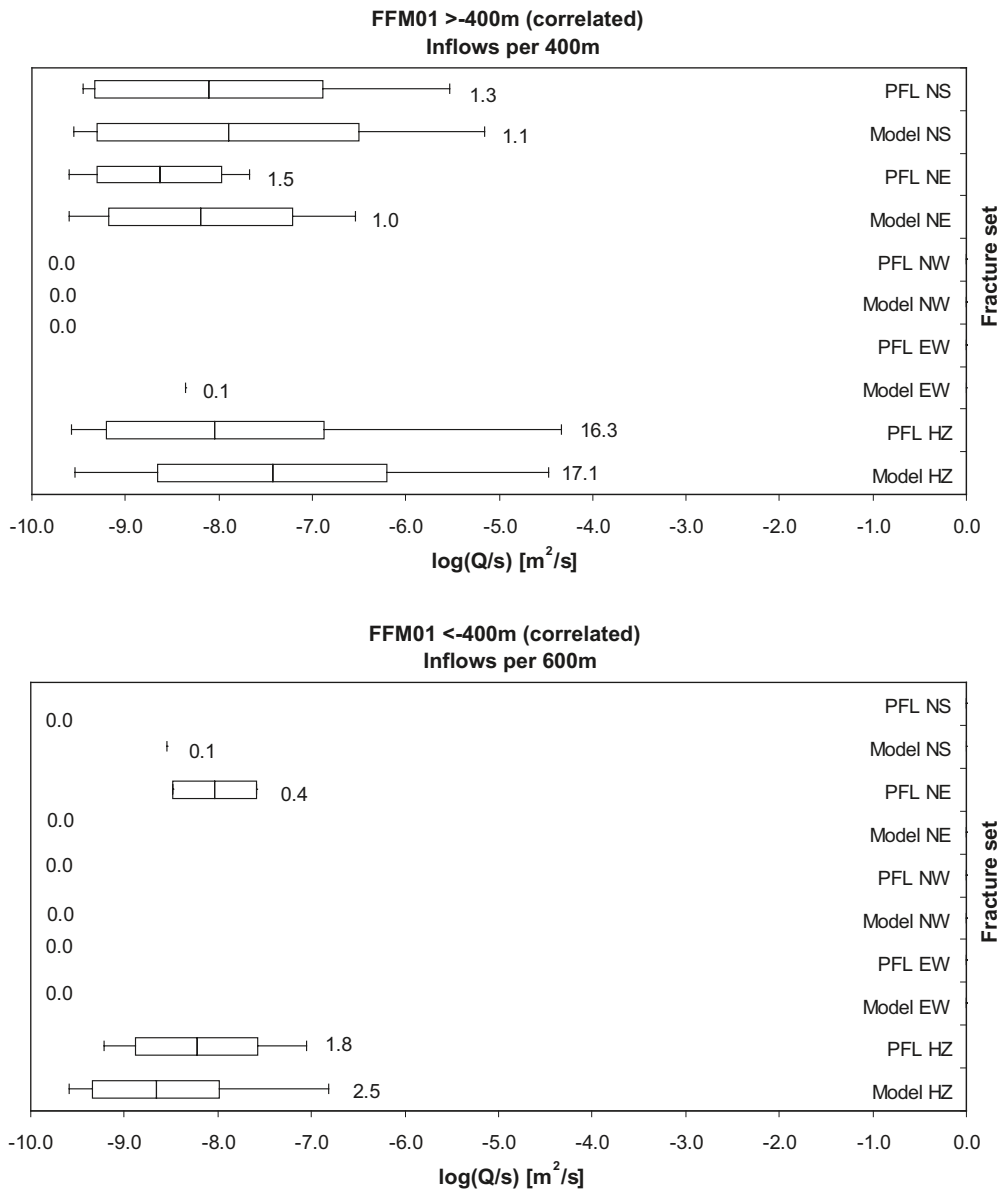


Figure B-4. Bar and whisker plots comparing statistics taken over each fracture set for the individual inflows, Q/s , for the PFL-f data from borehole sections within FFM01 against statistics taken from an ensemble over 10 realisations of the Hydro-DFN model with a correlated transmissivity. Top: above an elevation of -400 m; Bottom: below -400 m. The centre of the bar indicates the mean value, the ends of the bar indicate ± 1 standard deviation, and the error bars indicate the minimum and maximum values. Above -400 m the total numbers of fractures with inflows per 400 m section of borehole above the detection limits is given; below -400 m the numbers of inflows per 600 m section of borehole is given. For the data, statistics are taken over the identified flow-anomalies within each set, and for the model are taken over the fractures generated within each set and an ensemble over 10 realisations.

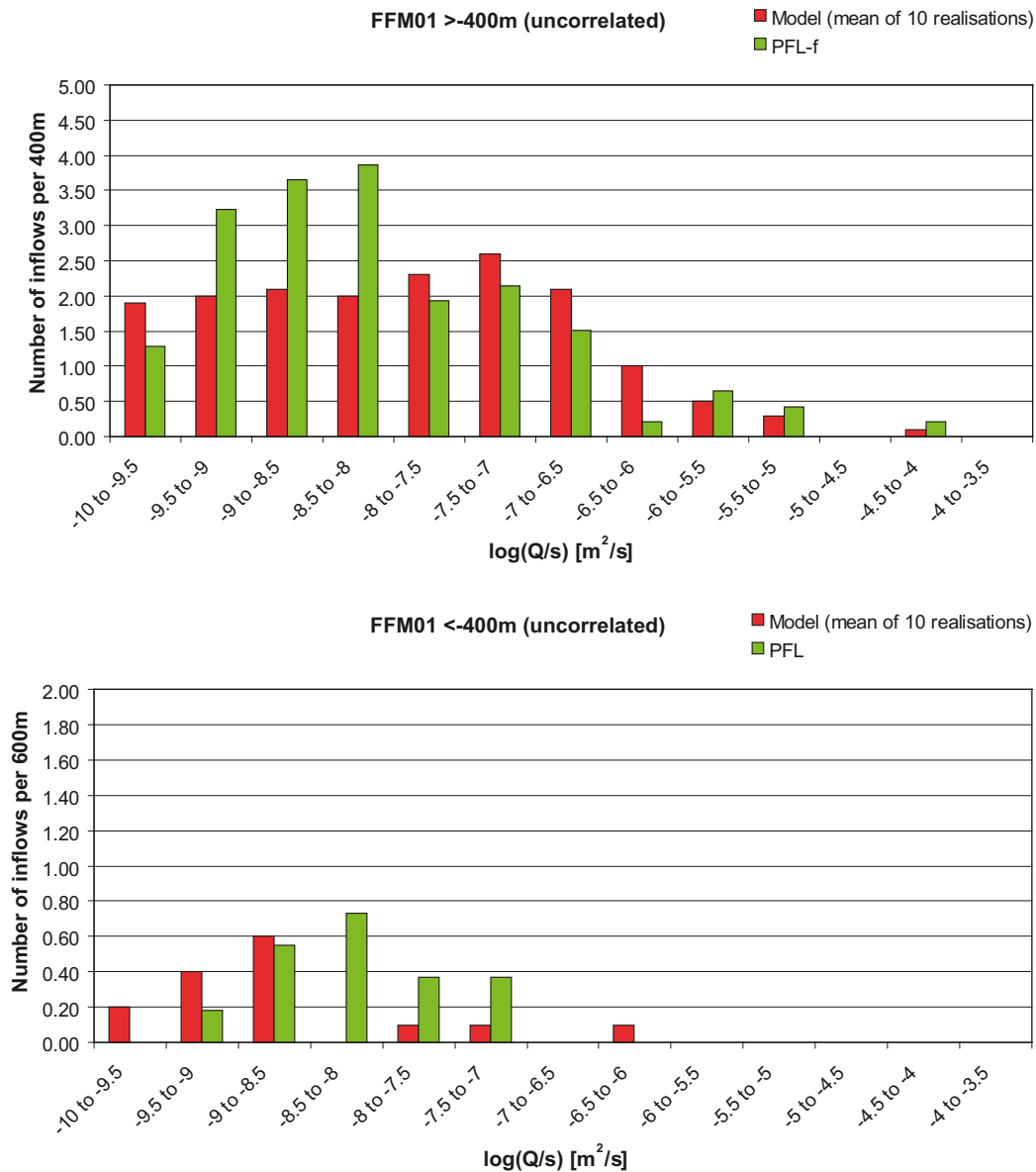


Figure B-5. Histogram comparing the distribution of the magnitude of inflows divided by drawdown, Q/s , at abstraction boreholes in FFM01 with an uncorrelated transmissivity (see Table 11-18 for parameter values). Top: above an elevation of -400 m; Bottom: below -400 m. The PFL-f measurements are treated as ensemble over all boreholes sections within FFM01. Above -400 m the number of inflows is normalised with respect to a borehole section of 400 m length, and below relative to a 600 m section. The simulations are represented by statistics taken from an ensemble over 10 realisations of the Hydro-DFN model.

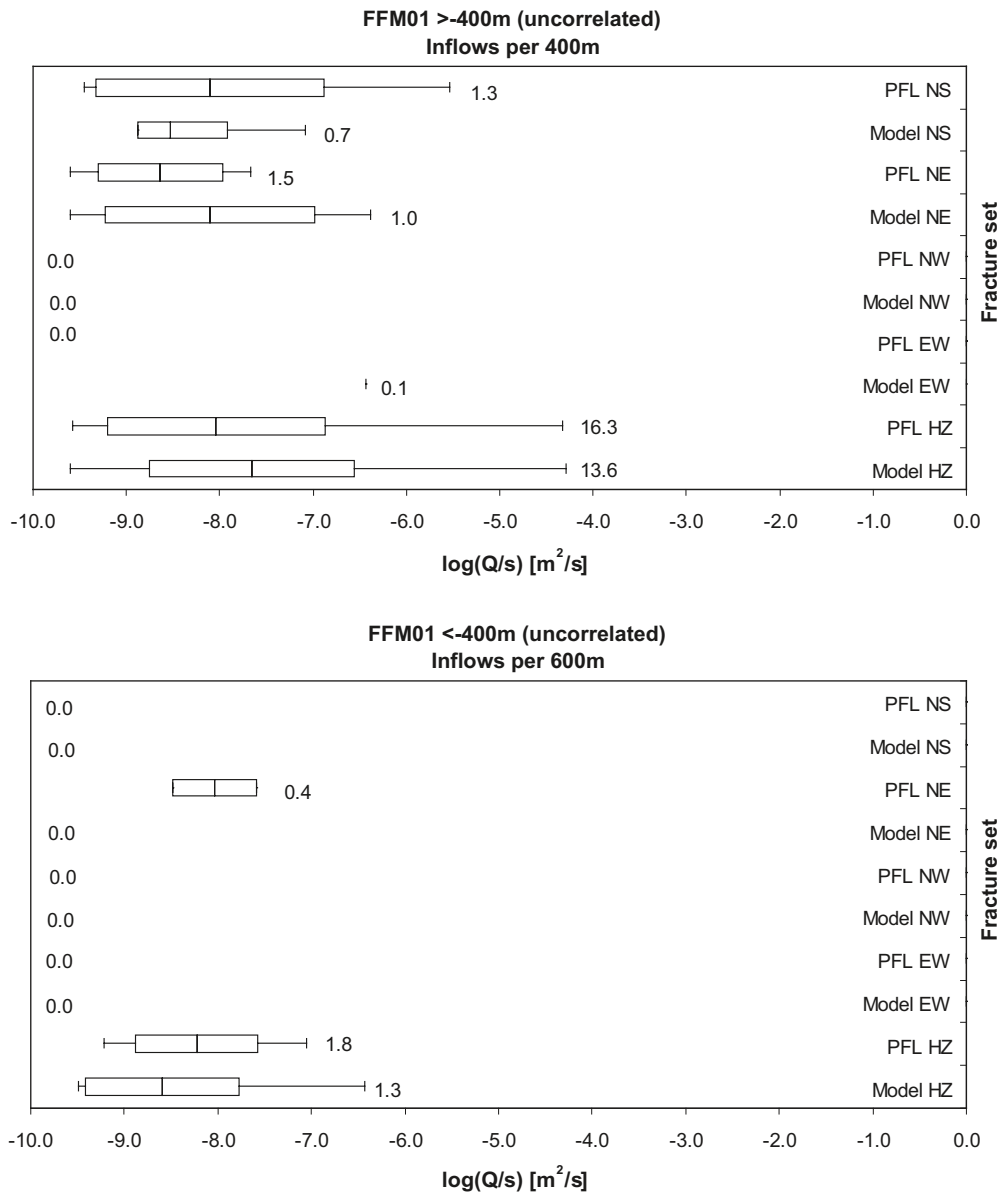


Figure B-6. Bar and whisker plots comparing statistics taken over each fracture set for the individual inflows, Q/s , for the PFL-f data from borehole sections within FFM01 against statistics taken from an ensemble over 10 realisations of the Hydro-DFN model with an uncorrelated transmissivity. Top: above an elevation of -400 m; Bottom: below -400 m. The centre of the bar indicates the mean value, the ends of the bar indicate ± 1 standard deviation, and the error bars indicate the minimum and maximum values. Above -400 m the total numbers of fractures with inflows per 400 m section of borehole above the detection limits is given; below -400 m the numbers of inflows per 600 m section of borehole is given. For the data, statistics are taken over the identified flow-anomalies within each set, and for the model are taken over the fractures generated within each set and an ensemble over 10 realisations.

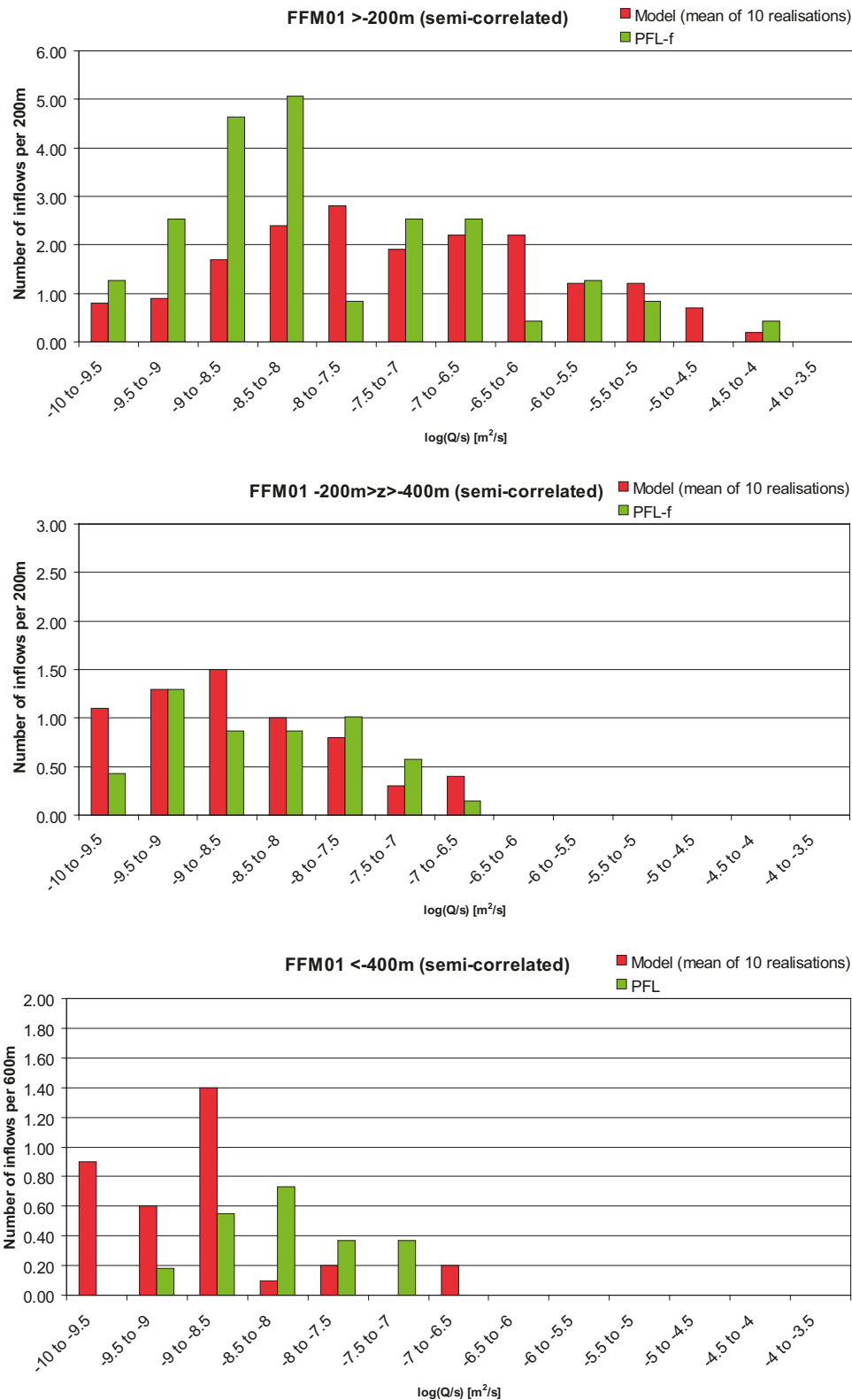


Figure B-7. Histogram comparing the distribution of the magnitude of inflows divided by drawdown, Q/s , at abstraction boreholes in FFM01 with a semi-correlated transmissivity (see Table 11-20 for parameter values). Top: above an elevation of -200 m; Middle: between -200 m and -400 m; Bottom: below -400 m. The PFL-f measurements are treated as ensemble over all boreholes sections within FFM01. Above -200 m and between -200 m and -400 m, the number of inflows is normalised with respect to a borehole section of 200 m length, and below -400 m relative to a 600 m section. The simulations are represented by statistics taken from an ensemble over 10 realisations of the Hydro-DFN model.

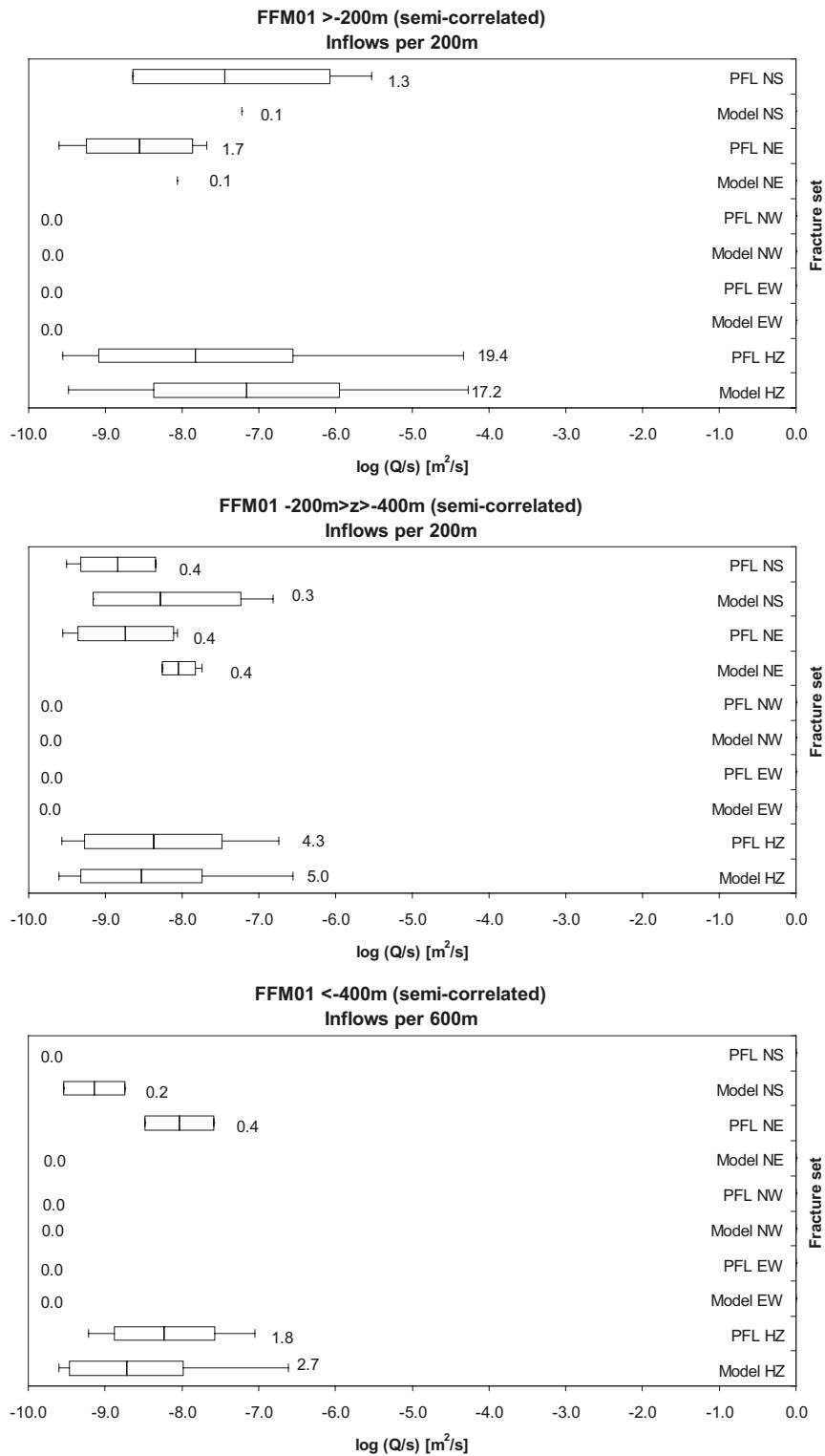


Figure B-8. Bar and whisker plots comparing statistics taken over each fracture set for the individual inflows, Q/s , for the PFL-f data from borehole sections within FFM01 against statistics taken from an ensemble over 10 realisations of the Hydro-DFN model with a semi-correlated transmissivity. Top: above an elevation of -200 m; Middle: between -200 m and -400 m; Bottom: below -400 m. The centre of the bar indicates the mean value, the ends of the bar indicate ± 1 standard deviation, and the error bars indicate the minimum and maximum values. Above -200 m and between -200 m and -400 m, the total numbers of fractures with inflows per 200 m section of borehole above the detection limits is given; below -400 m the numbers of inflows per 600 m section of borehole is given. For the data, statistics are taken over the identified flow-anomalies within each set, and for the model are taken over the fractures generated within each set and an ensemble over 10 realisations.

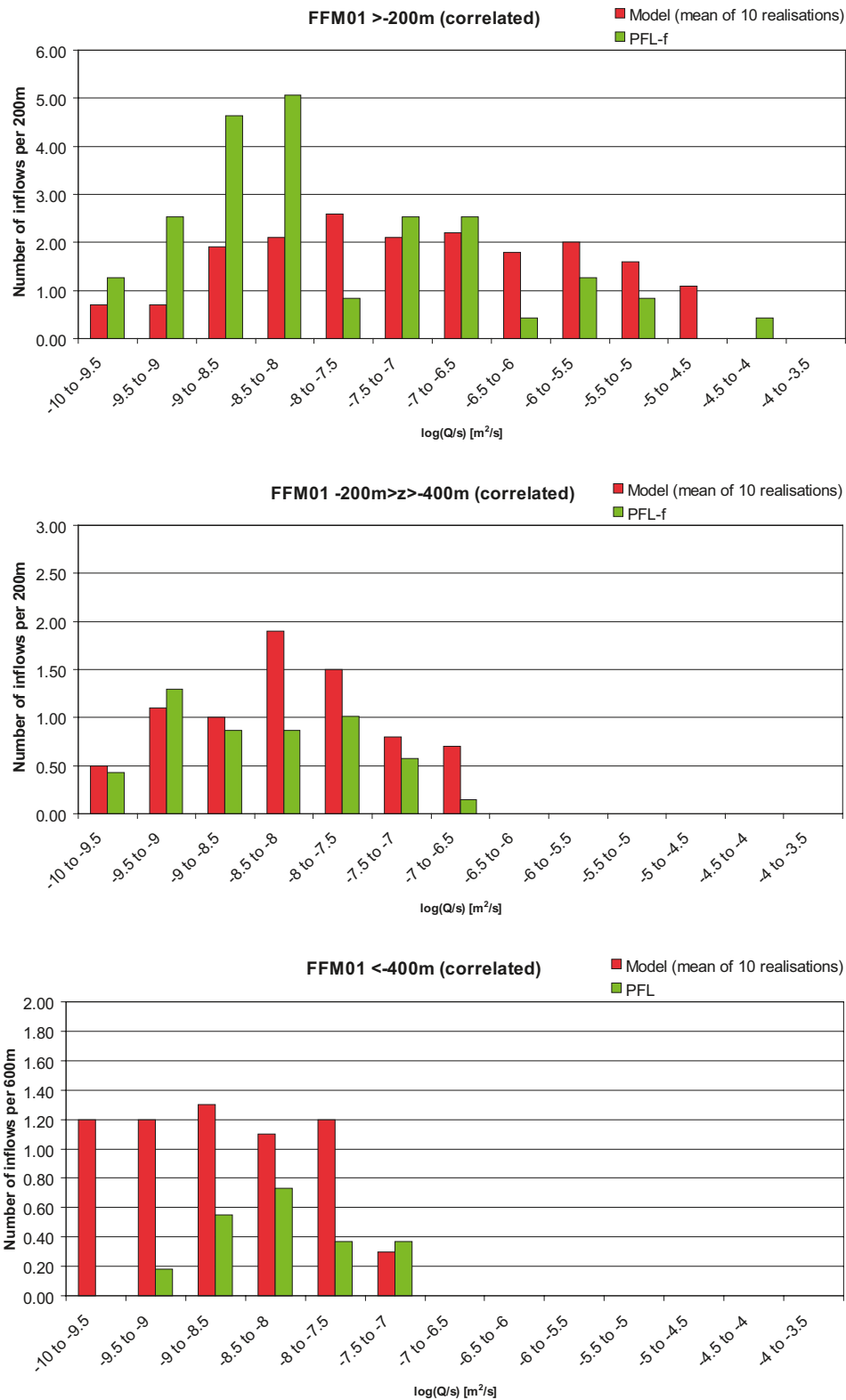


Figure B-9. Histogram comparing the distribution of the magnitude of inflows divided by drawdown, Q/s , at abstraction boreholes in FFM01 with a correlated transmissivity (see Table 11-20 for parameter values). Top: above an elevation of -200 m; Middle: between -200 m and -400 m; Bottom: below -400 m. The PFL-f measurements are treated as ensemble over all boreholes sections within FFM01. Above -200 m and between -200 m and -400 m, the number of inflows is normalised with respect to a borehole section of 200 m length, and below -400 m relative to a 600 m section. The simulations are represented by statistics taken from an ensemble over 10 realisations of the Hydro-DFN model.

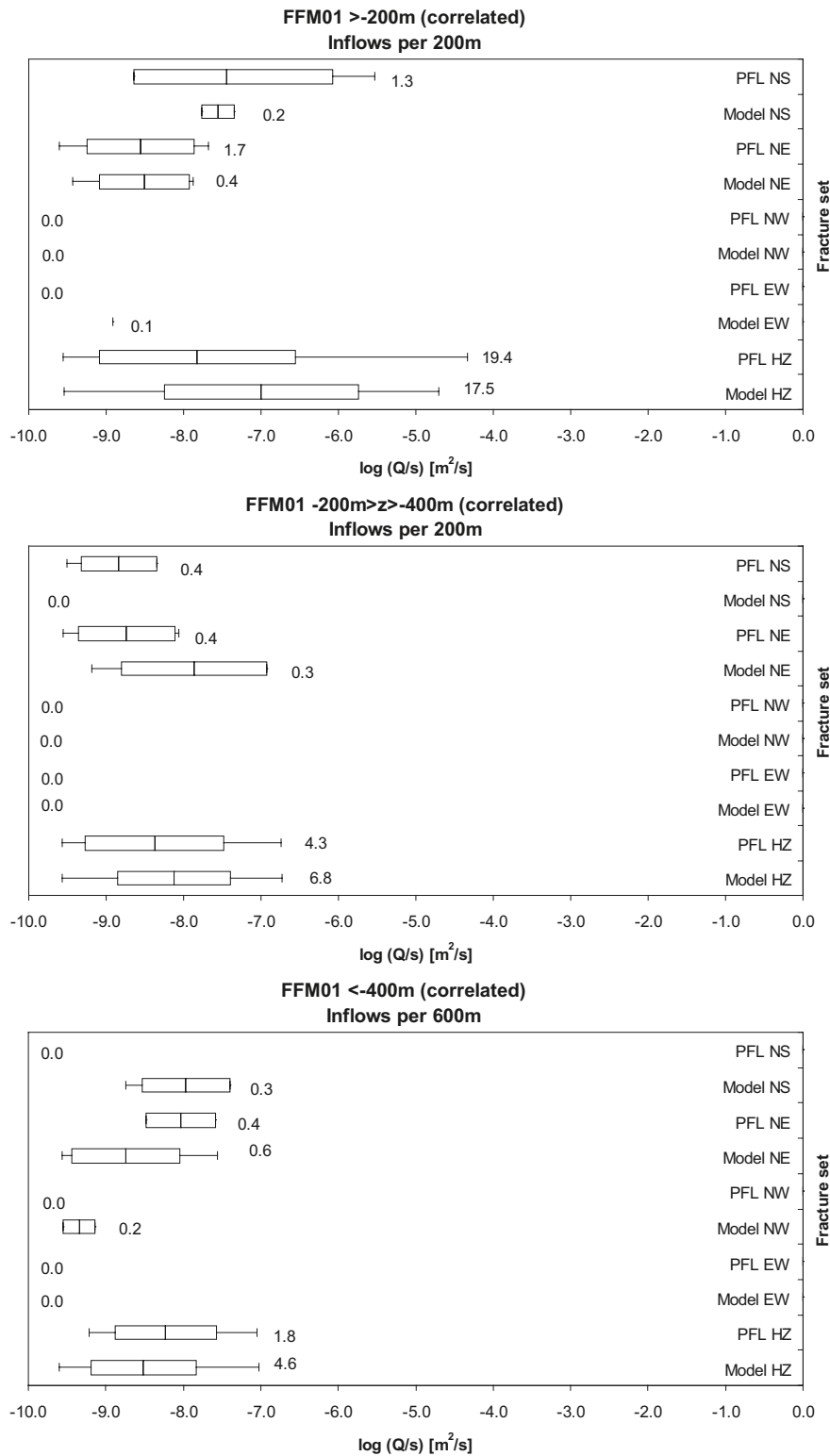


Figure B-10. Bar and whisker plots comparing statistics taken over each fracture set for the individual inflows, Q/s , for the PFL-f data from borehole sections within FFM01 against statistics taken from an ensemble over 10 realisations of the Hydro-DFN model with a correlated transmissivity. Top: above an elevation of -200 m; Middle: between -200 m and -400 m; Bottom: below -400 m. The centre of the bar indicates the mean value, the ends of the bar indicate ± 1 standard deviation, and the error bars indicate the minimum and maximum values. Above -200 m and between -200 m and -400 m, the total numbers of fractures with inflows per 200 m section of borehole above the detection limits is given; below -400 m the numbers of inflows per 600 m section of borehole is given. For the data, statistics are taken over the identified flow-anomalies within each set, and for the model are taken over the fractures generated within each set and an ensemble over 10 realisations.

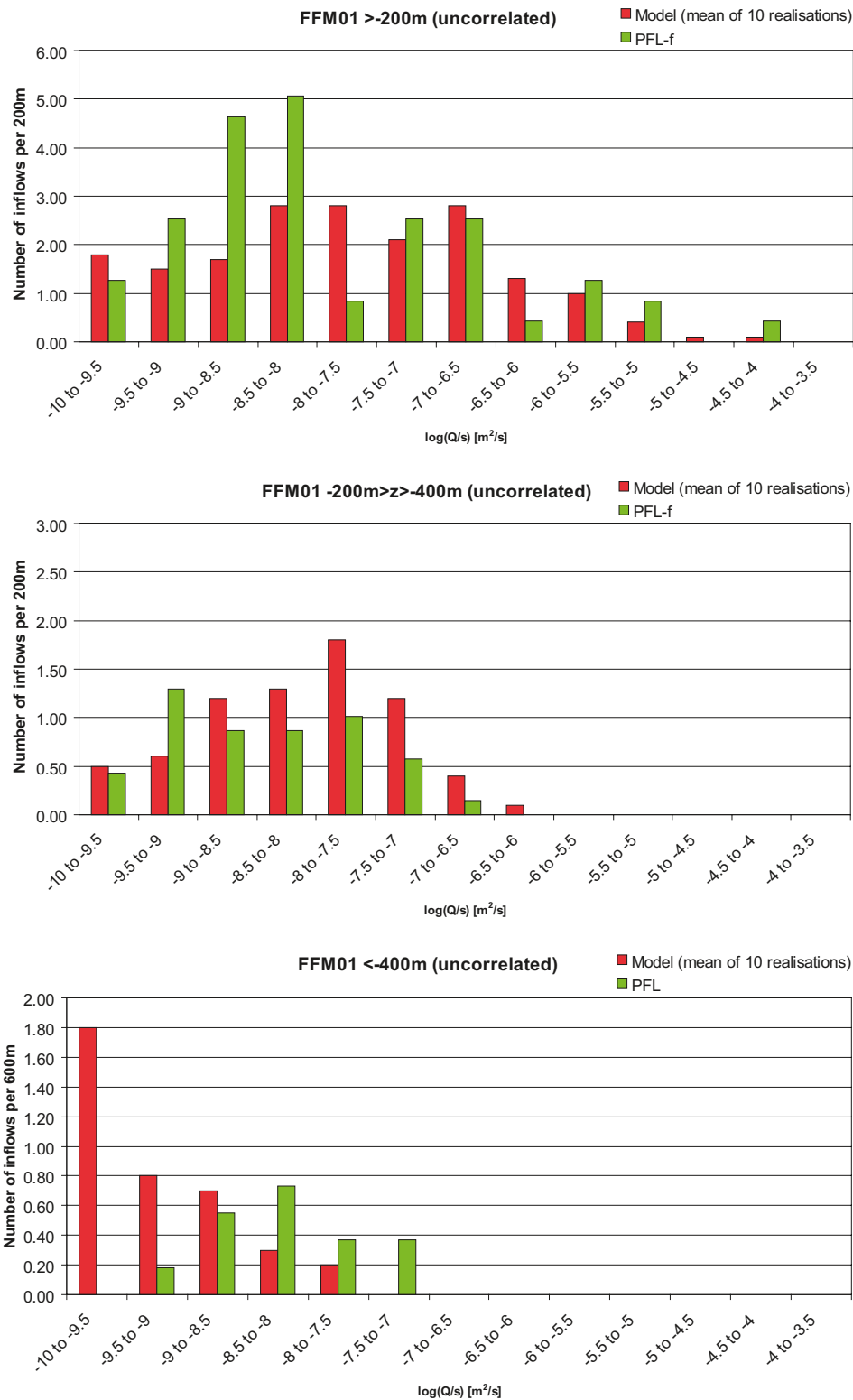


Figure B-11. Histogram comparing the distribution of the magnitude of inflows divided by drawdown, Q/s , at abstraction boreholes in FFM01 with an uncorrelated transmissivity (see Table 11-20 for parameter values). Top: above an elevation of -200 m; Middle: between -200 m and -400 m; Bottom: below -400 m. The PFL-f measurements are treated as ensemble over all boreholes sections within FFM01. Above -200 m and between -200 m and -400 m, the number of inflows is normalised with respect to a borehole section of 200 m length, and below -400 m relative to a 600 m section. The simulations are represented by statistics taken from an ensemble over 10 realisations of the Hydro-DFN model.

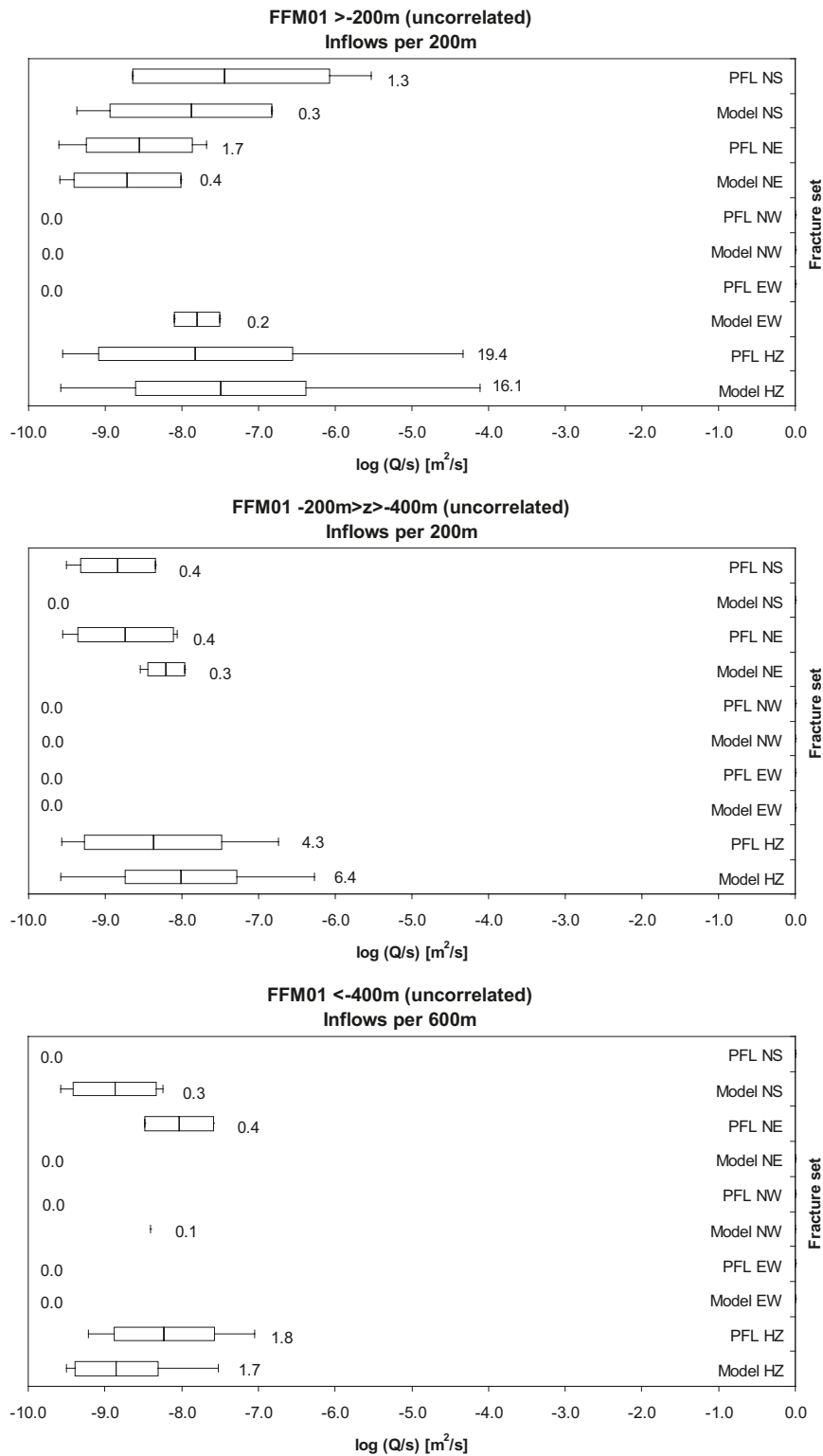


Figure B-12. Bar and whisker plots comparing statistics taken over each fracture set for the individual inflows, Q/s , for the PFL-f data from borehole sections within FFM01 against statistics taken from an ensemble over 10 realisations of the Hydro-DFN model with an uncorrelated transmissivity. Top: above an elevation of -200 m; Middle: between -200 m and -400 m; Bottom: below -400 m. The centre of the bar indicates the mean value, the ends of the bar indicate ± 1 standard deviation, and the error bars indicate the minimum and maximum values. Above -200 m and between -200 m and -400 m, the total numbers of fractures with inflows per 200 m section of borehole above the detection limits is given; below -400 m the numbers of inflows per 600 m section of borehole is given. For the data, statistics are taken over the identified flow-anomalies within each set, and for the model are taken over the fractures generated within each set and an ensemble over 10 realisations.

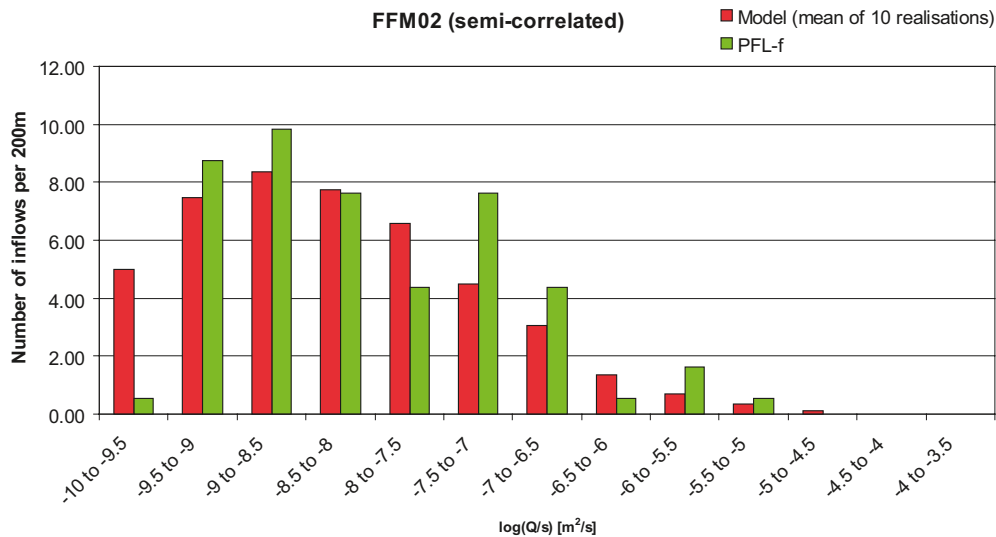


Figure B-13. Histogram comparing the distribution of the magnitude of inflows divided by drawdown, Q/s , at abstraction boreholes in FFM02 with a semi-correlated transmissivity (see Table 11-22 for parameter values). The PFL-f measurements are treated as ensemble over all boreholes sections within FFM02. The number of inflows is normalised with respect to a borehole section of 200 m length. The model is represented by statistics taken from an ensemble over 10 realisations of the Hydro-DFN.

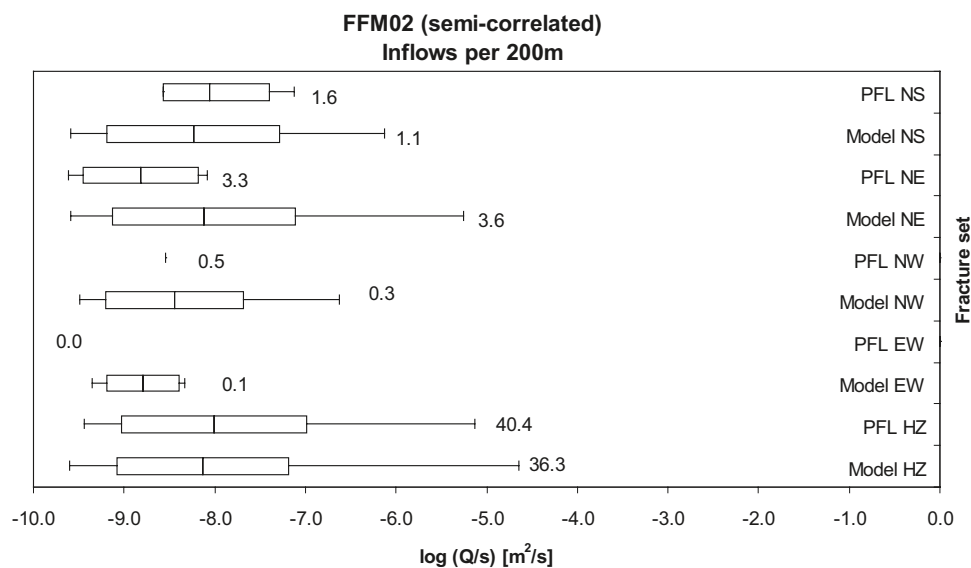


Figure B-14. Bar and whisker plots comparing statistics taken over each fracture set for the individual inflows, Q/s , for the PFL-f data from borehole sections within FFM02 against statistics taken from an ensemble over 10 realisations of the Hydro-DFN model with a semi-correlated transmissivity. The centre of the bar indicates the mean value, the ends of the bar indicate ± 1 standard deviation, and the error bars indicate the minimum and maximum values. The total numbers of fractures with inflows per 200 m section of borehole above the detection limits is given. For the data, statistics are taken over the identified flow-anomalies within each set, and for the model are taken over the fractures generated within each set and an ensemble over 10 realisations.

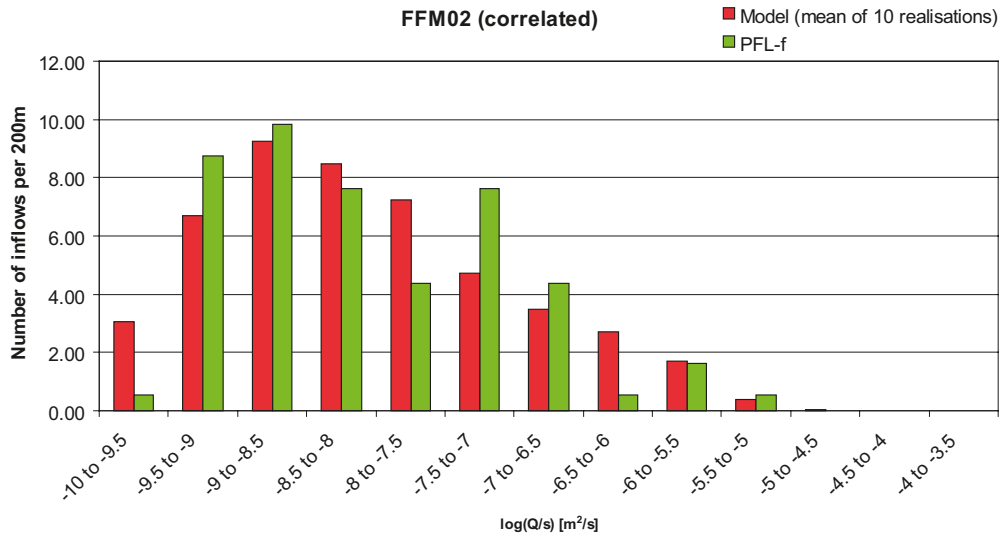


Figure B-15. Histogram comparing the distribution of the magnitude of inflows divided by drawdown, Q/s , at abstraction boreholes in FFM02 with a correlated transmissivity (see Table 11-22 for parameter values). The PFL-f measurements are treated as ensemble over all boreholes sections within FFM02. The number of inflows is normalised with respect to a borehole section of 200 m length. The model is represented by statistics taken from an ensemble over 10 realisations of the Hydro-DFN.

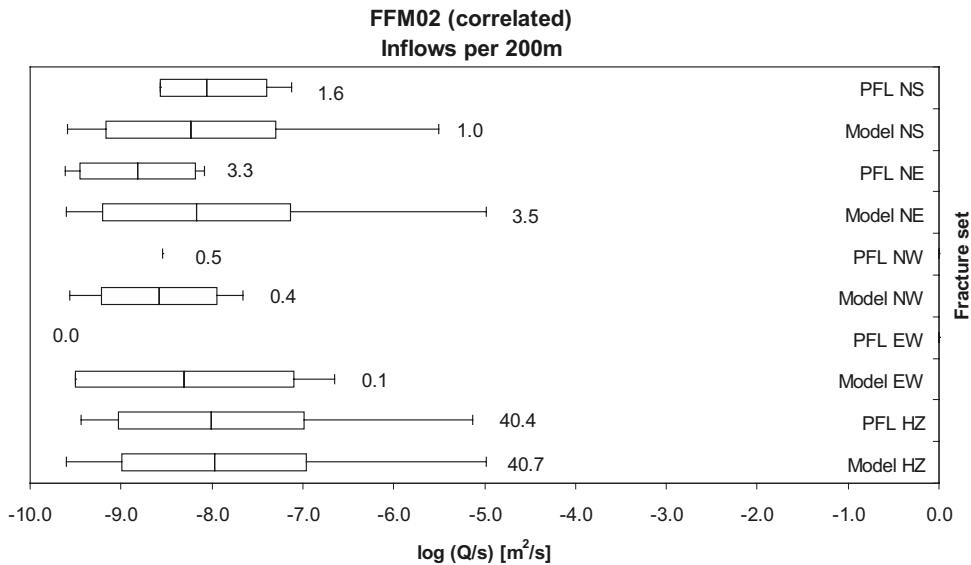


Figure B-16. Bar and whisker plots comparing statistics taken over each fracture set for the individual inflows, Q/s , for the PFL-f data from borehole sections within FFM02 against statistics taken from an ensemble over 10 realisations of the Hydro-DFN model with a correlated transmissivity. The centre of the bar indicates the mean value, the ends of the bar indicate ± 1 standard deviation, and the error bars indicate the minimum and maximum values. The total numbers of fractures with inflows per 200 m section of borehole above the detection limits is given. For the data, statistics are taken over the identified flow-anomalies within each set, and for the model are taken over the fractures generated within each set and an ensemble over 10 realisations.

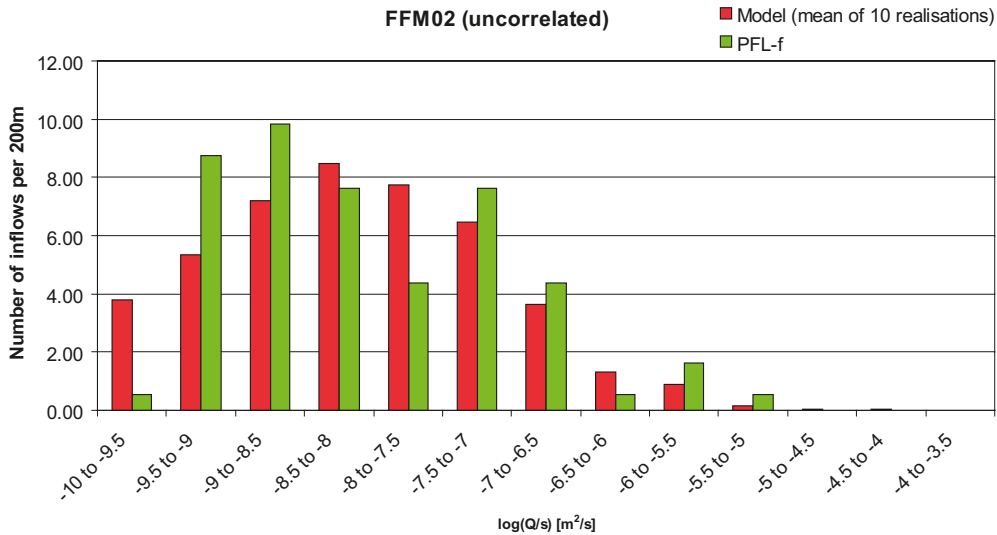


Figure B-17. Histogram comparing the distribution of the magnitude of inflows divided by drawdown, Q/s , at abstraction boreholes in FFM02 with an uncorrelated transmissivity (see Table 11-22 for parameter values). The PFL-f measurements are treated as ensemble over all boreholes sections within FFM02. The number of inflows is normalised with respect to a borehole section of 200 m length. The model is represented by statistics taken from an ensemble over 10 realisations of the Hydro-DFN.

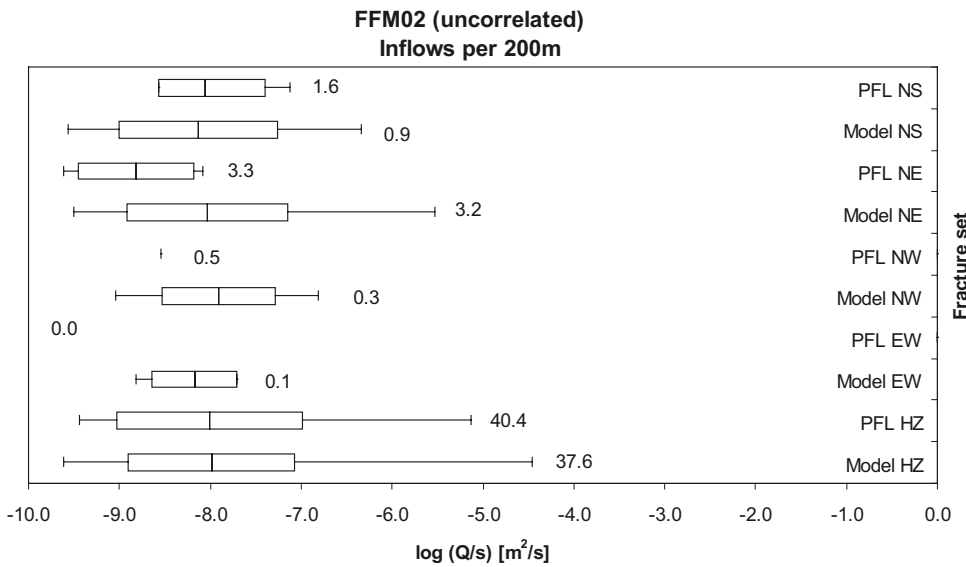


Figure B-18. Bar and whisker plots comparing statistics taken over each fracture set for the individual inflows, Q/s , for the PFL-f data from borehole sections within FFM02 against statistics taken from an ensemble over 10 realisations of the Hydro-DFN model with an uncorrelated transmissivity. The centre of the bar indicates the mean value, the ends of the bar indicate ± 1 standard deviation, and the error bars indicate the minimum and maximum values. The total numbers of fractures with inflows per 200 m section of borehole above the detection limits is given. For the data, statistics are taken over the identified flow-anomalies within each set, and for the model are taken over the fractures generated within each set and an ensemble over 10 realisations.

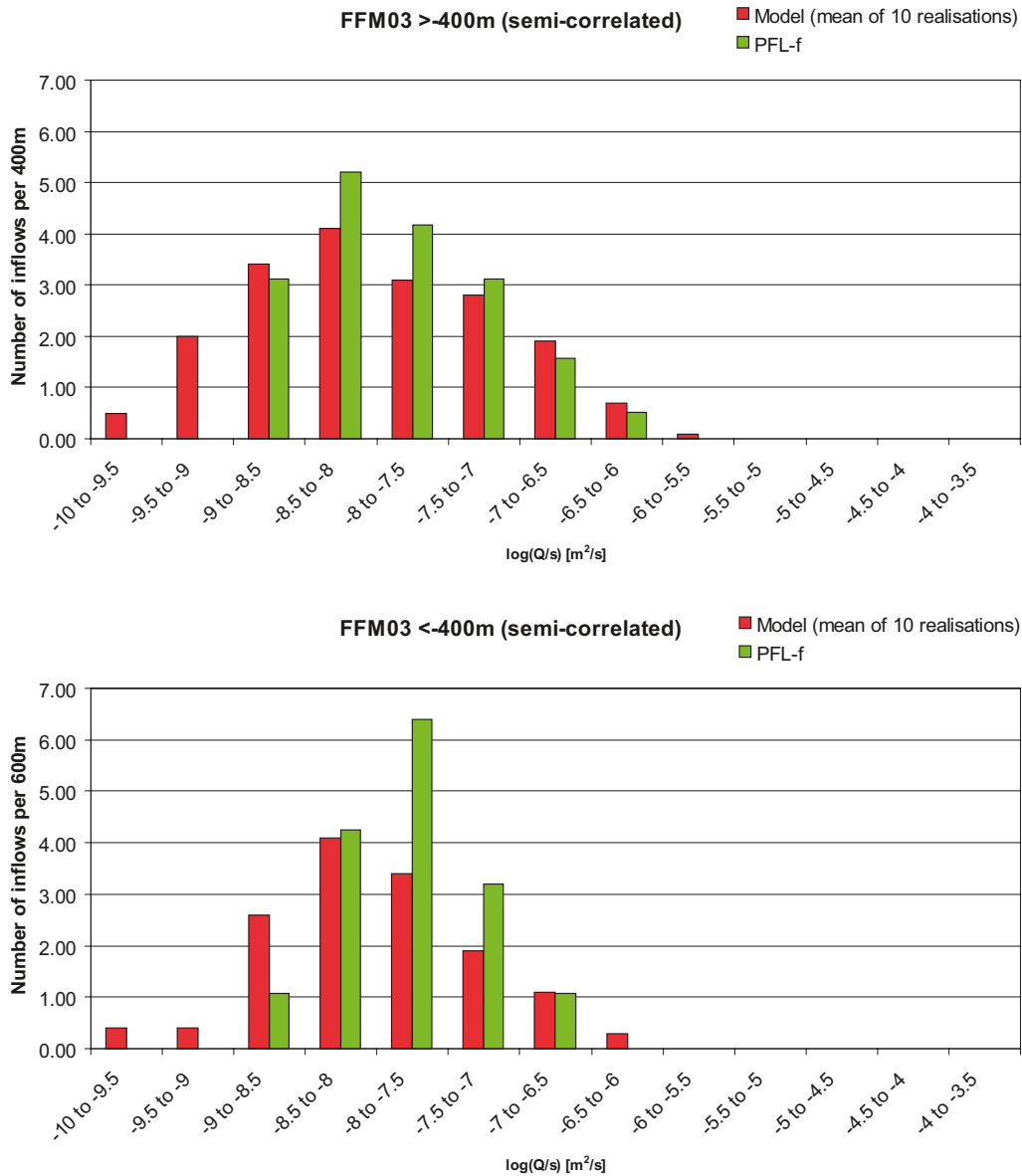


Figure B-19. Histogram comparing the distribution of the magnitude of inflows divided by drawdown, Q/s , at abstraction boreholes in FFM03 with a semi-correlated transmissivity (see Table 11-25 for parameter values). Top: above an elevation of -400 m; Bottom: below an elevation of -400 m. The PFL-f measurements are treated as ensemble over all boreholes sections within FFM01. Above -400 m the number of inflows is normalised with respect to a borehole section of 400 m length, and below relative to a 600 m section. The simulations are represented by statistics taken from an ensemble over 10 realisations of the Hydro-DFN model.

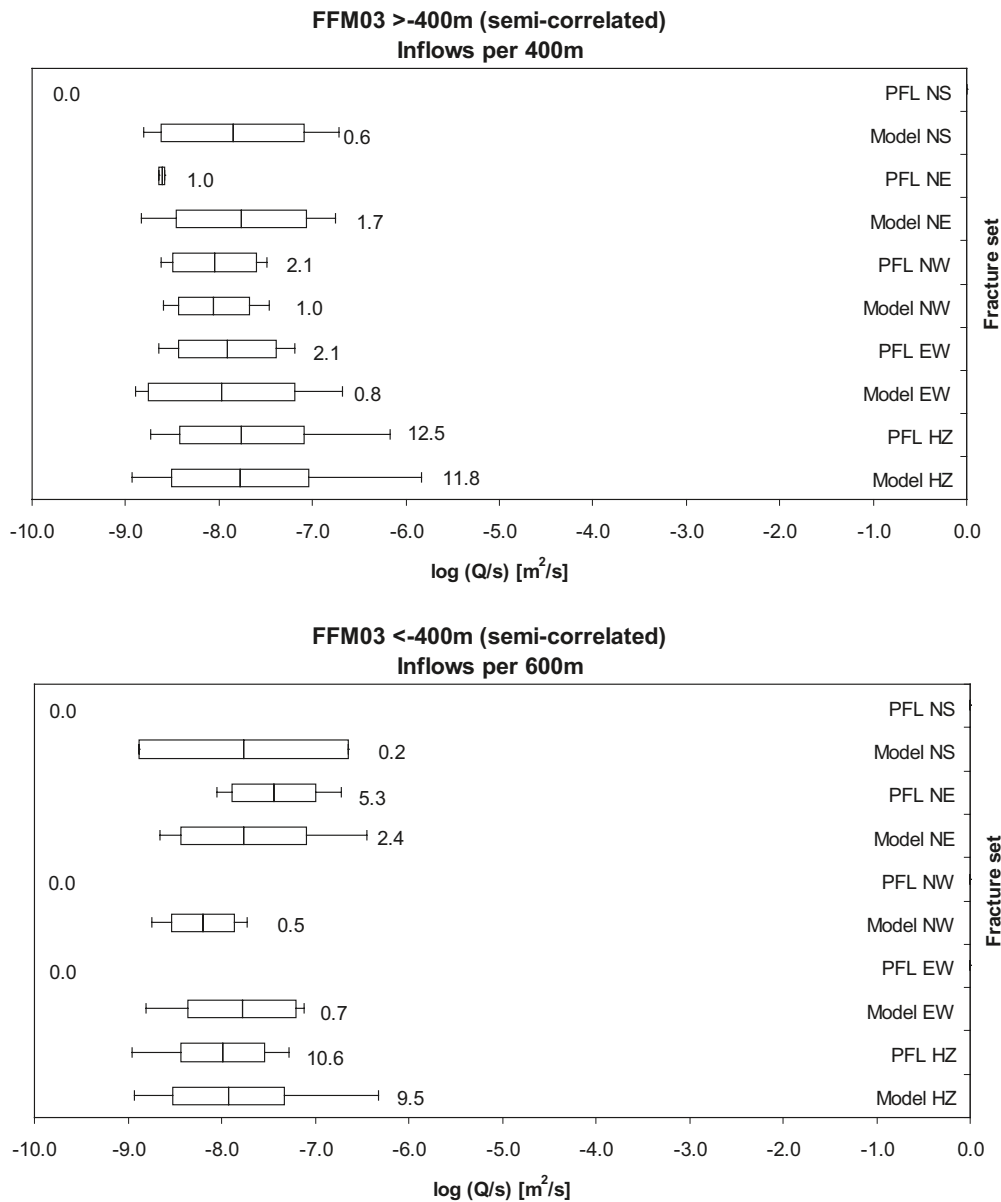


Figure B-20. Bar and whisker plots comparing statistics taken over each fracture set for the individual inflows, Q/s , for the PFL-f data from borehole sections within FFM03 against statistics taken from an ensemble over 10 realisations of the Hydro-DFN model with a semi-correlated transmissivity. Top: above an elevation of -400 m; Bottom: below an elevation of -400 m. The centre of the bar indicates the mean value, the ends of the bar indicate ± 1 standard deviation, and the error bars indicate the minimum and maximum values. Above -400 m the total numbers of fractures with inflows per 400 m section of borehole above the detection limits is given; below -400 m the numbers of inflows per 600 m section of borehole is given. For the data, statistics are taken over the identified flow-anomalies within each set, and for the model are taken over the fractures generated within each set and an ensemble over 10 realisations.

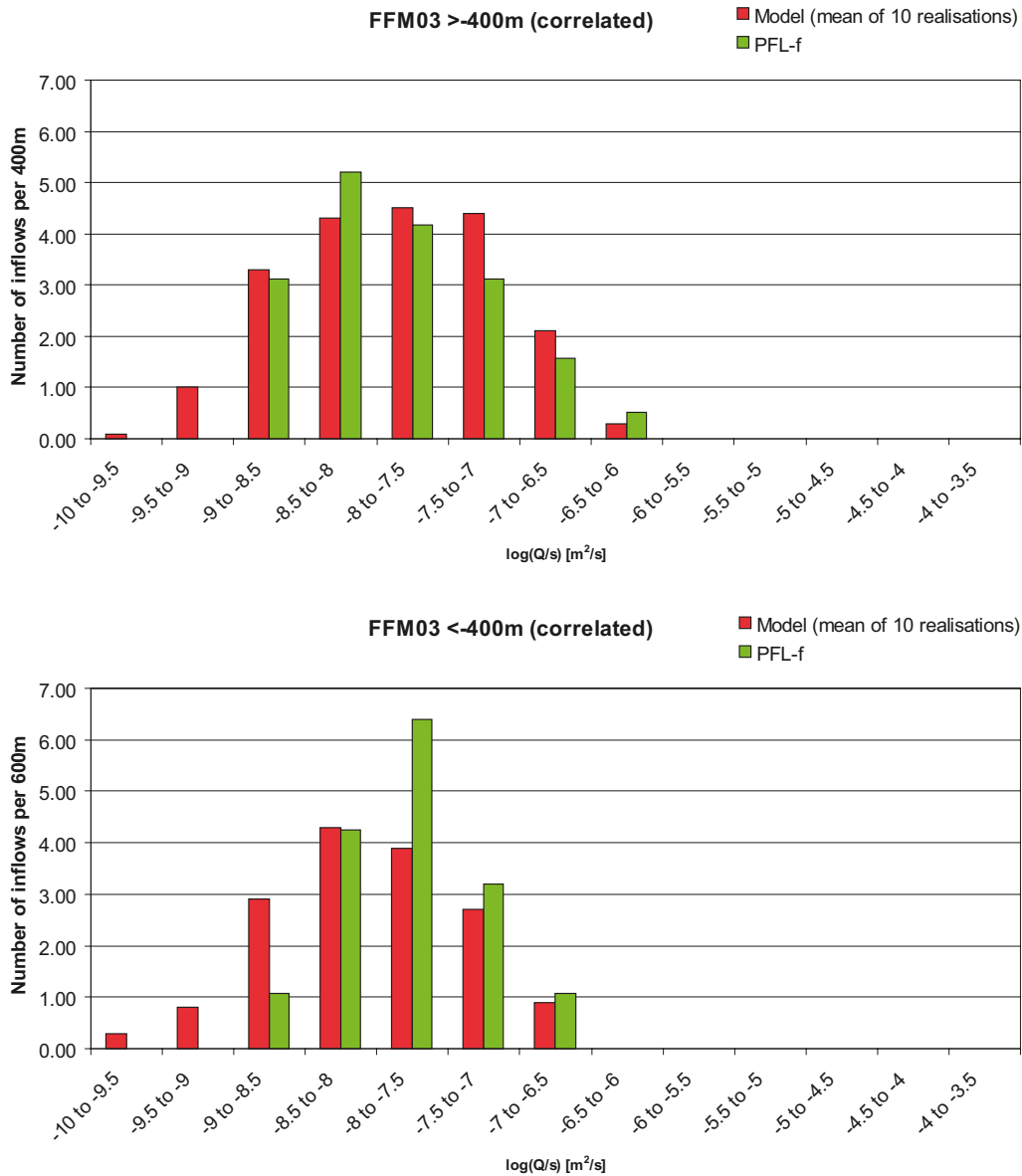


Figure B-21. Histogram comparing the distribution of the magnitude of inflows divided by drawdown, Q/s , at abstraction boreholes in FFM03 with a correlated transmissivity (see Table 11-25 for parameter values). Top: above an elevation of -400 m; Bottom: below an elevation of -400 m. The PFL-f measurements are treated as ensemble over all boreholes sections within FFM01. Above -400 m the number of inflows is normalised with respect to a borehole section of 400 m length, and below relative to a 600 m section. The simulations are represented by statistics taken from an ensemble over 10 realisations of the Hydro-DFN model.

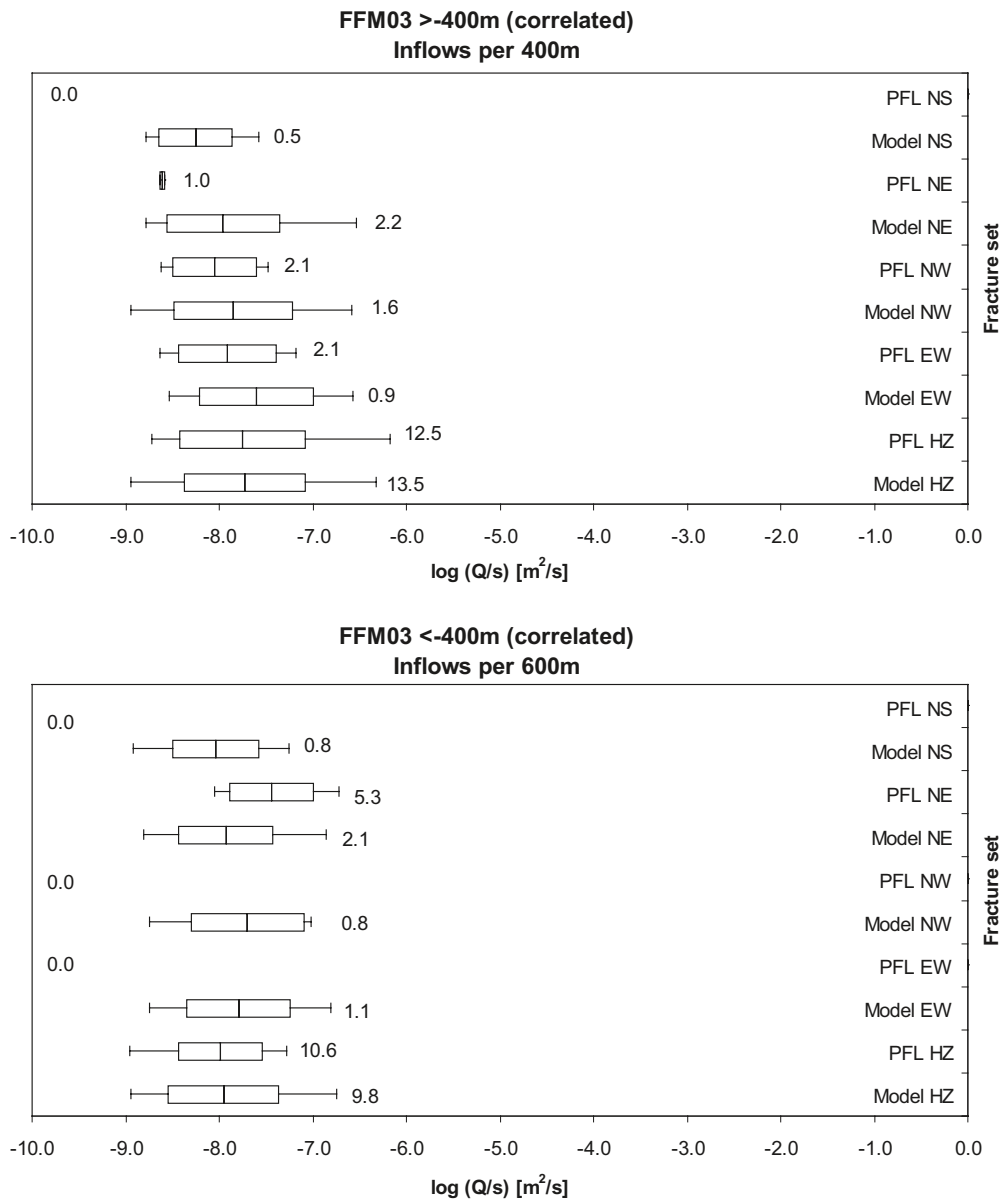


Figure B-22. Bar and whisker plots comparing statistics taken over each fracture set for the individual inflows, Q/s , for the PFL-f data from borehole sections within FFM03 against statistics taken from an ensemble over 10 realisations of the Hydro-DFN model with a correlated transmissivity. Top: above an elevation of -400 m; Bottom: below an elevation of -400 m. The centre of the bar indicates the mean value, the ends of the bar indicate ± 1 standard deviation, and the error bars indicate the minimum and maximum values. Above -400 m the total numbers of fractures with inflows per 400 m section of borehole above the detection limits is given; below -400 m the numbers of inflows per 600 m section of borehole is given. For the data, statistics are taken over the identified flow-anomalies within each set, and for the model are taken over the fractures generated within each set and an ensemble over 10 realisations.

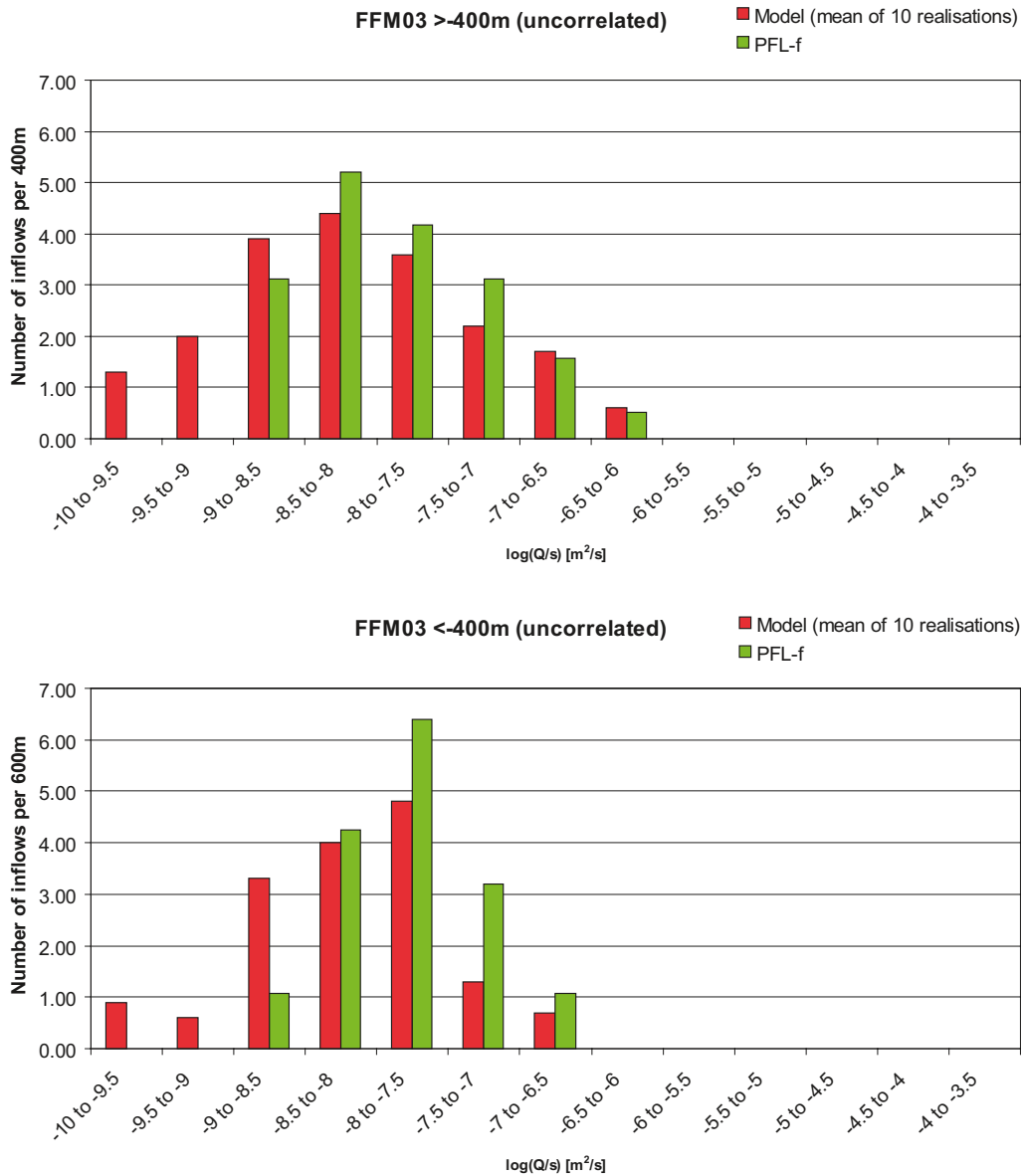


Figure B-23. Histogram comparing the distribution of the magnitude of inflows divided by drawdown, Q/s , at abstraction boreholes in FFM03 with an uncorrelated transmissivity (see Table 11-25 for parameter values). Top: above an elevation of -400 m; Bottom: below an elevation of -400 m. The PFL-f measurements are treated as ensemble over all boreholes sections within FFM01. Above -400 m the number of inflows is normalised with respect to a borehole section of 400 m length, and below relative to a 600 m section. The simulations are represented by statistics taken from an ensemble over 10 realisations of the Hydro-DFN model.

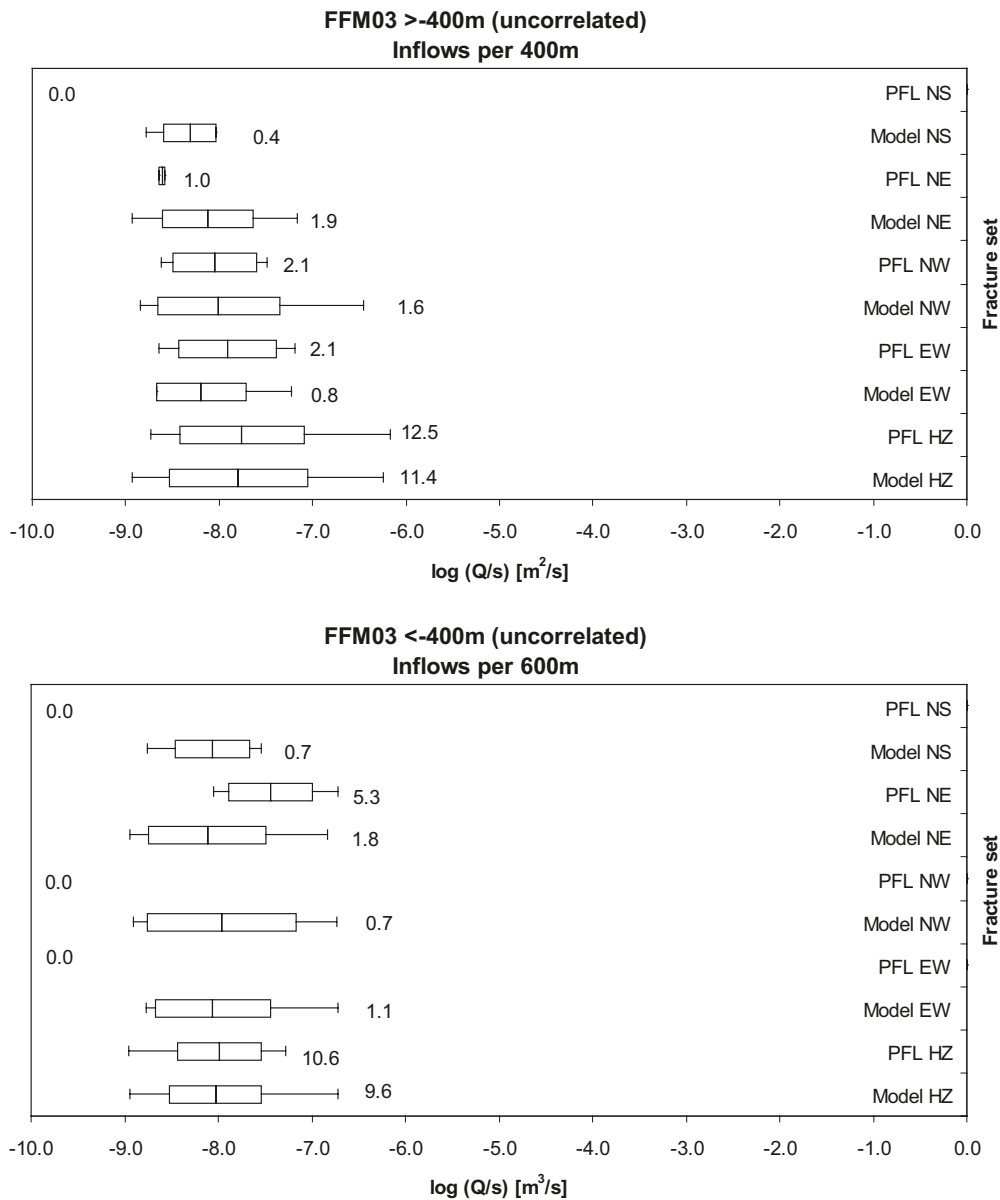


Figure B-24. Bar and whisker plots comparing statistics taken over each fracture set for the individual inflows, Q/s , for the PFL-f data from borehole sections within FFM03 against statistics taken from an ensemble over 10 realisations of the Hydro-DFN model with an uncorrelated transmissivity. Top: above an elevation of -400 m; Bottom: below an elevation of -400 m. The centre of the bar indicates the mean value, the ends of the bar indicate ± 1 standard deviation, and the error bars indicate the minimum and maximum values. Above -400 m the total numbers of fractures with inflows per 400 m section of borehole above the detection limits is given; below -400 m the numbers of inflows per 600 m section of borehole is given. For the data, statistics are taken over the identified flow-anomalies within each set, and for the model are taken over the fractures generated within each set and an ensemble over 10 realisations.